ECN

iea wind

Final report of IEA Wind Task 29 Mexnext (Phase 3)

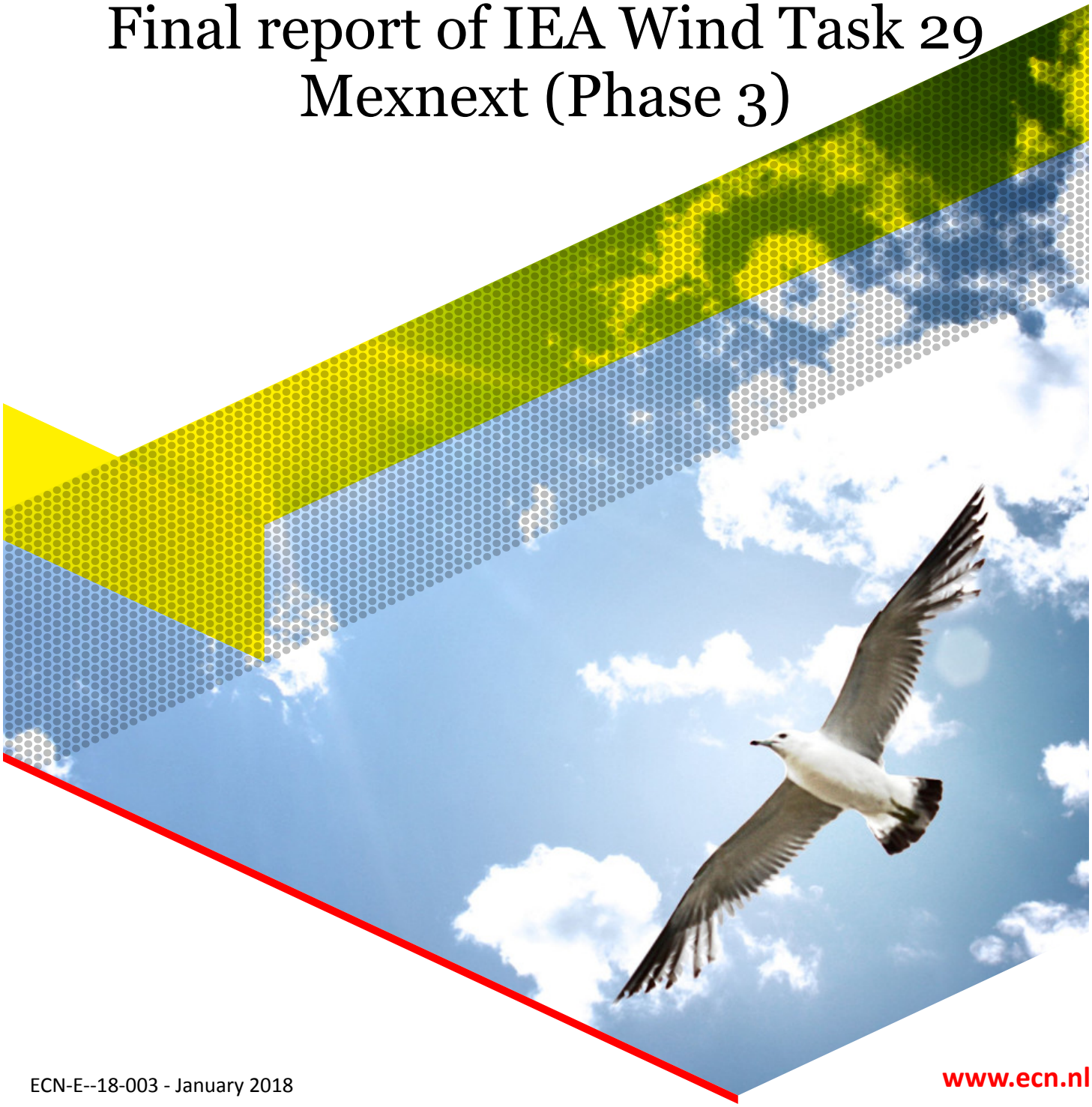

ECN-E--18-003 - January 2018

www.ecn.nl

Final report of IEA Wind Task 29 Mexnext (Phase 3)

revised

Author(s)

K. Boorsma, J.G. Schepers (ECN)
S. Gomez-Iradi (CENER)
I. Herraez (UAS Emden)
T. Lutz, P. Weihing (University of Stuttgart)
L. Oggiano (IFE)
G. Pirrung, H.A. Madsen, W.Z. Shen (DTU)
H. Rahimi (ForWind)
P. Schaffarczyk (Fachhochschule Kiel)

Acknowledgement

The authors would like to thank IEA TCP Wind for facilitating the Mexnext project in their framework.

The contributions of the participants to Mexnext have been funded in various national programmes:

- The participation from the Dutch partners in IEA TCP Wind Task 29 has been funded through the Dutch Ministry of Economic affairs.
- The participation from University of Uppsala was funded by the Swedish Energy Agency, SNIC (The Swedish National Infrastructure for Computing) and StandUp for Wind.
- The participation by DTU Wind Energy was funded by the Danish Ministry of Energy through the funding agency EUDP. Contract EUDP-II, J.nr. 64014-0543.
- The participation of CENER was funded thanks to two projects: ADITECH 2016 - OFEN (tool for calculating the transition from laminar to turbulent flow in aerodynamic profiles) and ADITECH 2017 - CENERVGs-Design of vortex generators. ADITECH, Advanced Innovation and Technology Corporation, being a private entity that brings together Navarre technology centres.

Several activities were aligned with the EU project AVATAR which received funding from the European Union's Seventh programme for research, technological development and demonstration under Grant Agreement NO FP7-ENERGY-2013-1/no 608396. The data sharing was made possible by the Dutch national e-infrastructure with the support of SURF Foundation.

Executive Summary

This report describes the results from the third phase of IEA TCP Wind Task 29 Mexnext, denoted as Mexnext-III, in which 22 parties from 10 countries participated. The main impact of the Mexnext-III project lies in the insights offered in the accuracy of design models by which it is possible to assess design calculations in a more thorough way. Moreover improved design models and recommendations on model use are provided which will reduce uncertainties in design calculations. Based on the project results it can be stated that current state of the art design models provide accurate aerodynamic load predictions for design conditions in constant axial and uniform inflow, while more scatter is observed in modeling the turbulent wake state, separated flow, 3d effects and tip effects. A prerequisite for accurate results is a careful consideration of input parameters and output post-processing. This especially holds for CFD simulations, of which the results are highly dependent on the large number of input- and output related choices. Guidelines to reduce the associated uncertainties have been given. Improvements have been made to engineering models describing amongst others yawed and dynamic inflow effects. However, it is shown that still large uncertainties exist in oblique, dynamic and/or non-uniform inflow conditions. Following this result it is recommended to further improve unsteady aerodynamic modeling in the fourth phase of IEA TCP Wind Task 29.

Dedicated aerodynamic measurements, mainly from the New MEXICO experiment have been used to validate, improve and understand aerodynamic models. In the New MEXICO experiment pressure and flow field measurements were taken on a 4.5 meter diameter rotor in the large German Dutch Wind Tunnel, DNW. The New MEXICO experiment is a follow-up of the MEXICO experiment which was the subject of analysis in the first phase Mexnext-I. In Mexnext-I significant and unexpected discrepancies were found between simulations and measurements in terms of blade loads and induced velocities. Resolving the reason for these discrepancies and reducing them has been accomplished in Mexnext-III. Thereto, the entire New MEXICO database has been documented and delivered to the Mexnext-III consortium. With this database a large comparison exercise has been performed, featuring six simulation cases in axial and yawed inflow conditions, containing results of over 20 codes ranging from BEM to CFD. More than 10 different variable types ranging from lifting line variables to pressures, loads and velocities have been compared for the different conditions, resulting in over 250 comparison plots. Apart from benchmarking much effort was spent on understanding the the flow physics of various phenomena. The result is a unique insight in the current status and accuracy of rotor aerodynamic modeling. More specifically it can be concluded that most questions from Mexnext-I have been answered and so a much better understanding of the aerodynamics of the MEXICO rotor in terms of blade aerodynamics as well as near wake aerodynamics has been gained. This is illustrated by the better agreement between calculations and measurements compared to the agreement in Mexnext-I. This is true for pragmatic engineering models but also for high fidelity models. Opposite to the situation after the first MEXICO campaign, the relation between loads and velocities now fulfills the momentum balance, not only in axial direction but even in the tangential direction.

Table of contents

1. Introduction

This report describes the results of Mexnext-III, i.e. the third phase of the project Mexnext. This third phase, like the first and second phase (denoted as Mexnext-I and Mexnext-II) is carried out as an IEA TCP Wind Task. The number which is assigned to Mexnext is 29, by which the project is identified as IEA TCP Wind Task 29. Such IEA TCP Wind Tasks are collaborative international projects organized under the auspices of the International Energy Agency (IEA) Technology Collaboration Programme (TCP) Wind Energy Systems.

In Mexnext-III the following countries and parties participated (between brackets the main contact persons are listed:

- China: Chinese Wind Energy Association, CWEA (H. Dexin), Sinoma and China Aerodynamics Research and Development Center, CARDC (L. Zuowu)
- Denmark: Technical University of Denmark, DTU (H. Madsen, N. Sørensen, G. Pirrung and W. Z. Shen)
- Germany: ForWind (I. Herraez, H. Rahimi, B. Dose), Fraunhofer IWES (B. Stoevesandt, H. Rahimi and B. Dose), Kiel University of Applied Sciences (P. Schaffarczyk), University of Stuttgart (T. Lutz, P. Weihing), WindNovation (D. Schulze), Enercon (A. Altmikus), Deutsches Zentrum für Luft- und Raumfahrt e.V., DLR (T. Schwarz and M. Imiela), University of Applied Sciences Emden (I. Herraez)
- Israel: Israel Institute of Technology, Technion (A. Rosen)
- Japan: Mie University/National Institute of Advanced Industrial Science. AIST (T. Maeda, Y. Kamada, J. Murata) (only in the first year of Mexnext-III)
- Netherlands: Energy Research Centre of the Netherlands, ECN (G. Schepers, K. Boorsma), Delft University of Technology, TUDelft (G. van Bussel, Y. Zhang), DNV-GL (M. Kloosterman), Suzlon Blade Technology, SBT (L. Broersma, D. Veldkamp) and University of Twente, UTwente (A. van Garrel)
- Norway: Institute for Energy Technology, IFE/Norwegian University of Science and Technology NTNU (L. Oggiano)
- Spain: National Renewable Energy Centre, CENER (S. Gomez-Iradi, X. Munduate, A. Gonzalez, M. Aparicio, R. Martin and A. Carrera) (Only in second and third year of Mexnext-III)
- Sweden: Uppsala University Campus Gotland, HGO (S. Breton and S. Ivanell)
- USA: National Renewable Energy Laboratory, NREL (S. Schreck, R. Damiani and J. Jonkman)

The focus of Mexnext-III was on validating, improving and understanding aerodynamic calculational models by means of dedicated aerodynamic measurements, mainly (but not only) in the wind tunnel. As such the character of the third phase was very similar to the character of the first and second phase Mexnext-I and Mexnext-II, see [68] and [69]. However, the focus of Mexnext-III was on the measurements which have been taken in the New MEXICO experiment, i.e. measurements taken in 2014 on a 4.5 meter wind turbine model in the large low speed facility LLF of the German Dutch Wind Tunnel DNW. Opposite to Mexnext-I a wide variety of measurements is considered in Mexnext-III, where Mexnext-I mainly considered the measurements from

the EU project MEXICO as taken in 2006 on a 4.5 meter wind turbine model in the large low speed facility LLF of the German Dutch Wind Tunnel DNW. Moreover, in the course of the Mexnext-III funding was found for an additional experiment on the MEXICO wind tunnel model by which the preparation and the performance of this 'New MEXICO' experiment also entered Mexnext-III.

Before discussing the results of the project in some detail, this report first describes the background of the project in section 1.1. In order to understand the relevance of the the project results it is essential to understand the importance of Mexnext's playing field (wind turbine aerodynamic modelling and measurements). This is explained in section 1.2 which then culminates in the goal of the project, see section 1.3.

Then the working procedure and the work plan of Mexnext is described in chapter 2 after which the database presentation and uncertainties of the New MEXICO experiment are described in chapter 3. The results of the comparison round between experiment and simulations are described in chapter 4. The project is carried out in different research tasks, the results of these tasks are reported in chapter 5 to 13. Conclusions and recommendations are given in chapter 14.

1.1 History and background of Mexnext-III

In the past the accuracy of wind turbine design models has often been assessed in validation projects using measurements of global wind turbine quantities (power, blade root bending moments etc.), see e.g. [71]. These projects showed that the modeling of a wind turbine response (i.e. the power or the loads) is subject to large uncertainties. As explained in section 1.2 these uncertainties mainly find their origin in the aerodynamic modeling. Several phenomena, like 3D geometric and rotational effects, instationary effects, yaw effects, stall, tower effects etc., contribute to unknown responses in particular at off-design conditions. These unknown responses make it very difficult to design cost-effective and reliable wind turbines. Turbines behave unexpectedly, experiencing instabilities, power overshoots, or higher loads than expected. Alternatively, the loads may be lower than expected which implies an over dimensioned (and costly) design. The availability of high quality measurements is considered to be the most important pre-requisite to gain insight into these uncertainties and to validate and improve aerodynamic wind turbine models. However, it should be realised that conventional experimental programs on wind turbines generally do not provide sufficient information for the validation and improvement of aerodynamic models, since they only measure the integrated, total (blade or rotor) loads. These loads consist of an aerodynamic and a mass induced component and they are integrated over a certain spanwise length. In the late 80s and the 90s it was realized that more direct aerodynamic information was needed in order to improve the aerodynamic modelling. For this reason several institutes initiated experimental programs in which pressure distribution and the resulting normal and tangential forces at different radial positions were measured. Under the auspices of the IEA TCP Wind, many of these measurements were stored into a database in Task XIV and XVIII, see [70]. The results of these measurements turned out to be very useful and important new insights on e.g. 3D stall effects, tip effects and yaw were formed which have been translated into models which are included in all nowadays state of the art wind turbine design models.

However, the IEA TCP Wind Tasks XIV and XVIII also identified some downsides of these measurements, the most important one was due to the fact that the measurements were taken on turbines in the free atmosphere, where the uncertainty due to the unsteady, inhomogeneous and uncontrolled wind conditions formed an important problem (as it is in all field measurements). This problem was overcome in NREL's NASA-Ames wind tunnel experiment which was carried out in 2000 [52]. In this experiment a heavily instrumented rotor with a diameter of 10 meter was placed in the world's largest wind tunnel, i.e. the NASA-Ames (24.4×36.6 m^2 cross section) wind tunnel. As such, measurements were performed at stationary and homogeneous conditions. The huge size of the wind tunnel allowed for a rotor diameter of 10 m, with little blockage effects. Obviously this rotor diameter is still (much) smaller than the diameter of the nowadays commercial wind turbines, but nevertheless the blade Reynolds number (in the order of 1 Million) is sufficiently high to make the aerodynamic phenomena at least to some extend representative for modern wind turbines. NREL made the measurements from this experiment available to other institutes and they were analysed within IEA TCP Wind Task XX. This Task was finished in December 2007 see [123].

Mexnext can be considered as the successor of IEA TCP Wind Task XX. The first phase focussed on the wind tunnel measurements which became available in December 2006 within the EU project MEXICO [67]. In this project detailed aerodynamic measurements were carried out on a wind turbine model with a diameter of 4.5 m, which was placed in the largest European wind tunnel, the German Dutch Wind Tunnel, DNW with a nozzle

cross section of 9.5 x 9.5 m^2. The most unique feature of the MEXICO measurements is the fact that the flow field around the rotor plane was measured simultaneously with the blade properties. The MEXICO project was finished at the end of 2006 very shortly after the measurements were taken. As such a large database was created but analysis of the data could not be carried out within the MEXICO project and had to wait until Mexnext-I was started. This happened on June 1, 2008 where Mexnext-I ended on June 1, 2011. The final findings of Mexnext-I are reported in [68]. At the end of Mexnext-I most of the originally scheduled tasks were finished and many questions have been answered. Still several new questions came up which led to the recommendation to carry out a follow-up phase (second). Thereto it must be noted that the MEXICO experiment was the first experiment in which detailed aerodynamic blade pressures are measured together with an extensive and detailed flow field mapping. This enabled the experimental determination of the relation between loads and velocities but this relation was found to be very puzzling. The results became even more confusing to a non-understood apparent vortex shedding at the inner part of the mapped flow field. Moreover, and possibly connected to these puzzling effects was the observation that differences between calculated and MEXICO measured blade loads are larger than found in other validations. In order to shed light on these non-understood phenomena it was recommended to investigate a number of (sometimes almost forgotten) aerodynamic experiments which are not fully explored yet. Such measurements could potentially deliver new insights and they were hoped to offer explanations for the non understood phenomena from the MEXICO measurements.

Therefore it was very much appreciated that the EU Aerospace program ESWIRP approved a 'New MEXICO' project in which two weeks of (expensive) DNW-LLF tunnel time were granted to the Mexnext-II project group in order to perform more measurements on the MEXICO tunnel model. The preparations as well as the performance of the New MEXICO experiment was then included in Mexnext-II which ran from January 1st 2012 until December 31st 2014.

One of the preparations consisted of measurements on the non-rotating MEXICO blades placed in the LST wind tunnel of TU Delft. After these preparatory tests the rotating New MEXICO measurements were carried out in the LLF of DNW in June/July 2014. In [69] it is explained that these experiments were very successful. The New MEXICO experiment improved the quality of the database because lessons learned from the MEXICO experiment could be taken into account and the database could be complemented with additional data. Most important is that the New MEXICO experiment led to a consistent relation between loads and velocities see [111].

Hence the New MEXICO experiment was very successful and provided a huge amount of data which was still largely unexplored. This made the situation very comparable to the situation in 2006 just after the MEXICO experiment: Like the MEXICO database in 2006, the New MEXICO database was still in a rather rudimentary form and only limited analyses have been carried out. However the amount of data was very vast which made the time needed to analyse all data extremely long for a single country (in this respect it should be noted that the New MEXICO base contains even more measurements than the MEXICO base: 1366 data points versus 950). Hence, like the situation after the MEXICO experiment, it was considered very beneficial to organise the analysis of the New MEXICO data under IEA TCP Wind, since this makes it possible to share tasks. Added value also lies in the fact that the task will serve as a forum for discussion and interpretation of the results. It is then possible to generate more value from the data than the summed value from the individual projects.

As a result Mexnext-III was proposed which started on January 1st 2015 and ended on December 31st 2017.

It is noted that Mexnext-III also considers the analysis of several interesting 'other than MEXICO' data. Part of Mexnext-III was also the organization of some annual progress meetings together with IEA TCP Wind Task 11 in the form of informal 'aerodynamic brainstorming meetings'.

1.2 Relevance of aerodynamic research

In order to acknowledge the relevance of wind turbine aerodynamics (research) and Mexnext in particular, the following should be understood:

- First it should be realized that the main aim of a wind turbine is to convert kinetic energy from the wind into mechanical energy of a wind turbine. This transformation of energy is an aerodynamic process. Therefore it is fair to consider a wind turbine as an aerodynamic machine. Moreover, it should be realised that aerodynamics drives the noise production of a wind turbine (where wind turbine noise is considered to be

a main hindrance for social acceptance) and the aerodynamics of a wind turbine determines the wake flow behind it and as such the very important wind farm losses.

- Aerodynamic models form the backbone of every wind turbine design code (roughly speaking it can be said that 80% of the computational effort for a design calculations is devoted to the aerodynamics part).

- Aerodynamic problems are very complex due to the fact that every aerodynamic process is described by means of the so-called Navier Stokes equations which cannot be solved in an analytical way. The extreme complexity of modelling aerodynamic problems is illustrated by the fact that solving the Navier Stokes equation (as a matter of fact 'only' proving that a smooth solution exists) is one of the seven Millenium Prize Problems as formulated by the Clay Mathematics institute in 2000.

  A numerical solution of the Navier Stokes equations is also out of reach due to the extreme demands on computational resources. This remains true even on the most modern computer clusters. [131] shows that for wind energy applications the computational effort is even more extreme than it is for most other applications (e.g. aerospace).

- The fact that aerodynamic problems cannot be solved in an exact nor numerical way requires that every wind turbine aerodynamic model suffers from many simplifications. These simplifications inevitably lead to an uncertainty band in design calculations. This uncertainty band is known to be very large for wind turbine aerodynamic models, see e.g. [71] and [146].

- The model uncertainties make it very difficult to design cost-effective and reliable wind turbines. Turbines behave unexpectedly, experiencing instabilities, or higher loads than expected leading to the risk of failure which can only be overcome with high (costly) safety margins. Alternatively, the loads may be lower than expected, which implies an over dimensioned (and costly) design.

The complexities inherent to aerodynamics, together with the fact that aerodynamic models do not provide the exact solution make that fundamental physical phenomena crucial to wind turbine operation remain hidden. The availability of high quality measurements is the only way to unravel these hidden phenomena and to gain insight into model uncertainties and to validate and improve aerodynamic wind turbine models. It is this important area of high quality aerodynamic measurements which forms the playing field of IEA TCP Wind Task 29 Mexnext.

1.3 Goal

The main objective of the third phase of IEA Wind Task Mexnext is to validate, improve and develop aerodynamic models for wind turbines. The importance of these activities is explained in [68] which describes the impact of aerodynamics for the successful implementation of wind energy.

More specifically models will be considered for boundary layer transition, yawed flow, unsteady aerodynamics, 3D effects (on both lift and drag), tip effects, non-uniformity of flow between the blades, near wake aerodynamics, turbulent wake, standstill, aerodynamic devices (Guerney flaps and root spoilers) and pitch misalignments. Acoustic models will be considered too. Different categories of models will be considered (CFD, free vortex wake methods, engineering methods etc.). Where possible standard engineering models will be recommended for inclusion in design tools

The model assessment will largely, but not exclusively, be based on the New Mexico measurements. The common denominator in all experiments is the fact that they should provide detailed aerodynamic data.

2. Workplan, deliverables and meetings

2.1 Workplan

The workplan of Mexnext-III has been approved at the 74th Executive Committee Meeting in October 2014 in Charlottetown, Canada. Mexnext-III started on January 1st 2015 and ended on December 31st 2017.

Mexnext-III was (apart from a management work package WP0) divided in 4 technical work packages (WP's):

- WP1: Inventory of experiments/historical research. In this Work Package the usefulness of various 'historical' experiments was established. Thereto the participants have critically reviewed all data and their documentation to check which data are suitable for use in the other WP's in particular WP3 (i.e. the validation of different codes, see below) or WP4, (the investigation of several aerodynamic phenomena, see below)

- WP2: Processing/presentation of data, uncertainties.
  In this Work Package the data have been processed and documented. The Work Package also included an assessment of the measurement quality. The measurements considered mainly come from the New MEXICO experiment.

- WP3: Comparison of calculated results from different types of codes with New MEXICO measurement data.
  In this WP, the calculated results from several codes were compared to the data which are selected in WP1. It formed a thorough validation of different codes from which insights were gained into phenomena which need further investigation (see WP4). The calculations were carried out in two rounds. Every round consisted of the following phases:

  – Definition of the calculational round;
  – Performance of calculations;
  – Processing of data and comparing with measurements;
  – Evaluation and interpretation of results

  Both rounds required several iterations in which the insights from the former iterations could be taken into account. These insights could be misunderstandings on sign conventions etc but also more fundamental insights, i.e. the need for additional output properties in order to understand the results better.

- WP4: Deeper investigation into phenomena.
  In this WP a deeper investigation of different phenomena took place. The phenomena were investigated with isolated submodels, simple analytical tools or by physical rules. The work package was subdivided in the following tasks (between brackets the leaders and the participants of each task are mentioned)

  – Task 4.1 Parked conditions and IEC Aerodynamics (DNV-GL with substantial input from IFE)
  – Task 4.2 Sensitivity of results and rotational speed (In consultation with the IEA ExCo this has been put on hold and no acitvities were carried in Mexnext-III)

- Task 4.3 Angle of attack (DTU, with substantial input from Forwind, USTUTT, DLR, UAS Emden and ECN)
- Task 4.4 Near wake aerodynamics (USTUTT with substantial input from IFPEN and DLR)
- Task 4.5 Non-uniformity of flow in the rotor plane (i.e. tip corrections) (ECN with substantial input from TUDelft)
- Task 4.6 3D effects (both on lift and drag) (Forwind with substantial input from UAS Emden)
- Task 4.7 Yawed conditions and instationary airfoil effects (NREL with substantial input from Forwind and ECN)
- Task 4.8 Dynamic Inflow (DTU with substantial input from IFPEN and ECN)
- Task 4.9 Boundary layer transition (UAS Kiel with substantial input from ECN and DTU)
- Task 4.10 Acoustics (DTU with substantial input from ECN)
- Task 4.11 Devices (ECN/TUDelft)

The Work Packages 2 to 4 are described in chapters 3, 4 and 5 to 13. The results from WP1 are described along the deliverable DIII.1 see section 2.2.

2.2 Deliverables and reports

This report summarizes the status of the deliverables as promised in the Description of Work, which was approved at the 74th Executive Committee meeting in Charlottetown Canada.

- WP1: DIII.1 (First results of useful measurements). An important result was formed by the delivery of FFA experimental data on a 5 meter diameter wind turbine model to the Mexnext database. These measurements were taken in the large Chinese CARDC tunnel in the end of the 1980 and the beginning of the 1990's by the Swedish Aerospace laboratory FFA. The project group found these measurements very interesting but a complete comprehensive overview of these data including a thorough description was lacking. This was partly caused by the fact that FFA does not exist anymore. However contacts with the former FFA researchers (in particular Goran Ronsten) could be re-established through the Swedish participation in the project after which the data were delivered in a structured way.

  Apart from the FFA measurements in the CARDC tunnel, data from the following experiments have been supplied, either in digital form or in reports:

  - Aerodynamic glove experiments, i.e. boundary layer experiments from UAS Kiel in field conditions
  - Measurements on the NREL Phase VI turbine placed in the NASA Ames wind tunnel
  - Measurements on a scaled down NREL Phase VI turbine placed in a wind tunnel from CARDC
  - Aerodynamic measurements on a 5 meter turbine placed on a towed mobile test facility taken by Cranfield university
  - Danaero field measurements taken by DTU
  - Measurements in the DNW KKK cryogenic tunnel taken by TUDelft and UAS Kiel
  - Helicopter experiments
  - Field measurements from IEA Task 14 and IEA Task 18 data, including measurements from DTU on a Tellus turbine with a diameter of 19 meter with different tips
  - Measurements on a scaled down Mexico rotor taken in the wind tunnel from INTA
  - Measurements on a scaled down Mexico and NREL Phase VI rotor taken by KARI in their wind tunnel.
  - Data from Mie University on a 2.4 meter turbine

- WP2: DIII.2 and DIII.3. Preliminary and final database. In 2015, after an initial analysis of data, the New MEXICO measurements were released to the Mexnext participants. Thereto the data are shared on the so-called Beehub facility of the Dutch Surfsara. This facility provides a general storage service for large datasets and easy sharing with collaborators. The database was accompanied by a detailed description of the experiment and the database [24] and a report describing the data reduction and analysis [110]. Since then the results in the database has been updated, in particular the description of the acoustic measurements.

- WP3: DIII.4 to DIII.8 (Model descriptions, descriptions of 2 calculational rounds and the comparison between calculations and measurements).
  - The model descriptions have been supplied continuously on the extranet site of www.mexnext.org. The results are described in appendix E and F/
  - The description of 2 calculational rounds has been distributed between the participants and uploaded to the extranet site of www.mexnext.org, see appendix C.
  - The comparison between calculations and measurements has been presented at the 2nd, 3rd and 4th plenary meeting [133], [134] and [135]. The results are reported in sections 4.2 and 4.3.
- WP4: The results from the tasks carried out in WP4 are described in the present report.
- WP0: DIII.9 to DIII.16: These are management deliverables (i.e. progress reports for every IEA ExCo meeting, minutes of plenary meetings and the present final report). The progress reports have, in line with IEA procedures, been delivered to the IEA ExCo at least two weeks before their bi-annual meetings. The minutes of the plenary meetings, see section 2.3 and [132], [133], [134] and [135] have been distributed between the Mexnext-III partners. The minutes are, together with the presentations, uploaded to the Mexnext extranet site.

Apart from the official deliverables Mexnext has led to a large number of publications and technical reports, e.g. [25, 111, 155, 106, 126, 15, 86, 26, 37, 38, 59]. Moreover the results from Mexnext were main contributors to 2 PhD thesis disserations: [141] and [178].

2.3 Meetings

Within Mexnext-III a total of 4 plenary meetings were held.

- The first meeting was held at ECN Amsterdam (NL) on March 4 2015 [132]. It served as the kick-off meeting where the participants presented their plans and where they informed the consortium about the chances of participation.
- The second meeting was held at NREL Boulder (USA) on January 11 and 12 2016. [133]. At that moment the consortium was more or less established and the progress of the various WP's was discussed. Special attention was paid to the first analyses of the New MEXICO experiment and the results of the first calculations at non-yawed conditions. Since many differences between calculations and measurements were caused by postprocessing issues and misunderstandings on conventions, the definition of cases were refined. The meeting was followed by an aerodynamic 'free wheeling meeting' organised together with IEA Task 11 where presentations were given on on non- Mexnext results
- The third meeting was held at ONERA Paris (France) on November 9 en 10 2016, [134]. The progress of the various WP's was discussed. Special emphasis was paid to the results from the first and second calculational round at non-yawed and yawed conditions. Moreover the results and relevance of Mexnext was evaluated leading to recommendations for a continuation.
- The final meeting was held in Beijing from December 4 to 6 2017, [135]. At that meeting the results from all WP's were discussed with the final evaluation of the Mexnext-III results . A visit to the Sinoma blade factory was included in the agenda.

The meetings were 'enligthened' with presentations on the lifes of famous scienticst like Ludwig Prandtl or Gustave Eifel, on sports aerodynamics, and with Christmas puzzles on aerodynamic problems. Apart from the official plenary meetings two intermediate meetings were organised which were combined with meetings from the EU FP7 project AVATAR in which many of the Mexnext members participate. These meetings were held at:

- University of Glasgow on June 7th 2016
- CENER in Pamplona Spain on April 6th 2017

These meetings mainly addressed the intermediate results from calculational rounds. As a result several refinements were made to the definition of the calculational rounds and the planning was refined.

3. WP2 Processing/presentation of data, uncertainties

The New MEXICO experiment produced about 4TB of data. The data were stored on an external server and made available to the Mexnext participants. Access details have been shared on the Mexnext teamsite [16]. On the server, the time series (of pressures and strain gauges) are given in raw form. In principle the data were organized in a self explanatory way but some further data reduction was performed. Thereto the pressure data has been reprocessed, taking into account the calibration and drift between the zero-runs just before and after a measurement run. In addition to that time- and azimuthally bin averaged pressure distributions and sectional loads have been shared. The PIV data were given in both raw and processed form (i.e. raw images as well as ASCII data of the velocity vectors at different x-y-z positions). The same holds for the acoustic microphone data, where the processed data contains noise source levels. In addition to that pictures and movies made during the experiment were shared. Explanatory information regarding the data files was added to [27].

During the course of Mexnext-III, several uncertainty aspects were studied. Although the uncertainty of the measurement apparatus used during the New MEXICO experiments are presented in [27], several other aspects that played a role in the project are highlighted in the sections below.

3.1 RISØ profile load discrepancy

From the comparison round a clear discrepancy is observed between measured and predicted normal force at the 60%R station which houses the RISØ profile, see also Figures 4.2(a) and 4.2(c). The discrepancy is observed both for lifting line as well as CFD predictions. A short investigation was carried out in an attempt to reveal the cause for this difference.

The lifting line codes have been fed with 2D airfoil data measurements of the RISØ-A1-21 profile since no measured data was available for the implemented RISØ-A2-21 profile. For both profiles the geometry coordinates are known. In addition to that the MEXICO blades were scanned digitally in Mexnext-I from which sectional cuts of the midboard part are available. All three geometries were fed to the RFOIL 2D panel code [100] to obtain a quick estimate of the differences between them for a tripped boundary layer at the appropriate Reynolds number. Similar studies using CFD were performed by DTU and CENER in the course of Mexnext-III. The panel code results are given in Figure 3.1. Although the pressure distribution between the A1 and A2 profile are quite different, the corresponding lift curves are very similar in the attached flow region. The latter also holds for the results between the scanned blade geometry versus design geometry of the RISØ-A2-21 profile. From the 10 m/s case in Figure 4.2(a) the difference in normal force is around 30 N/m, which translates to a ΔCl around 0.1. The operating angle of attack at this spanwise position is roughly 2° for this case. From Figure 3.1(a) the observed differences are much smaller. For the lifting line codes it is therefore unlikely that the usage of airfoil data from the A1 instead of A2 profile has caused the discrepancy. From this result also the difference between scanned and design geometry cannot explain the difference, which is in line with a previous CFD investigation on this topic [20].

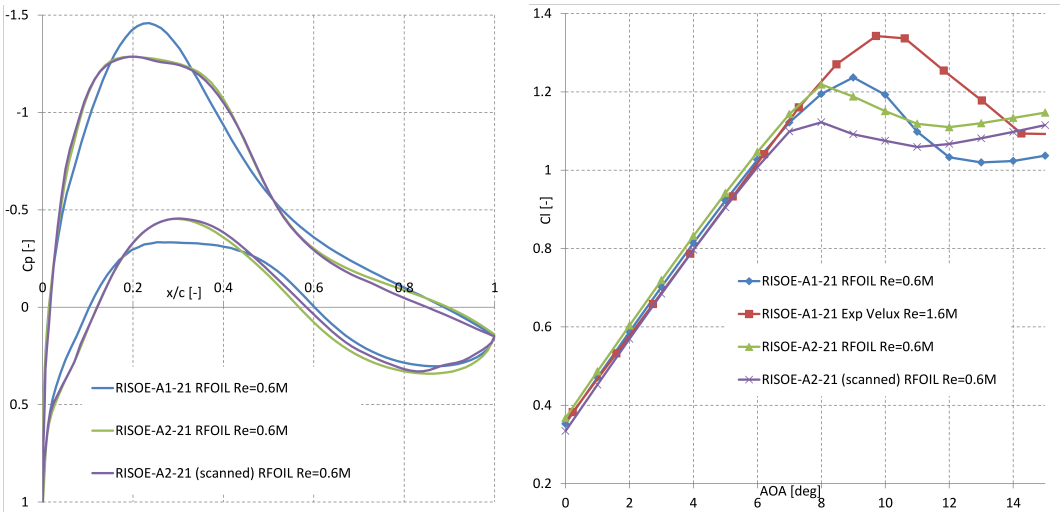

(a) Pressure distributions at AOA=2°

(b) Lift curves for tripped conditions

Figure 3.1: Comparison between RISØ profiles

A closer look at the corresponding pressure distribution comparison between CFD and experiment (e.g. Figure A.6(c)) shows a reasonable agreement on the lower side of the airfoil but a significantly lower measured suction level on the upper side. This is in line with the pressure distributions from the comparison rounds in Mexnext-I, although they were obtained with old pressure and tunnel speed calibrations. It has been posed that the different camber of the RISOE profile in comparison to the DU and NACA profiles and consequently the circulation discontinuity at the transition between the profiles could cause the decambering. However the non-rotating MEXICO blade measurements in the Delft Low speed low turbulence tunnel [24], hence featuring a totally different spanwise circulation distribution, give rise to exactly the same observation as the rotating measurements in the DNW (Figure 3.2). Hence for now the consistent over prediction of loads for this section

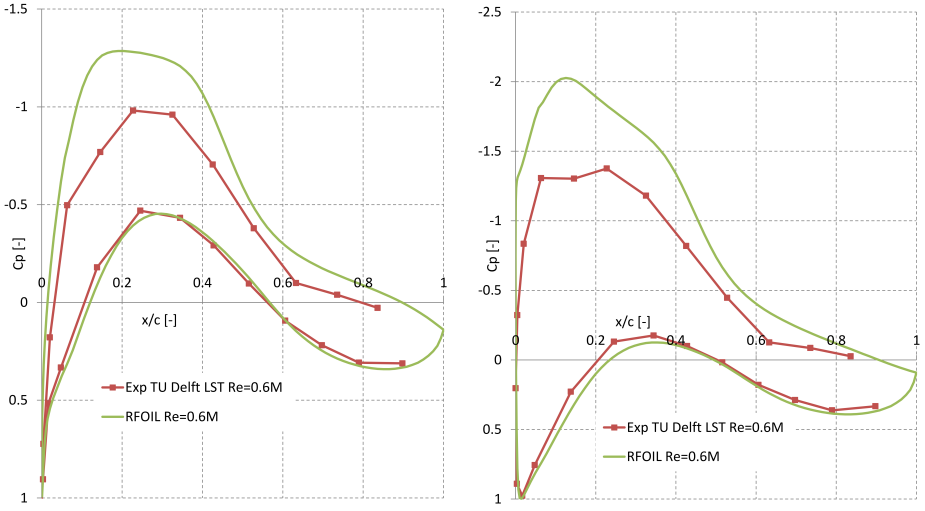

(a) Geometric AOA=2°

(b) Geometric AOA=7°

Figure 3.2: TU Delft LST measured and predicted pressure distributions for tripped conditions at the 60%R station

cannot be explained. As was earlier posed [68], the thickness of the tripping tape causes a thicker and hence more decambering boundary layer compared to solely making the boundary layer turbulent as was done in most computations. Figure A.10(c) contains results from USTUTT that actually model the strip by means of a

meshed disturbance, which is shown to significantly reduce the suction level opposed to the simulation without a meshed strip. However, as discussed in the next section, the strips were interrupted at the spanwise location of the sensors. It is recommended to further study the effect of the roughness strip on the profile performance experimentally.

3.2 Zigzag strip configuration

As reported in section 12, boundary layer transition was studied on the MEXICO blade using the unsteady pressure sensor data [90, 8]. In addition to the tests in the DNW, also the data from the non rotating wind tunnel test at the Low speed low turbulence tunnel in Delft were used [24]. These measurements gave the opportunity to validate the post-processing of the pressure sensors by using oil flow and stethoscope measurements. Previously attention was paid to the effect of the strip thickness and width and its chordwise positioning. Thanks to some well observing Mexnext participants another aspect of the roughness strip configuration was studied, as also reported in [27].

To prevent the zigzag strips from blocking the pressure sensors and/or measuring local pressure disturbances due to the strip, they were interrupted at the location of the pressure sensors on both pressure and suction side. This leaves a gap of about 10 mm in spanwise direction (i.e. approximate 5 mm on both sides), see also Figure 3.3(a). An exception lies in the 25%R and 35%R pressure side sections from blade 1, where the chordwise resolution of the sensors left enough space to accommodate the strip without interruption. For the interrupted sections it was anticipated that the spanwise extent of the turbulent wedges emanating from the strip edges would trip the boundary layer at the pressure sensor location as well, albeit slightly downstream. It can be expected that the spanwise extent of turbulent wedges emanating from the strip edges is less in a favorable pressure gradient (blade pressure side for positive angles of attack) rather than a positive pressure gradient (blade suction side for positive angles of attack), influencing the degree of turbulence in the boundary layer at the pressure sensors. This was confirmed in the above mentioned boundary layer transition study, see also the oil flow visualization in Figure 3.3(b). It has however to be realized that the described interruption of the strip will result in a difference when comparing between integrally measured blade loads (e.g. balance, strain gauges) and loads obtained from the pressure sensors. Especially the fact that the interrupted sections do not include the additional step increase in boundary layer thickness as induced by the thickness of the roughness strip result in the measured sectional characteristics not being representative for the full blade.

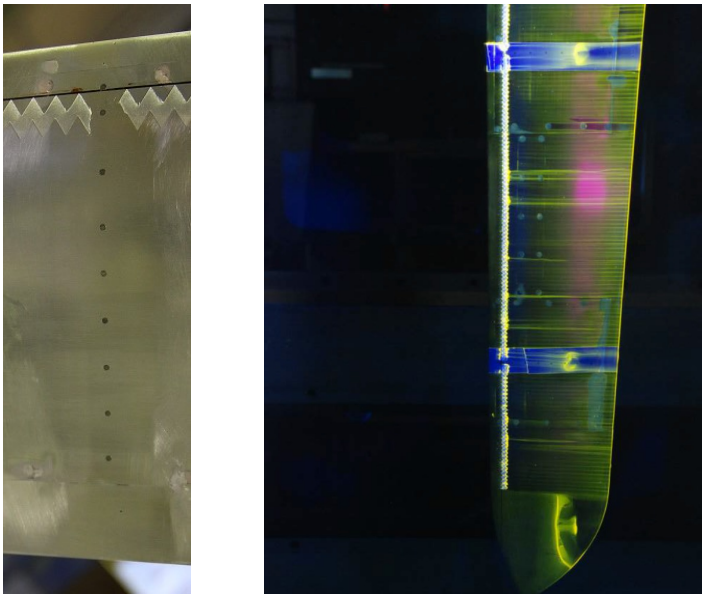

(a) Strip interruption at 60%R suction side, blade 2

(b) Blade 3 pressure side oil flow visualization showing the taped 82%R and 92%R sections, AOA$\approx 5^{\circ}$, Re=4.7×10^5 (Delft wind tunnel)

Figure 3.3: Visualization of the interruption of the zigzag strip on the MEXICO blade

3.3 Comparison round related uncertainties

As explained in appendix D, all loads variables are determined from the pressure sensors. This approach ignores frictional forces and includes resolution related uncertainties due to the limited amount of blade pressure sensors both in spanwise and chordwise direction. Using the available CFD results from DTU_EllipSys3D, an estimate can be made to quantify the influence of several comparison round related uncertainties.

The following data reduction is applied to CFD and experimental results, of which the item headers correspond to the legend in Figures 3.4 and 3.5.

- NewMexico
  Measured data which is post-processed as described in appendix D. This means the trailing edge pressure is obtained by averaging the readings of the last sensor on pressure and suction side.

- NewMexico_TE
  Same as above, but now the trailing edge pressure is estimated by extrapolating the last two sensors values for both pressure and suction side and averaging these.

- DTU_EllipSys3D
  The original resolution of the CFD simulation is used, featuring a fine spacing in both chordwise ($\sim$ 380 points) and radial direction ($\sim$ 200 points). Only pressure forces are considered.

- DTU_EllipSys3Dp1
  The radial resolution of the experiment is taken (5 points), the chordwise resolution is kept the same. The rotor integral variables are determined by linear interpolation identical to the post-processing of the experiment.

- DTU_EllipSys3Dp2
  The radial and chordwise resolution of the experiment (5 and approximately 20 points respectively) is taken. The trailing edge pressure is estimated by extrapolating the last two sensors values for both pressure and suction side and averaging these.

- DTU_EllipSys3Dp3
  Same as DTU_EllipSys3Dp2, but for the integration of pressures to tangential forces the sectional y/c coordinates are taken from the specified sensor location (used for reducing the experimental data) rather than from the IGES file which was used for the CFD simulation.

From Figure 3.4 it is apparent that the used ***trailing edge estimation*** technique hardly has an influence on normal force Fn. A small loading decrease at the 82%R station is observed, which is attributed to the limited number of sensors at the rear part of the suction side of this section (see e.g. Figure A.6(d)). This reduces the axial force up to 2% as shown in Table 3.1. The tangential force Ft is heavily impacted by the estimation method, especially for the outboard sections. The trailing edge extrapolation algorithm brings the measured results closer to the simulations, increasing the torque up to 14% for Case 1.1.

In addition to the above itemized analyses focusing on the influence of limited sensor resolution and post-processing techniques, also the effect of ***friction*** on integral rotor variables could be verified from the CFD simulations. From Table 3.1, friction hardly reduces the axial force but reduces the torque up to 25% for Case 1.1. This can be expected as skin friction forms a large portion of the total drag in attached flow conditions, directly influencing the rotor torque.

From the Figures and Table it becomes clear that the limited ***spanwise resolution*** in the experiment results in underestimation of the integrated normal and tangential force. Assuming a linear trend between the discrete radial stations results in cutting off area especially at the root and tip region. This results in up to 6% lower axial force for these load cases. The influence on the torque results in a decrease up to 10% depending on the load case. Therefore it was decided to enforce the same spanwise resolution as the experiment for calculation of axial force and torque from simulations in the comparison round (chapter 4). This procedure was further streamlined by supplying pre-determined weighting factors to be applied to normal and tangential forces, see also appendix C.

The influence of ***chordwise sensor resolution*** appears to be limited, changing integral variables in the order of 1%. This indicates that the chordwise sensor distribution was well designed to capture the pressure distributions. Here it is noted that the trailing edge estimation procedure extrapolates the last two sensors values for both pressure and suction side and averages these. As verified above using the measured pressure distributions, the effect of the limited number of chordwise pressure sensors would probably be larger if trailing edge pressure is estimated by simply averaging the readings of the last sensor on pressure and suction side.

A relatively large offset between measured and predicted tangential force can be observed, notably in the outboard sections for Case 1.1 and 1.2 (Figures 3.4(b) and 3.4(d)), which is unexpected based on the good agreement between measured and predicted pressure distributions (Figures A.6 and A.7). Although a more advanced trailing edge estimation algorithm brings the experiment closer to the simulations, the ***sensitivity to sectional y/c coordinates*** in the pressure integration to tangential force was investigated. A small offset was noted between the y/c coordinates from the specified sensor locations (used for post-processing the experimental pressure), opposed to the ones obtained from the CFD simulation (which was based on the IGES file of the blade). To quantify the influence of this effect, the y/c values from the CFD simulations were replaced with the ones from the experiment and tangential force based on CFD predicted pressures was calculated. The DTU_EllipSys3Dp3 results in Figures 3.4 and 3.5 and consequently also Table 3.1 indicate that this procedure increases tangential force and torque, driving them further away from the experiment.

Concluding it has to be stated that obtaining tangential force and torque from pressure sensors features a large measurement uncertainty, and large differences with simulations can be expected. Furthermore it has to be emphasized that the above results are only valid for the specific cases under consideration. Care should be taken when extrapolating these results to other turbine blades and conditions.

Table 3.1: Effect of friction, limited sensor resolution and post-processing on rotor axial force and torque

	Case 1.1		Case 1.2		Case 1.3	
	Fax [%]	Torque [%]	Fax [%]	Torque [%]	Fax [%]	Torque [%]
Effect of friction	0.3	-24.5	0.3	-6.4	0.5	-1.8
Effect of radial spacing	-5.8	-10.5	-5.1	-5.6	-2.5	0.1
Effect of chordwise spacing*	-1.0	1.6	-0.8	1.6	-1.3	2.2
Aggregate effect of spacing	-6.8	-9.1	-5.9	-4.1	-3.7	2.3
Effect of using experimental y/c	0.0	7.0	0.0	3.0	0.0	1.9
Effect of TE extrapolation†	-2.1	14.5	-1.5	3.2	-0.2	0.0

* employing trailing edge pressure estimation using average of extrapolation of 2 last sensors on pressure and suction side

† verified by application to measured results

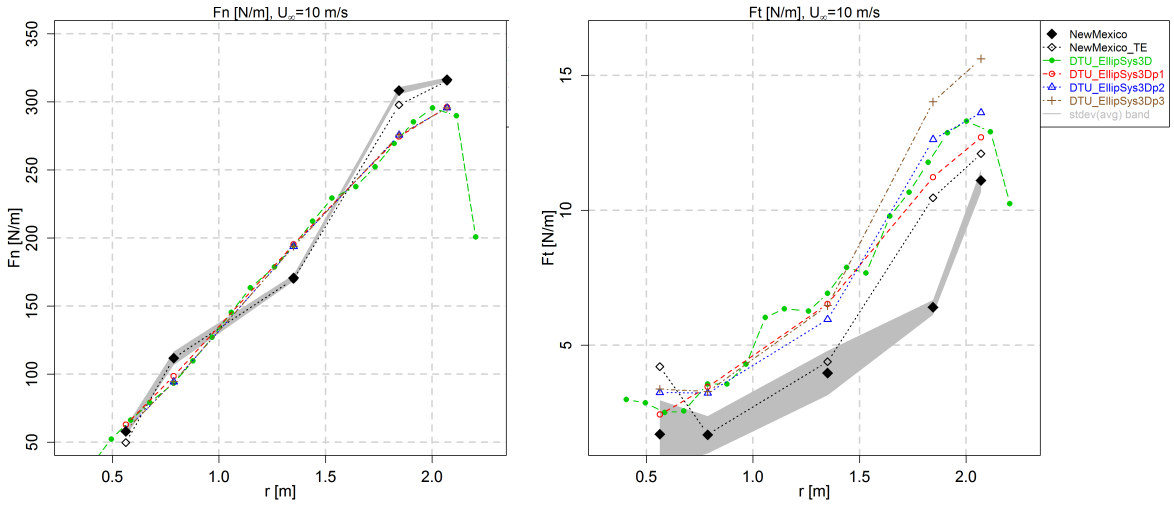

(a) Fn, Case 1.1

(b) Ft, Case 1.1

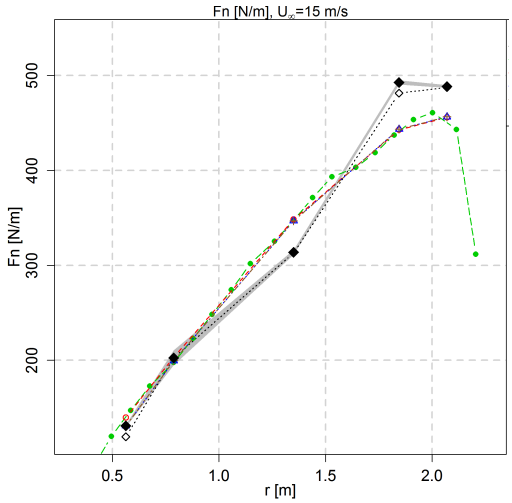

(c) Fn, Case 1.2

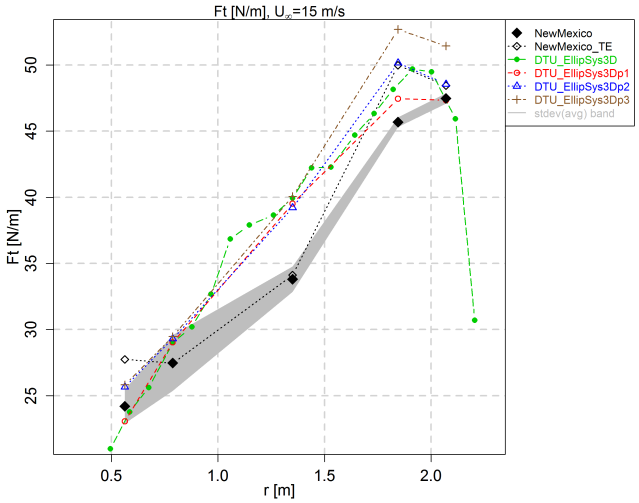

(d) Ft, Case 1.2

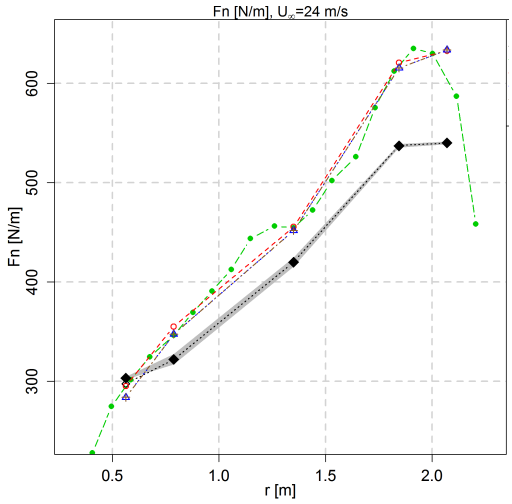

(e) Fn, Case 1.3

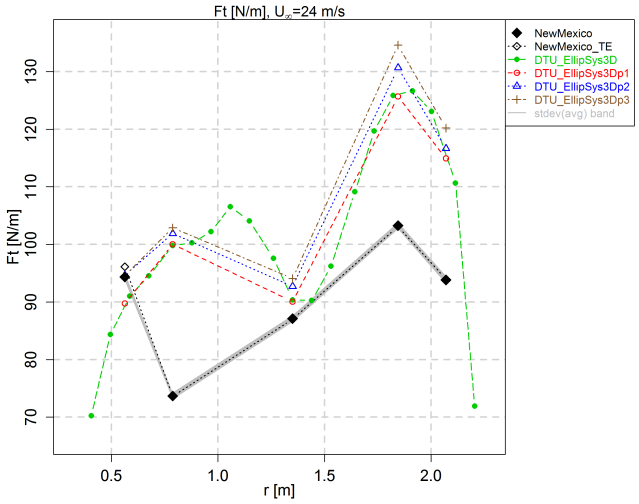

(f) Ft, Case 1.3

Figure 3.4: Influence of limited sensor resolution and post-processing on sectional forces

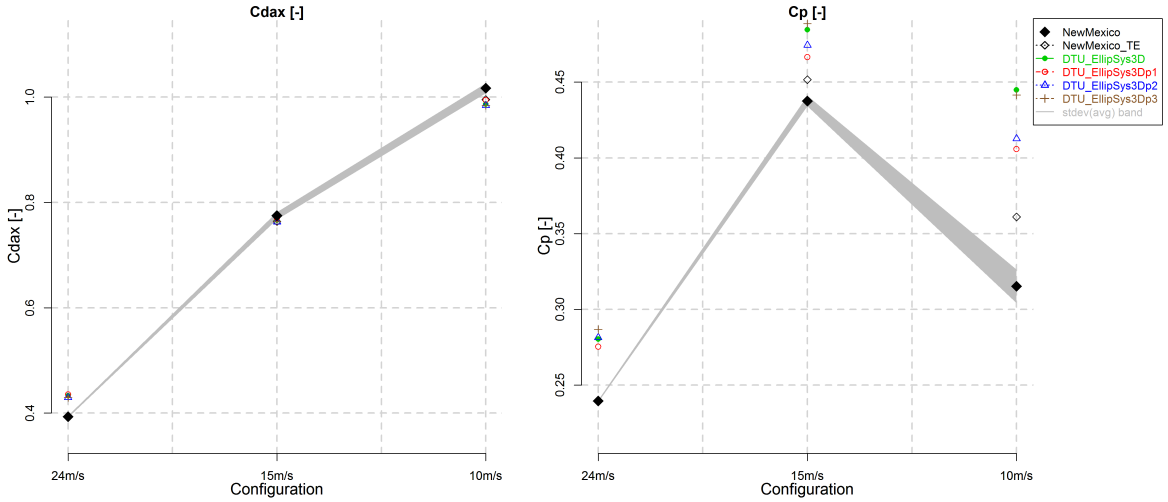

(a) Axial force coefficient Cdax

(b) Power coefficient Cp

Figure 3.5: Effect of limited sensor resolution and post-processing on rotor axial force and torque

4. WP3: Comparison between simulations and measurements

4.1 Introduction

Several participants of Mexnext performed turbine simulations with a variety of aerodynamic codes (both CFD and lifting line codes). The results from the calculations were compared mutually and with experimental values. After the comparison rounds of Mexnext-II, the focus shifted to the New MEXICO experiment.

The comparison has been performed for three axial flow and yawed flow cases. Appendix C gives detailed information on the compared cases and variables. Appendix D gives more information on the experimental data reduction applied. Appendix E and F can be consulted for all model descriptions corresponding to the displayed calculations. Section 4.2 is dedicated to the comparison results in axial flow. Section 4.3 describes the comparison results in yawed flow. The latter two sections describe the main results of the comparison, an overview of all comparison results in terms of figure plots is presented in appendix A and B. Finally section 4.4 provides a study into several possible sources of discrepancies between the CFD simulations.

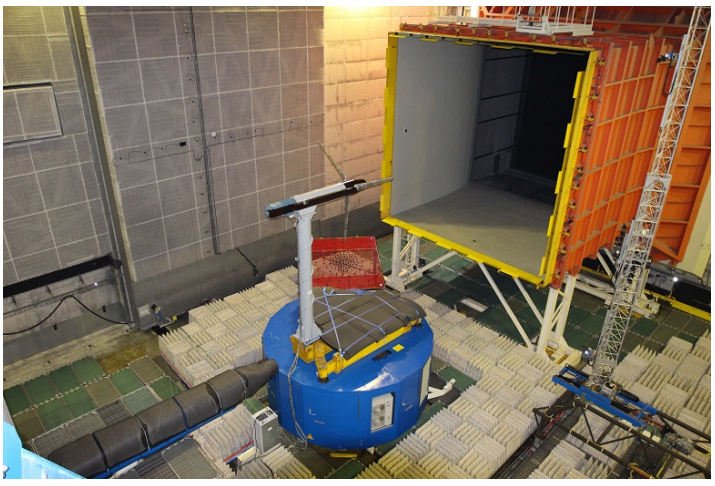

Figure 4.1: The New MEXICO experiment

4.2 First round: Axial flow

Three cases are created featuring a variety of angles of attack and axial induction, as summarized in Table 4.1, mixing a large number of experimental datapoints with similar inflow and operational conditions (see appendix D). A more detailed description of the conditions and the data format and variable definition can be found in appendix C. All variables are displayed as supplied. An exception lies in the axial force and torque which are post-processed to thrust and power coefficients Cd_{ax} and Cp using

$$Cd_{ax} = \frac{Fax}{0.5\rho {U_\infty}^2 \pi R^2}, \quad Cp = \frac{Torque \quad \omega}{0.5\rho {U_\infty}^3 \pi R^2}, \quad \text{with}$$

Cd_{ax}	[-]	Axial force coefficient
Cp	[-]	Power coefficient
Fax	[N]	Rotor axial force
Torque	[Nm]	Rotor torque
ω	[rad/s]	Rotor speed
ρ	[kg/m^3]	Air density
U_∞	[m/s]	Wind speed
R	[m]	Rotor radius

The legend of each graph refers to the parties and their codes that were used to perform the simulations. The model description corresponding to the legends can be found in section E and F. For the measurements, if multiple measured datapoints are available within one case, the standard deviation between the average experimental values gives an indication of the repeatability. The standard deviation is indicated in the graphs by a grey band around the mean value, as described in the experimental data reduction chapter (appendix D).

Table 4.1: New MEXICO comparison cases (axial flow)

Case nr	Wind speed U_∞ [m/s]	Pitch angle [°]	Rot. speed [rpm]	Tip speed ratio λ [-]	Angle of attack $\alpha^\dagger$@80%R [°]	Axial induction factor a†@80%R [-]
1.1	10.05	-2.3	425.1	10.0	3.0	0.5
1.2	15.06	-2.3	425.1	6.7	7.0	0.3
1.3	24.05	-2.3	425.1	4.2	14.0	0.13

† estimate

4.2.1 Lifting line codes

The ***lifting line variables*** comparison plots are given in section A.1. The effective velocity Ueff (Figure A.1) is in good agreement between the codes, indicating that the inputted operational conditions are consistent between the codes. Small differences can be observed in the inboard region, where induction starts to play a role over the elsewhere dominant rotational velocity. The angle of attack AOA shows larger variations, caused by the differences in axial and tangential induced velocities Ui and Vi as shown in Figure A.2. Apart from several outliers the agreement is better for Case 1.2 in design conditions than Case 1.1 in the turbulent wake state. Most codes feature an induction increase towards the tip, although several results show an opposite trend. This is due to a different implementation of the tip correction model which is also applied to the force coefficients rather than the conventional way of applying the Prandtl correction only to the induced velocities. We can also observe a large spread towards the root due the different models correcting for 3D rotational effects, especially for separated flow conditions in Case 1.3. Also apparent is the discontinuity of the induced velocity distribution at the RISØ profile transition around 1.1 m and 1.6 m spanwise position for this case (Figure A.2(e) and A.2(f)). A closer look reveals that only the free vortex wake (FVW) and actuator line or disk models are able to predict this dip due to the fact that they account for trailed vorticity effects in a non-uniform circulation distribution along the span. The differences in force coefficients Cn and Ct from Figure A.3 are less prominent than the variations

in induced velocity, because the sensitivity of angle of attack to induced velocities variations is often reduced within the effective velocity triangle. However the differences in modeling 3D rotational effects remain clearly to be observed.

The resulting ***loads*** in terms of sectional normal and tangential force Fn and Ft are given in Figure A.4. Consistent with the induced velocities, the agreement in Fn is good in design conditions (Case 1.2), where results start to diverge for the turbulent wake state (Case 1.1). An interesting observation can be made in Figure A.4(a) for the IFPEN and ECN results which feature both a BEM and free vortex wake result. It is hypothesized that the significant radial expansion, which is not accounted for in BEM, causes the consistent load increase towards the outboard region for the free vortex wake codes. A closer look at the corresponding axial induction levels from Figure A.2(a) show that, in contradiction to *annular* momentum theory, the FVW models predict a lower rather than higher induction. For the attached flow cases the spread in Fn is generally scattered around the experimental value, the 60%R value excepted (see also section 3.1). The tangential force Ft is more difficult to match, but it has to be considered that obtaining tangential force from pressure sensors features a large measurement uncertainty. Although the friction is embedded in the airfoil data used by the lifting line codes, while it is obviously not included in the pressure data, the trend indicates higher tangential forces for the predictions. See also section 3.3 for a more elaborate consideration of the underlying effects. The bad agreement of the sectional forces for Case 1.3 clearly illustrate the shortcoming of the airfoil data approach in separated flow conditions. The resulting rotor performance coefficients Cd_{ax} and Cp in Figure A.5 are in line with the trends of the sectional forces. The use of prescribed weighting factors for application to Fn and Ft to determine these coefficients has reduced the scatter between the codes. Although the predicted axial forces seem in agreement with the measured value for Case 1.3 (24 m/s), inspecting the sectional forces reveals this is a clear result of compensating errors.

4.2.2 CFD codes

The CFD results are given in section A.2, with the ***pressure distribution*** comparison plots in Figure A.6 to A.8 for the turbulent CFD and in Figure A.9 to A.11 for the transitional CFD simulations. For the inboard stations at 25%R and 35%R it is clear that the experimental resolution of the pressure sensors is insufficient, especially at the lower inflow speeds, resulting in non-smooth measured pressure plots. There is a clear offset between measured and predicted suction side pressure levels at 60%R, which is discussed in more detail in section 3.1. For the outboard stations the agreement with the experiment is quite satisfactory. Some outliers excepted, the same holds for the agreement between the predictions themselves. However, a small deviation in pressure levels can result in large integrated force differences. It is unclear why the ONERA results consistently feature slightly elevated suction levels in comparison to the other simulations. The largest spread between the simulations can be observed in Case 1.3, where the separation point location is challenging to predict. The effect of modeling the outboard part of the blades clean is nicely illustrated at 82%R and 92%R by the CFD results that feature a transition model. Especially for attached flow conditions, the transitional results exhibit slightly higher suction and pressure levels resulting in an increase of chord normal force. The Stuttgart results feature three variations herein; a fully turbulent simulation (Turbs), a fully turbulent simulation modeling zigzag strip by means of a geometric 'bump' (Transr), and a transitional simulation also modeling the zigzag strip by means of the meshed disturbance. A clear jump in the pressure distribution can be observed due to this disturbance for the 25%R, 35%R and 60%R sections.

Since normal force is mostly dictated by pressure forces, the resulting ***loads*** prediction for the CFD codes should be congruent to the pressure distributions. These are given in Figure A.12 and A.13 for the fully turbulent CFD simulations and in Figure A.14 and A.15 for the transitional CFD. Indeed, normal force is scattered around the measurements for attached flow conditions, whereas we observe more variability both between CFD and experiments as well as between CFD codes themselves for Case 1.3 featuring separated flow conditions. For Case 1.3 the predicted load distributions are far from smooth due to the spanwise variation of separated flow features, but the trend is in better agreement with the experiment than for the lifting line codes. Similar to the lifting line codes, tangential force is over predicted in comparison to the experiment. See also section 3.3 for a more elaborate consideration of the underlying effects. Modeling part of the boundary layer clean outboard of 70%R is seen to bring the Fn predictions closer to the experiment in Figures A.14(a) and A.14(c). However, the tangential force increases further due to the lower friction of the laminar boundary layer, which makes the agreement with the experiment worse. As for the lifting line codes, the usage of prescribed weighing factors has reduced the scatter in the resulting integral rotor variables Cd_{ax} and Cp.

4.2.3 Model types

In addition to displaying the loading results from the various codes as summarized in Appendix E and F, the supplied data also gives the opportunity to calculate an average result for each code type. Here the following code types are distinguished:

- BEM
  Blade Element Momentum methods using the airfoil data as prescribed in appendix C.
- FVW
  Lifting line free vortex wake methods, also using the prescribed airfoil data dataset.
- AM
  Actuator line and actuator disk models, also using the prescribed airfoil data dataset.
- CFD_turb
  Computational fluid dynamics codes, which model the rotor blade geometry and the 3D space around it. The blade boundary layer is modeled as fully turbulent.
- CFD_trans
  Similar to above but with a boundary layer transition model, starting with a laminar boundary layer on the leading edge of the blade.

A summary of the codes used to determine the average is given in Table 4.2.

Table 4.2: Summary of codes used for code type averaging (axial flow)

Code type	Code names
BEM	CENER_BEM, CENER_FAST, DTU_HAWC2, DTU_HAWC2NW, ECNAero-BEM, IFPEN_BEM Suzlon_BEM
FVW	ECNAero-AWSM, IFPEN_VL, ONERA_PUMA
AM	DTU_AL, Uppsala_AD, USTUTT_AL
CFD_turb	CENER_CFD, DLR_TAU, DTU_EllipSys3D, FW_IWES_CFD, IFE_CFD, Onera_ElsA, Technion_CFD USTUTT_FLOWer
CFD_trans	DTU_EllipSys3D_trans, Onera_ElsA_trans

To obtain the loading averages, first the normal and tangential force are determined at the same spanwise five positions as the instrumented sections using linear interpolation from the supplied radial distributions. A simple average $\overline{x}$ is determined using

$$\overline{x} = \frac{1}{n}\sum_{i=1}^{n}(x_i) \quad .$$

In addition to that, to give an indication of the variability between the results, a partly transparent band is plotted around the average of each code type illustrating the standard error x_{err} between the supplied results of a code type

$$x_{err} = \sqrt{\sum_{i=1}^{n}\frac{(x_i - \overline{x})^2}{n(n-1)}}.$$

The results for the sectional forces are illustrated in Figure 4.2. The differences in normal force between the various code types are relatively small in attached flow conditions (Figures 4.2(a) and 4.2(c)). A closer look

reveals that for Case 1.1 (turbulent wake state), FVW predictions deviate from BEM resulting in higher loads, in better agreement with CFD, whilst they are more or less aligned for Case 1.2 (design conditions). This observation illustrates the shortcoming of the BEM and its engineering additions in modeling high thrust cases. The largest differences between the various code types can be found in the tip region, where the lifting line approach has its limitations in comparison to CFD. The effect of modeling the blade clean or turbulent in CFD can clearly be observed from roughly 70%R onwards. The discrepancy between codes and experiment is consistent and puzzling for the 60%R section as was discussed in section 3. Differences between code types are more pronounced in the tangential force distribution to the right, also between the lifting line options (BEM, FVW and AM). However the differences are very small on an absolute scale. In separated flow conditions (Figures 4.2(e) and 4.2(f)) the trends of the lifting line codes are clearly off in comparison to the experiment, illustrating that using sectional airfoil data is not a valid approach. This is clearly improved by CFD.

Several observations can also be made from the bands showing the variability between results from each code type. Normal force is less variable than tangential force which results in the same observation between Cd_{ax} and Cp in Figure 4.3. Case 1.3 featuring separated flow conditions (Figure 4.2(e) and 4.2(f)) results in significant variability between CFD codes and also the rotational augmentation modeling in the inboard part between lifting line codes. Generally speaking more variability is observed between CFD codes, which could possibly be explained by the fact that these codes need careful considerations of a large number of input details. It is hypothesized that the 'human factor' would result in rather different results when various people use the same CFD code. See also section 4.4 for an effort to quantify the origin of the observed variability between CFD codes.

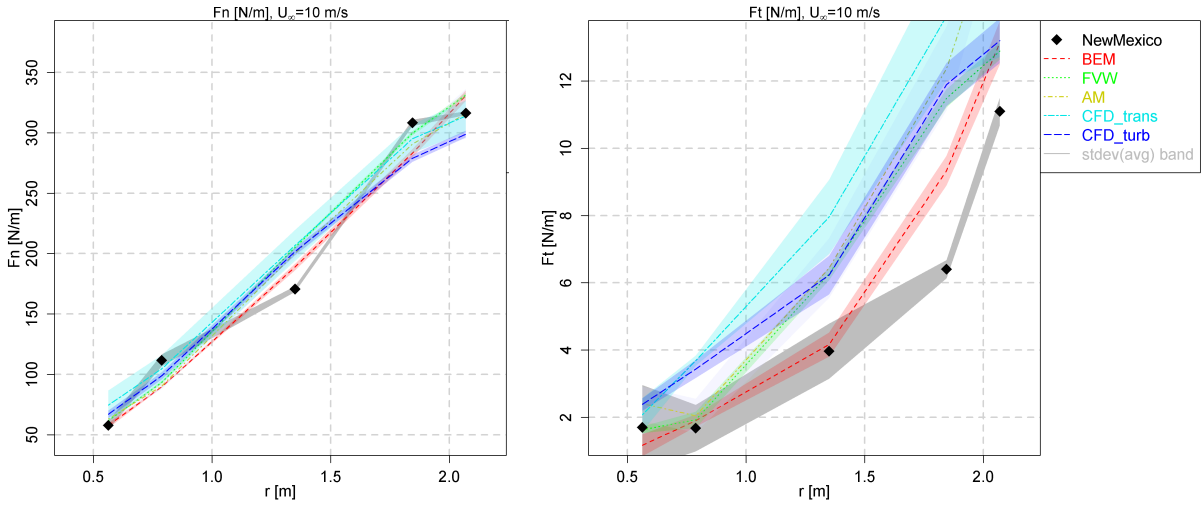

(a) Fn, Case 1.1

(b) Ft, Case 1.1

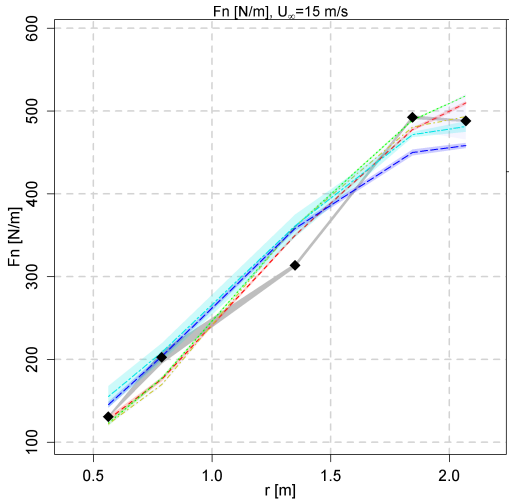

(c) Fn, Case 1.2

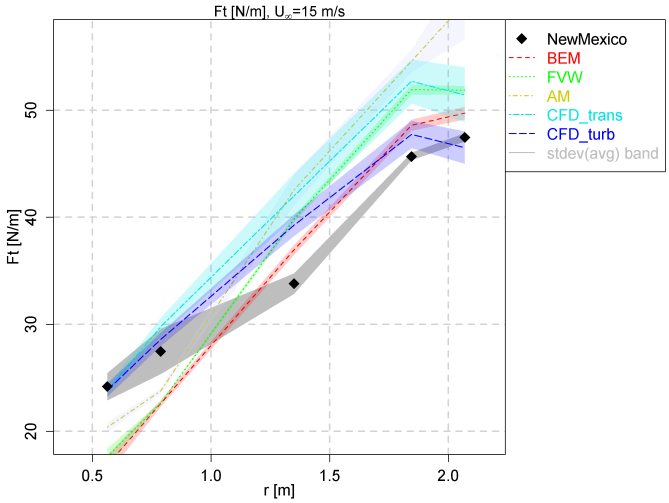

(d) Ft, Case 1.2

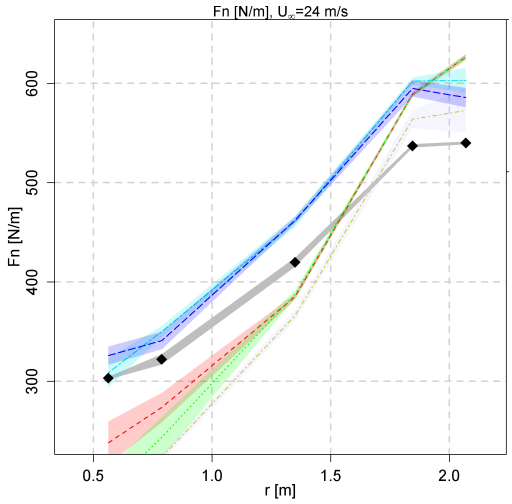

(e) Fn, Case 1.3

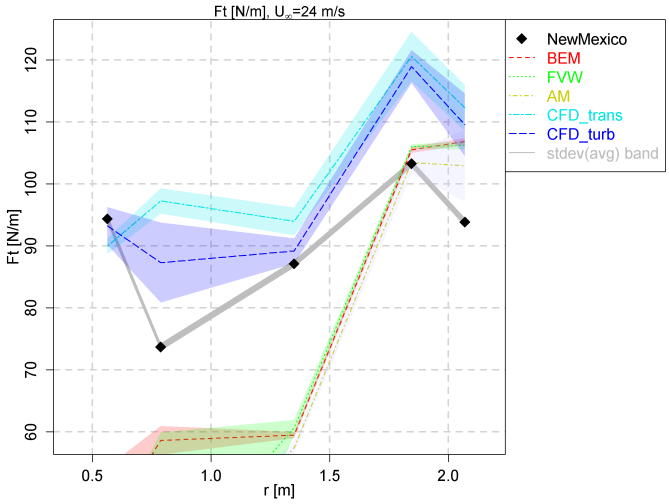

(f) Ft, Case 1.3

Figure 4.2: Comparison between model types: Chord normal and tangential force

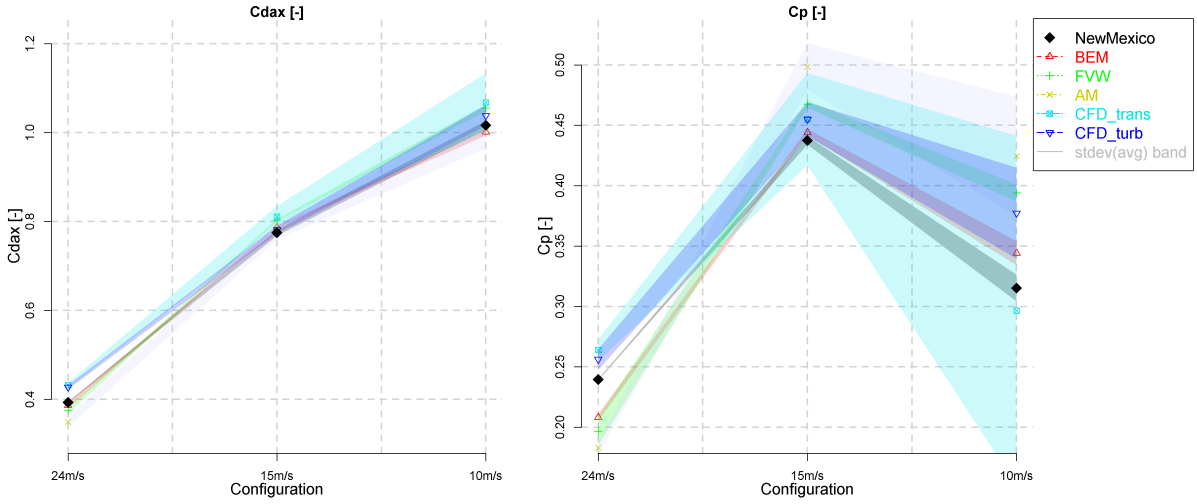

(a) Axial force coefficient Cdax

(b) Power coefficient Cp

Figure 4.3: Comparison between model types: Rotor integral forces and moments

4.2.4 Velocity traverses

The results of the velocity traverse are given in section A.3. The ***axial traverse*** of axial, radial and tangential velocities u, v and w are displayed in Figures A.16 to A.18 for the two radial locations at r=0.5 m and r=1.5m. The inboard traverses at r=0.5 m slice through the root vortex in the downwind half, which causes large fluctuations. A small offset in root vortex position will give a totally different traverse, which is the reason for the variability between the different codes. It is however surprising to see the large variation in u for the upwind part for Case 1.1 (Figures A.16(a) and A.16(b)), with the ONERA_ElsA constantly being elevated, similar to the load results as observed above. The v component shows the radial expansion approaching the rotor plane, which is influenced by the presence of the nacelle for the inboard location. Since not all participants model the nacelle geometry, this effect is clearly distinguishable observing the difference between them. The traverse of tangential velocity w slices through the convected blade wake for the downstream locations, which is difficult to match exactly. For separated flow (Case 1.3), the wake deficit becomes larger which can clearly be observed in the corresponding w plot (Figure A.18(f)).

The ***radial traverse*** plots are given in Figures A.19 to A.21 for an upwind and downwind position relative to the rotorplane at x=-0.3 m and x=+0.3 m. It is noted that the velocities represent an azimuthal average which is determined by averaging the velocities of individual azimuth angles using prescribed weighting factors. Generally speaking the predicted trends are in good agreement with the experiment. The axial velocity u still shows a large spread between the different code results, mostly over predicting the velocity in comparison to the experiment. This is confirmed by revisiting the axial traverse plots, but this difference seems only to be present at locations nearby to the rotorplane. The radial velocity component shows an underestimation of the radial expansion by the lifting line code results in comparison to the CFD results. For the upwind plot at x=-0.3 m the influence of the nacelle is visible again. The experimental results for the w component confirm the absence of tangential induction for the upwind location, where the small variations are an indication of the uncertainty of the PIV measurements. Some codes however still seem to predict tangential induction upstream of the rotor plane. The downwind locations at x=+0.3 m show the swirl as induced by the root vortex, gradually decreasing towards the tip. The variability between the codes is larger for the separated flow case.

The numerous ***azimuth traverse*** plots are given in Figures A.22 to A.39. They feature velocity variations at a fixed point in space as a function of azimuth angle for both upwind and downwind locations x=-0.3 m and x=+0.3 m at five radial positions r/R=25,35,60,82,92%. Acknowledging the fact that the PIV measurements are taken at the 9 o'clock position, this means that blade 2 will pass this position at a rotor azimuth angle of 30° (see also the conventions in appendix C). The upwash and downwash of the blade can be identified just before and after this azimuth angle in the plots. Generally speaking this trend is well captured, although there tends to be quite some difference in absolute levels. Apart from this effect, the variation in radial and tangential

velocity v and w is dictated by proximity of the root and tip vortex for the downwind positions. For Case 1.3 also the presence of the separated blade wake influences the v and w components variation with azimuth (see e.g. Figures A.38(c) and A.39(c)). Some of the codes do a good job in predicting this effect, which is believed to be difficult to model.

4.3 Second round: Yawed flow

Three cases are created featuring a variety of angles of attack and axial induction, as summarized in Table 4.3, mixing a large number of experimental datapoints with similar inflow and operational conditions (see appendix D). A more detailed description of the conditions and the data format and variable definition can be found in appendix C. All variables are displayed as supplied. An exception lies in the axial force and torque which are post-processed by the coordinator applying pre-defined weighting factors to the sectional forces. In addition to these two variables, also the flapwise aerodynamic blade root moment is calculated from the supplied normal and tangential load variation. For the measurements, if multiple measured datapoints are available within one case, the standard deviation between the average experimental values gives an indication of the repeatability. The standard deviation is indicated in the graphs by a grey band around the mean value, as described in the experimental data reduction chapter (appendix D).

Table 4.3: New MEXICO comparison cases (yawed flow)

Case nr	Wind speed U_∞ [m/s]	Yaw angle [°]	Pitch angle [°]	Rot. speed [rpm]	Tip speed ratio λ [-]	Angle of attack $\alpha^\dagger$@80%R [°]	Axial induction factor a†@80%R [-]
2.1	10.03	30	-2.3	425.1	10.0	3.0	0.45
2.2	15.01	30	-2.3	425.1	6.7	6.0	0.28
2.3	24.08	30	-2.3	425.1	4.2	12.0	0.15

† Estimate of azimuth averaged value

4.3.1 Lifting line codes

The ***lifting line variables*** comparison plots are given in section B.1. The effective velocity Ueff variation (Figures B.1 to B.3) shows a good agreement between the codes, indicating consistency between the inputted operational conditions. The axial induced velocity variation Ui in Figures B.4 to B.6 reveal large variations and opposite trends between the underlying models. The largest variations occur between the BEM codes due to the differences between the used skewed wake models. For the tangential induced velocity (Figures B.7 to B.9) differences are even larger showing large amplitude variations for the free vortex wake and actuator models in comparison to BEM. The effect on angle of attack AOA is however limited, relatively reducing the scatter. For Case 2.3 an abrupt kink is observed in the inboard sections (25%R and 35%R) due to leading edge separation in the lift polar for these angles of attack. This case poses a challenge for the dynamic stall modeling. The same feature is observed in the normal and tangential force coefficients Cn and especially Ct (Figure B.18).

The ***loads*** comparison can be found in Figures B.19 to B.24 for normal force Fn and axial force Fax and tangential force Ft and Torque. The largest variations between experiments and simulations are observed for the inboard sections, where the outboard sections seem to be dominated by the advancing and retreating effect. The over prediction of Fn at 60%R from the axial flow comparison is also present in yawed flow conditions, judging by the level offset. Case 2.3 shows abrupt force variation measurement for the inboard sections due to the variation of leading edge separation and attachment which was also observed in the lifting line variables. However, none of the codes seem to be able to predict the trend correctly. Also the 60%R section shows a consistent amplitude overshoot prediction in Fn compared to the experiment for this case in Figure B.23(c). The corresponding tangential force Ft comparison in Figure B.24(c) shows a totally different trend with rather constant measurements and a large azimuthal variation of the predictions. Perhaps this is related to the discontinuous spanwise circulation distribution at the airfoil transitions for the RISØ profile in combination with separated flow features.

4.3.2 CFD codes

Section B.2 shows the CFD related plots in yaw. The ***pressure distributions*** are given for all five radial stations at 0°,90°,180° and 270° azimuth in Figures B.25 to B.39. Generally speaking the trend with azimuth is well

captured, but the separated flow conditions for Case 2.3 remain a challenge. For the inboard sections the dynamics associated with leading edge separation is difficult to predict, although some codes are close to the experiment. For the more outboard sections the onset and extent of trailing edge separation is a challenge to simulate.

The corresponding ***loads*** comparison can be found in Figures B.40 to B.45. As expected the results are in agreement with the pressure distributions and generally speaking the CFD codes are able to predict the azimuthal variation of the loads, except for the separated flow case. Only the Stuttgart and Fraunhofer simulations are able to predict the measured abrupt load variation due to leading edge separation at the 25%R and 35%R sections. These two predictions are also seen to feature high frequency load oscillations, likely due to the unsteadiness accompanied by separated flow. Since the measurements are averaged over approximately 35 revolutions, possible high frequency oscillations are likely to be smoothed out in the measurements. Contrary to the lifting line codes, Figure B.45(c) shows the predicted tangential force variation at 60%R for case 2.3 to be in better agreement with the experiment.

4.3.3 Model types

Similar to the axial flow analysis as described in section 4.3.3, results between code types have been averaged to give a better overview of the differences between them. The same code types are distinguished, where all CFD simulations feature a fully turbulent boundary layer and are indicated by 'CFD' in the legends. A summary of the codes used to determine the average is given in Table 4.2. To obtain the loading averages and standard error,

Table 4.4: Summary of codes used for code type averaging (yawed flow)

Code type	Code names
BEM	CENER_FAST, DTU_HAWC2, DTU_HAWC2NW, ECNAero-BEM, IFPEN_BEM Suzlon_BEM
FVW	ECNAero-AWSM, IFPEN_VL, ONERA_PUMA
AM	DTU_AL, Uppsala_AD
CFD	DLR_TAU, DTU_EllipSys3D, FW_IWES_CFD, IFE_CFD, Onera_ElsA USTUTT_FLOWer

the same data reduction procedure is adopted as for axial flow. Since we are interested in the load variation as a function of azimuth, all supplied code results are linearly mapped onto an azimuth angle distribution with a step of 5°, prior to calculating the average and standard error for each code type.

The results for the sectional forces are illustrated in Figure 4.4 to 4.9. It can be confirmed that for yawed flow conditions CFD outperforms BEM models in terms of trend and absolute level agreement with respect to the experiment. For the attached flow cases (2.1 and 2.2) the predicted trend of FVW models is seen to be in close agreement with CFD and experiment. Judging by the red error band of the BEM code type, the variability between the used engineering extension models is significant. As for axial flow conditions, the variability between CFD simulations is also noticeably present. This is most significant the case in separated flow conditions. As was commented upon already in the lifting line and CFD sections, predicting the measured tangential force variation at 60%R for Case 2.3 is demonstrated to be a challenge for lifting line models in Figure 4.9(c). Although the trend of CFD is much better in this case, the large error band indicates large variability between the underlying CFD codes.

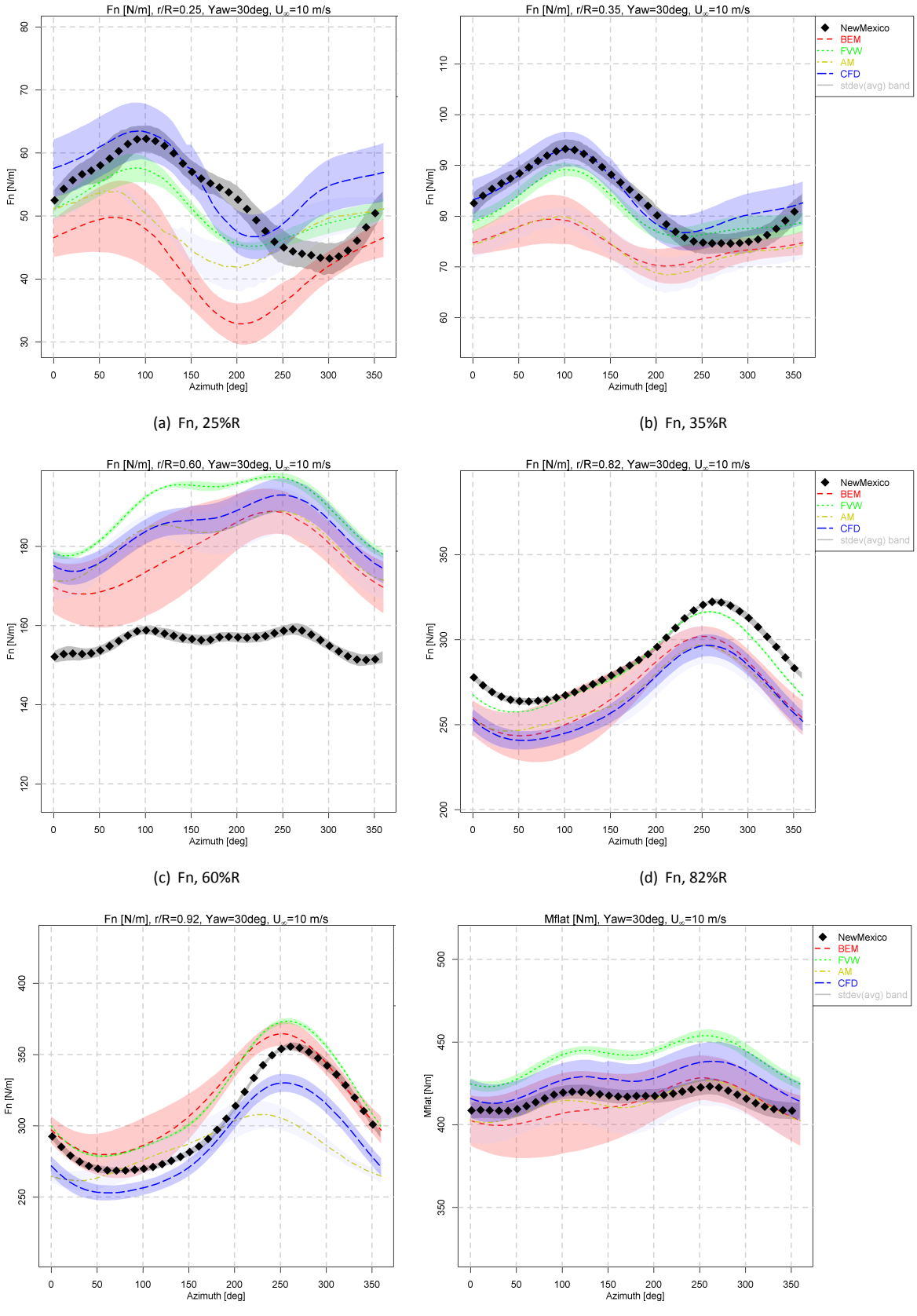

(a) Fn, 25%R

(b) Fn, 35%R

(c) Fn, 60%R

(d) Fn, 82%R

(e) Fn, 92%R

(f) Mflat

Figure 4.4: Chord normal force and flatwise blade root moment, Case 2.1

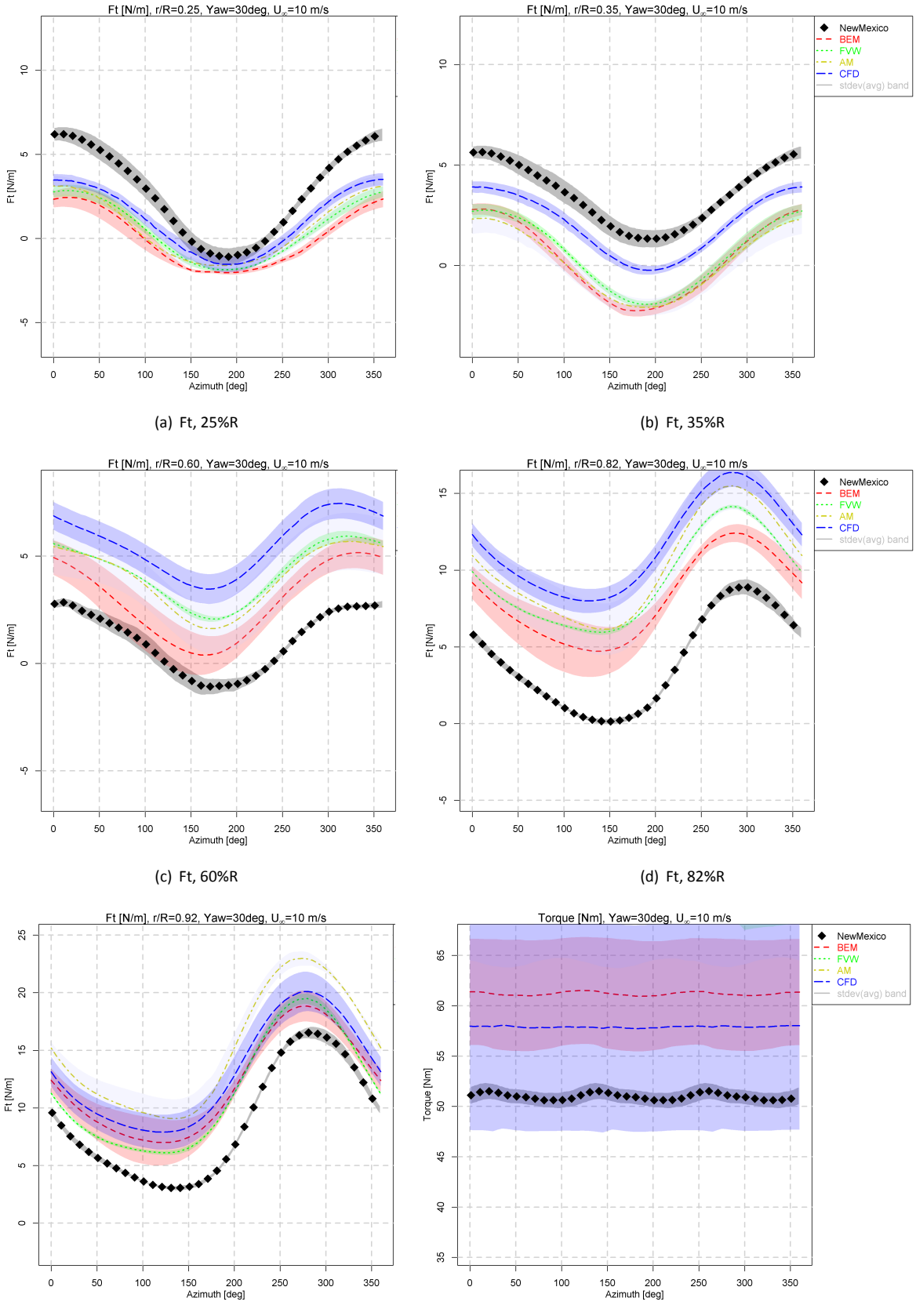

(a) Ft, 25%R

(b) Ft, 35%R

(c) Ft, 60%R

(d) Ft, 82%R

(e) Ft, 92%R

(f) Torque

Figure 4.5: Chord tangential force and torque, Case 2.1

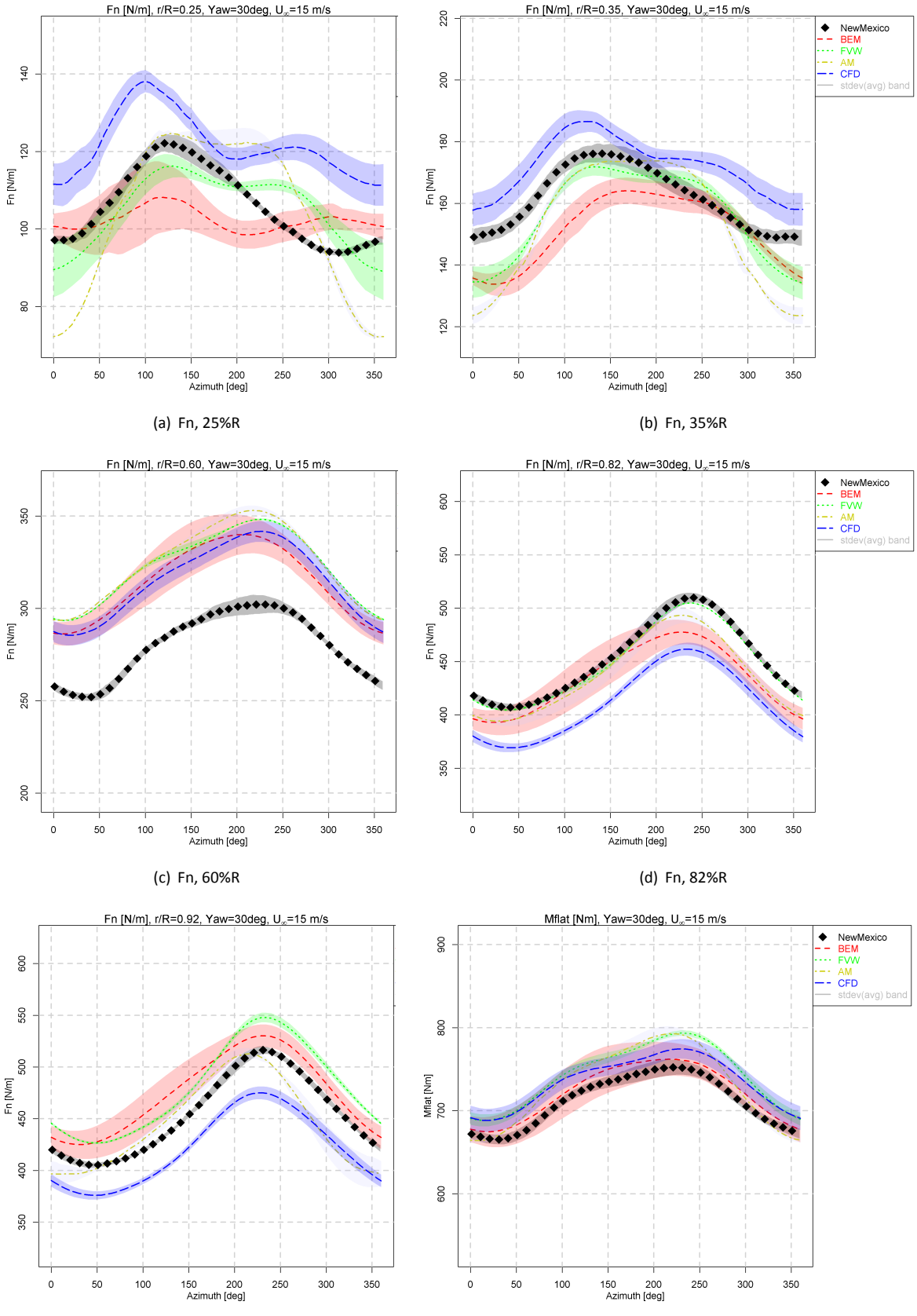

(a) Fn, 25%R

(b) Fn, 35%R

(c) Fn, 60%R

(d) Fn, 82%R

(e) Fn, 92%R

(f) Mflat

Figure 4.6: Chord normal force and flatwise blade root moment, Case 2.2

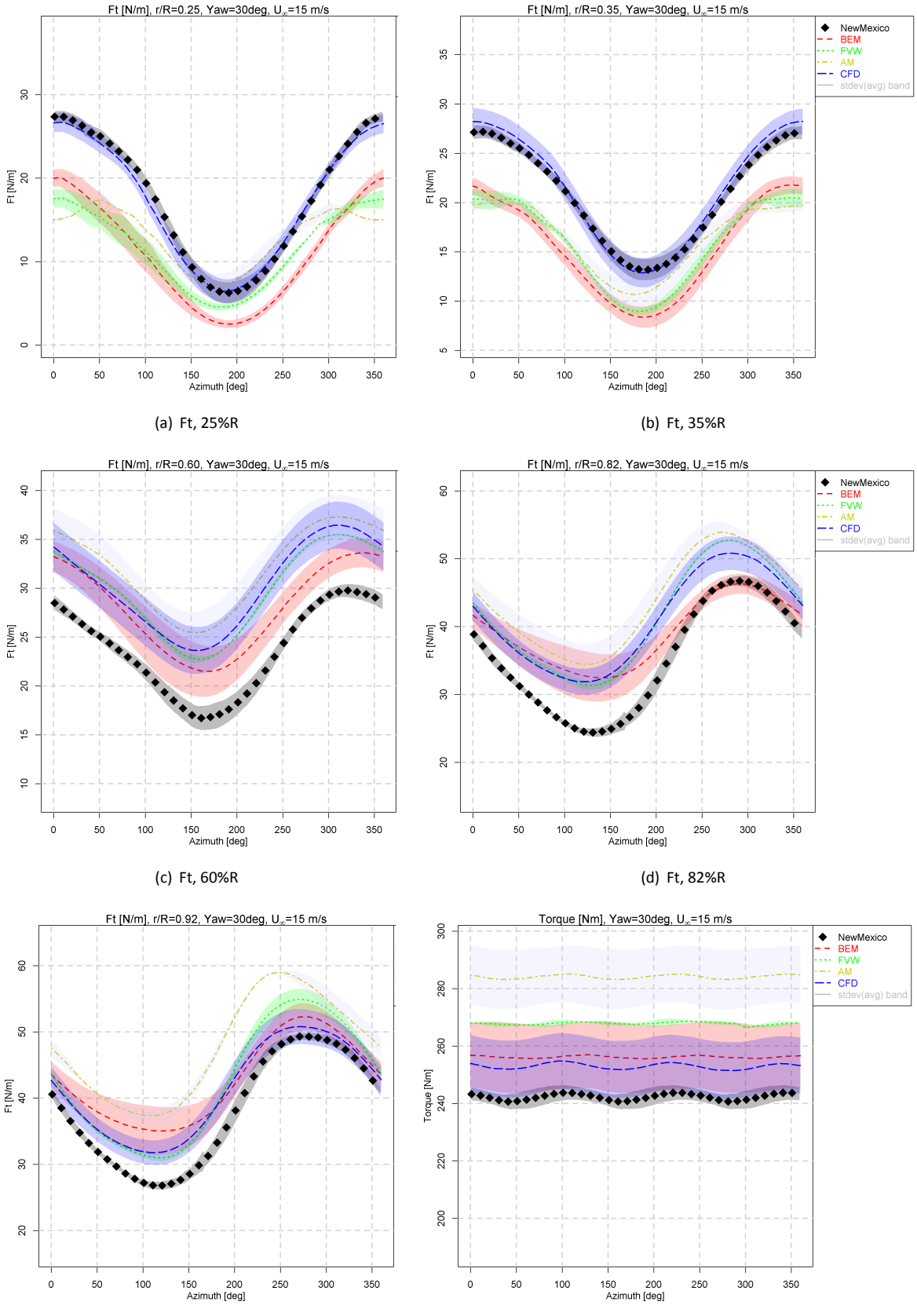

(a) Ft, 25%R

(b) Ft, 35%R

(c) Ft, 60%R

(d) Ft, 82%R

(e) Ft, 92%R

(f) Torque

Figure 4.7: Chord tangential force and torque, Case 2.2

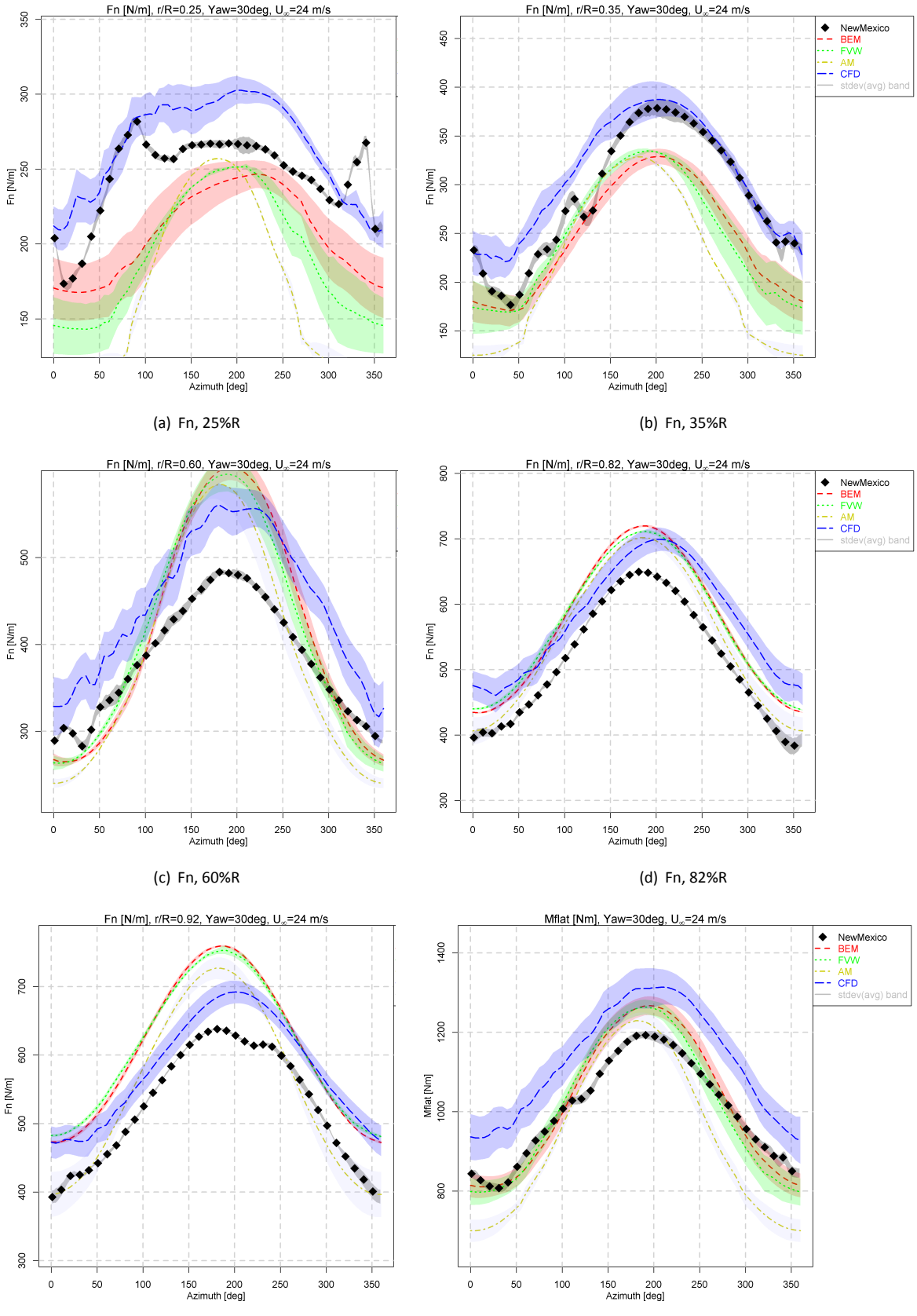

(a) Fn, 25%R

(b) Fn, 35%R

(c) Fn, 60%R

(d) Fn, 82%R

(e) Fn, 92%R

(f) Mflat

Figure 4.8: Chord normal force and flatwise blade root moment, Case 2.3

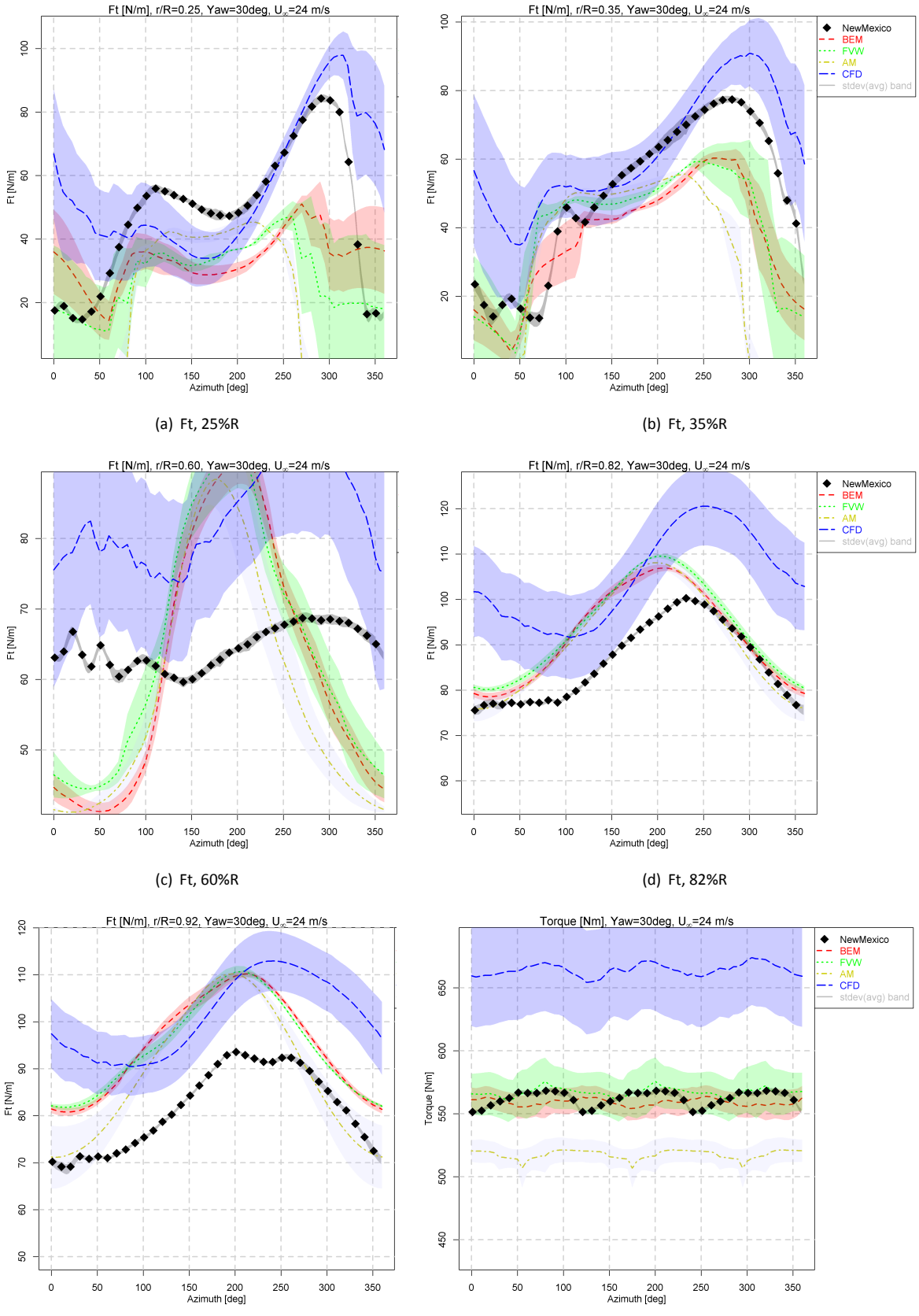

(a) Ft, 25%R

(b) Ft, 35%R

(c) Ft, 60%R

(d) Ft, 82%R

(e) Ft, 92%R

(f) Torque

Figure 4.9: Chord tangential force and torque, Case 2.3

4.3.4 Velocity traverses

The results of the velocity traverse are given in section B.3. The ***axial traverse*** plots are shown in Figure B.46 to B.48 for the axial, radial and tangential velocities u, v and w at y=-1.5 m and y=+1.5m for the three defined cases. Where the upwind part of the plots yields reasonable agreement between measurements and predictions, differences in convection of tip vortices and blade wake result in a large scatter downwind. The same can be observed for the ***radial traverse*** plots shown in Figure B.49 to B.51 at x_m=-0.3 m and x_m=+0.3 m for the three defined cases. In addition to that, the codes simulating the blockage of the nacelle can clearly be distinguished.

4.4 Convergence of CFD simulations

4.4.1 Objective

The objective of this work was to study the sources of the discrepancies within the CFD computations shown during Mexnext-III. Few aspects have been studied, like computational boundary influence and convergence issues and criteria. In order to have more robust comparisons and understand better different partners results, a table has been generated where the details of each computation are summarized. The table, that is useful for this project, could be improved and therefore modified for the next project and general research papers, since it contains quite detailed data of the computations and results (includes information about the inputs, computations and the post-processing). Finally, Appendix F gives the detailed definitions of all CFD methods and meshes employed within Mexnext-III.

4.4.2 Convergence criteria

During Mexnext-III, the difference in results were tried to explain sometimes due to the lack of convergence, or due to the different level or convergences. Some of the cases were challenging, like the 10 m/s case (turbulent-state) and the 24 m/s where the flow has massive separation regions. On the top of that, apart of the blade loads, the wind flow was also compared since it was also measured through PIV during the experiments.

Several researchers has proposed different convergence criteria, and it can be said that despite we have advanced, this is still an open work. However, the studied criteria are presented in the following sub-sections.

Criterion 1

Initial proposal focuses in the overall load convergence of the wind turbine. It considers a converged solution when in the last revolution, the variation of the Thrust and Torque forces are smaller than 0.25% and 0.50% respectively. Regarding the flow convergence, longer computational times were required and the criterion was less precise, since was said that the convergence was obtain, when no visual differences on U (axial flow) at the last downwind measured location were found. The application of this criterion can be seen in Figure 4.10.

One of the problems that could have this criterion is that when significant stall exist, there could be large load fluctuations despite the solution is converged. And also that the more unsteady inboard stations, that normally reach convergence later has less weight when total forces are studied. To avoid this last point, a small deltas in thrust and torque were selected.

Criterion 2

The second criterion states that the load and flow convergences should be achieved together. This is a kind of *running mean* that allows to smooth out the short-term fluctuations and highlight the long-term. In theory is valid for more cases than the first criterion since it is a more general and more conservative assumption. However, the coupled convergence could be reached later and have to be set the length of the *running mean*?

Criterion 3

This criterion is based on the Coefficient of Variation (CV) = STD / avg, also known as RSD.

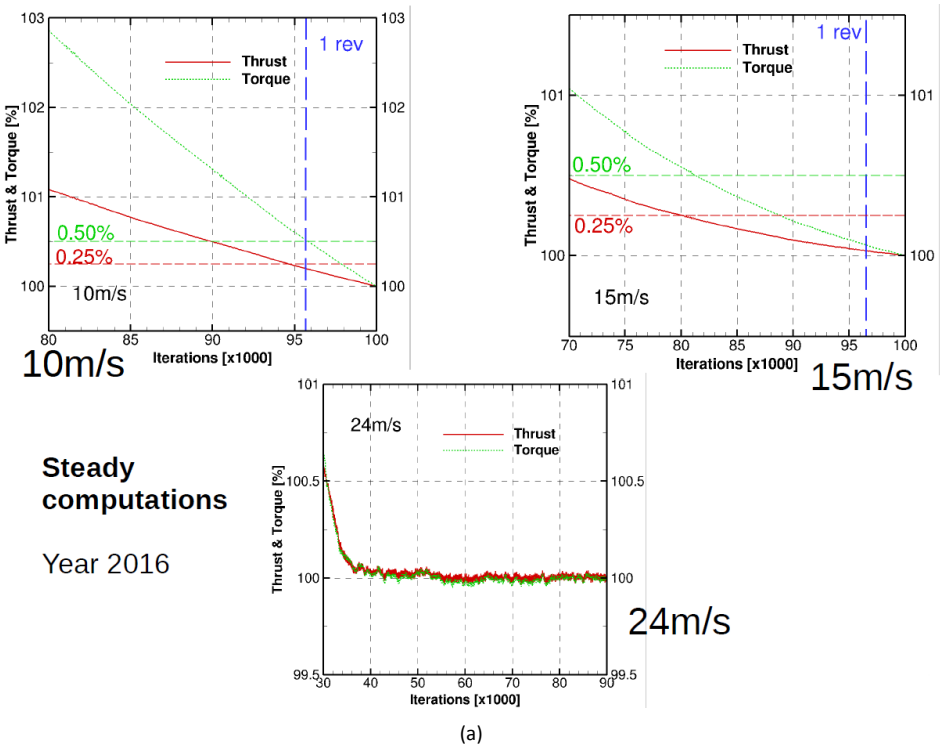

(a)

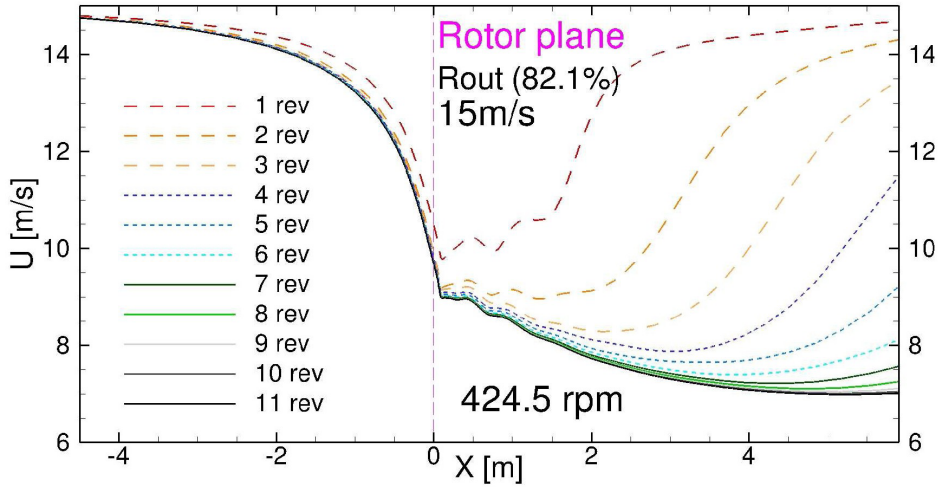

(b)

Figure 4.10: First convergence criterion: for the loads (above) and flow (below) of the MEXICO turbine

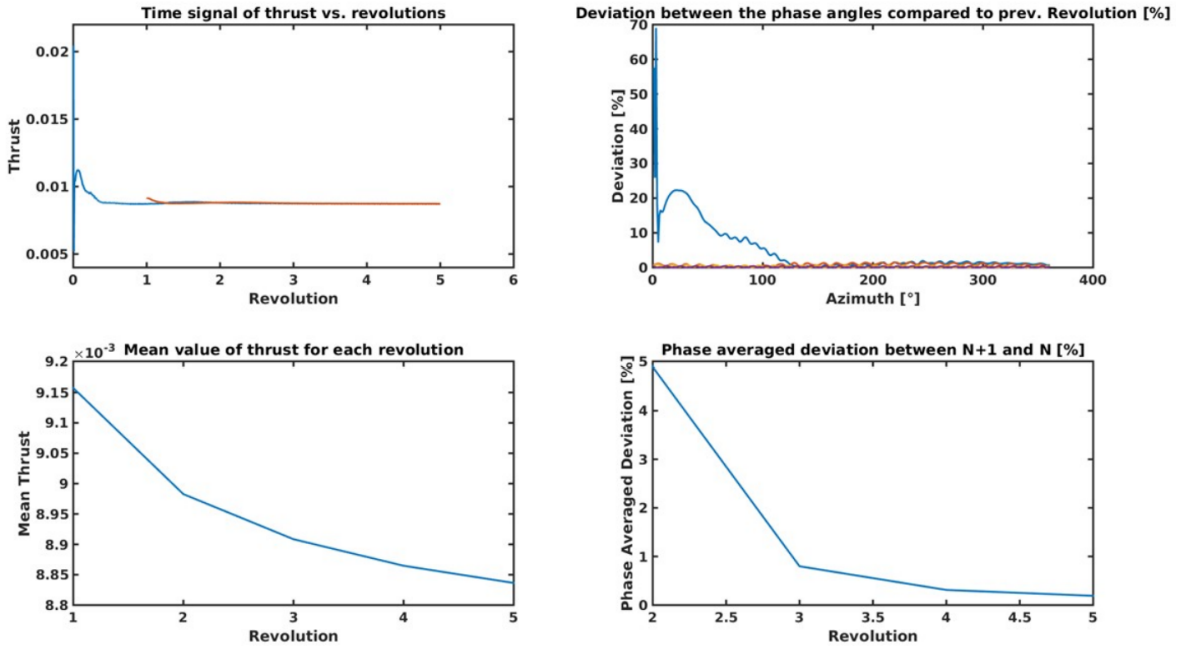

Figure 4.11: Fourth convergence criterion: Phase method (MEXICO turbine)

After calculating it for different number of steady steps, it could be established that a variation of CV smaller than 0.005% indicates that the total loads are converged (when checking the worst CV of the Thrust and the Torque values). From previous experiments, the NREL Phase VI, the following values were obtained: 0.086% for the Thrust and 0.287% for the Torque in solutions that were considered converged. A drawback of this criterion is that in order to define an universal CV value, there is a need of a large amount of post-processed results. So this point is open to be improved with a more accurate CV value.

Criterion 4

This criterion is similar to the first one, but it is included due to the phase approach that it does. The objective here is to measure the phase difference in loads (for example 1°with 361°, 2°with 362°,... or even 1°with 121°in a 3 bladed rotor with no yaw, no tilt,... (which is the case for the MEXICO rotor). Focusing in the deep stall case (24m/s of New MEXICO experiments analyzed in Mexnext-III), a criterion was set that the difference in load between phases should be smaller than 0.05% (see Figure 4.11). Like the rest of the criteria, where a value is given, it is mentioned that these values are not final. So far they are the best estimated that have been found, but if more experiments and computations are included in the comparison, they should be updated to a more robust value.

4.4.3 Computational boundaries location influence

A computational domain variation study have been performed for a single CFD method (WMB). The domain dimensions were modified in flow direction leaving constant the radial boundaries (far-field), as can be seen in the Figure 4.12. The main characteristics of the meshes used in this study are summarized in the Table 4.5 and cell distribution can be observed in the lower part of the Figure 4.12. Identical cell distribution has been maintained from -2.7R to 8.3R.

The three baseline cases of the Mexnext-III comparison round were computed (the 10, 15 and 24m/s cases at 425 rpm, and with 0° of yaw angle that replicates the New MEXICO experiment) in both meshes. For that,

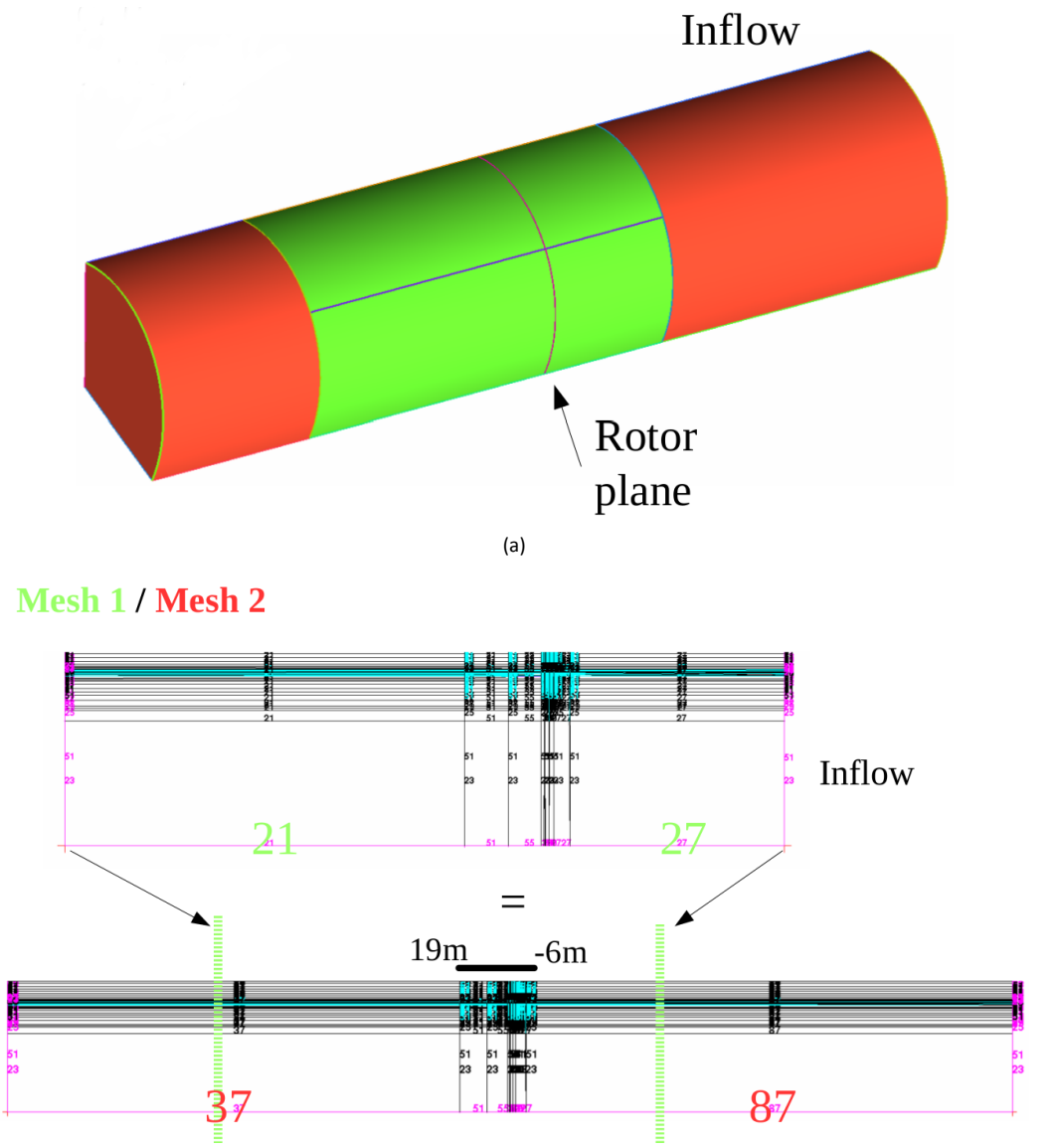

Figure 4.12: Computational domain boundaries and cell distribution along them

Table 4.5: Main characteristics of the meshes used for the computational boundary location influence study

	Mesh 1 (Short)	Mesh 2 (Large)
Cells chord-wise	417 (+37 TE)	417 (+37 TE)
Cells span-wise	412	412
1^{st} cell height	1e-5c (c=0.24m)	1e-5c (c=0.24m)
Total number of cells	71,153,232	83,606,640
Domain		
Inflow	6R	20R
Outflow	12R	20R
Far-field	5R	5R

WMB (a compressible CFD method) has been used. The computations were periodic in time and space (just one third of the rotor was modeled which included o single blade, the nacelle and the hub) and the k-ω SST turbulence model was used.

The integrated loads show in Table 4.6 that the differences are larger for slower wind speeds. However, the lower values obtained at smaller wind speeds also help to increase this percentile differences. The distributed force coefficients along the blade are shown in Figure 4.13 where these differences can be observed on the entire blade span (the effect being smaller towards the tip of the blade). So the differences could be explained due to increase on the inflow speed, as shown in Figure 4.14. Here can be observed that the inflow wind speed is larger for the three cases, being more sensible for the 10 and 15m/s cases. At -0.3m location, just before the wind turbine rotor plane, the velocity is reduced by 1.7%, 1.2% and 0.3% (10, 15 & 24m/s).

Table 4.6: Differences in the final integrated loads due to the computational boundary locations

Loads	Case [m/s]	Mesh 1 (Short) [N] & [Nm]	Mesh 2 (Large) [N] & [Nm]	Difference [%]
Thrust	10	978	963	1.6
Torque		96	92	4.0
Thrust	15	1,683	1,665	1.0
Torque		349	341	2.3
Thrust	24	2,403	2,400	0.1
Torque		842	839	0.3

In previous figures, has been observed that the inflow speed decreases with a larger domain, and therefore the loads also decrease. So, it can be concluded that the computational domain boundaries are more sensible with the inverse of the wind speed. However, this study also leaves an open questions: What will happen if the Far-field direction is modified?

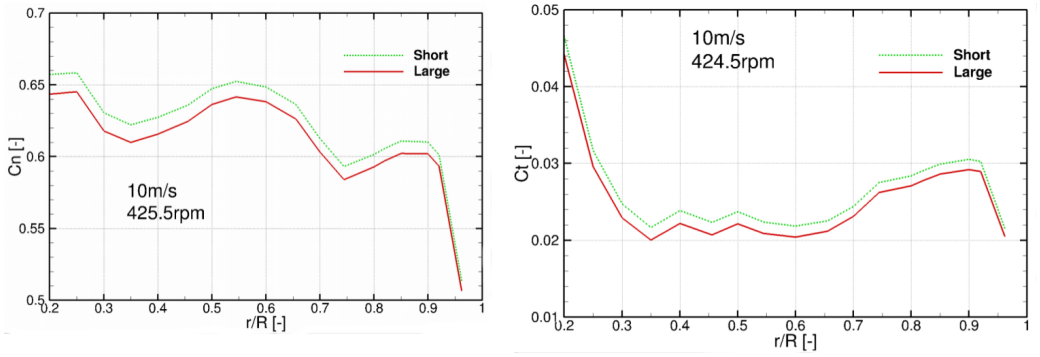

(a)

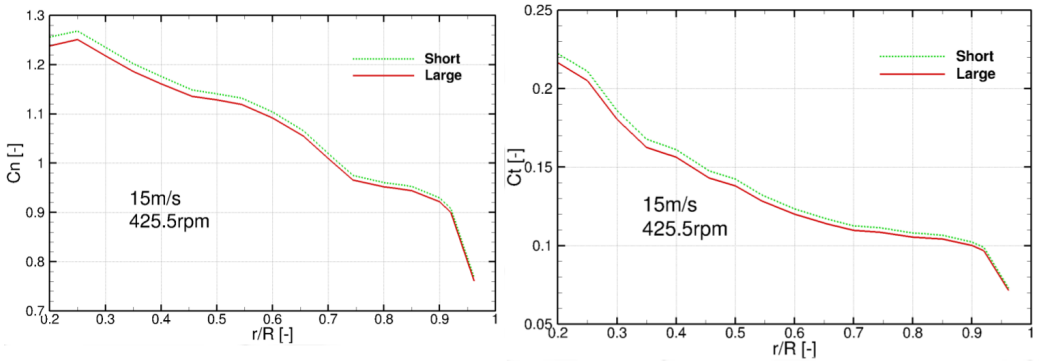

(b)

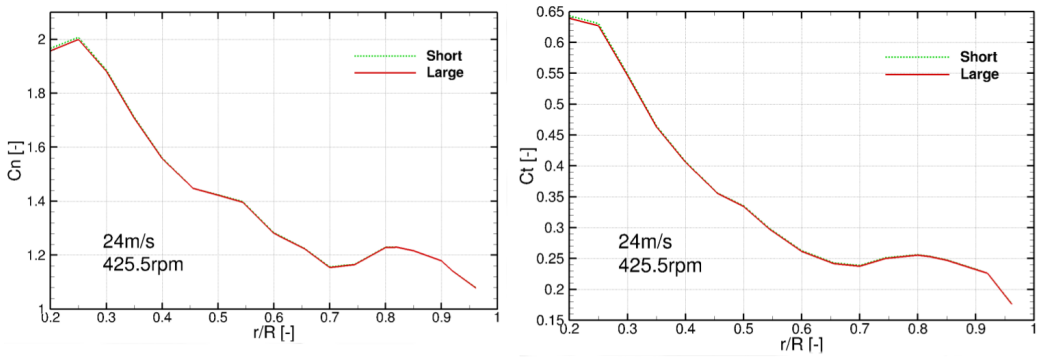

(c)

Figure 4.13: Comparison between the force coefficients for the three wind speeds and both computational domains (Short/Mesh1 and Large/Mesh2)

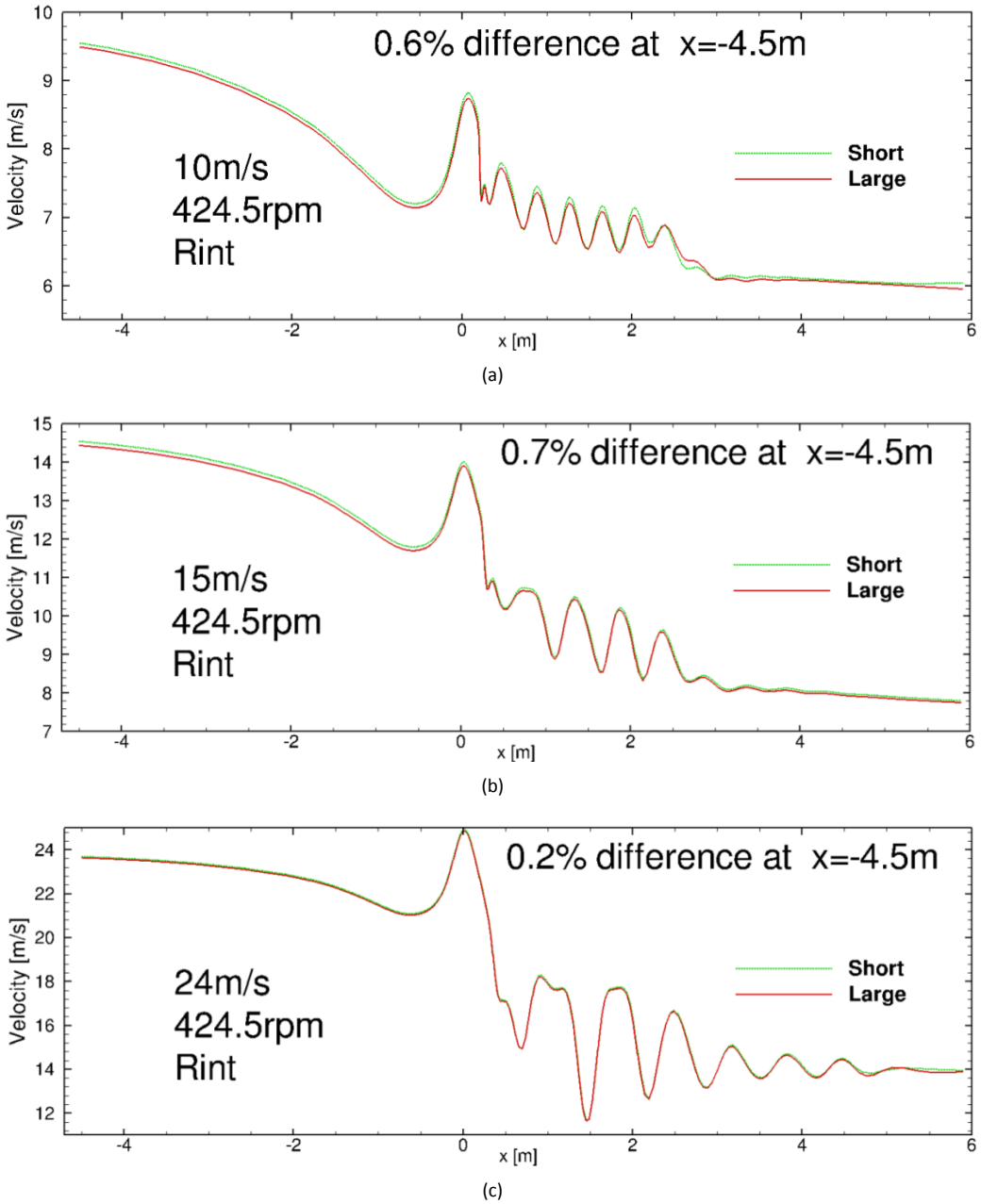

Figure 4.14: Comparison between the axial velocity of the flow at 22%R station of the blade for the three wind speeds and both computational domains (Short/Mesh1 and Large/Mesh2)

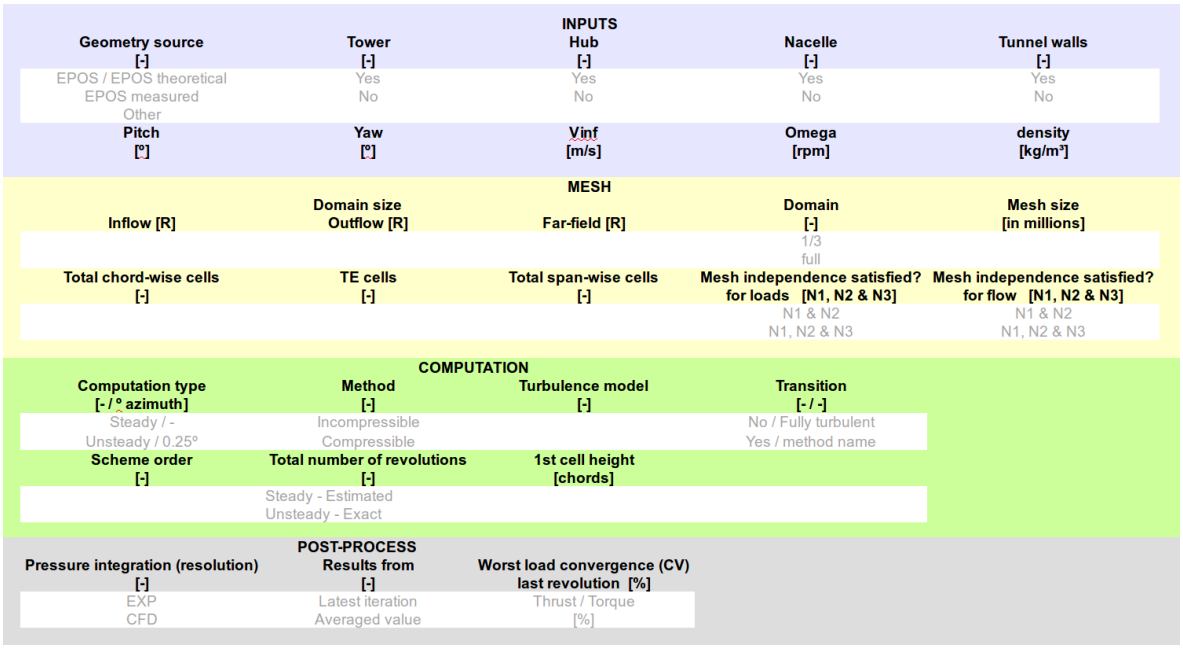

Figure 4.15: The list of the parameters that have been agreed within the Mexnext-III project to provide when a computation is performed in order to obtain better comparisons and conclusions

4.4.4 What to provide together with results

It has been agreed by the project participants to share some data in order to make comparison more meaningful and error proof. For that, the data that has to be provided was categorized in four aspects, as is also shown in Figure 4.15.

The first one was named **Inputs** and collects the geometrical aspects of the model and experimental set-up. This includes blade geometry source, if the tower, hub and/or nacelle were included, as well as the wind tunnel walls, the pitch and yaw angles of the turbine, its rotational speed, the inflow speed and the air density that has been used.

The second category is the **Mesh**. There the computational domain size is defined (inflow, outflow and far-field), as well as the domain that has been modeled (full or a segment). Then the characteristics of the mesh are described (total mesh size, the number of cells that have been used at each section, along the span and also at the trailing edge). To finalize with the mesh section, if mesh independence studies were carried out is asked for loads and for the flow. The nomenclature in this case, N1, N2 and N3 relates to mesh variation of two times in the three dimensions (for example, N1 mesh will have 8 times less, 2 in *x*, 2 in *y* and 2 in *z*, cells than the N2 mesh). Perhaps another parameter that could be added is to define whether the mesh was structured, unstructured or hybrid.

Then, the **Computation** parameters are requested. Here the type of computation is defined (steady or unsteady, and the azimuth steps in degrees for the unsteady ones), the employed method (compressible or incompressible), the used turbulence model and the transitional model, if any, as well as the scheme of the solver. Finally, the computed number or revolutions are asked together with the 1^{st} cell height. This last parameter could fit perhaps better in the mesh section. And as an addition, it could be added the employed solver name.

The fourth, and the last section, is the **Post-process**, where the pressure integration comes from (full CFD or the experimental resolution), if the provided results were taken from a fixed time-step or solution or they were the average of several, and the worst convergences in thrust and torque based on the *Convergence Criterion 1*, shown in the subsection 4.4.2.

4.4.5 General analysis of what has been provided

Based on the inputs added to the table from the majority of the participants, some general conclusions can be derived.

Regarding the first category, **Inputs**, the 90% of the computations that were presented in the report, were performed with the theoretical geometry of the MEXICO blade. The tower was neglected by 90% of the computations. However, when yawed flow was studied, the tower was present at 25% of them. The hub and the nacelle were taken into account (modeled) in the 90% of the simulations since at inboard stations the effects are noticeable, as well as for the yawed cases, where they were included in the 75% of the simulations. The wind tunnel walls were neglected by all (100%), since their influence was negligible according to Mexnext-I project. In all the computations the pitch and yaw angles were set in the same way agreeing with the experimental set-up (100%). The inflow velocity of the wind was common for the 67% of the cases at each baseline wind speed, and the rotational speed at 83% of the simulations (the differences in the rotational speed were minimal, of 0.26%, between the different 17% and the rest). The density follows the same trend as the inflow wind speed, being common for the 67% of the simulations.

Regarding the **Mesh** parameters, the computational boundaries were located in average at 18.3R towards the inflow, and another 18.3R towards the outflow, being the far-field located at 14.4R. However, the largest and smallest inflows were located at 32R and 5R, as well as the outflows, and the far-fields. The entire domain (full rotor) was modeled for the 50% of the axial flow simulations, being the unsteady computations modeled as entire in all the cases (100%), and the 40% of the steady simulations. In average, the employed mesh size was of 53 million cells, being the maximums of 145 millions for the entire domain and 83 millions for the one third domain. The minimum was of 21 million cells for the full domain configuration. The average chord-wise and span-wise cell distributions were of 273 and 208 respectively, with 25 cells in the trailing edge. The maximum chord-wise cells were set in 417 and the minimum in 180. For the span-wise distribution the maximum was of 412 and the minimum of 139 cells. For the trailing edge, the cell distribution ranged from 37 to 15 cells. To finalize this section, the mesh independence study was done for the 50% of the simulations. However, this section was not defined as clear as it should be so the values on mesh independence study should be taken with care.

Moving towards the **Computation**, as expected the 100% of the yawed flow cases were computed as unsteady with an average azimuth steps of 0.65°, being the maximum of 1° and the minimum of 0.25°. From the simulations that have been collected in the table, 80% of them were done with compressible methods. The most employed turbulence model was Menter's k-ω SST model (73%), followed by SA-DDES (20%) and Wilcox's k-ω (7%). 80% of the simulation were performed as fully turbulent, and all of the computations (100%) were done with second order schemes. The computations were run in average for 17 revolutions having a maximum of 36 and a minimum of 3 revolutions. Despite the lowest wind speeds needed more revolutions to converge, the amount of revolutions for each of the three baseline cases are scattered and do not follow the logical pattern of more revolutions at lower wind speeds and less at higher wind speed. The average 1^{st} cell height is located at 4.3x10^{-6}chords, being the largest difference between the simulation of one order (1x10^{-6} vs. 1x10^{-5}).

To finalize with the **Post-process**, mention that the pressure data was obtained in 80% of the simulations from full CFD resolution, and the solution was given from the last iteration in 60% of the cases. When just yawed flows are taken into account, this value goes to 50%. To finalize, the averaged thrust and torque variation on the last revolution are quite similar and are set in 0.13% and 0.14%. These values needs to be taken with care since the post-processing was partners base and these are the results of the first iteration.

4.5 Conclusions

A large comparison exercise has been performed featuring six simulation cases in axial and yawed inflow conditions, containing results of over 20 codes ranging from BEM to CFD. More than 10 different variable types ranging from lifting line variables to pressures, loads and velocities have been compared for the different conditions, resulting in over 250 comparison plots. The result is an unique insight in the current status and accuracy of rotor aerodynamic modeling.

Averaging over model types has provided a quantification of the uncertainty and variability of different code types depending on operational conditions. In steady axial inflow and attached blade flow conditions, lifting line models are shown to reasonably accurate predict wind loading provided that good quality airfoil data is

used. For separated flow conditions the lifting line assumption does not hold and CFD codes start outperform lifting line codes. However the variability between CFD results remains significant. Unsteady conditions represented by yawed inflow are challenging to model for BEM type codes, although free vortex wake code loading results are in good agreement with the corresponding CFD simulations and measurements. Dynamic separation on the blade appears to be challenging to model for all code types including CFD. The velocity traverses indicate that generally speaking rotor blockage and the associated wake expansion are well predicted in comparison to the measurements. More challenging are the wake characteristics in terms of tip and root vortices and their locations as well as the dissipation of the blade wake.

To study the sources of the discrepancies between CFD simulations and give some guidelines, an attempt was made to quantify the influence of computational domain size and (grid) convergence. Although this helps in reducing the variability between CFD results, it can be concluded that the large number of actions and parameters to define make the result of CFD simulations prone to discrepancies due to the 'human factor'.

5. Task 4.1: Standstill and IEC Aerodynamics

5.1 Introduction

This task has been carried out from June 2015 to June 2017 and was created in order to provide modelers with experimental data that can be used to validate the models in conditions where wind turbines experience failures. Particular attention was given to the parked load case (representing one of the design load cases in the IEC-61400 standard [1]) and on a load case (off-pitch) where one of the blades is pitched off 20 deg, (representing again the pitch deviation mentioned in the IEC-64100 standard [1]) which was considered to be useful for future analysis and comparisons with common design standards. The parked load case measurements were widely analyzed already in Mexnext-I [68] and were repeated due to uncertainties and errors in the previous measurements. The off-pitch measurements are novel. The idea of carrying out a measurement campaign on off-pitched load cases came from the fact that, when in operation, wind turbine controllers or mechanical faults could possibly lead to under or over pitching of one or more rotor blades with consequent rotor imbalance and increase in fatigue loads on bearings and gearbox but also to drastic change in power production. Even if guidelines for design and certification are prescribed in the IEC-61400-1 standard [1] and it is well known that pitch fault conditions are quite likely to happen in operational conditions [160], limited data is currently available and it is somehow unknown how the performance of each blade is affected by a pitch misalignment.

A description of standstill and off-pitched experiments and the main measured parameters is hereby described. This is followed by a description of simulations done for the off pitched case. It is followed by an analysis of these including conclusions.

5.2 Experimental overview

The MEXICO rotor is a three bladed rotor model of 4.5 m diameter equipped with a speed controller and pitch actuator. The rotor blades specifically designed for the MEXICO wind tunnel measurement campaign and they are instrumented with 148 fast Kulite® XCQ-95-062-5 to measure the pressure distribution along the airfoil sections at different span locations The pressure sensors are distributed on the three blades (see Figure 5.2). Blade 1 (25% and 35% span), blade 2 (60% span), blade 3 (82% and 92% span).

Stand still Measurements

The standstill measurements were all done at a wind speed of 30m/s with a locked rotor in order to avoid rotation. From global to local measurements, the three forces and the three moments were measured at the root of the tower with a 6-components balance. At the root of each blade, the edge-wise and the flat-wise bending moments were also measured using strain gauges. Pressure distributions measurements were also measured at the five section of the blades. A range of measurements with different pitch angles were carried out for clean configuration (where the blade were left clean), rough configuration (with trip wire), spoiler configuration (where a spoiler was added to the blades) and serration configuration (where a serration add-on was added to the blades).

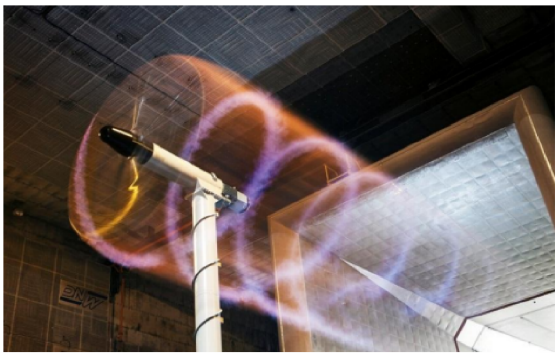

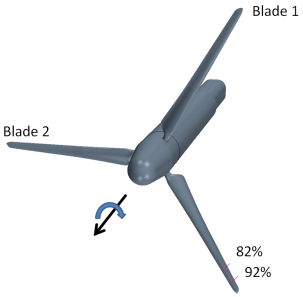

Figure 5.1: The MEXICO rotor in the DNW wind tunnel (left) and the CAD model of the of the rotor with blade 2 off-pitched (right).

Table 5.1: Measured data points with relative pitch angles for different configurations

Rough	**Pitch [deg]**	90	87	85	83	81	79	77	75	73	71	60	30	69	67	65	55	50	40	35
Clean	**Pitch [deg]**	90	88.5	87	85.5	84	82.5	81	79.5	78	76.5	75	73.5	72	70.5	69	67.5	66	64.5	63
Spoilers	**Pitch [deg]**	90	88.5	87	85.5	84	82.5	81	79.5	78	76.5	75	73.5	72	70.5	69	67.5	66	64.5	63
Serrations	**Pitch [deg]**	90	88.5	87	85.5	84	82.5	81	79.5	78	76.5	75								

Table 5.2: Measured data points with relative yaw angles - Pitch Angle=90deg

Yaw [deg]	90	60	45	30	15	-15	-30

The measurements carried out are presented in Table 5.1 and Table 5.2. In addition, PIV measurements in the wake were also carried out at different wind speeds and for different configurations (Table 5.3).

Off-Pitch experiments

In normal operational conditions, all the sensors are fully functional. For the pitch misalignment runs, the pitch angle of blade 2 was reduced by 20deg in comparison to the other blades. The rotational speed was limited to 325 rpm to minimize instabilities. In the pitch misalignment test, the pressures were then measured only from the sensors placed in the tip area on blade 3 (82% and 92% span). The blades have been instrumented with strain gauges at the root of all three blades to measure the flatwise and edgewise root bending moments. The strain gauges were applied at 5 cm in spanwise direction from the blade root. A number of configurations and combinations of different pitch angles and wind speeds were tested and they are shown in Figure 5.2.

5.3 Description of simulations

The present section describes the simulations to reproduce the experiments on a imbalanced rotor with one blade off pitched by 20 deg carried out within Mexnext-III. Models of increasing complexity were used (Blade Element Method simulation (BEM) lifting line with free vortex wake (FVW) and URANS CFD) and the results were compared. The three different load cases corresponding to a tip speed ratio of 5.24, 7.6 and 11.2 were chosen from the test matrix performed during the experiments. The rotor speed was kept constant at 325 rpm.

Introduction

While the current status in wind turbine modelling is mostly based on blade element momentum theory, it is well known that these methods are not applicable in highly unsteady flow, stalled conditions and under yawed conditions due to the nature of the theoretical formulation behind them, which is based on independence between blade elements and actuator disk assumption. More generally, complex turbine conditions like yawed

Table 5.3: Measured data points with relative pitch angles and traverse positioning

	V	Pitch	x-trav	y-trav
	m/s	deg	m	m
Standstill PIV 1	10.02	90	-0.12	1.525
	12.53	90	-0.12	1.525
	14.96	90	-0.12	1.525
	17.48	90	-0.12	1.525
	19.98	90	-0.12	1.525
	22.42	90	-0.12	1.525
	24.95	90	-0.12	1.525
	27.42	90	-0.12	1.525
	29.96	90	-0.12	1.525
Standstill PIV 2	30	90	-0.12	0.925
	27.52	90	-0.12	0.925
	24.97	90	-0.12	0.925
	22.43	90	-0.12	0.925
	19.97	90	-0.12	0.925
	17.5	90	-0.12	0.925
	14.99	90	-0.12	0.925
	12.53	90	-0.12	0.925
	10.1	90	-0.12	0.925
Standstill PIV 3	10.08	90	-0.12	0.6
	12.5	90	-0.12	0.6
	14.98	90	-0.12	0.6
	17.49	90	-0.12	0.6
	19.97	90	-0.12	0.6
	22.42	90	-0.12	0.6
	24.96	90	-0.12	0.6
	27.42	90	-0.12	0.6
	30.01	90	-0.12	0.6

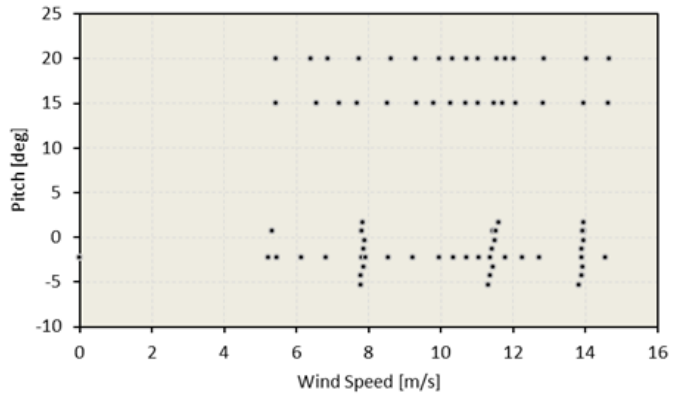

Figure 5.2: Measured data points for off-pitch configurations referring to blade 2

Table 5.4: Load cases

	Load Cases	Wind Speed (m/s)	Rotational speed (rpm)	Pitch angle Blade1,3 (deg)	Pitch angle Blade2 (deg)	Tip Speed Ratio
	LC1	6.89	324.9	-2.3	-2.3	11.118
Normal	LC2	9.99	324.9	-2.3	-2.3	7.66
	LC3	14.52	324.9	-2.3	-2.3	5.274
	LC1OFF	6.81	324.9	-2.3	-22.3	11.248
Fault	LC2OFF	9.97	324.9	-2.3	-22.3	7.667
	LC3OFF	14.56	324.9	-2.3	-22.3	5.259

inflow, pitch asymmetry, or heavily deflected rotor that result in non-uniform induction like blades violate the assumptions of BEM and its correction models limiting its range of applicability [148, 83].

More sophisticated and elegant approaches which imply fewer limitations and a larger range of applicability are currently available. The lifting-line theory models combined with a free vortex wake methods allow to reproduce the complex flow phenomena on wind turbine rotors and, even if local corrections are needed, lifting-line free vortex wake method (FVW) proved to be more accurate in determining wind turbine loads than BEM codes even in individual pitch conditions. Some examples that have been coupled to wind turbine simulations are the AWSM code developed at the Energy Research Centre of the Netherlands, the GENUVP code developed at the National Technical University of Athens [170] the WinDS code developed at the university of Massachussets [44], and the prescribed vortex model implemented in some versions of AeroDyn [34].

An even more advanced approach is to model the full rotor and solve the Reynolds-averaged Navier-Stokes equation (RANS) of the flow around the model. The RANS equations are averaged version of the governing equations where turbulent stresses are modelled in order to provide different levels of closure for the equations. With this approach, statistically unsteady (or non-stationary) flows can be treated [60, 49] and the near wake can be accurately computed [138, 154].

Methods

Load Cases

Three load cases were chosen from the experimental test matrix for reduced rotational speed in order to represent three typical different operational conditions: a load case with low free stream velocity and high TSR (LC1), a load case around design conditions (LC2) and a load case with low TSR and high free stream velocity where the rotor operates in stalled conditions (LC3). Similarly, three load cases were chosen from the pitch misalignment test matrix so that the free stream velocity and thus the loads were comparable and they were named LC1OFF, LC2OFF and LC3OFF. In these three load cases blade 1 and 3 were kept with the design pitch angle of -2.3 deg while blade 2 was pitched at -22.3 deg. See also Table 5.4 for a summary.

BEM and FVW (ECN Aero Module)

The ECN Aero Module [21] was used for the lifting line calculations. It includes both BEM as well as a lifting line free vortex wake formulation, allowing the same external input (e.g. wind, tower, airfoil data) to be used for both models. The BEM formulation is based on PHATAS [89], including state of the art engineering extensions which have matured over decades of research in wind turbine rotor aerodynamics. The free vortex wake method is based on the AWSM code [165]. For the free vortex wake simulation with AWSM, the number of wake points was chosen to make sure that the wake length was developed over at least 3 rotor diameters downstream of the rotor plane. The wake convection was free for approximately 2 rotor diameters downstream. In addition to the BEM and AWSM free wake results, also AWSM simulations were ran using a prescribed wake formulation. A hybrid free-prescribed wake was adopted, drastically reducing the computational effort. Here only a small portion of the near wake was free, whilst the convection of the remainder was prescribed based on the calculated blade induction.

URANS CFD (StarCCM+)

The multipurpose StarCCM+ code from CD-Adapco was used for the CFD simulations and, in the present work, an unsteady RANS (Reynolds Average Navier Stokes) approach was chosen to reproduce the experiments. A sliding mesh technique was used in the rotor plane for the URANS simulations to reproduce the rotor.

The full rotor consisting of three blades, hub and nacelle was modeled. The wind tunnel was not modeled. A trimmed meshing technique was used to discretize the rotor surface. The cell size on the surface was chosen so that the final grid consisted of a minimum number of 180 cells in the chordwise direction. A local surface grid refinement was applied at the leading edge. 15 cells in the boundary layer growing with a growing factor of 1.25 were used and the first cell placed so that a maximum wall y+ of 1 could be achieved on the blade, allowing thus the first cell to be placed in the viscous sublayer area of the boundary layer. A preliminary grid dependency study was carried out on a simpler configuration (one blade, 1/3 of the domain and steady state configuration) in order to ensure a grid independent solution in steady state conditions. A coarser mesh with only 5 cells layers of prismatic cells in the boundary region was generated on the nacelle and hub. The volume grid consisted of cubical cells with three cylindrical levels of grid refinement, progressive coarsening upstream and downstream was obtained by doubling the cell's characteristic length. The first refinement region, closer to the rotor plane, extends from -0.15m upstream to 0.4m downstream and it has a radius of 2.5m and a characteristic length of 0.02m, the second refinement region extends from -1m upstream to 1m downstream, it has a radius of 2.6m and it has a characteristic length of 0.4m and the third region extends from the inlet to 4m downstream, it has a radius of 4m and a characteristic length of 0.08m. A progressive coarsening was used in the rest of the domain (Figure 5.3).

The numerical wind tunnel has a square section of 30mx30m and a length of 80m. The rotor was placed at a distance of 15m from the inlet. The final mesh consisted of ca. 15.000.000 cells

Fully turbulent conditions were used in the simulations and the k-omega SST turbulence model introduced by Menter [96] was used throughout the whole simulation matrix. One degree per time step and 10 iterations per time step resulted to be sufficient in order to ensure convergence. A second order precision central difference numerical scheme was used to solve the Navier Stokes equations. A total number of 2 complete rotor revolutions were recorded and torque, thrust and pressure fields were averaged in time after the monitored values converged. Velocity inlet boundary conditions for the inlet, pressure outlet for the outlet and symmetry for the side walls were used in the simulation.

5.4 Simulation results

In this section, the results obtained with URANS, FVW and BEM are presented and compared with the experimental data from the New Mexico campaign. Torque and axial force on each blade and on the total rotor are presented and pressure distribution on blade 3 from CFD simulations are compared with experimental values. Finally 3D effects are briefly discussed.

Axial Force and Torque on Full rotor and single blade

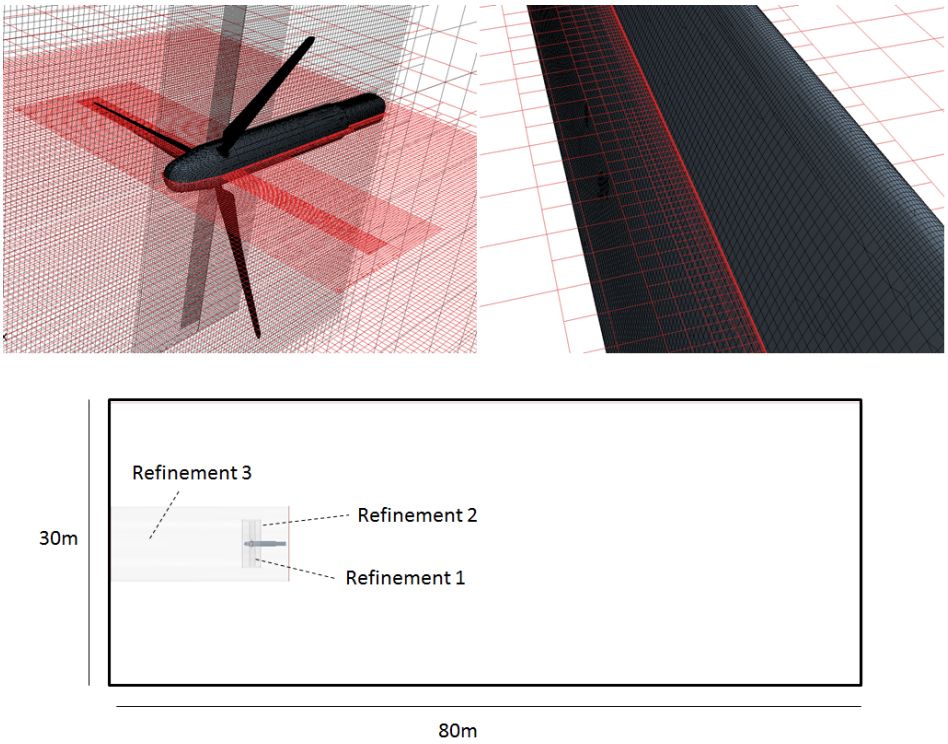

Figure 5.3: Mesh details and domain size.

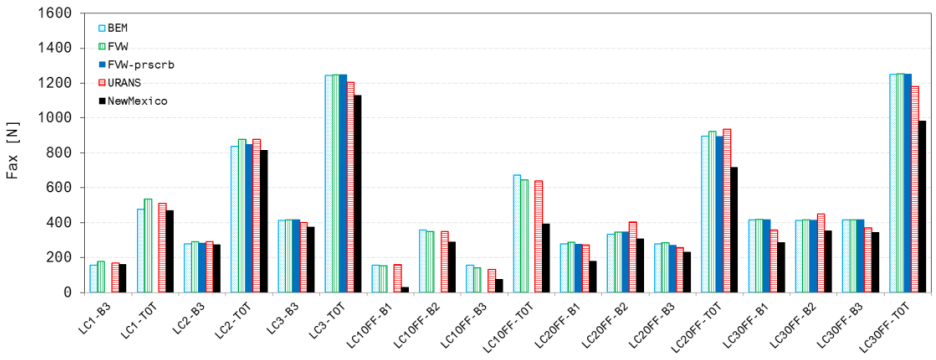

Figure 5.4: Comparison between thrust (Fax) from simulations and experimental values.

The results relative to all 6 load cases are presented in the histograms in Figure 5.4 and Figure 5.5. URANS simulations tend to overestimate the axial force Fax, particularly when the rotor is operating in stalled conditions and the k-omega SST turbulence model only partially manages to correctly reproduce the massively separated flow in the suction side of the blade. This behaviour is also clear when looking at the axial force on blade 2 for the off pitched load cases. With the turbine operating in design conditions, a general good agreement can be however found while larger differences and larger scattering between the models are noticeable in the fault conditions. All the models tend to overestimate the axial force.

Larger scattering between the models is noticeable when comparing the generated torque presented in Figure 5.5. All the models show an overall satisfactory comparison with the experimental data for normal operation conditions while larger scattering can be seen in the fault conditions especially in LC1OFF were the URANS simulations provide a better solution.

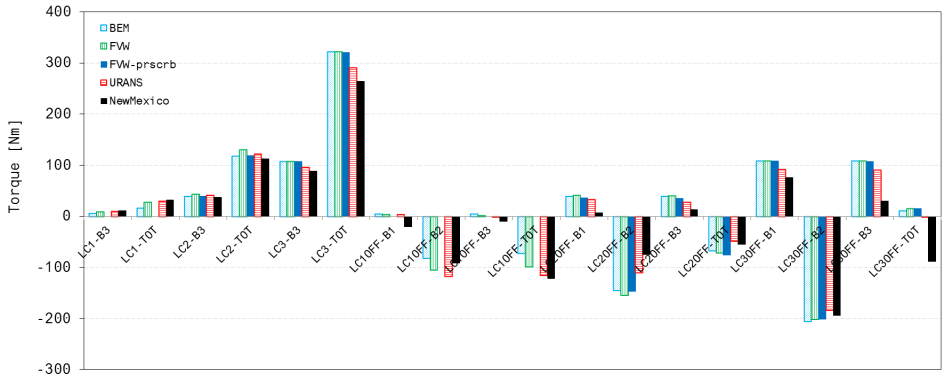

Figure 5.5: Comparison between generated torque from simulations and experimental values.

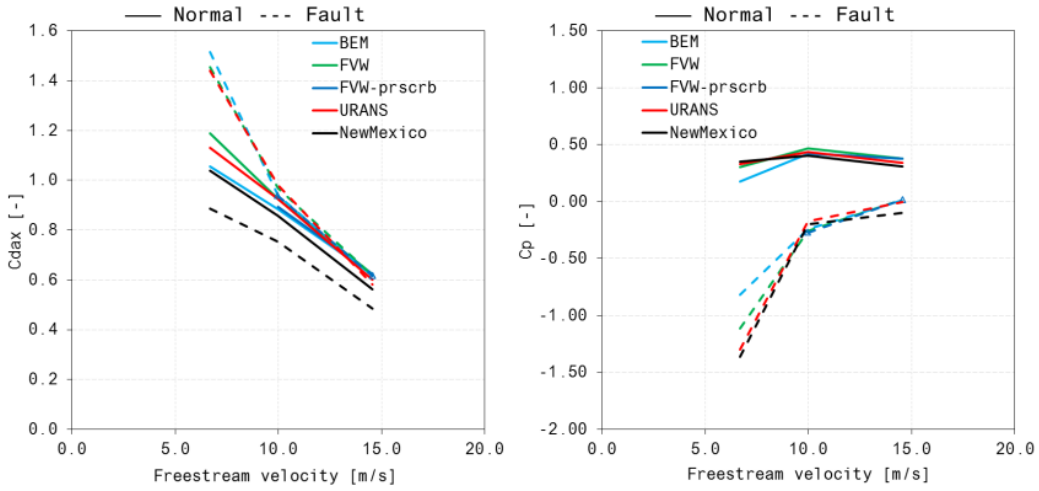

Figure 5.6: Thrust coefficient and power coefficient for Normal operational (Normal) and fault conditions (Fault) for the full rotor from simulations and experiments

A similar trend can be seen in Figure 5.6 and Figure 5.7 where thrust coefficient (Cdax) and power coefficient (Cp) are plotted against the freestream velocity Minimal scattering between the models can be noticed for normal operational conditions while the differences are more pronounced in fault conditions. A comparison between normal operational and fault conditions shows that the overall measured performance of the rotor decreases in fault conditions with blade 2 operating in fully stalled conditions and generating lower axial loads and negative torque. None of the models was able to reproduce the decrease in total thrust visible in the experimental data.

However, all the models predict a larger axial force in fault conditions than in normal operational conditions. This is mostly due to the over prediction of the axial force on blade 2 in combination with a reduced force on the other two blades which is not properly accounted for. For the misaligned blade, the decrease in torque from operational to fault conditions is well predicted by all the models. In fault conditions, blade 3 operates in the turbulent wake created by the off-pitched blade 2 resulting in lower axial force and lower generated torque. The BEM model fails to predict the decrease in axial force for this blade showing similar levels to normal conditions. This is due to the fact that the blades are modelled independently in BEM, allowing no interference between them. For the FVW model this is different and a small decrease in axial force and torque is noticeable for the high tip speed ratio cases. Compared to the experiment the level decrease is very small due to the fact that lifting line methods do not explicitly model (drag dominated) separated flow areas, which

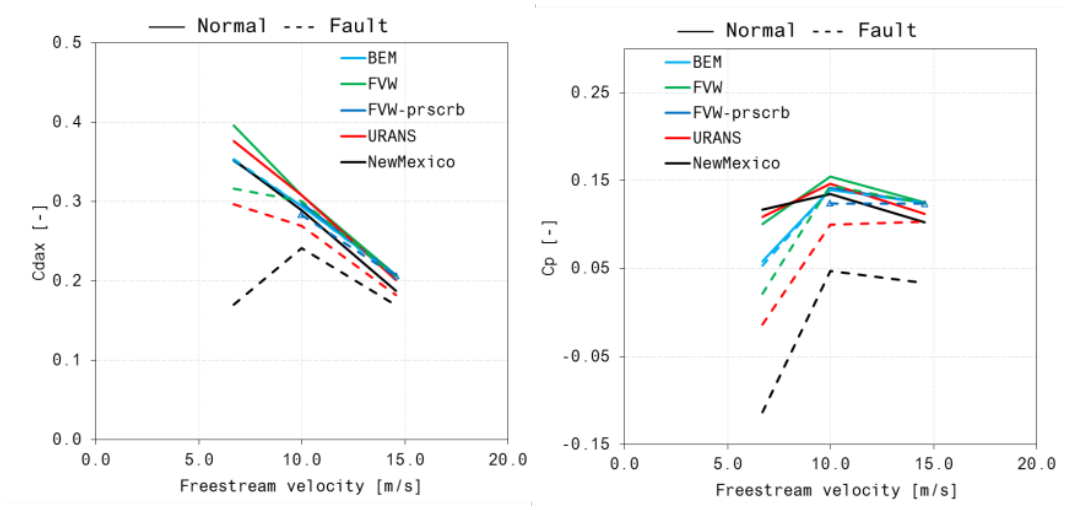

Figure 5.7: Axial force coefficient and power coefficient for Normal operational (Normal) and fault conditions (Fault) for blade 3 from simulations and experiments.

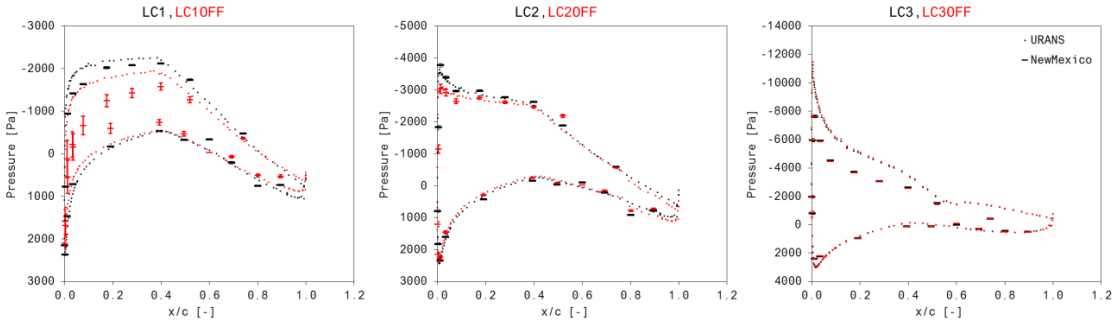

Figure 5.8: Pressure distribution plots at 82% span of blade 3 for normal operational (LC1,LC2 and LC3) and fault conditions (LC1OFF,LC2OFF,LC3OFF) from experiments and URANS simulations.

is the major cause for the decrease. URANS simulations, due to a better resolution of the wake behind blade 2 are able to catch the trend but still overestimate the generated axial force and torque probably due to an underestimate of the velocity deficit in the tangential velocity.

Pressure distributions on Blade3 from URANS simulations and Experiments

The pressure distribution plots along the blade are a useful tool in order to be able to better understand the loads acting on a wind turbine blade. The loads plotted on Figure 5.8 are relative to two sections of the blade 3 (82% and 92%) and refer to both normal operational conditions (LC1, LC2 and LC3) and fault conditions (LC1OFF, LC2OFF and LC3OFF). For lower freestream velocities or high tip speed ratios (LC1, LC1OFF) large differences between the normal operational and fault conditions can be seen. The large error bars visible in the experimental data for LC1 off at both 82% and 92% indicate that large fluctuations in pressure at the leading edge were measured. Since the fluctuations are limited to the leading edge area, large vibrations are probably excluded as a possible cause. A more likely explanation is the turbulent flow caused by the large separation behind blade 2. The iso-surface plots for the vorticity field in Figure 5.11 give a qualitative picture of the large vortices detaching from the tip area of blade 2 and hitting the tip of blade 1.

The pressure plots from the URANS simulations show that the URANS approach is able to capture the trend but over predicts the loads. This behaviour is probably due to an incorrect estimate of the velocities in the

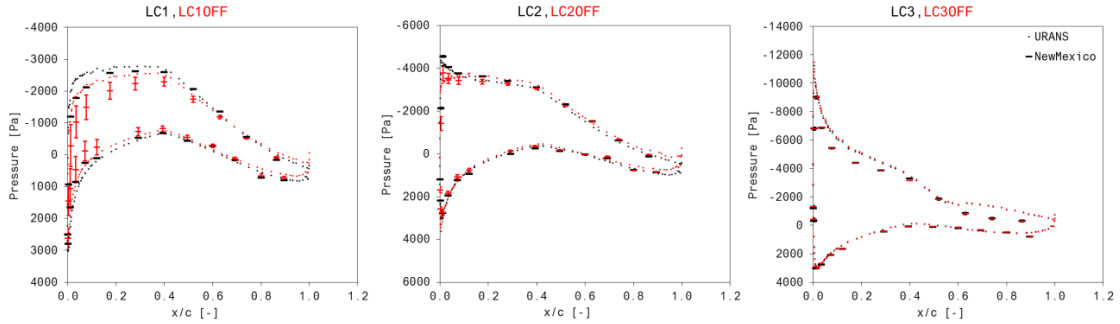

Figure 5.9: Pressure distribution plots at 92% span of blade 3 for normal operational (LC1,LC2 and LC3) and fault conditions (LC1OFF,LC2OFF,LC3OFF) from experiments and URANS simulations.

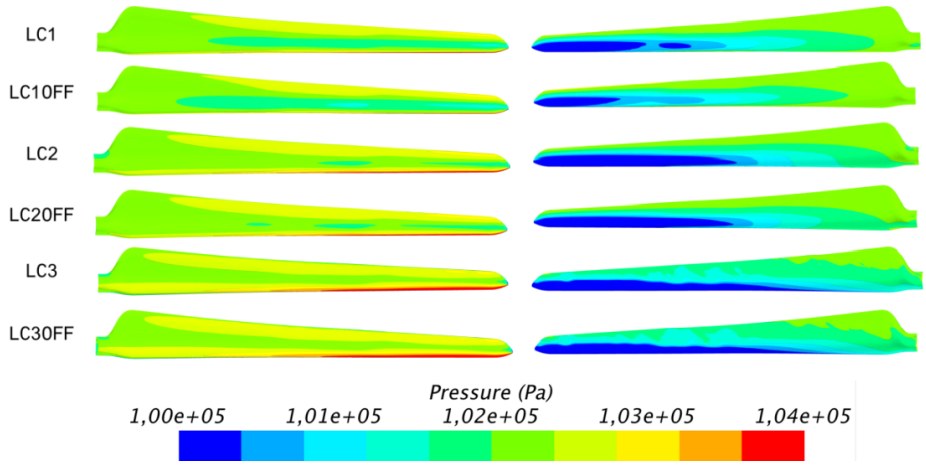

Figure 5.10: Contour pressure plots on the blades for pressure (left) and suction (right) side

separation area. With increasing wind speed (reduced tip speed ratio) the differences between the pressure plots for the operational conditions and fault conditions are reduced since the vortices generated by blade 2 are convected away from the rotor plane and blade 3 only partially sweeps in the turbulent wake generated by blade 2. In LC3 and LC3OFF, where the wind turbine is acting in stalled conditions, the pressure distributions plots for operational and fault conditions are overlapping each other both for the experiments and the URANS simulations. While the pressures on the pressure side of the blade are correctly computed, differences in this case are present in the suction side. This is a limitation of the RANS and URANS models that tend to over predict the negative pressure on the suction side of a wind turbine blade that operates in stalled conditions [69, 85].

From the contour plots on the blades in Figure 5.10 clear difference can be noticed when comparing LC1 with LC1OFF load case both in the pressure and suction side. On the pressure side, a higher pressure on the leading edge in experienced by the blade when operating in normal conditions and on the suction side a lower pressure is experienced by the blade along the span. Similar findings can be seen also comparing LC2 with LC2OFF and LC3 with LC3OFF. However, with increasing wind speeds the differences are less evident, as previously discussed.

A qualitative analysis of the vorticity (Figure 5.11) field for the three fault conditions show that for LC1OFF the long coherent vortical structures generated by blade 2 are kept and in the rotor plane and blade 3 sweeps through a highly turbulent area justifying the high standard deviation measured by the pressure sensors. With

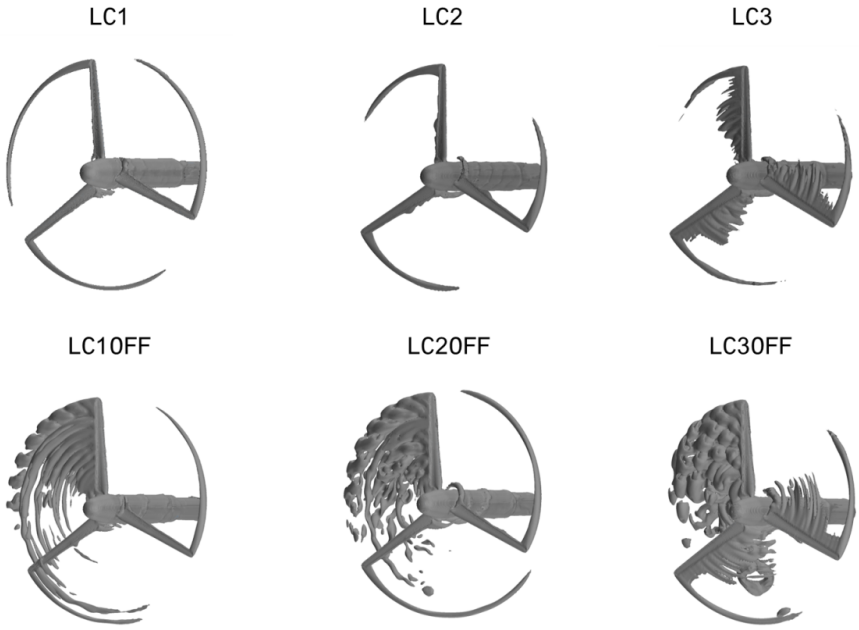

Figure 5.11: Iso vorticity fields for normal operational and fault conditions.

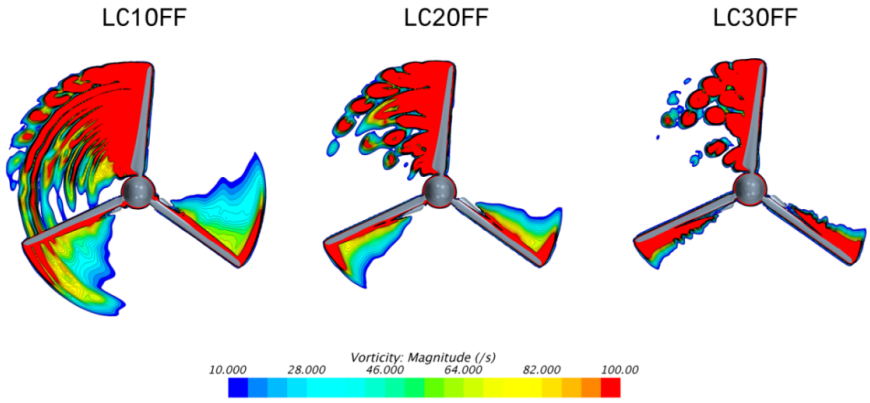

Figure 5.12: Vorticity field in the rotor plane.

increasing velocity the vortical structures are covected in the streamwise direction behind the rotor and thus the incoming flow experienced by blade 2 and blade 3 is less influenced by the turbulence generated by the large structures detaching from blade 2. The stucture of the vortical structures is also affected and the vortices are broken into smaller structures.

The same qualitative analysis is done for Figure 5.12 where the vorticity field on the rotor plane for the three fault load cases tested is represented showing that for LC1OFF the vortex generated by blade 2 are confined to the rotor plane and blade 3 experiences an incoming flow affected by the vorticity generated by blade 2.

Conclusions

A comparison between models of increased complexity was featured in the present chapter. All the models used are only partially able to reproduce the complex flow generated by the off pitched blade and the loads on the immediately following blade. All the models over predict the axial force generated both in normal and

fault conditions but general trends are well predicted. BEM and to a lesser extent FVW experience difficulties in modeling the inflow conditions for the blade immediately following the off pitched blade while URANS simulations provide a better match with the experimental possibly due to a better prediction of the near wake and flow conditions in the rotor plane.

6. Task 4.3: Angle of Attack

6.1 Goal of the task

In aerodynamic simulation codes using airfoil data, such as Blade Element Momentum (BEM) methods or Actuator Disc/Line/Surface Navier-Stokes techniques, the angle of attack is an important quantity which is required to be known at each cross-section on rotor blades [38]. When the angle of attack is known, the loading on each cross-section can be calculated by using the blade element theory and tabulated airfoil data obtained from 2D wind tunnel measurements or CFD computations with the correction to rotational effects. A wrong estimation of the angle of attack on a rotor blade can influence the subsequent prediction of the rotor performance. However the definition, determination and measurement of the angle of attack on a rotating wind turbine blade is far from straightforward. In this task, the goal is to evaluate different determination techniques for flows past two 10 MW wind turbines designed in the EU AVATAR [3] and INNWIND [4] projects. The task period is from the 1st of January, 2015 to the 31st of December, 2017 and the following 8 partners: DLR, DTU, DUT, ECN, University of Applied Sciences Emden/Leer, University of Malta, University of Oldenburg-Fraunhofer IWES, University of Stuttgart, participated in the task.

6.2 Methods for the determination of angle of attack

To determine the angle of attack (AoA) on rotor blades, eight different methods are used: Inverse BEM, Azimuth average, 3-Point, Shen1, Shen2, Ferreira-Micallef, Line average and Herráez method. The eight methods are summarized here:

1. Inverse BEM method
   The computed or measured load distribution is used as an input to estimate the induction and AoA using the general BEM theory formulation [149] [88]. This technique may be expected to give reasonable results in axial flow conditions. However due to the fact that the BEM theory is one-dimensional and many empirical relations are employed, the accuracy of this method is limited. This also holds for the root and tip where the flow shows its 3D nature. In addition, just like in BEM, the simple momentum theory does not hold anymore when the axial induction factor becomes larger than approximately 0.3. Therefore, an empirical relation between the thrust coefficient and the induction factor has to be used in order to correct for this effect.

2. Azimuth average technique
   This technique is based on the annularly averaged axial velocity at several upstream and downstream locations [54]. The velocity fields in an annulus upstream and an annulus downstream of the rotor plane at a given radial location are averaged. Afterwards, the value of the velocity in the rotor plane is estimated by interpolating the upstream and downstream velocity values. The azimuth average technique (AAT) provides an annular averaged induced velocity which is known to differ from the local induced velocity near the tip. Another shortcoming of this method lies in the fact that this model is only valid for axial conditions (or for the mean value of axial induction factor over one rotation) and it can not capture the dynamics of the induced velocity of yawed flows. It is also noted that the results might depend on the positions of the monitor points and the interpolation algorithm.

3. 3-Point method
   This method first introduced in [120] uses only three points along the chord length on each side of the

airfoil cross-section. This greatly simplifies the average procedure. Moreover, unlike the AAT method, this method is able to reproduce the dynamic behavior of the induction at each azimuthal position, e.g in a yawed flow. In addition, the local induced velocity near the tip and root of the blades can be reproduced and finally, by choosing three points at each section, the effect of upwash and downwash on the averaged velocity can be reduced. In Figure 6.1, a schematic representation of this method is presented. For this method, 3 points on each side of a particular section which is modeled as an airfoil, will be assigned. These points are located at 25, 50 and 75 % chords along an airfoil. Then, each pair of points (P1, P4), (P2, P5) and (P3, P6) are averaged independently to get the three velocities at the airfoil section. Finally, the resulting velocity points are averaged to get the estimated velocity which is induced at the blade section (red point). However, it should be noticed that the selection of the 3 points on each side of the airfoil will be dependent on the pitch axis and location of the bound circulation.

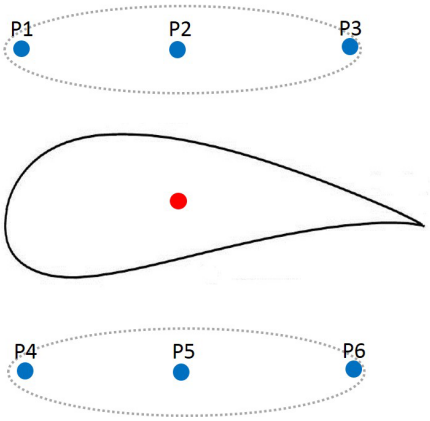

Figure 6.1: Monitor points in the 3-Point method

4. Shen1 method
   The technique presented in [142] is a simple way to determine the AoA on a rotor blade. As input to this technique, the force distribution along the blade (typically projected along the chordwise and normal to the chordwise directions) and the velocity at a set of monitor points in the vicinity of the blade is assumed to be known from CFD computations or experiments [176]. The AoA is determined by (1) estimating the lift force by projecting the force along the incoming and normal to the incoming directions; (2) calculating the bound vortex using the Kutta-Joukowski law; (3) calculating the induced velocity by the bound vortex using Biot-Savart's law; (4) computing the relative velocity at the monitor points by subtracting the induced velocity from the bound vortex; (5) computing the AoA from the relative velocity. This procedure continues until the convergence is reached. The positions of the monitoring points are important for this method as the bound vortex is considered as a line vortex along the blade. The points cannot be chosen too close to the bound vortex since this is a singularity where the induced velocity approaches infinite.

5. Shen2 method
   In order to overcome the difficulty of singularities in the previous method, an alternative technique was presented in [143], where a distributed bound circulation along the airfoil/blade surface is used instead of the concentrated bound vortex at the force center. In this case, the monitor points can be chosen closer to the blade. Another advantage is that this method takes the chordwise variation of aerodynamic forces into account, which is neglected when the vorticity is concentrated in a bound vortex. Additionally, this method is not iterative. However, the difficulty of using this method may be related to find the separation point (SP), where the local circulation changes sign [143].

6. Ferreira-Micallef method
   Assuming that the flow around a blade section is 2D, incompressible and irrotational, then the velocity at any point near the blade section can be decomposed in the linear addition of three elements: (i) induced velocity by the free vorticity in the flow, (ii) induced velocity by the vorticity bound to the surface of the airfoil, (iii) local uniform wind velocity (the result of U_∞ and the induction of all other elements in the 3D domain). Of these three elements, only the distribution of free vortices can be calculated directly from the velocity/vorticity field. To determine the local wind velocity, a system of equations based on potential flow

vortex theory is solved (see [77]) simultaneously, thus determining the local wind velocity and the strength of the vortices bound to the blade section surface. In this approach, the free vorticity and the vorticity bound to the surface of the airfoil are approximated by point vortices with a Rankine vortex distribution (see [77]), having a strength $\Gamma_\omega = \omega_z \Delta x \Delta y$. Figure 6.2(a) shows a schematic of the free vortex points distributed at each grid point. Bound vortex points of strength Γ_{bi} are placed on the blade surface, where i is the index of the point vortex. The control points for the evaluation of the system of equations are collocated in the vicinity of the blade section, as represented in Figure 6.2(b);however, it is not necessary for the locus of the control points to be a closed contour around the blade section, as represented in Figure 6.2(b). The unknowns of the system of equations are the vortex strengths of each element and the velocities (U_l, V_l) which are the components of the local wind velocity at the blade's quarter chord. This results in an over-constrained system which is solved using a least squares approach. Finally, (U_l, V_l) can then be used to determine the angle of attack. The relative inflow angle is thus given by $\phi = tan^{-1}(V_l/U_l)$.

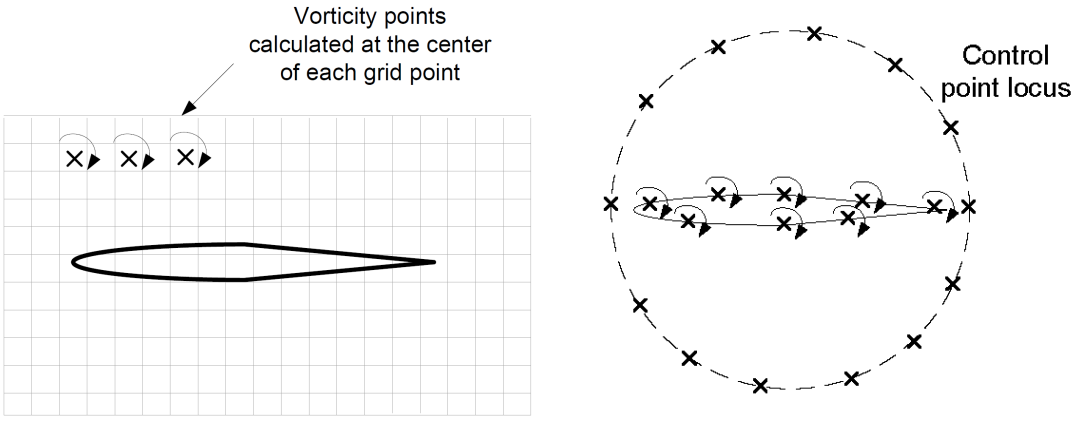

(a) Free vortex points distributed at each grid point

(b) Bound vortices and monitor/control points

Figure 6.2: Schematics

7. Line average method
   The Line average (LineAve) method determines the AoA by averaging the flow velocities along a symmetric, closed line around the rotor blade [76]. In the present study, a circle is chosen for this purpose as illustrated in Figure 6.3. The circle center is placed at the quarter chord position, where, like in a lifting line representation the bound vortex is located. The idea is that the induced velocity at opposed points on the circle extinguishes each other. By averaging the flow velocities along the circle, the influence of bound circulation is eliminated and the local inflow velocity and AoA can be determined. Since it needs to be solely ensured that the shapes are symmetric to the quarter chord point, in theory a variety of closed shapes are possible. However, in earlier works [76] the circle shape provided convincing results. The local circle radius is varied along the blade span and chosen dependent on the local chord length c. In this study, $r_{circ} = 4c$ is used.

8. Herráez method
   This method obtains the undisturbed flow rotor velocities by extracting them directly from a position in the rotor plane where the influence of the blade bound circulation from each blade is canceled out by the other blades [59]. In the case of axi- symmetric, homogeneous inflow, this position corresponds to the bisectrix of the angle between two arbitrary blades. For a wind turbine with 3-blades, the undisturbed velocities can be obtained along the radial traverses located 60^o ahead and behind an arbitrary blade. In the case of a 2-bladed rotor, the velocities should be probed at the radial traverses located 90^o ahead and behind an arbitrary blade. The difference between the free stream velocity and the axial velocity component obtained in this way for each radial position corresponds to the local axial wake induction. The local tangential velocity extracted from the radial traverse corresponds to the local tangential wake induction after changing its sign. The main advantage of this method is its simplicity, which makes the calculation of the AoA very straightforward. The main limitation of the method is that its use for non- axi-symmetric or inhomogeneous inflow becomes much more complicated because of the dependence of the blade bound circulation on the azimuthal blade position.

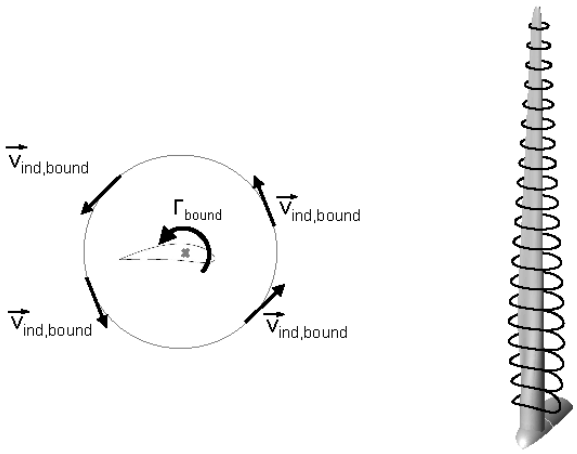

Figure 6.3: Line average method

6.3 Results

In this section, results obtained from the eight methods will be summarized and discussed for both the AVATAR and InnWind rotors in axial inflow conditions. To check how the obtained lift-drag polar is used in BEM, the numerical results using FAST V8 [75], developed by the National Renewable Energy Laboratory (NREL) are also included for comparison.

InnWind rotor

To check the performance of different methods of determination of AOA, the first considered case is the InnWind rotor. The InnWind rotor has a diameter of 178.3 m, a rated power of 10 MW, and a rated rotor speed of 9.6 rpm which results a rated tip speed of 90 m/s. A wind speed of 9 m/s is considered at which the rotor runs at 7.23 rpm. In Figure 6.4, the axial induced velocity and angle of attack are plotted. For the axial induction, the results are discussed in 3 different regions ($r/R < 0.3$, $0.3 < r/R < 0.75$, $r/R > 0.75$).

1. $r/R < 0.3$
   Deviations are observed in the root region of the blades. Herráez, Shen1 and Shen2 methods are forming one group of results as they share similar monitoring point locations in this part, while all others (AAT, Line average, 3P, InvBEM and Ferreira-Micallef) are forming the second group as an averaged velocity at control points is used. One reason for this deviation could be the 3D nature of the flow in the root region. Hence since different methods are using different ways of monitoring velocity, this could lead to some deviations in this area.

   AOAs are usually big in this region and very hard to estimate due to the complicated flow situation. Nevertheless AoAs seem close between the different methods with a maximum of 5 degree difference.

2. $< 0.3 < r/R < 0.75$
   In general, a good agreement is observed between all the methods in the mid-span region in terms of induced velocity (Figure 6.4(a)) and also in terms of AoA (Figure 6.4(b)).

3. $r/R > 0.75$
   In the tip region of the blades, deviations are observed in terms of induced velocity between the Line average and Ferreira-Micallef (FM), and the remaining methods. The flow in the blade tip region is 3D and due to the presence of the tip vortex it is very difficult to capture the flow physics correctly. Hence by having different ways of monitoring velocity, the results could differ. Nevertheless, the level of the agreement between all the methods beside the Line average and FM model at the tip remains good. Near the tip it is known that there is a strong dependency of the induced velocity on the azimuthal position in the rotor plane. As regards to the FM and Line average approach the main reasons for the discrepancies are associated with the fact that these methods calculate the bound circulation on a 2D airfoil section from a highly three dimensional flow field towards the tip. These methods would therefore seem to necessitate

some form of tip correction which is left for a future work. In terms of AoA, it is important to note that AoA is the difference between the inflow angle and the twist angle. The inflow angle is the arctangent of the rotational speed and the axial velocity. Due to the high value of the rotational velocity in particular near the tip, differences in induced velocity are ”hidden” and so the AoA from the different methods will remain in a very good agreement all over the blade span. However at the very tip of blade where the Line average and Ferreira-Micallef method have up to 2 degree deviation from the other methods.

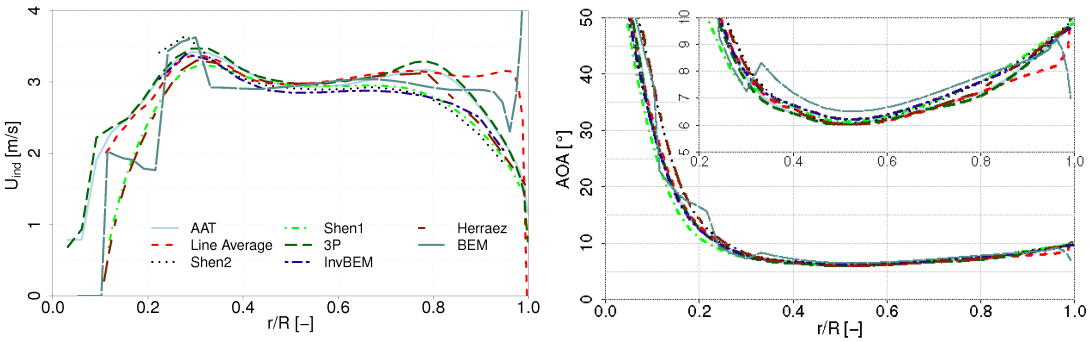

(a) Induced velocity (b) Angle of attack

Figure 6.4: Lifting line variables at the InnWind rotor at a wind speed of 9 m/s

In figure 6.5, the Cl and Cd are plotted in function of radial position. For the lift coefficient, good agreements are seen between the different methods for all radius positions while the drag coefficient has a deviation in the root and tip regions.

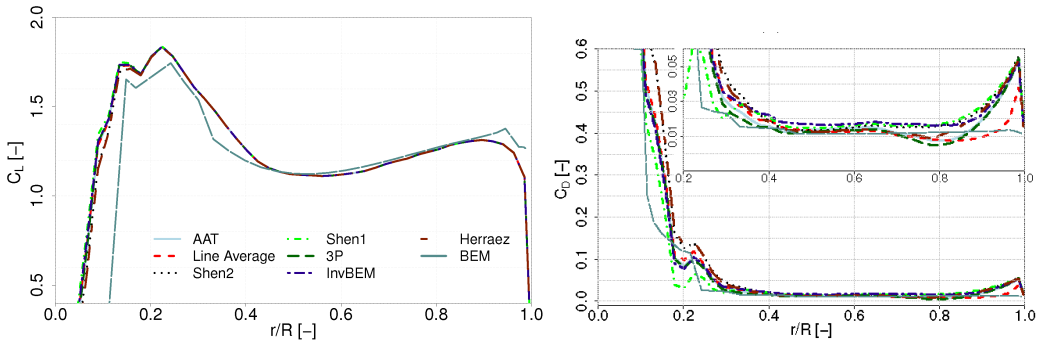

(a) Lift (b) Drag

Figure 6.5: Force coefficients on the InnWind rotor at a wind speed of 9 m/s

AVATAR rotor

To check how the different methods work on a different rotor, we consider the AVATAR rotor. The AVATAR rotor has a diameter of 205.8 m, a rated power of 10 MW, and a rated rotor speed of 9.6 rpm which results a rated tip speed of 103.4 m/s. A wind speed of 9 m/s is also considered at which the rotor runs at 6.87 rpm. It should be noted that AVATAR turbine compare to InnWind turbine has lower induction. In Figure 6.6, the axial induced velocity and angle of attack are plotted. For the axial induction and angle of attack, the variation of results is quite similar to that for the InnWind rotor and can be divided into 3 different regions ($r/R < 0.3$, $0.3 < r/R < 0.75$, $r/R > 0.75$). However for AVATAR rotor, in general less deviation is observed when comparing different methods.

In Figure 6.7, Cl and Cd are plotted in function of radial position. For the lift coefficient, good agreements are seen between the different methods for all radius positions while the drag coefficient has a deviation in the root and tip regions.

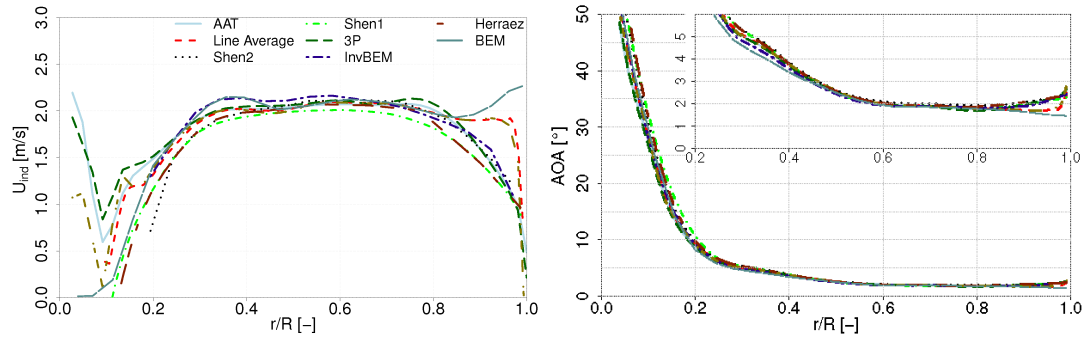

(a) Induced velocity (b) Angle of attack

Figure 6.6: Lifting line variables on the AVATAR rotor at a wind speed of 9 m/s

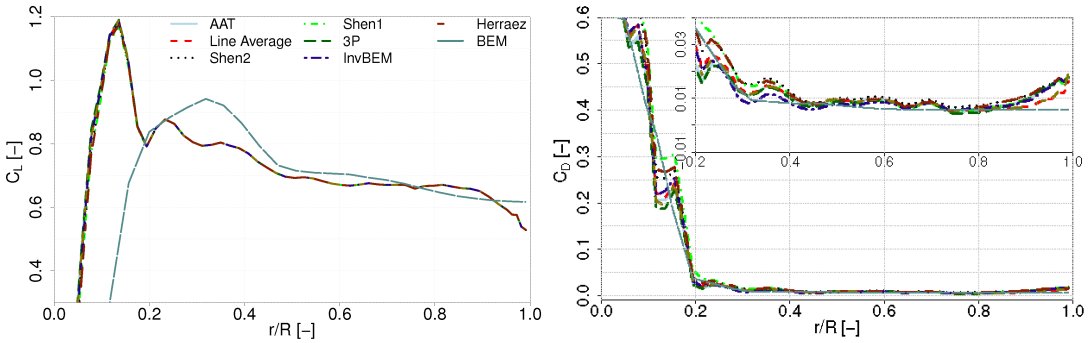

(a) Lift (b) Drag

Figure 6.7: Force coefficients on the AVATAR rotor at a wind speed of 9 m/s

6.4 Conclusion

In this work, eight methods for extracting the induced velocity and AoA from CFD computations in axial inflow conditions for flows past two 10MW reference wind turbines, namely the EU AVATAR and INNWIND.EU turbines, are presented. Based on the results presented, it can be concluded that all the methods are in good agreements in the mid-span. However, at the very root and the very tip of the blade deviations are observed. At the root ($r/R = 0.0$ to 0.3) the Herráez method, Shen1 and Shen2 methods are in a very close agreement with respect to each other. This could be due to the fact that the positions of monitoring point for these methods are very similar. They are forming the first group of results. The AAT, 3P, Ferreira-Micallef and Line average methods are also forming the second group of results which are in a closer agreement with each other. At the tip ($r/R = 0.75$ to 1.0) Ferreira-Micallef and Line average are forming one group of the results. The similarity in the approach and the position of monitoring point at the tip between these two methods could be the reason for this close agreement. This group (Ferreira-Micallef and Line average) deviates in the tip region with respect to the other methods. These deviations have less impact on the resulting AoA and also C_l and C_d due to the high value of the rotational velocity in particular near the tip. New correction models can be derived using the extracted airfoil characteristics for blade element momentum calculations. In future work, these methods will be tested in asymmetric inflow conditions.

7. Task 4.4: Near Wake Aerodynamics

7.1 Introduction

The near wake of a wind turbine is typically defined as the region close behind the rotor where the wake is still stable and no mutual interaction of the tip vortices has taken place [125]. In contrast to the far wake, which is initiated by the break down of the tip vortices, and where the wake state is an outcome of the dynamic interaction with meteorologic effects as atmospheric turbulence and stratification, the near wake is more dependent on the operational point of the turbine and the aerodynamic details in the rotor plane. For example the tip speed ratio (TSR) and the associated induction directly determines the wake deficit and expansion. Further, it defines how close to each other the tip vortices trail and therefore, how strong the mutual induction becomes that finally leads to the break down of the wake. This mutual interaction can be further enhanced when tip vortices undergo a shifting during one revolution for example due to sheared or yawed inflow, a tilted rotor axis or atmospheric turbulence [174]. For the turbulent wake state, no such "additional disturbance" is necessary. The high induction in the rotor plane results such a strong shear layer at the wake edge that the wake becomes unstable quite close behind the rotor even for uniform inflow. The resulting flow reversal generates complex flow features which also affect the turbine loading.

Since in the near wake there is a close relationship between loading and induction, accurate predictions of loads and the wake necessitate each other. If complex, unsteady features are expected to occur in the wake region and the capturing of vortical features is essential. However, this requires a high spatial resolution and enhanced numerical schemes as well as turbulence models that allow for eddy resolving simulations. The influence of these numerical parameters as well as that of the turbine representation on the tip vortex development shall be analyzed for the axial cases. Furthermore, for the turbulent wake state case, thrust versus axial induction curves shall be summarized based on CFD results from all partners. For the yawed inflow, the wake deflection shall be evaluated and compared for full turbine and isolated rotor simulations.

Apart from the University of Stuttgart, Germany (USTUTT), results were provided by Frédéric Blondel from IFPEN and Manfred Imiela from the German Aerospace Center (DLR).

7.2 Near wake analyses for axial inflow

For the axial flow cases the focus will be on the tip vortex development. The tip vortices originate from the equalization of pressure around the blade tip and can be characterized by position, core strength, core radius, as well as integral circulation. These properties are analyzed using a vortex evaluation macro for Tecplot developed at IAG within the Mexnext-I project [68] which is based on the methods of [169]. The vortex core position is determined at that point, where the local vorticity is maximum. Its radius is defined as the half distance between the maximum and minimum tangential velocity near the vortex center. The circulation is calculated by integrating the vorticity within a circular area around the tip vortex center. This procedure is applied to the PIV measurements as well as on the simulation results. The horizontal plane is chosen for the evaluation and the time when one blade is just passing it (nine o'clock position). Unsteady RANS simulations are compared to free-wake simulations. Further, the impact of higher order convection schemes as well as the influence of the turbulence modeling approach shall be investigated for the $24\,{}^{m}/_{s}$ case.

Computational details

The computational setup of USTUTT takes into account all aerodynamically important components including the tower and nacelle, the rotating and non-rotating part of the hub and the rotor blades. These are separately meshed and embedded into a Cartesian background mesh of different refinement levels with the overset grid technique as shown in Fig. 7.1(a). The meshes around the rotor blades have been created using the software *Gridgen* and the IAG tool *Automesh* that allows y^+-adaptation of the boundary layer in radial direction. Different grids were used for the URANS simulations and the Detached Eddy simulations (DES) of the $24\,{}^m/_\mathrm{s}$ case. The dimensions the URANS grid and the grid optimized for DES are 224/384 cells in span-wise-, 224/256 cells in chord-wise- and 136/152 cells in wall normal direction. For the DES grid, the cells are equally spaced in span-wise direction over a wide range of the blade, whereas the URANS grid implies a tanh-type distribution. Both meshes are refined near the root and tip. The cell sizes of the fine levels of the background mesh that expand downstream to $x/R \approx 3.5$ are $\Delta = 0.02$ m in the wake center and $\Delta = 0.01$ m in the tip region.

The time step was set equivalent to $1\,^\circ$ for the 10 and $15\,{}^m/_\mathrm{s}$ cases and equal to $0.125\,^\circ$ for the $24\,{}^m/_\mathrm{s}$ case.

For the latter, a comparison shall be drawn on the effect of the numerical convection scheme. Thereby, a fifth order WENO scheme [72] will be employed for calculation of the inviscid fluxes and compared to the standard JST scheme [65]. Further, these schemes shall be combined the DES concept [144], which is a hybridization of RANS and LES within the turbulence model, allowing to treat regions of flow separation and turbulent mixing with LES-like behavior. All simulations were run fully turbulent, as the turbine blades were tripped over the whole span when the tip vortex PIV measurements were conducted.

The results provided by IFPEN employ a free vortex code, where the wake is represented by shedding and trailing vortex filaments as shown in Fig. 7.1(b), while the blades are represented by bound vortex filaments (lifting-line approach). In the present work, the core radius size is based on the Lamb-Oseen vortex model, the core growth is based on the Ramasamy-Leishman formulation, and the Vatistas formulation is taken into account for the stretching effects. Thanks to the Lagrangian formulation, the vortex solver exhibit a very low diffusion. Non-rotating parts are not represented in this solver. Some validation elements can be found in [14] and [15]. Each blade consists of 34 elements that are distributed in cosine shape. Contour plots of the velocity field are performed in a post-processing step, and induced velocities are computed on a regular, cartesian grid. The time step is equivalent to $10\,^\circ$ azimuth movement and the total simulation was run over 18 revolutions. With such a high number of revolutions, one ensures the full development of the rotor near-wake. GPUs (Graphical Processing Units) are used to compute wake inductions, thus strongly reducing the computational time when compared with standard CPUs implementations: a single test case takes approximatly 20 minutes on a $k40m$ Nvidia GPU.

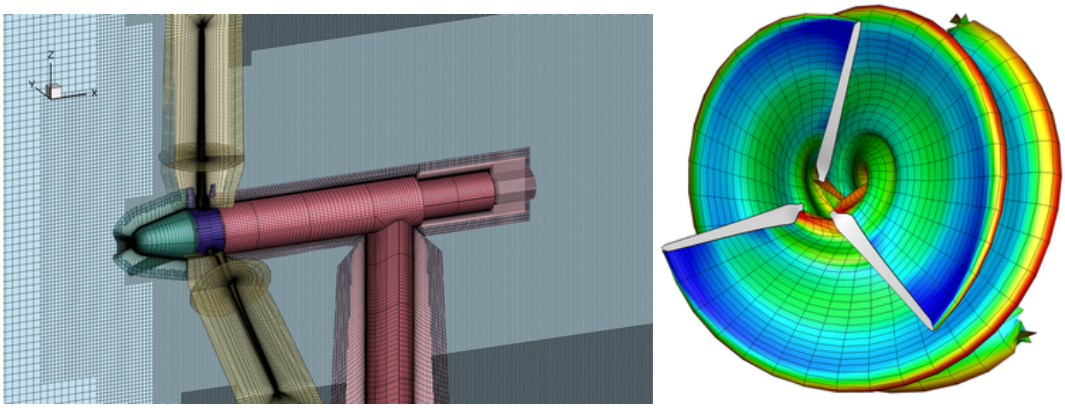

(a) Overset mesh topology of USTUTT (not every gridline shown) (b) Vortex filaments of the IFPEN free wake code

Figure 7.1: Computational grids of USTUTT and vortex filaments of IFPEN

Comparison of tip vortex properties

The tip vortex properties of the $10\,{}^m/_\mathrm{s}$ case are shown in Fig. 7.2. An impression of the wake expansion can be gained from the graph of the vortex core positions. Due to the high induction the expansion is very strong

and further, the distance until the wake is fully expanded is rather short with only about 1.5 rotor lengths. The maximum expansion is about 1.22 R. Further downstream the wake begins to destabilize in course of tip vortex pairing (see Fig. 7.3). While the wake continues expanding, the vortices roll up to larger sub-structures that finally result the stream-tube to collapse around 3.5 R downstream of the rotor. Up to the point where the tip vortices are still intact, the wake expansion is well captured by the former USTUTT CFD results from Mexnext-II using the scanned rotor geometry. The new results slightly underestimate the expansion. The IFPEN results show also good agreement with the measurements, however reveal a small upstream shift of the vortex positions as indicated by the symbols. Concerning the predictions of the vortex strength, this directly depends on the formation of the tip vortex is directly dependent on the pressure difference at the blade tip, its integral strength is linked to the lift distribution along the blade radius. Thus, inaccuracies in prediction of the lift will be deposited on the circulation. All predictions depicted in Fig. 7.2 agree well with the experiment for the first four vortices. Further downstream the former USTUTT results show a jump in the circulation. This is due to the fact that those simulations were performed on a coarser mesh and the vortices start to merge due to numerical diffusion, so that the area of integration most likely covers more than one vortex. The impact of the numerical diffusion of the vortices becomes particularly problematic when comparing the vortex radius and the core vorticity. In the measurements the vorticity is highly concentrated within a small radius of 0.015-0.02m. For the CFD simulations the vortex core radius is over predicted, whereas the vortex core vorticity is under predicted by about an order of magnitude. According to Spalart [156] a at least second order scheme could resolve vortices of the wave length $\lambda = 5 - 10\Delta$. For the employed grid spacing of 0.01 m a tip vortex radius of approximately 0.025-0.05 m could be expected. However, the vortex size is almost double due to the artificial dissipation introduced by the JST scheme. It is interesting to note, that the free-vortex results are in the same range of the CFD results. The zig-zag type variation in the vortex radius is due to the clustering of the discrete vortex filaments.

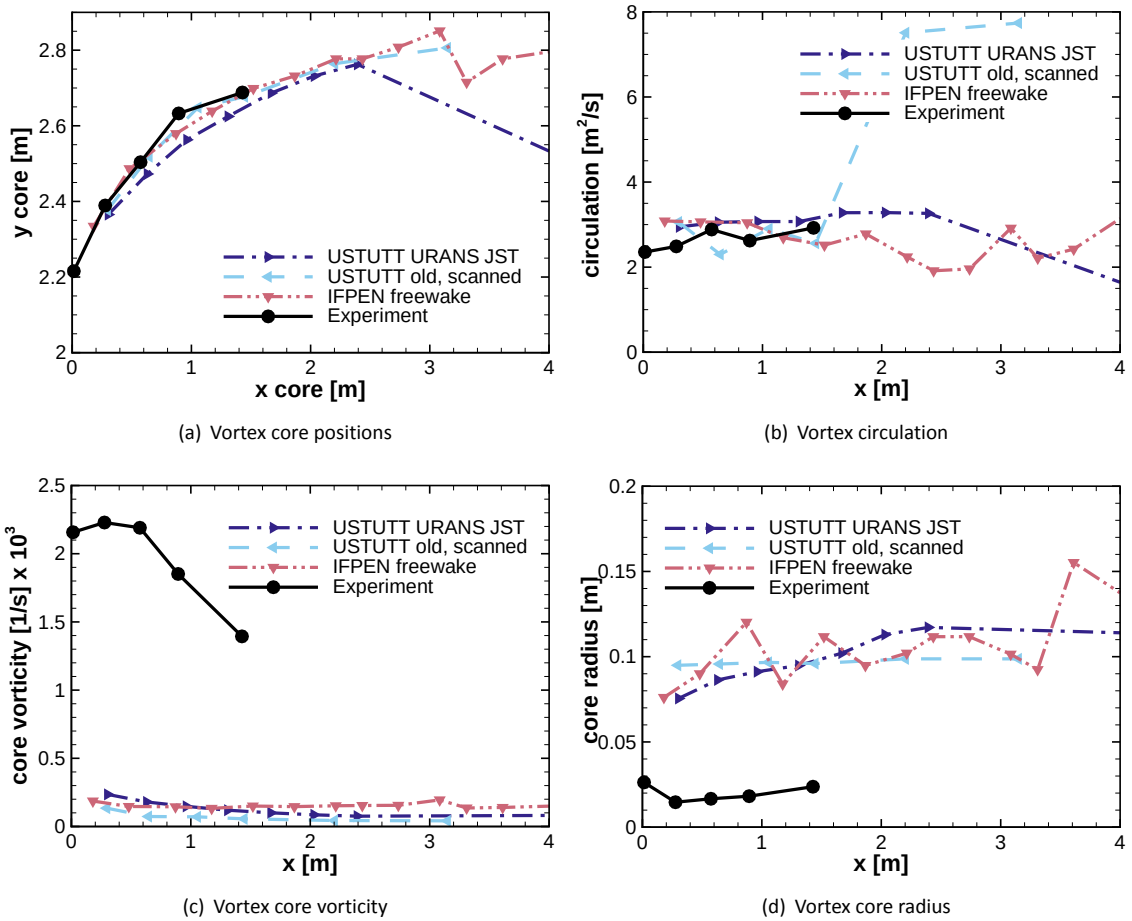

(a) Vortex core positions

(b) Vortex circulation

(c) Vortex core vorticity

(d) Vortex core radius

Figure 7.2: Tip vortex properties for the $10\,m/s$ case

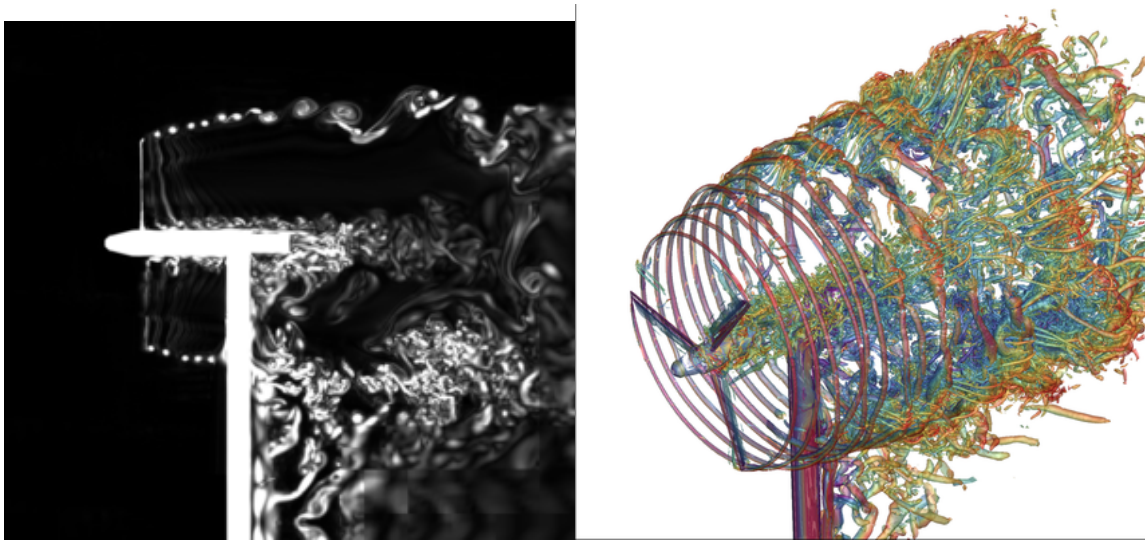

(a) Contour of the vorticity magnitude (light shading indicates high values)

(b) Iso-surface of λ_2

Figure 7.3: Tip vortex break down for the $10\,{}^{m}/_{s}$ case

The vortex development for the design TSR $\Lambda = 6.7$ is depicted in Fig. 7.4. Compared to the turbulent wake state case the wake expansion rate is smaller, but the expansion length which is about $x/R = 2.7$ is significantly longer. The total wake expansion almost reaches the extension of the high TSR. Downstream of that point, first vortex pairings could be observed, however within the fine wake mesh of the computational domain no wake instability could be observed. Comparing the vortex properties of simulations and measurements, the trends are the same as for the $10\,{}^{m}/_{s}$ case. Vortex positions as well as the circulation are well captured, whereas core vorticity and radius are over/ under predicted, respectively. For the vortex core radius, however the relative difference decreases, as the "physical extent" increases due to the higher circulation near the tip, while the numerical resolution capabilities remain the same.

Turning to the low TSR case of $24\,{}^{m}/_{s}$ wind speed the wake structure significantly differs from the previous cases. It is clear that due to the small induction of the rotor, the wake expansion is quasi absent revealing an extension of only 1.07 R at $x/R = 4.5$. Therefore, no wake instability by tip vortex pairing could be observed within the computational domain. IFPEN Lagrangian flow model shows a correct agreement with measurements and USTUTT CFD results. However, agreement is not as good as design and high TSR cases, since the inviscid lifting-line approach is not able to catch the massive separation zones. An interesting effect that could be observed is that the flow mechanisms which are responsible for the formation of the vortices is different to the previous cases. Apart from the inviscid trailing vortices also shedding vortices emerge from the massive flow separation over the blade. As will be shown later, these mechanisms interact with each other in the tip region.

Comparing the classical unsteady RANS concept and the scale resolving DES approach, with different numerical schemes a visual impression of the effect on the resolution of vortical structures can be obtained from Fig. 7.5. As a first conclusion it is clearly visible that the resolved content of the DES simulation is strongly dependent on the dissipation of the employed numerical scheme. Applying the fifth order WENO scheme with the *l^2Roe* Riemann solver resolves smaller scale turbulence which is completely absent in the standard JST solution. For URANS these structures are not resolved even with the high order scheme. When looking at the span-wise evolution of the vortices is to be noted that the three selected airfoils, which have quite different stall characteristics, are blended over a relatively small span-wise segment: In the section $r/R = 0.45$-0.54 from the *DU91-W2-250* to the *RISØ-A1-21* and finally between $r/R = 0.65$-0.74 to the *NACA64-418*. Consequently, high span-wise gradients of bound circulation induce quasi-steady trailing vortices that interact with the shed vortices of the separated boundary layer. The resolution of this mixing process seems to be suppressed by the URANS, while DES is able to capture it, which is expressed in the fact, that the trailing vortices in the blending regions of the airfoil disintegrates.

When looking at the tip region an interaction of the separated shear layer of the blade with the tip vortex can

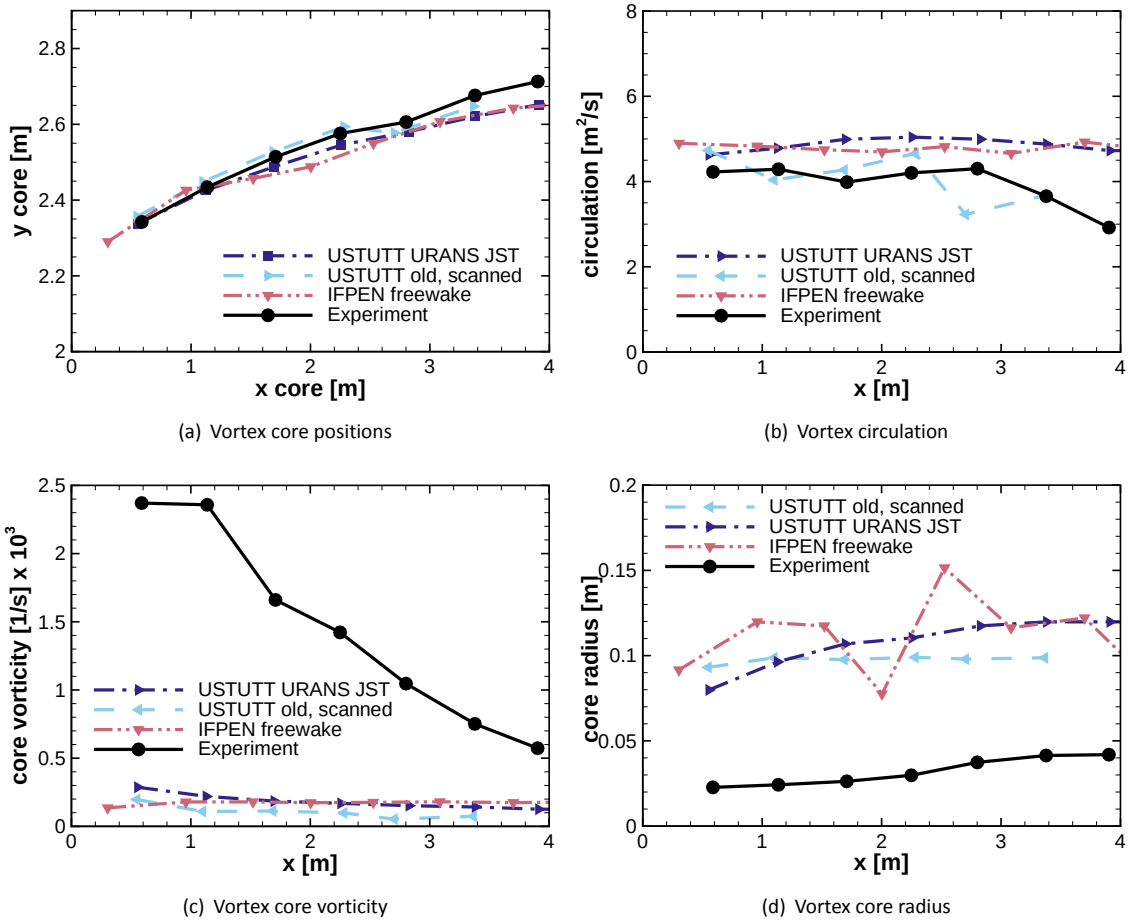

(a) Vortex core positions

(b) Vortex circulation

(c) Vortex core vorticity

(d) Vortex core radius

Figure 7.4: Tip vortex properties for the $15\,m/s$ case

be observed and so-called ”turbulent worms” emerge which roll over the main tip vortex. The mechanism that leads to these worms can be understood from analyzing the radial and tangential velocity components of the axial traverses as well as by considering the distribution of shedding and trailing vorticity in the near wake. As can be seen from the radial velocity component, separated fluid moves in outward direction due to centrifugal forces. In tangential direction the shedding vortices generate peaks opposed to the tangential velocity induced by the entire wake. This results in a strong vorticity component oriented perpendicular to the trailing tip vortex. It is to be noted that the gradient is expected to be higher compared to a virtually non-rotating case. Lastly, the axial induction of the rotor causes a deceleration of the axial convection of the shear layer. Hence, it can be summarized that for an observer in the inertial frame the shear layer moves upstream, outward and running after the blade, which means that it enters the area of influence of the tip vortex, so that its induction initiates the roll-over. This process can be followed by considering the shedding and trailing vorticity distribution in the wake shown in Fig. 7.6. Note that the level of both components is of the same order. In the right sub-figure it can be observed that within the time period between the third and the fourth tip vortex the shear layer stretches and becomes thinner. According to Helmholtz’ theorem this inherently increases the shear layer vorticity component perpendicular to the tip vortex, which seems to be the reason for the visibility of the ”worms” from the fourth tip vortex on. It is difficult to find experimental evidence for these secondary vortices. From the smoke visualizations depicted in Fig. 7.7 at least an indication can be found for the second, third and fourth smoke ring which respectively correspond to the third, fifth and sixth vortex number in the simulation. For those, a sharper smoke core is surrounded by a ”halo” of less dense smoke as marked in the picture by the green curves. Another indication is given by plotting the tangential velocity around the vortex core (Fig. 7.8), which represents any fluid motion aligned normal to the tip vortex. In the simulations particularly for vortex four, the roll-over of the shear layer and the formation of the worms is correlated with a change in sign of the tangential velocity in a ring around the vortex core. This behavior can also be observed in the instantaneous PIV results. The phase averaged PIV data smeared out this effect.

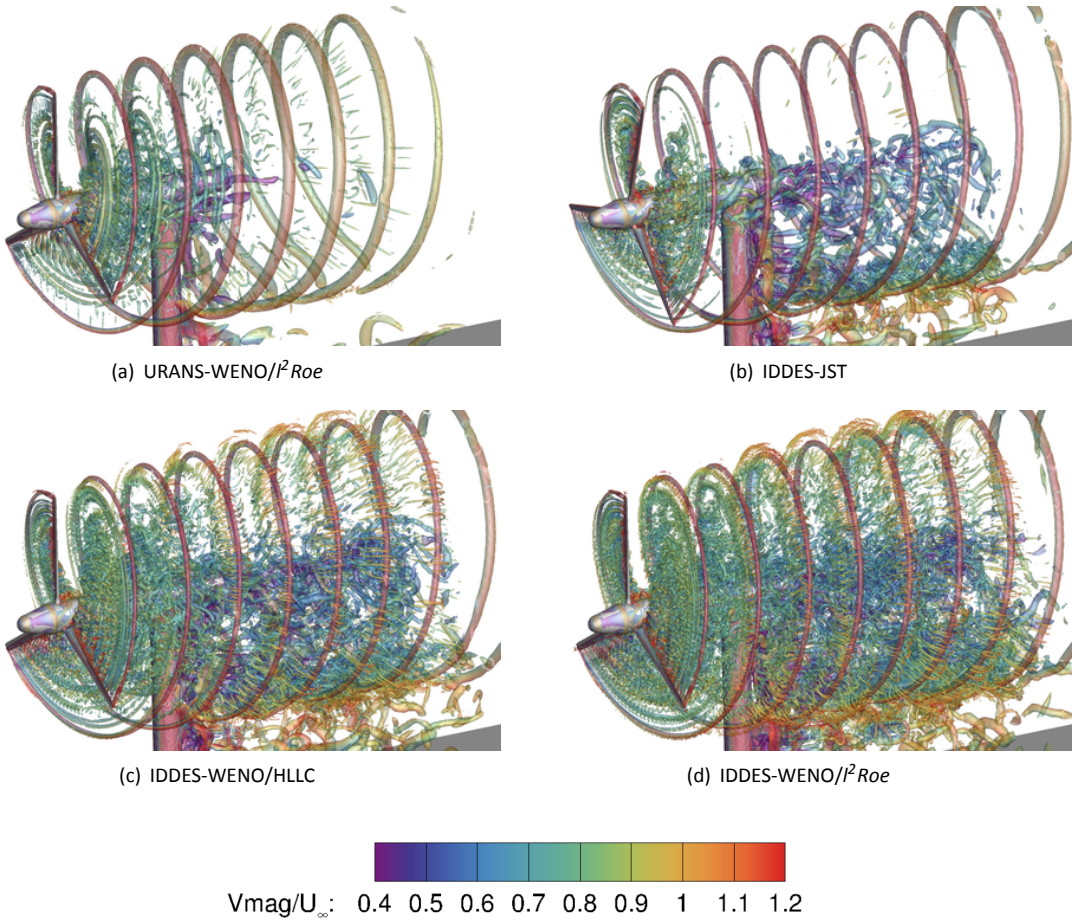

Figure 7.5: Wake of the MEXICO rotor predicted by different turbulence models and numerical convection schemes, $\lambda_2 = -0.015$ iso-surface

Regarding the requirements for the numerical resolution of these structures it is important to decrease artificial numerical diffusion as much as possible, without introducing spurious oscillations. The JST scheme adds such artificial dissipation in order to guarantee stability of the central differencing , however also excessively damps high gradients and therefore would require an even finer grid to resolve small scale vortices. The conservation of these can be notably improved by employing the fifth order WENO scheme. This essentially non-oscillatory scheme comes without the need of additional artificial dissipation. In combination with DES, which further reduces the eddy viscosity that suppresses the physical resolution of turbulence interaction, a significant improvement of the resolution of small scale eddies could be made. Similar observations as the present ones have been made by [31] who predicted those secondary vortices in a helicopter wake.

In order to obtain a quantitative measure for the quality of the different simulation methods, again the vortex position, circulation, core vorticity and the core radius are compared with the PIV data and plotted in Fig. 7.9. The vortex positions of the URANS/WENO and DES perfectly agree with the measurements. The former USTUTT results over-predict the wake expansion, whereas the free-wake simulations apart from the previously observed phase shift show a contraction of the wake for the third and fourth vortex. All models over estimate the circulation which confirms the general trend that most models over-predicted the lift near the blade tip. However, the DES in combination with WENO comes rather close for the second and third vortices. When looking at the properties that are critical in terms of numerical diffusion it can be concluded that DES increases the predicted core vorticity, particularly in combination with WENO. For the core radius the numerical diffusion of the scheme is dominant over the effect of the turbulence model, since the vortex smearing in the DES/JST simulation is larger than for the URANS/WENO simulation. The combination of DES with WENO yields the best results. It is interesting to see that compared to all previously performed simulations, for the first time at least the growth rate of the vortex size seems to be predicted correctly. The parallel shift could be further reduced either by investing in one finer grid level, by further increasing the error order of the numerical scheme or by

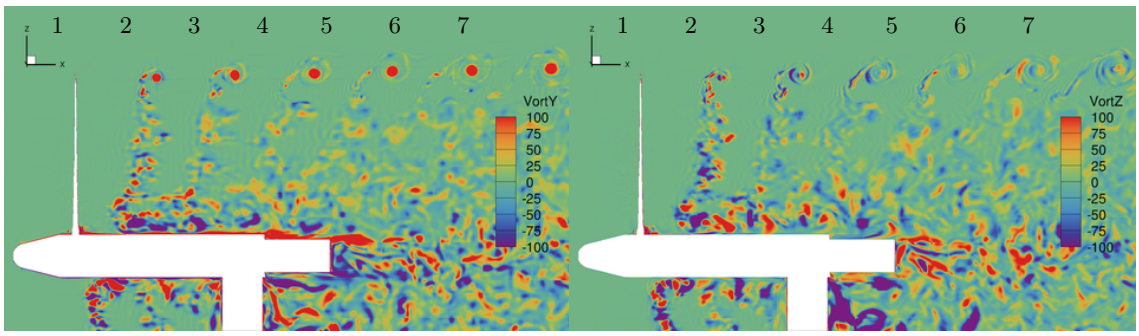

(a) Vorticity -Y (b) Vorticity -Z

Figure 7.6: Vorticity contours to visualize the interaction of trailing vorticity (a) and shedding vorticity (b)

Figure 7.7: Smoke visualization of the tip vortices for $\Lambda = 4.2$. In a virtual vertical slice, the first and second and the third and fourth smoke rings correspond respectively to the second and fourth and fifth and sixth vortices in the simulation shown in Fig. 7.6

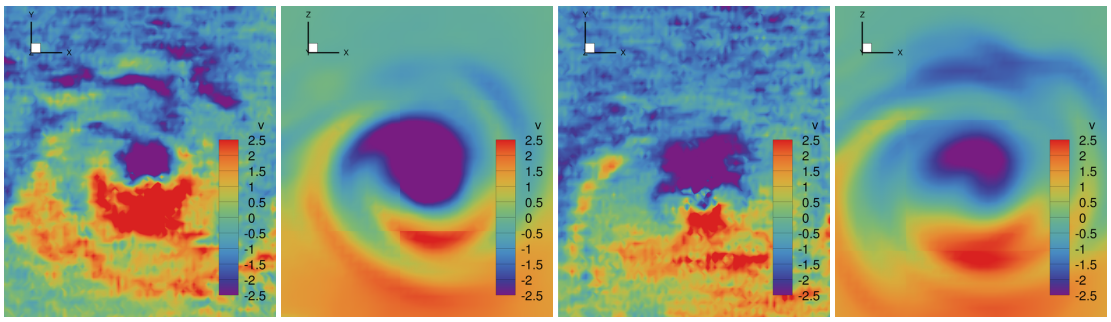

(a) PIV vortex 3 (b) DES vortex 3 (c) PIV vortex 4 (d) DES vortex 4

Figure 7.8: Tangential velocity in the vortex region for vortex three and four. Instantaneous PIV measurement and DES.

employing a DES method which comes close to implicit LES in quasi two dimensional flow regimes.

7.3 Near wake analyses of the yawed inflow cases

Two aspects have been worked out for the cases with yawed inflow. The first is dedicated to the deflection of the wake and the influence of tower and nacelle on this deflection. Secondly, the effect of the yaw angle on the tip vortex development shall be presented. To separate the effect of tower and nacelle, simulations of an isolated rotor performed by DLR and simulations including tower and nacelle by USTUTT are compared.

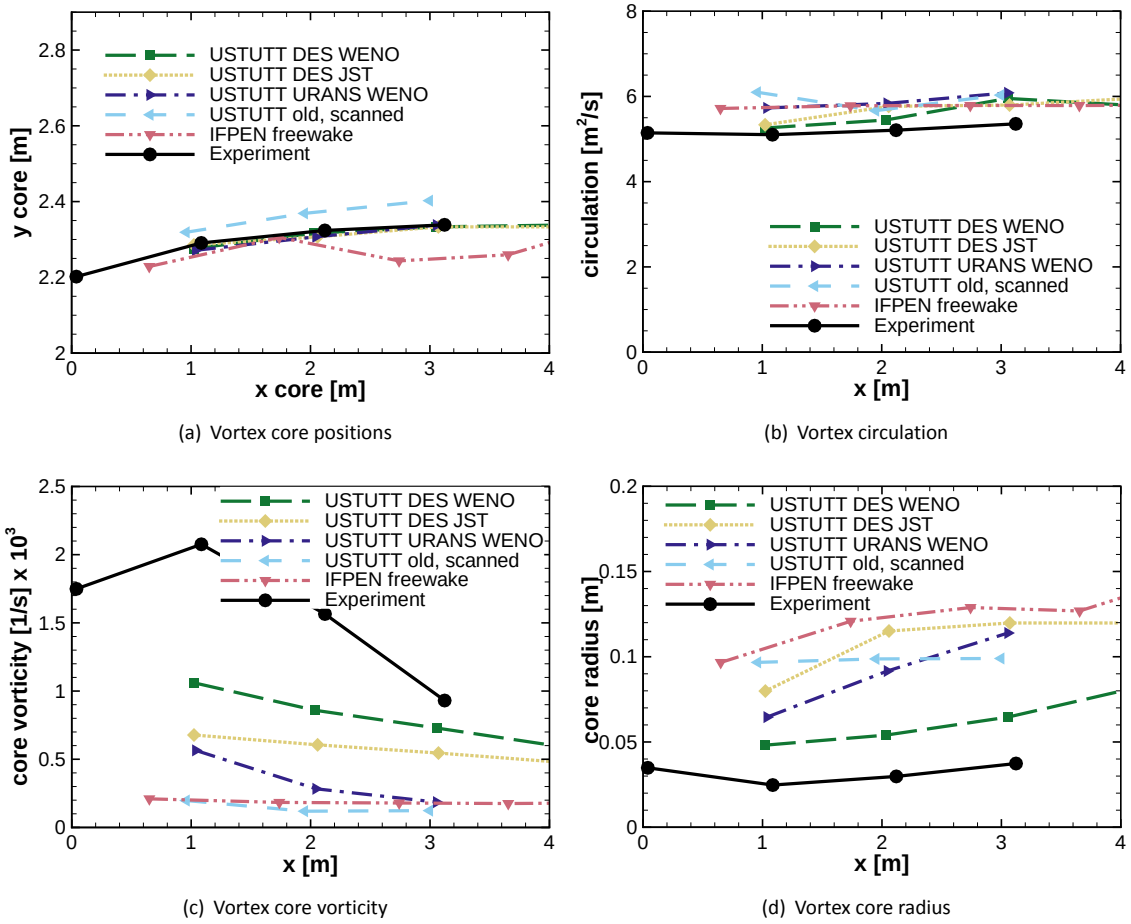

(a) Vortex core positions

(b) Vortex circulation

(c) Vortex core vorticity

(d) Vortex core radius

Figure 7.9: Tip vortex properties for the $24\,m/s$ case.

Computational details

The computational details simulations performed by DLR and USTUTT are compared in Tab. 7.1.

Table 7.1: Simulation parameters for the simulations of DLR and USTUTT

	DLR-TAU	USTUTT-FLOWer
Solver	compressible	compressible
Mesh type	unstuctured	structured
Convection scheme	CDS + matrix dissipation	CDS + scalar dissipation in the blade meshes, WENO in the background mesh
Turbulence model	SST, SA-neg	SA-R
Considered components	Isolated rotor	Rotor, tower, nacelle
Wake mesh	Structured with refinement near the tip	Cartesian mesh with $\Delta = 0.02\,\mathrm{m}$
Azimuthal time step	$0.25 - 0.05\,^\circ$	$0.25 - 0.0625\,^\circ$

Wake deflection

Wake deflection is commonly understood as the shift of the velocity deficit with respect to the axis of rotation of the turbine. A geometric description of the wake is however not trivial. One possibility is to define the wake edge as an isotach, e.g. 95 % of the undisturbed inflow velocity, and then to derive the wake center point as the mid point on the array of various radial traverses in the wake that begin and end on the wake edges. This methods works well in cases where the edge of the wake remains smooth and intact [137], however it may become problematic to extract the wake edge using an isotach in the presence of atmospheric gusts or when the wake is already highly turbulent due to break down of the tip vortices. For such cases an alternative method for the calculation of a representative wake center was presented in [94, 91]. The idea is based on

defining an appropriate mass center of the wake and therefore also accounting for the "amount of deficit" in the description of the wake direction. For a radial traverse, the equation reads:

$$y_{center} = \frac{\int y\,(u - U_\infty)\,dy}{\int (u - U_\infty)\,dy}, \tag{7.1}$$

where u is the local axial velocity and U_∞ the undisturbed axial wind speed. The wake movement can be traced by defining multiple radial traverses in downstream direction. Both, the isotach methods and the mass center method will be applied to the MEXICO rotor in yawed inflow to characterize the deflection of the wake.

The general effects of wake deflection can be explained based on the vortex structures visualized using the Λ_2 criterion in Fig. 7.10. A trailing tip vortex that leaves the rotor plane, naturally begins to align with the inflow vector. Therefore, an asymmetry of the distances between the tip vortices in the wake and the current blade position develops, becoming smaller from the upwind wake edge to the downwind rotor half and larger the other way around. This directly follows that, according to Biot-Savart's law, the axial induction on the downwind side becomes larger than on the upwind rotor half, resulting in a deflection of the wake beyond the pure alignment with the wind vector. Thus a total skew angle of the wake can be defined as

$$\chi = \gamma + \chi_\tau, \tag{7.2}$$

where χ_τ denotes the additional deflection to the yaw angle γ. From the visual impression in Fig. 7.10 this deflection is particularly strong for the high induction case with $10\,m/s$ inflow velocity. It is further interesting to see, that compared to the other cases the first helix trailing from the blade on the upwind side is still approximately aligned with the rotor axis before it gets deflected. On this side, just upstream of the nacelle vortex pairing initiates the break down of the wake. The break down is then amplified when the pairing vortices hit the rear part of the nacelle and the tower. On the downwind side the triggering of the wake instability is slightly delayed. Once, the tip vortices start breaking down their axes realign with the inflow vector. For the 15 and $24\,m/s$ cases no wake instability can be observed. However, local effects as the displacement and destruction of the tip vortices is found as a result of the interaction with the nacelle as well as with the tower and its associated vortex shedding. When looking at root vortices those are deflected to negative y-values as well. Additionally, also a vertical downward deflection can be noted in all cases. This effect is associated with a positive angle of attack acting on the rear part of the nacelle due to a positive w-component (see Fig. 7.3). In the axial traverse this positive w-component was predicted by all simulation tools taking into account the nacelle. The PIV sheets in the direct vicinity of the nacelle for the $15\,m/s$ case provide evidence for this as well. Since the inflow direction on the nacelle is yawed, its profile is now an ellipsis instead of a cylinder, therefore producing lift under a positive angle of attack and a down-wash on the other side, which is most likely the reason for the vertical downward deflection of the hub vortices.

Table 7.2: Approximate additional wake skew angle χ_τ for a yaw angle $\gamma = +30°$ at various TSR for isolated rotor and full turbine simulations.

		Isolated rotor (DLR)	Full turbine (USTUTT)
10 m/s	isotach method	$7.0\,°$	$7.5\,°$
	mass center method	$14\,°$	$17.5\,°$
15 m/s	isotach method	$7.0\,°$	$6.0\,°$
	mass center method	$7.5\,°$	$7.0\,°$
24 m/s	isotach method	$5.0\,°$	$2.9\,°$
	mass center method	$6\,°$	$3.5\,°$

The wake deflection in the horizontal plane can be quantified by applying the wake center line determination methods presented above and is shown in Fig. 7.12. The isolated rotor simulations of the DLR are plotted in the left column, the full turbine simulations of USTUTT in the right column. The isotach method, where the contour $u/U_\infty = 0.96$ was chosen to estimate the wake edges, is shown by the solid line, whereas the dashed lines indicate the wake center-line computed with mass center method. At a first glance, it becomes apparent that the wake edge of the isolated rotor simulation is much smoother than that of the full turbine simulation. Particularly, on the upwind rotor half the USTUTT results reveal a wavy and unsteady wake edge as a consequence of the interaction with the nacelle. Furthermore, the latter is responsible for a deflection of the wake edge in positive y-direction. At the downwind side, the wake edge is similarly predicted in both approached. $10\,m/s$ case, the very irregular shape seen in the USTUTT results is a consequence of the initiating wake instability.

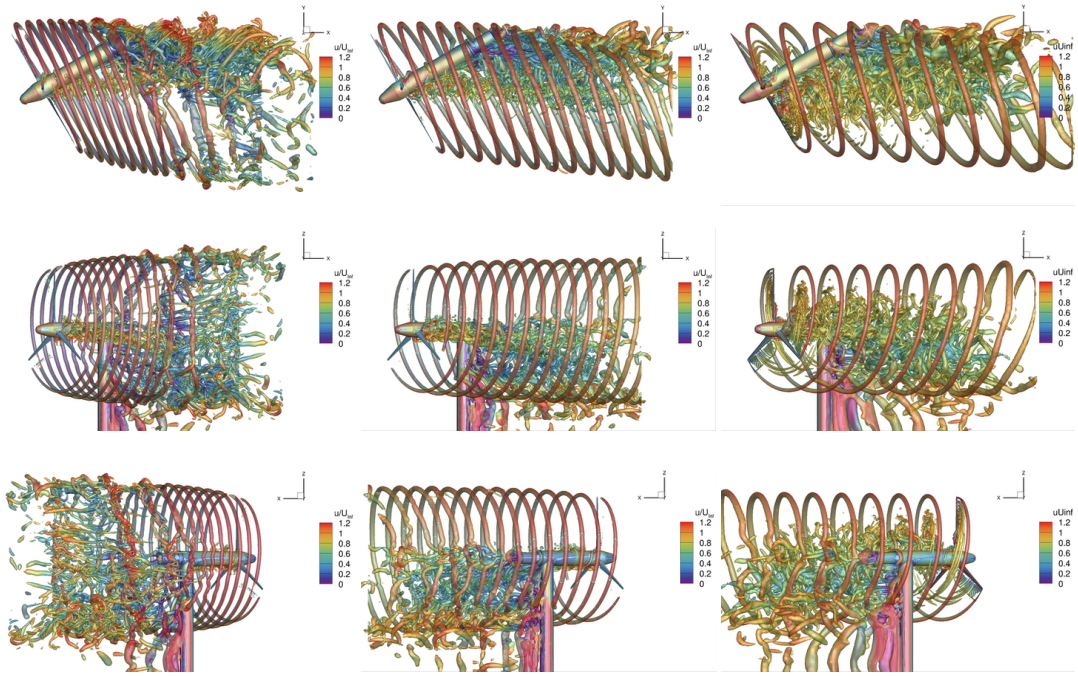

(a) High TSR $\Lambda = 10$. (b) Design TSR $\Lambda = 6.7$. (c) Low TSR $\Lambda = 4.2$.

Figure 7.10: Wake of the MEXICO rotor in yawed conditions for different TSR, $\lambda_2 = -0.015$ iso-surface.

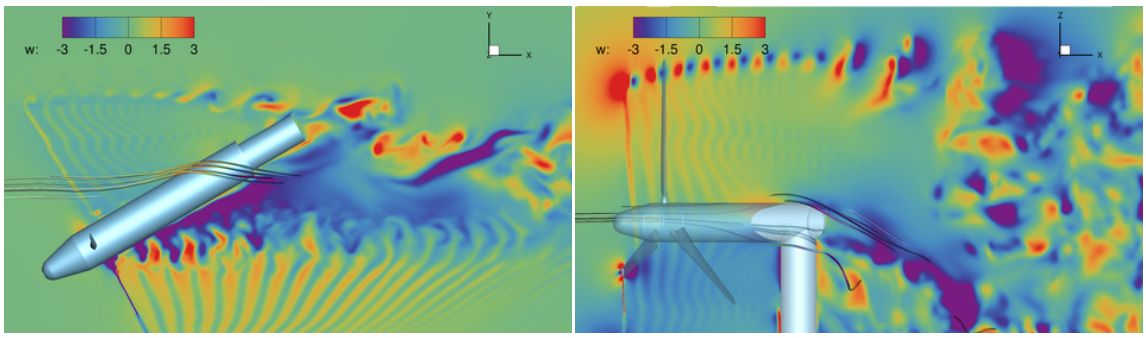

(a) Vertical velocity component w in the horizontal plane for the $\Lambda = 10$ case. (b) Vertical velocity component w in the vertical plane $y = 1m$ for the $\Lambda = 10$ case.

Figure 7.11: Down-wash effect in the rear part of the nacelle

Turning to the flow in the hub region a distinct jet and its associated hub vortices are seen in the DLR results. In contrast to the lower TSR cases where the deflection of the hub vortices is more or less aligned with the global wake deflection, the 10 m/s implies a significantly smaller deflection of the hub wake compared to the outer part. For the DLR results this is even slightly deflected towards positive y-values. In the full turbine simulations the nacelle hampers the generation of such a hub jet and deforms the hub vortices that cannot follow the rotor axis any more and ”stumble” over the nacelle.

When comparing the centerlines obtained from the different evaluation methods it must be restated that the mass center method accounts for the amount of deficit in the wake and moves the center point towards areas of smaller axial velocities. Thus, local effects like the wake of the nacelle yield a bump in the center-line. Additionally, a yaw specific result is that due to the asymmetry of the wake in terms of axial induction, which is always higher on the downwind rotor side, the wake center lines are moved to smaller y-values indicating a stronger wake deflection compared to the isotach method. As the asymmetry of the induction is particularly

high for the $10\,^{m}/_{s}$ case, the wake deflection obtained from the mass center method is more than double compared to the isotach method. For the other cases similar deflection values are obtained.

The approximately derived additional wake skew angles χ_τ are summarized in Tab. 7.2. Overall, the agreement of the DLR and USTUTT results are reasonable. Due to the presence ot the nacelle in the USTUTT simulations the deviations are stronger in the mass center method. A systematic difference is only obtained for the $24\,^{m}/_{s}$ case, where the deflection in the USTUTT simulation is about $2\,^{\circ}$ smaller than in the DLR results. A possible explanation on that is given by studying the tip vortex properties in the next section.

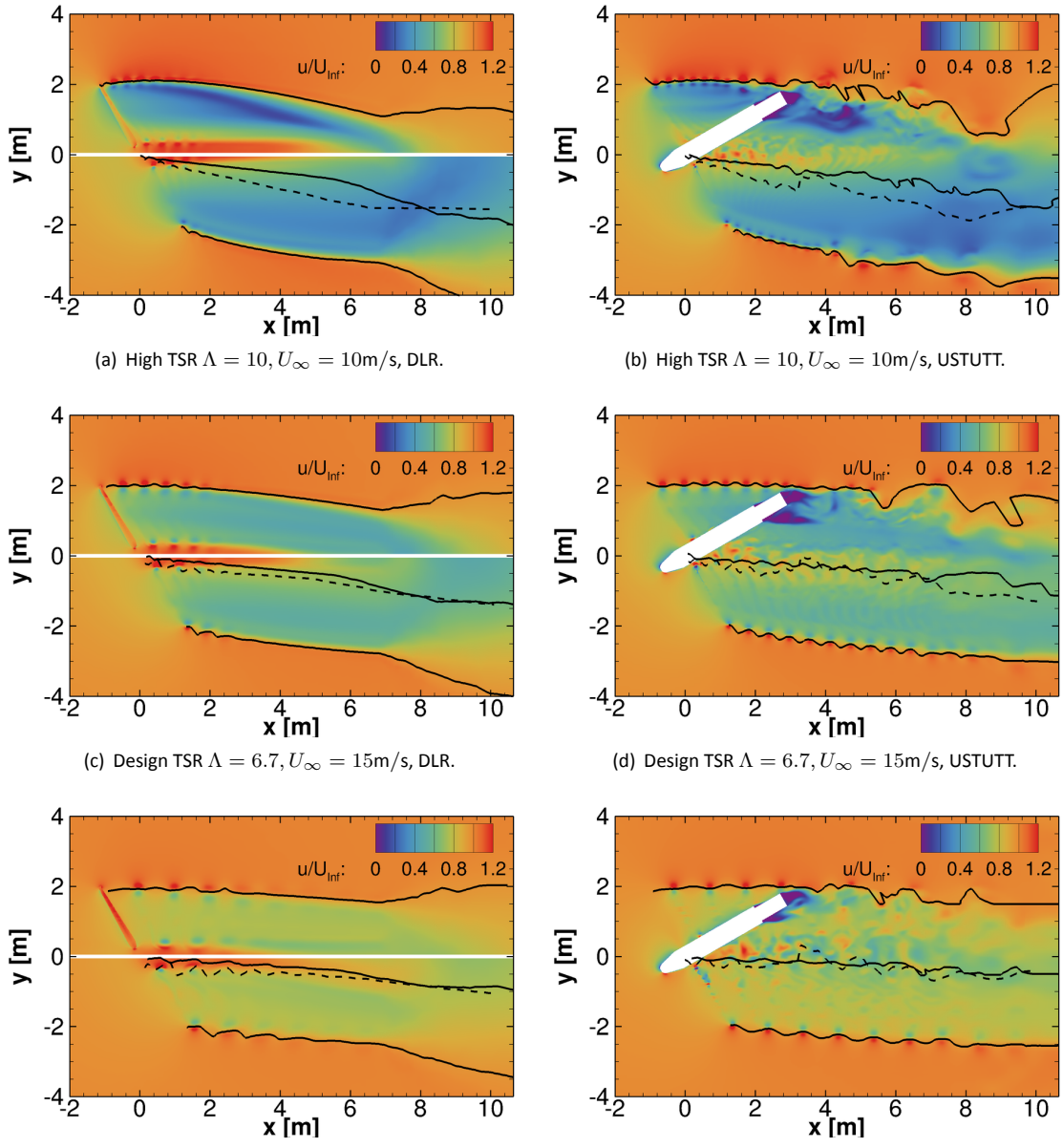

(a) High TSR $\Lambda = 10, U_\infty = 10\text{m/s}$, DLR.

(b) High TSR $\Lambda = 10, U_\infty = 10\text{m/s}$, USTUTT.

(c) Design TSR $\Lambda = 6.7, U_\infty = 15\text{m/s}$, DLR.

(d) Design TSR $\Lambda = 6.7, U_\infty = 15\text{m/s}$, USTUTT.

(e) Low TSR $\Lambda = 4.2, U_\infty = 24\text{m/s}$, DLR.

(f) Low TSR $\Lambda = 4.2, U_\infty = 24\text{m/s}$, USTUTT.

Figure 7.12: Wake centerlines and wake edges evaluated with the isotach method (solid) and using the mass center method (dashed). Isolated and full rotor simulations with various TSR.

Comparison of tip vortex properties

The development of the tip vortex properties on the upwind rotor side is shown in Fig. 7.13. Regarding the vortex positions good agreement between DLR and USTUTT is obtained for the $10\,^{m}/_{s}$ case, since the evaluated tip vortices due not hit the nacelle and also the blockage effect of the latter is moderate. This however drastically

changes when increasing the wind speed. Even if the vortices have not hit the nacelle yet, the blockage already deflects the tip vortices in radial direction. Particularly for the $24\,m/s$ case the difference is obvious, where the vortex path seen in the USTUTT results is even pointing into positive y-direction. Therefore, the distance of these vortices to the rotor plane and also to the other side of the wake increases reducing its inductive effects which is one reason why the wake deflection is more pronounced for the $24\,m/s$ case of the DLR. In addition, a stronger asymmetry was observed in the load distribution of the DLR results with higher values for the upwind rotor side. The effect of this can be seen in the integrated vortex circulation which is particularly higher for the $24\,m/s$ case. Hence, apart from the smaller distance to the rotor plane also the vortex strength is higher for the isolated rotor simulation, which is believed to be the reason for the higher wake deflections seen in the DLR results. Lastly, the core vorticity and vortex core radius show similar trends than for the axial cases. As expected, the core vorticity is comparatively low compared to the experimental level due to dissipative effects. However, it must be stressed, that in contrast to the axial cases where for the USTUTT simulations a background grid resolution of 0.01 m was used in the tip region, the yawed cases employ a grid spacing of 0.02 m in the wake. Since all simulations were further performed in URANS mode, a more dissipate character is present than seen in Fig. 7.9, meaning smaller core vorticity and a larger core radius. When comparing the DLR and USTUTT results the level of the latter properties is about the same. As the USTUTT simulations employed the higher order WENO scheme in the wake region the tip vortices are a bit more concentrated.

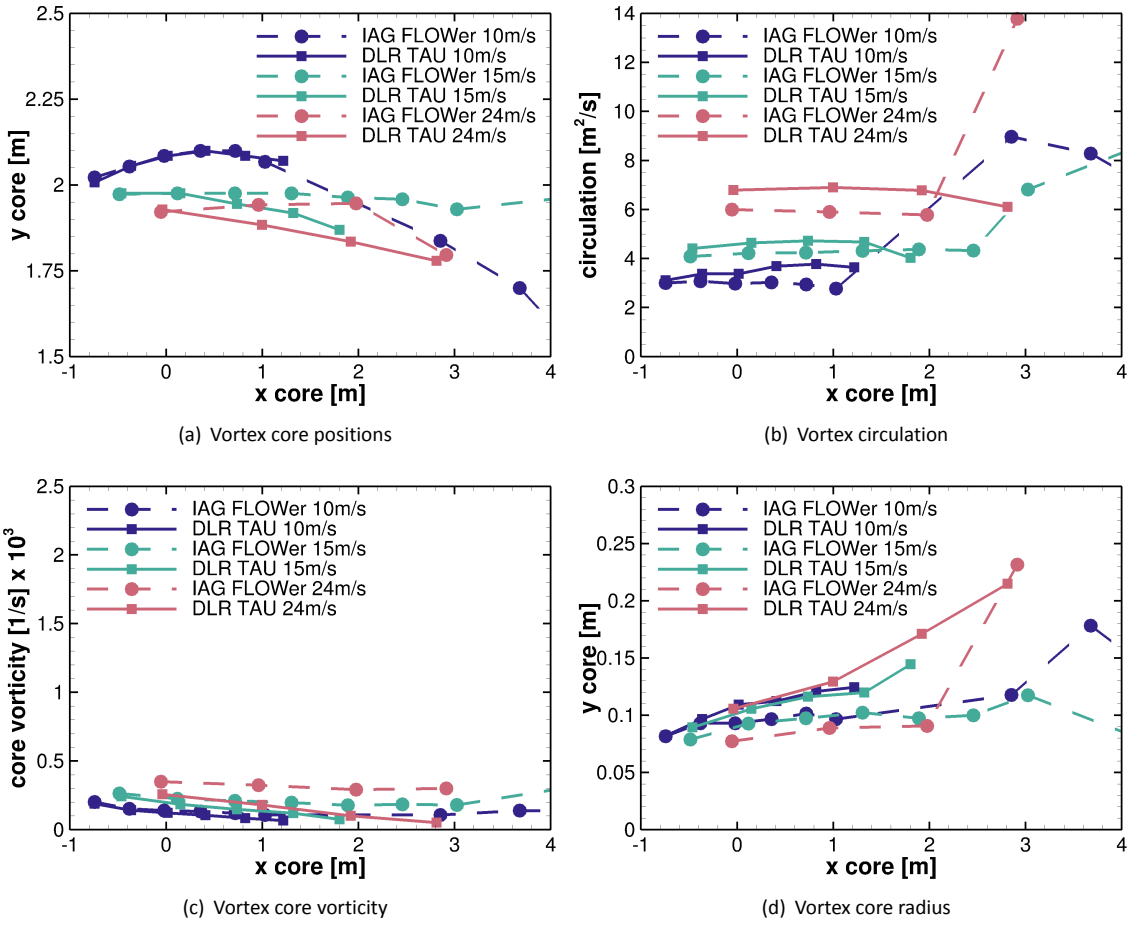

(a) Vortex core positions

(b) Vortex circulation

(c) Vortex core vorticity

(d) Vortex core radius

Figure 7.13: Comparison of tip vortex properties for yawed inflow.

7.4 Conclusions

For the axial inflow conditions the effect of different numerical parameters and turbine representations on the development of tip vortices have been evaluated. Already the computationally very inexpensive free wake code of IFPEN provided reasonable results of the tip vortex properties that don't need to hide from computationally more elaborate CFD methods. Regarding those, vortex diffusion could be reduced by employing a higher order numerical scheme and further by applying Detached Eddy simulations. With the latter for the $24\,m/s$ case close

agreement to the measured vortices was obtained and secondary vortices originating from viscous effects were predicted.

Concerning the yawed inflow cases, a comparison between isolated rotor and full turbine simulations have been performed. The wake deflection is evaluated using two different wake center calculation methods, the first being purely defined as the geometric midpoint of the wake edges and the second taking into account the local axial induction. As vortex nacelle interaction occurs for the 15 and $24\,{}^{m}/_{s}$ cases, the associated blockage displaces the vortices towards the upwind rotor side and results in a slightly larger wake deflection for the isolated rotor simulations. In the root region the nacelle is responsible for deformation and disintegration of the root vortices which are seen to be displaced also in vertical direction.

Overall, it can be concluded, that increasing the model fidelity improves predictions in the near wake. However, at a price of more complex simulation set ups and higher computational effort.

8. Task 4.5: Non-uniformity of flow

8.1 Introduction: Flow non-uniformities in the rotor plane and Prandtl tip loss factor

An important simplifications in the momentum theory is the representation of the rotor by an actuator disc. Such actuator disc is a hypothetical concept which to some extent can be seen as a rotor with an infinite number of blades since the flow in the rotor plane is assumed to be uniform. However, the fact that a real rotor has a finite number of blades makes the actual flow in the rotor plane non-uniform. This non-uniformity is generally covered with the Prandtl tip loss correction F, (or modifications to it, see e.g. [175]). In its basis the Prandt tip loss factor gives the ratio between the local axial induction factor at the blade (as applied in the blade element theory) and the azimuthally averaged axial induction (as applied in the momentum theory). Prandtl derived the factor in the pre-computer era (1919). This necessitated the use of a very simplified vortex wake concept by which it was possible to derive the factor analytically

The simplified model from Prandtl consisted of vortex planes which move with a constant transport velocity without wake expansion, see Figure 8.1.

In the study described in [121] the formulation of the Prandtl tip loss factor is written in a generalised form representative for the way as it is often implemented in wind turbine design codes (for details on the precise derivation and assumptions made, reference is made to [121]).

$$\mathsf{F} = \frac{2}{\pi} arccos(exp(F_1)) \tag{8.1}$$

with:

$$\mathsf{F}_1 = \frac{-B(R-r_1)}{2r_2} \frac{\sqrt{V_n^2 + V_t^2}}{V_n} \tag{8.2}$$

In 8.2, V_n is the axial velocity of wake vortices =$V_w(1-a)$ and V_t represents the tangential velocity which includes the induction in tangential direction.

It is then observed that 72 variations are possible for the practical implementation of 8.1 and 8.2 in design codes, where knowledge is lacking on the best performing implementation. The freedom lies in the values of r_1(for which usually the local value is taken) but in particular for r_2 which is sometimes taken as local value but in other cases as tip value. Moreover different implementations are possible in V_t. For the axial induction factor in V_n the local value can be used but also the tip value where an additional difference lies in applying the annulus averaged value of the induction or the local induction value at the blade section. In some cases the induction factor is even ignored or the average between the wake and free stream value (where a =0) is taken.

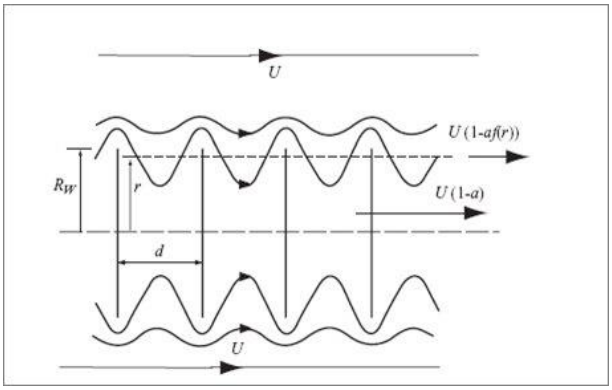

Figure 8.1: Wake model used to derive the Prandtl tip correction, from [29] (U denotes the free stream wind speed and d the distance between the vortex planes)

8.2 Assessment of free vortex wake method AWSM in predicting flow non-uniformaties

In [121] the lifting line free vortex wake ASWM [165] is applied to assess the Prandtl tip loss factor. This model has a much more physical basis to calculate the induction than the simplified wake representation from Figure 8.1 which was needed in the pre-computer area to get an analytical expression for the tip losses.

The good performance of AWSM for the assessment of flow non-uniformities in the rotor plane can amongst others been seen in the results discussed in 4.2.4 where the azimuthal traverses from the AWSM code just upstream and just downstream of the rotor are generally in good agreement with the measurements. Although the results from 4.2.4 are not taken exactly in the rotor plane the flow non-uniformity so close upstream and downstream of the rotor is considered representative for the non-uniformity in the rotor plane. In the MEXICO project opposite to the situation in New MEXICO PIV measurements were taken in the rotor plane itself (note that in MEXICO the blade azimuth differs at least 10 degrees from the 270 degrees azimuth where the PIV sheet is positioned. This allows PIV measurements to be taken in the rotor plane without laser reflections from the blade. In New MEXICO the blade azimuths are very close to the 270 degrees by which PIV measurements in the rotor plane lead to heavy reflections and so the PIV measurements are done just upstream and downstream of the blade). The results given in [68] compare the performance of AWSM in predicting the non-uniformity with that measured in the MEXICO project, precisely in the rotor plane.

In Figure 8.3 a representative comparison is shown. The axial velocities are presented as function of streamwise coordinate, from 30 cm upstream of the rotor to 30 cm downstream of the rotor. The different lines in this figure denote different blade azimuth positions, the colour legend of which is indicated in Figure 8.2 where the zero azimuth angle of one blades (denoted as blade number 1) is defined to be at '12 o' clock'.

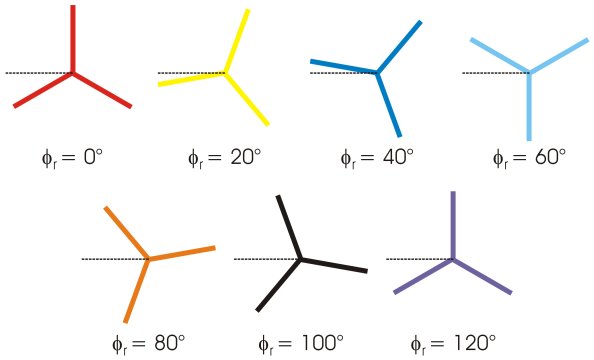

Figure 8.2: Position of blade 1 at $\phi_r = 0, 20, 40, 60, 80, 100, 120°$

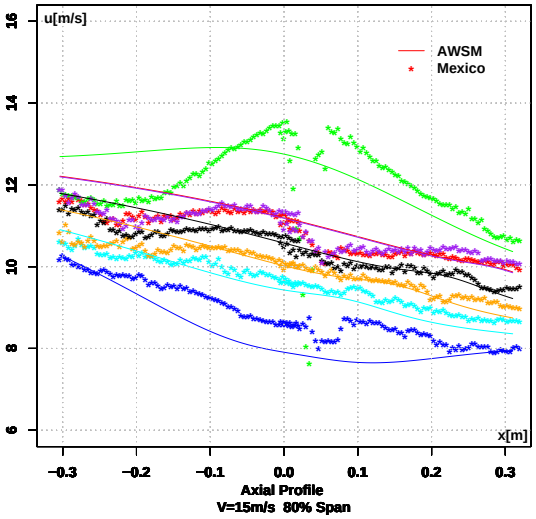

Figure 8.3: IEA Task 29 Mexnext): Axial traverse near the rotor at 80% span and V_{tun} = 15 m/s, different blade positions. Measured and calculated with AWSM

A clear jump in velocities is seen when blade 1 rotates from azimuth angle 20 to 40 degrees, i.e. when blade 3 passes the 9 o clock position where the PIV sheet is positioned. Generally speaking a good agreement between AWSM and measured velocities is found at all azimuth angles.

8.3 Assessment of Prandtl tip loss factor with free vortex wake code AWSM

The good performance of ASWM in predicting flow-non uniformities in the rotor plane from section 8.2 justifies the use of this code for an assessment of the Prandtl tip loss factor.

In [121] the assessment has been done for different tip speed ratios and various rotors:

- A hypothetical rotor which has been derived from the MEXICO rotor with a diameter of 4.5 meter but with a constant loading along the blade. Such hypothetical rotor with constant loading makes the rotor to some extent comparable to the rotor which has been used by Prandtl in the derivation of the tip loss factor since that rotor assumes a constant circulation along the blade as well. Obviously some other assumptions made by Prandtl (e.g. neglect of wake expansion, constant vortex convection velocities in the wake, no trailed vortices along the blade) are still violated.
- The MEXICO rotor with a diameter of 4.5 meter
- The NREL Phase VI rotor with a diameter of 10.0 meter [52]
- A 10 MW reference wind turbine designed in the EU project AVATAR [3] with a diameter of 206 meter
- A 10 MW reference wind turbine designed in the EU project INNWIND.EU [4] with a diameter of 178.4 meter

Note that the main difference between the AVATAR and INNWIND.EU reference wind turbine lies in the fact that the AVATAR turbine is designed for a low axial induction factor (in the order of 0.24) where the INNWIND.EU turbine is designed along a more classical design philosophy leading to an axial induction factor in the order of 0.3

Some examples of the resulting values for the Prandtl tip loss factor in comparison to the tip loss factor from AWSM are given as function of relative radial position r/R for the outer part of the blade (i.e. from r/R =0.8 to

r/R = 1.0) from the constant circulation turbine in the Figures 8.4 and 8.5. Note that only a limited selections of Prandtl tip loss factor implementations is given since some implementations yield results which are so similar that they can be grouped together into 1 common line. The most important observation on Figures 8.4 and 8.5 is then the fact that different implementations of the Prandtl tip loss factor yield very different results. On the other hand there is a qualitative agreement on the tip speed ratio dependency: The tip loss factors at the low tip speed ratio (λ = 4.2) are much lower than they are at the high tip speed ratio of λ = 11.9). This is true for all Prandtl tip loss factor implementations but also for the AWSM tip loss factor.

From the compilation of results for all rotors and for all tip speed ratios the best Prandtl tip implementation for each rotor has been determined (i.e the implementation which averaged over all tip speed ratios yields for the particular rotor the least difference with the AWSM tip loss factor). Also an overall best implementation is determined which yields the least differences with the ASWM tip loss factor for all rotors and all tip speed ratios. These implementations are compared in Figure 8.6 for the MEXICO rotor at a high tip speed ratio of 10 and in Figure 8.7 for a low tip speed of 4.2. In this Figure the implementation of the ECN tip loss factor is given too. This ECN implementation uses the so-called roller bearing assumption for the determination of V_n, i.e. an average value for the induction value between the wake and the free stream is taken (note that the free stream induction is zero).

The comparison between the results from Figure 8.6 with those from Figure 8.7 shows that the differences are much larger in Figure 8.6. This is due to the fact that the tip loss factor is a correction on the induced velocities where these induced velocities are highest at λ = 10 from Figure 8.6.

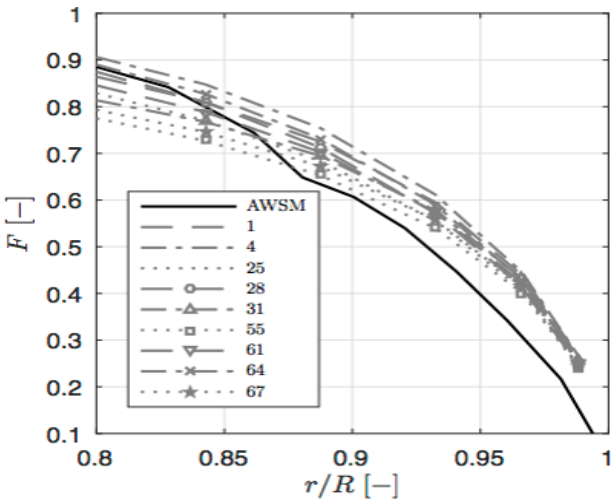

Figure 8.4: Tip loss factor as function of relative radial position for the hypothetical rotor at a tip speed ratio of 4.2: AWSM tip loss factor compared with various implementations of the Prandtl tip loss factor)

8.4 Recommendation on implementation of Prandtl tip loss factor

The most important conclusion from all analyses which then forms a recommendation for BEM modellers, turns out to be the observation that when using the Prandt tip loss factor from equations 8.1and 8.2, the best implementation (i.e. the implementation with the least differences to the AWSM tip loss factor) is found when the distance r_2 and V_n is evaluated locally. This is true for the "rotor's best" as well as the "overall best" implementation of the factor. The dependency on the precise implementation of V_t turns out to be very limited. For r_1 the local value can be used. For more information reference is made to [121].

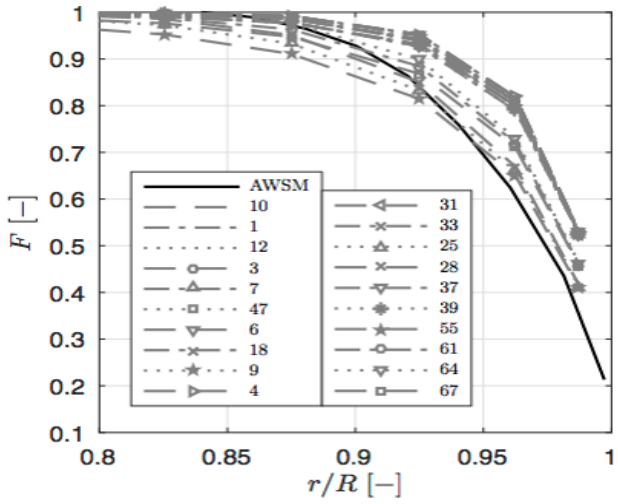

Figure 8.5: Tip loss factor as function of relative radial position for the hypothetical rotor at a tip speed ratio of 11.9: AWSM tip loss factor compared with various implementations of the Prandtl tip loss factor)

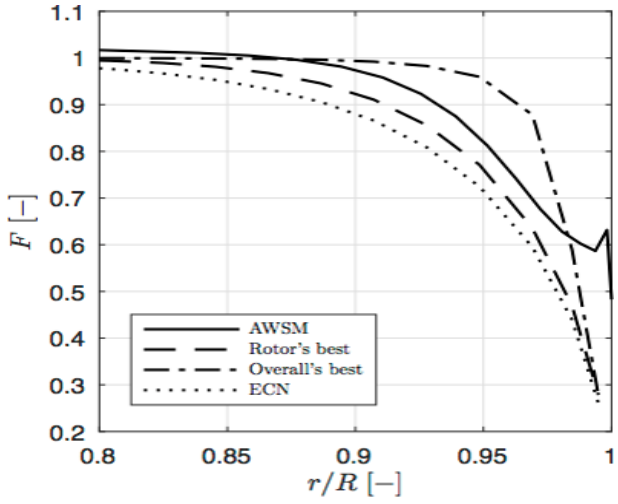

Figure 8.6: Tip loss factor as function of relative radial position for the MEXICO rotor at a tip speed ration of 10.0: AWSM tip loss factor, ECN tip loss factor and rotors and overall best implementation)

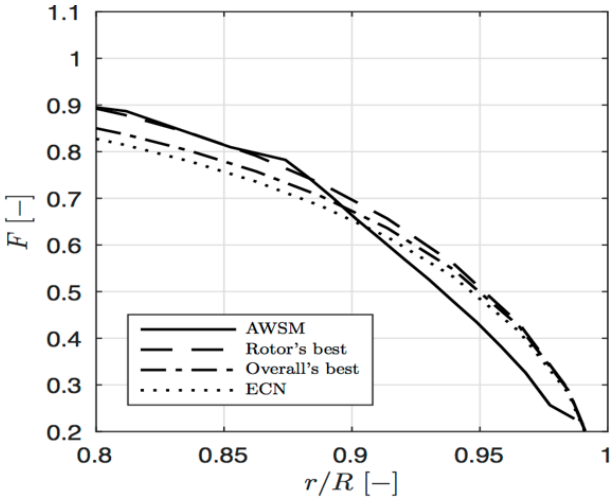

Figure 8.7: Tip loss factor as function of relative radial position for the AVATAR rotor at a tip speed ration of 10.0: AWSM tip loss factor, ECN tip loss factor and rotors and overall best implementation)

9. WP4.6: 3D Effects

9.1 Introduction to Task 4.6

The so called 3D effects, also known as Himmelskamp effect, rotational augmentation or stall delay, were first documented seven decades ago by Himmelskamp [62], who observed that at high angles of attack the blade section characteristics in the inboard blade region differ considerably from the corresponding 2D characteristics. However, the physical mechanisms leading to this effect are still not well understood.

In this task, numerical simulations of different rotors have been performed in order to gain a better understanding on how 3D effects can affect the performance of different wind turbines.

A summary of the work carried out by ForWind (University of Oldenburg) to simulate the TU-Delft-A turbine [58] as well as the Institute of Aerodynamics and Gas Dynamics (IAG) of the University of Stuttgart to simulate the MEXICO turbine [10] are presented in the sections 9.2 and 9.3, respectively. The conclusions of this task are then summarized in section 9.4 .

9.2 3D effects on the TU-Delft-A wind turbine

The TU-Delft-A wind turbine is a two bladed rotor with a diameter of 2 m. The chord and twist distributions are shown in Figure 9.1.

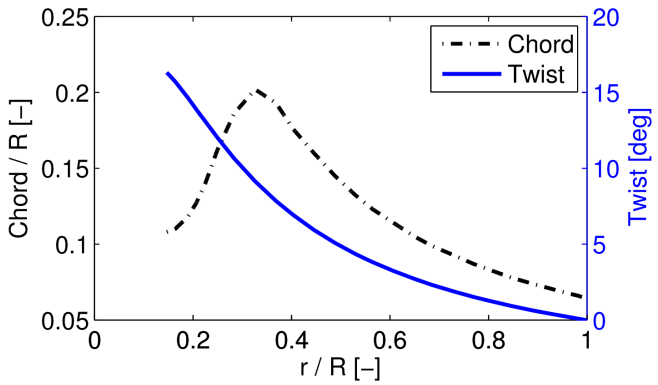

Figure 9.1: Chord and twist distribution of the TU-Delft-A wind turbine along the blade span.

The considered case assumes rated conditions with a free speed of $U_\infty = 6\ m/s$ and a rotational speed of $\omega = 400rpm$, resulting in a tip speed ratio of $\lambda = 7$. The available experimental data comprise Stereo Particle Image Velocimetry (SPIV) measurements in a plane orthogonal to the blade axis all along the span. The measurement campaign took place in the Open Jet Facility of Faculty of Aerospace Engineering at the Delft University of Technology [5].

In the current study, a RANS simulation was performed using the finite-volume code OpenFOAM [107]. The turbulence model $k-\omega\ SST$ by Menter [95] was chosen because of its proven reliability for separated flows. However, it is worth to recall that assuming fully turbulent flow might be a non-negligible source of uncertainty, since the transition from laminar to turbulent flow should not be disregarded.

The mesh was created with the software Pointwise [119] and contains 9.8×10^6 cells. The dimensionless height of the first cells in the boundary layer Y+ was smaller than one along the whole blade, what allowed to run the simulations without any wall function.

The velocity field at a distance of 10 mm from the suction side of the blade surface was reconstructed from the PIV and CFD results in order to study the flow in the blade surface proximity. As shown in Figure 9.2, 9.3 and 9.4, the agreement between experiments and simulations is quite good for all velocity components, what allows to build confidence on the reliability of the numerical model.

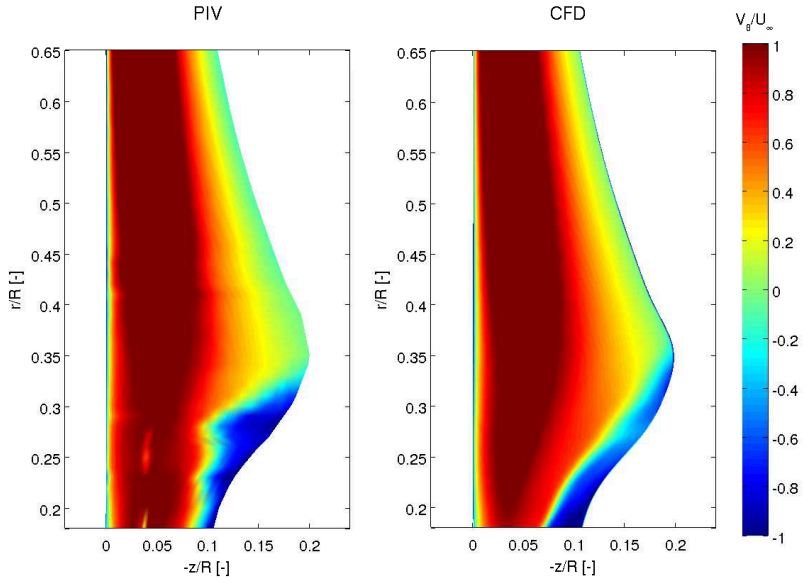

Figure 9.2: Experimental and numerical results of the azimuthal velocity component 10 mm off the blade suction side.

In terms of 3D effects, the radial velocity component is especially relevant, since it is known to play a substantial role in the mentioned type of aerodynamic effect. As it is clear from Figure 9.4, the root of the blade presents strong radial flows up to the spanwise position corresponding to the position of maximum chord length.

In Figure 9.5, the numerical results are used for plotting the limiting streamlines over the suction side of the blade root against the isobars in order to study the origin of the radial flows. As it can be seen from this figure, the flow over the regions with separated flow do not follow the pressure gradients. This implies that the driving force pushing the flow from the root to larger spanwise positions must be attributed to the centrifugal force.

Figure 9.6 shows the C_p distribution corresponding to the radial position $r/R = 0.26$. At this location, the angle of attack (AoA), which was obtained applying the method by [143] , is $AoA \approx 13°$. The corresponding distribution from $2D$ airfoils obtained from numerical and experimental results are also shown. As it can be seen, the C_p distribution corresponding to the 3D case differs substantially from the one of the 2D case. Interestingly, the differences affect not only the suction side, but also the pressure side. The suction peak is significantly reduced in the 3D case. The same happens with the slope of the adverse pressure gradient, what implies that the stall is delayed. The point of separation is easily identifiable in the 2D case as the point where the adverse pressure gradient meets the region with zero pressure gradient ($x/c \approx 0.39$). In the 3D case, however, this point can not be easily identified, since the adverse pressure gradient seems to extend until the trailing edge. This suggests that the flow might remain attached all along the chord. In order to elucidate if that is the case, the wall shear stress in chordwise direction is analysed in Figure 9.7.

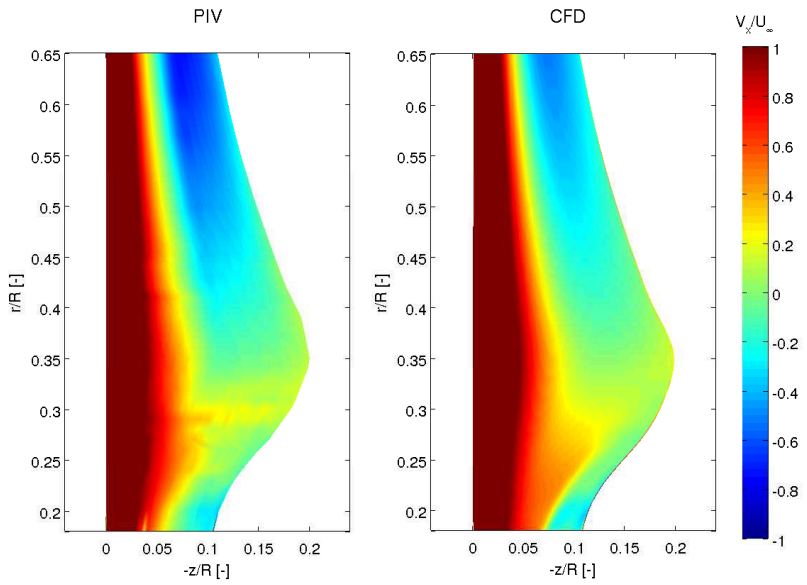

Figure 9.3: Experimental and numerical results of the axial velocity component 10 mm off the blade suction side.

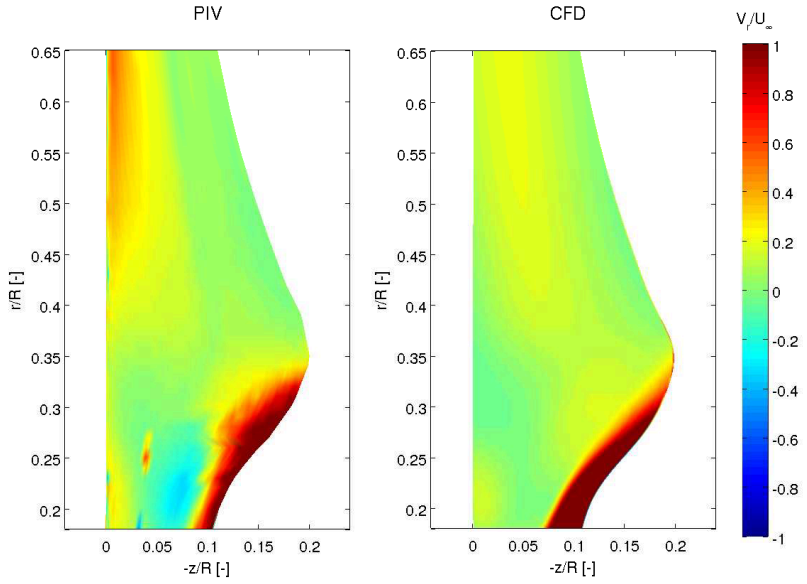

Figure 9.4: Experimental and numerical results of the radial velocity component 10 mm off the blade suction side.

A change in the sign of the wall shear stress along the chord would indicate the location of the flow separation point. However, in the 3D case the wall shear stress remains positive for the whole chord. This confirms that the flow remains attached all along the suction side as a consequence of the 3D effects. The resulting C_l and C_d for this radial position as well as for the corresponding 2D case are presented in Table 9.1.

Table 9.1: C_l and C_d for the simulated 2D airfoil and 3D blade at r=0.26R, AoA$\approx 13°$

	Cl	Cd
2D	0.97	0.07
3D	1.06	0.07

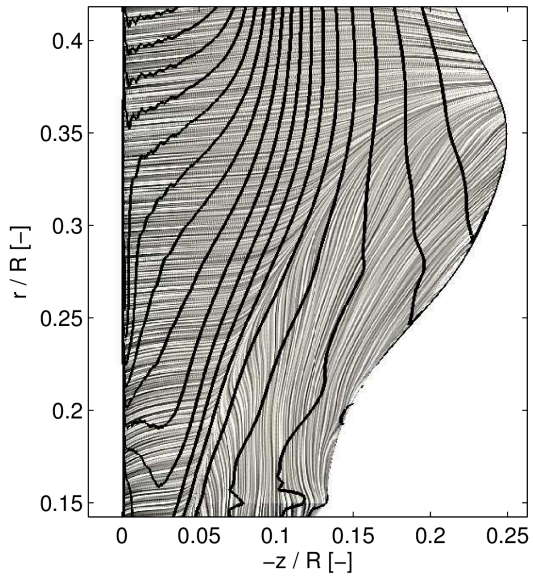

Figure 9.5: Isobars and limiting streamlines over the suction side of the blade root region (obtained from the numerical results).

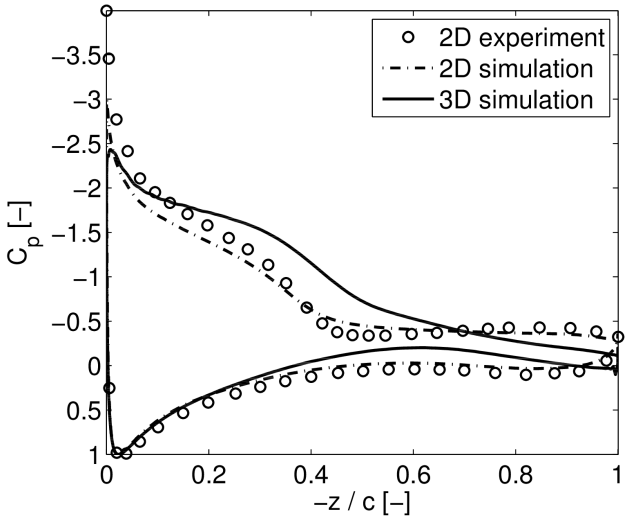

Figure 9.6: Cp distributions at $AoA \approx 13°$. The corresponding Reynolds numbers are $Re \approx 1 \times 10^6$ for the 2-D experimental results, $Re \approx 1 \times 10^5$ for the simulated 2-D airfoil, and $Re \approx 1 \times 10^5$ for the 3-D blade ($r = 0.26R$).

The lift force is clearly influenced by the 3D effects in spite of the relatively small angle of attack ($AoA \approx 13°$), but this is not the case for the drag force, which remains unaltered. In terms of the aerodynamic forces, the reduction of the suction peak previously described partly counteracts the reduction of the adverse pressure gradient. Therefore, the influence of the 3D effects is more obvious in the C_p distribution than in the integrated aerodynamic sectional loads.

9.3 3D effects on the MEXICO wind turbine

The simulations performed by the IAG (University of Stuttgart) are based on the MEXICO wind turbine [10]. The details of this 3-bladed rotor with a diameter of 4.5 m can be found in Ref. [27]. The operating conditions

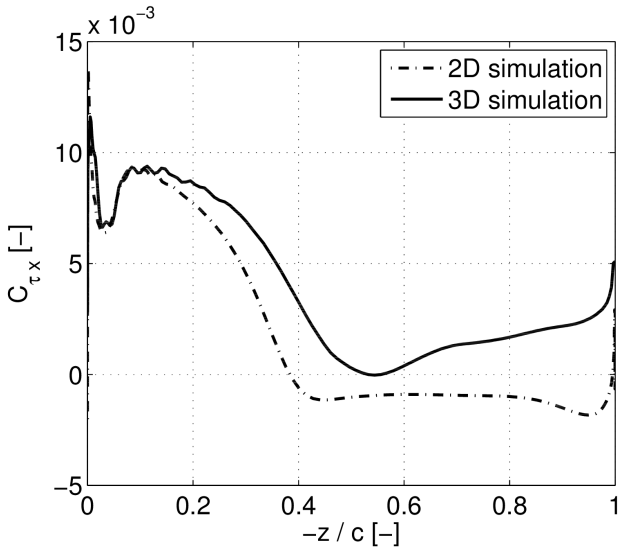

Figure 9.7: Wall shear stress in the chordwise direction over the suction side for the 2-D and 3-D (r D 0:26R) cases.

considered for this case are $U_\infty = 24\,m/s$ and $\omega = 424\,rpm$, corresponding to a tip speed ratio $\lambda = 4.16$. The pitch angle is kept constant at $-2.3°$. Under these conditions, the flow over the blades is completely stalled.

The simulation is of the type Delayed Detached Eddy Simulation (DDES) and the Menter's SST model [95] is employed as RANS model near the wall. The time is advanced with a rate of $1°$ per time step. The Chimera method is used for combining efficiently different high-quality meshes of different parts of the domain. The total number of elements is 37.5×10^6.

In order to extract the angle of attack from the numerical results, the azimuthal averaging technique [55] is used. As in the previous study (section 9.2), the nacelle and hub were here not modelled. This leads to an acceleration of the flow in the proximity of the rotor axis due to a nozzle effect. However, this is not expected to play a significant role for the 3D effects.

Figure 9.8 shows the dimensionless radial velocity component for 4 different spanwise positions of the blade.

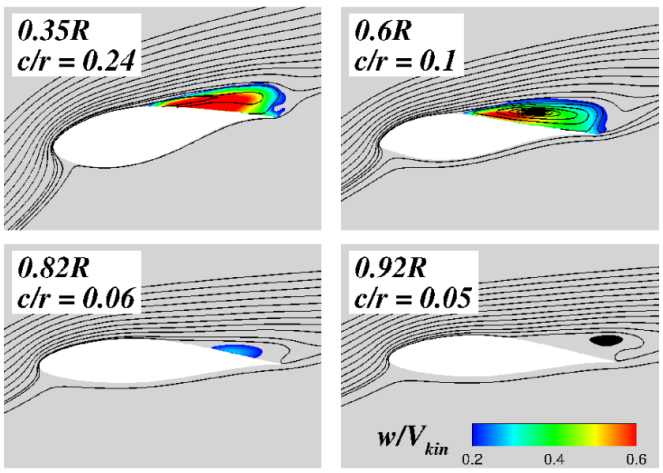

Figure 9.8: Time-averaged dimensionless radial velocity in rotating frame of reference at several radial stations, $r/R = 0.35$, 0.6, 0.82 and 0.92.

As it can be seen, the radial velocity is only substantial up to $r/R = 0.6$, in spite of the fact that the flow is also separated at larger spanwise positions. From these results it is concluded that radial flows only occur for $c/R < 0.1$, and they only take place in regions with separated flow. This is in contrast with the results observed in the TU-Delft-A turbine [58] (see section 9.2), where it was observed that the radial flows can also be significant with attached flow. From Figure 9.9, it can be seen that C_l is increased in the 3D case with respect to the 2D case at inboard radial positions.

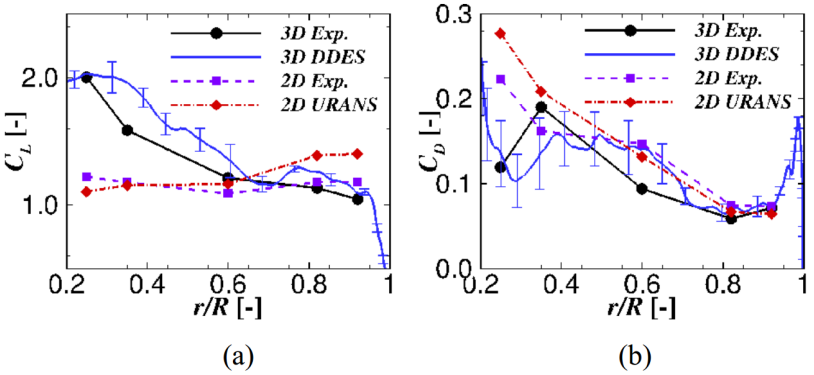

Figure 9.9: (a) Lift and (b) drag coefficients along the blade radius from CFD and experiment. The error bars indicate the standard deviation of the unsteady fluctuations.

Two main reasons have been documented to cause this lift increase:

1. The centrifugal force 'pumps' the separated flow from the root to larger spanwise positions, what reduces the thickness of the boundary layer.
2. The Coriolis force pushes the flow in the chordwise direction, counteracting the adverse pressure gradient.

Both effects contribute to delay the flow separation and correspondingly to the enhancement of the lift force.

As also shown in Figure 9.9, the drag force does not seem to be significantly influenced by the 3D effects. This is in good agreement with the study of the TU-Delft-A wind turbine (section 9.2) and previous analysis on the MEXICO wind turbine [61]. A slight decrease of C_d with respect to the 2D case is attributed to the reduced area with separated flow.

9.4 Conclusions of Task 4.6

Within this task two different wind turbines have been simulated for obtaining a better understanding of the flow mechanisms leading to the so called 3D effects: on one hand the two bladed TU-Delft-A wind turbine (rotor diameter $D = 2\ m$) has been simulated at nominal operating conditions [58]. On the other hand, the three-bladed MEXICO turbine (rotor diameter $D = 4.5\ m$) has been computed at stall conditions [10]. In the case of the TU-Delft-A turbine, substantial radial flows were found even before the flow separation took place. Indeed, the flow separation was completely avoided as a consequence of the 3D effects. However, in the MEXICO turbine, radial flows were only found in regions with separated flow and for $c/R < 0.1$. In both studies it was concluded that the radial flows played a crucial role in the development of 3D effects. The origin of the radial flows has been attributed to the centrifugal force and not to spanwise pressure gradients.

The 3D effects affect strongly the C_p distributions by reducing significantly the suction peak and the adverse pressure gradient. Both effects counteract each other in terms of the resulting loads, but the adverse pressure gradient reduction dominates over the reduction of the suction peak. As a consequence, the lift force C_l is increased in regions affected by 3D effects. On the other hand, the drag force C_d does not seem to be substantially influenced, although in the case of the MEXICO turbine, a slight reduction of the drag force has been observed. This effect was attributed to the reduction of the area with separated flow.

10. Task 4.7: Yawed Conditions and Instationary Airfoil Aerodynamics

10.1 Goal of the task

Modeling of wind turbines at yawed conditions is an important research area since wind turbines in the atmospheric boundary layer (ABL) are operating in a fluctuating wind, by which they are continuously exposed to a misalignment of the velocity vector with respect to the rotor plane. This leads to higher fatigue loads and a reduced power see e.g. Ref. [17]. Yawed inflow can even be applied deliberately in order to deflect the wake behind the upstream so that wind farm losses are decreased (the expense of an (unknown) lower power at the upstream turbine going together with higher loads). Therefore, accurate models for the prediction yawing moment are needed to design control algorithms for yawed controlled turbines so that yaw errors are corrected in a passive way. Still despite several decades of research, the results from Mexnext and AVATAR have shown that yaw remains one of the most challenging conditions to model.

The task 4.7 period is from the 1st of January, 2015 to the 31st of December, 2017 in a joint effort by Forwind, ECN and Fraunhofer IWES. It focused on the improvement of an engineering yaw model by tuning the parameters in such a model with results from a higher fidelity model. The work was largely funded by AVATAR. Additional support from the EU IRPWIND program and the Federal Ministry for Economic Affairs and Energy (Bundesministeriums für Wirtschaft und Energie) was received in order to fund the exchange or researchers between Forwind and ECN. The work is described in detail in Ref. [37]. The present chapter only gives a very brief summary of the main activities and results.

10.2 Background

For a better understanding of different aspects of wind turbines that operate under yaw misalignment, the convention for the yaw moment M_z, yaw and azimuth angle, respectively ψ and ϕ is presented in Figure 10.1. Figure 10.1(a) shows the positive definition of the yaw moment (positive means a restoring yawing moment) and the yaw angle. For positive yawed inflow, the upwind side of rotor plane is on the left side and between 180° to 360°. Figure 10.1(b) shows the definition of the azimuth angle, where at 12 o'clock ϕ = 0° and rotating clockwise, the ϕ = 180° is at 6 o'clock.

The azimuthal variation of blade loads (and its effect on the yawing moment) is mainly driven by two unsteady phenomena:

1. Advancing and retreating blade effect:

   In the case of positive yaw the blade will advance in the lower half of the rotor plane and retreat in the upper side. In this case the tangential component of the wind velocity is no longer negligible and should be considered for computing the angle of attack. This leads to a 1P variation of the angle of attack and the effective inflow velocity. It leads to a cosine type-like azimuthal distribution and it is symmetric around

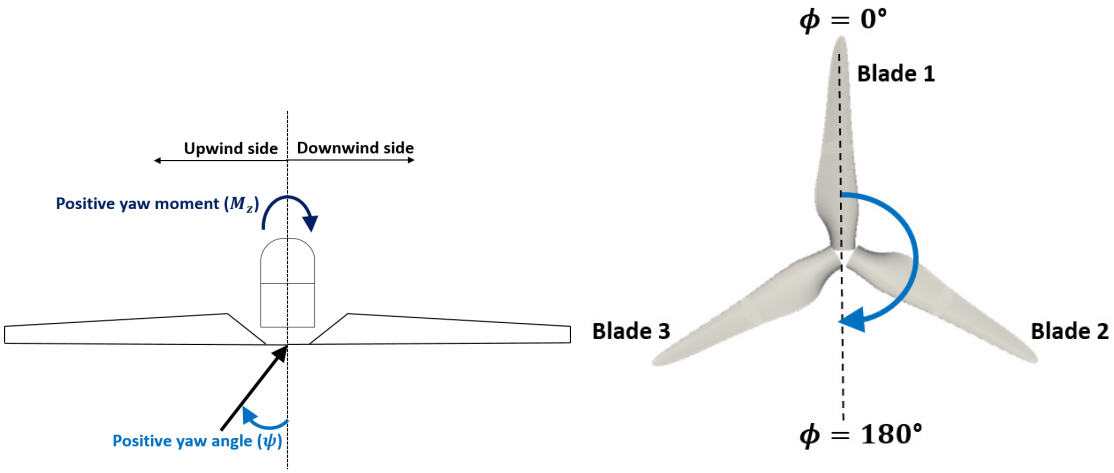

(a) Convention of yaw angle ψ and yaw moment M_z

(b) Convention of azimuth angle ϕ

Figure 10.1: Convention for the yaw angle ψ, yaw moment M_z and azimuth angle ϕ

ϕ =180° (blade pointing down in vertical position). Therefore, the maximum thrust will occur at ϕ =180° due to higher effective velocity. This effect leads to an aerodynamic tilt moment but no restoring yaw moment [129]. Its effect is relatively straightforward to model and it was already included in the first generation of wind turbine design codes [167]. It should be noted that although the advancing and retreating blade effect itself is relatively straightforward to model it can be shown to occur mainly at low tip speed ratios ([50] and [136]). These low tip speed ratio generally go together with large angles of attack which may lead to strong dynamic stall effects. These dynamic stall effects are extremely difficult to model.

2. Skewed wake effect:

   As shown in Figure 10.2, due to the asymmetric position of the wake (root and tip free vortex) relative to the rotor plane, the trailing tip vorticity is on average closer to the downwind side, therefore, the axial induction over the rotor plane will vary. The consequent load unbalance between the upwind and downwind side of the rotor plane results in a yaw moment.

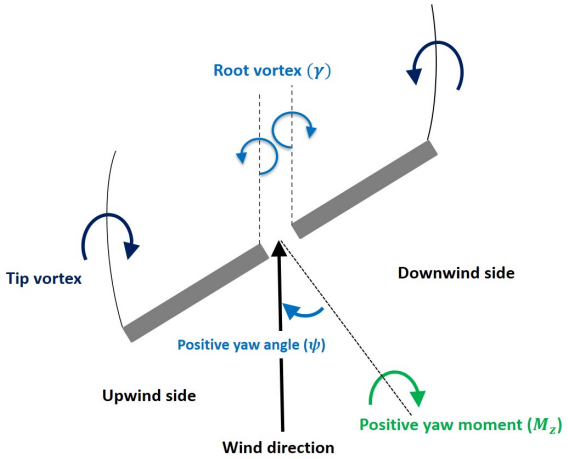

Figure 10.2: Schematic view of the root and tip vortices trailing from the rotor at yawed condition. Adapted from [51]

To correct for this load unbalance Glauert developed a model based on his work on the autogyro [45]. He proposed that $a = a_{average}\left(1 + K\frac{r}{R}sin\phi\right)$ in order to correct the induction factor at the blades for non-axial conditions, where: a is axial induction at each section and each azimuthal position, $a_{average}$ is the averaged axial induction at each section over one rotation, K is a constant, r is the sectional radial station, R is the rotor radius and ϕ is the azimuthal position of the rotor blade.

Although a large number of variants to this model have been developed (the difference mainly lies in the K) they all rely on a sinusoidal variation. Such sinusoidal variation is induced by skewed tip vortices only and it leads to a stabilizing yawing moment.

10.3 Derivation of the new model

In the wind energy society the first attempts to include the skewed wake effect was done in the JOULE projects Dynamic Inflow [50]. Later in 1999 Schepers [129] used inflow measurements on a model turbine placed in the TU-Delft wind tunnel to develop a new model for the prediction of induction variation with azimuth position. In this work, the measurements of the axial velocity at several radial positions and yaw angles have been expanded in a Fourier series as a function of azimuth angle. A second-order Fourier series, as Equation 10.1, was derived for the variation in axial induction.

$$a = a_{average}\big(\, 1 - A_1 cos\big(\phi - \psi_1\big) - A_2 cos\big(2\phi - \psi_2\big)\big) \tag{10.1}$$

The amplitudes A_1 and A_2 and phases ψ_1 and ψ_2 have been tuned as a function of the radial position and yaw angle. In 1999 it was not allowed to publish the precise values of the model parameters but they were in 2012, see [131].

The main difference in comparison to the previous models lies in the inclusion of root vortex effects which were clearly observed in the measurements of velocities in the inner part of the blade. This led to a deviation from the pure sinusoidal behaviour and destabilizing yawing moments at the inner part of the blade. It was interesting to note that in retrospective, the root vortex effects were observed in precisely the same qualitative way in FVW calculations from NTUA as carried out earlier in the above mentioned projects on Dynamic Inflow ([50] and [136]).

The 2nd order model with root vortex effects was often found to give significant better prediction of the loads at yawed conditions than a conventional Glauert based model. However, recently comparisons were made to fully resolved CFD simulation and experiments. Rahimi et al. [120] showed that for modern turbines (multi-MW class), at the sections near the blade tip, the qualitative behavior of the induced velocity for Schepers model is slightly poorer due to an over-prediction of the root vortex effects for this section. This can be due to the fact that Schepers used the experimental data from a small sized turbine (2 bladed with the rotor diameter of 1.2m) with a strong root vortex. The current wind turbine blades are far bigger and have a smoother transition at the root. Therefore, improvement can be done for the current yawed models not only in terms of root vortex modelling but also to enhance the general validity for larger turbine and their functionality at extreme yaw angles [120]. Last but not least for most of the skewed wake models, the wake is assumed to be cylindrical, where for high loading the wake expands considerably [101].

However one of the major limitations for the improvement of low complexity tools, lies in the fact that there are very limited or almost no extensive experimental results available for large turbines. Hence one possibility could be to use so-called high or intermediate (medium) fidelity models, such as fully resolved Computational Fluid Dynamics (CFD), free vortex wake [165] or Actuator Line Models (ALM), [152] to calibrate the BEM correction models. CFD with fully resolved geometry has a very high computational demand and can be used for limited cases, unlike the free vortex wake or ALM. Therefore the present study mainly relies on results from the ALM- OWFA CFD package developed by the National Renewable Energy Laboratory (NREL) [33] with supporting FVW calculations using the ASWM code [165].

Calculations have been performed on 3 types of rotors the NREL 5MW [74], the 10MW AVATAR [3] and the INNWIND.EU [4] turbine for a wide range of conditions.

Figure 10.3 shows a comparison between AWSM FVW and ALM calculated axial induction factor with respect to the azimuth position for 35, 65 and 90 % span for both the AVATAR and INNWIND.EU turbine at rated speed and ψ=30°. For both turbines and for all three sections, the ALM results and AWSM results are in excellent agreement in terms of the location of the maximum and phase, thus, ensuring the validity of the calculations

from both ALM and AWSM. Next from the ALM simulations new parameters have been fitted to the 2nd order equation 10.1.

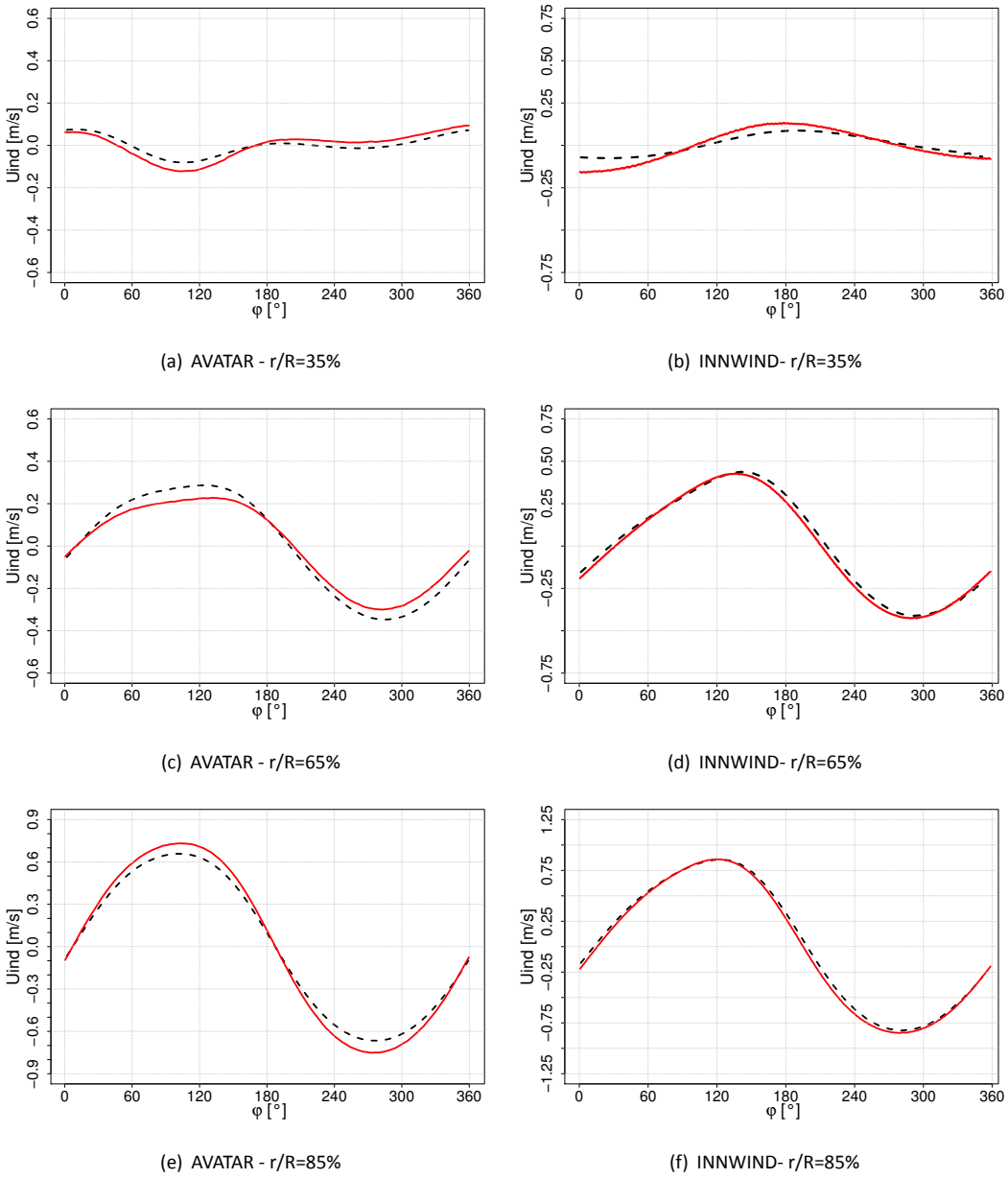

(a) AVATAR - r/R=35%

(b) INNWIND- r/R=35%

(c) AVATAR - r/R=65%

(d) INNWIND- r/R=65%

(e) AVATAR - r/R=85%

(f) INNWIND- r/R=85%

Figure 10.3: Axial induction factor vs azimuth positions at 3 different radial position for the AVATAR $U_\infty = 10.5m/s$ and ψ=30° (left) and INNWIND turbine for $U_\infty = 9m/s$ and ψ=30° (right) . ALM ——, AWSM - · - · ,

Figure 10.4 presents the results obtained for a representative example. It shows the axial induction factor with respect to the azimuth position (left) for one blade and the yawing moment generated by the local blade segments from the three blades (right) at five different radial positions for the INNWIND.EU turbine. Results are shown for the ALM model (i.e. the higher fidelity model, which are assumed to be 'true'), the results from the models developed by Glauert and Schepers as well as the newly proposed model. Also the Generalized Dynamic Wake (GDW) model as derived for helicopter aerodynamics, based on a potential flow solution for the Laplace's equation is added. It can be noted that (as explained above) the model from Glauert deviates at the root: This is reflected in the phase difference in axial induction factor compared to the ALM results and a positive stabilizing yawing moment contribution where the ALM predicts a generally negative destabilizing yawing moment contribution. On the other hand the model of Schepers predicts a too strong root vortex

Table 10.1: Sectional yawing moment for AVATAR $U_\infty = 6m/s$ and ψ =20°.

	Sectional yawing moment (M_z)				
Model	**35%**	**50%**	**65%**	**80%**	**90%**
ALM	-0.372	-0.253	2.47	11.28	15.83
Glauert	0.74	6.50	7.38	12.3	17.16
Schepers	-1.64	-0.575	−0.52	6.19	8.68
Proposed	-.45	-0.36	1.98	9.84	12.28

Table 10.2: Sectional amplitude values of yawing moment for AVATAR $U_\infty = 6m/s$ and ψ =20°.

	Sectional amplitude values of yawing moment (M_z)				
Model	**35%**	**50%**	**65%**	**80%**	**90%**
ALM	0.54	0.93	2.41	3.31	5.55
Glauert	0.37	1.69	5.3	9.15	10.36
Schepers	0.62	0.49	2.61	6.27	7.27
Proposed	0.52	0.92	2.23	3.45	6.89

effect at the outer part of the blade. This is in particular visible through the dip in axial induction factor at an azimuth angle of 90 degrees. This leads to an underpredicton of the yawing moment (although the other models overpredict this moment).

Table 10.1 shows the rotor averaged yawing moment over one revolution at five different sections for the AVATAR turbine, at $U_\infty = 6m/s$ and ψ =20°, using different skewed wake models in comparison to ALM. Results indicate that with almost all models the stabilising moment at the outboard area is predicted correctly. However, at 65% of the span length, Schepers' model predicts a small negative yawing moment, which, is due to incorrect prediction of root vortex.

At the inboard sections the ALM model predicts a destabilizing moment. The Glauert model completely fails to predict this behavior. Schepers model predicts the correct sign but at a higher value than that predicted by the ALM.

The proposed model is the closest to ALM, and it has less deviation in terms of amplitude compared to GDW and Schepers model as presented in Table 10.2.

Generally speaking speaking the newly proposed model outperforms the other models.

As such the newly developed model (described in [37]) can be recommended for inclusion in BEM based models. However it must be noted that during the AVATAR project an insight grew which slightly complicates the validity of the present model (and all other yaw models!). This complication is related to the fact that equation 10.1 models the variation of the induced velocity relative to an annulus averaged value. It should then be known that the solution of BEM equations can be done in different ways, e.g. an annulus averaged approach (based on momentum equilibrium using the annulus averaged conditions) or a local equilibrium approach where the conditions at the particular blade element are used in the calculation of momentum equilibrium. The use of the present yaw model is consistent to the annulus averaged approach but not to the local equilibrium approach due the variation of induced velocities from the advancing and retreating blade effect!

Still as described in [19] the modeling of turbulent sheared flow is preferred to be done with a local equilibrium approach. As such further research is needed to find a method which predicts the correct variation of induced velocities in a local equilibrium approach.

10.4 Conclusion

In this task a new engineering skewed wake model for the prediction of loads in aeroelastic tools was developed and introduced. The new model was derived from a second order Fourier fit for the induction azimuthal variation, obtained from ALM simulations of three multi-MW class wind turbines, for several yaw angles, wind speeds and tip speed ratios. This model covers the dependency of the axial induced velocity as a function of azimuth angles, radial positions, yaw angles and tip speed ratios. Based on the results presented, the following observations can be made:

- The proposed model is implemented into the NREL FAST V8 code and validated by using a set of simulations on the different turbines. Results indicated that the new model in many cases considerably improved the prediction of the azimuthal variation of axial induction factor, loads and the yawing moment at yawed inflow conditions.
- The engineering model for azimuthal variation of induced velocities, which takes into account root vortex effects, performs better than the conventional Glauert model and also Schepers model, in particular at the root section.

In the future, the effect of aeroelasticity, turbulent flow, tilt, cone and shear inflow conditions in combination with yaw should be investigated. Moreover fatigue analysis of a MW class turbine under yawed flow should be conducted. Besides, although, the ALM considers the root vortex into the account, but more research should be conducted on the origin, effect, and characteristics of the root vorticity at the inboard area using experiments and fully resolved CFD simulations.

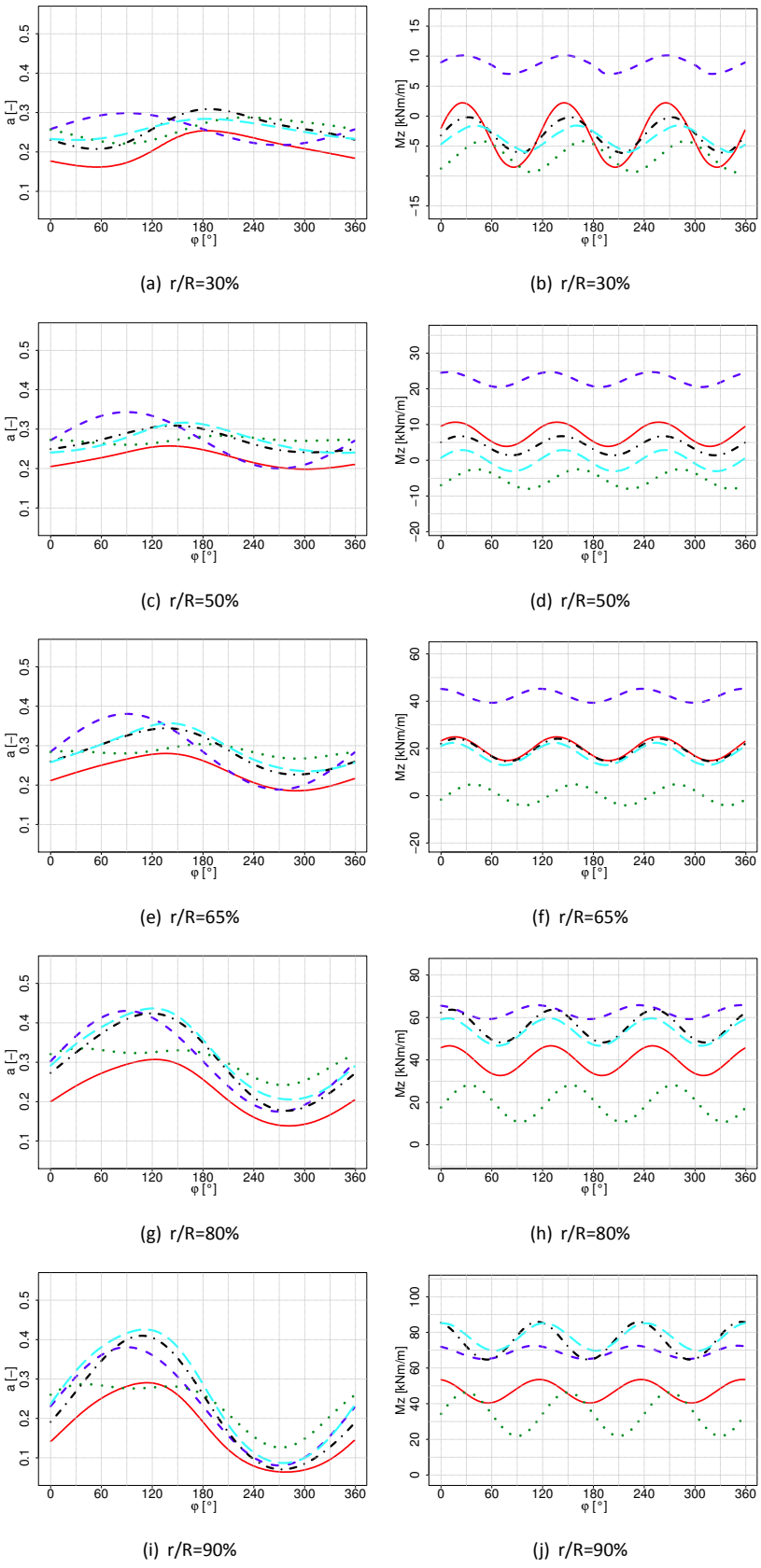

(a) r/R=30% (b) r/R=30%

(c) r/R=50% (d) r/R=50%

(e) r/R=65% (f) r/R=65%

(g) r/R=80% (h) r/R=80%

(i) r/R=90% (j) r/R=90%

Figure 10.4: Axial induction factor(left) and yawing moment (right) with respect to the azimuth position at five radial positions for the INNWIND.EU turbine for $U_\infty = 9m/s$ and ψ =30°. ALM ——, Schepers model ·····, Glauert model - - -, Proposed model -·-·-, GDW model - - -.

11. Task 4.8 Dynamic inflow

This report contains the results and conclusions from code-to-measurement comparisons with both the Nasa-AmesNREL UAE Phase VI experiment and the New MEXICO experiment. Also a more general investigation of the NREL UAE Phase VI dynamic inflow run at 5 m/s is included, which helps to identify basic challenges when using measurement data to improve dynamic inflow models.

Because both experiments have been performed using relatively small wind turbines with very high rotor speeds compared to modern wind turbines, the pitch step durations relative to one rotor revolution are longer than what could be realized on a large wind turbine. For this reason a code comparison for smaller pitch steps on the AVATAR 10 MW turbine has been included in the report. At these higher relative pitching speeds, the effect of the blade passage, i.e. when a blade passes the trailed wakes of previous blades, becomes visible.

The following section briefly presents the runs from the experiments that have been selected for comparison with the aerodynamics codes. While most of the model descriptions can be found in Chapter E, the new developments in HAWC2 that are relevant for dynamic inflow are introduced in Section 11.2. In Section 11.3, some fundamental dynamic inflow effects are explained. A more detailed version of these explanations can be found in [114]. The code-to-measurement comparisons are shown and discussed in Section 11.4, and Section 11.5 contains the code comparison for the pitch step case on the AVATAR turbine. The focus here is on the investigation of the blade passage related staircase shape of the force response due to the relatively fast pitching time. Finally the conclusions from the dynamic inflow work as well as recommendations for future model improvements are given in Section 11.6.

11.1 Experimental data

NASA Ames Phase VI

In the NREL/NASA Ames Phase VI Experiments, [52], a 2-bladed wind turbine with 10 m diameter has been placed in the NASA Ames open loop wind tunnel. One of the turbine blades was instrumented at 30%, 47%, 63%, 80% and 95% (corresponding to radii of 1.510 m, 2.343 m, 3.185 m 4.023 m and 4.780 m) with 22 pressure taps at each location. A large number of experiments in both parked and rotating conditions have been performed. The basis for the dynamic inflow investigations in [130] are pitch step experiments at 5 m/s wind tunnel speed and at a rotor speed of 72 rpm. That case is denoted as *Q0500000* in Table 11.1. Also included in this report is case *Q0800000* at 8 m/s, where the induction value is much lower and thus the dynamic inflow effects are expected to be much less pronounced. The maximum pitch rate in both cases was roughly 66 degrees per second.

In the *Q0500000* case 20 pitch steps between -5.9 degrees pitch (heavily loaded rotor, induction factor $a \approx 0.5$) and 10.02 degrees pitch (unloaded rotor, $a \approx 0$) have been performed. After each pitch step, a 15 second waiting time ensured that the flow conditions can reach an equilibrium. The previous analyses, as well as the present work, are based on the force response obtained by averaging the responses to the 20 pitch steps.

The *Q0800000* case 20 pitch steps between 0 degrees pitch (lightly loaded rotor, induction factor $a \approx 0.15$) and 18 degrees pitch (unloaded rotor, $a \approx 0$) have been performed.

Case	Tunnel speed [m/s]	Rot. speed [rpm]	Density [kg/m3]
Q0500000	5.10	71.62	1.245
Q0800000	8.02	71.76	1.246

Table 11.1: NASA Ames Phase VI cases for code to measurement comparison.

New Mexico

In the New Mexico experiments [27], a turbine with 4.5 meters diameter was placed in the Large Scale Low Speed Facility of the German Dutch Wind Tunnels. Pitch steps of 7.3 degrees have been performed at a maximum pitch rate of 40 deg/s. Due to the smaller rotor diameter and thus higher rotor speed compared to the NASA Ames Phase VI turbine the pitch duration is longer in comparison to one rotor revolution. The cases used in the code-to-measurement comparison in Section 11.4 are shown in Table 11.2. Some of these cases are measured at yaw errors of 15 or 30 degrees.

One blade was instrumented with pressure taps at 25, 35, 60, 82 and 92% radius. The forces have been integrated using the extrapolation and averaging approach for the trailing edge pressure that is described in [110].

Case	Tunnel speed [m/s]	Yaw angle [deg]	Rot. speed [rpm]	density [kg/m3]
R59P97D1146	9.97	0	425.1	1.2088
R59P98D1149	10.01	15	425.1	1.2072
R59P99D1152	7.68	0	324.9	1.2068
R59P100D1155	7.66	15	324.9	1.2068
R59P101D1158	7.67	30	324.9	1.2067

Table 11.2: New Mexico cases for code to measurement comparison.

11.2 Participating codes

The participating codes in the code-to-measurement comparisons are:

BEM codes

- DTU HAWC2
- DTU HAWC2 NW
- IFPEN AeroDeep
- ECNAero-BEM

Free wake codes

- IFPEN CASTOR
- ECN AWSM

CFD codes (only AVATAR case)

- DTU EllipSys

The code descriptions of these codes can be found in Chapter E.

Specifically for the AVATAR turbine pitch step case described in Section 11.5 the DTU HAWC2 near wake code has been updated to model the blade passage phenomenon that was observed in the high fidelity simulations of this case. The modification of the near wake code is related to the grid formulation in the far wake BEM. Therefore a brief description of the BEM grid implementation is given in the following, and then a description of the HAWC2 NW modification follows in Section 11.2.

HAWC2: Induction grid based BEM model and relevant submodels

One of the main features of the HAWC2 BEM model is that the induced velocities are not computed on annular ring elements, but instead on an induction grid, see Figure E.2. This makes it possible to compute local variations of the induction, for example due to wind shear, turbulence or half wake situations.

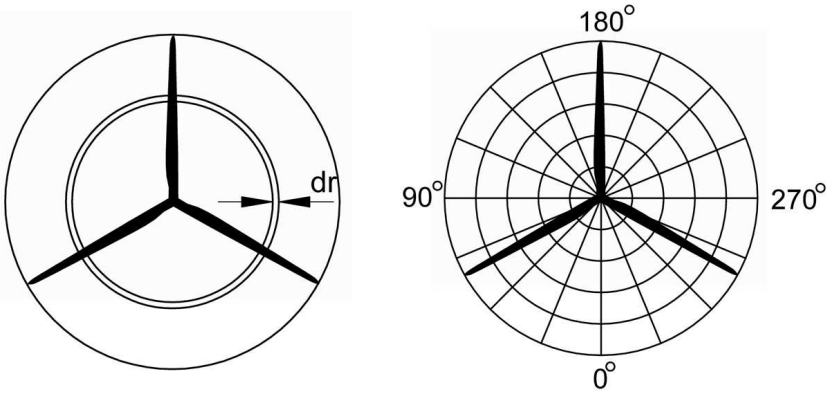

Figure 11.1: Illustration of the BEM approach. Left: Classic approach using an annular element to which the load is assumed contant over the element (mean value of blade forces). Right: Induction grid with annular elements and further subdivided azimuthally

The induction at each grid point is computed as following:

1. determine the free wind speed at each grid point, including effects of shear and turbulence
2. add the induced velocity at that grid point at the previous time step
3. for each of the 2 blades b that are closest to the grid point:
   a) compute angle of attack and relative velocity based on blade motion, blade pitch and deflection as if the blade was located at the grid point
   b) compute thrust coefficient $C_{T,b}$
   c) compute Prandtl tip loss factor F_b, as presented by Glauert [46]
4. perform azimuth based interpolation of the two thrust coefficients and tip loss factors to the grid point to compute C_T/F
5. compute induction factor $a = f(C_T/F)$
6. apply dynamic inflow filters with time constants depending on radial position and downwind wake convection speed, [153]

HAWC2 NW: Coupled near and far wake model

A near wake model can be used in HAWC2 to compute the induction due to the trailed vorticity close to the individual blades while ensuring a roughly real time computation speed, [116, 118, 117]. The induction due to the remaining wake is computed by a far wake model, which is a modification of the BEM model described above.

The modifications of the far wake model with respect to the pure BEM model are:

- The tip loss correction is turned off ($F = 1$), because the near wake model computes the local effect of the tip vortex
- The thrust coefficient is multiplied by a coupling factor $k_{FW} < 1$ which leads to a reduced induction, $a = f(C_T k_{FW})$. The determination of the coupling factor is described in [116].

- In the AVATAR pitch step case, see Section 11.5: The C_T value is based on the pitch angle and blade motion of the last blade that passed the grid point, at the moment it passed the grid point. The velocity triangle also includes the near wake induction at that blade at that instant.

The modified handling of the induction grid has only been implemented recently and was only used in the AVATAR pitch step case case. The previous grid implementation, which is also used in the HAWC2 BEM and in the code-to-measurement comparisons with HAWC2 NW, means that all the grid points see a collective pitch step immediately. The new implementation implies that the pitch step is only felt at a grid point if a blade has passed that grid point after the pitch step. Therefore the immediate force overshoot after a pitch step is only governed by the near wake model and the 2D unsteady airfoil aerodynamics model for dynamic stall and Theodorsen effects. After a third of a rotor rotation the blades enter the grid region that has been affected by the pitch step of the previous blade. The far wake induction felt at the blade then increases rapidly, and the repeated occurence of this effect creates a characteristic staircase shaped decay of the overshoot, see Section11.5.

11.3 Basic observations from the NASA Ames Phase VI experiment

The dynamic inflow behavior seen in the NASA Ames Phase VI experiment at 5 m/s can be explained with the help of a very simple vortex cylinder model, [114]. Figure 11.2 shows the measured scaled normal force response to a deloading pitch step (left plot) and a loading pitch step (right plot) at the different radial positions of the Phase VI rotor. These force responses have been studied previously by Schepers, [130] and Sørensen and Madsen, [153]. Two surprising effects are visible in these force responses:

- The radial dependency of the dynamic inflow time constants is clearly visible for the deloading pitch step. However, the extent of the radial dependency is much smaller than expected, [130].
- When reversing the pitching direction and loading the rotor (right plot of Figure 11.2, the radial dependency of the time constants appears to be reversed, with the tip section reacting the slowest.

In previous analyses these effects could be reproduced by CFD and free wake vortex simulations, however their cause remained unclear.

It is shown in [114] that the same effects can be obtained by a very simple cylindrical wake model. The geometry of such a model is sketched in Figure 11.3. The main assumptions for the computed induced velocities from this model are:

- A cylindrical vortex sheet is trailed from the tip with a constant strength beginning at the start of the pitch step. The pitch step duration is neglected.
- The downwind convection velocity of the wake is a constant $v_\infty(1 - 1.5a)$, where v_∞ is the free stream velocity and a the induction factor.
- Wake expansion is neglected.

It is apparent from Figure 11.2 that the time constants only become visible in the aerodynamic forces roughly 0.35 seconds after the pitch step. The induced velocities from the cylindrical wake model from that point in time are shown in Figure 11.4 for the deloading pitch step (left) and the loading pitch step (right). The induced velocities at each section are scaled such that they start at zero at t=0.35s and approach 1 for a wake length of 10 diameters. Comparing Figures 11.2 and 11.4 clearly shows a qualitative agreement: In the deloading case (left plots) there is a moderate radial dependency of the time constants, and in the loading case (right plots) all sections react similarly fast, except the tip section which lags behind. This shows that evaluating the time constants some time after the pitch step and based on the force response caused these effects to appear. Therefore it is difficult to directly extract dynamic inflow time constants from force measurements or force computations from high fidelity codes. Free wake vortex codes are more suitable to estimate the time constants, since they directly compute the time series of the induced velocities.

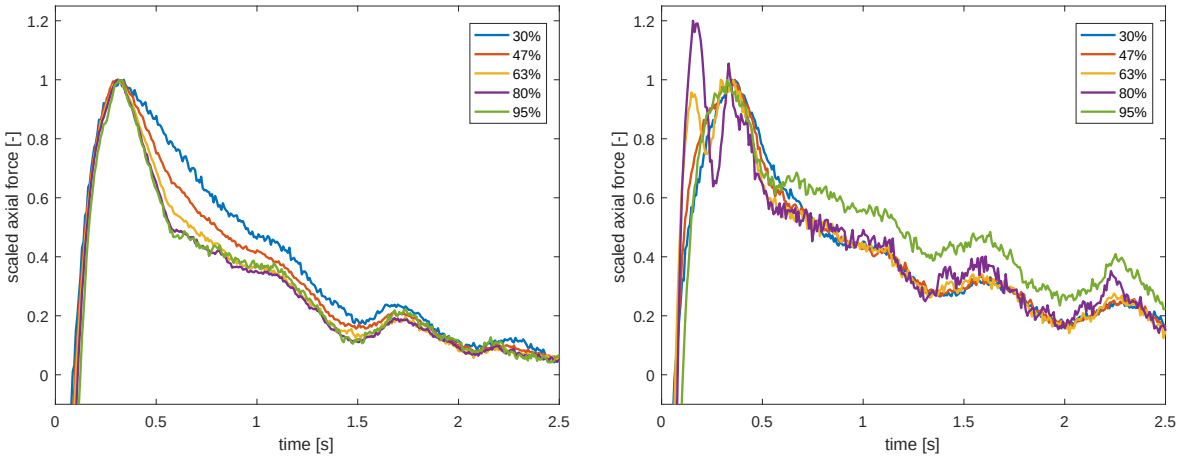

Figure 11.2: Scaled axial force measurements from the Phase VI experiment at 5 m/s. The pitch steps are deloading the rotor (induction factor from a=0.5 to a=0.0, left plot) and loading the rotor (a=0.0 to a=0.5, right plot). From [114].

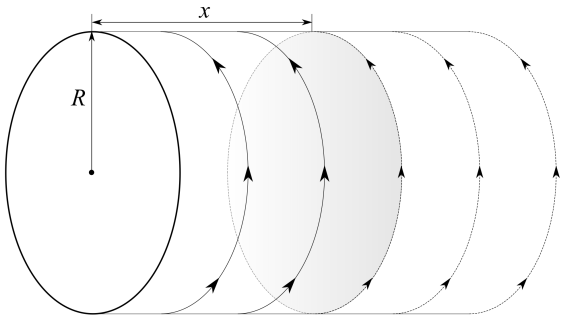

Figure 11.3: Sketch of cylindrical wake with radius R and a step change in vortex strength at a distance x from the rotor. From [114].

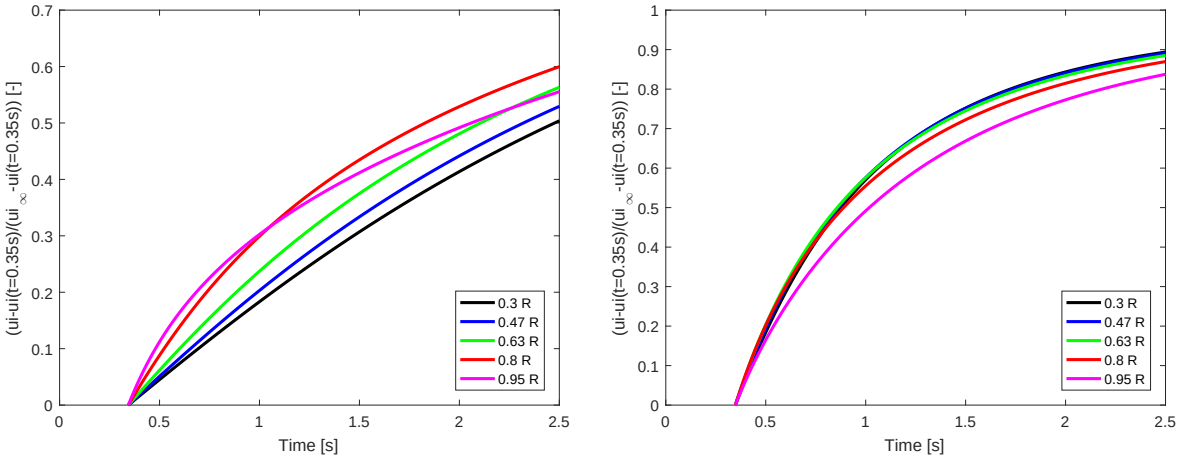

Figure 11.4: Scaled induced velocities predicted by the cylindrical wake model for the deloading (left plot) and loading (right plot) of the rotor. The scaling is such that the velocities range from 0 at the time instant just after the maximum force overshoot. The scaled induced velocities show the same qualitative trends as observed in the force measurements, see Figure 11.2. From [114].

11.4 Comparison of simulations and measuread data

This section contains the comparison of the simulated aerodynamic force time series with the sectional forces obtained from the pressure tabs in the Phase VI and new mexico experiments. Plots for all the runs named in Section 11.1 are available [113]. Here only a limited number of results is shown to illustrate the general trends that can be observed in the measurements.

All the force time series in this section are scaled such that the steady state values are 0 (low loading operation) and 1 (higher loading operation). In this way the differences in steady state values do not distract from the dynamic behaviour when comparing the different time series. This scaling is different than in Figure 11.2, because in the previous investigations by Schepers, [130] and Madsen and Sørensen, [153] the focus was on the time constant of the dynamic force decay after the overshoot. As shown in Section 11.3, the size of the overshoot is an important part of the dynamic inflow effect. This effect is clearly visible when the forces are scaled as presented in the following.

The quality of the pitch signal for the new mexico dynamic inflow experiments has been a concern, thus in the left plot of Figure 11.5, the pitch signal is shown before and after a low pass 5th order butterworth filter has been applied backwards and forwards to ensure that the phase of the signal is preserved. The corresponding code-to measurement results of F_N at 35% radius are shown in the right plot of Figure 11.5. It is seen that the drop in pitching speed after about 80% of the pitch step causes a drop in force that is visible in both the codes and the experiment. Also the smaller variations in pitch after the pitch step are visible in measured and experimental loading. Thus it appears that the necessary strong low pass filtering of the pitch signal was able to preserve the main features of the pitch signal that were otherwise hidden behind the noise.

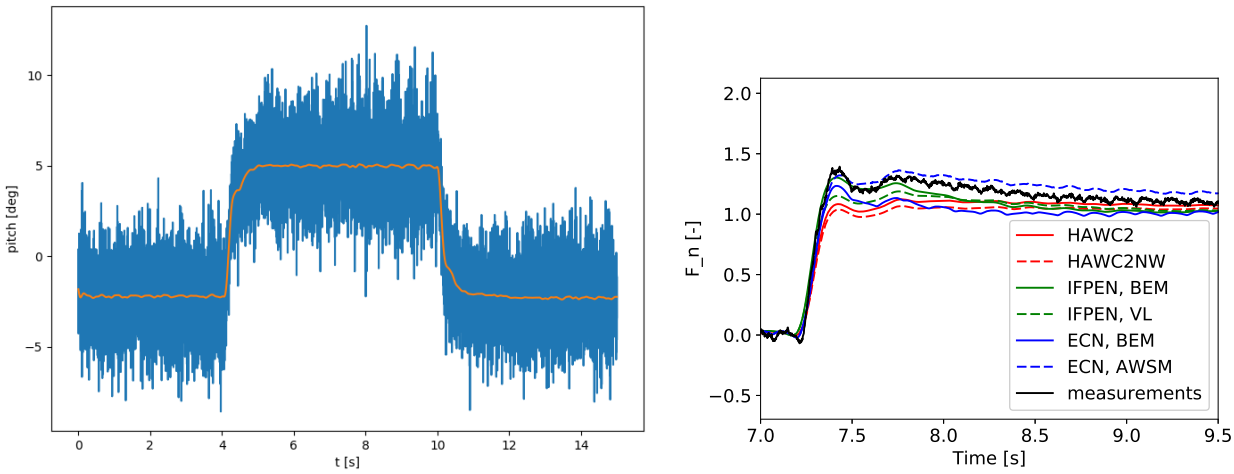

Figure 11.5: Normal force on the Mexico rotor at 35% radius after a pitch step towards increased loading from case R59P97D1146. The good agreement on the dip in forcing at roughly 7.5 seconds indicates that the strong filtering of the noisy pitch signal preserved the important characteristics of the pitch step.

Figures 11.6 and 11.7 contain the measured and predicted normal forces of the Phase VI runs at 5 and 8 m/s, respectively. The left and right plots in both figures differ pitch direction, to highlight the influence of the different wake velocities on the dynamic force response. At 5 m/s, Figure 11.6, the difference in loading between the pitch settings is very large ($a \approx 0$ vs $a \approx 0.5$). Due to the different wake velocities the force overshoot is expected to be smaller in the pitch step towards higher loading, which is confirmed by the experimental data. All codes except the ECN BEM predict this lower overshoot when pitching towards higher loading in comparison to the other pitching direction. However the influence of the pitching direction appears exaggerated in the HAWC2 and IFPEN BEM simulations. The HAWC2 NW simulations predict too low overshoots in general, whereas the AWSM simulations agree best with the measurements in this case.

At 8 m/s (Figure 11.7) the induction is much lower ($a < 0.1$ for both pitch settings), and thus both the overshoots and the influence of the pitching direction is very small in the measurements. However the overshoot in the HAWC2 results is exagerrated when pitching towards lower loading (left plot), and the IFPEN BEM simulations predict a larger overshoot when pitching towards higher loading. Therefore it is recommended that

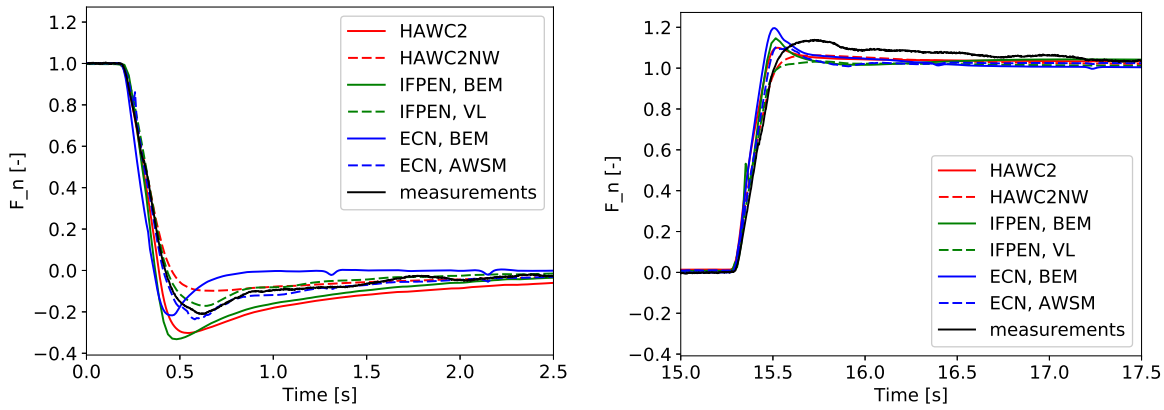

Figure 11.6: Influence of pitching direction, Phase VI, 5 m/s tunnel speed. Normal Forces at 95% radius for pitching towards low loading (left) and high loading (right). All the codes except the ECN BEM predict that the overshoot is smaller for the pitching towards higher loading, which is expected due to the higher wake velocity at the start of the pitch step.

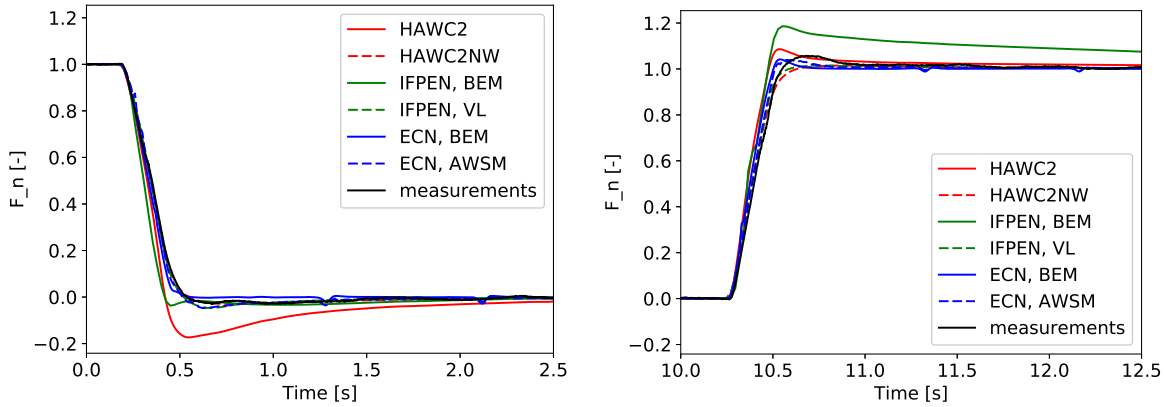

Figure 11.7: Influence of pitching direction, Phase VI, 8 m/s tunnel speed. Normal Forces at 95% radius for pitching towards low loading (left) and high loading (right). Due to the much lower induction at this tunnel speed, the overshoots are generally smaller. The HAWC2 and IFPEN BEM codes overpredict the overshoot when pitching to lower and higher loading, respectively.

the adjustment of the dynamic inflow time constants with changing wake velocity might be modified in these codes.

Figure 11.8 contains the normal and tangential force at 47% radius of the Phase VI turbine at 5 m/s during and after the deloading pitch step. In this case the dynamic induction response predicted by the IFPEN and ECN BEM models is too slow compared to the measurements, leading to an exaggerated overshoot in the normal forces (left plot). The tangential force response in this case (right plot) looks qualitatively different than the normal force response. This is because the angle of attack at the section has a positive value before the deloading pitch step, crosses zero and reaches a negative value during the pitch step and then approaches zero while the induced velocities decrease as a response to the deloading of the rotor. While the normal force changes sign during the pitch step as the lift becomes negative for angles of attack below the zero lift angle, the tangential force component due to the projection of the lift force is positive for both positive and negative angles of attack. This explains the shape of the tangential force response shown in the right plot of Figure 11.8: The tangential force is positive for positive AOA, reaches a slightly negative drag dominated value around the zero lift angle, becomes positive again for negative AOA and then approaches a drag dominated value as the AOA approaches zero due to the dynamic induction response. The slower dynamic inflow effect predicted by the IFPEN and ECN BEM models leads to a more negative AOA at roughly 0.5 seconds and thus a larger tangential force that takes a longer time to reach the steady state value at roughly 2.5 seconds.

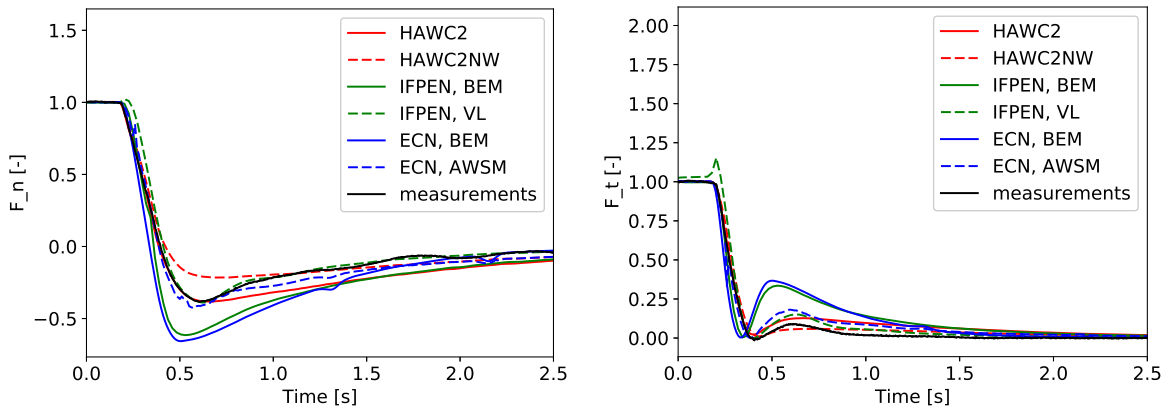

Figure 11.8: Normal force and tangential force at 47% rotor radius when deloading the rotor, Phase VI, 5 m/s tunnel speed.

Figure 11.9 contains time series of the normal and tangential force measured in the new mexico experiment in the case with lower rotor speed and no yaw error. It can be seen that the overshoot is larger on the inboard section (left plot) than on the outboard section (right plot), which agrees well with the expected decrease of the dynamic inflow time constants towards the tip of the blade. Also from these results it is apparent that the heavily filtered pitch time series used in the simulations agree well with the pitch step that was performed in the wind tunnel.

Measurements and simulation results of the normal and tangential forces in the New Mexico run at 15 degrees yaw error are shown in Figure 11.10. The 1P variations due to the yaw error make a scaling of the results difficult, since the scaling would also change the amplitudes of the variations. The plots show that there are slight force overshoots due to dynamic inflow effects and that the different yaw modeling in the different codes leads to different shapes and amplitudes of the observed force variations.

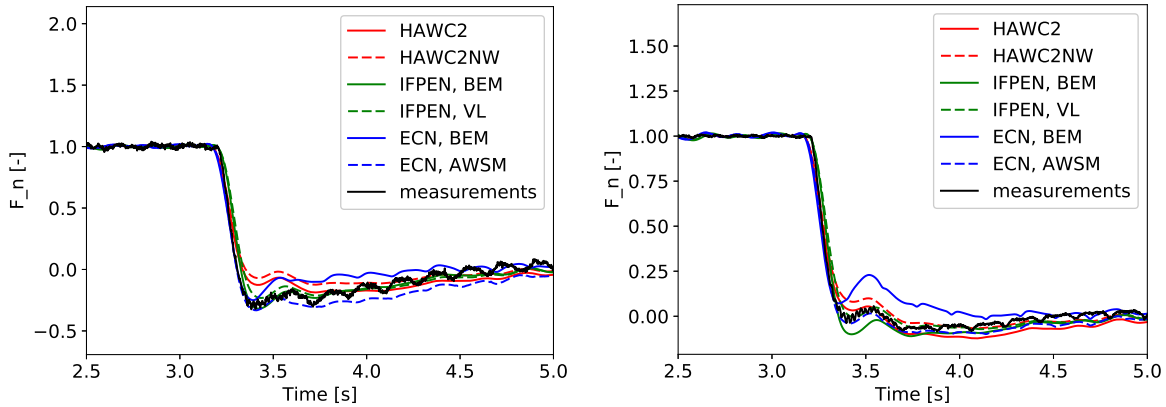

Figure 11.9: Normal force at 35% (left) and 92% (right) radius measured in the New Mexico experiment at 7.68 m/s tunnel speed and 324.9 rpm. All models predict the decrease in overshoot towards the tip due to the faster dynamic induction response.

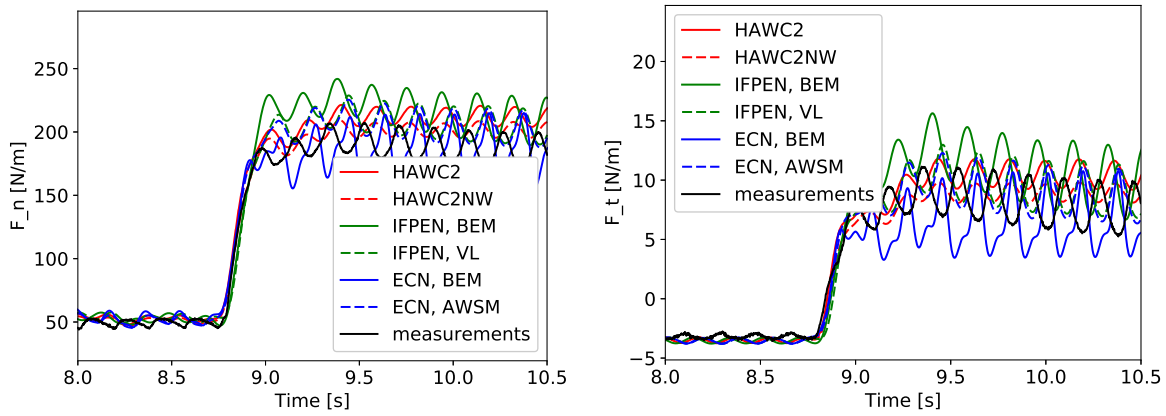

Figure 11.10: Normal force (left) and tangential force (right) at 92% radius measured in the New Mexico experiment at 7.68 m/s tunnel speed and 324.9 rpm at 15 degrees yaw error.

11.5 AVATAR turbine pitch step

In the AVATAR project a pitch step case was defined as part of a larger set of aerodynamic comparison cases. Due to the relevance for the present dynamic inflow task and because some of the related model development and results analysis at DTU has been carried out within Mexnext III, a short section on this case is included here.

Pitch steps of $+/-$ 2 degrees have been performed at a maximum pitch rate of 10 degrees per second. The complete pitch step duration was thus roughly 4 times faster in relation to a rotor revolution than in the Phase VI measurements. Also, due to the smaller pitch step size the loading is varying less between the different pitch angles than in the Phase VI measurements, therefore the wake velocities and dynamic responses to the different pitching directions are more similar.

The codes shown in this comparison are HAWC2, which uses a BEM based engineering model as well as a coupled BEM + near wake model, as well as the free wake vortex code AWSM and the CFD code EllipSys. Thus the codes are representative of a range of fidelity of aerodynamic models.

The predicted effect of the pitch steps on the thrust curves is shown in Figure 11.11. The left plot includes the thrust response to the three consecutive pitch steps. Clearly the time constants for the different pitching directions and load levels are much more similar than what has been observed in the Phase VI measurements, cf. Section 11.3. The right plot of Figure 11.11 is a zoom to the first pitch step towards lower loading. In this plot it becomes apparent that the BEM results from HAWC2 exhibit the expected smoothly decreasing force overshoot due to the low pass time filter applied directly on the induced velocity. The free wake and CFD computations, on the other hand, show a staircase decay of the overshoot, where the width of each stair is one third of a rotor revolution. Thus the sudden drop in forcing can be explained by the blades moving past the trailed wake of the previous blades. This behavior can be captured by the modified HAWC2 near wake implementation described in Section 11.2.

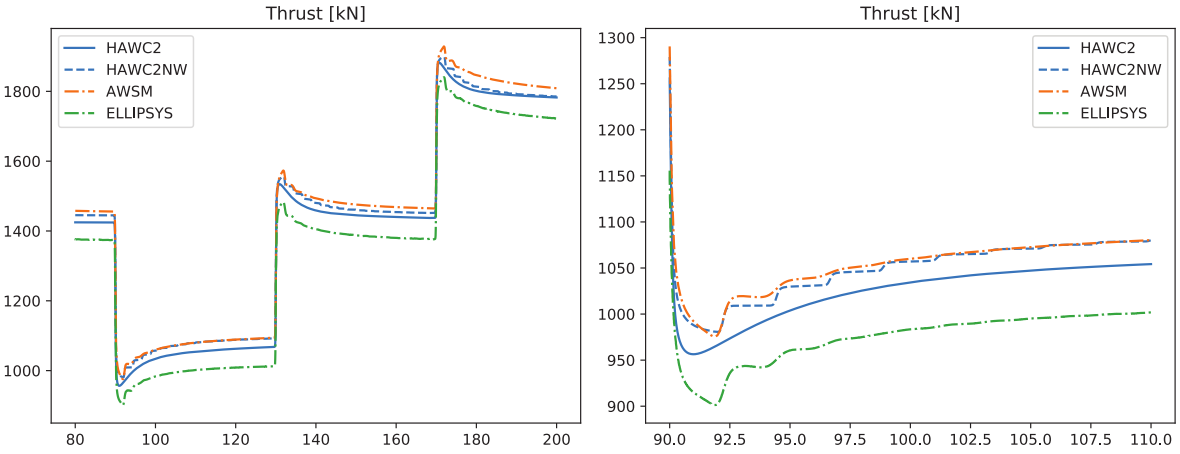

Figure 11.11: Comparison of the thrust response.

This staircase effect is only visible if the pitch step duration is short compared to one rotor revolution. Otherwise the force response becomes smeared out, as shown in the torque comparison in Figure 11.12. This Figure contains results from a simulation where the pitching speed was reduced by a factor of 4 to match the conditions of the Phase VI experiment. The disappearing stair case agrees well with the measurements and predictions from Phase VI, cf. Section 11.4. The figure also illustrates the influence of the pitching speed on the size of the force overshoot, which again highlights the importance of the immediate dynamic inflow response, as described previously in Section 11.3.

It is helpful to look at the basic flow field behind a wind turbine blade. The shed and trailed vorticity is shown in Figure 11.13, where the shed vorticity refers to vorticity shed parallel to the blade, depending on the temporal gradient of the bound circulation. Trailed vorticity refers to the vorticity shed perpendicular to a straight blade, and the trailed vortex strength depends on the radial bound circulation gradient. Also shown in the figure is the tip vortex from the previous blade, which is the most dominant part of the vortex wake from the previous

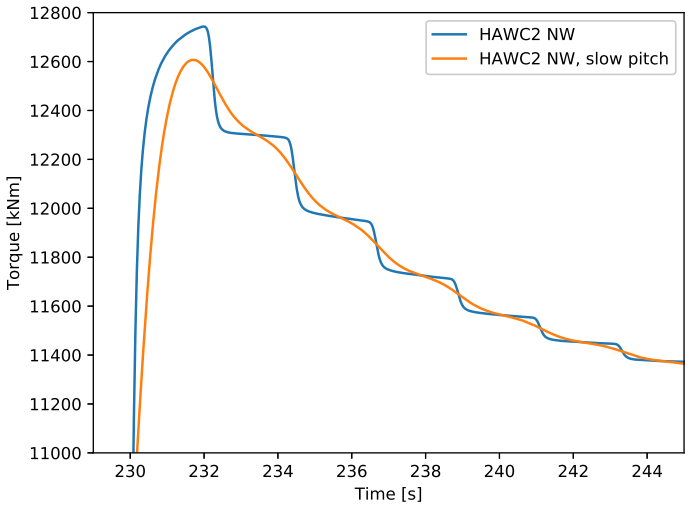

Figure 11.12: Influence of the pitching speed on the torque response. In the slow pitch case the pitch step duration relative to the rotor speed is equivalent to the NASA Ames experiment, which is roughly 4 times slower than the original AVATAR turbine case.

blade. The blade passage in front of these previous wakes is responsible for the staircase effects.

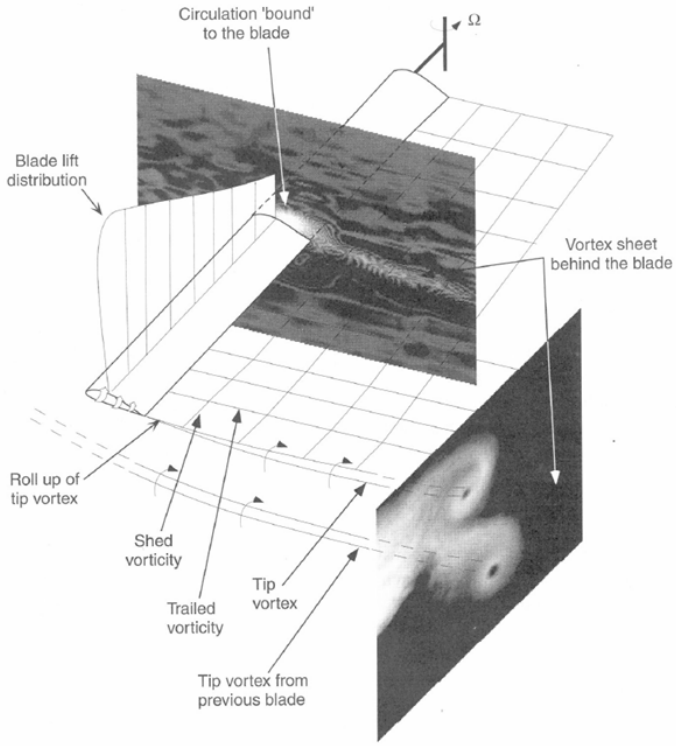

Figure 11.13: Illustration of shed vorticity and trailed vorticity of the blade's own wake and the recurring wakes of previous blades. From [84].

A more detailed look at Figure 11.11 reveals that the position of the overshoot predicted by BEM is earlier after the pitch step than the positions predicted by the more advanced codes. Figure 11.14 includes additional results from BEM and NW codes where the influence of the shed vorticity on the aerodynamic forces, the so-called Theodorsen effect, is excluded. In the 'HAWC2 NW QS 2D' case without shed vorticity effects on the forcing, the trailed vorticity is still computed using the unsteady bound vorticity including shed vorticity effects. Thus the trailed vorticity in the 'HAWC2 NW' and 'HAWC2 NW QS 2D' cases is identical to easier distinguish

between the different effects. In the BEM QS 2D and NW QS 2D cases the torque decreases after the pitch step due to the increasing induced velocity. However in the BEM case, where the dynamic induction is averaged for the whole rotor and does not include blade passage effects, the torque decreases faster after the pitch step. If the shed vorticity effects on the aerodynamic forces are added, the torque in the BEM still decreases after the pitch step, but at a slower rate. In the NW computation, however, the trailed vorticity induction slowly reaches the value due to the wake behind one blade, while the 2D shed vorticity effects still lead to an increase of the forcing with time. These two effects add up to a positive torque gradient just after the pitch step, followed by a strongly negative gradient when passing the wake from the previous blade at roughly 232 seconds. Thus it can be said that up to 232 seconds the force response is governed mainly by the trailed and shed wake behind the individual blades. In this HAWC2 NW induction therefore a change of the dynamic inflow time constants will not affect the shape or size of the overshoot.

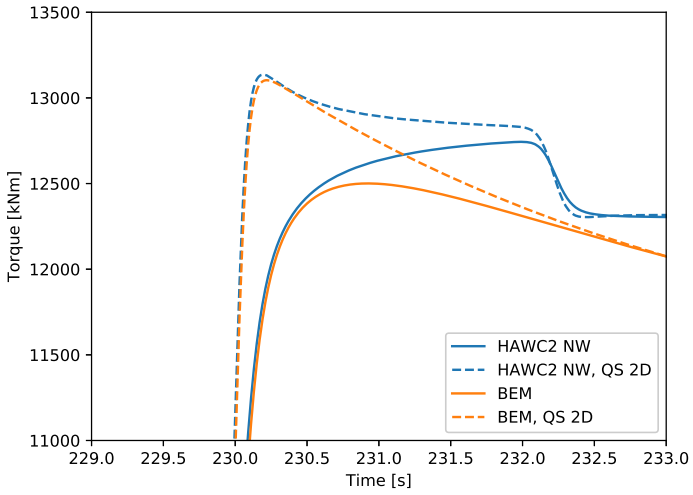

Figure 11.14: Comparison of torque response with or without 2D Theodorsen effects enabled. When enabled, the Theodorsen effects impose mainly a time lag on the angle of attack used for the force computation. The unsteadyness of the bound circulation that is necessary to compute the correct unsteady trailed vorticity in the NWM computations is active in all cases.

11.6 Conclusions

The investigations of the NASA Ames Phase VI experiment showed that the changing behavior of the dynamic force response with pitch direction is due to the large difference in wake velocity in the loaded and unloaded state. Therefore the wake is convected much further downstream just after the pitch step in the unloaded case, which is when the time constants of the decay of the force overshoot can be analyzed. This leads to an apparently reversed radial dependency in the force time series, where the dynamic inflow effect appears to be slowest at the tip. This clearly shows that a two time constant dynamic inflow model is necessary.

As previous work has shown the same effects can be observed on the force time series predicted by high fidelity codes, which means that these are also not immediately suitable for extracting dynamic inflow time constants. Free wake vortex codes, though, have the advantage of providing the dynamic induction response at the blades, which is difficult to obtain from CFD, directly.

In the AVATAR pitch step case it was found that a staircase shaped force response appears when the pitch step duration is short in comparison to a rotor revolution. This staircase response can not be modeled by traditional BEM methods using induced velocities on ring elements of the rotor disc, because the effect is caused by the blades passing in front of the wake of the other blades. A combination of a model for the shed and trailed vortex wake behind each blade and a BEM model in a grid implementation can capture this effect.

The code to measurement comparisons with the Phase VI and New Mexico experiments showed that all codes are able to qualitatively model the dynamic inflow effects observed in the measurements. However some codes predicted dynamic inflow effects in low induction conditions (Phase VI, 8m$/$s tunnel speed) where the measurements do not show evidence of dynamic inflow. Also some codes are better able to capture the influence of changing pitching direction on the varying time constants. To improve this and prevent overpredicting dynamic inflow effects the scaling of the time constants with the wake velocity might be revisited in the participating BEM codes. The HAWC2 NW implementation used in the code-to-measurement comparison generally tends to underpredict the extend of the dynamic inflow effects. It is expected that the modified implementation used for the AVATAR pitch step case performs better in these cases. The free wake codes, especially the AWSM code, generally perform very well in these dynamic inflow cases.

Finally it is noted that a new model for predicting dynamic inflow effects has been developed at TUDelft but this model arrived too late to be included in the Mexnext-III validation cases. The model is developed and validated with a free vortex wake code and it has two time constants where the fast one has a strong radial dependancy. As such it is very much in line with the above given recommendations. The model is reported in [177].

12. Task 4.9: Boundary Layer Transition

12.1 Introduction

This report deals with the results of work conducted in subtask 4.9 *Boundary layer transition*. Participant were:

DTU Wind Energy, Denmark, ONERA, France, IWES/FORwind, IAG - U Stuttgart and UAS Kiel, Germany.

Related work is summarized in table 12.1

Table 12.1: Related work.

Name of Project	Date	Remark	source
HAT25	1983	transition detection via microphone	[73]
MEXICO	2006 and 2014	PIV and Kulite data	[67, 25]
DAN Aero	2007 - 2009	Full Scale LM 38.8	[40]
Aerodynamic Glove	2011	E 33 with 15 m blade	[128]
AVATAR	2011 - 2017	2D measurements and CFD for a DU profile	[30]
Free Field Thermography	2014 - 2016	LM37 (meter) blade	[9]

12.2 Boundary Layer Transition

Due to renewed interest in boundary layer experiments of wind-turbine blades operating in the free atmosphere [73, 40, 139, 127, 128] a work-plan for Mexnext was released in the beginning of 2013 to phase 2 (2012 - 2014) but most of the work was performed in phase 3 (2015 - 2017) only.

A set of measurements without tripping the blades during wind-tunnel measurements were performed and reported in 2014 [158, 24, 18].

It has to be noted that very recently during the EU-funded AVATAR project (see [3]), remarkable consistent findings were published for predicting c_L and c_D data using transition predicting tools like e^N [168] or Menter's Correlation based model [97]. Reynolds-number was varied from 3 to 12 million and turbulence intensity (TI) ranged from about 0.5 % to 0.086 %. Some impressions can be found in Figs 12.1 and 12.2.

In contrast to applications for pure 2D flow for airfoils complete 3D transitional simulations esp. for rotating wings are much more rare.

Experiments on Rotating Wind Turbine Blades

Earliest approach of this kind goes back to 1983 [73, 166]. The then used blade had a length of 14 m and profiles from the NACA 4-digit 44 series were used. Rated power of this turbine was 300 kW. Reynolds-number varied

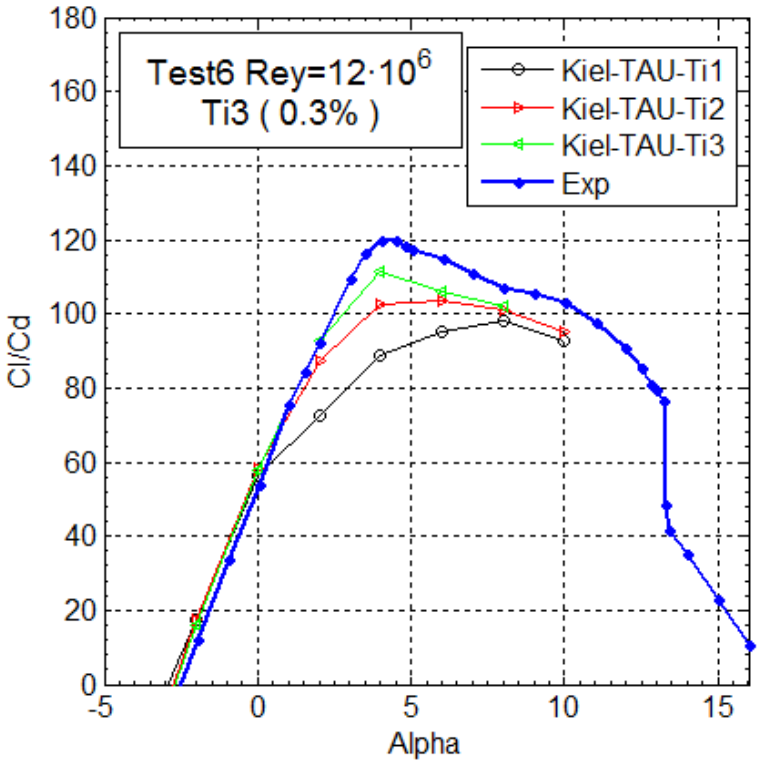

Figure 12.1: CFD results showing dependence of lift-to-drag-ratio on turbulence intensity, [30]

from 1 to 3 million. Main findings were the save detection of laminar parts even under apparently high inflow turbulence.

A considerable time later in Denmark [40, 42] a MultiMW (NecMicon NM80 with LM38 blades) was investigated in much more detail. Due to the much faster signal-processing much sharper detection of transition locations and even chances during one revolution ($T \approx 5$ sec) could be detected. Main finding here was pronounced laminar parts (20 % to 40 % with regard to x/c) and the very interesting fact that the energy increase within the turbulent boundary layer starts not before about 500 Hz. This then explains that even under the seemingly much higher turbulent inflow only a small part is *aerodynamically active* due to the assumed acting mechanism of *receptivity*.

This was confirmed by the *Aerodynamic Glove* experiment [128] performed on a 15 m blade of an ENERCON E30 machine, in size rather comparable to the original HAT25 experiment [166]. It was found that the energy content (of the turbulent atmosphere) in a frequency range above 0.5 kHz is about 6 (!) orders of magnitude smaller than at its maximum at about 10^{-2} Hz. Due to the different sensor used (hot films instead of microphones) only a very limited range ($0.24 \leq x/c \leq 0.31$) in chordwise direction could be screened. Nevertheless some of the over 700 recorded data-sets clearly showed transition detected by the same type of reasoning and criteria as used above.

Another project [9] used thermography to detect laminar-turbulent transition on a LM37 blade by measuring temperature differences. A 3D RANS-CFD model was set up by Mommsen [99] but could not confirm the experimental findings so far. A much less laminar part was seen only. However this may not be contradicting because some of the operating conditions of the turbine like wind velocity and pitch were known not very accurately.

Results from Re-Analysis of New MEXICO Kulite Data

New MEXICO data, esp. the high-frequency Kulite-data has been re-processed by Lobo [90] for possible detection of transition by comparing the energy content in various frequency ranges. A rather similar dependency

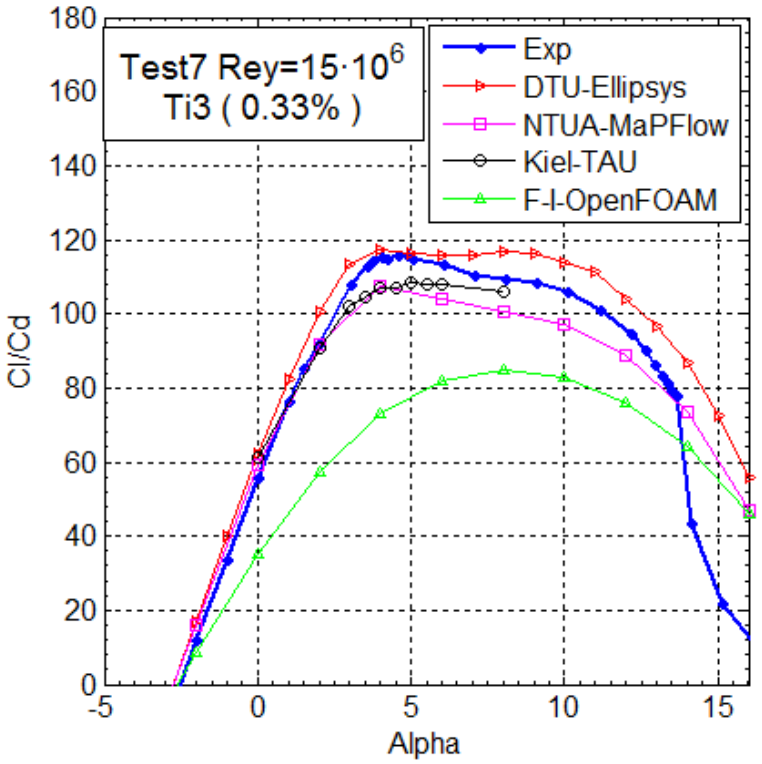

Figure 12.2: CFD results for lift-to-drag-ratio from various CFD-codes and methods[30]

was found if all measurements were collapsed to one graph by relating them to their corresponding angle-of-attack calculated by Rfoil (see Fig 12.3).

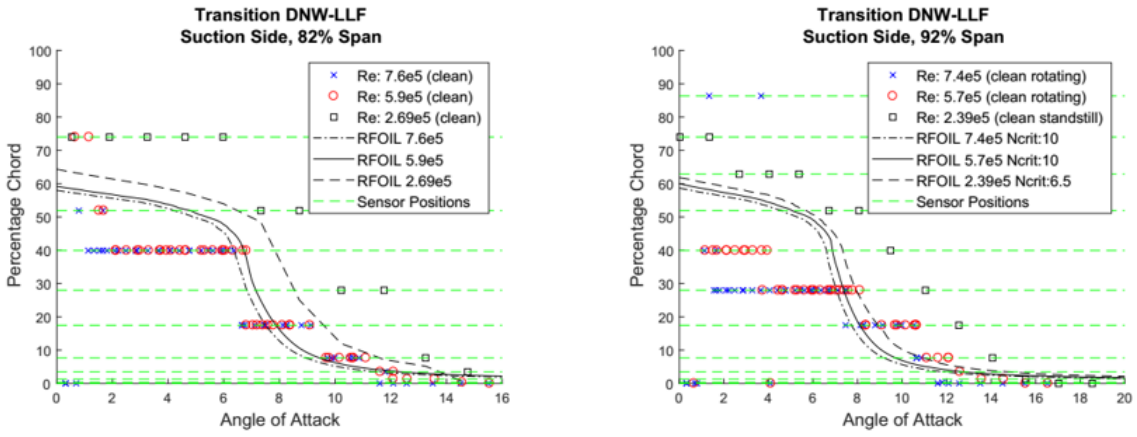

Figure 12.3: Transition locations from Kulite data. Both rotating and standstill conditions are included [90]

CFD comparison for New MEXICO data

Global results for thrust and torque

During Mexnext-III a lot of (some of them new) codes were able to produce results. Table 12.2 summarizes the findings for cases 1.1 (10 m/s) and 1.2 (15 m/s). These may be compared to the fully turbulent modeling (table 12.4) and the experiment(s) itself (table 12.3). Finally indications of general deviations from an average over all contributions is given in table 12.5.

It must be noted that the measurements from 2014 seem to be somewhat more reliable because some systematic errors from the 2004 run could be identified and corrected as described in [155].

Table 12.2: Global results for thrust (N) and torque (Nm) from transitional CFD codes.

Code	Thrust (case 1.1)	Torque (case 1.1)	Thrust (case 1.12)	Torque (case 1.2)
eLSa	1086	33	1791	302
CFX	840	50	1790	250
FLOWer	953	81	1793	357
OF kkL omega	1047	85	1875	364
OF gamma Re	990	76	1729	333
EllipSys [155]	984	58	1752	278
tau	1025	74	1800	465

Table 12.3: Global results for thrust (N) and torque (Nm) from MEXICO and New MEXICO experiment. Data from 2014 are considered more reliable

Experiment	Thrust (case 1.1)	Torque (case 1.1)	Thrust (case 1.2)	Torque (case 1.2)
MEXICO (2006)	854	61	1517	285
New MEXICO (2014)	974	68	1663	301

Table 12.4: Global results for thrust (N) and torque (Nm) from fully turbulent CFD computations.

Year	Code	Thrust (case 1.1)	Torque (case 1.1)	Thrust (case 1.12)	Torque (case 1.2)
2010	EllipSys	1000	70	1550	370
2016	EllipSys	969	59	1704	278
2012	tau (Kiel)	1036	30	1608	220
2015	tau (DLR)	1050	75	1800	360
2016	elsA	1064	32	1781	295
2017	FLOWer	920	77	1725	350

Table 12.5: Comparison for averages (AVR) and standard deviation (STD) for thrust (N) and torque (Nm) at 10 m/s and 15 m/s inflow. N is the number of data points or different computational runs. Values in brackets for experimental data are from New MEXICO

type	velocity (m/s)	Thrust (AVR)	Thrust (STD)	Torque (AVR)	Torque (STD)
Experiment	10	914 (974)	42	65 (68)	2
N = 2	15	1590 (1663)	52	301 (317)	11
fully turbulent	10	994	5	64	24
N = 8	15	1709	19	316	5
transitional	10	983	29	62	7
N = 7	15	1790	26	337	26

Radial resolved data

Figs 12.4 and 12.5 give an impression of the calculated deviations of radial resolved tangential forces. Results are form three groups (DTU, ONERA and U Stuttgart) Transitional and turbulent data are rather close inside one's group.

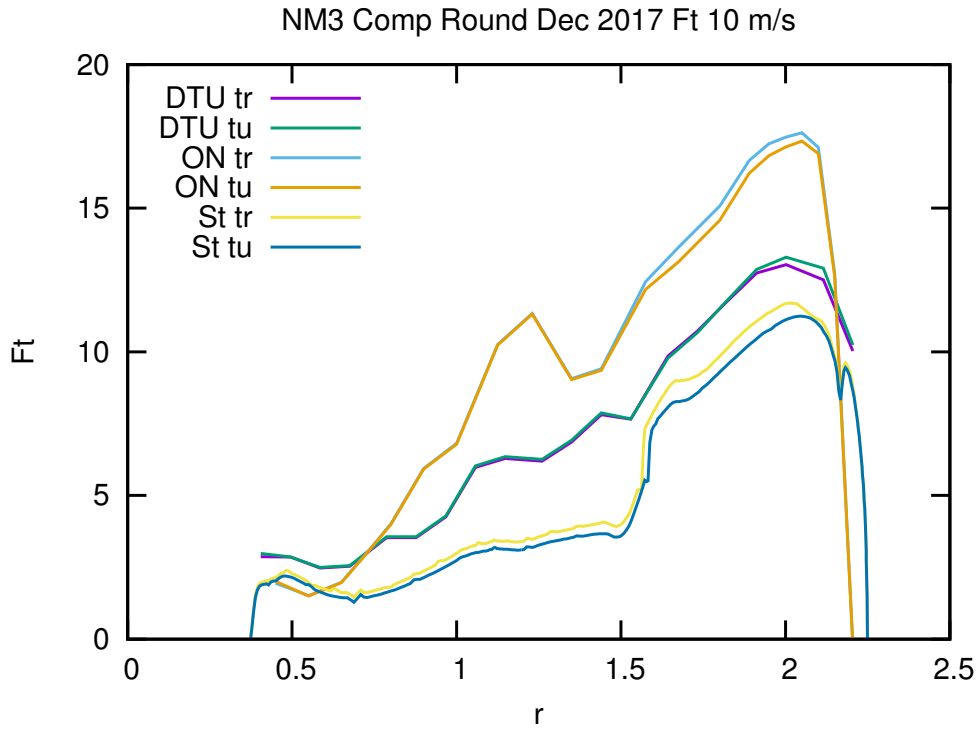

Figure 12.4: Radial resolved tangential force (in N/m) from fully turbulent and transitional CFD calculations, case 1.1: 10 m/s inflow

Impact on pressure distribution

Fig 12.6 the pressure on first downstream half of the suction side is shown for comparison. Even from the pressure a clear indication where the transition takes place can be deduced: $z_{tr} \approx 0.02$ for Onera's simulation and $z_{tr} \approx 0.035$ for DTU. In general both transitional pressures give raise to more lift than in the fully turbulent case as may be expected.

Prediction of location of transition

Finally Fig. 12.7 gives more insight into the details of a transitional simulation. Usually (in CFD simulations) transition is blended by an *intermittency* function from laminar (low) to turbulent (high) wall shear stess. This is clerly seen in this figure - esp. ONERA's c_f-data being very smooth - although the location itself is different. This may be related directely to the different turbulence models and prediction models used.

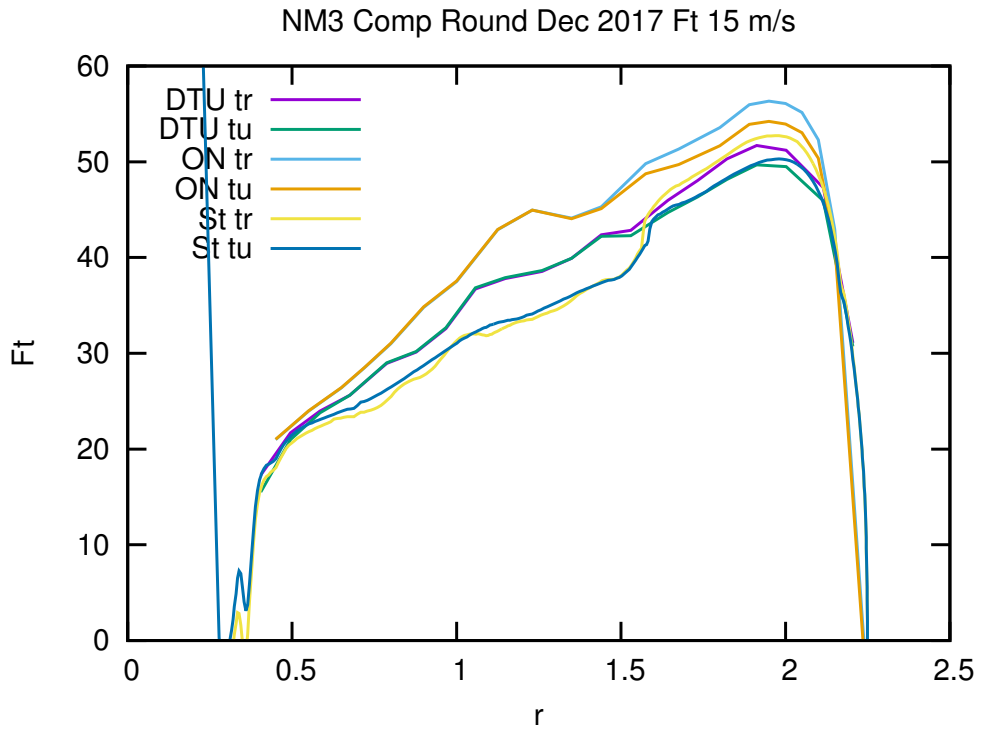

Figure 12.5: radial resolved tangential force (in N/m) from fully turbulent and transitional CFD calculations, case 1.2: 15 m/s inflow

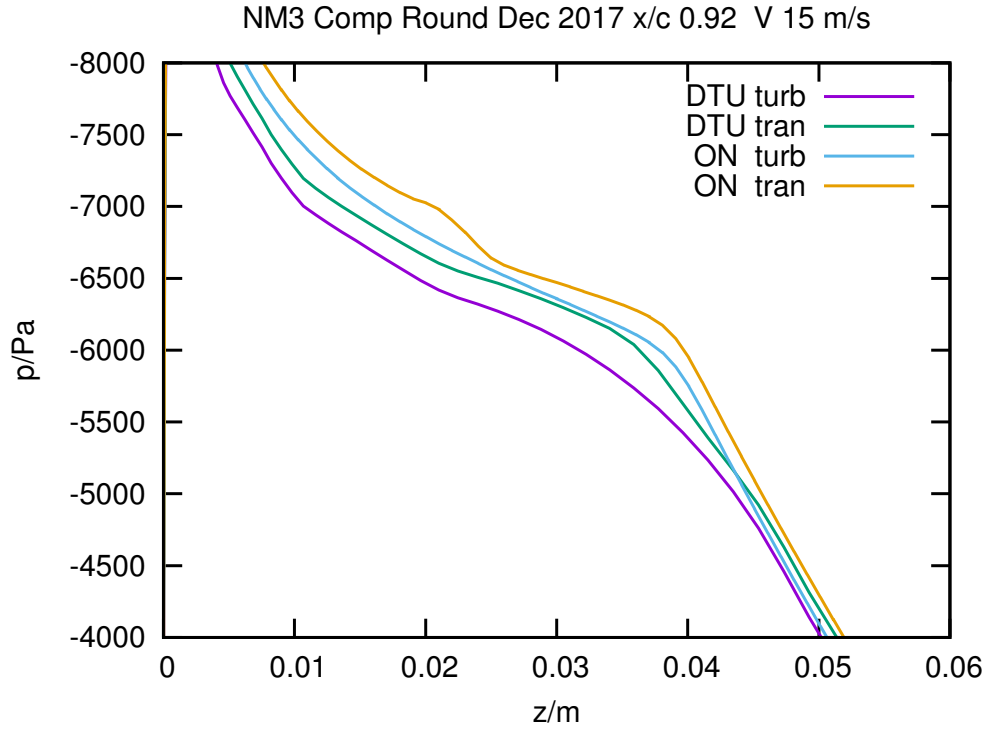

Figure 12.6: Pressure on (first part of) suction side from fully turbulent and transitional CFD calculations

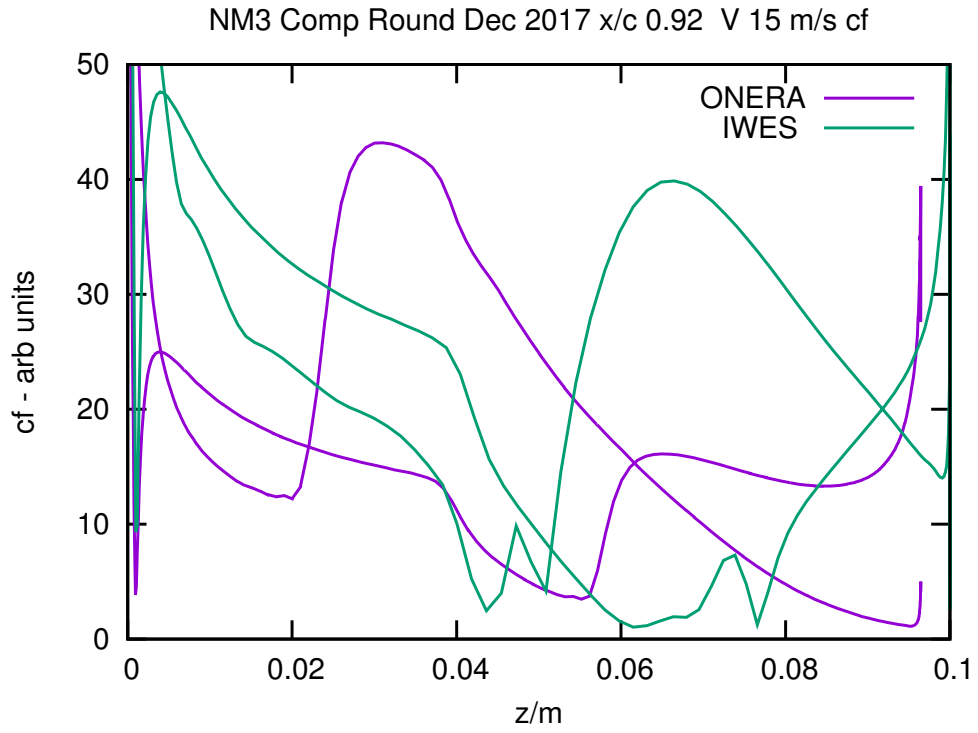

Figure 12.7: Prediction of location of transition (first minimum of c_f) from CFD calculations, case 1.2, 15 m/s inflow at x/c = 0.92, Data kindly from IWES and ONERA, resp.

12.3 Discussion, Summary and Conclusion

During Mexnext-III 7 transitional CFD calculations from 4 groups (DTU, FORwind, FH Kiel, Onera and U Stutt) were able to perform 3D transitional CFD computations.

In addition high frequency pressure data was re-processed and transition location could be deduced which agree reasonably with RFoil simulations

Due to decambering and larger turbulent wall shear stress it was expected that transitional simulations should give slightly larger integrated force values at non-tripped outboard sections.

This is easily confirmed even by a simple Xfoil estimation for the 92% section at Re = 1 million and an assumed AOA of 6°: Lift is increased from 0.96 to 1.06 and drag is reduced from 0.015 to 0.0086. As it is typically for Xfoil even the transition location is visible as a cusp in c_p. An comparable cusp at z = 0.02 m seems to be present in Fig 12.6 for Onera's transitional case 1.2.

Further, the following more specific conclusions may be drawn separately for case 1.1 and 1.2:

- Inflow 10 m/s (Case 1.1, TSR = 10)

  Transitional thrust and torque agree (within the statistical standard deviation (std) obtained from all computational runs) with the experiment and fully turbulent flow. An expencted increase of force/moment data is barely visible.

- Inflow 15 m/s (Case 1.2, TSR = 7) Both thrust and torque statistically significant increase if transition is enabled but seem to depart from the experimental values even further.

As a summary it must be said, that, unfortunately, 3D data do not have the consistency of 2D results from the recently finished AVATAR project as described in [30]. In general our data (for integral thrust and torque) show approximately the same scattering as in previous computational rounds.

As an outlook efforts should be made in direction of suggestions proposed by [48]. As a first step it may be appropriate to use identical meshes to investigate exclusivley the effects of the predictions modules. However, turbulence and transitions moduls are know to be very sentitive to them and may prevent it.

13. Task 4.10: Acoustics

13.1 Introduction

Uncertainty in aerodynamic noise prediction is an important parameter driving the price of wind energy [69, 68]. An accurate prediction of noise can aid the design of more quiet blades but also noise mitigation strategies.

There have been many modeling efforts in the field of wind turbine noise, which for modern turbines mostly focus on aerodynamic noise from the blades [171]. Mechanical noise is often not considered an important source, as long as tonal components are not present [112]. Where rotational harmonics are dictating the low frequency spectrum for downwind rotors, they seem to be insignificant above 20 Hz for upwind placed rotors [63, 93]. Both aerodynamic source modeling as well as its propagation have hence been subject of investigation, mostly for upwind placed rotors.

Source modeling ranges from simple empirical one-equation models to computational aeroacoustic (CAA) simulations resolving both the flow field and acoustic perturbations around the wind turbine blades [102]. A compromise between accuracy and computational effort can be found in semi-empirical methods that divide the wind turbine blades into segments and treat these as two-dimensional airfoil sections producing incoherent sound sources [23, 43]. The most popular model for predicting these sectional sources is the Brooks, Pope and Marcolini (BPM) model [161]. It includes a prediction method for turbulent boundary layer trailing edge noise, which is believed to be the dominant source for wind turbine applications [105]. However, the TNO model [109] which includes a more physics based approach, is gaining popularity as well [13].

Validation by experiments is the most plausible route to model improvement. Although many field measurements on wind turbines exist [41], the uncertainty in inflow conditions (turbulence, shear, gusts) and turbine specifications complicates progress. To reduce this uncertainty, experiments in controlled conditions as featured in wind tunnels are a prerequisite. However, high quality wind tunnel campaigns on horizontal axis wind turbine models are scarce due to the large wind tunnel size needed and consequently high associated costs [124, 32].

Within the current task it is investigated how the New MEXICO measurements can contribute to improve and validate acoustic modeling of wind turbines. The main participant is ECN. Hermann Holthusen (DNW) is acknowledged for data reduction of the raw time series into beamforming plots and resulting spectra plus the corresponding explanations. An overview of the acoustic part of the experiment is given, including selected results together with a comparison to noise predictions. A more detailed report of the work can be found in the dedicated publication [26].

13.2 Acoustic instrumentation

An acoustic array was positioned between nozzle exit and the model, below the jet (depicted in red in Figure 13.1). As can be observed the array could not be placed directly upstream of the model, but was positioned slightly sideways due to the restricted space available between the nozzle (depicted in orange) and external balance (depicted in blue). The 4m x 4m phased array consisted of 140 electret microphones (circular arrangement) sampled at a frequency of 51.2 kHz over a period of up to 60 s for each data point. In addition to that 48 far field microphones, arranged in three horizontal rows on the side wall of the test chamber (covering directivity from about 40° to 140° with respect to the rotor center, where 90° denotes sideways propagation) were

used, featuring the same data acquisition parameters as the array. Although all microphones are positioned

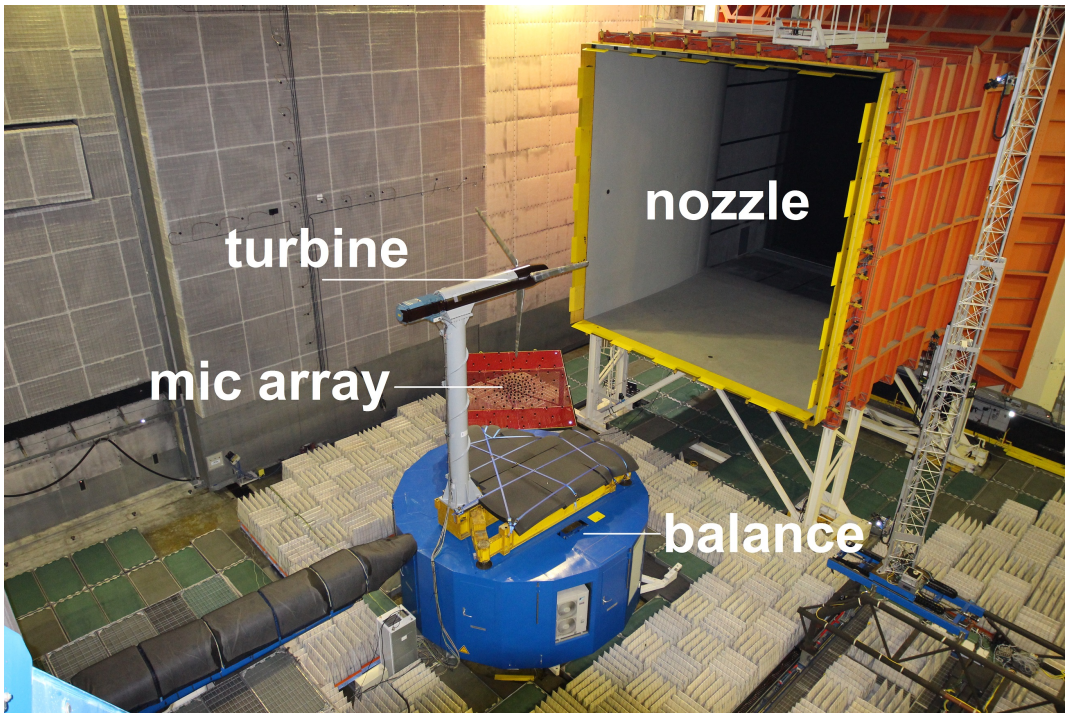

Figure 13.1: Test set-up of the experiment

outside of the open jet, they are protected by so-called foam 'wind balls' against wind noise from secondary flows in the test hall. All microphones were calibrated using a certified pistonphone, providing a pure tone of 94dB at 1 kHz. Acoustic lining was applied to the test chamber side walls, floor and ceiling wherever possible to prevent reverberations. Foam padding was applied to the top side of the balance (depicted in grey in Figure 13.1) to prevent noise disturbance from the impingement of the jet shear layer onto the sharp objects of the model support frame. More details about model, test set-up and instrumentation can be found in [27, 24, 35].

Post-processing and uncertainty

To reduce the enormous amount of acoustic data resulting from the raw time series of the far field microphones, DNW has applied a fast Fourier transform using a block size of 4096 yielding a narrow band frequency resolution of 12.5Hz. Since the model was initially not designed to perform aero-acoustic research with, the motor/generator and gearbox appeared to be rather noisy. Unfortunately this noise over shadowed the aerodynamic rotor noise, which is the subject of research, for all conditions. The background noise caused by the wind tunnel itself was shown to be lower than the model noise for all conditions. The first observation makes it rather difficult to separate rotor noise from the motor/generator/gearbox noise. As such the results from the farfield noise measurements are not discussed in the current paper.

The array data are processed by DNW using beamforming with the same block size as the far field microphones. The CLEAN-SC enhanced beamforming algorithm [145] has been used to separate the rotor noise from the motor/generator and gearbox noise by defining the scan grid as the outer part of the rotor plane ($r/R > 0.7$). This way the contamination from the motor noise, which is located in the nacelle about 2 meter downwind of the rotor plane, is minimized. Integrating over the scan grid then yields the narrow band and 1/3-Octave band power spectra. The resulting spectra have been corrected for shear layer diffraction of the open jet. A distance correction was employed using the 1/r law. It was found that after transformation of all array results to 0.28 m relative to the scan grid location, the measured Sound Pressure Level (SPL) would equal the Sound Power Level (PWL). Therefore this distance has been used throughout the processing. Weighting has not been applied. The resulting frequency range resolved by the array spans between 125 Hz and 10000 Hz, although the spatial resolution in the lower end of the range is regarded insufficient to distinguish noise sources.

It has been shown by former tests at DNW that the absolute accuracy of the sound levels, calculated from the integrated scan areas by enhanced CLEAN-SC beam forming processing, is about $\pm$3 dB. However, for the relative (delta) accuracy of the sound levels, calculated from the integrated scan areas by enhanced CLEAN-SC beam forming processing, this figure improves to about $\pm$1.5 dB (or better). More details about the DNW applied post-processing can be found in [35].

Sectional forces (normal and tangential to the local chord) at the five sections have been obtained by linearly integrating the measured pressure distribution along suction and pressure side. The rotor axial force was determined by decomposing these forces in the axial direction and integrating them linearly over the span from blade root to tip, assuming zero loading at the ends. The axial force coefficient Cdax was obtained by dividing this quantity by the freestream dynamic pressure and rotor disk area.

13.3 Experimental results

An example of resulting beamformning plots is given in Figure 13.2 for the rough and clean blade configuration. The results clearly show the dominance of turbulent boundary layer trailing edge noise at the outboard part of the blade which features the highest incoming flow speeds. Acknowledging the clockwise rotation of the blade, the most noisy part of the revolution is the downgoing motion of the blade in agreement with previous research on this topic [104, 41]. However it is noted that the peak is observed slightly before the 3 o'clock position, which is attributed to the off-axis location of the array. As described in section 13.2 the scangrid used only considers the last 30% span of the rotor, which results in a sharp transition at this radial position. The fact that the maximum noise levels appear well within this region justifies the approach taken.

Resulting 1/3-Octave band spectra are depicted in Figure 13.3(a) for several operational conditions. A haystack shaped spectrum is observed which is common for this noise source type. A lower tip speed ratio λ will result in a higher angle of attack increasing the noise level but also lower the frequency for which the peak occurs. For the low wind speeds (high tip speed ratios) University of Stuttgart has, by comparing noise levels between blade off and rotating blade measurements, demonstrated that for low frequencies (below approximately 1000 Hz) the rotor scan area is contaminated by the engine noise. Although the trailing edge noise peak usually exceeds this frequency for high tip speed ratios, the low frequency part of the spectra for these conditions should be interpreted with care. From the spectra, overall noise levels in terms of Overall Power Watt Level (OAPWL) are obtained which can be plotted and compared for a variety of conditions as shown in Figure 13.3(b). This plot also shows an estimate of the local angle of attack variation with tip speed ratio at the 82%R section. The same variation with tip speed ratio (or local angle of attack) can be observed as was noted from the spectra. The first increase from λ=9 to 7 could originate from turbulent transition moving forward causing more turbulent conditions at the trailing edge. For lower tip speed ratios trailing edge separation occurs, rapidly increasing the noise levels even further. Some of the operational conditions at -2.3° pitch angle were repeated many times ($>$5 as illustrated by the clustering of symbols at $\lambda = 6.7$ in Figure 13.3(b)) giving an indication of the repeatability. The dependency on pitch angle is also clearly illustrated, confirming that lowering the pitch will increase noise levels due to the higher local angles of attack and consequently more turbulence at the trailing edge. A rule of thumb originating from field test [164] was established in the past estimating 1 dB noise reduction per degree increase of pitch angle. Judging by the graph the actual amount depends on the tip speed ratio (or local aerodynamic state) under consideration and varies between 0.6 dB and 1.3 dB per degree pitch.

Effect of roughness

The effect of removing the strips from the outboard region is illustrated in Figure 13.2(e) and 13.2(f) for two frequencies at design conditions. Comparing around the spectrum peak frequency (f=2500 Hz) to the rough configuration from Figure 13.2(c) clearly shows the highest noise levels to move further inboard which still has the roughness strips applied. Also it can be observed that at f=10000 Hz the dominant noise source moves further outboard to the tip again indicating the dominance of tip noise at these high frequencies.

The effect on the noise levels can be observed in Figure 13.6. For the 425 rpm case, a rather large noise increase due to roughness of about 5dB is observed above λ=6.7 in attached flow conditions. The larger than expected increase could be related to the thickness effect of the roughness strip which adds extra to the boundary layer thickness. Because the boundary layer has now already been triggered to a turbulent state and hence transition does not creep up, there is no steep increase in noise levels below λ=7 as for the partially clean case. For separated flow conditions at very low tip speed ratios the noise levels converge because at these high angles

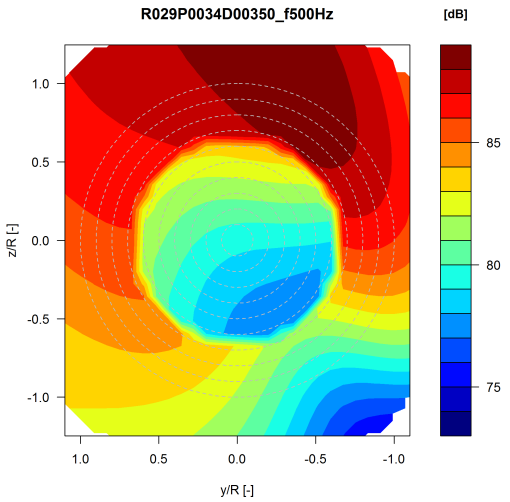

(a) B0, f=500 Hz

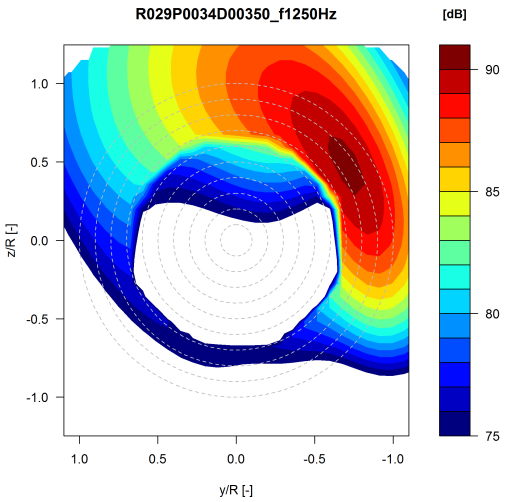

(b) B0, f=1250 Hz

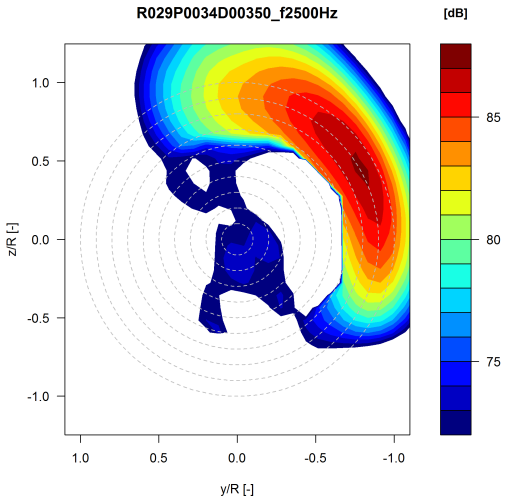

(c) B0, f=2500 Hz

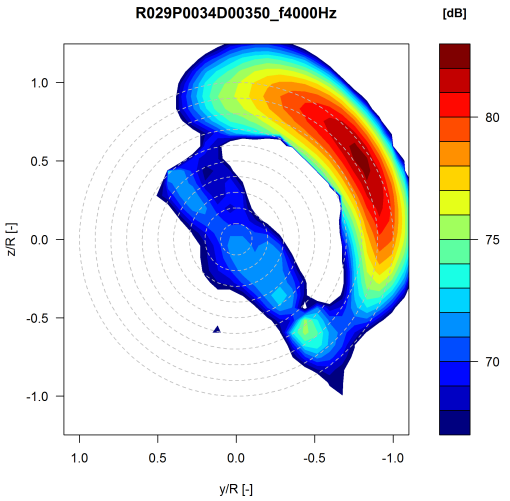

(d) B0, f=4000 Hz

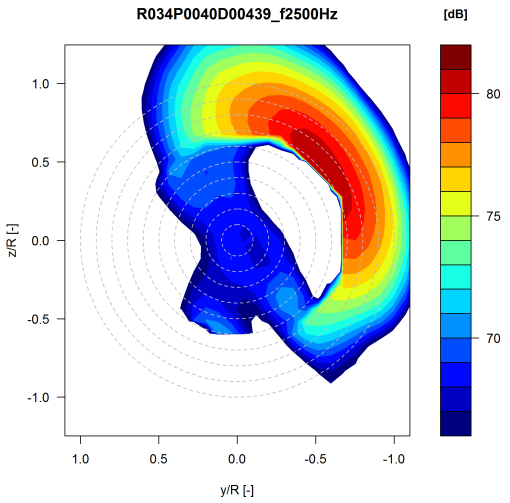

(e) B3, f=2500 Hz

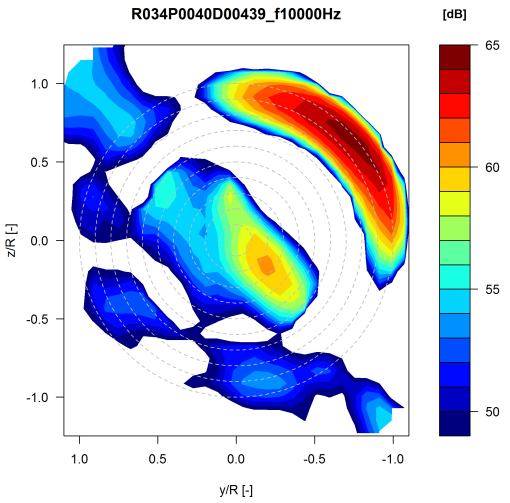

(f) B3, f=10000 Hz

Figure 13.2: Selected beamforming plots for rough (B0) and partially clean blade configuration (B3), λ=6.7, 425 rpm, pitch=-2.3°

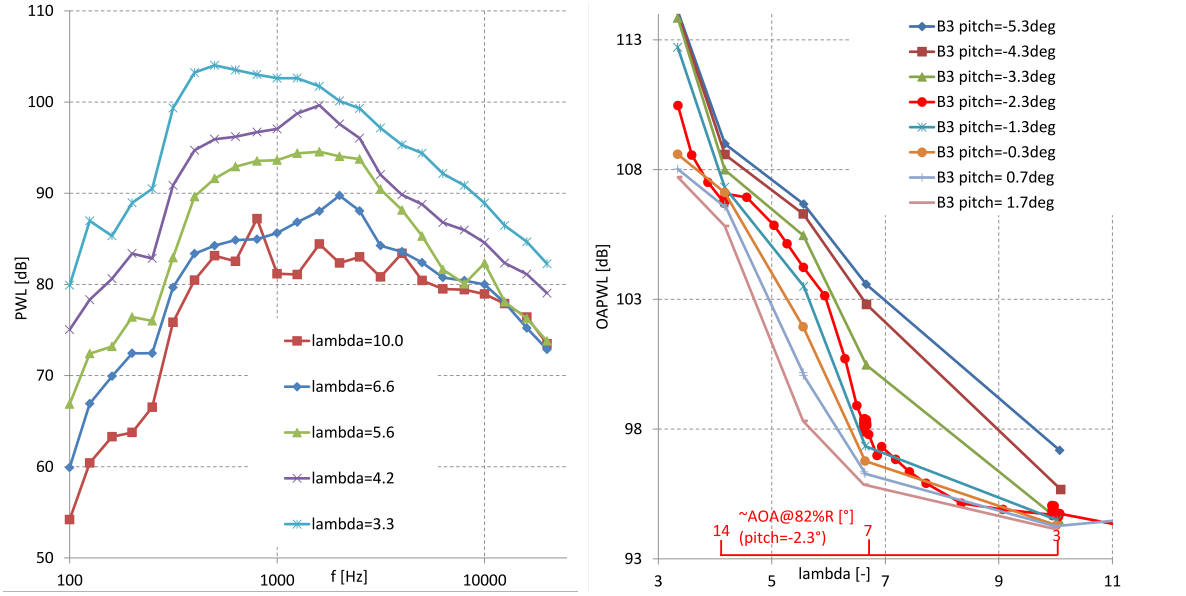

(a) 1/3 Octave band PWL spectra for pitch=-1.3°

(b) OAPWL levels versus tip speed ratio. Local angle of attack (AOA) estimate on secondary horizontal axis for pitch=-2.3°

Figure 13.3: Noise plots for partially clean configuration B3, 425 rpm

of attack natural transition occurs prior to the trigger position. Similar differences between partially clean and rough conditions are observed for the other pitch angles.

It was also observed that for partially clean blades the repeatability of the noise levels for identical operating conditions was not always perfect. For attached flow conditions differences larger than 1 dB were observed between identical runs which were performed on different days. Although great care was taken to clean the blades each morning, dust particles or similar could have triggered early transition in some cases influencing the noise level. It indicates how sensitive emitted noise levels are to soiling.

Yawed flow

The influence of **yaw**ing the turbine on the overall noise levels is shown in Figure 13.4(a). Small yaw angles up to 15° hardly influence the noise levels. Exceeding this misalignment, which is not very common for regular wind turbine operation, can offset the noise levels to about 4dB at 45°. Due to the skewed wake and advancing and retreating effect, local angle of attack and apparent velocity at the blade sections vary with azimuth angle, causing fluctuations during a rotor revolution. Combining these effects with the directivity effect changes the azimuth position for which the maximum noise levels are perceived, together with a decrease of the time averaged noise level. This is illustrated by the source plot in Figure 13.4(b) in comparison to the corresponding plot in axial flow conditions in Figure 13.2(e). This effect also explains why positive and negative yaw misalignment $\pm$ 30° result in different perceived noise levels. So although source levels principally are the same between positive and negative yaw, the perceived noise levels on the ground differ due to this effect.

The above results are only a small portion of the available data, as there still is a large amount of data which is untouched. It is recommended to analyze the data using blade tracking as well to analyse sectional noise levels better as a function of azimuth angle. Since the acoustic and aerodynamic measurements were synchronized in the time domain, it is possible to perform cross correlations between microphone and unsteady pressure sensors.

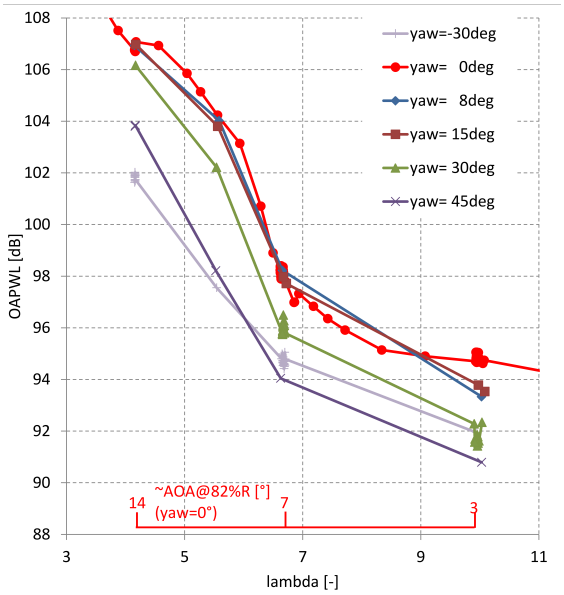

(a) 1/3 Octave band PWL spectra. Local angle of attack estimate on secondary horizontal axis

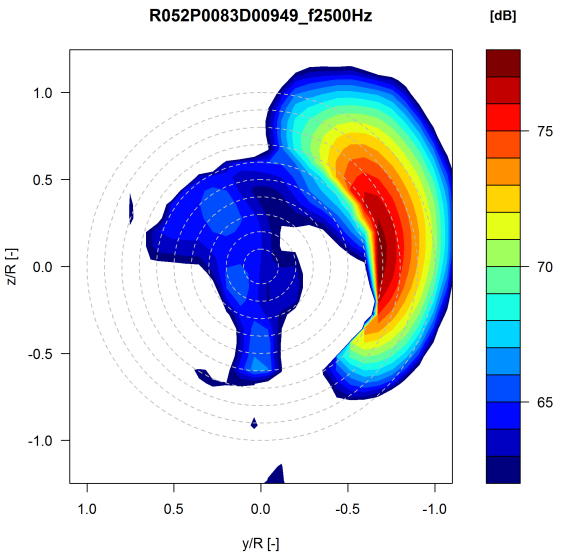

(b) Source plot at f=2500Hz for 45° yaw, λ=6.7

Figure 13.4: Influence of yawing the turbine for partially clean configuration B3, pitch=-2.3°, 425 rpm

13.4 Comparison to predictions

A comparison has been made to predictions from an engineering model widely used throughout the wind industry. First the model implementation named Silant is described together with the applied settings. Acknowledging that the noise is driven by the underlying aerodynamics a comparison of measured and prediction forces is given first, after which the noise levels are studied.

Silant model

Silant originated in 1996 from a Dutch consortium consisting of Stork Product Engineering BV, the Netherlands Organisation for Applied Scientific Research (TNO) and the Dutch Aerospace Laboratory (NLR). The model was designed to calculate noise emission of wind turbines, based on the sources that are considered most important: trailing edge noise (including separation-stall noise) and inflow noise. After ECN became the manager of the tool several improvements have been made, partly in cooperation with NLR.

Silant divides the rotor blades into a number of segments, usually in the order of 10 to 20 per blade. For each element, the trailing edge and inflow noise source are calculated. For the tip element, the contribution of tip noise is added. To determine the total emission, the element contributions are acoustically summed, assuming the sources to be incoherent.

The BPM turbulent boundary layer trailing edge noise model [161] is implemented to model the first noise source. This model necessitates the input of boundary layer parameters at the trailing edge for both pressure and suction side of the airfoil. In this case these are obtained from an a priori created database generated by `R-FOIL`[100], which is based on XFOIL [36], and essentially is a 2D panel code featuring a viscous inviscid interaction scheme. Airfoil coordinates of the profiles used in the blade serve as input to this code. The roughness strips were mimicked by prescribing the laminar to turbulent transition location. The critical amplification factor needed for transition as used in the underlying e^n model was set at 9, corresponding to smooth, low turbulence inflow conditions. In addition to the boundary layer variables this model needs several rotor aerodynamic variables (sectional angle of attack and apparent velocity), which are estimated by a BEM based code [87] after feeding the operational conditions. Here the relevant airfoil polars originate from dedicated airfoil wind tunnel tests, with the exception of the midboard RISØ profile. The tip noise model for rounded tips from [161] is also implemented, where level and spectral content of the tip noise are determined using the spanwise extent of separation at the trailing edge due to the tip vortex. Here the spanwise extent is estimated using a

representative angle of attack in the tip region, obtained from the BEM code.

Although inflow noise due to the interaction of the airfoil with turbulence in the oncoming flow is predicted by Silant, this noise source is discarded from the current comparison due to the low turbulence levels in the tunnel (~0.2%) and the expected dominance of turbulent boundary layer trailing edge noise. For more details about Silant please consult the relevant publication [23].

Load verification

To assess the validity of the BEM simulations of which the results are used as input to the Silant code, a comparison is made in terms of axial force coefficient Cdax obtained from the pressure sensors for pitch=-2.3° and 425 rpm in Figure 13.5(a). To prevent differences due to the limited number of sensors, the experimental resolution in spanwise direction is used to obtain the axial force from the simulations. Although the experimental axial force is deduced from the pressures and hence does not include the contribution of friction, this was previously demonstrated to affect axial force less than 1% [69]. The agreement is quite good for a variety of operational conditions, although results seem to slightly diverge for high tip speed ratios towards the turbulent wake state. It is noted here that these conditions feature relatively low tunnel speeds and consequently low dynamic pressures utilizing only a small fraction of the measurement range (plus the fact that absolute differences are non-dimensionalized with a lower velocity enlarging differences in Cdax). Because a good agreement in axial force can also be a result of compensating errors along the blade span and since the outboard part of the blade is mostly responsible for the noise, a comparison of chord normal force at 82%R is given in Figure 13.5(b). Except for the kink due to stall just below λ=6, the trend is well captured. The smooth stall characteristics from the measured two dimensional polars that were used as input to the predictions are apparently different from the more abrupt stall encountered in the rotating experiment. Because the loading in the inboard stations is underpredicted in stalled conditions (λ <6), the agreement in Cdax is still good for these conditions. In attached flow conditions (λ >6), the predicted normal forces are roughly 20 N/m lower (in agreement with the observed discrepancy in Cdax), which is a satisfactory agreement.

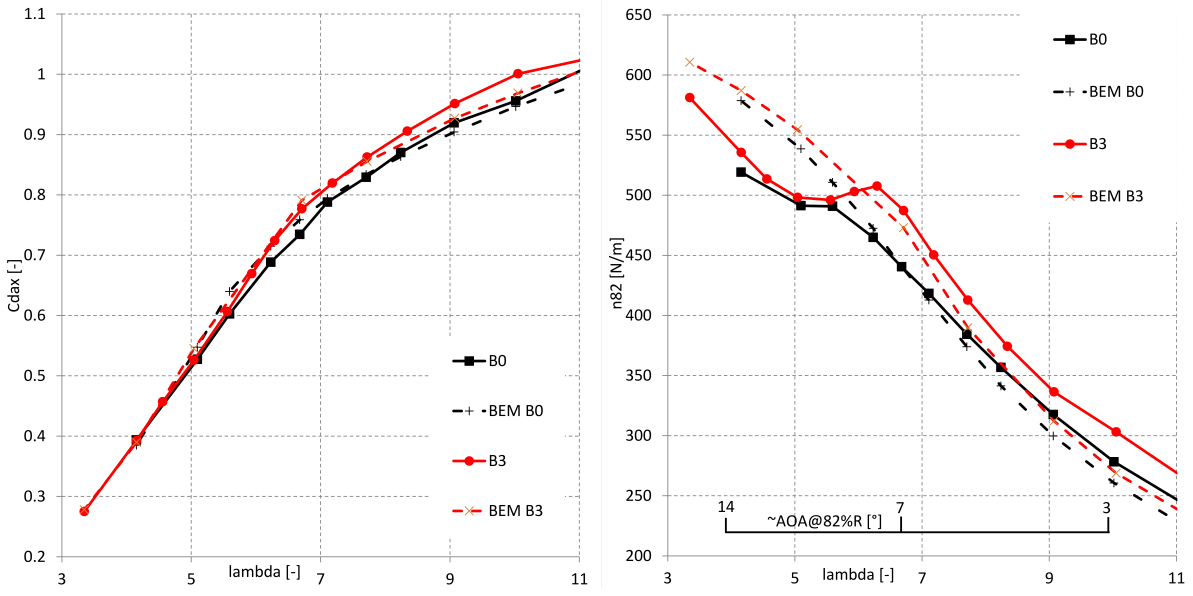

(a) Axial force coefficient

(b) Normal force at 82%R. Local angle of attack estimate on secondary horizontal axis

Figure 13.5: Comparison to predicted loads (dashed) at pitch=-2.3° and 425 rpm for partially clean (B3) and rough configuration (B0)

Noise validation

The comparison of predicted noise levels to the measurements is shown in Figure 13.6 for the two different rotational speeds, while a selection of underlying spectra at 425 rpm is given in Figure 13.7. For the clean

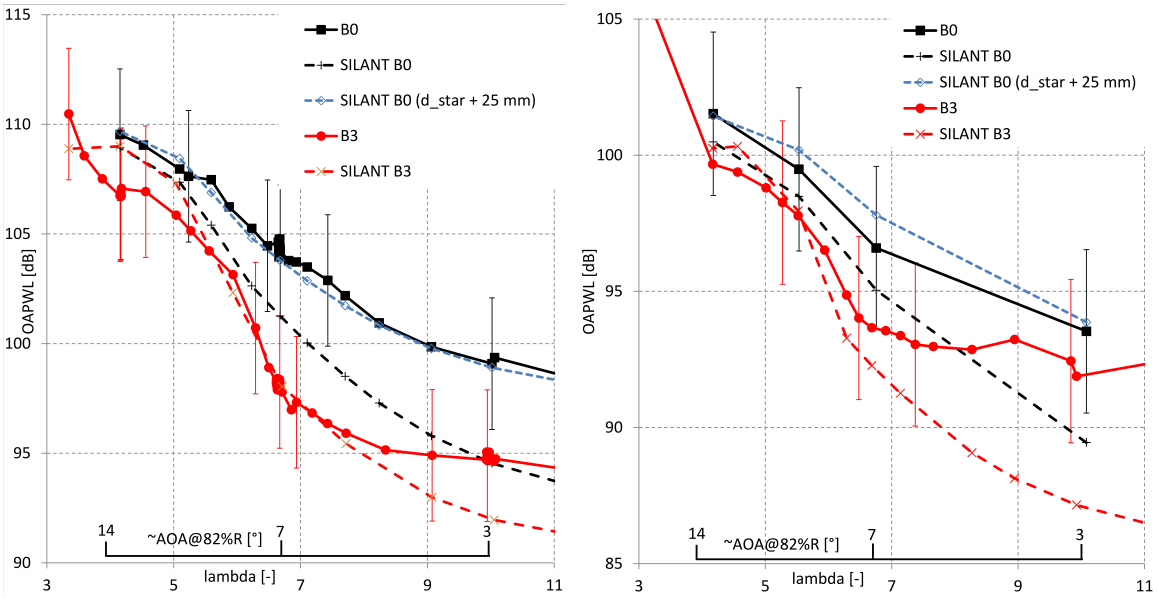

Figure 13.6: Comparison to predicted OAPWL (dashed) at two different rotational speeds for partially clean (B3) and rough configuration (B0), pitch=-2.3°. A local angle of attack estimate is given on a secondary horizontal axis. Error bars give an indication of the absolute uncertainty of the measurements.

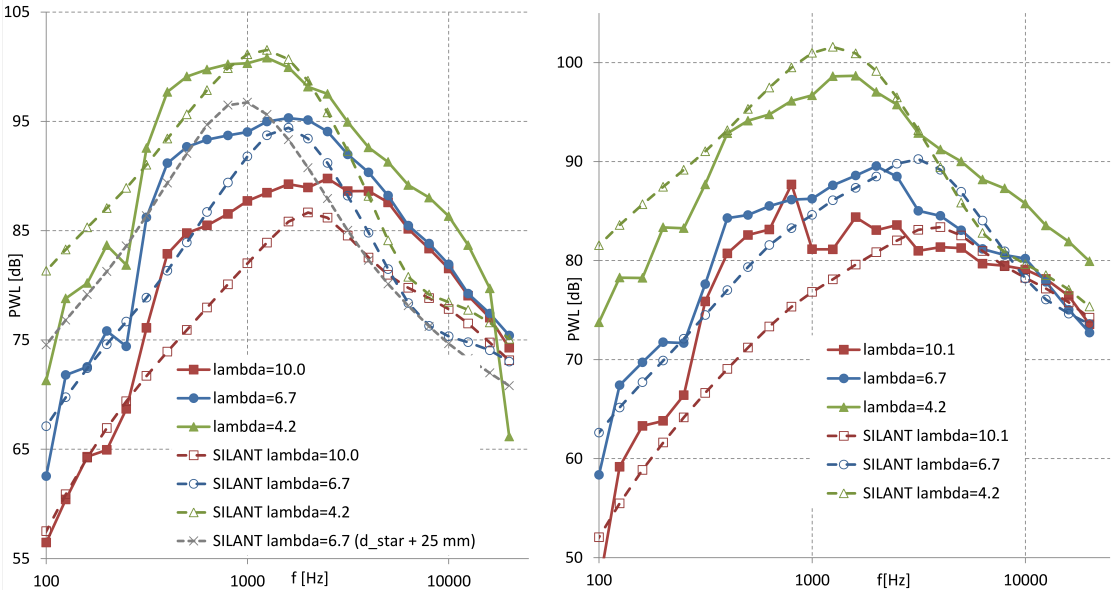

Figure 13.7: Comparison to predicted spectra (dashed) for partially clean (B0) and rough conditions (B3), pitch=-2.3°, 425 rpm

configuration the agreement is within 1 dB below $\lambda = 7$. The implemented switch to separation-stall noise seems to yields a good agreement for low tip speed ratios. However the measured sharp noise increase trend towards λ=3 in massively separated flow is not captured by the calculations. For higher tip speed ratios the results seem to diverge slightly, similar to what was shown for the loads. Hence the question that can be asked is whether this discrepancy arises from a shortcoming of the BPM model or the aerodynamic input to this model.The scaling of the noise between the two different rotational (or tip) speeds is well predicted by the code, confirming the validity of the underlying model for this purpose. The underlying spectra in Figure 13.7 show a surprisingly good agreement. The maximum levels and their corresponding frequency are well approximated and the shape agreement is also fair. Generally speaking the measured peaks are slightly more broad than the predictions.

The effect of the roughness strip on the noise appears to be underestimated by the predictions. In addition to enforcing laminar to turbulent transition, turbulators have a finite thickness which is known to induce an increase in boundary layer thickness. This thickness effect is not modeled in the `R-FOIL`code which was used to create the airfoil database. Possibly this effect is responsible for the larger discrepancy between measured and predicted noise levels for the rough configuration. To attempt to mimic this effect, the boundary layer thickness database of the NACA profile was manipulated with a constant offset for both the pressure and suction side. Figure 13.6 shows that for an increase in trailing edge boundary layer displacement thickness of 25 mm, the predicted noise levels come closer to the measurements, especially for the 425 rpm case. However the corresponding spectrum at λ=6.7 in Figure 13.7(a) shows the underlying physics are far from modeled correctly, illustrated by the discrepancy in peak frequency and spectral shape. More investigation is necessary to verify to what extent this is a shortcoming of the underlying acoustic model or the incorrect input given to it.

13.5 Conclusions

Wind turbine noise measurements have successfully been performed in the wind tunnel for a variety of operational conditions and model configurations. The rule of thumb stating that per degree of pitch angle increase the noise roughly reduces with 1dB was assessed. Addition of roughness by means of zigzag strips increased the overall noise levels up to 5 dB for the experiment under investigation. Yawing the turbine is found to significantly decrease the perceived noise levels at the array position above 15° misalignment. The influence of various configurations on the noise signature has been assessed.

For the standard blade configuration (clean blade in the outboard region) the predictions of the BPM model were found to agree well within the specified uncertainty band of the experiment. Generally speaking trends are well captured. An excellent agreement in overall noise levels was obtained for design conditions. For off-design conditions such as cases in the turbulent wake state and cases with large portions of separated flow (high and low tip speed ratio), larger discrepancies can be observed. Here it must be stated that the BPM model is dependent on the accuracy of the inputted airfoil data and rotor aerodynamic state.

The present chapter describes a selection of the acoustic analysis performed in Mexnext-III. In [26] more observations are reported. It is amongst others observed that caution is needed on the design of Guerney flaps, in particular the radial extent of them. Extending the Guerney flaps from 40 to 60 % span led to a considerable noise increase.

14. Conclusions and recommendations

In this section the main results, conclusions and recommendations from Mexnext-III are given. The main objective of this third phase of IEA TCP WInd Task 29 Mexnext-III was to analyze, in a collaborative way, the detailed aerodynamic measurements from the New Mexico experiment and more specifically to solve the puzzling results from the first phase Mexnext-I. This objective has been met. Thereto the entire New Mexico database has been documented and delivered to the Mexnext-III consortium. With this database a large comparison exercise has been performed, featuring six simulation cases in axial and yawed inflow conditions, containing results of over 20 codes ranging from BEM to CFD. More than 10 different variable types ranging from lifting line variables to pressures, loads and velocities have been compared for the different conditions, resulting in over 250 comparison plots. The result is a unique insight in the current status and accuracy of rotor aerodynamic modeling. More specifically it can be concluded that most questions from Mexnext-I have been answered and so a much better understanding of the aerodynamics of the MEXICO rotor in terms of blade aerodynamics as well as near wake aerodynamics has been gained. This is illustrated by the better agreement between calculations and measurements compared to the agreement in Mexnext-I. This is true for pragmatic engineering models but also for high fidelity models. Opposite to the situation in MEXICO the relation between loads and velocities now fulfills the momentum balance, not only in axial direction but even in the tangential direction.

By using the measurements from New MEXICO and computational results from higher fidelity models it has been possible to improve engineering models, e.g for the prediction of tip losses and yaw. Recommendations for grid size and refinements were important to improve predictions from CFD.

The analysis of data led to many new insights, e.g. on the following fields:

- 'IEC Aerodynamics': It was found that a faulted pitch situation leads to an aerodynamic influence from the blade with the pitch error to the other blades
- Dynamic Inflow: The earlier found deficiency with regard to the radial dependency of the dynamic inflow time constant in state of the art models is now understood and a new model was developed.
- Acoustics:
  - A good agreement has been found between BPM prediction and measurements at design conditions.
  - The 1dB(A) per degree pitch angle rule (which originates from the 90s) was confirmed in the present measurements.
  - Caution is needed on the design of Guerney flaps, in particular the radial extent of them. Extending the Guerney flaps from 40% to 60% span led to a considerable noise increase.
- Determination of lifting line variables from measurements or CFD: Several methods have been assessed with which lifting line variables could be determined from measurements. They compare well at the mid-span of the blade, say from 30% to 70% span. This now makes it possible to validate induction models from measured results (at least for the mid-span of the blade).

- Transition: It was possible to determine the transition point from the response of the fast Kulite pressure transducers. As such this might act as an alternative method for transition detection in case more conventional methods (microphones, flow visualization, infrared etc.) are lacking.

Based on the project results it can be stated that current state of the art design models provide accurate aerodynamic load predictions for design conditions in constant axial and uniform inflow. Despite the better agreement between calculations and measurements, several challenges remain. This is amongst others true for the difficult turbulent wake cases, the stalled cases and the yawed cases where differences between calculations (in particular from engineering methods) and measurements were larger than for the conditions relatively close to design situations. The same holds for dynamic and/or non-uniform inflow conditions. It is then interesting to observe that these phenomena were best (though not perfectly) predicted by the highest fidelity models (with the longest computational effort). It was also found that intermediate free vortex wake methods predict induction dominated phenomena almost as good as CFD.

Another unsolved question remains the relatively large differences between calculated and measured results at the 60% span station.

As such it is important to emphasize that wind turbine rotor aerodynamics research is not 'finished'. Following this result it is recommended to further improve (unsteady) aerodynamic modeling in the fourth phase of IEA TCP Wind Task 29. This observation then supports the recommendations which were already given in [68] and [69] and which remains true after Mexnext-III: The publicly available amount of aerodynamic validation material is far too limited and much more detailed aerodynamic measurements (with extensive analyses) are needed where measurements should be taken both in the field (full scale) as well as in the wind tunnel since wind tunnel and field experiments are complimentary!

Other recommendations are:

- Several New Mexico data are still untouched. They should be investigated in future studies.
- Reliable 2D airfoil data of all blade sections on a wind turbine model should be known at the appropriate conditions to understand the aerodynamics of the rotating model.
- Objective measures should be defined to determine differences between calculations and measurements.

Finally it is noted that a selection of data has been made available for third parties. As such many institutes and companies have improved and validated their approach to simulate rotor aerodynamics using the database and this will continue in the future.

Bibliography

1 *IEC 61400-1 Ed. 3, Wind Turbines. Part 1: Design Requirements*. 2005.

2 *Code_Saturne* 4.0.0 Theory Guide. Technical Report , www.code-saturne.org, EDF R&D, 2015.

3 AVATAR: Advanced Aerodynamic Tools for Large Rotors. (EERA) European Energy Research Alliance report, May 2016.

4 INNWIND.EU: Design of state of the art 10-20MW offshore wind turbines. (EERA) European Energy Research Alliance report, May 2016.

5 B. Akay, D. Ragni, C.J. Sim ao Ferreira, and G.J.W. van Bussel. Experimental investigation of the root flow in a horizontal axis wind turbine. *Wind Energy*, 17(7):1093–1109, 2014.

6 F. Archambeau, N. Méchitoua, and M. Sakiz. *Code_Saturne*: a Finite Volume Code for the Computation of Turbulent Incompressible Flows - Industrial Applications. *International Journal on Finite Volumes*, 1(1), 2004.

7 A. Arnal, M. Habiballah, and E. Coustols. Laminar Instability Theory and Transition Criteria in Two and Three-Dimensional Flow. *La Recherche aérospatiale*, 1984-2, 1984.

8 K. Boorsma B.A. Lobo and A.P. Schaffarczyk. In *Investigation into Boundary Layer Transition on the MEXICO Blade*, To be published in the Proceedings of the Science of Making Torque from Wind, POLIMI, Italy, 2018.

9 N. Balaresque, S. Bicker, C. Dollinger, A. Fandrich, S. Gatz, M. Hölling, K. Irischick, T. Reichstein, A.P. Schaffarczyk, and C. von Zengen. Investigation for Improvement of Energy Yield of Rotor-blades form the 1.5 MW Class. In *J. Phys. Conf. Ser., 753*, page 072012, October 2016.

10 G. Bangga, T. Lutz, and E. Krämer. Root flow characteristics and 3D effects of an isolated wind turbine rotor. *Journal of Mechanical Science and Technology*, 31(8):3839–3844, 2017.

11 A. Bechmann, N.N. Sørensen, and F. Zahle. CFD simulations of the MEXICO rotor. *Wind Energy*, 14(5):677–689, 2011.

12 J.A. Benek, J.L. Steger, F.C. Dougherty, and P.G. Buning. In *Chimera. A Grid-Embedding Technique.*, 1986.

13 F. Bertagnolio. Trailing edge noise model applied to wind turbine airfoils. Technical Report Risø-R-1633(EN), Risø, 2008.

14 F. Blondel, R. Boisard, M. Milekovic, G. Ferrer, C. Lienard, and D. Teixeira. Validation and comparison of aerodynamic modelling approaches for wind turbines. In *Journal of Physics: Conference Series*, volume 753. IOP Publishing, 2016.

15 F. Blondel, G. Ferrer, M. Cathelain, and D. Teixera. In *Improving a BEM Yawmodel based on New Mexico Experimental Data and Vortex/CFD simulations*, Congres Francais de Mecanique, 28-1 September 2017, Lille, France, 2017.

16 K. Boorsma. https://mexnext.ecn.nl. In *Password protected environment for exchange of Mexnext data*, Petten, the Netherlands, 2008. ECN.

17 K. Boorsma. Power and loads for wind turbines in yawed conditions. Technical Report ECN-E-12-047, Energy Research Centre of the Netherlands, ECN, Petten, The Netherlands, 2012.

18 K. Boorsma. Mexnext Progress overview presentation. MexNext Phase 2, meeting, Mianyang, China, 2014.

19 K. Boorsma, P. Chasapogiannis, D. Manolas, M. Stettner, and M. Reijerkerk. Comparison of aerodynamic models for calculation of fatigue loads in turbulent inflow. AVATAR Deliverable AVATAR Deliverable D4.6, 2016.

20 K. Boorsma, S. Gomez-Iradi, and C. Schulz. On the influence of MEXICO blade shape deviations, Compar-

ison of CFD results using scanned and design blade geometry. ECN-X–13-038, Energy Research Center of the Netherlands, April 2013.
21 K. Boorsma, F. Grasso, and J.G. Holierhoek. Enhanced approach for simulation of rotor aerodynamic loads. Technical Report ECN-M–12-003, ECN, presented at EWEA Offshore 2011, Amsterdam, 29 November 2011 - 1 December 2011, 2011.
22 K. Boorsma, M. Hartvelt, and L.M. Orsi. Application of the lifting line vortex wake method to dynamic load case simulations. *Journal of Physics: Conference Series*, 753(2):022030, 2016.
23 K. Boorsma and J.G. Schepers. Enhanced wind turbine noise prediction tool SILANT. Technical Report ECN-M–12-004, presented at the Fourth International Meeting on Wind Turbine Noise, Rome, Italy, April 2011.
24 K. Boorsma and J.G. Schepers. New MEXICO Experiment, Preliminary overview with initial validation. Technical Report ECN-E–14-048, ECN, September 2014.
25 K. Boorsma and J.G. Schepers. In *Rotor experiments in controlled conditions continued: New Mexico*, Proceedings of the Science of Making Torque from Wind, Technical University of Munich, 2016.
26 K. Boorsma and J.G. Schepers. Wind turbine noise measurements in controlled conditions. *International Journal of Aero-acoustics*, 16(7-8):649–665, 2017.
27 K. Boorsma and J.G. Schepers. New Mexico Experiment, Description of experimental setup. Technical Report ECN-X–15-093 (v3), ECN, February 2018.
28 M.L. Buhl. A New Empirical Relationship between Thrust Coefficient and Induction Factor for the Turbulent Windmill State. Technical Report NREL/TP-500-36834, NREL, 2005.
29 T. Burton, D. Sharpe, N. Jenkins, and E. Bossanyi. *Wind Energy Handbook*. Wiley, 2001.
30 O. Ceyhan, O. Pires, X. Munduate, N. Sørensen, T. Reichstein, A.P. Schaffarczyk, K. Diakakis, G. Papadakis, E. Daniele, M. Schwarz, T. Lutz, and R. Prieto. Summary of the Blind Test Campaign to predict High Reynolds number performance of DU00-W-210 airfoil. *AIAA 2017-0915*, 915, 2017.
31 N.M. Chaderjian. Advances in rotor performance and turbulent wake simulation using DES and adaptive mesh refinement. In *Seventh International Conference on Computational Fluid Dynamics (ICCFD7)*, July 2012.
32 T. Cho, C. Kim, and D. Lee. Acoustic measurement for 12% scaled model of NREL Phase VI wind turbine by using beamforming. *Current Applied Physics*, 10:5320–5325, 2010.
33 M. Churchfield and S. Lee. NWTC Information Portal (SOWFA) - Simulator fOr Wind Farm Applications. https://nwtc.nrel.gov/SOWFA, May 2016.
34 H.D. Currin, F.N. Coton, and B. Wood. Dynamic Prescribed Vortex Wake Model for AERODYN/FAST. *Journal of Solar Energy Engineering*, 120, August 2008.
35 DNW. New MEXICO test. Technical report, To be published in 2014.
36 M. Drela. Xfoil: An analysis and design system for low reynolds number airfoils. In *Conference on Low Reynolds Number Airfoil Aerodynamics*. University of Notre Dame, June 1989.
37 H. Rahimi et al. An engineering model for wind turbines under yawed conditions derived from high fidelity models. *Wind Energy (in review)*, June 2017.
38 H. Rahimi et al. Evaluation of different methods for determining the angle of attack on wind turbine blades with cfd results under axial inflow conditions. *Journal of Renewable Energy (in review)*, June 2017.
39 H.A. Madsen et al. Validation and Modification of the Blade Element Momentum theory based on comparisons with actuator disc simulations. *Wind Energy*, 13(4), 2009.
40 H.A. Madsen et al. The DAN-AERO MW experiments. *AIAA*, 2010-645:1–13, 2010.
41 J.G. Schepers et al. Sirocco: Silent rotors by acoustic optimisation. In *Conference proceedings European Wind Energy Conference*, Athens, Greece, March 2006.
42 N. Troldborg et al. The DAN-AERO MW II Experiments Final report. Technical Report DTU Wind Energy E-0027, DTU, April 2013.
43 P. Fuglsang and H.A. Madsen. Implementation and verification of an aeroacoustic noise prediction model for wind turbines. Technical Report Risø-R-867(EN), Risø, 1996.
44 E.M. Gaertner and M.A. Lackner. Modeling dynamic stall for a free vortex wake model. *Wind Engineering*, 39(6):675–691, 2015.
45 H. Glauert. *A general theory of the autogyro*. HM Stationery Office, 1928.
46 H. Glauert. "Airplane Propellers, Division L in Aerodynamic Theory, vol. IV, Durand WF (ed.).". pages 169–360. Springer, 1935.
47 S. Gomez-Iradi and G.N. Barakos. Computational fluid dynamics investigation of some wind turbine rotor design parameters. *Proceedings of the Institution of Mechanical Engineers, Part A: Journal of Power and Energy*, 222(5):445–470, 2008.
48 S. Gomez-Iradi, I. Herraez, N. Sørensen, and P. Weighin. Simulation convergence MexNext 3, April 2017.

49 S. Gomez-Iradi, R. Steijl, and G.N. Barakos. Development and validation of a CFD technique for the aerodynamic analysis of HAWT. *Journal of Solar Energy, Engineering-Transactions of the ASM*, 131(3), 2009.

50 H. Snel H. and J.G. Schepers. JOULE1: Joint investigation of Dynamic Inflow Effects and Implementation of an Engineering Method. ECN-C-94-107, Energy Research Centre of the Netherlands, ECN, December 1994.

51 W. Haans. Wind turbine aerodynamics in yaw, unravelling the measured rotor wake. PhD Thesis, Technical University of Delft, September 2011.

52 M.M. Hand, D.A. Simms, L.J. Fingersh, D.W. Jager, J.R. Cotrell, S. Schreck, and S.M. Larwood. Unsteady Aerodynamics Experiment Phase VI Wind Tunnel Test Configurations and Available Data Campaigns. NREL/TP-500-29955, National Renewable Energy Laboratory, NREL, December 2001.

53 M.O.L. Hansen. *Aerodynamics of Wind Turbines*. Earthscan, second edition, 2008.

54 M.O.L. Hansen and J. Johansen. Tip studies using CFD and computation with tip loss models. *Wind Energy*, (7):343–356, 2004.

55 M.O.L. Hansen, N.N. Sørensen, J.N. Sørensen, and J.A. Michelsen. Extraction of lift, drag and angle of attack from computed 3D viscous flow around a rotating blade. In *Scientific Proceedings from European Wind Energy Conference, EWEC'97*, pages 499–501, Dublin, Ireland, October 1997.

56 C.C. Heister. Approximate Transition Prediction for the ONERA 7AD Rotor in Forward Flight using a Structured and Unstructured URANS solver. In *Proceedings of the AHS International 72nd Annual Forum., Mira Conference*, West Palm Beach, Florida, US, 2016.

57 C.C. Heister. RANS Simulation of the New MEXICO Rotor Experiment Including Laminar-Turbulent Transition. In *20. DGLR-Fach-Symposium der STAB*, 2016.

58 I. Herráez, B. Akay, G.J.W. van Bussel, J. Peinke, and B. Stoevesandt. Detailed analysis of the blade root flow of a horizontal axis wind turbine. *Wind Energy Science*, 1:89–100, 2017.

59 I. Herraez, E. Daniele, and J.G. Schepers. Extraction of the wake induction and angle of attack on rotating wind turbine blades from piv and cfd results. *Wind Energy Science Conference 2017*, (WES-2017-43), June 2017.

60 I. Herraez, H. Plischka, B. Stoevesandt, and J. Peinke. Simulation and validation of the mexico-wind turbine with openfoam. *6th OpenFOAM Workshop PennState University*, pages 13–16, June 2011.

61 I. Herraez, B. Stoevesandt, and J. Peinke. Insight into Rotational Effects on a Wind Turbine Blade Using Navier-Stokes Computations. *Energies*, 7(10):6798–6822, 2014.

62 H. Himmelskamp. *Profile investigations on a rotating airscrew*. Reports and translations. Völkenrode MAP, 1947.

63 H.H. Hubbard and K.P. Shepherd. Wind turbine acoustics. Technical Report NASA-TP-3507, NASA, 1990.

64 A. Jameson. Time Dependent Calculations Using Multigrid, with Applications to Unsteady Flows past Airfoils and Wings. In *AIAA 91-1596, AIAA 10th Computational Fluid Dynamics Conference*, June 1991.

65 A. Jameson, W. Schmidt, and E. Turkel. Numerical Simulation of the Euler Equations by finite Volume Methods using Runge-Kutta Time Stepping Schemes. *AIAA Journal No. 1259*, 1981.

66 A. Jameson, W. Schmidt, and E. Turkel. Numerical solutions of the euler equations by finite volume methods using runge-kutta time-stepping schemes. *AIAA paper*, 1259:1981, 1981.

67 J.G. Schepers and H. Snel. MEXICO, Model experiments in controlled conditions. ECN-E-07-042, Energy Research Center of the Netherlands, 2007.

68 J.G. Schepers and K. Boorsma et al. Final report of IEA Task 29, Mexnext (Phase 1): Analysis of MEXICO wind tunnel measurements. ECN-E-12-004, Energy Research Center of the Netherlands, February 2012.

69 J.G. Schepers and K. Boorsma et al. Final report of IEA Task 29, Mexnext (Phase 1): Analysis of MEXICO wind tunnel measurements. ECN-E-14-060, Energy Research Center of the Netherlands, December 2014.

70 J.G. Schepers et al. Final report of IEA Annex XVIII' Enhanced Field Rotor Aerodynamics Database. ECN-C-02-016, Energy Research Centre of the Netherlands, ECN, February 2002.

71 J.G. Schepers et. al. Verification of European Wind Turbine Design Codes. ECN-C-01-055, ECN, April 2002.

72 G.S. Jiang and C.W. Shu. Efficient implementation of weighted eno schemes. *Journal of computational physics*, 126(1):202–228, 1996.

73 J.L. van Ingen and J.G. Schepers. Prediction of boundary layer transition on the wind turbine blades using th e^N methid and a comparison with experiment. priv comm, 2012.

74 J. Jonkman, S. Butterfield, W. Musial, and G. Scott. Definition of a 5-mw reference wind turbine for offshore system development. Technical report, National Renewable Energy Laboratory, 2009.

75 J.M. Jonkman and M.L. Buhl Jr. FAST user's guide. NREL/EL-500-38230: National Renewable Energy Laboratory, 2005.

76 E. Jost, L. Klein, L. Leipprand, T. Lutz, and E.Kramer. Extracting the angle of attack on rotor blades from CFD simulations. *Wind Energy*, page submitted, 2017.

77 J. Katz and A. Plotkin. Low-Speed Aerodynamics. Cambridge Aerospace Series, Cambridge University Press, 2001.

78 T.T. Kim, A.M. Hansen, and K. Branner. Development of an anisotropic beam finite element for composite wind turbine blades in multibody system. *Renewable Energy*, 59:172, 2013.

79 U. Kowarsch, C. Oehrle, M. Keßler, and E. Krämer. High order cfd-simulation of the rotor-fuselage interaction. 2013.

80 N. Krimmelbein and R. Radespiel. Transition prediction for three-dimensional flows using parallel computation. *Computers&Fluids*, 38:121–136, 2008.

81 N. Kroll, C.-C. Rossow, K. Becker, and F. Thiele. The megaflow project. *Aerospace Science and Technology*, 4(4):223–237, 2000.

82 T.J. Larsen, H.A. Madsen, G.C. Larsen, and K.S. Hansen. Validation of the dynamic wake meander model for loads and power production in the Egmond aan Zee wind farm. *Wind Energy*, 16(4):605–624, 2013.

83 J.G. Leishman. Challenges in modelling the unsteady aerodynamics of wind turbines. *Wind Energy*, 5(11):85–132, 2002.

84 J.G. Leishman. *Principles of Helicopter Aerodynamics*. Cambridge Aerospace Series. Cambridge University Press, 2002.

85 Y. Li, K. Paika, T. Xing, and P.M. Carricac. Dynamic overset cfd simulations of wind turbine aerodynamics. *Renewable Energy*, 37:285–298, 2012.

86 C. Lienard and R. Boisard. In *Investigation of the MEXICO rotor aerodynamics in axial flow, including boundary layer transition effects,*, AIAA Scitech conference, 2018, 2018.

87 C. Lindenburg. Bladmode, program for rotor blade mode analysis. Technical Report ECN-C–02-050-r2, ECN, 2002.

88 C. Lindenburg. Investigation into rotor blade aerodynamics. Technical Report ECN-C-03-025, Energy Research Center of the Netherlands, Petten, Netherlands, 2003.

89 C. Lindenburg and J.G. Schepers. Phatas-IV aeroelastic modelling, release ”dec-1999” and ”nov-2000”. Technical Report ECN-CX–00-027, ECN, 2000.

90 B. Lobo. Investigation into Boundary Layer Transition on the MEXICO Blade. Master’s thesis, University of Applied Sciences Flensburg, 2018.

91 T. Lutz, C. Schulz, P. Letzgus, and A. Rettenmeier. Impact of Complex Orography on Wake Development: Simulation Results for the Planned WindForS Test Site. In *Journal of Physics: Conference Series*, volume 854, page 012029. IOP Publishing, 2017.

92 H.A. Madsen. *A CFD analysis of the actuator disc flow compared with momentum theory results*, pages 109–124. Technical University of Denmark. Department of Fluid Mechanics, 1997.

93 H.A. Madsen. Low frequency noise from mw wind turbines - mechanisms of generation and its modelling. Technical Report Risø-R-1637(EN), Risø, 2008.

94 K. Meister, T. Lutz, and E. Krämer. Time-Resolved CFD Simulation of a Turbulent Atmospheric Boundary Layer Interacting with a Wind Turbine. In *Wind Energy-Impact of Turbulence*, pages 191–196. Springer, 2014.

95 F.R. Menter. Zonal Two Equation Kappa-Omega Turbulence Models for Aerodynamic Flows. In 23^{rd} *Fluid Dynamics, Plasmadynamics, and Lasers Conference*, July 1993.

96 F.R. Menter. Two-Equation Eddy-Viscosity Turbulence Models for Engineering Applications. *AIAA Journal*, 32(8):1598–1605, 1994.

97 F.R. Menter, R.B. Langtry, S.R. Likki, Y.B. Suzen, P.G. Huang, and S. Völker. A Correlation-Based Transition Model Using Local Variables - Part I: Model Formulation. *Journal of Turbomachinery*, 128:413–422, 2006.

98 R. Mikkelsen. Actuator disc methods applied to wind turbines. *Technical University of Denmark*, 2003.

99 K. Mommsen. 3D Laminar-Turbulent Transition on Wind Turbine Blades by CFD. Master’s thesis, University of Applied Sciences Flensburg, 2017.

100 B.O.G. Montgomerie, A.J. Brand, J. Bosschers, and R.P.J.O.M van Rooij. Three-dimensional effects in stall. Technical Report ECN-C–96-079, ECN, 1996.

101 P.J. Moriarty and C. Hansen. Aerodyn theory manual. Technical Report NREL/TP-500-36881, National Renewable Energy Laboratory Golden, Colorado, 2005.

102 P.J. Morris, L.N. Long, and K.S. Brentner. An aeroacoustic analysis of wind turbines. In *42nd AIAA Aerospace Sciences Meeting and Exhibit*, pages 429–433, Reno, Nevada, 2004.

103 S.A. Ning. Development and Validation of a New Blade Element Momentum Skewed-Wake Model within AeroDyn. In *Proceedings of the AIAA*, 2015.

104 S. Oerlemans. *Detection of Aeroacoustic Sound Sources on Aircraft and Wind Turbines*. PhD thesis,

University of Twente, 2009.
105 S. Oerlemans and B.M. Lopez. Localisation and quantification of noise sources on a wind turbine. In *Wind Turbine Noise: Perspectives for Flow Control*, Berlin, Germany, 2005.
106 L. Oggiano, K. Boorsma, G. Schepers, and M. Kloosterman. In *Comparison of simulations on the NewMexico rotor operating in pitch fault conditions*, Proceedings of the Science of Making Torque from Wind, Technical University of Munich, 2016.
107 OpenFOAM. OpenFOAM: the open source CFD toolbox, 2015. Accessed: October 2015.
108 S. Øye. Dynamic Stall Simulated as Time Lag of Separation. In *Proceedings of the EWEC*, 1994.
109 R. Parchen. Progress report DRAW, a prediction scheme for trailing-edge noise based on detailed boundary-layer characteristics. Technical Report HAG-RPT–980023, TNO Institute of Applied Physics, 1998.
110 E.A. Parra. Data Reduction and Analysis of New MEXICO Experiment . Technical Report ECN-WIND-2015-189, ECN, July 2015.
111 E.A. Parra, K. Boorsma, J.G. Schepers, and H.Snel. In *Momentum considerations on the New MEXICO experiment,*, Proceedings of the Science of Making Torque from Wind, Technical University of Munich, 2016.
112 J.N. Pinder. Mechanical noise from wind turbines. *Wind Engineering*, 16(3), 1992.
113 G.R. Pirrung. WP4.8 comparison plots. https://mexnext.ecn.nl/do/document?id=18541-646f63756d656e74, January 2018.
114 G.R. Pirrung and H. Aa. Madsen. Dynamic inflow effects in measurements and high fidelity computations. *Wind Energy Science Discussions*, 2018:1–10, 2018.
115 G.R. Pirrung, H.A. Madsen, and T. Kim. The influence of trailed vorticity on flutter speed estimations. *Journal of Physics: Conference Series (Online)*, 524, 2014.
116 G.R. Pirrung, H.A. Madsen, T. Kim, and J. Heinz. A coupled near and far wake model for wind turbine aerodynamics. *Wind Energy*, 2016. doi:10.1002/we.1969.
117 G.R. Pirrung, H.A. Madsen, and S. Schreck. Trailed vorticity modeling for aeroelastic wind turbine simulations in stand still. *Wind Energy Science Discussions*, 2017:1–20, 2017.
118 G.R. Pirrung, V. Riziotis, H.A. Madsen, M. Hansen, and T. Kim. Comparison of a Coupled Near and Far Wake Model With a Free Wake Vortex Code. *Wind Energy Science Discussions*, 2016:1–28, 2016.
119 Pointwise. Pointwise inc, version 17.3r2, 2015. Accessed: October 2015.
120 H. Rahimi, M. Hartvelt, J. Peinke, and J.G. Schepers. Investigation of the current yaw engineering models for simulation of wind turbines in BEM and comparison with CFD and experiment. *Journal of Physics*, (753):022016, 2016.
121 Ramdin, S.F.. "Prandtl tip loss factor assessed". ECN-Wind 2017–023, ECN, February 2017.
122 P.E. Réthoré, N.N. Sørensen, F. Zahle, A. Bechmann, and H.A. Madsen. MEXICO Wind Tunnel and Wind Turbine modelled in CFD. In *AIAA Conference*, June 2011.
123 S. Schreck. IEA Wind Annex XX: HAWT Aerodynamics and Models from Wind Tunnel Measurements. NREL/TP-500-43508, The National Renewable Energy Laboratory, NREL, December 2008.
124 G. Guidati et al S. Wagner. Design and Testing of Acoustically Optimized Airfoils for Wind Turbines (DATA). Technical Report Publishable Final Report - Contract JOR3-CT98-0248, , 2001.
125 B. Sanderse, S.P. van der Pijl, and B. Koren. Review of computational fluid dynamics for wind turbine wake aerodynamics. *Wind energy*, 14(7):799–819, 2011.
126 S. Sarmast, W.Z. Shen, W.J. Zhu, R.F. Mikkelsen, S.P. Breton, and S. Ivanell. In *Validation of the actuator line and disc techniques using the New MEXICO measurements*, Proceedings of the Science of Making Torque from Wind, Technical University of Munich, 2016.
127 A.P. Schaffarczyk. *Introduction to Wind Turbine Aerodynamics*. Springer Verlag, Berlin, 2014.
128 A.P. Schaffarczyk, D. Schwab, and M. Breuer. Experimental Detection of Laminar-Turbulent Transition on a Rotating Wind Turbine Blade in the Free Atmosphere. *WIND ENERGY*, 19:DOI 10.1002/we.2001, 2016.
129 J.G. Schepers. An engineering model for yawed conditions, developed on basis of wind tunnel measurements. Technical Report AIAA-1999-0039, AIAA, 1999.
130 J.G. Schepers. *IEA Wind Task XX: Dynamic Inflow effects at fast pitching steps on a wind turbine placed in the NASA-Ames wind tunnel*. ECN-E-07-085, 2007.
131 J.G. Schepers. *Engineering models in wind energy aerodynamics, development, implementation and analysis using dedicated aerodynamic measurements*. PhD thesis, University of Delft, ISBN 978-94-6191-507-8, 2012.
132 J.G. Schepers and K. Boorsma. Minutes of the kick-off meeting of Mexnext-III, held at Amsterdam (Holland), on March 4 2015, March 2014.
133 J.G. Schepers and K. Boorsma. Minutes of the second meeting of Mexnext-III, held at NREL (USA), on

January 11 and 12 2016, January 2016.
134 J.G. Schepers and K. Boorsma. Minutes of the third meeting of Mexnext-III, held at ONERA (France), on November 9 and 10 2016, November 2016.
135 J.G. Schepers and K. Boorsma. Minutes of the fourth meeting of Mexnext-III, held at CWEA (China), from December 4 to 6 2017, December 2017.
136 J.G. Schepers and H. Snel. JOULE2: Dynamic Inflow: Yawed Conditions and Partial Span Pitch. ECN-C-95-056, Energy Research Centre of the Netherlands, ECN, June 1995.
137 C. Schulz, P. Letzgus, Thorsten T. Lutz, and E. Krämer. CFD study on the impact of yawed inflow on loads, power and near wake of a generic wind turbine. *Wind Energy*, 20(2):253–268, 2017.
138 C. Schulz, K. Meister, T. Lutz, and E. Kramer. Investigations on the wake development of the mexico rotor considering different inflow conditions. *Notes on Numerical Fluid Mechanics and Multidisciplinary Design*, 132, 2016.
139 D. Schwab, S. Ingwersen, A.P. Schaffarczyk, and M. Breuer. Pressure and hot film measurements on a wind turbine blade operating in the atmosphere. *Journal of Physics, Conference Series*, 555(012092), 2014.
140 D. Schwamborn, T. Gerhold, and R. Heinrich. The DLR TAU-Code: Recent Applications in Research and Industry. In *European Conference on Computational Fluid Dynamics, ECCOMAS CFD 2006*, Delft, The Netherland, 2016.
141 M. Sessarego. *Design of Large Wind Turbines using Fluid- Structure Coupling Techniqued*. PhD thesis, Technical University of Denmark, PhD thesis, 2017.
142 W.Z. Shen, M.O.L. Hansen, and J.N. Sørensen. Determination of angle of attack (AOA) for rotating blades. Berlin Heidelberg: Springer-Verlag, 2006.
143 W.Z. Shen, M.O.L. Hansen, and J.N. Sørensen. Determination of the Angle of Attack on Rotor Blades. *Wind Energy*, (12):91–98, 2009.
144 M.L. Shur, P.R. Spalart, M.Kh. Strelets, and A.K. Travin. A hybrid rans-les approach with delayed-des and wall-modelled les capabilities. *International Journal of Heat and Fluid Flow*, 29(6):1638–1649, 2008.
145 P. Sijtsma. CLEAN based on spatial coherence. Technical Report AIAA paper 2007-3436, presented at the 13th AIAA/CEAS aeroacoustics conference, Rome, Italy, May 2007.
146 D.A. Simms, S. Schreck, M.M. Hand, and L.J. Fingersh. NREL Unsteady Aerodynamics Experiment in the NASA-Ames Wind Tunnel: A Comparison of Predictions to Measurements. NREL/TP-500-29494, The National Renewable Energy Laboratory, NREL, June 2001.
147 H. Snel. Heuristic modelling of dynamic stall characteristics. In *Conference proceedings European Wind Energy Conference*, pages 429–433, Dublin, Ireland, October 1997.
148 H. Snel. Review of the present status of rotor aerodynamics. *Wind Energy*, 1:46–69, 1998.
149 H. Snel, R. Houwink, and J. Bosschers. Sectional prediction of lift coefficients on rotating wind turbine blades in stall. ECN-C-93-052, Energy Research Center of the Netherlands, 1994.
150 H. Snel, R. Houwink, G.J.W. van Bussel, and A. Bruining. Sectional prediction of 3d effects for stalled flow on rotating blades and comparison with measurements. In *Proc. European Community Wind Energy Conference*, 1993.
151 H. Snel and J.G. Schepers. JOULE1: Joint investigation of Dynamic Inflow Effects and Implementation of an Engineering Model. Technical Report ECN-C–94-107, ECN, 1994.
152 J.N. Sørensen and W.Z. Shen. Numerical modeling of wind turbine wakes. *J. Fluids Eng*, 124(2):393–399, 2002.
153 N. N. Sørensen and H. A. Madsen. *Modelling of transient wind turbine loads during pitch motion (paper and poster)*. European Wind Energy Association (EWEA), 2006.
154 N.N. Sørensen, A. Bechmann, P.E. Réthoré, and F. Zahle. Near wake reynolds-averaged navier–stokes predictions of the wake behind the mexico rotor in axial and yawed flow conditions. *Wind Energy*, 17(1):75–86, 2012.
155 N.N. Sørensen, F. Zahle, K. Boorsma, and J.G. Schepers. In *CFD computations of the second round of MEXICO rotor measurements*, Proceedings of the Science of Making Torque from Wind, Technical University of Munich, 2016.
156 P.R. Spalart and C. Streett. Young-person's guide to detached-eddy simulation grids. NASA/CR-2001-211032, NASA, 2001.
157 R. Steijl, G.N. Barakos, and K. Badcock. A framework for CFD analysis of helicopter rotors in hover and forward flight. *International Journal for Numerical Methods in Fluids*, 51(8), 2006.
158 T. Cho and C. Kim. Wind tunnel test for the NREL phase VI rotor with 2 m diameter. *Renewable Energy*, 65(C), 2014.
159 T. Lutz and K. Meister and E. Krämer. Near Wake Studies of the Mexico Rotor. In *EWEA Annual Event held at Brussels*, March 2011.

160 P.J. Tavner, J. Xiang, and F. Spinato. Reliability analysis for wind turbines. *Wind Energy*, 10(1):1–18, 2007.
161 D.S. Pope T.F. Brooks and M.A. Marcolini. Airfoil self noise and prediction. Technical Report Reference publication 1218, NASA, 1989.
162 L.A.M. Tossas and S. Leonardi. Wind turbine modeling for computational fluid dynamics. *National Renewable Energy Laboratory (NREL), Technical Report No. NREL/SR-5000-55054*, 2013.
163 N. Troldborg. Actuator line modeling of wind turbine wakes. Master's thesis, Technical University of Denmark, 2009.
164 N.J.C.M. van der Borg and P.M. Vink. Acoustic Noise Measurement on Wind Turbines Performed in the Frame of JOU2-CT92-0233. Technical Report ECN-C–95-112, ECN, November 1995.
165 A. van Garrel. Development of a wind turbine aerodynamics simulation module. Technical Report ECN-C–03-079, ECN, 2003.
166 G.J.H. van Groenewoud, L.M.M. Boermans, and J.L. van Ingen. (In Dutch:) Onderzoek naar de Omslag Laminair-Turbulent van de Grenslaag op de Rotorbladen van de 25m HAT Windturbine. Technical Report LR-390, Technische Hogeschool Delft, May 1983.
167 H.J. van Grol, H. Snel, and J.G. Schepers. Wind Turbine Benchmark Exercise on Mechanical loads. A state of the art report. Volume 1, part A & B. ECN-C-91-031, Energy Research Center of the Netherlands, ECN, May 1991.
168 J.L. van Ingen. The e^N method for transition prediction. Historical review of work at TU Delft. *AIAA 2008-3830*, 3830, 2008.
169 H. Vollmers. Detection of vortices and quantitative evaluation of their main parameters from experimental velocity data. *Measurement Science and Technology*, 2001.
170 S. G. Voutsinas. Vortex methods in aeronautics: How to make things work. *International Journal of Computational Fluid Dynamics*, 20:3–18, 2006.
171 S. Wagner, R. Bareiss, and G. Guidati. *Wind Turbine Noise*. Springer-Verlag, 1996.
172 P. Weihing, J. Letzgus, G. Bangga, T. Lutz, and E. Krämer. Hybrid rans/les capabilities of the flow solver flower-application to flow around wind turbines. In *Notes on Numerical Fluid Mechanics and Multidisciplinary Design (to be published)*. Springer, 2017.
173 P. Weihing and T. Lutz. Numerical simulation of wake turbine interactions in alpha ventus. In *RAVE R&D Conference*, 2015.
174 P. Weihing, C. Schulz, T. Lutz, and E. Krämer. Comparison of the actuator line model with fully resolved simulations in complex environmental conditions. In *Journal of Physics: Conference Series*, volume 854, page 012049. IOP Publishing, 2017.
175 W.Z. Shen et al. Tip Loss Corrections for Wind Turbine Computations. *Wind Energy*, 8(4), 2005.
176 H. Yang, W.Z. Shen, J.N. Sørensen, and W.J. Zhu. Extraction of airfoil data using PIV and pressure measurements. *Wind Energy*, (14):539–556, 2011.
177 W Yu. *The wake of an unsteady actuator disc*. PhD thesis, University of Delft, ISBN ISBN: 978-94-6366-020-4, 2018.
178 Y. Zhang. *Wind Turbine Rotor Aerodynamics: The IEA Mexico rotor explained*. PhD thesis, University of Delft, 2017.

A. WP3 Comparison plots: Axial flow

A.1 Lifting line codes

Lifting line variables

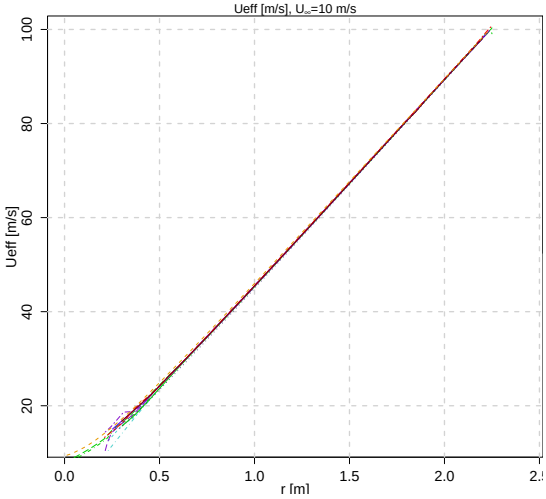

(a) Ueff, Case 1.1

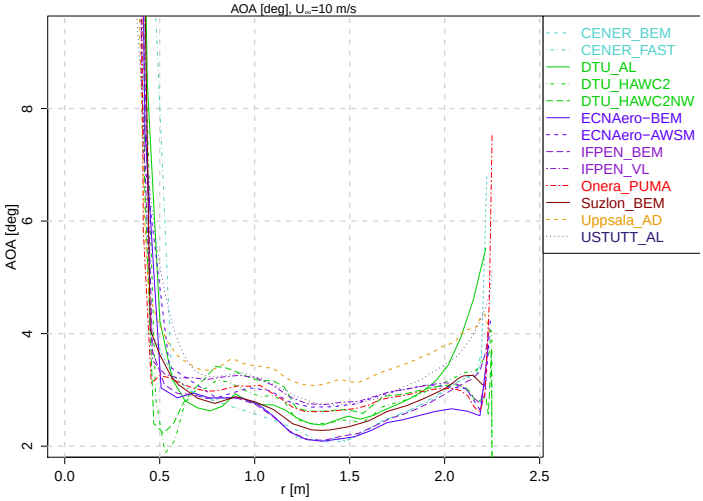

(b) AOA, Case 1.1

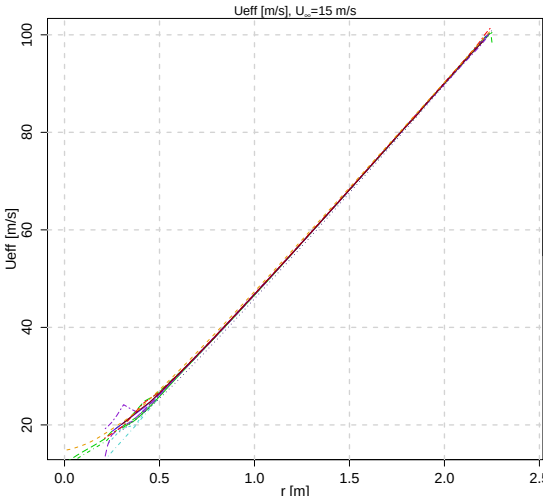

(c) Ueff, Case 1.2

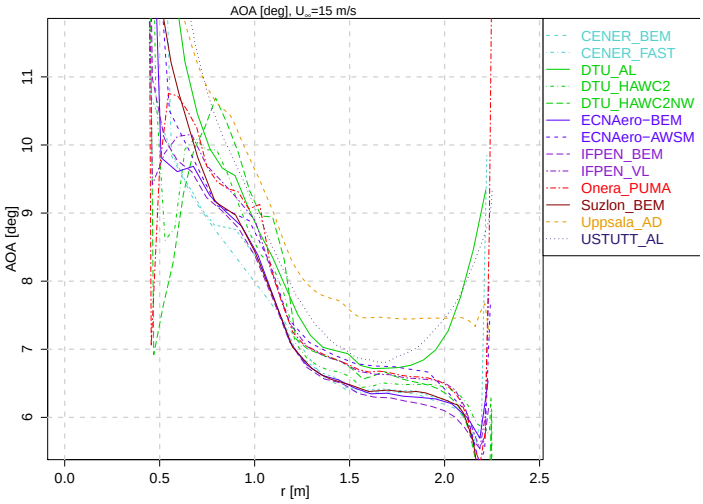

(d) AOA, Case 1.2

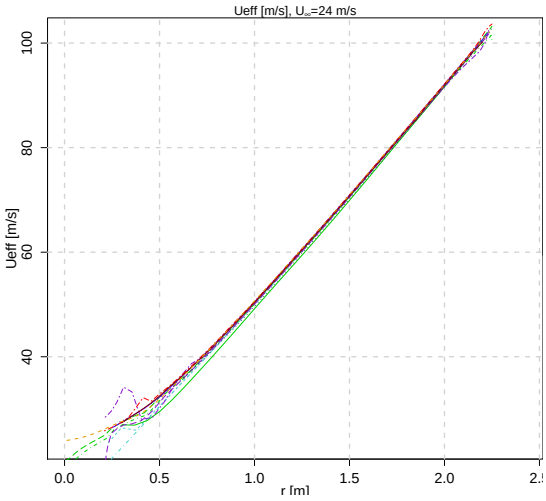

(e) Ueff, Case 1.3

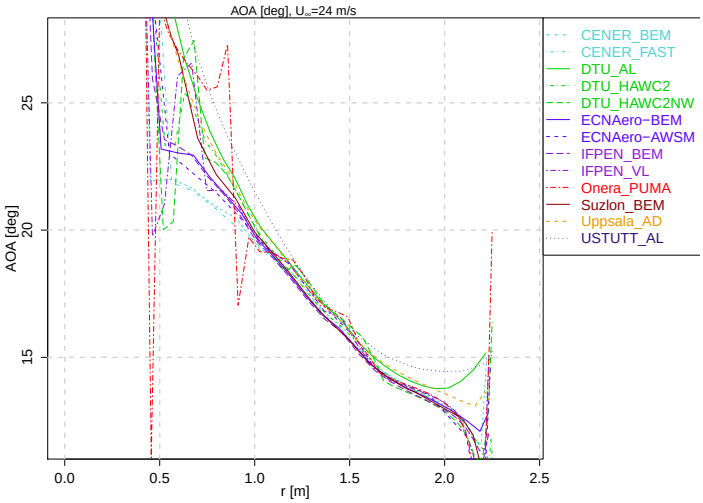

(f) AOA, Case 1.3

Figure A.1: Lifting line variables (1)

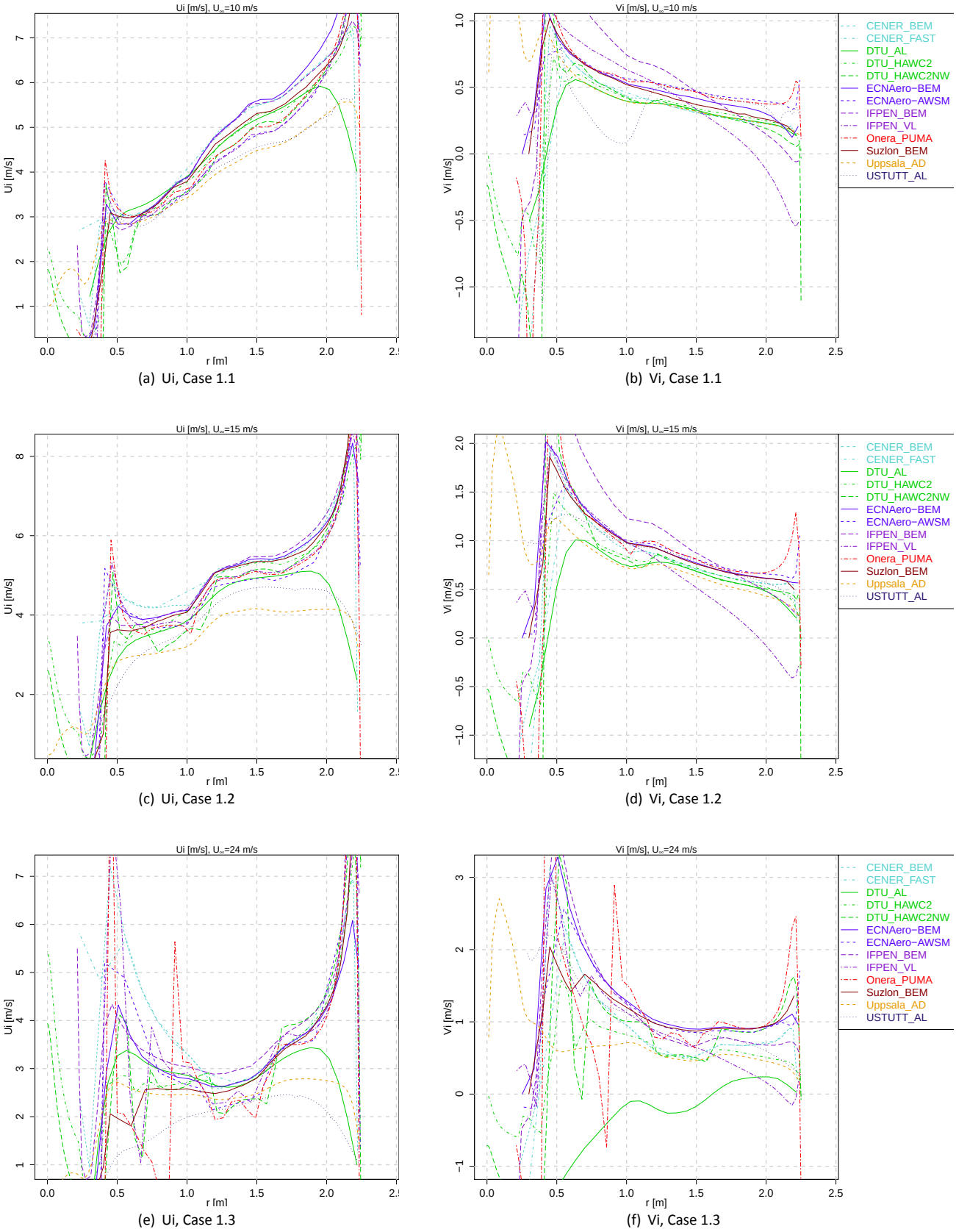

Figure A.2: Lifting line variables (2)

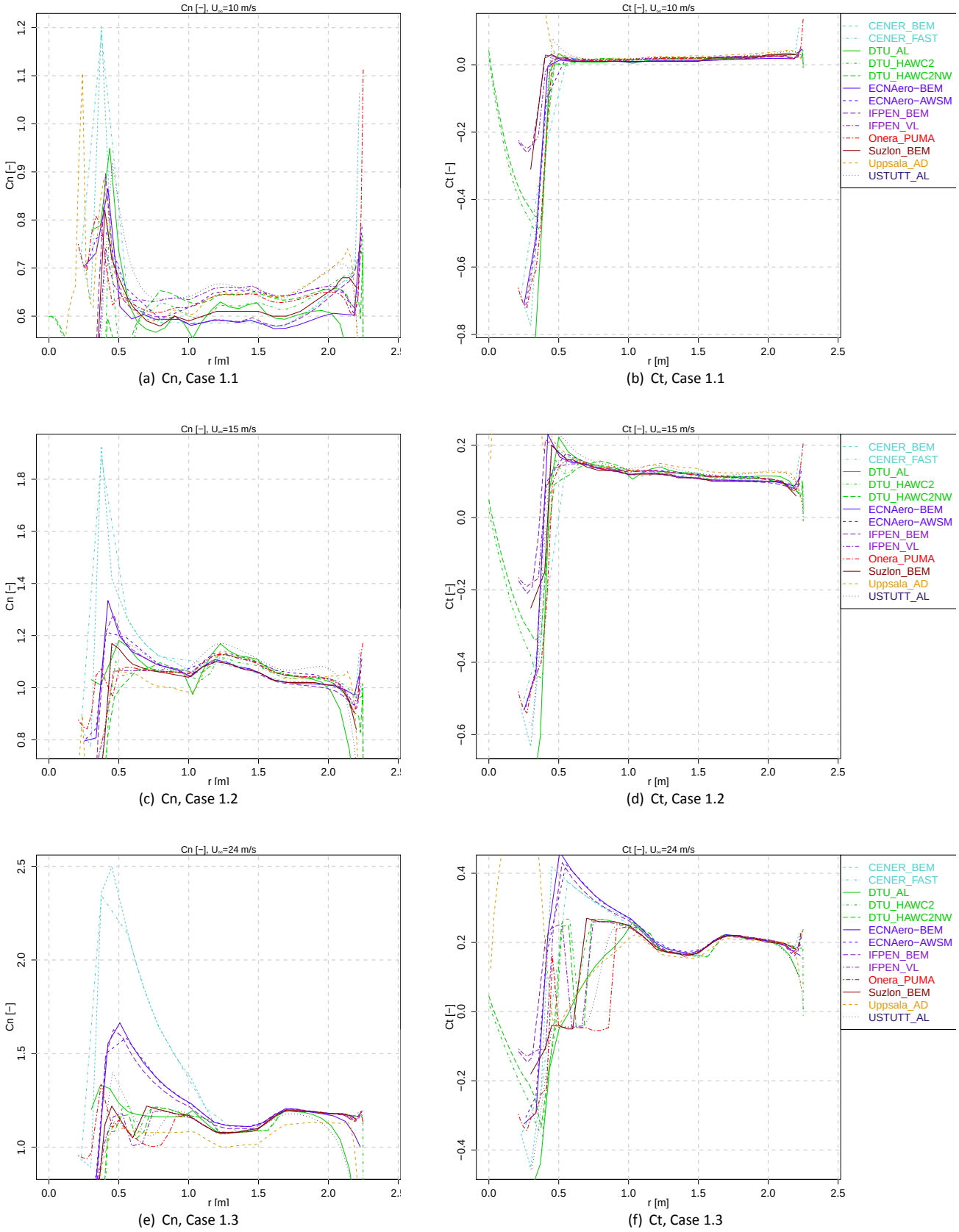

Figure A.3: Lifting line variables (3)

Loads

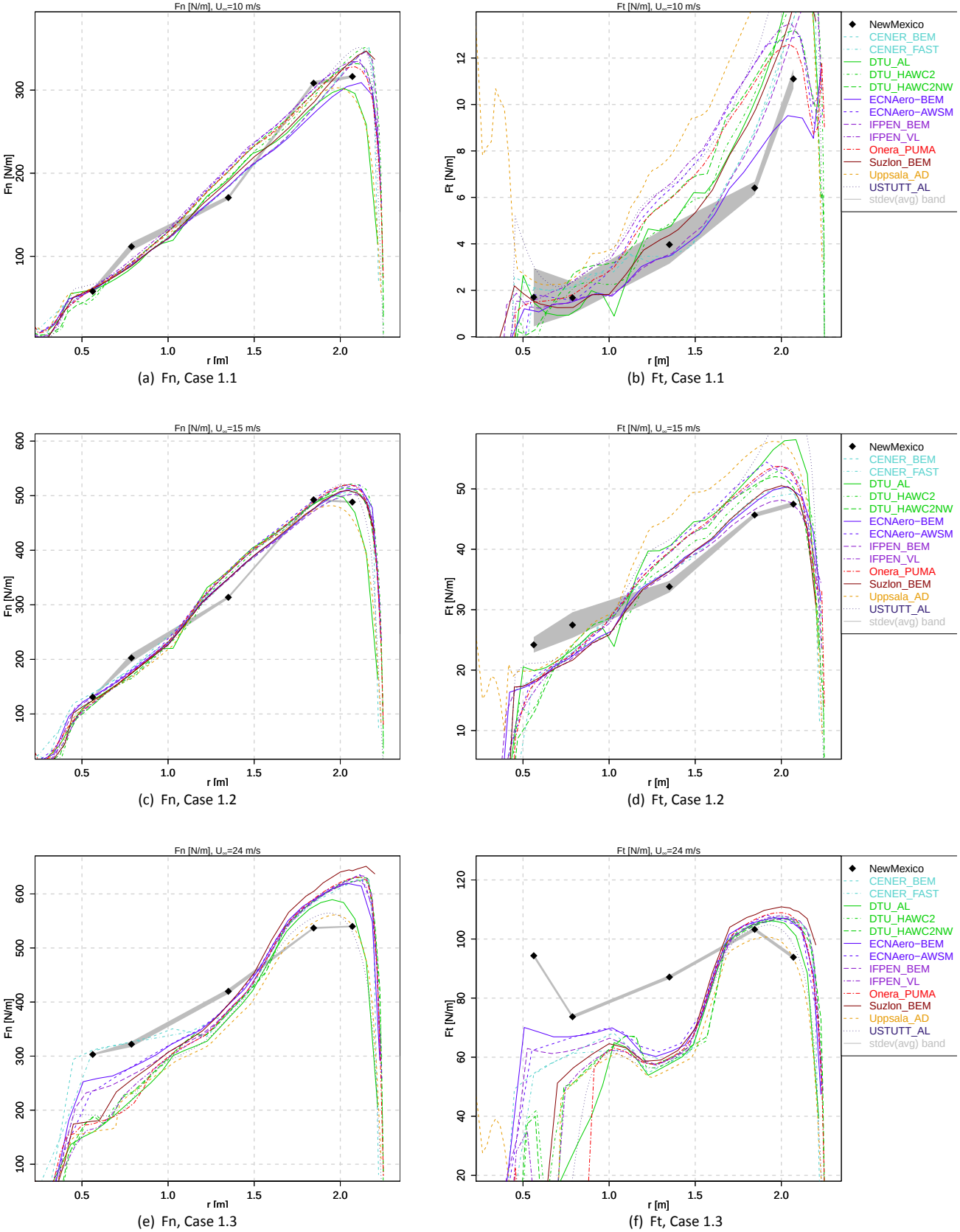

(a) Fn, Case 1.1 (b) Ft, Case 1.1

(c) Fn, Case 1.2 (d) Ft, Case 1.2

(e) Fn, Case 1.3 (f) Ft, Case 1.3

Figure A.4: Lifting line codes: Chord normal and tangential force

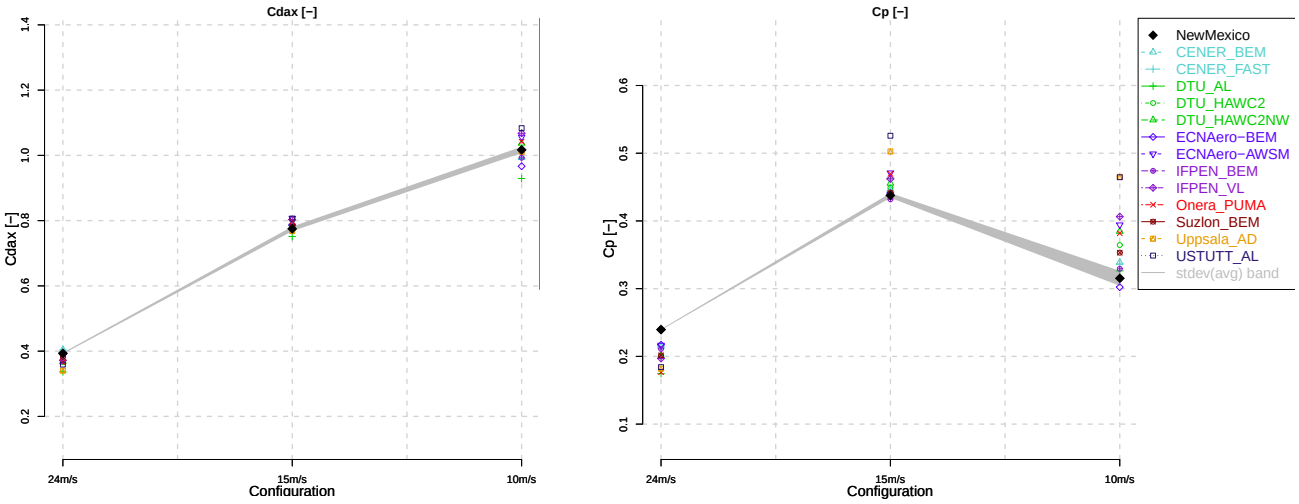

(a) Axial force coefficient Cdax

(b) Power coefficient Cp

Figure A.5: Lifting line codes: Rotor integral forces and moments

A.2 CFD codes

Pressure distributions

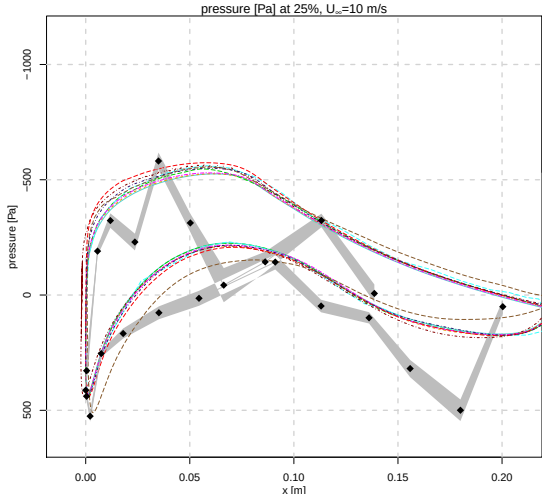

(a) 25%R

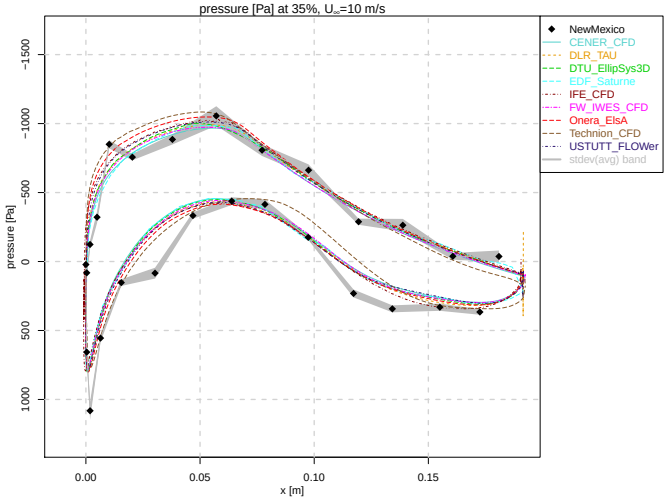

(b) 35%R

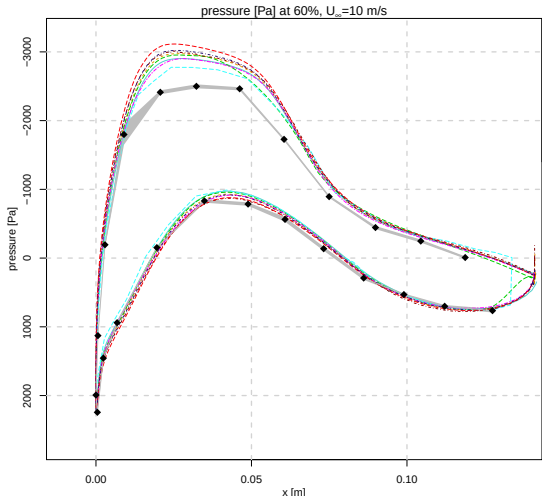

(c) 60%R

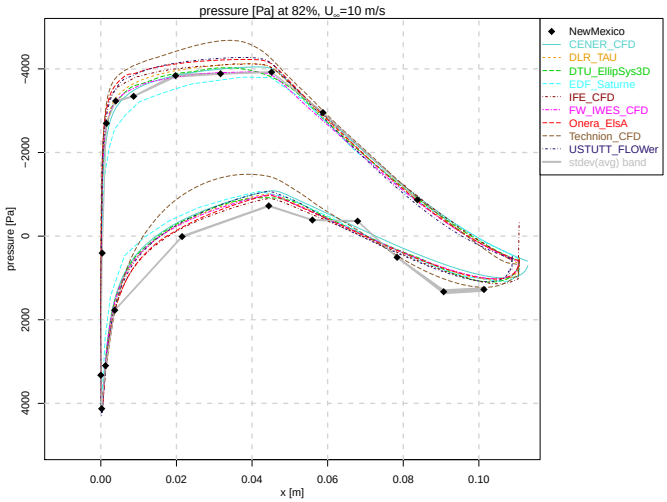

(d) 82%R

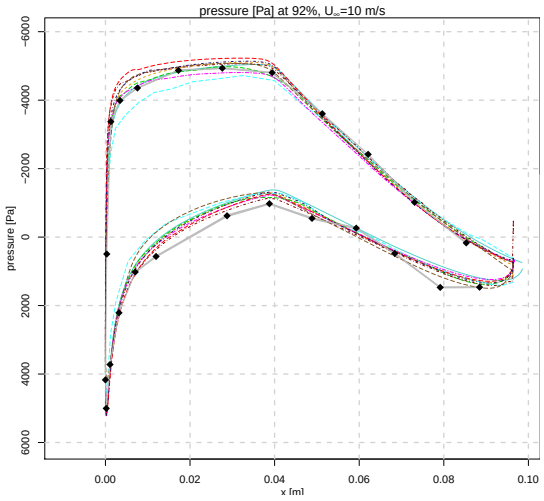

(e) 92%R

Figure A.6: Pressure distributions, Case 1.1 (turbulent boundary layer)

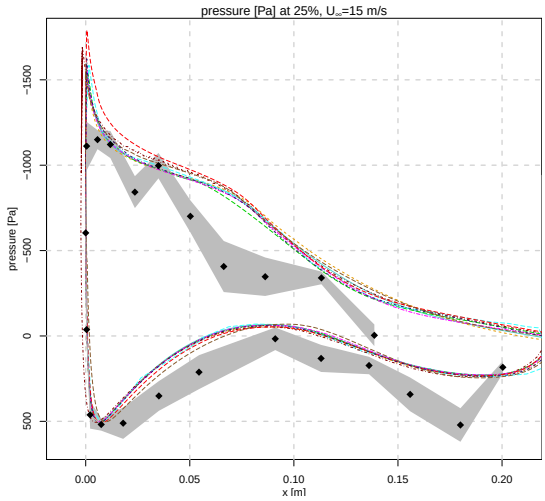

(a) 25%R

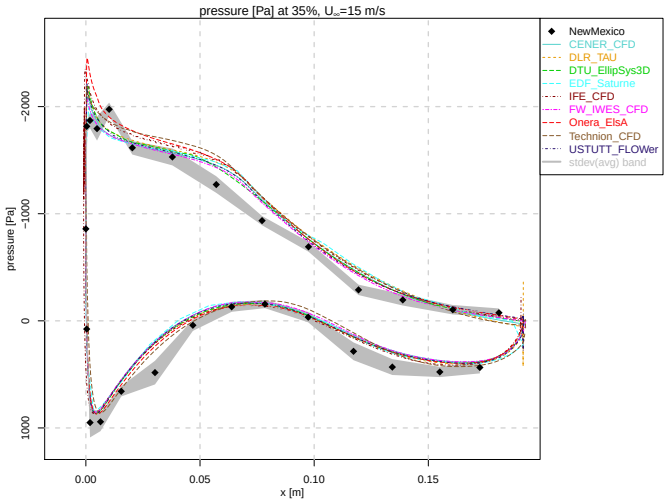

(b) 35%R

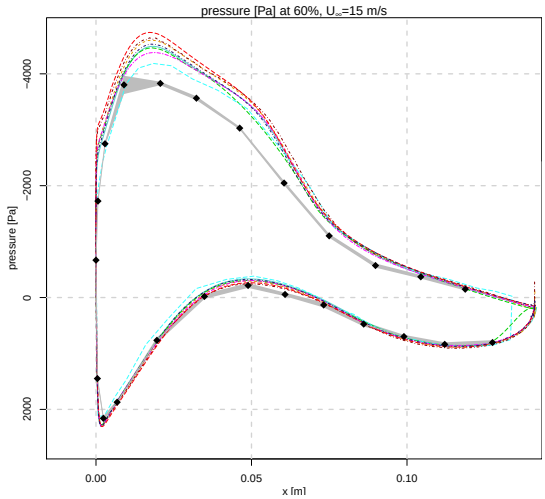

(c) 60%R

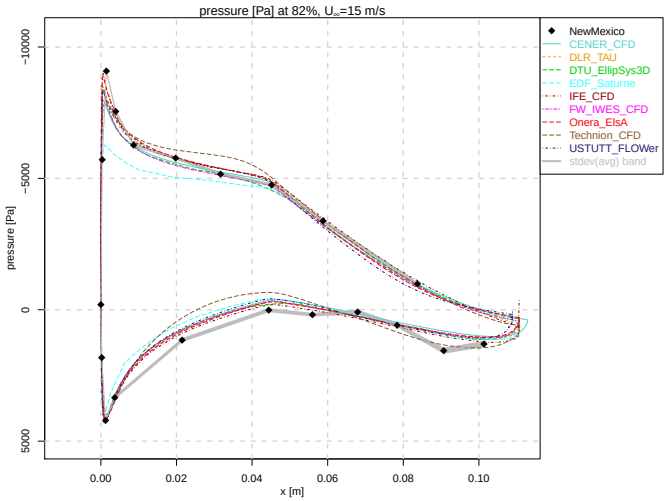

(d) 82%R

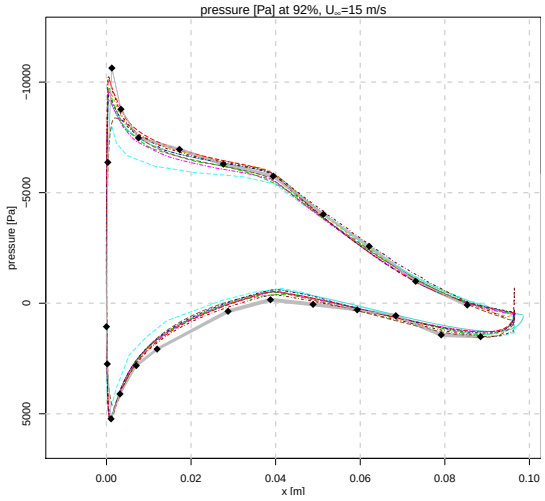

(e) 92%R

Figure A.7: Pressure distributions, Case 1.2 (turbulent boundary layer)

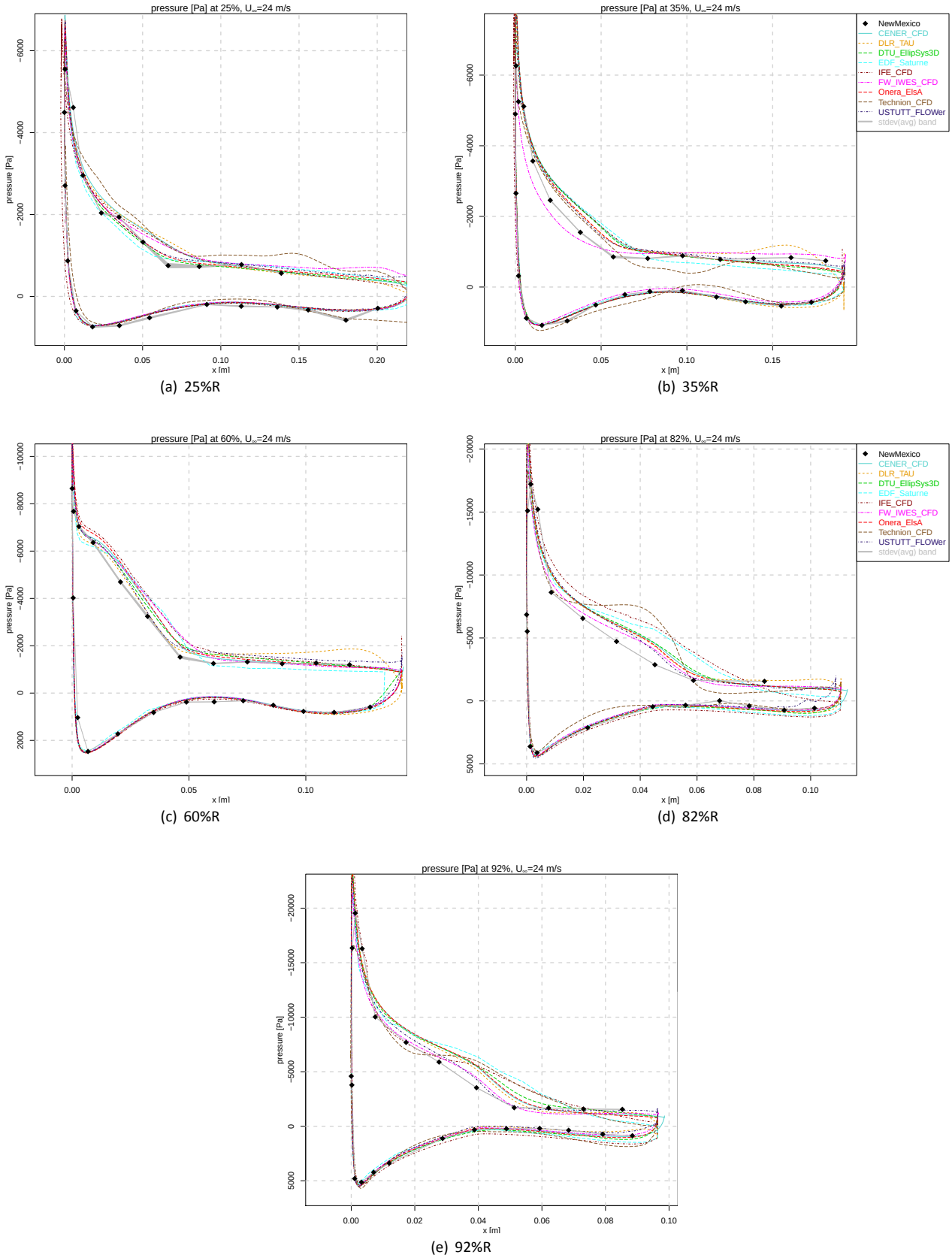

Figure A.8: Pressure distributions, Case 1.3 (turbulent boundary layer)

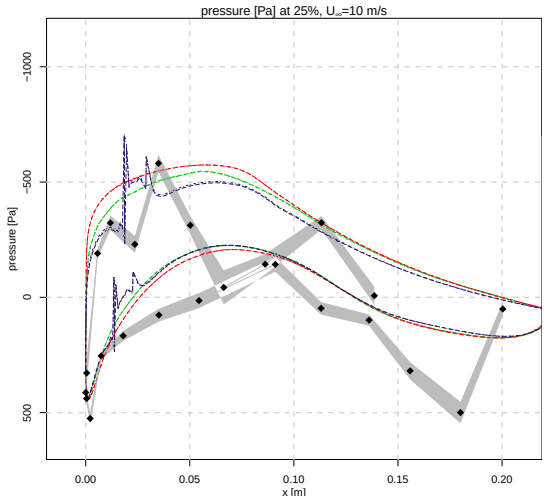

(a) 25%R

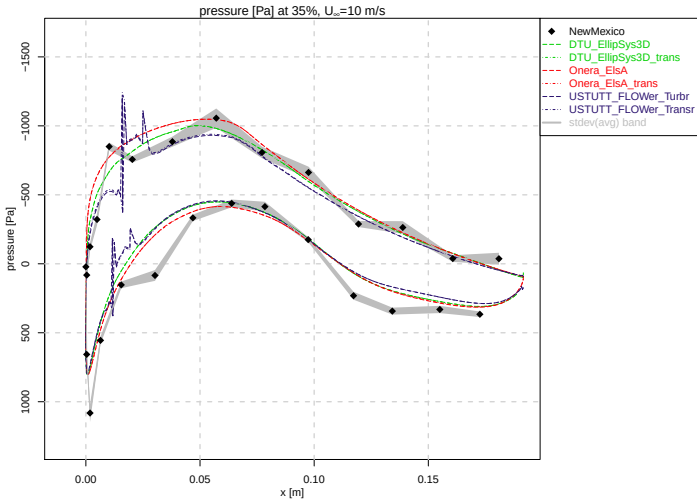

(b) 35%R

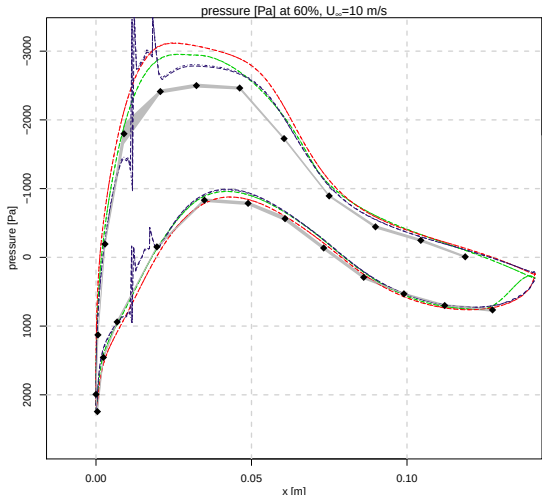

(c) 60%R

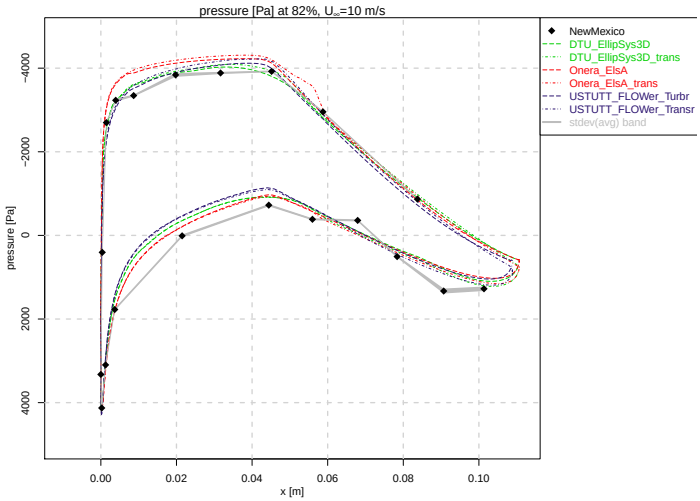

(d) 82%R

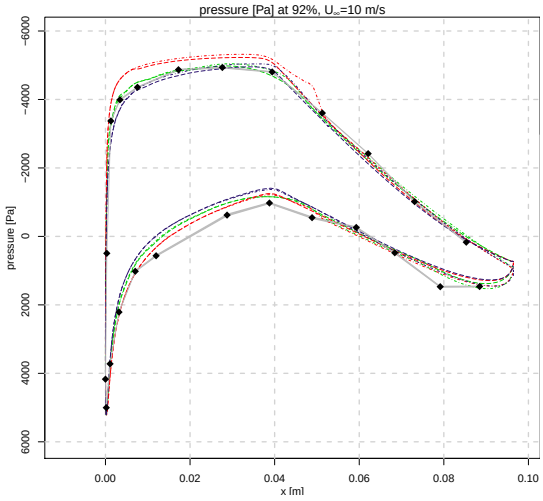

(e) 92%R

Figure A.9: Pressure distributions, Case 1.1 (transitional boundary layer)

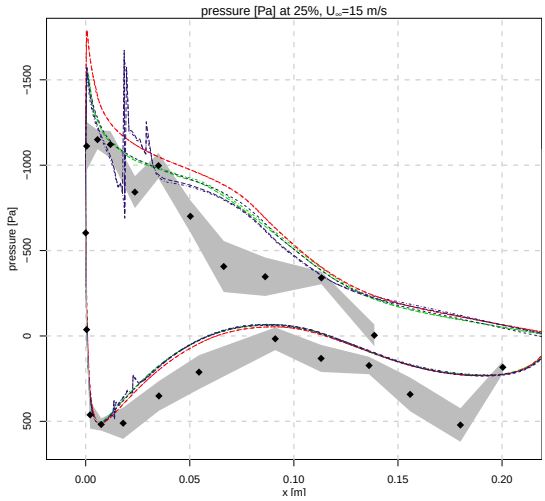

(a) 25%R

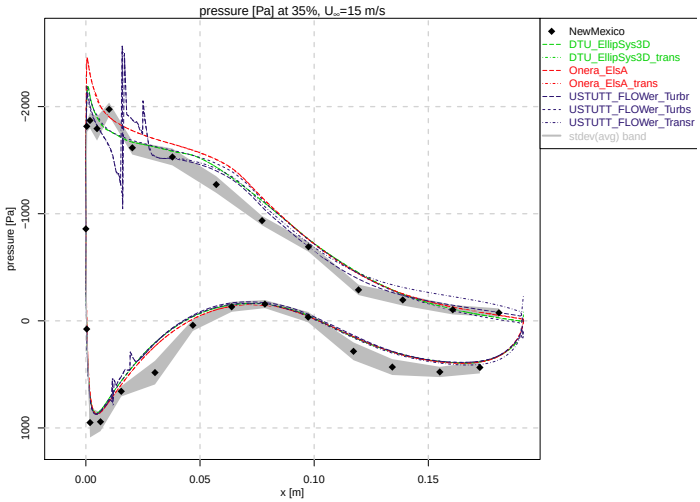

(b) 35%R

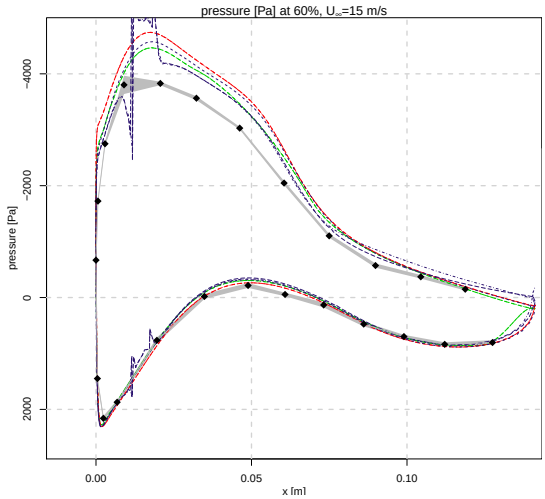

(c) 60%R

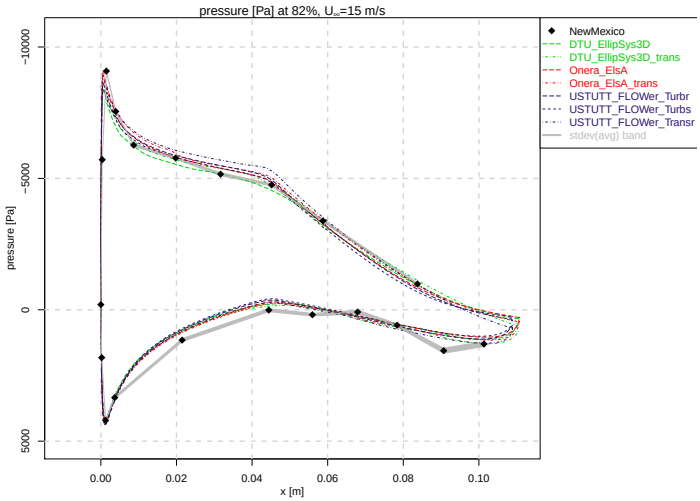

(d) 82%R

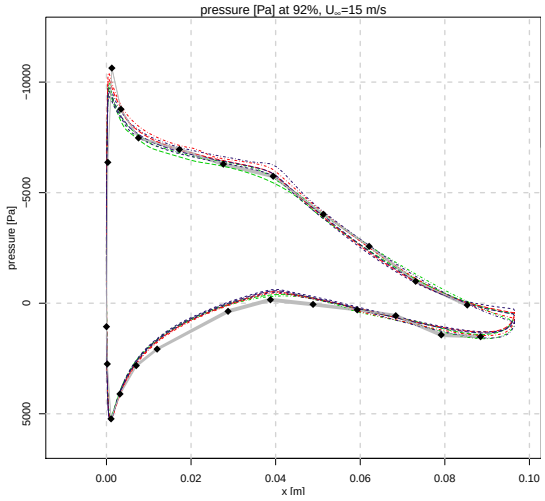

(e) 92%R

Figure A.10: Pressure distributions, Case 1.2 (transitional boundary layer)

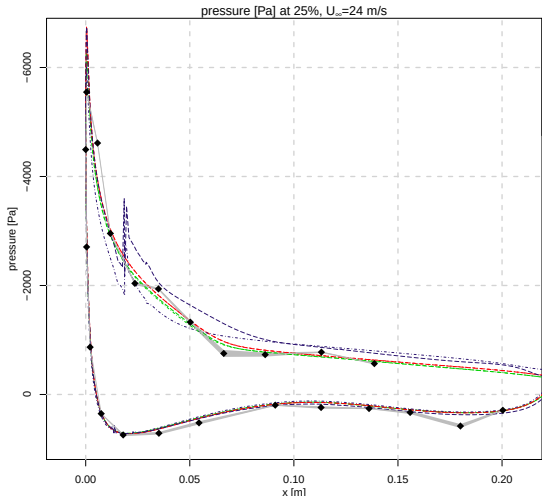

(a) 25%R

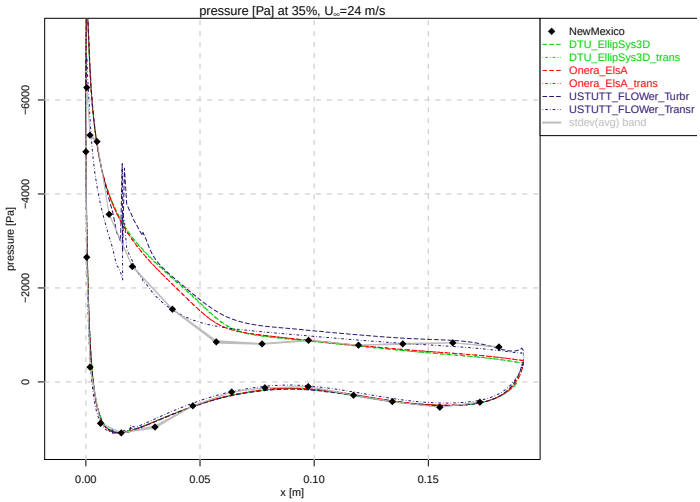

(b) 35%R

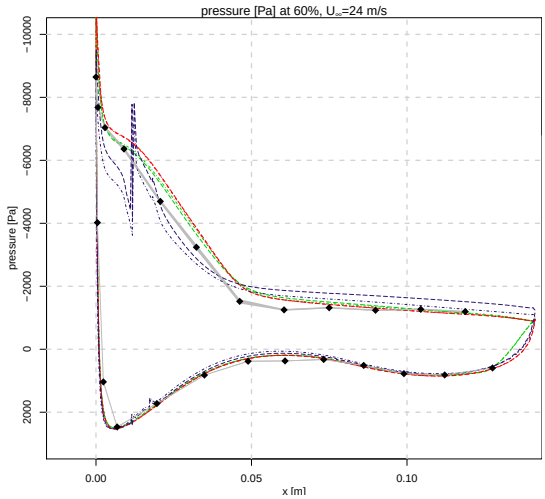

(c) 60%R

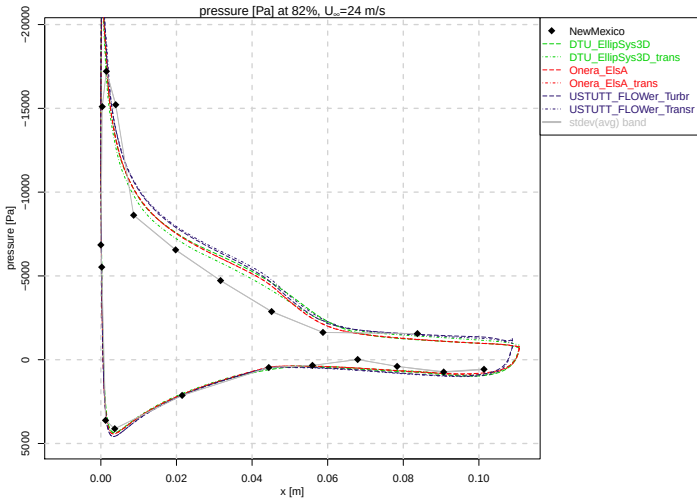

(d) 82%R

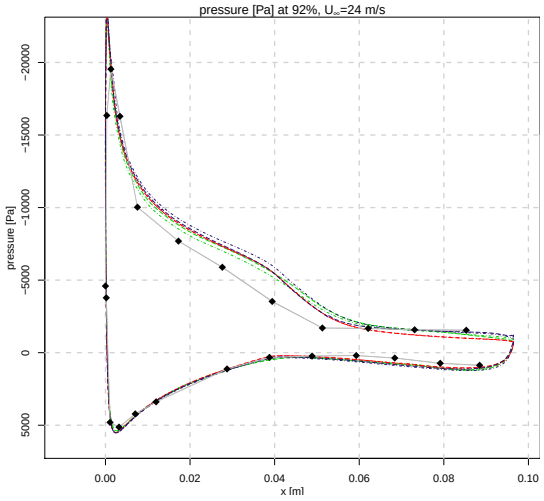

(e) 92%R

Figure A.11: Pressure distributions, Case 1.3 (transitional boundary layer)

Loads

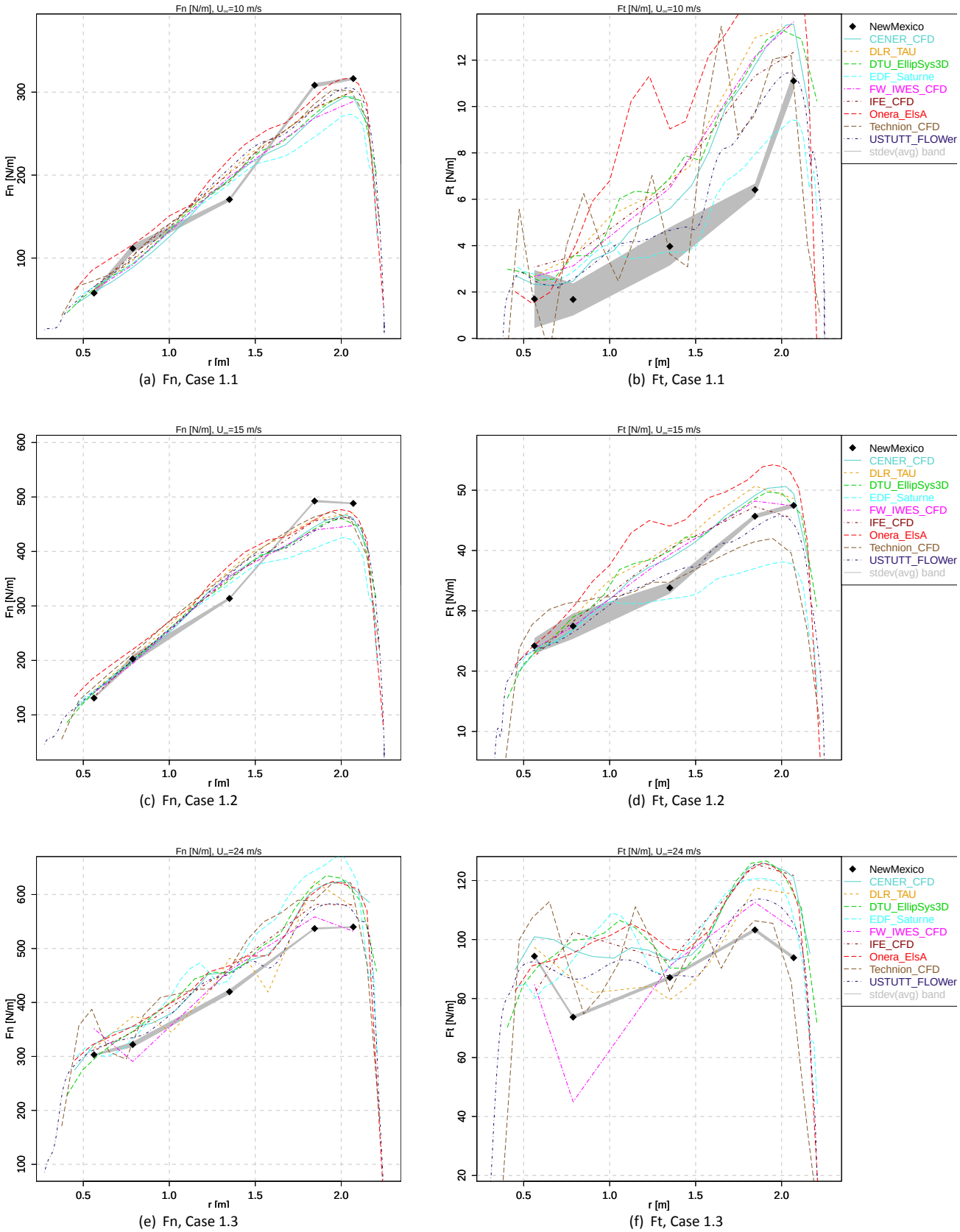

(a) Fn, Case 1.1 (b) Ft, Case 1.1

(c) Fn, Case 1.2 (d) Ft, Case 1.2

(e) Fn, Case 1.3 (f) Ft, Case 1.3

Figure A.12: CFD codes: Chord normal and tangential force (turbulent boundary layer)

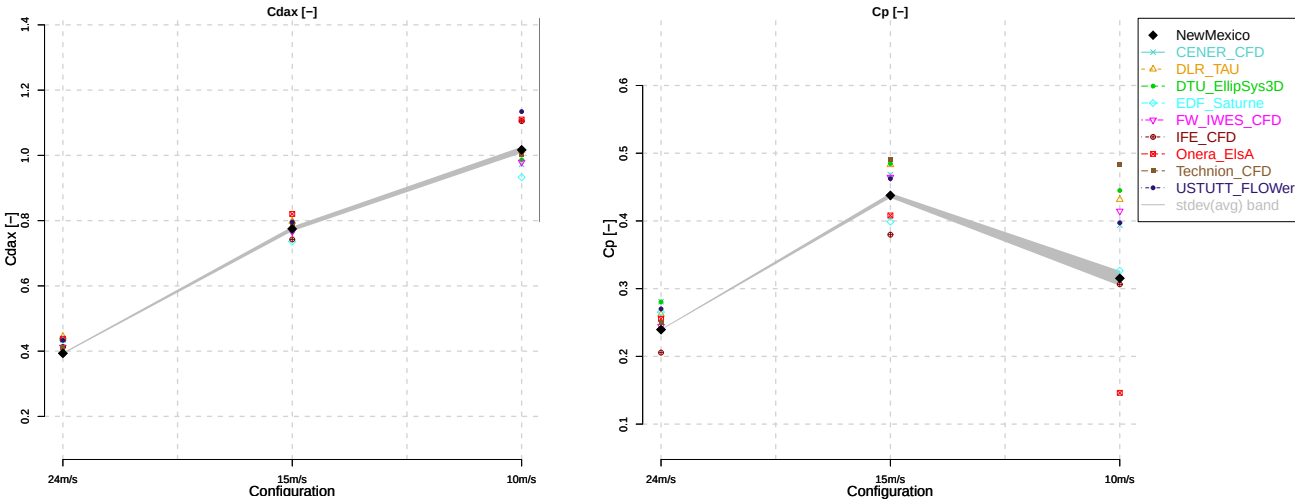

(a) Axial force coefficient Cdax

(b) Power coefficient Cp

Figure A.13: CFD codes: Rotor integral forces and moments (turbulent boundary layer)

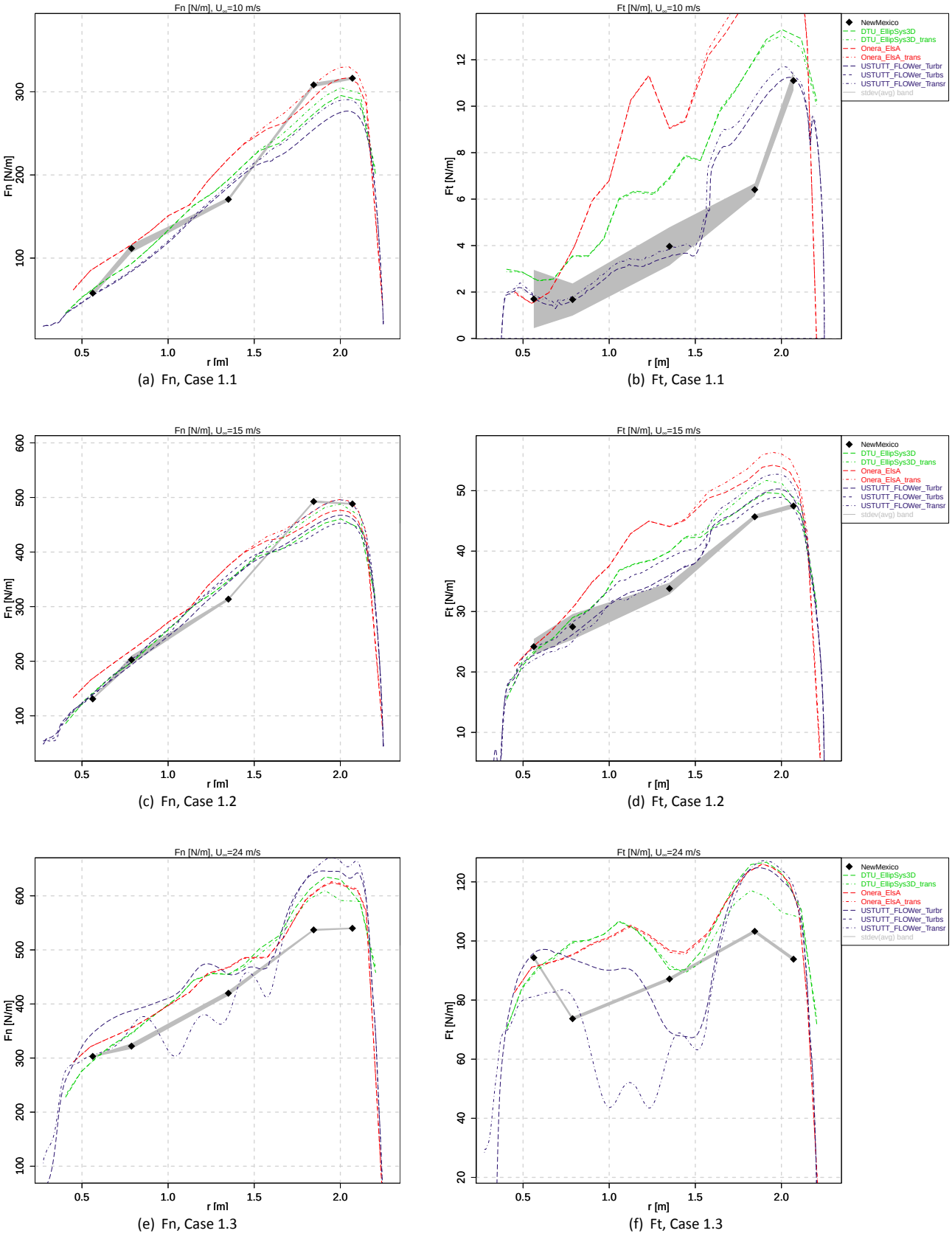

Figure A.14: CFD codes: Chord normal and tangential force (transitional boundary layer)

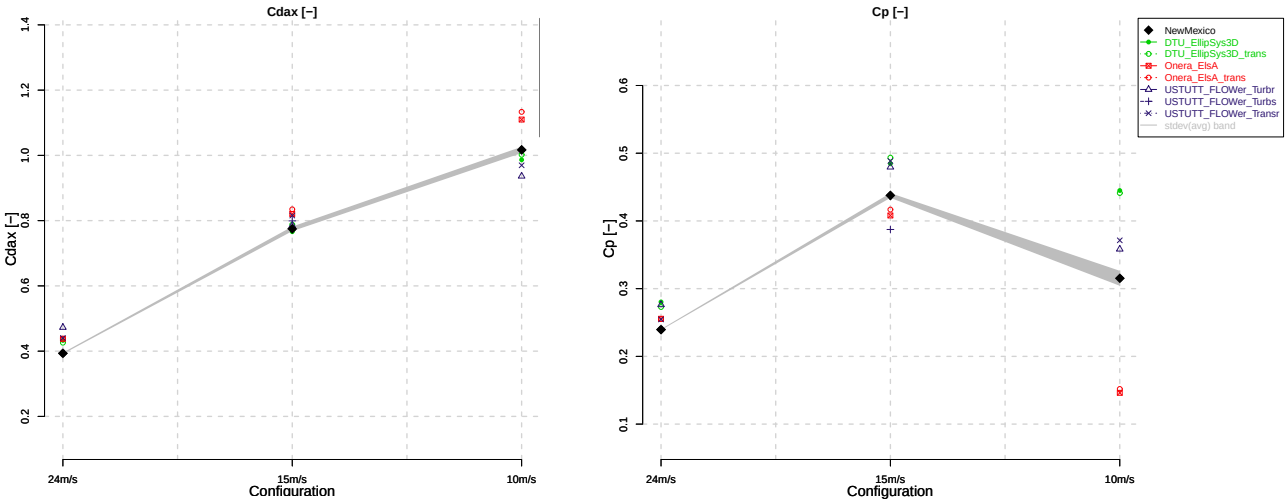

(a) Axial force coefficient Cdax

(b) Power coefficient Cp

Figure A.15: CFD codes: Rotor integral forces and moments (transitional boundary layer)

A.3 Velocity traverses

Axial traverse

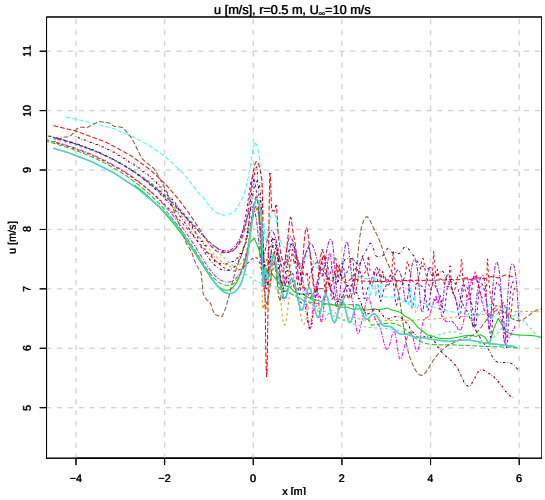

(a) u, r=0.5 m

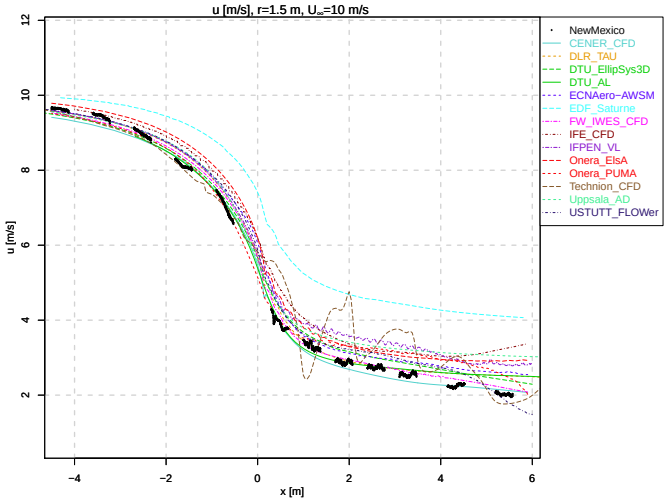

(b) u, r=1.5 m

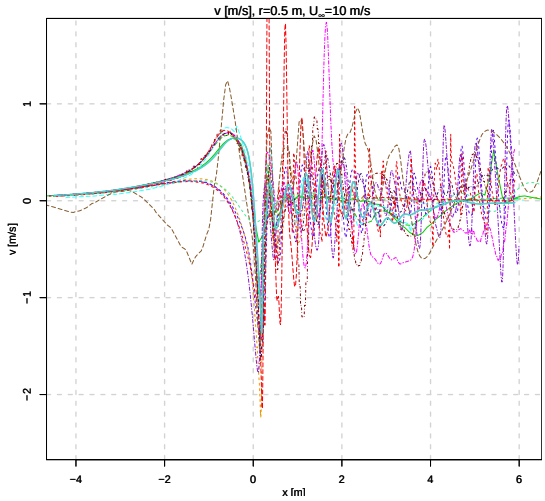

(c) v, r=0.5 m

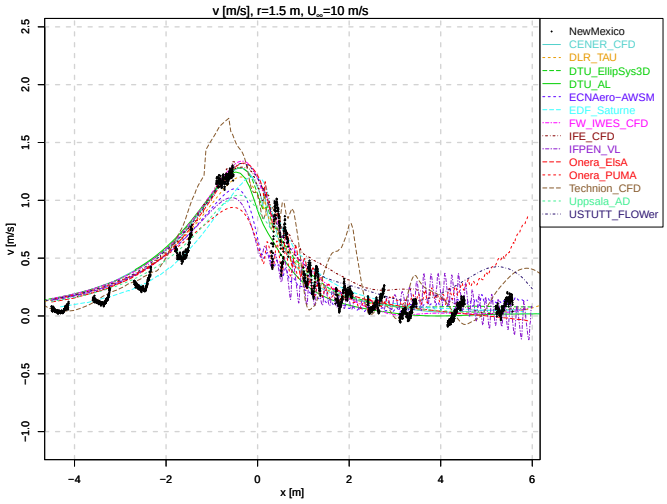

(d) v, r=1.5 m

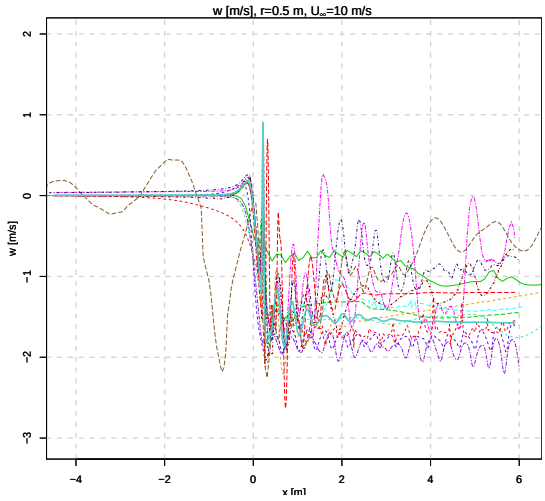

(e) w, r=0.5 m

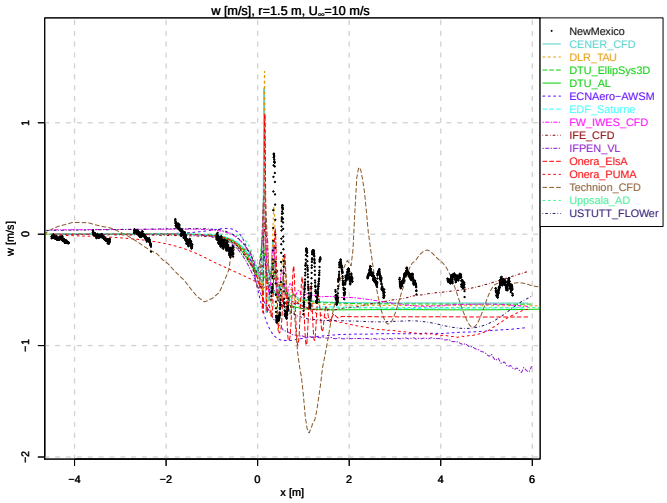

(f) w, r=1.5 m

Figure A.16: Axial traverse of velocity , Case 1.1

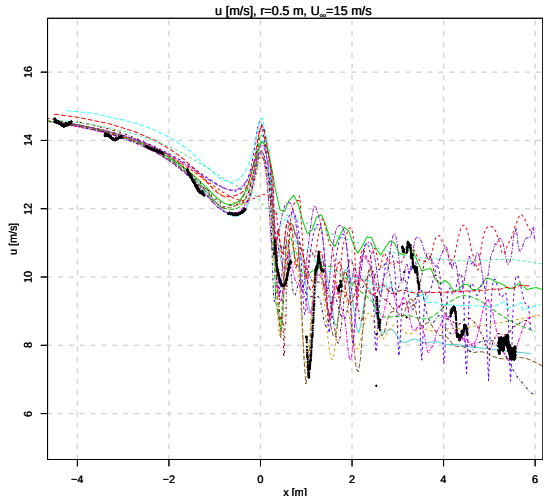

(a) u, r=0.5 m

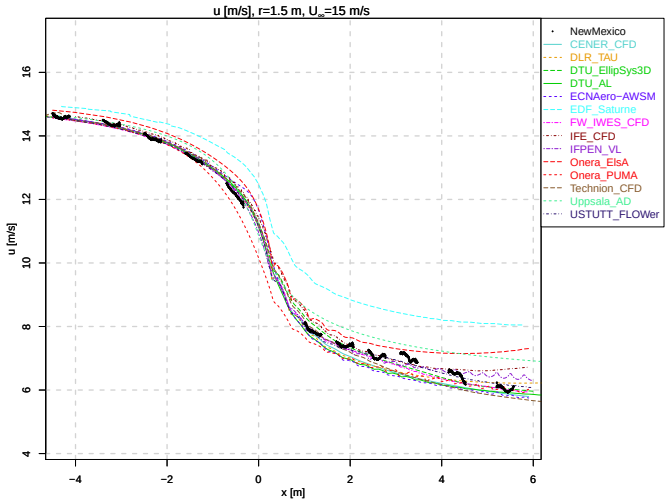

(b) u, r=1.5 m

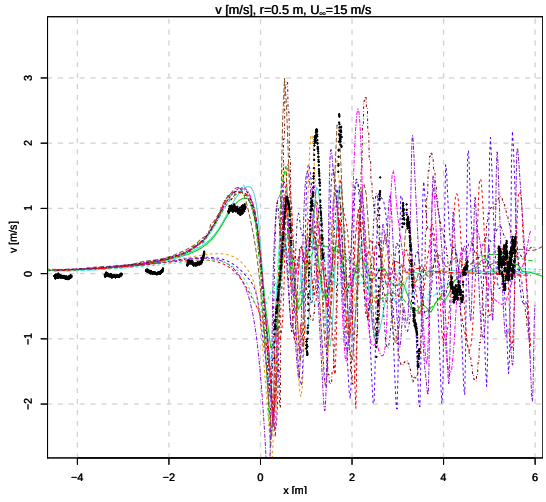

(c) v, r=0.5 m

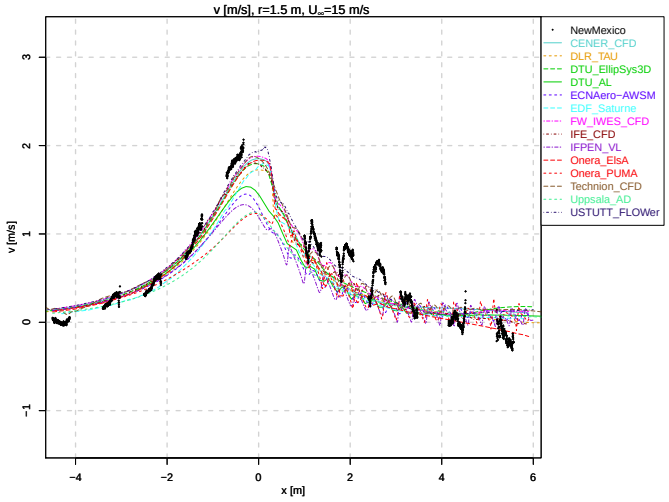

(d) v, r=1.5 m

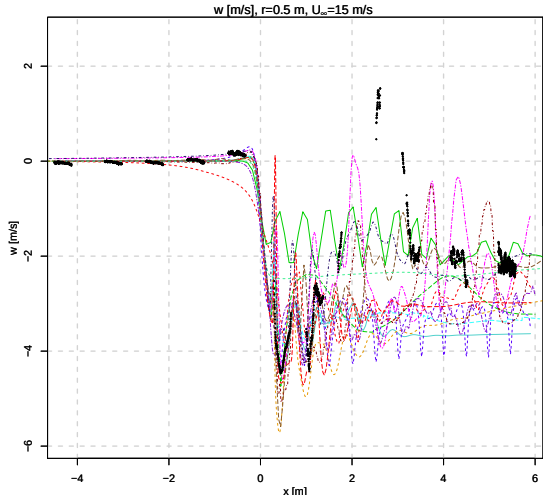

(e) w, r=0.5 m

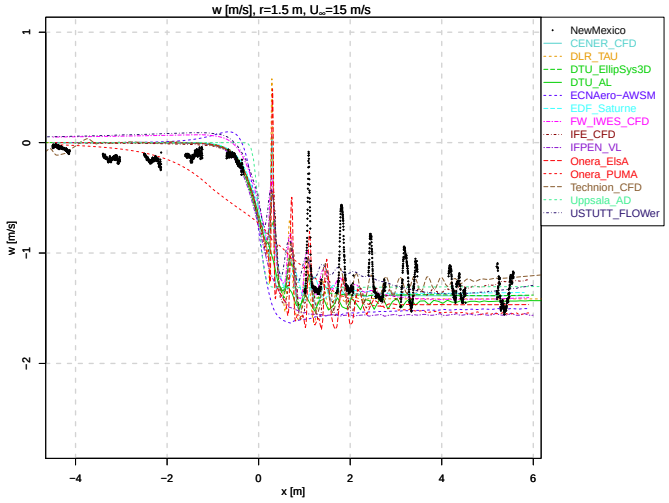

(f) w, r=1.5 m

Figure A.17: Axial traverse of velocity , Case 1.2

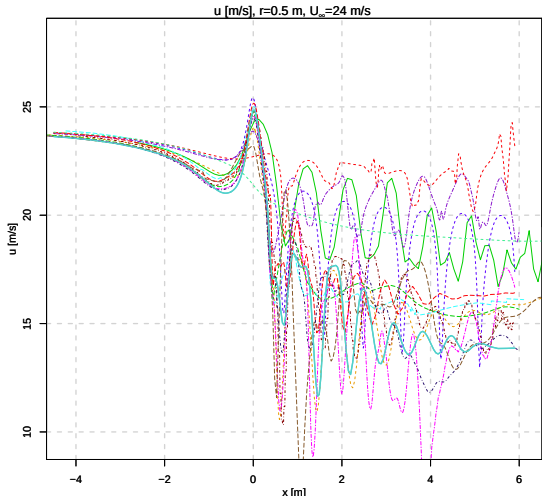

(a) u, r=0.5 m

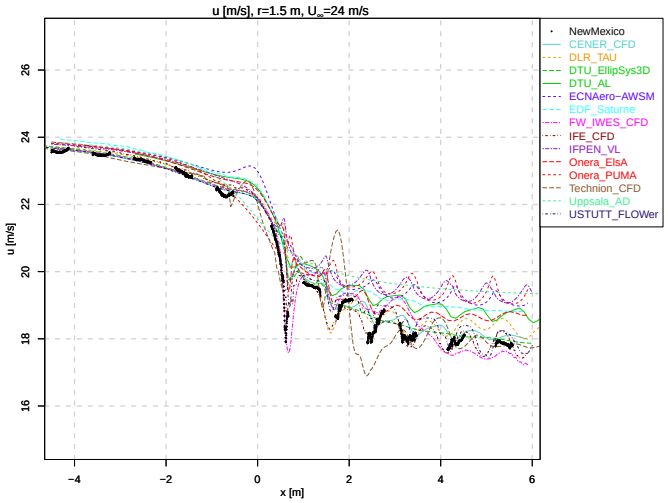

(b) u, r=1.5 m

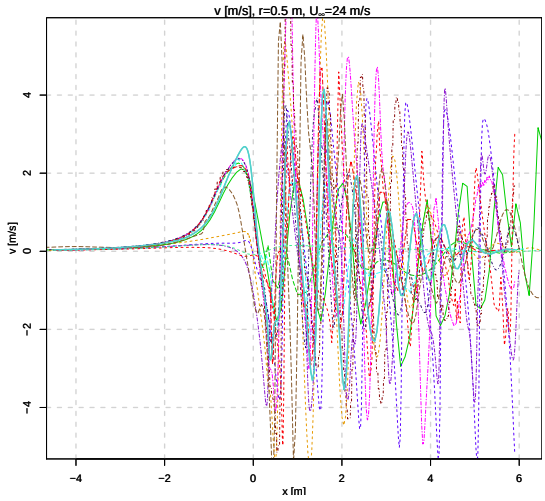

(c) v, r=0.5 m

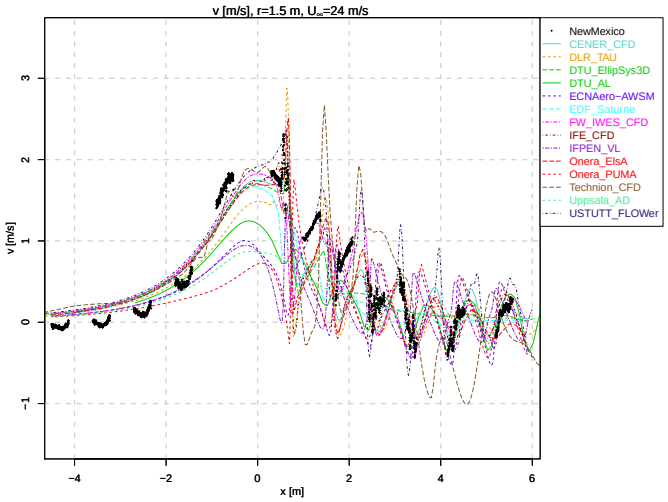

(d) v, r=1.5 m

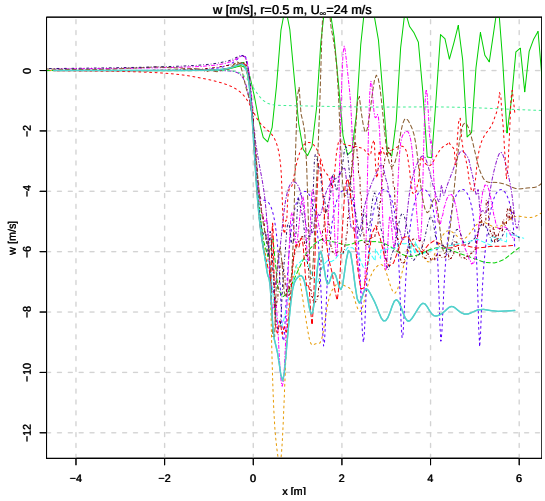

(e) w, r=0.5 m

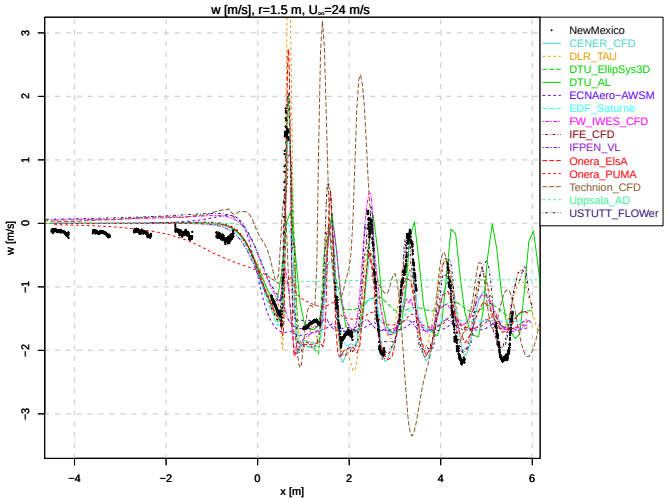

(f) w, r=1.5 m

Figure A.18: Axial traverse of velocity , Case 1.3

Radial traverse

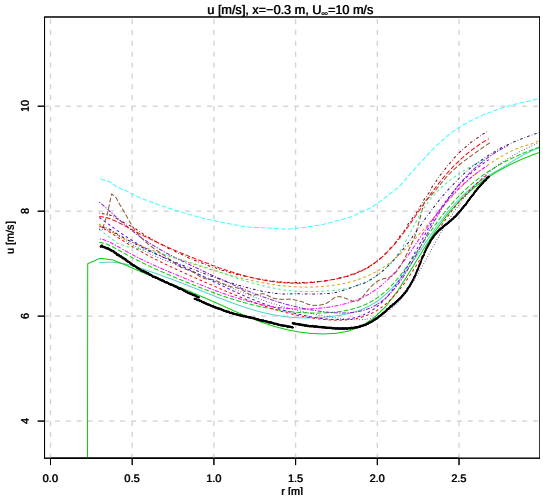

(a) u, x=-0.3 m

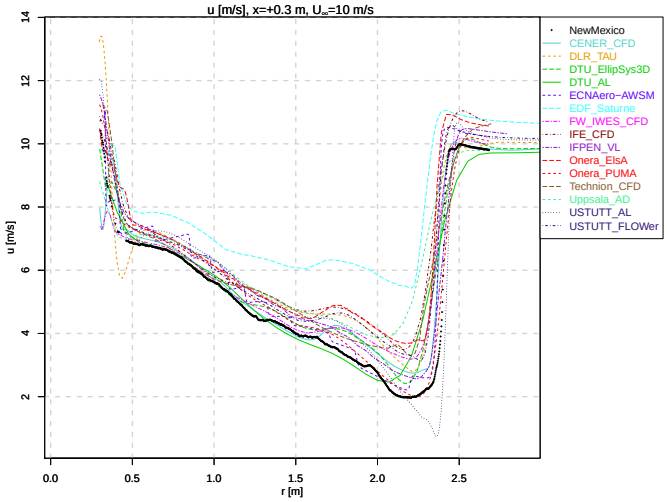

(b) u, x=+0.3 m

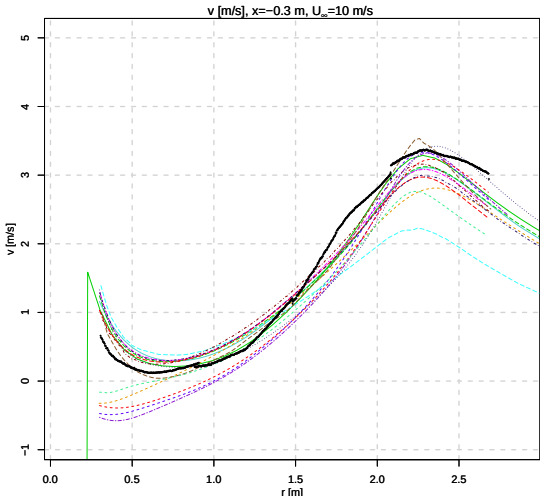

(c) v, x=-0.3 m

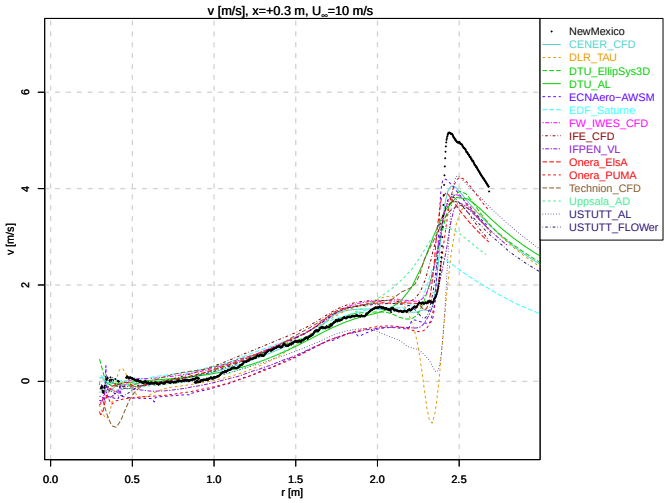

(d) v, x=+0.3 m

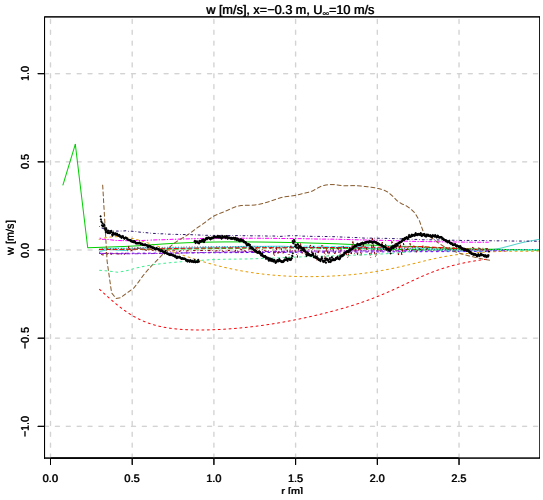

(e) w, x=-0.3 m

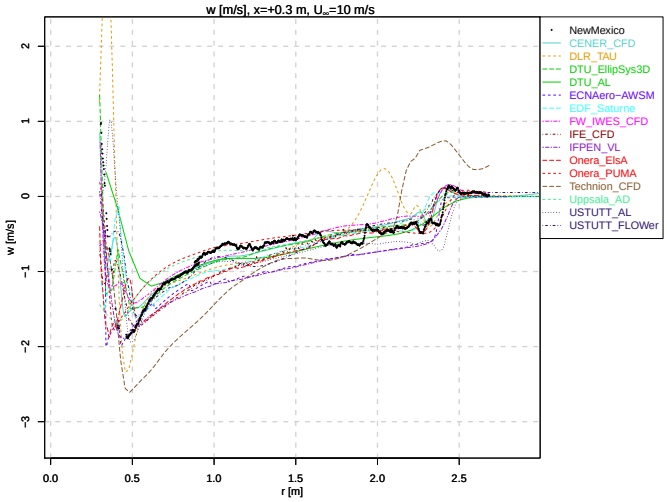

(f) w, x=+0.3 m

Figure A.19: Radial traverse of velocity , Case 1.1

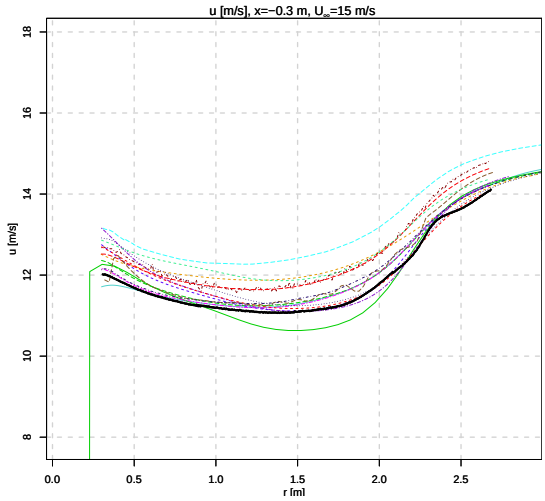

(a) u, x=-0.3 m

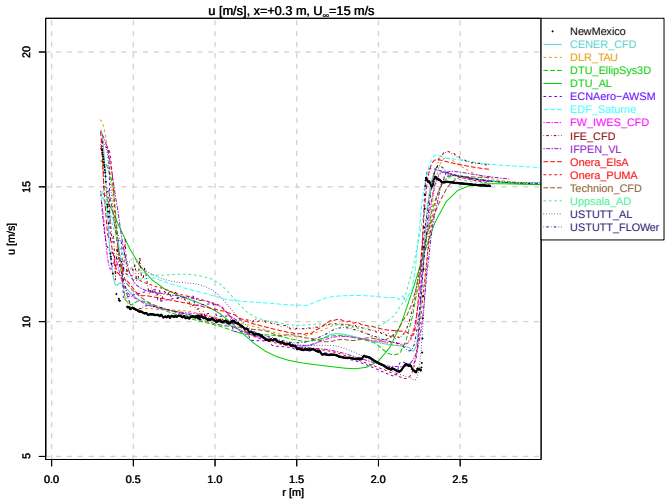

(b) u, x=+0.3 m

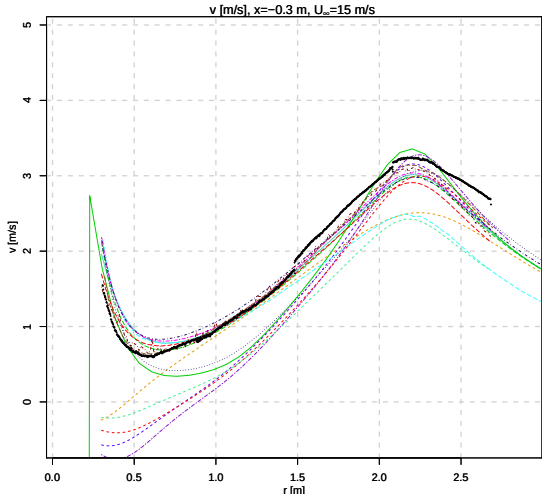

(c) v, x=-0.3 m

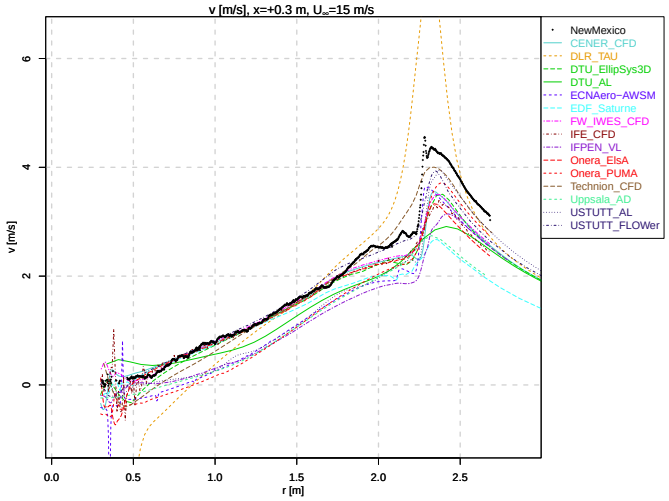

(d) v, x=+0.3 m

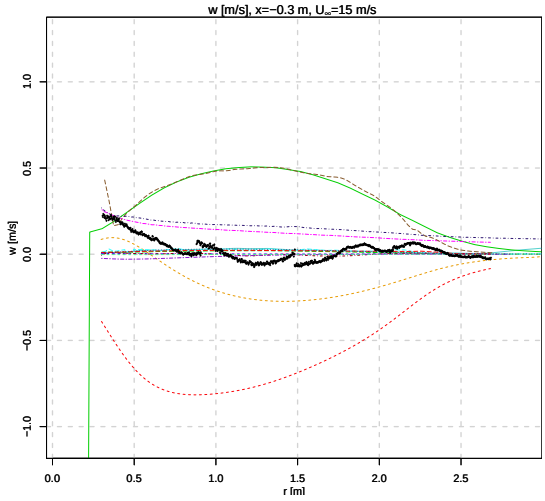

(e) w, x=-0.3 m

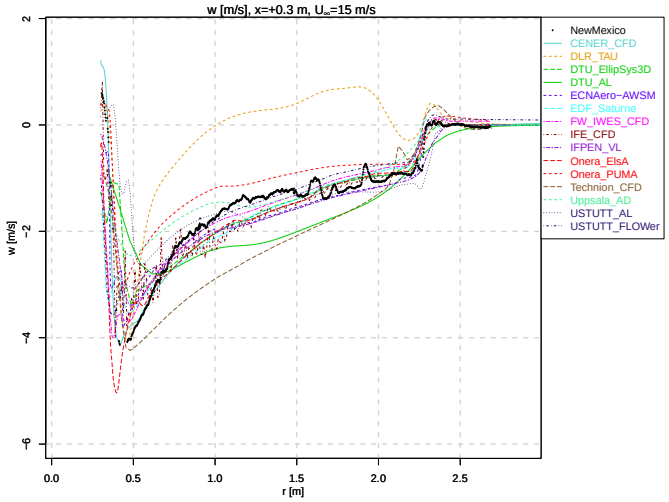

(f) w, x=+0.3 m

Figure A.20: Radial traverse of velocity , Case 1.2

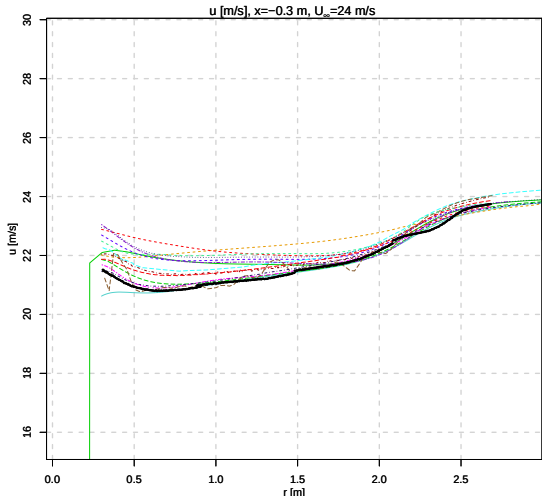

(a) u, x=-0.3 m

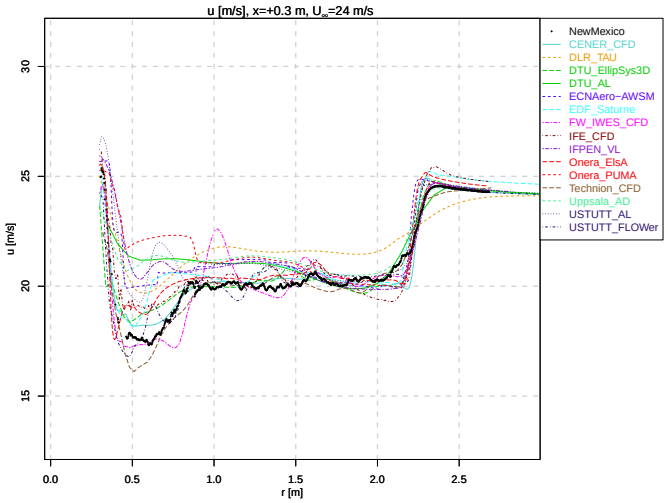

(b) u, x=+0.3 m

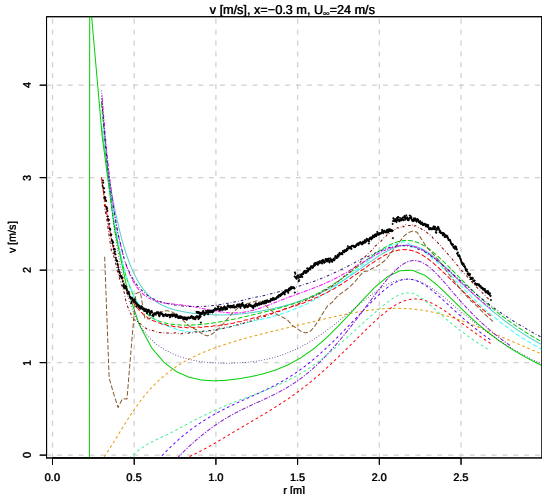

(c) v, x=-0.3 m

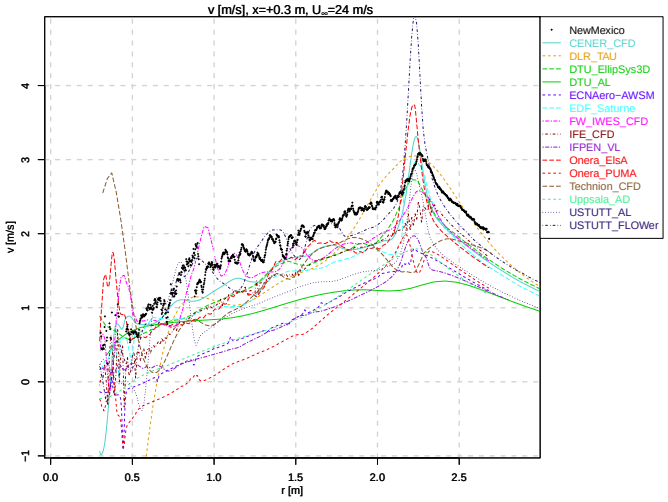

(d) v, x=+0.3 m

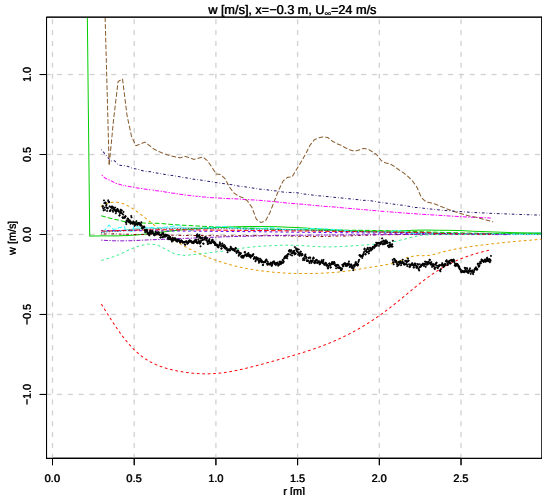

(e) w, x=-0.3 m

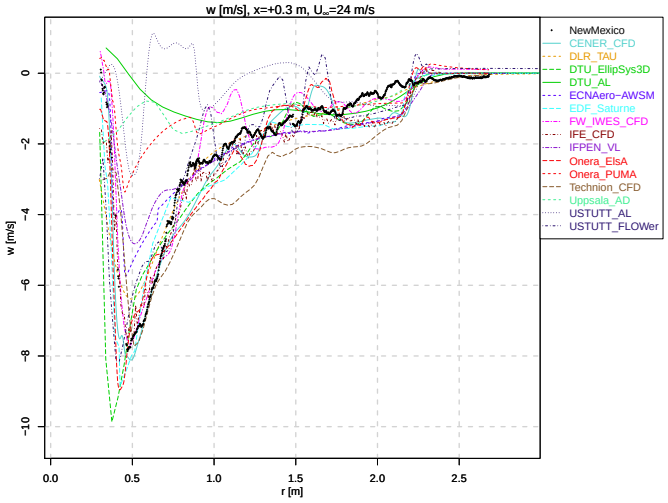

(f) w, x=+0.3 m

Figure A.21: Radial traverse of velocity , Case 1.3

Azimuth traverse

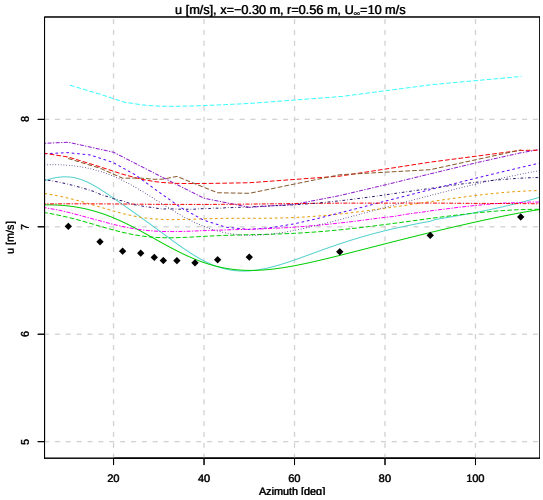

(a) u, x=-0.3 m, r=25%R

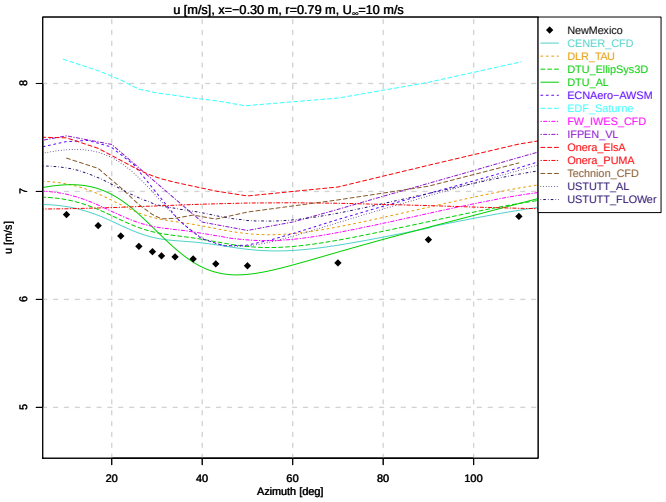

(b) u, x=-0.3 m, r=35%R

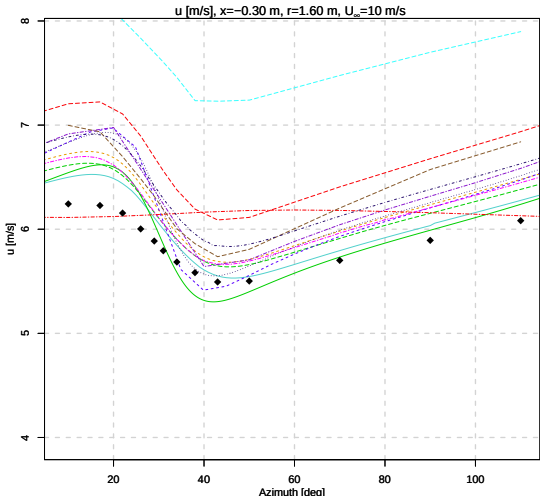

(c) u, x=-0.3 m, r=60%R

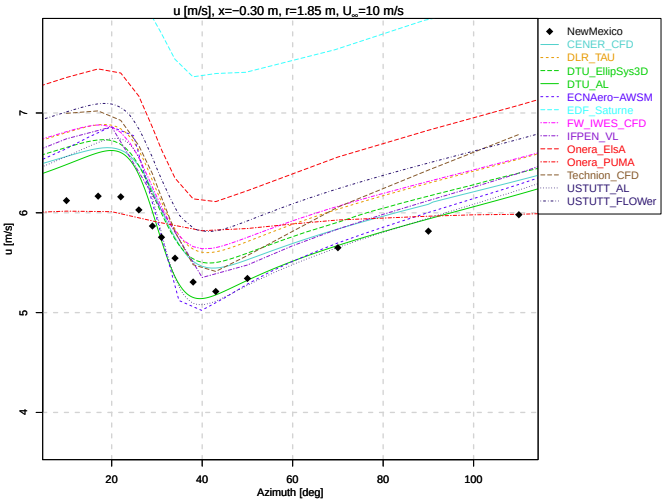

(d) u, x=-0.3 m, r=82%R

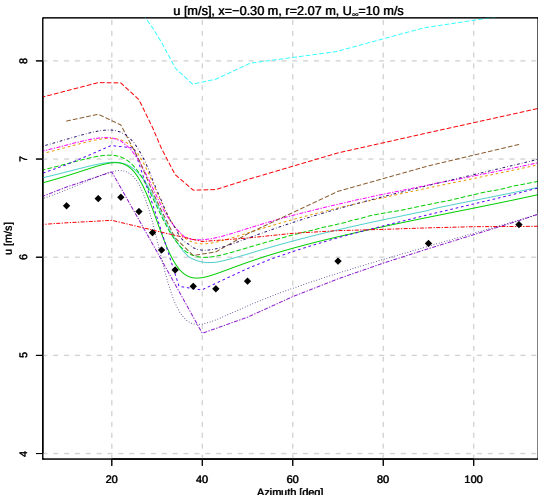

(e) u, x=-0.3 m, r=92%R

Figure A.22: Azimuth traverse of axial velocity u at x=-0.3 m, Case 1.1

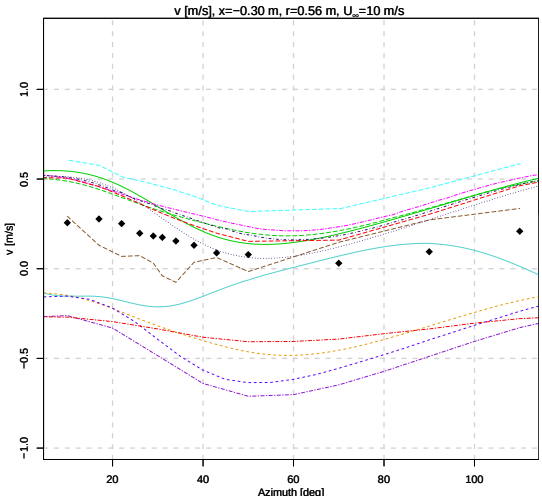

(a) v, x=-0.3 m, r=25%R

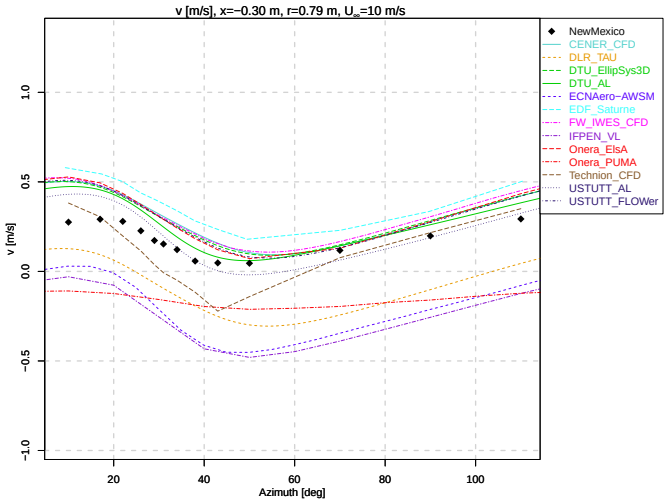

(b) v, x=-0.3 m, r=35%R

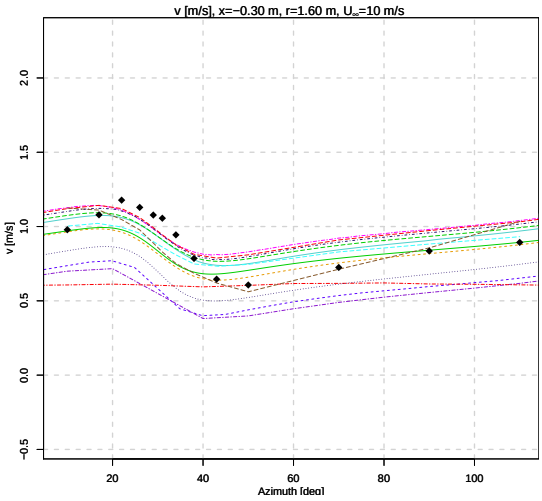

(c) v, x=-0.3 m, r=60%R

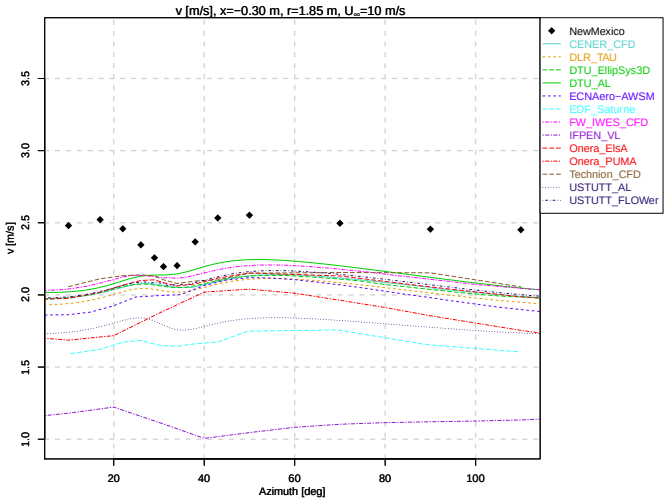

(d) v, x=-0.3 m, r=82%R

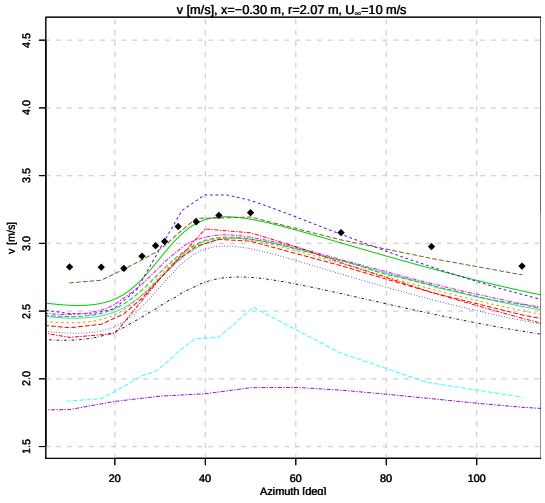

(e) v, x=-0.3 m, r=92%R

Figure A.23: Azimuth traverse of radial velocity v at x=-0.3 m, Case 1.1

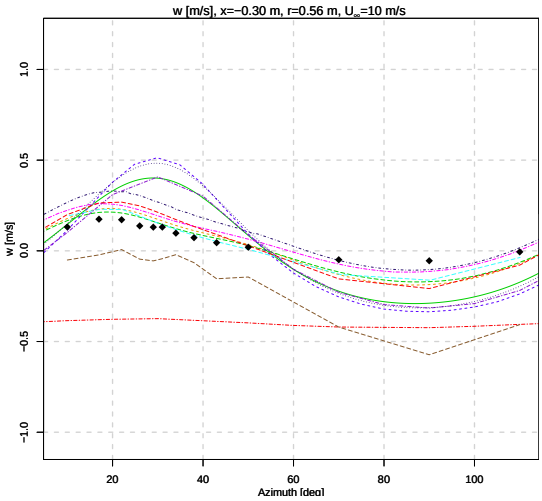

(a) w, x=-0.3 m, r=25%R

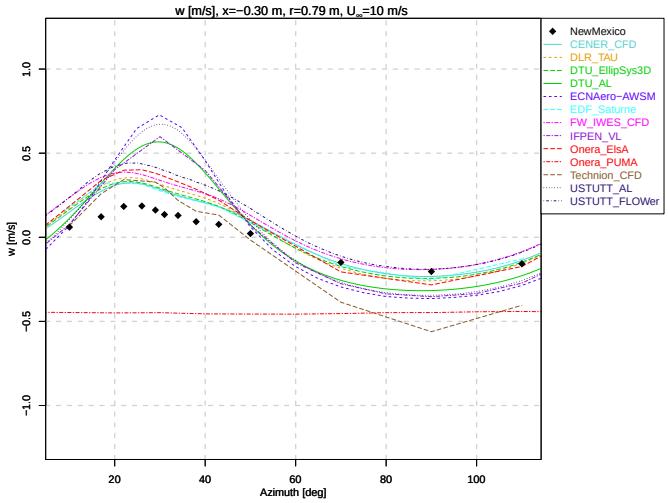

(b) w, x=-0.3 m, r=35%R

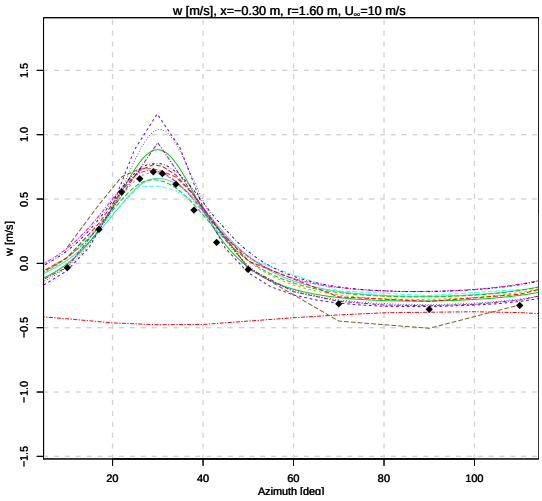

(c) w, x=-0.3 m, r=60%R

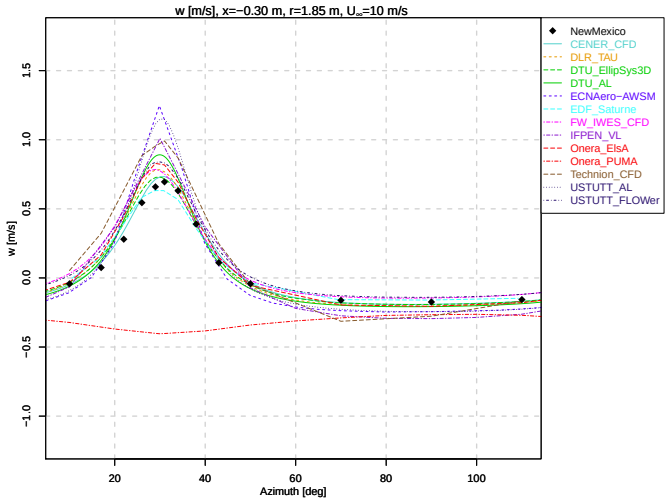

(d) w, x=-0.3 m, r=82%R

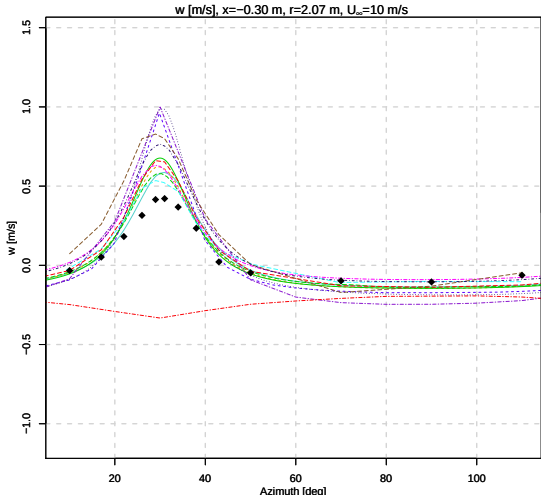

(e) w, x=-0.3 m, r=92%R

Figure A.24: Azimuth traverse of tangential velocity w at x=-0.3 m, Case 1.1

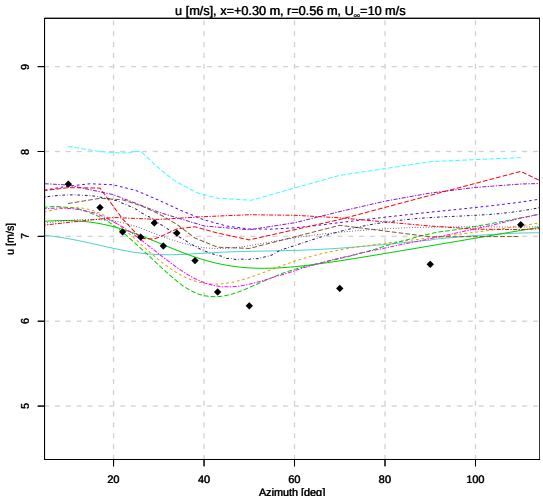

(a) u, x=+0.3 m, r=25%R

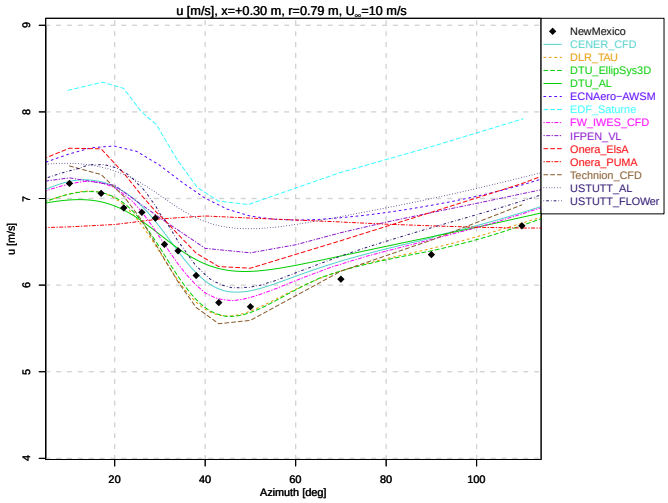

(b) u, x=+0.3 m, r=35%R

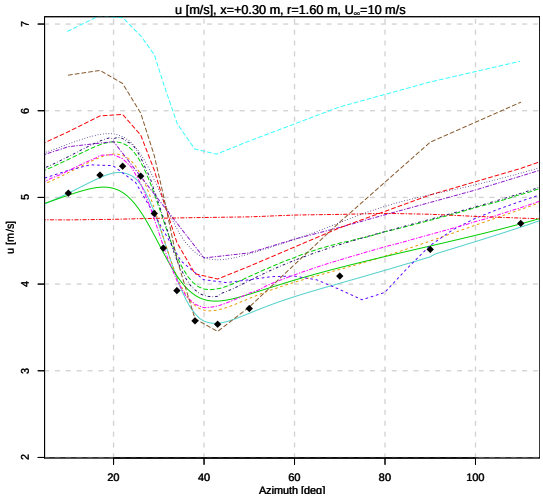

(c) u, x=+0.3 m, r=60%R

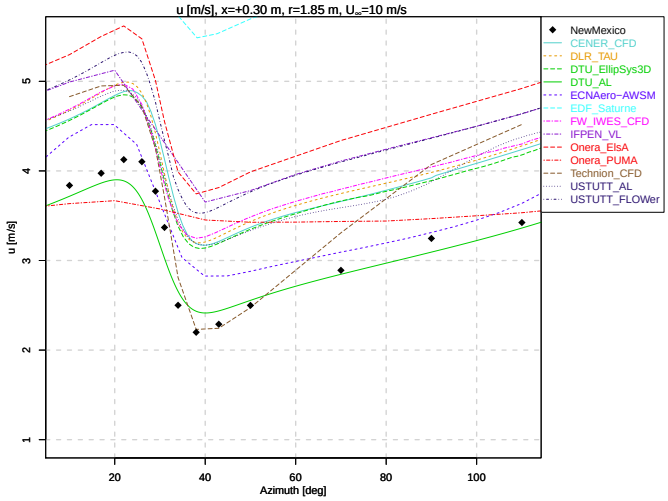

(d) u, x=+0.3 m, r=82%R

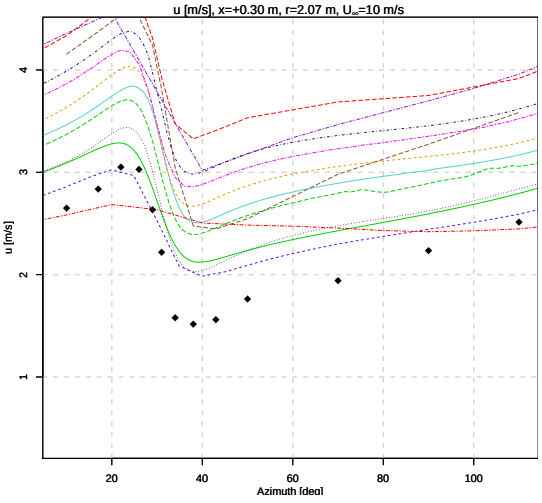

(e) u, x=+0.3 m, r=92%R

Figure A.25: Azimuth traverse of axial velocity u at x=+0.3 m, Case 1.1

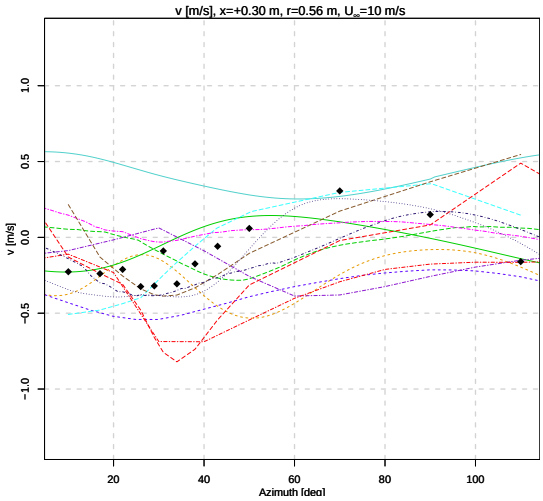

(a) v, x=+0.3 m, r=25%R

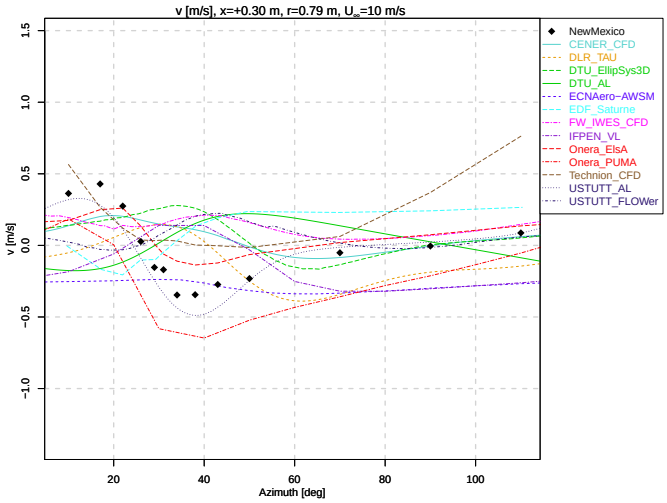

(b) v, x=+0.3 m, r=35%R

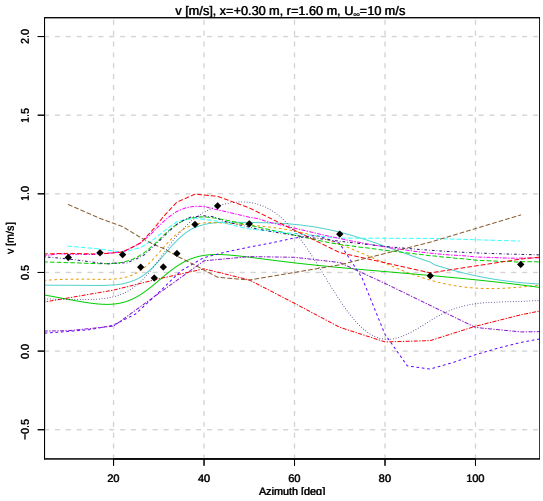

(c) v, x=+0.3 m, r=60%R

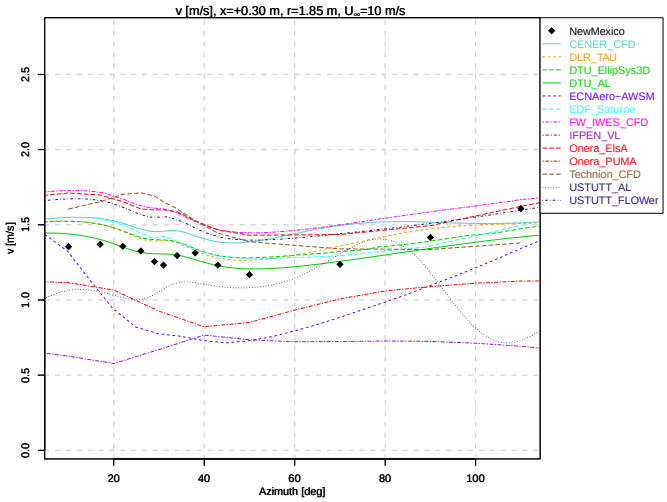

(d) v, x=+0.3 m, r=82%R

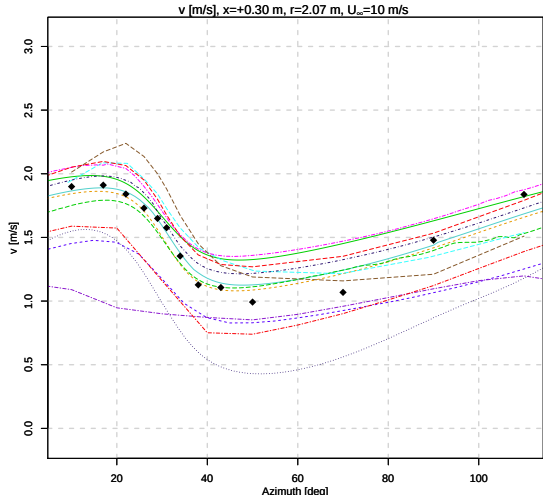

(e) v, x=+0.3 m, r=92%R

Figure A.26: Azimuth traverse of radial velocity v at x=+0.3 m, Case 1.1

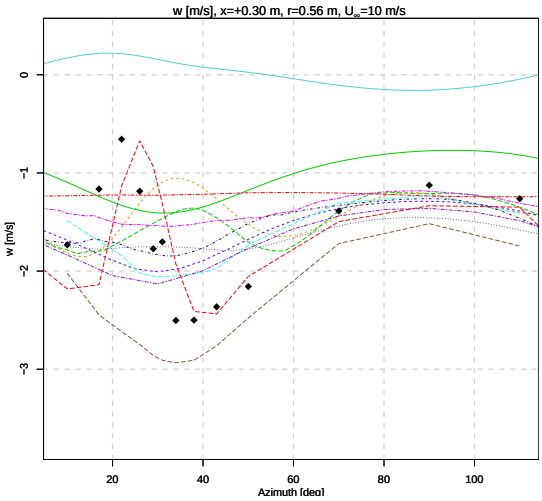

(a) w, x=+0.3 m, r=25%R

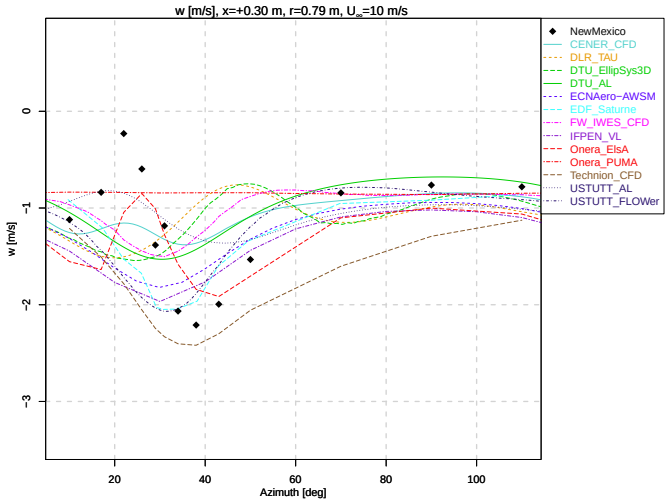

(b) w, x=+0.3 m, r=35%R

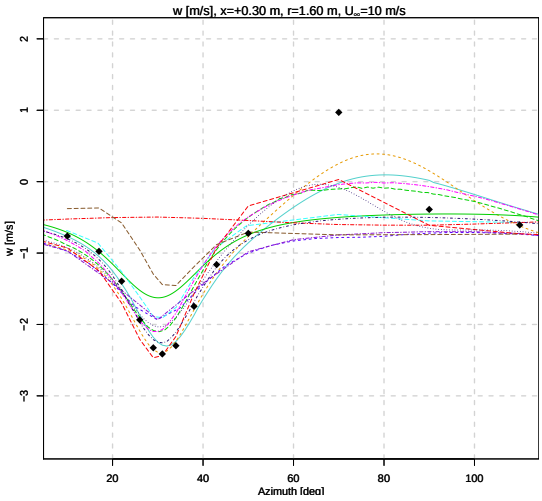

(c) w, x=+0.3 m, r=60%R

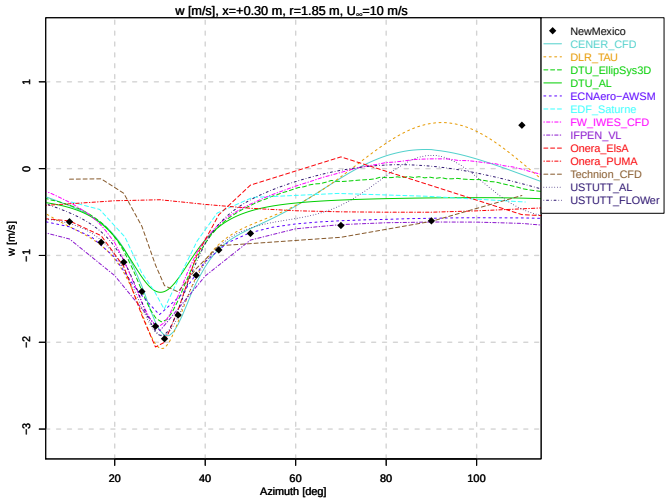

(d) w, x=+0.3 m, r=82%R

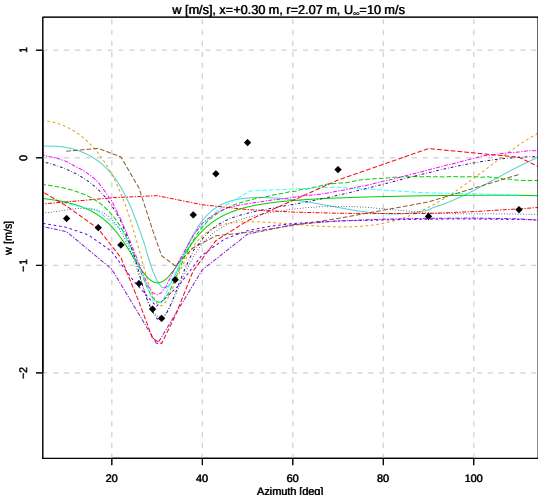

(e) w, x=+0.3 m, r=92%R

Figure A.27: Azimuth traverse of tangential velocity w at x=+0.3 m, Case 1.1

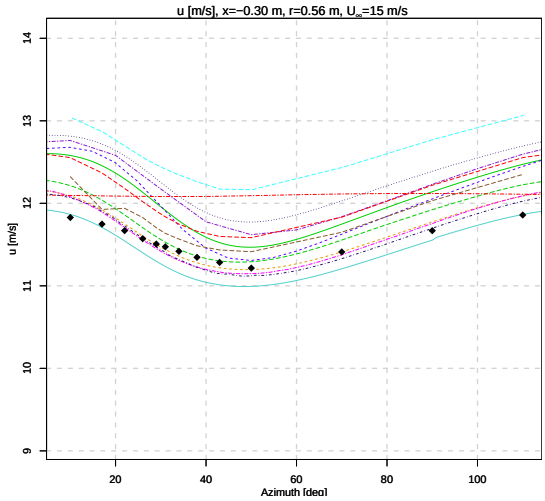

(a) u, x=-0.3 m, r=25%R

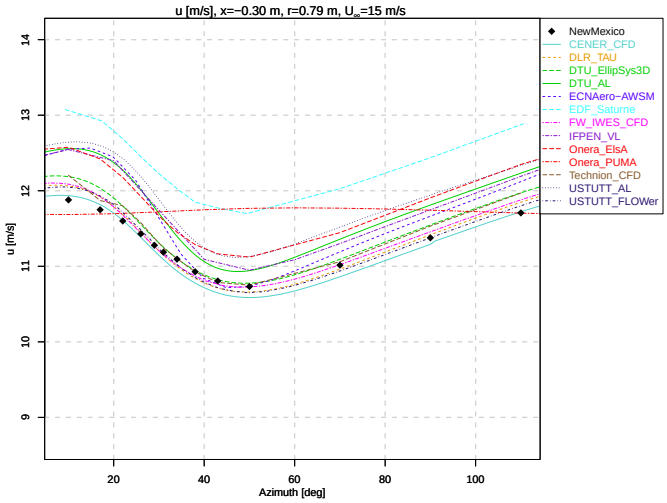

(b) u, x=-0.3 m, r=35%R

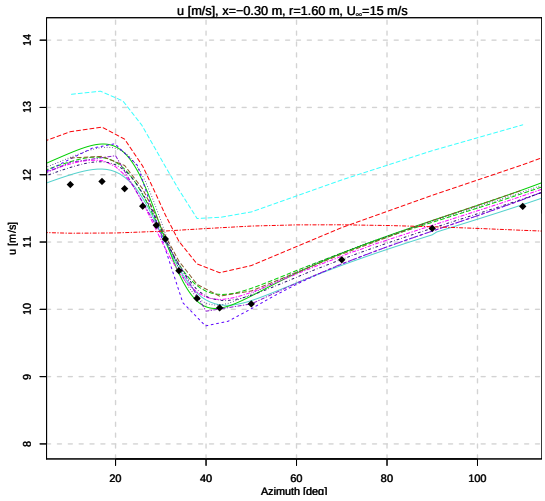

(c) u, x=-0.3 m, r=60%R

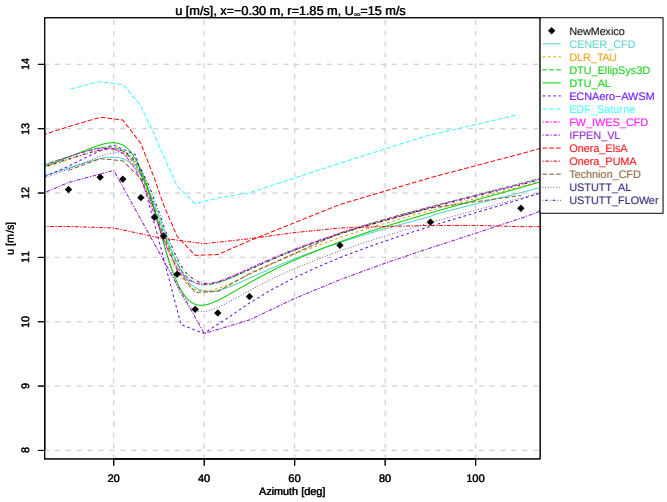

(d) u, x=-0.3 m, r=82%R

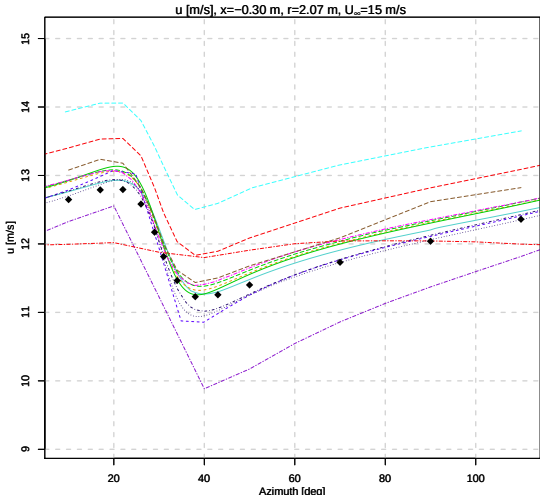

(e) u, x=-0.3 m, r=92%R

Figure A.28: Azimuth traverse of axial velocity u at x=-0.3 m, Case 1.2

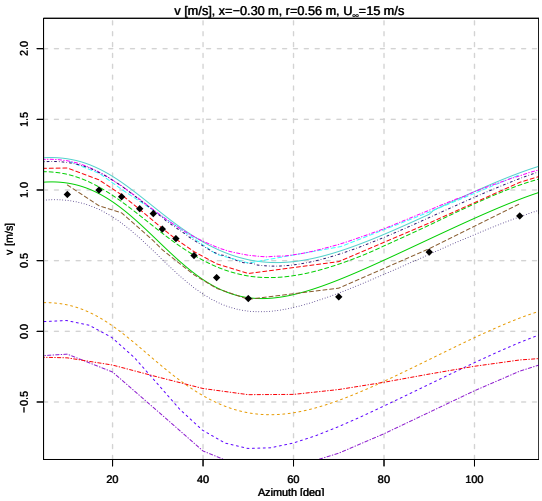

(a) v, x=-0.3 m, r=25%R

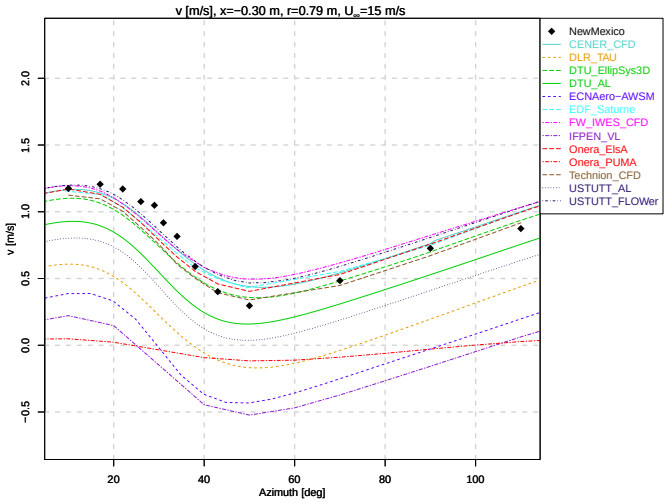

(b) v, x=-0.3 m, r=35%R

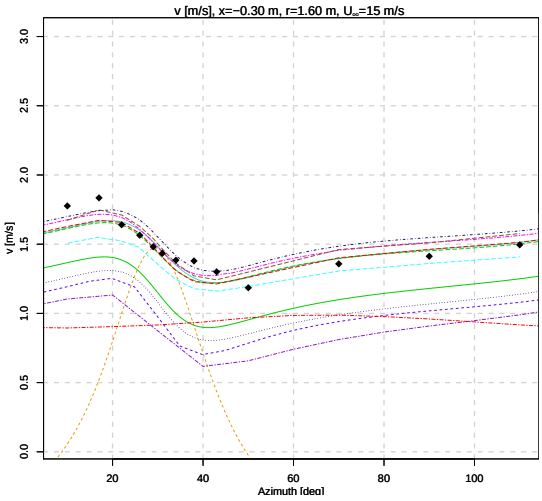

(c) v, x=-0.3 m, r=60%R

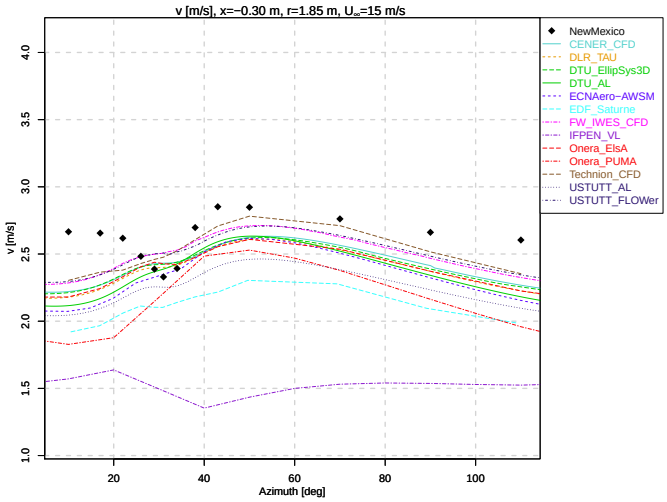

(d) v, x=-0.3 m, r=82%R

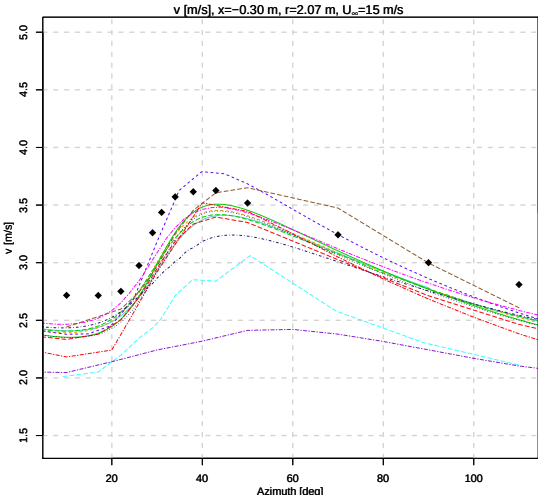

(e) v, x=-0.3 m, r=92%R

Figure A.29: Azimuth traverse of radial velocity v at x=-0.3 m, Case 1.2

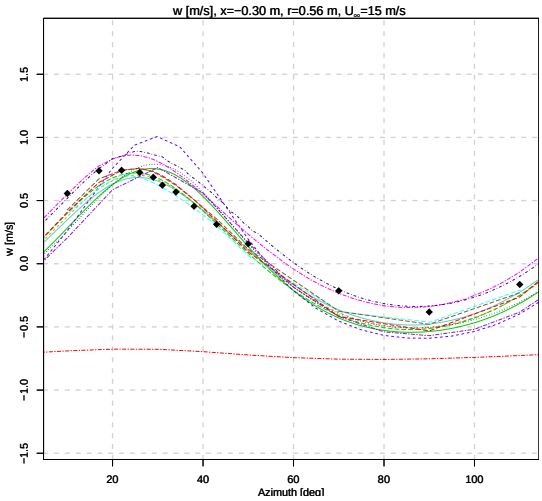

(a) w, x=-0.3 m, r=25%R

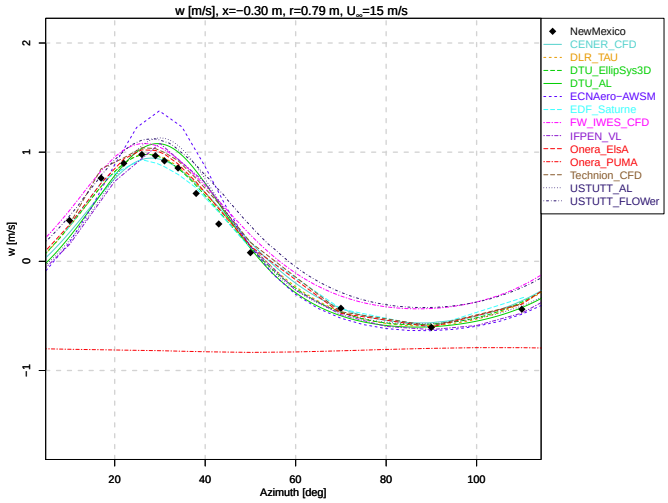

(b) w, x=-0.3 m, r=35%R

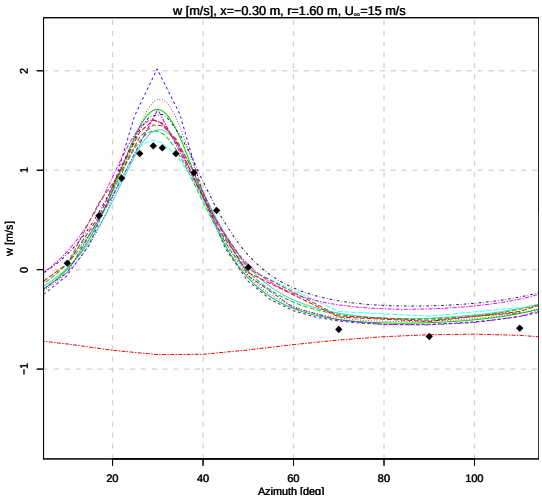

(c) w, x=-0.3 m, r=60%R

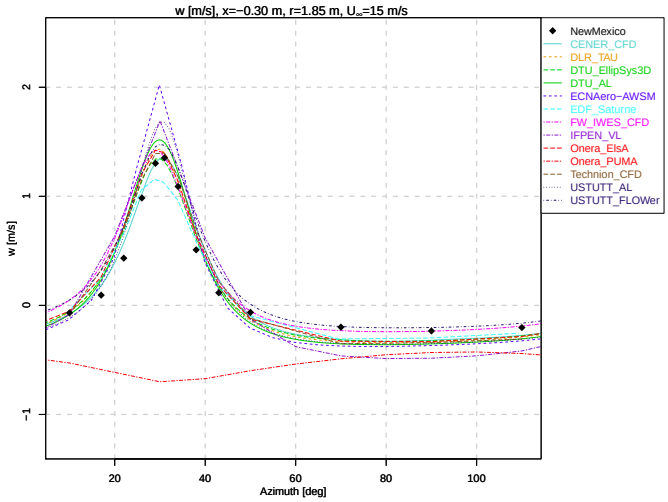

(d) w, x=-0.3 m, r=82%R

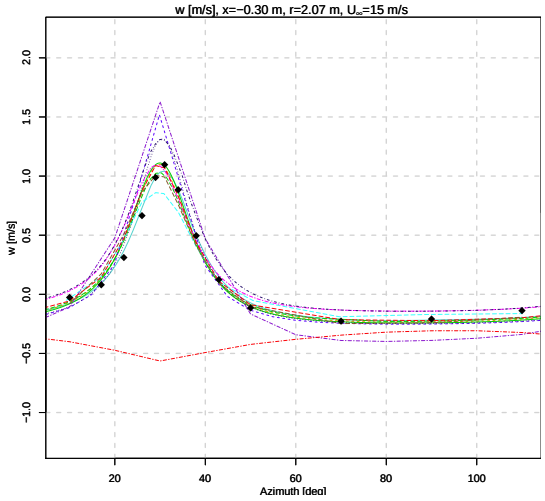

(e) w, x=-0.3 m, r=92%R

Figure A.30: Azimuth traverse of tangential velocity w at x=-0.3 m, Case 1.2

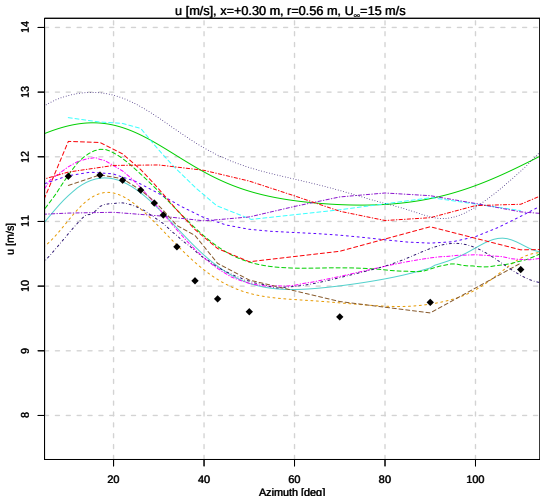

(a) u, x=+0.3 m, r=25%R

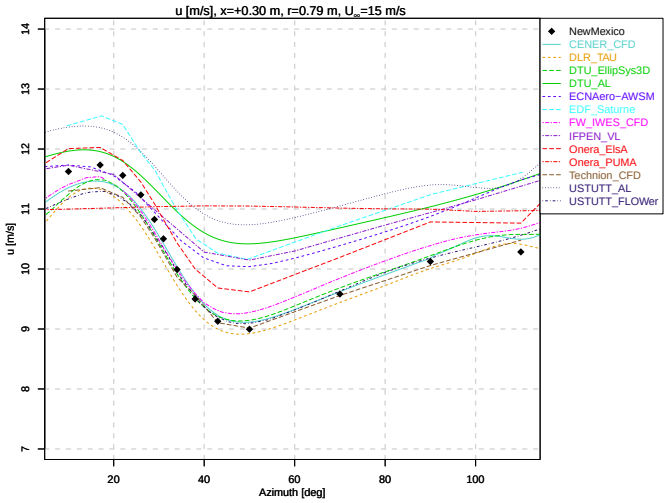

(b) u, x=+0.3 m, r=35%R

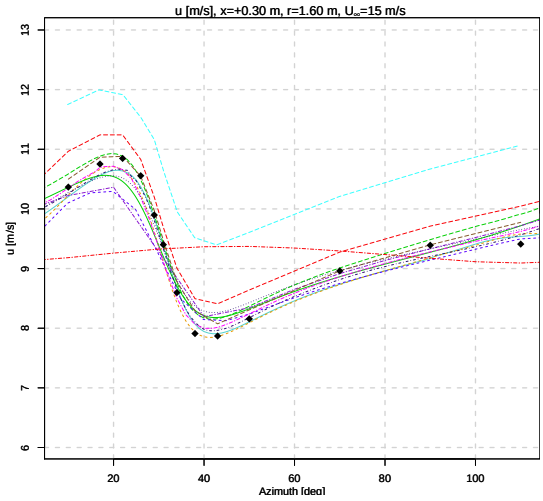

(c) u, x=+0.3 m, r=60%R

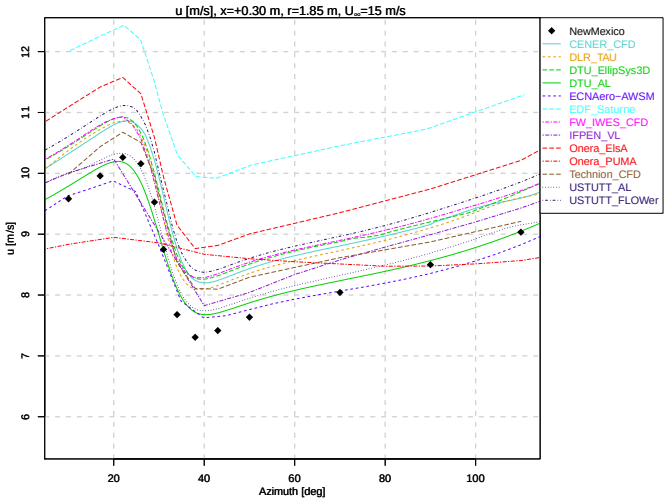

(d) u, x=+0.3 m, r=82%R

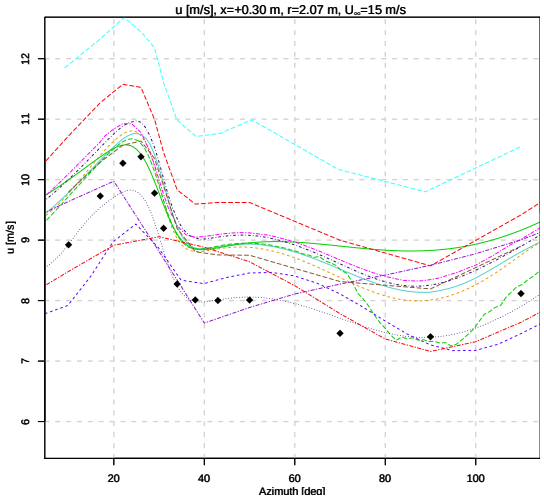

(e) u, x=+0.3 m, r=92%R

Figure A.31: Azimuth traverse of axial velocity u at x=+0.3 m, Case 1.2

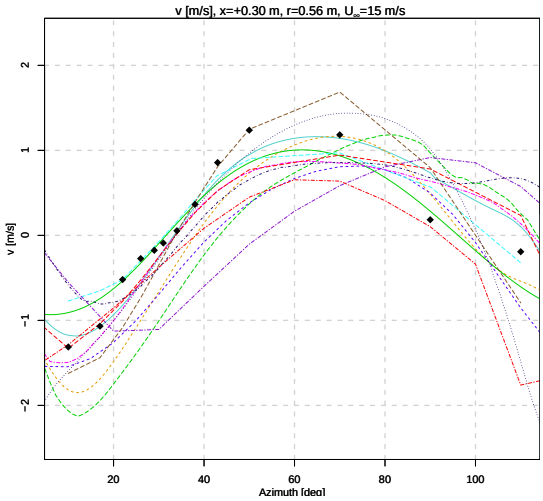

(a) v, x=+0.3 m, r=25%R

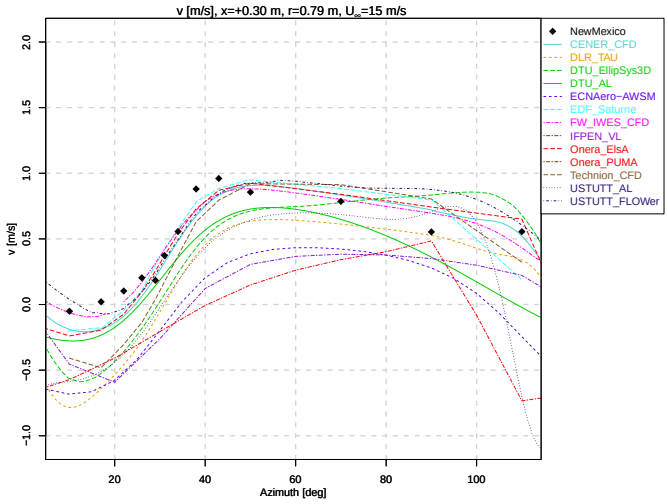

(b) v, x=+0.3 m, r=35%R

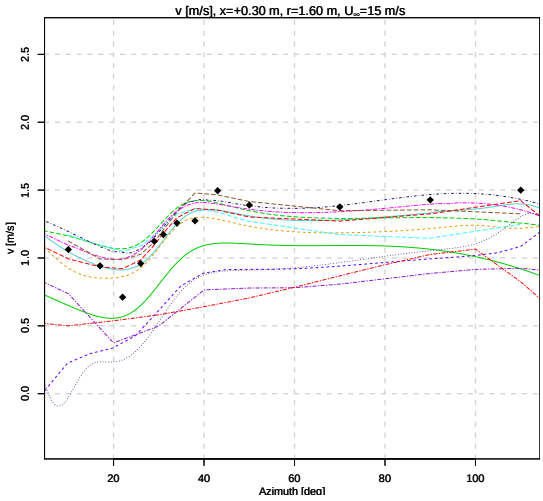

(c) v, x=+0.3 m, r=60%R

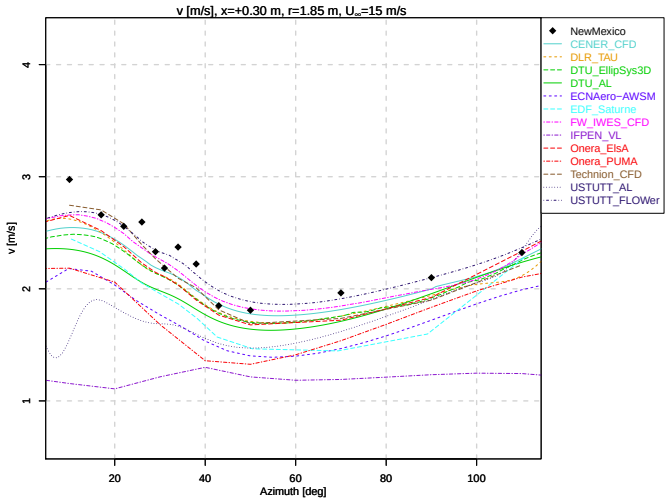

(d) v, x=+0.3 m, r=82%R

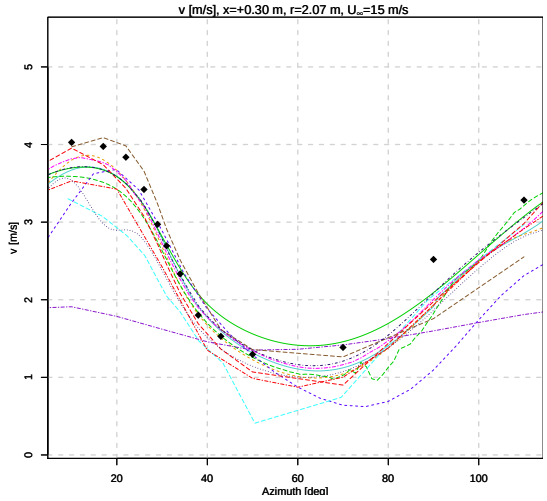

(e) v, x=+0.3 m, r=92%R

Figure A.32: Azimuth traverse of radial velocity v at x=+0.3 m, Case 1.2

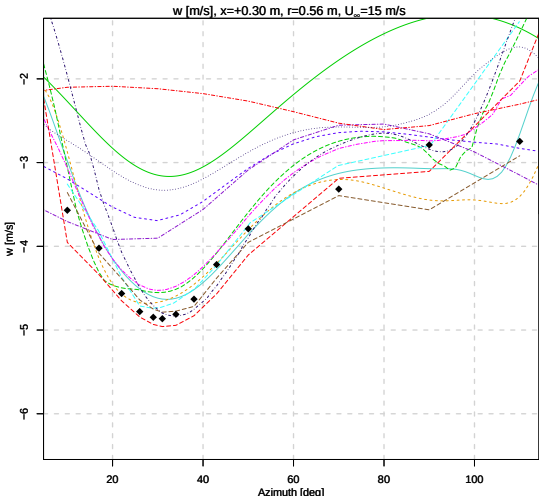

(a) w, x=+0.3 m, r=25%R

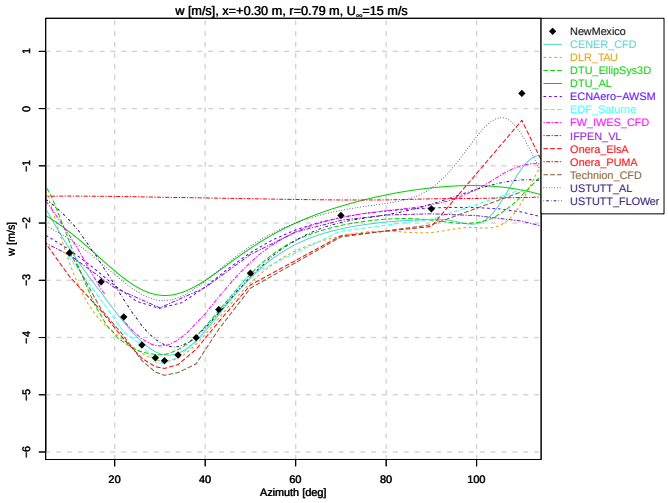

(b) w, x=+0.3 m, r=35%R

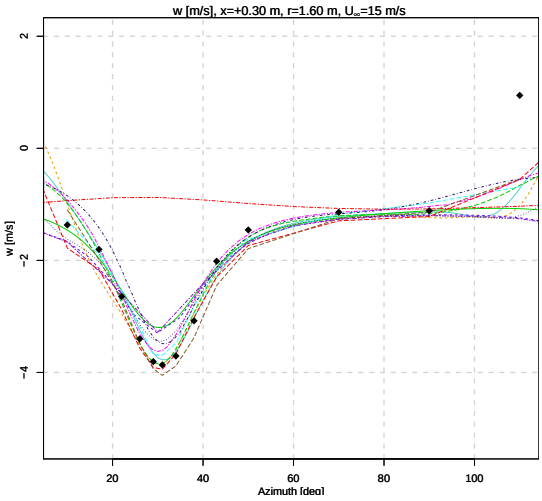

(c) w, x=+0.3 m, r=60%R

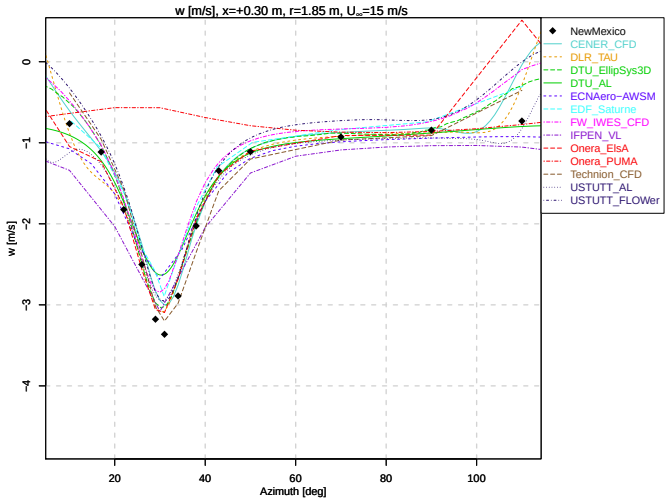

(d) w, x=+0.3 m, r=82%R

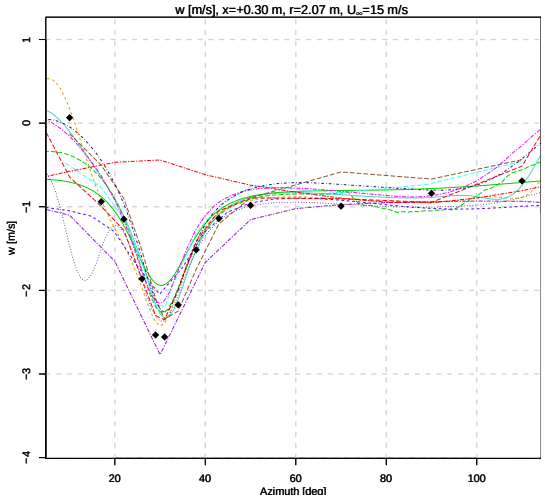

(e) w, x=+0.3 m, r=92%R

Figure A.33: Azimuth traverse of tangential velocity w at x=+0.3 m, Case 1.2

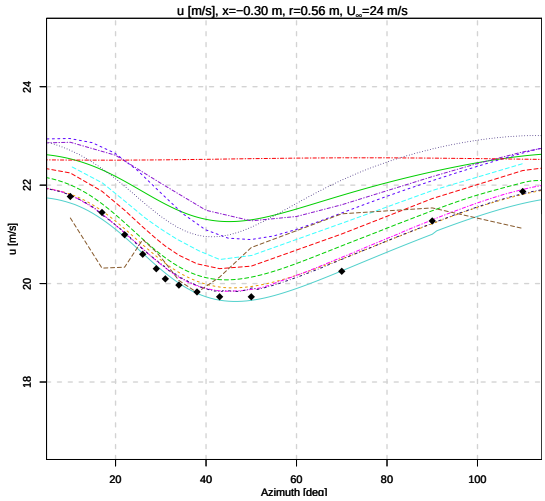

(a) u, x=-0.3 m, r=25%R

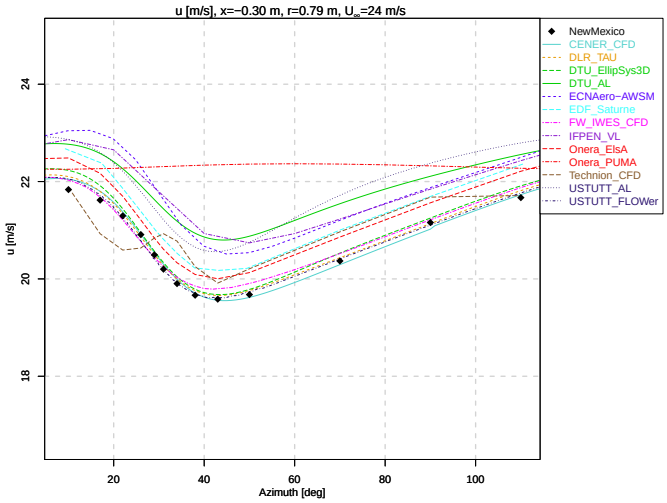

(b) u, x=-0.3 m, r=35%R

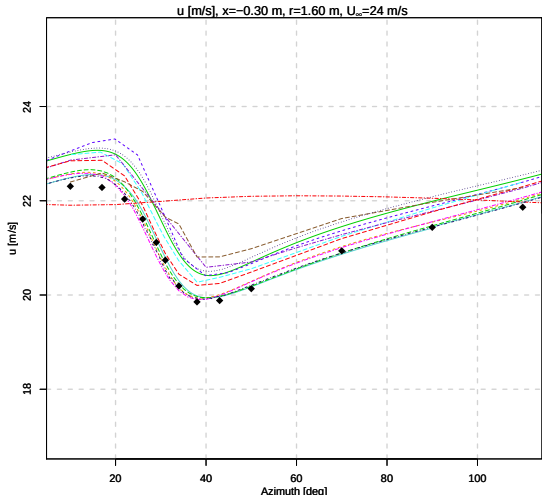

(c) u, x=-0.3 m, r=60%R

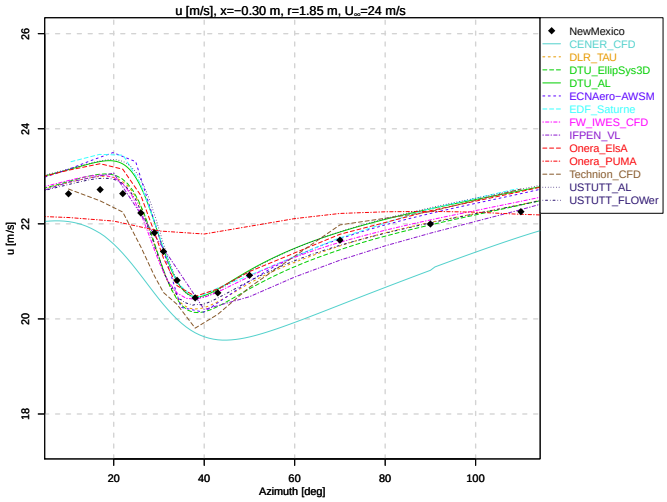

(d) u, x=-0.3 m, r=82%R

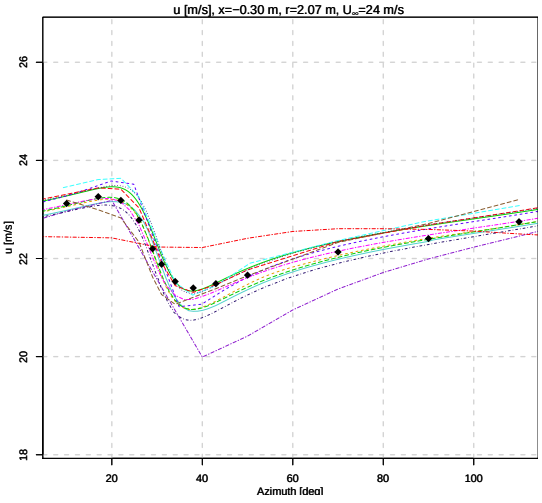

(e) u, x=-0.3 m, r=92%R

Figure A.34: Azimuth traverse of axial velocity u at x=-0.3 m, Case 1.3

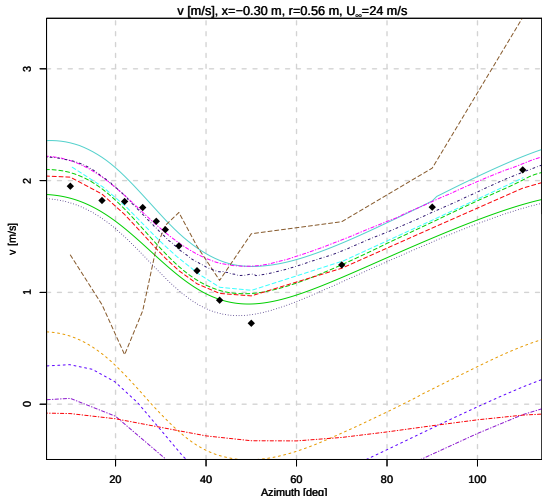

(a) v, x=-0.3 m, r=25%R

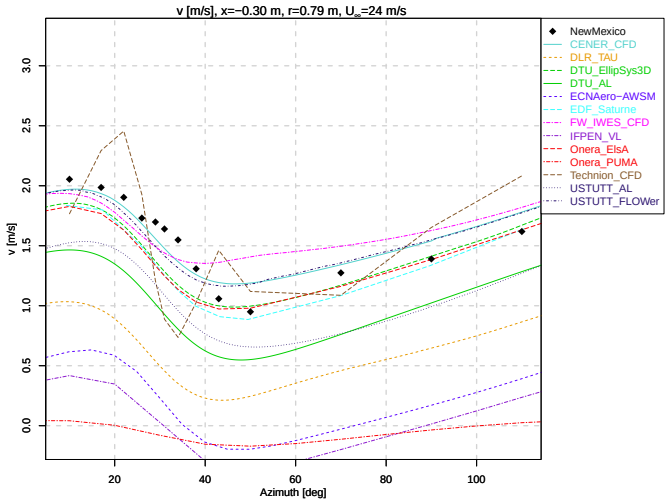

(b) v, x=-0.3 m, r=35%R

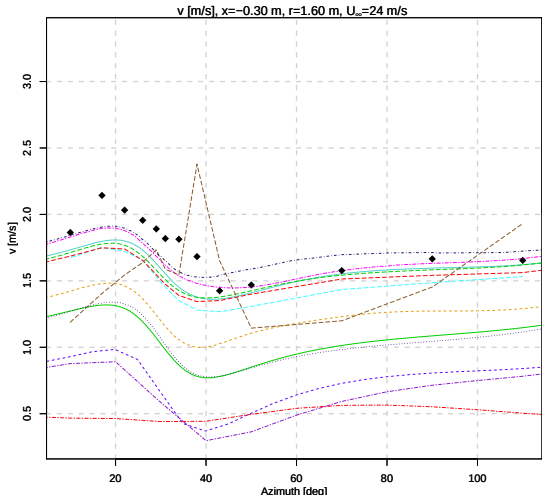

(c) v, x=-0.3 m, r=60%R

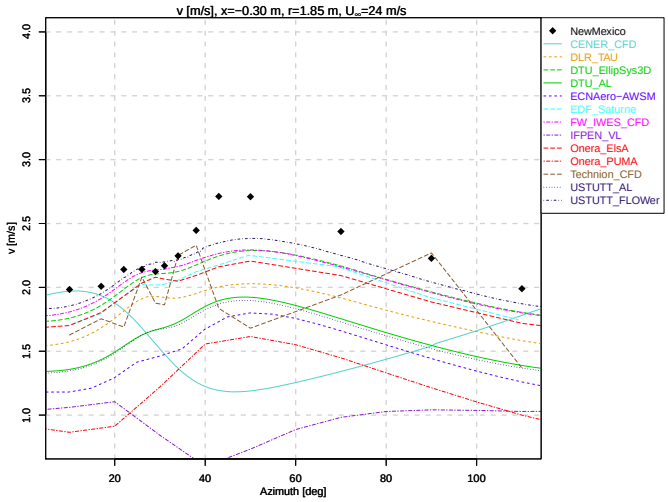

(d) v, x=-0.3 m, r=82%R

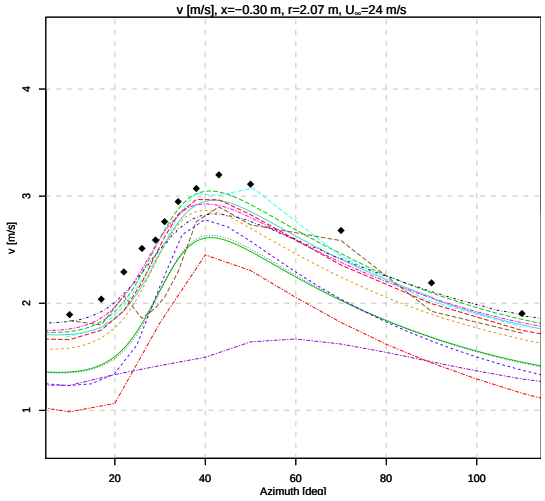

(e) v, x=-0.3 m, r=92%R

Figure A.35: Azimuth traverse of radial velocity v at x=-0.3 m, Case 1.3

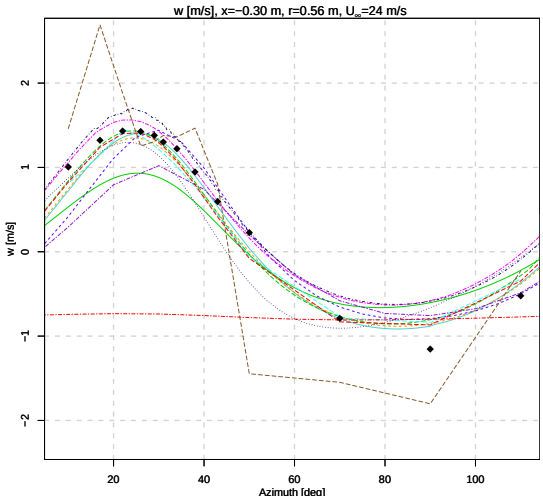

(a) w, x=-0.3 m, r=25%R

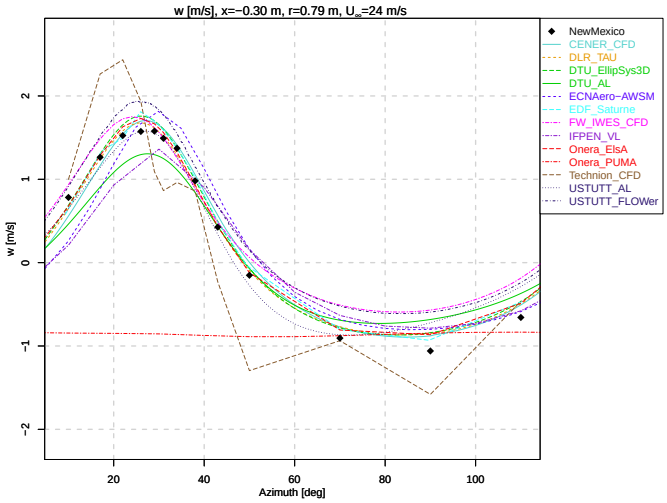

(b) w, x=-0.3 m, r=35%R

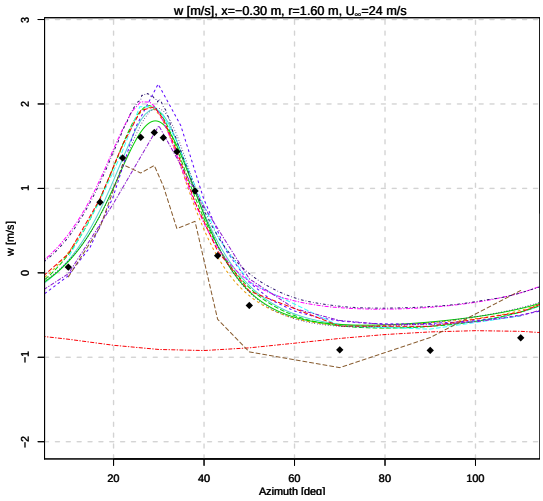

(c) w, x=-0.3 m, r=60%R

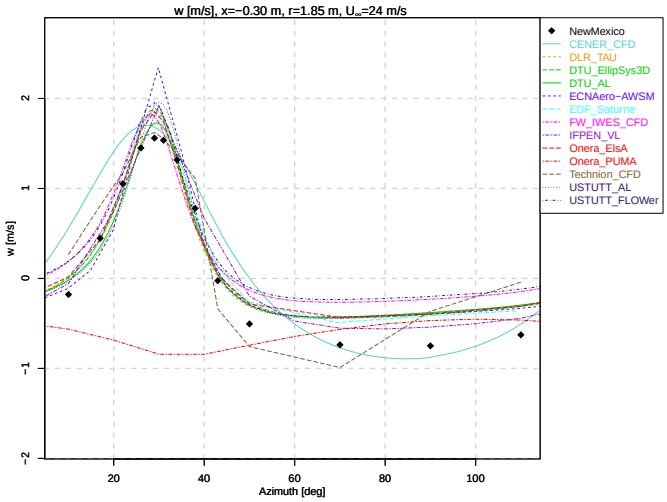

(d) w, x=-0.3 m, r=82%R

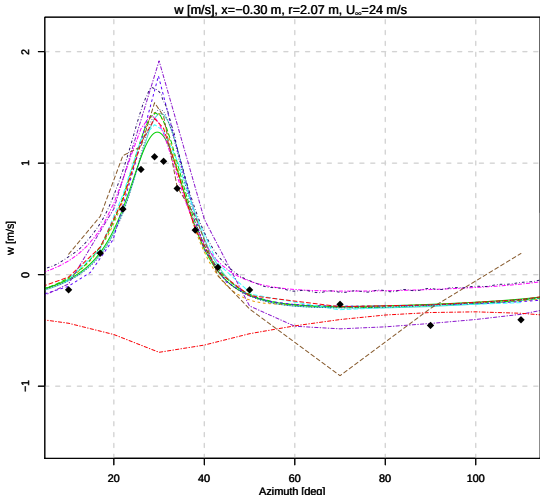

(e) w, x=-0.3 m, r=92%R

Figure A.36: Azimuth traverse of tangential velocity w at x=-0.3 m, Case 1.3

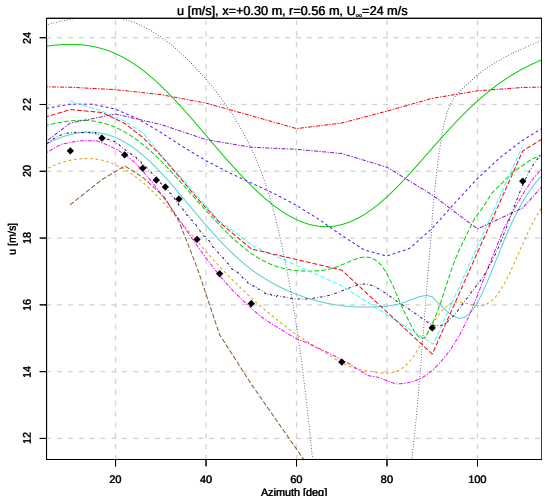

(a) u, x=+0.3 m, r=25%R

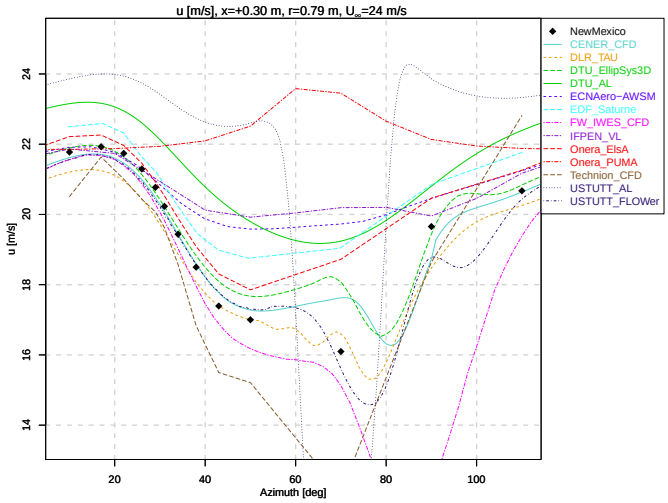

(b) u, x=+0.3 m, r=35%R

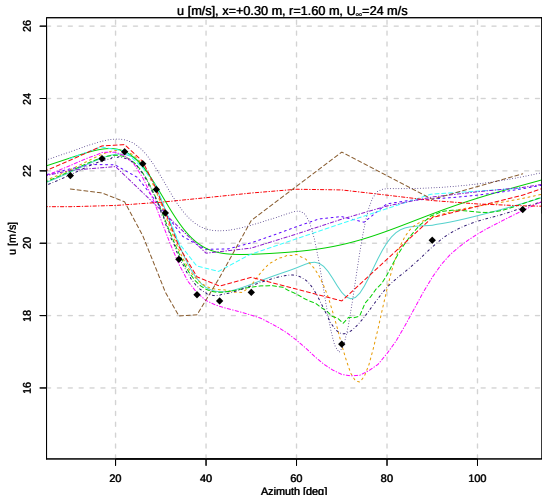

(c) u, x=+0.3 m, r=60%R

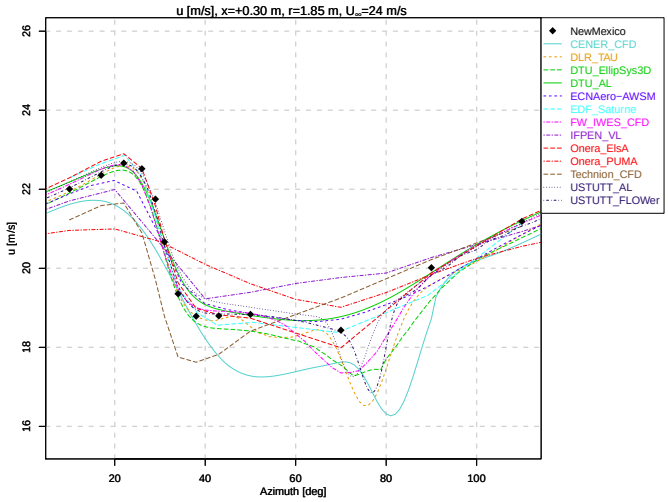

(d) u, x=+0.3 m, r=82%R

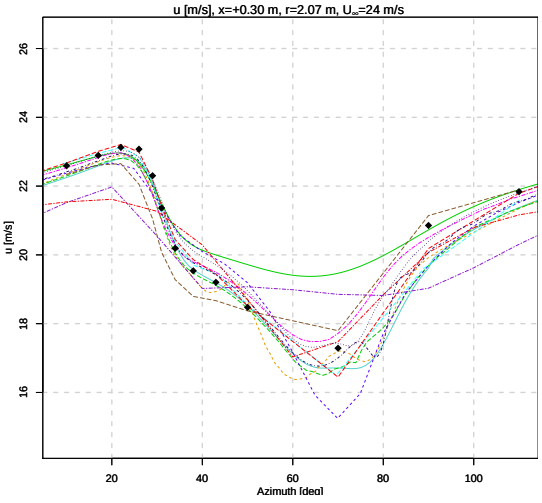

(e) u, x=+0.3 m, r=92%R

Figure A.37: Azimuth traverse of axial velocity u at x=+0.3 m, Case 1.3

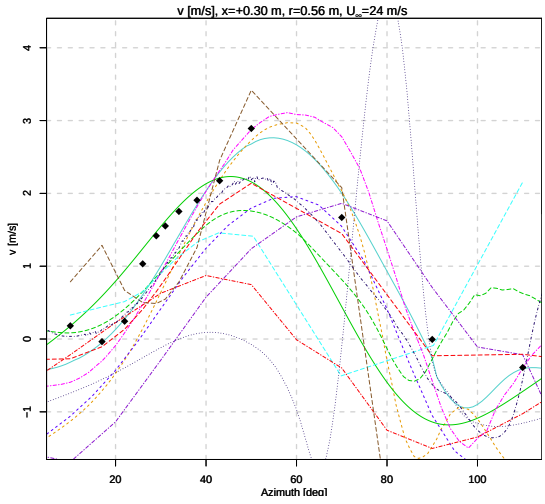

(a) v, x=+0.3 m, r=25%R

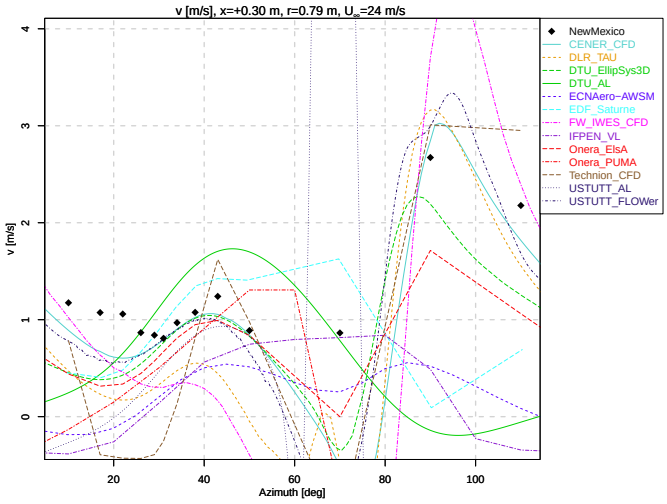

(b) v, x=+0.3 m, r=35%R

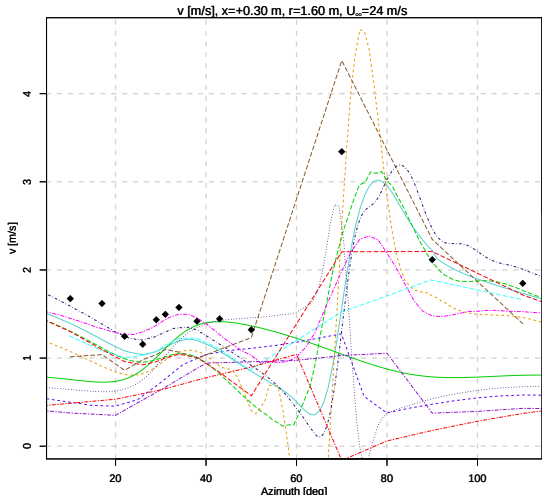

(c) v, x=+0.3 m, r=60%R

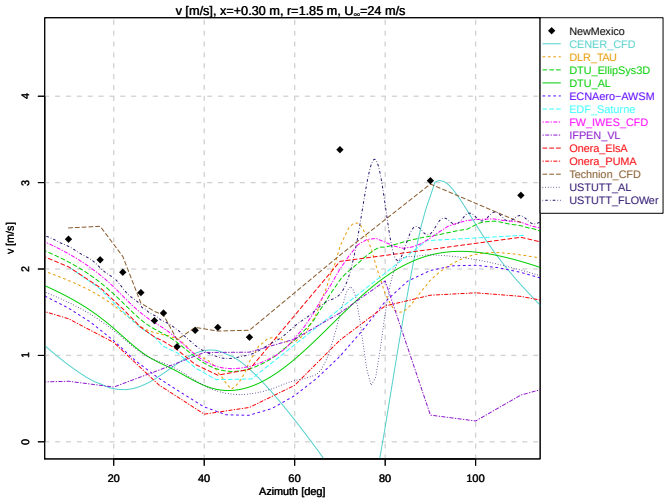

(d) v, x=+0.3 m, r=82%R

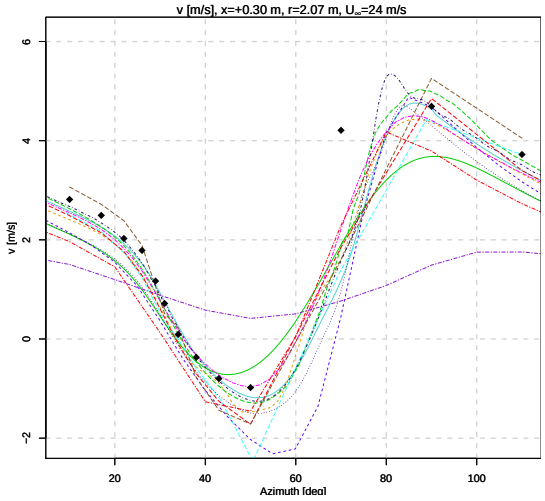

(e) v, x=+0.3 m, r=92%R

Figure A.38: Azimuth traverse of radial velocity v at x=+0.3 m, Case 1.3

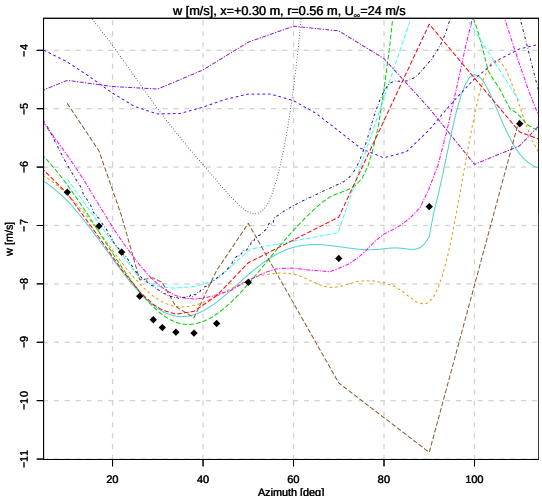

(a) w, x=+0.3 m, r=25%R

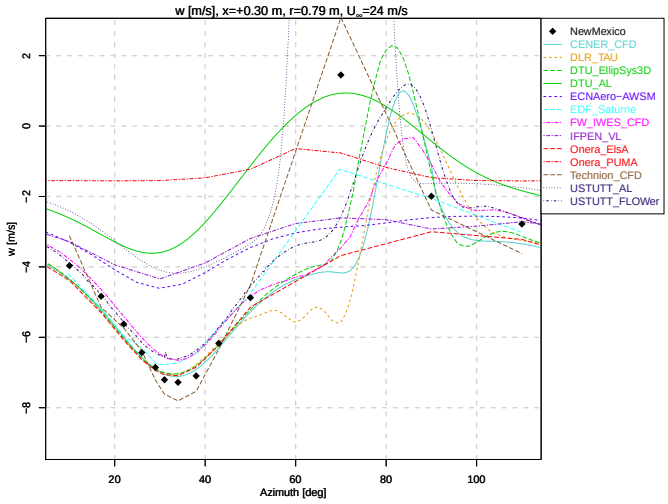

(b) w, x=+0.3 m, r=35%R

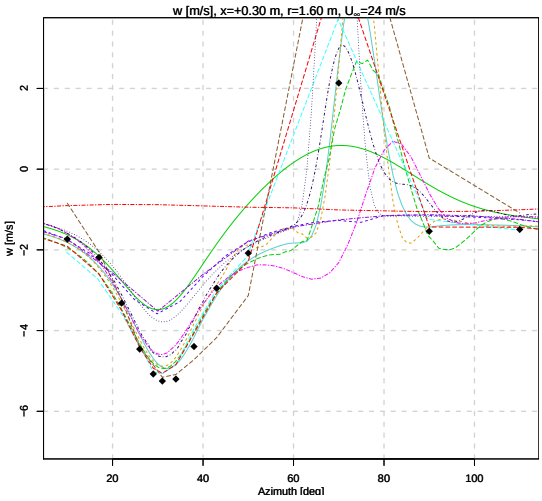

(c) w, x=+0.3 m, r=60%R

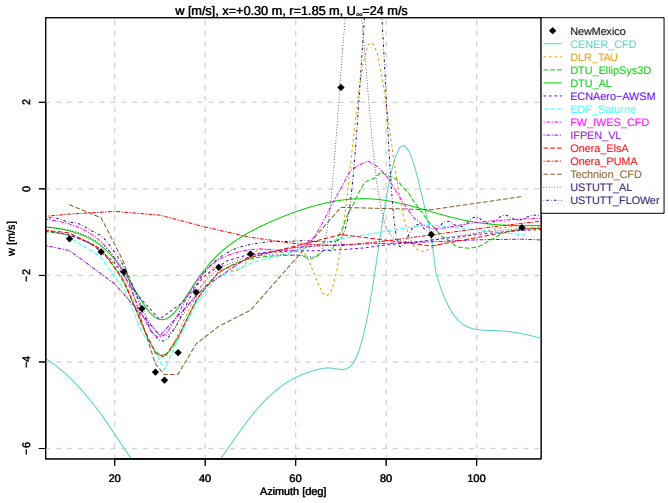

(d) w, x=+0.3 m, r=82%R

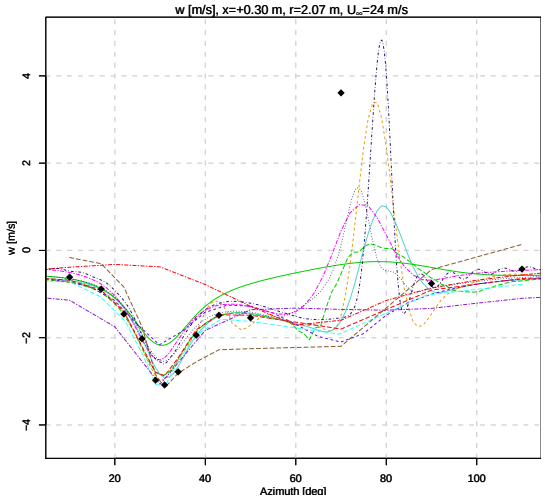

(e) w, x=+0.3 m, r=92%R

Figure A.39: Azimuth traverse of tangential velocity w at x=+0.3 m, Case 1.3

B. WP3 Comparison plots: Yawed flow

B.1 Lifting line codes

Lifting line variables

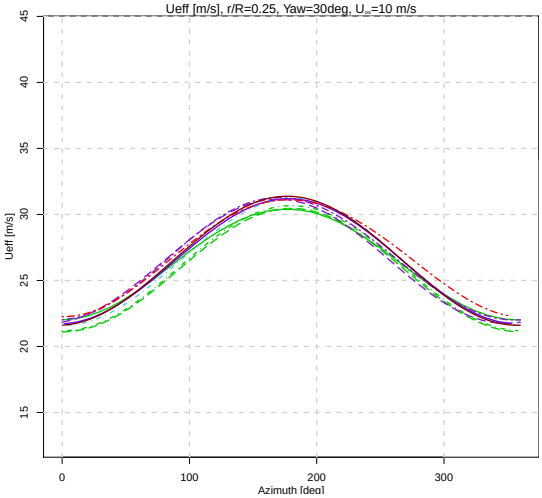

(a) Ueff, 25%R

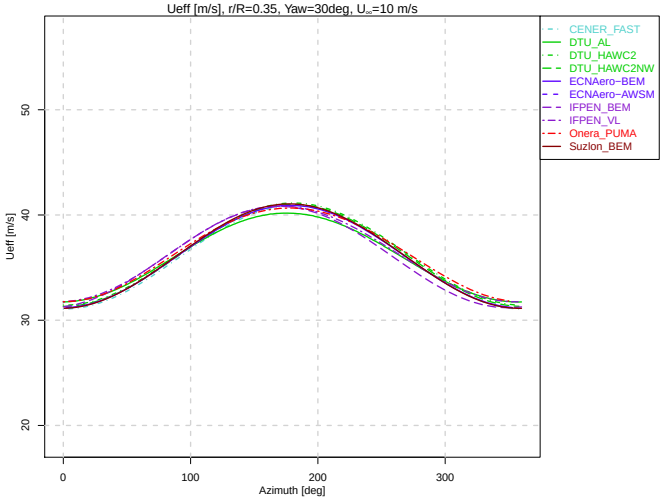

(b) Ueff, 35%R

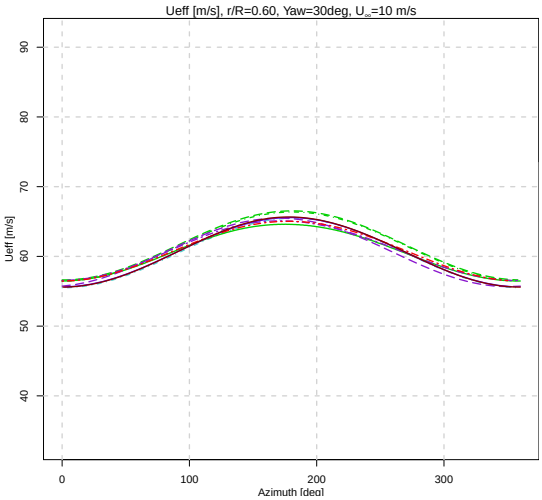

(c) Ueff, 60%R

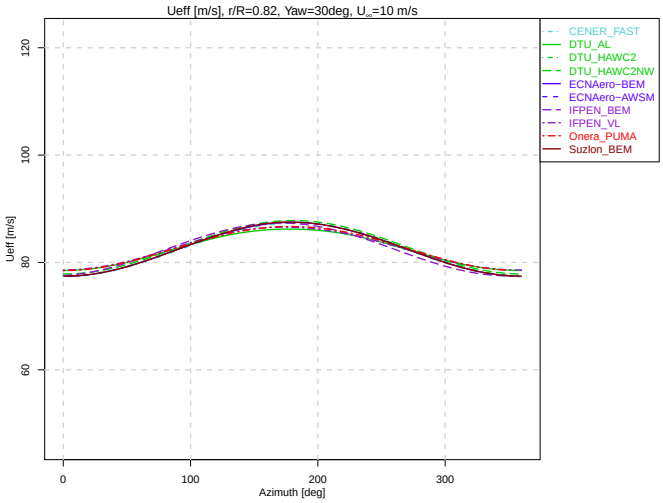

(d) Ueff, 82%R

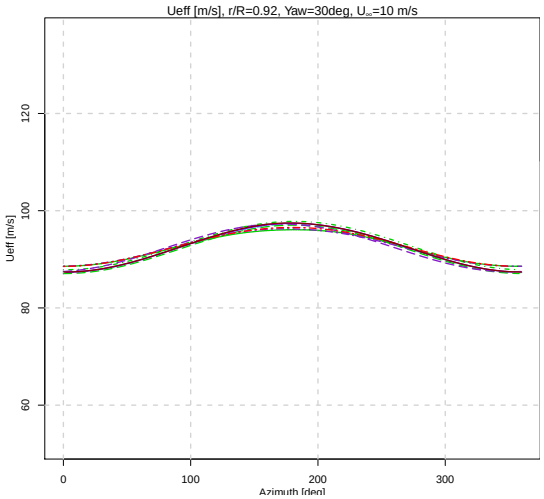

(e) Ueff, 92%R

Figure B.1: Ueff, Case 2.1

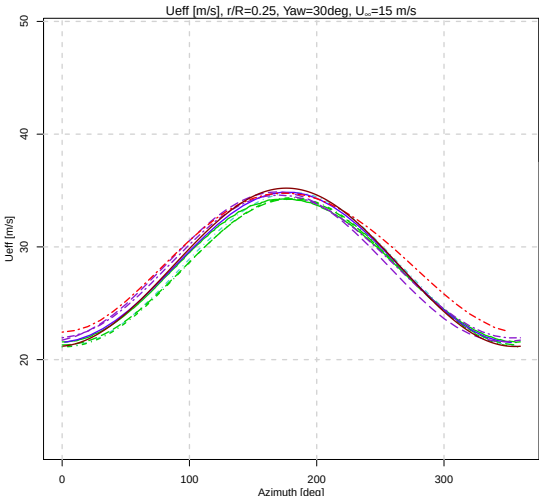

(a) Ueff, 25%R

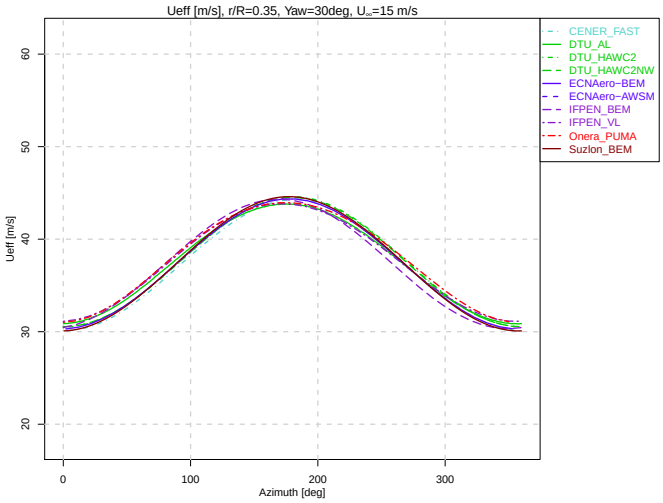

(b) Ueff, 35%R

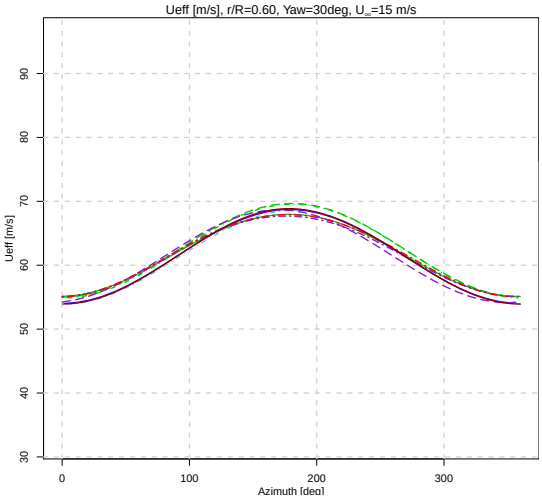

(c) Ueff, 60%R

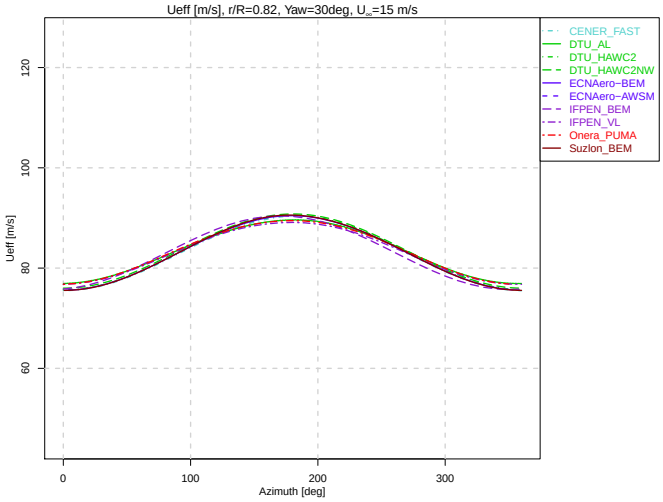

(d) Ueff, 82%R

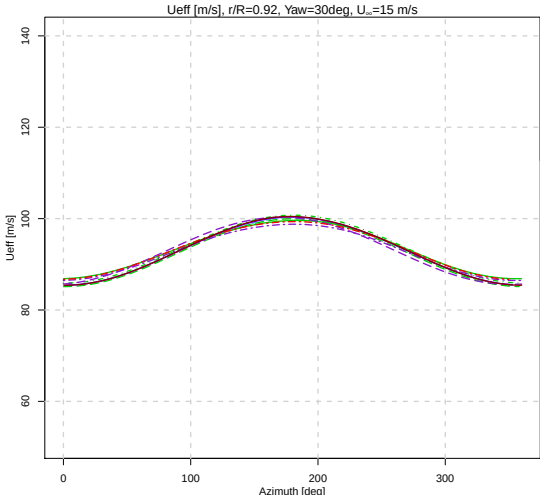

(e) Ueff, 92%R

Figure B.2: Ueff, Case 2.2

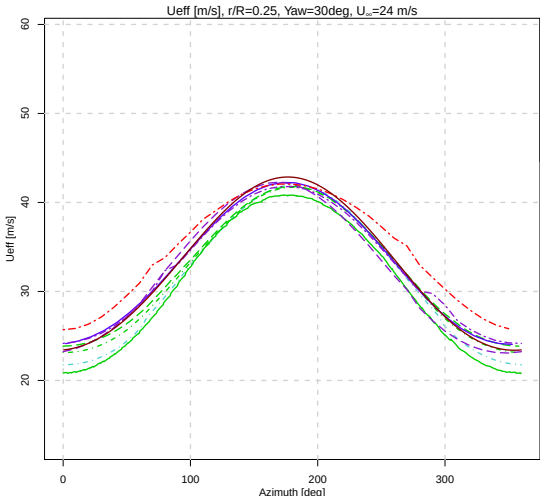

(a) Ueff, 25%R

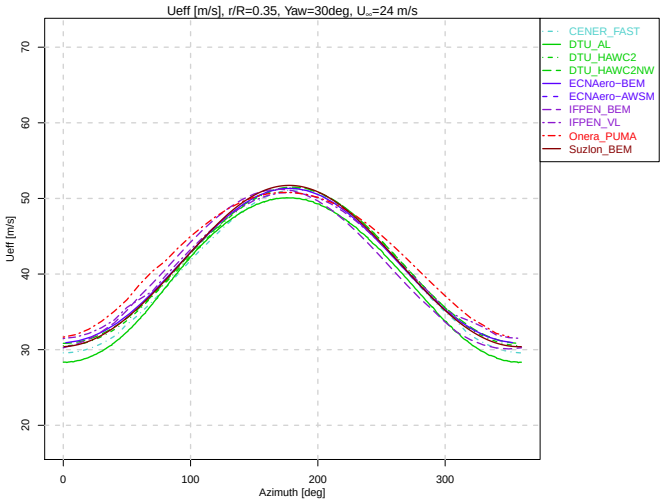

(b) Ueff, 35%R

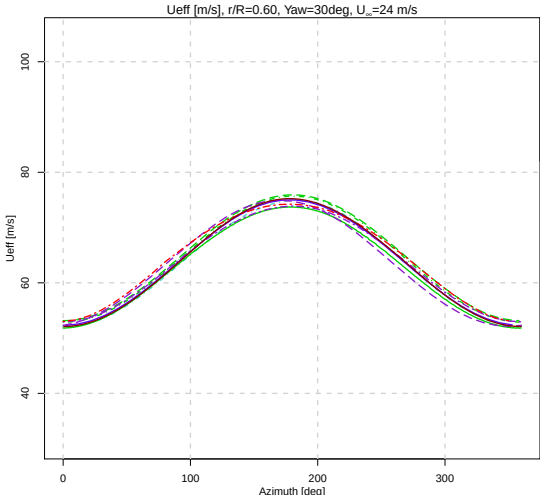

(c) Ueff, 60%R

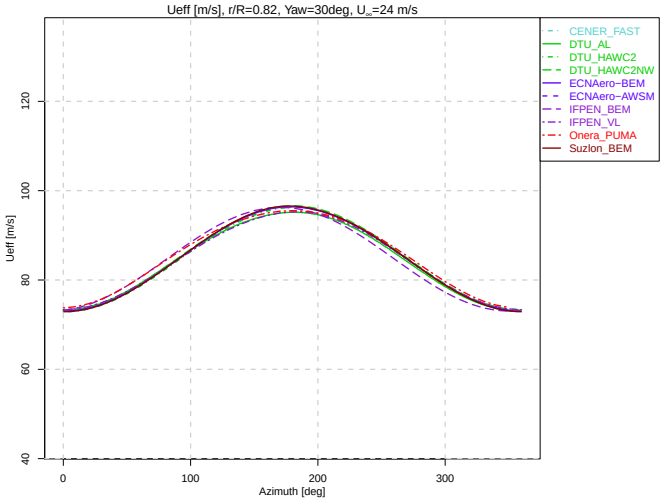

(d) Ueff, 82%R

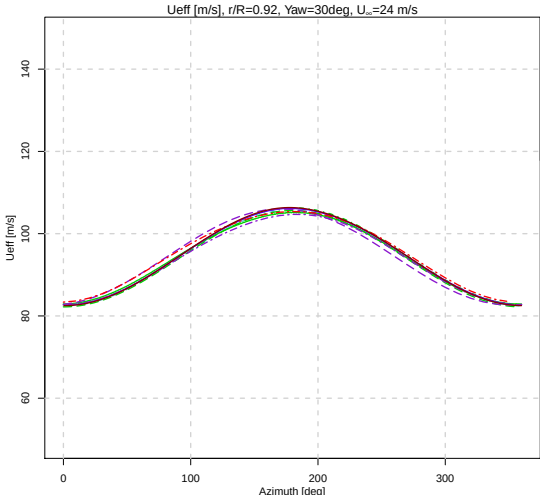

(e) Ueff, 92%R

Figure B.3: Ueff, Case 2.3

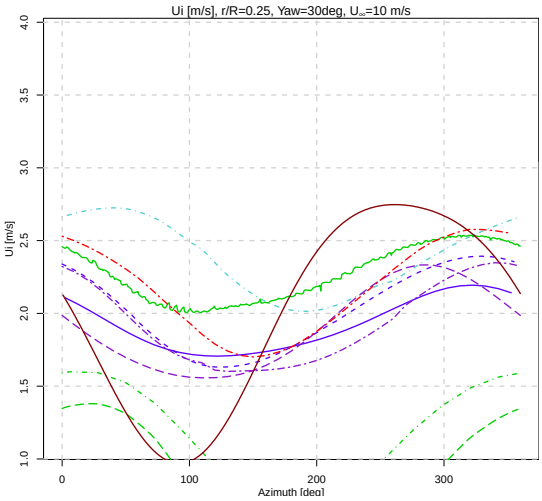

(a) Ui, 25%R

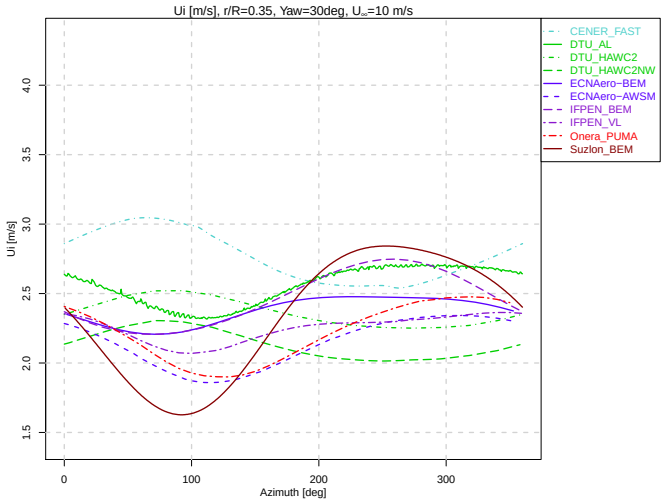

(b) Ui, 35%R

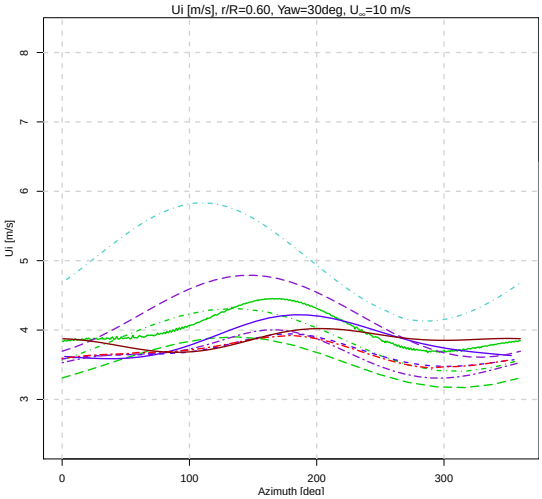

(c) Ui, 60%R

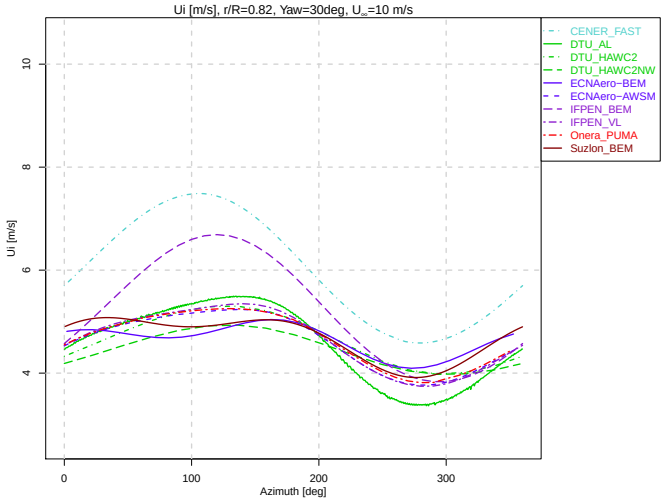

(d) Ui, 82%R

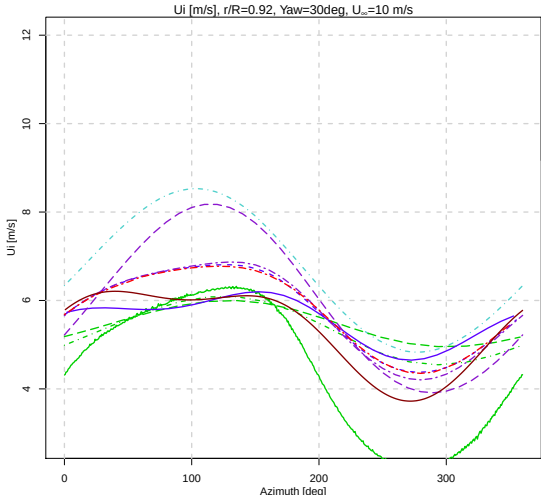

(e) Ui, 92%R

Figure B.4: Ui, Case 2.1

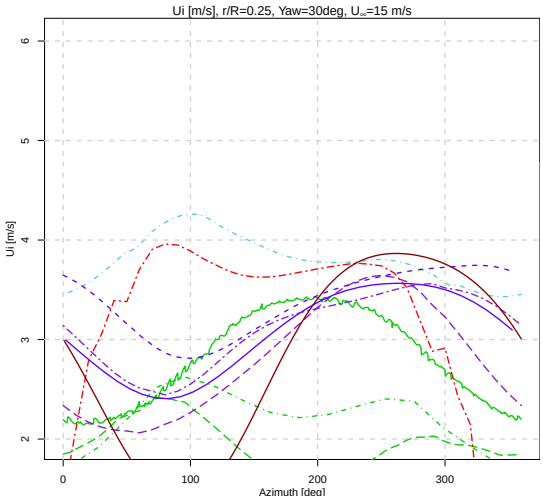

(a) Ui, 25%R

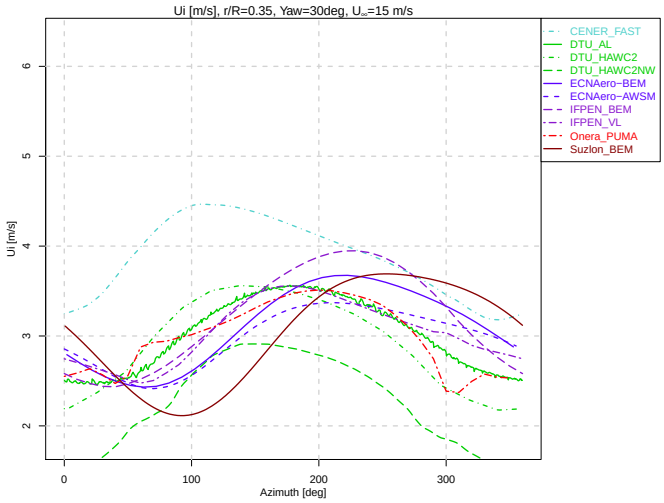

(b) Ui, 35%R

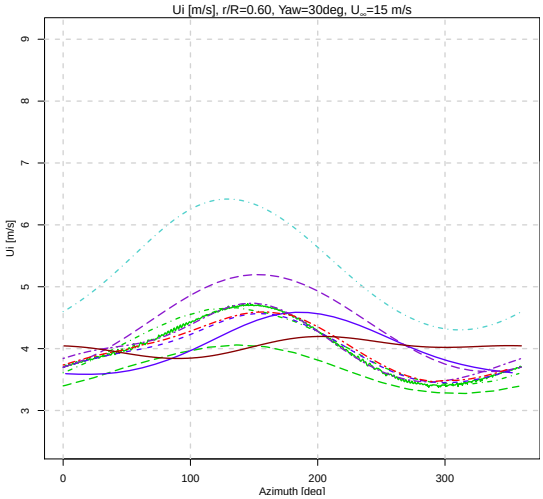

(c) Ui, 60%R

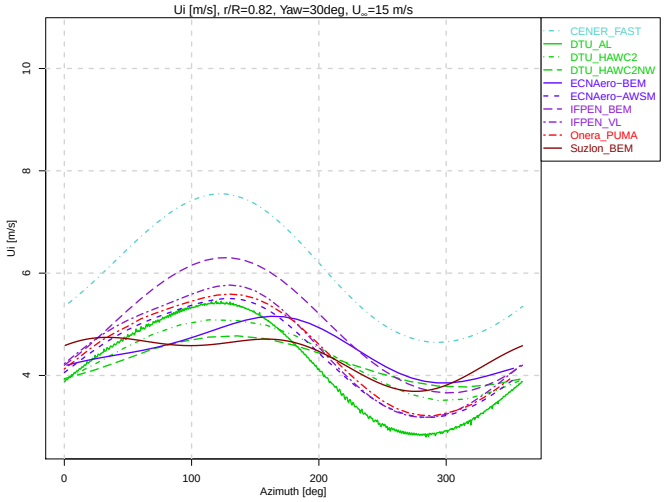

(d) Ui, 82%R

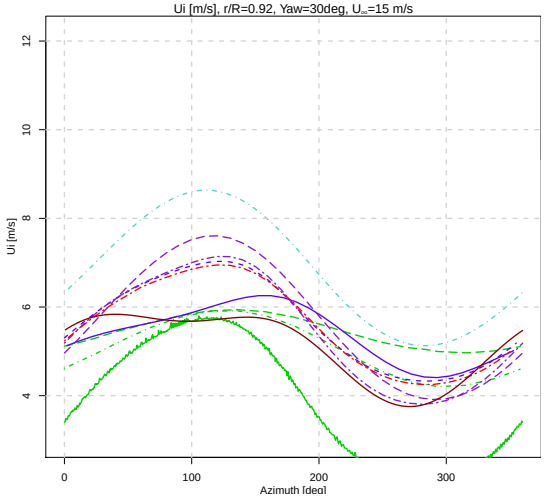

(e) Ui, 92%R

Figure B.5: Ui, Case 2.2

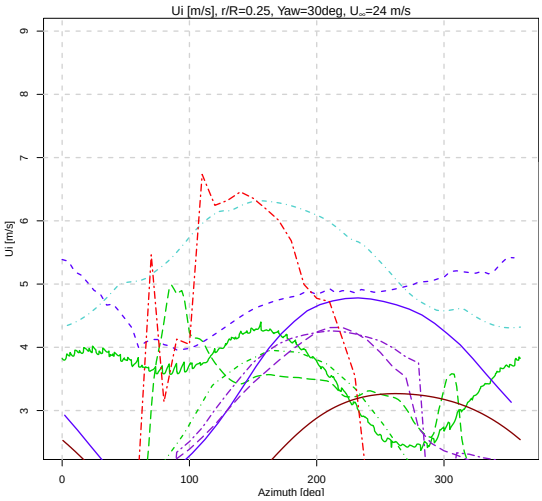

(a) Ui, 25%R

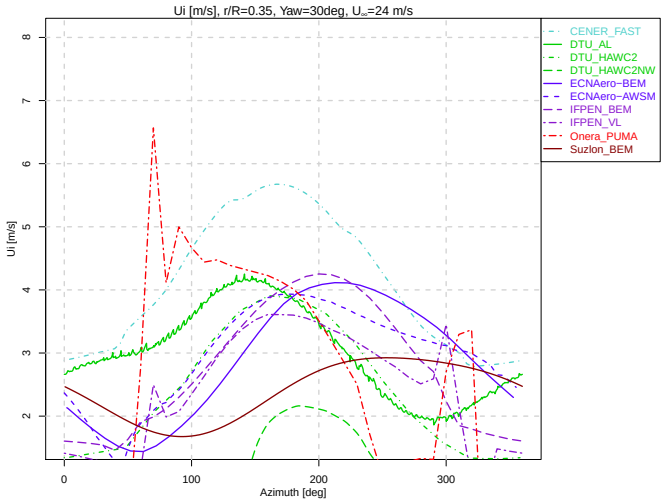

(b) Ui, 35%R

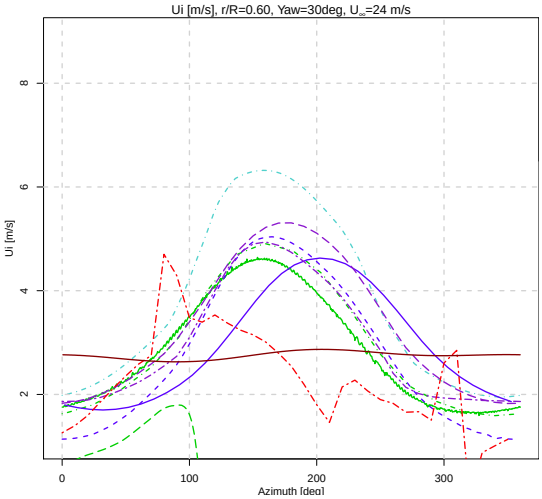

(c) Ui, 60%R

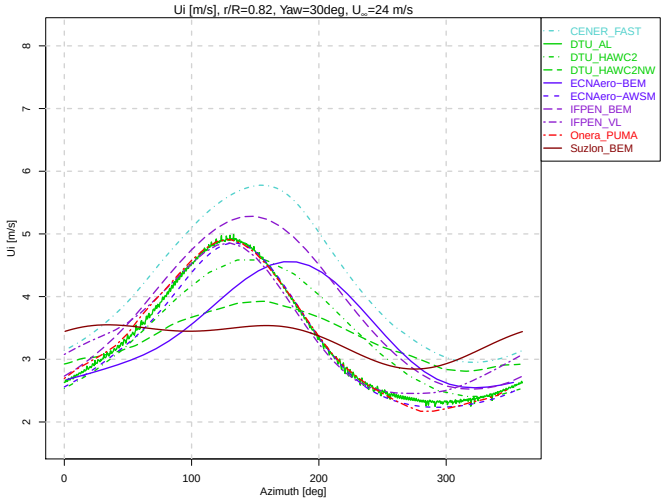

(d) Ui, 82%R

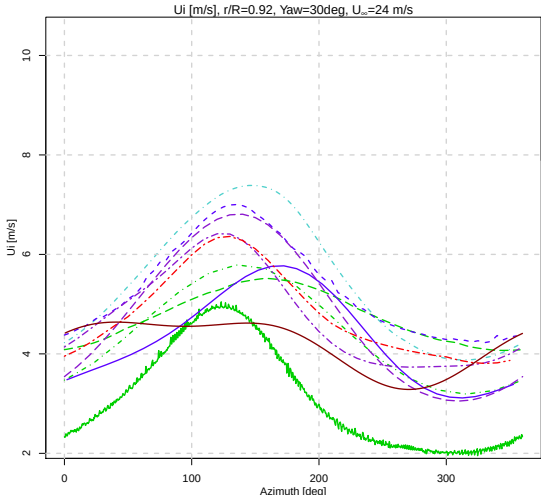

(e) Ui, 92%R

Figure B.6: Ui, Case 2.3

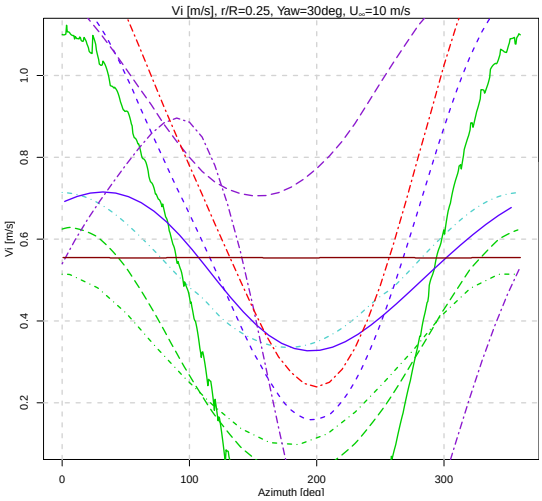

(a) Vi, 25%R

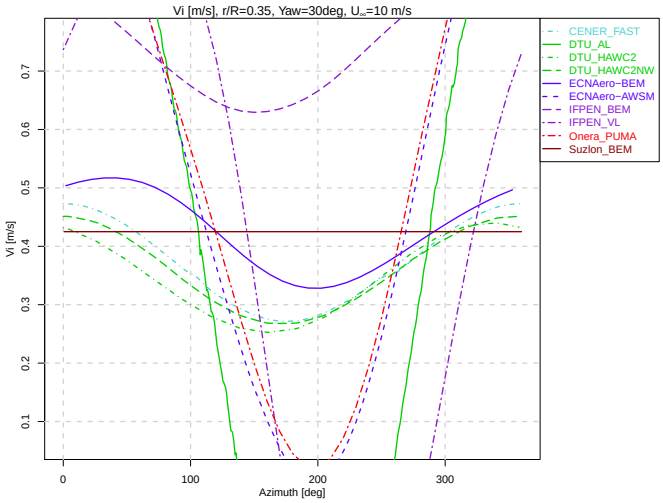

(b) Vi, 35%R

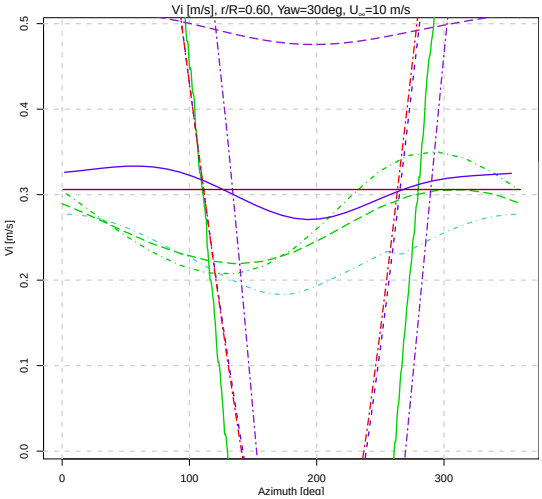

(c) Vi, 60%R

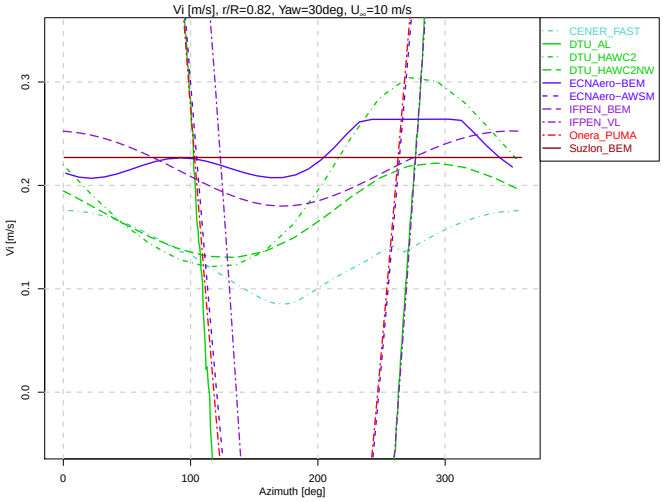

(d) Vi, 82%R

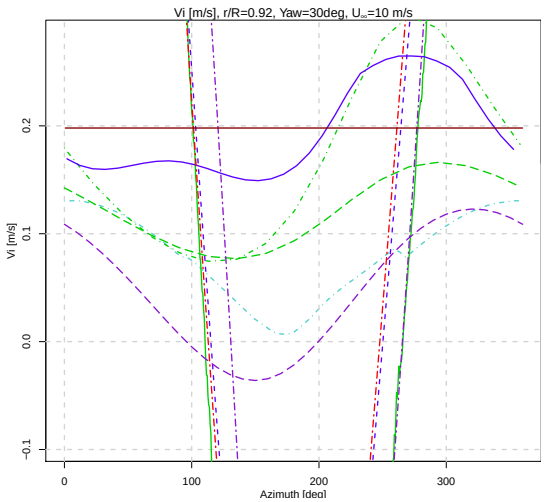

(e) Vi, 92%R

Figure B.7: Vi, Case 2.1

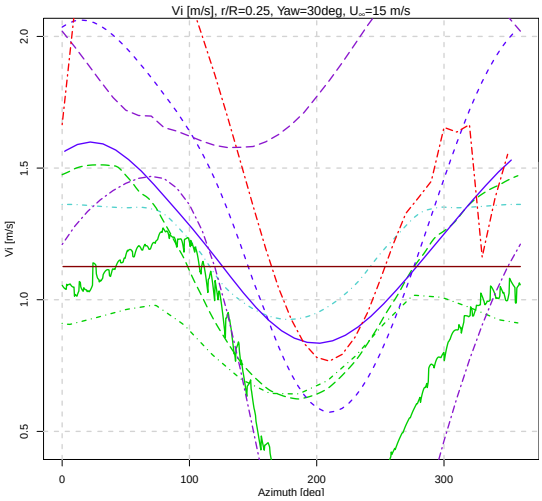

(a) Vi, 25%R

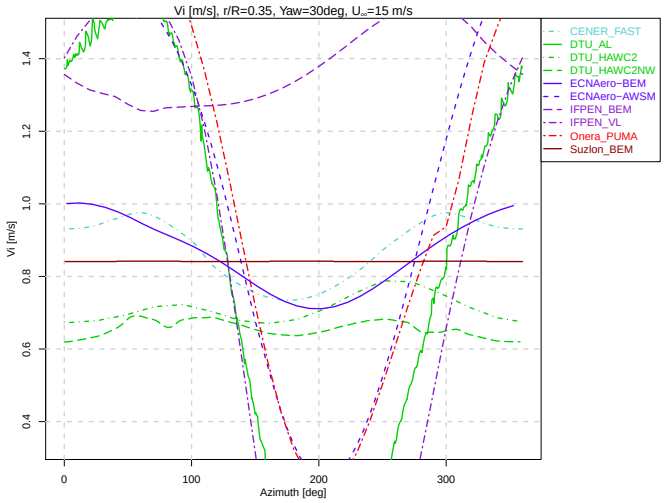

(b) Vi, 35%R

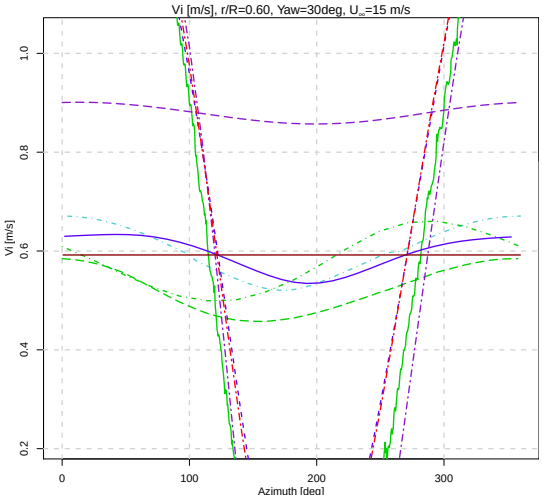

(c) Vi, 60%R

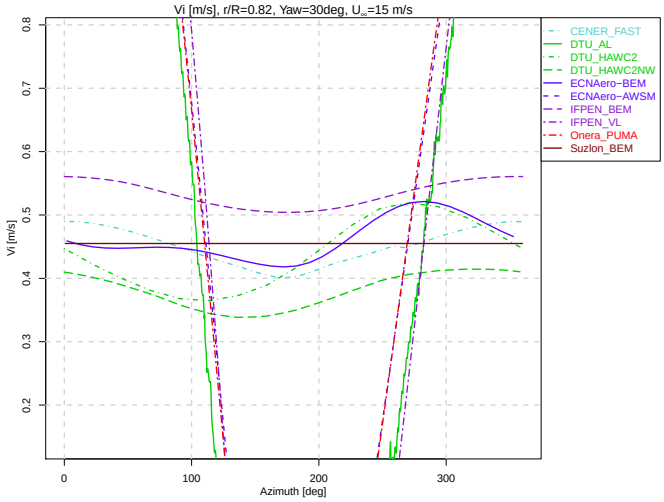

(d) Vi, 82%R

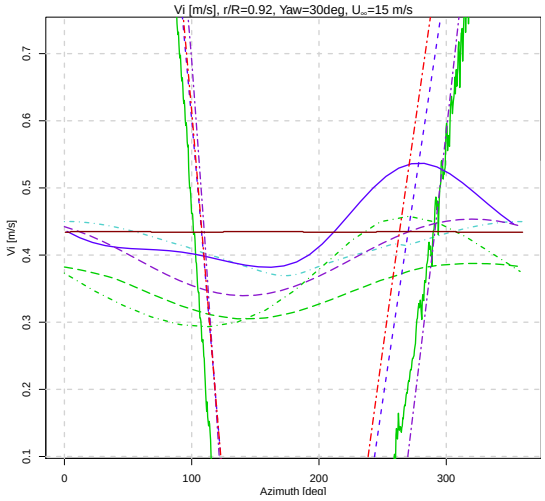

(e) Vi, 92%R

Figure B.8: Vi, Case 2.2

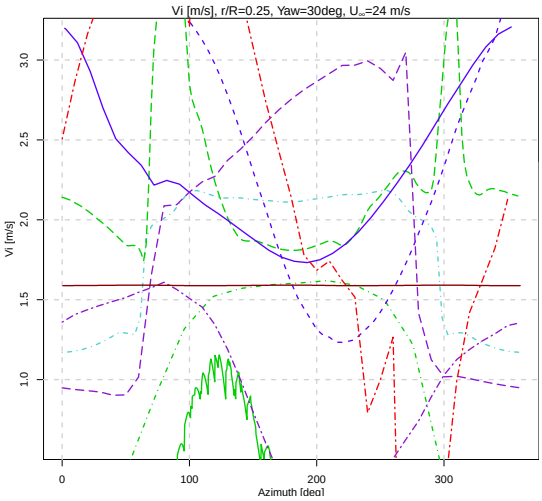

(a) Vi, 25%R

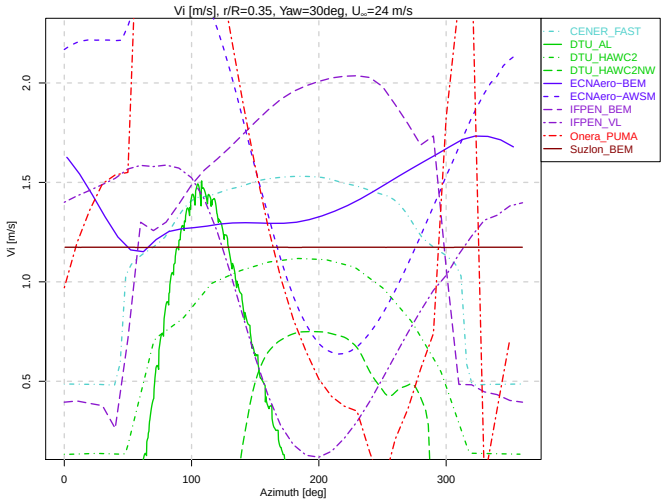

(b) Vi, 35%R

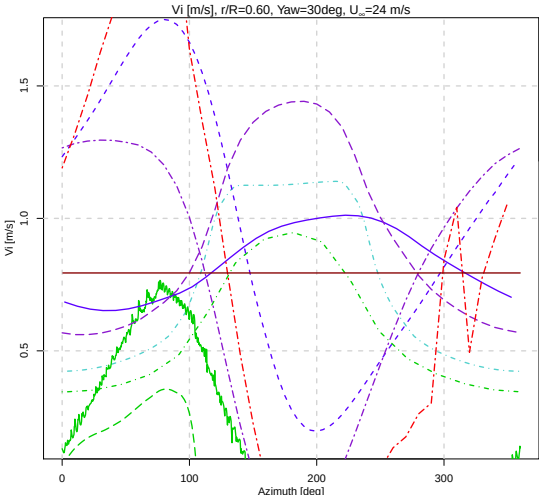

(c) Vi, 60%R

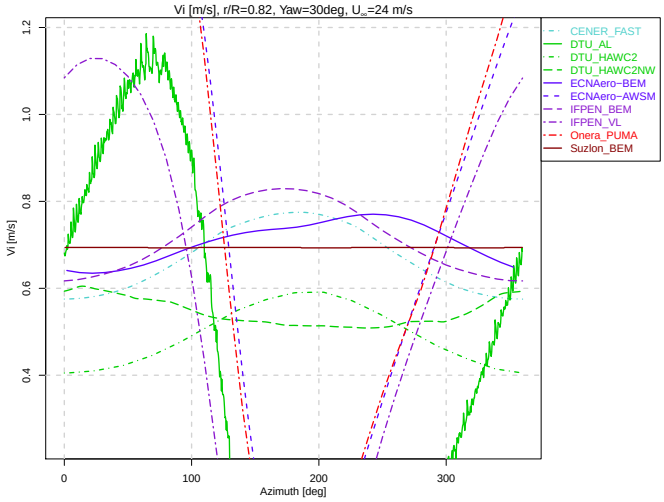

(d) Vi, 82%R

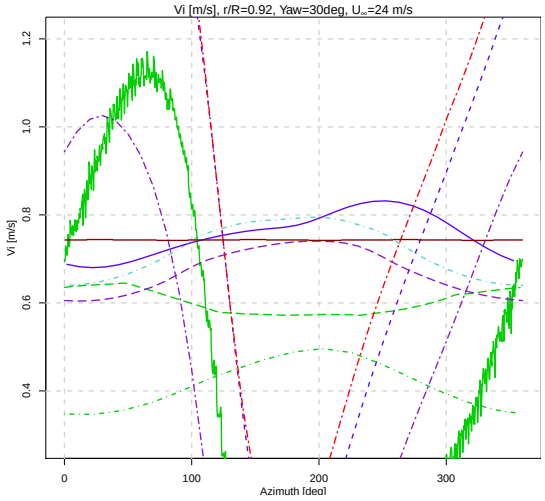

(e) Vi, 92%R

Figure B.9: Vi, Case 2.3

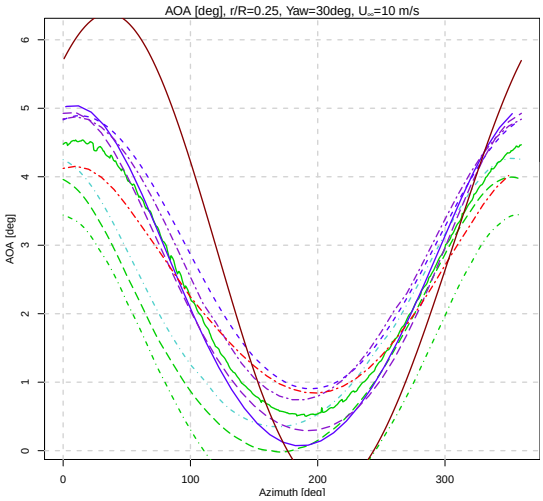

(a) AOA, 25%R

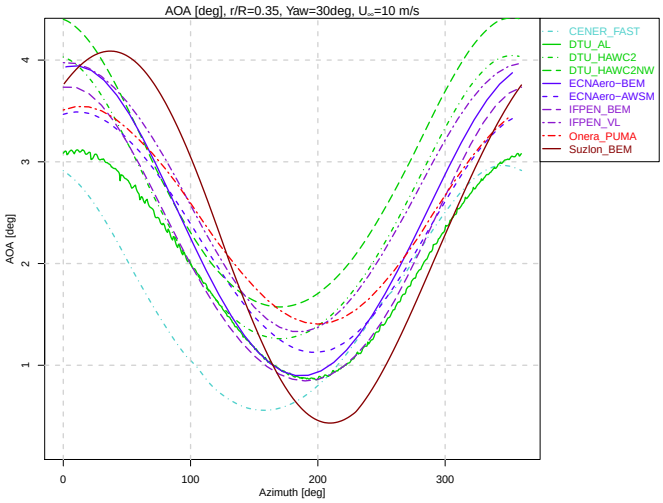

(b) AOA, 35%R

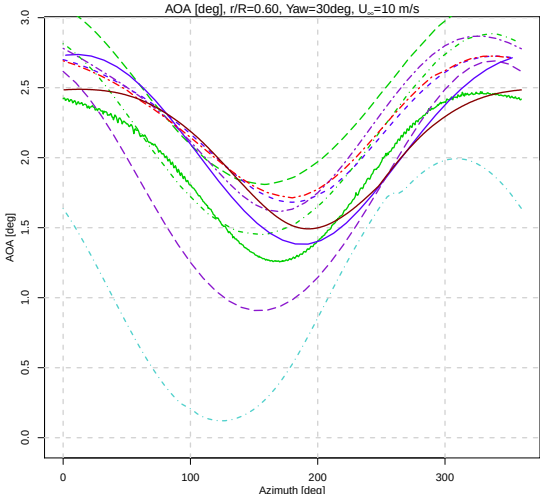

(c) AOA, 60%R

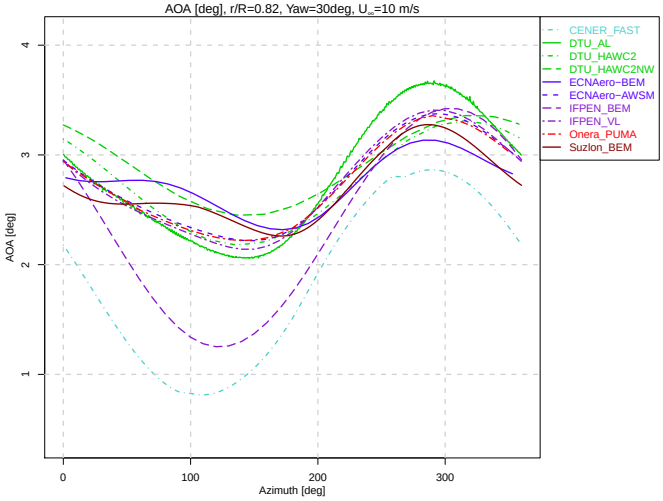

(d) AOA, 82%R

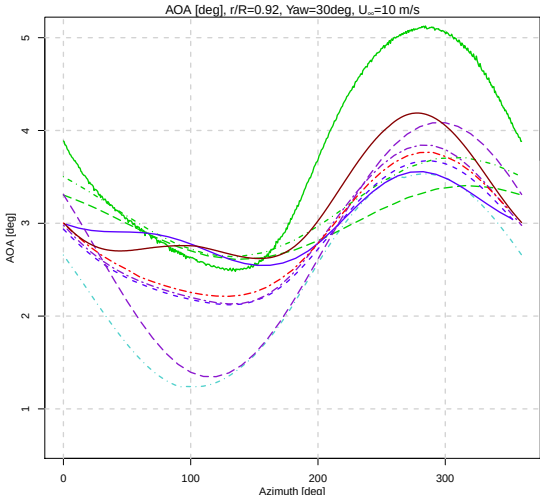

(e) AOA, 92%R

Figure B.10: AOA, Case 2.1

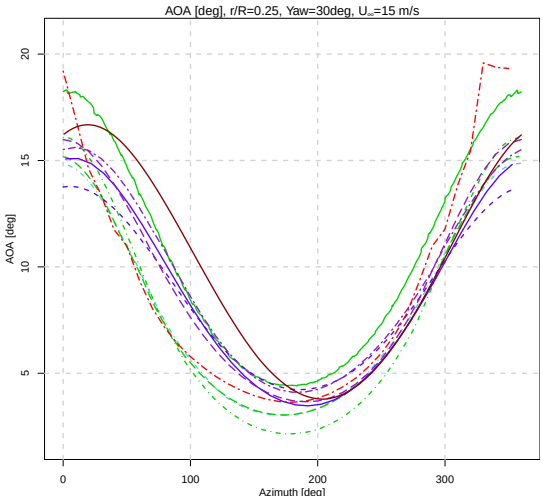

(a) AOA, 25%R

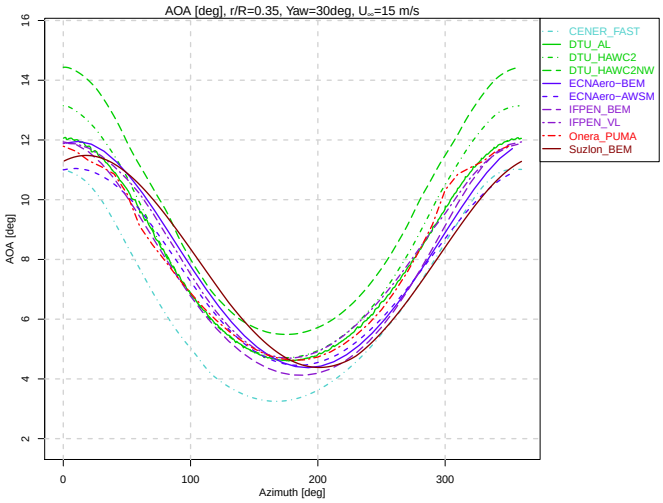

(b) AOA, 35%R

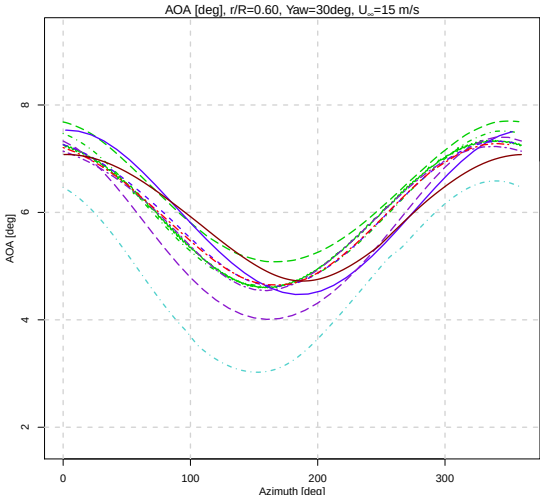

(c) AOA, 60%R

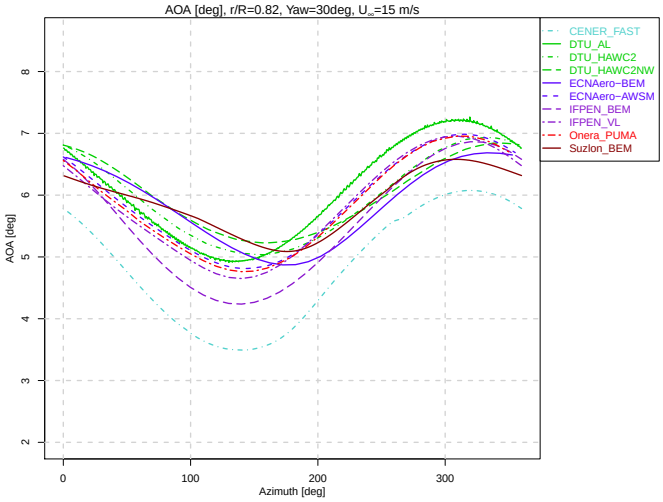

(d) AOA, 82%R

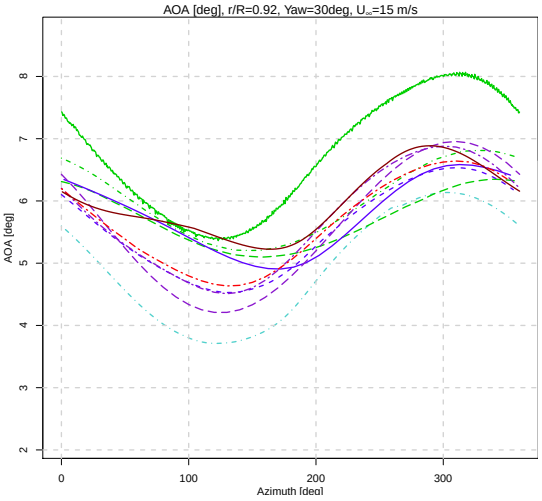

(e) AOA, 92%R

Figure B.11: AOA, Case 2.2

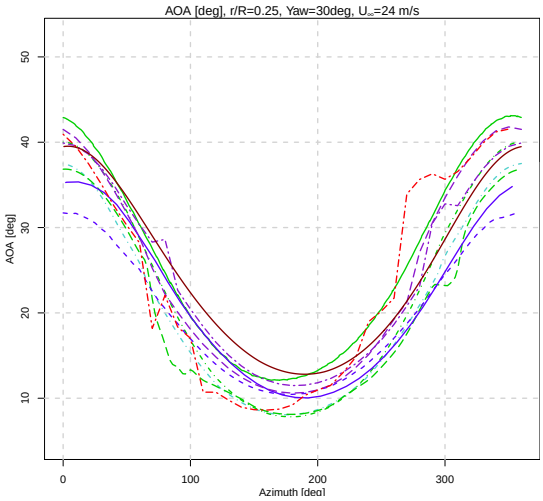

(a) AOA, 25%R

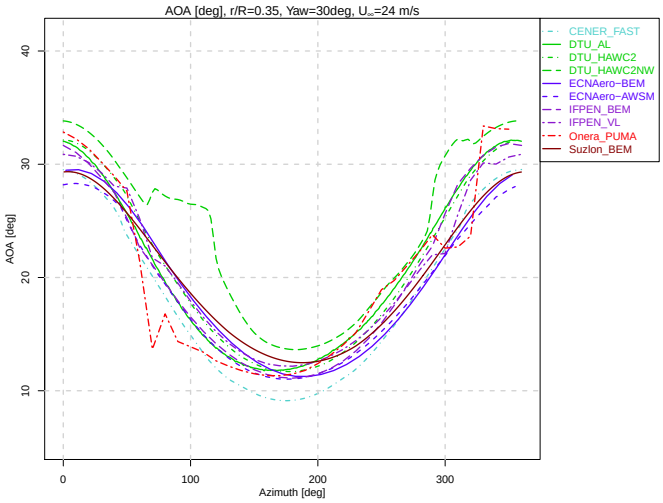

(b) AOA, 35%R

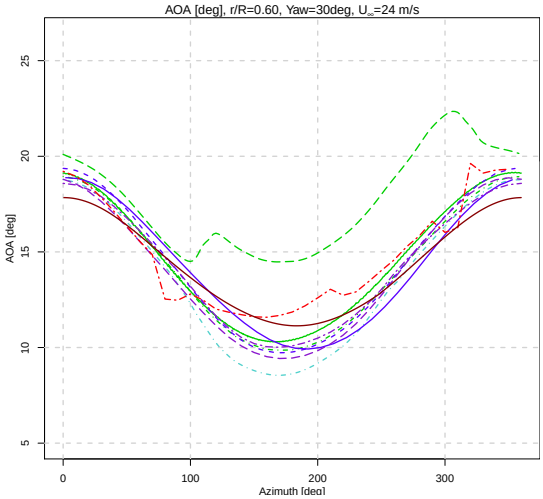

(c) AOA, 60%R

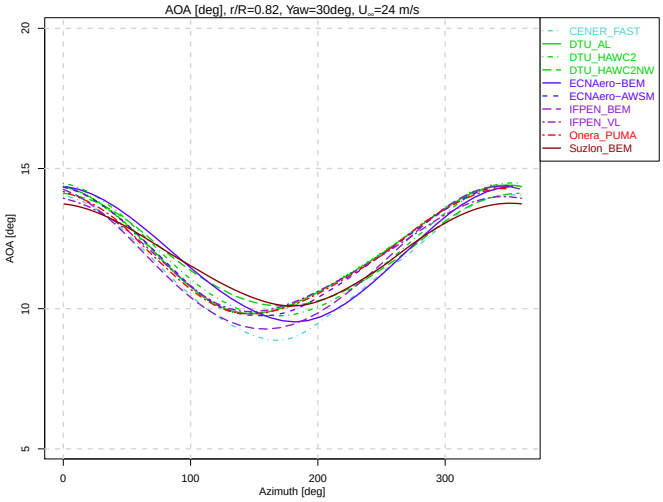

(d) AOA, 82%R

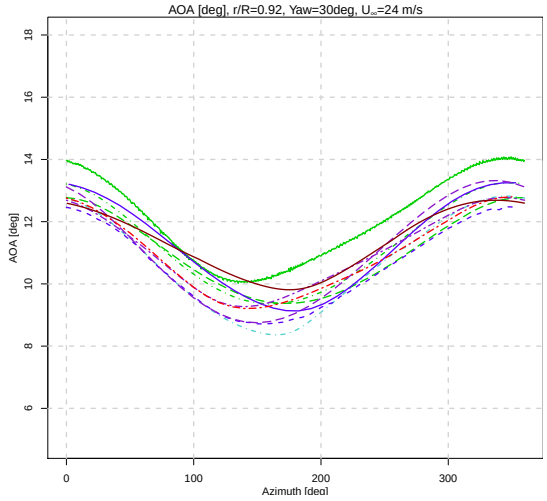

(e) AOA, 92%R

Figure B.12: AOA, Case 2.3

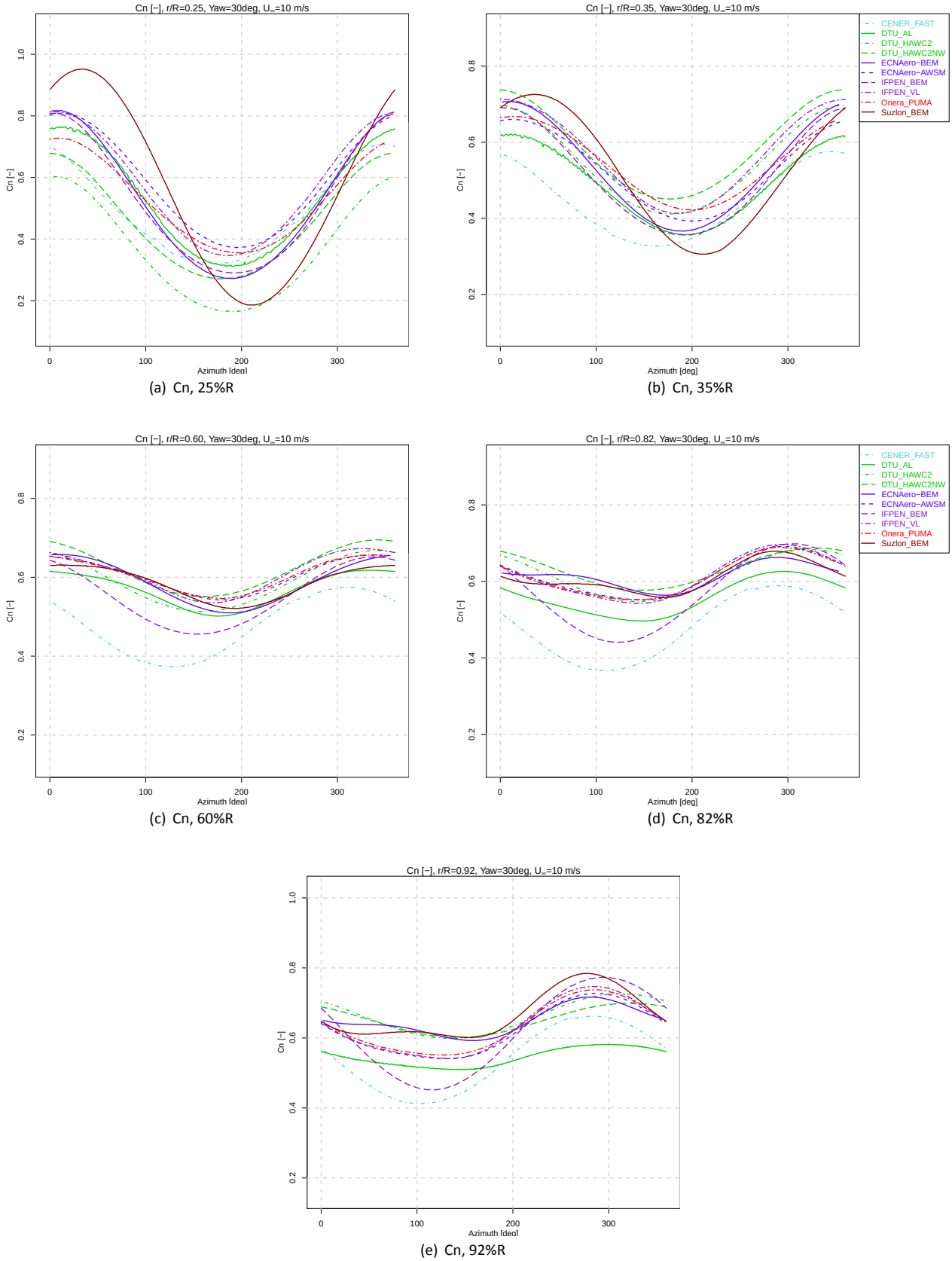

(a) Cn, 25%R

(b) Cn, 35%R

(c) Cn, 60%R

(d) Cn, 82%R

(e) Cn, 92%R

Figure B.13: Cn, Case 2.1

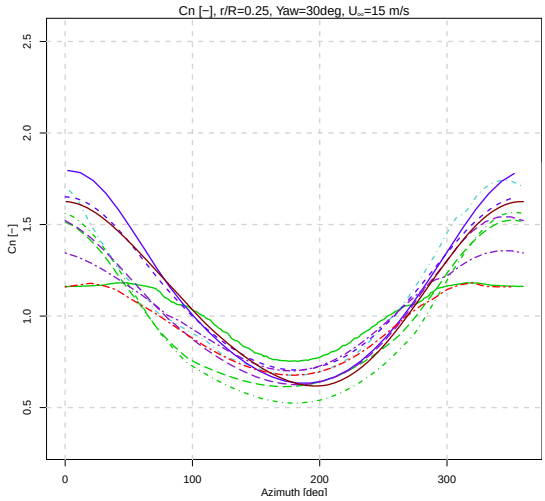

(a) Cn, 25%R

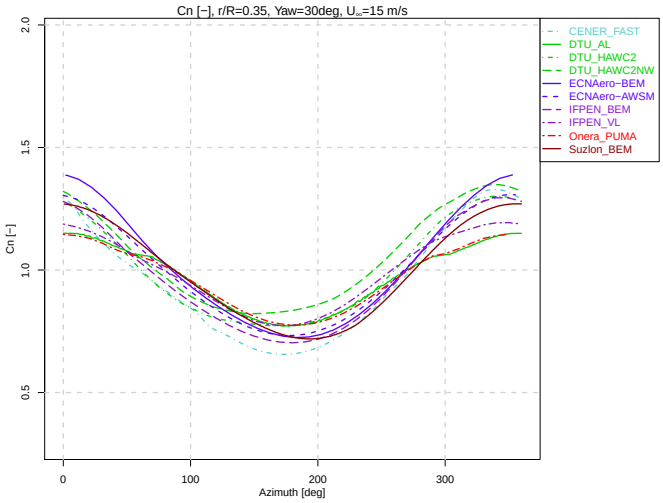

(b) Cn, 35%R

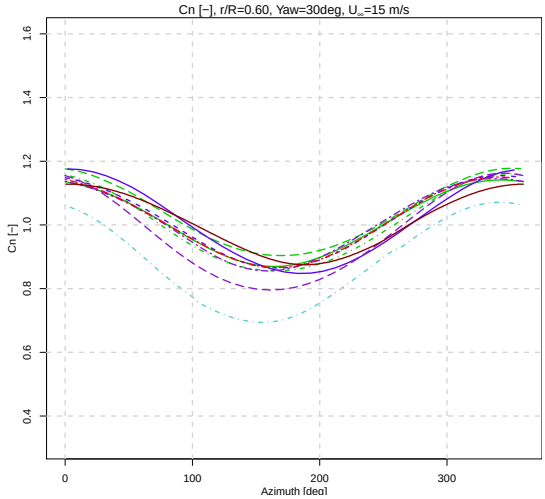

(c) Cn, 60%R

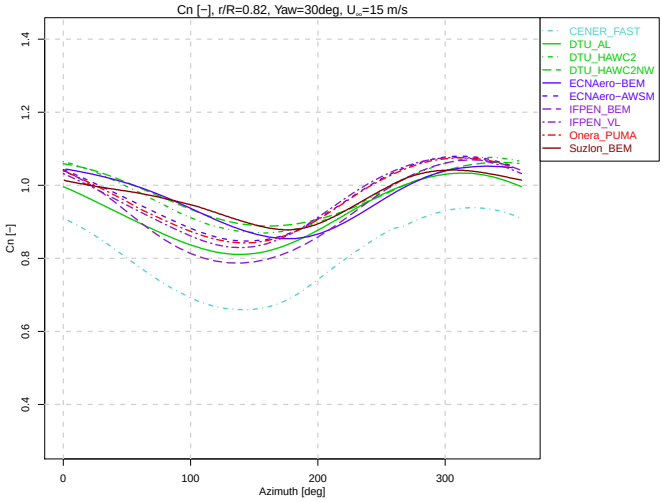

(d) Cn, 82%R

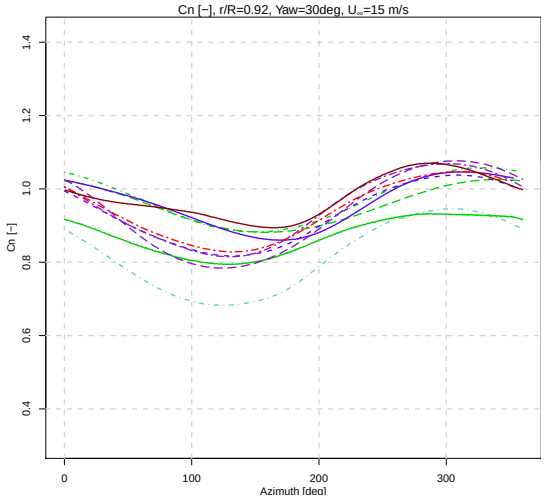

(e) Cn, 92%R

Figure B.14: Cn, Case 2.2

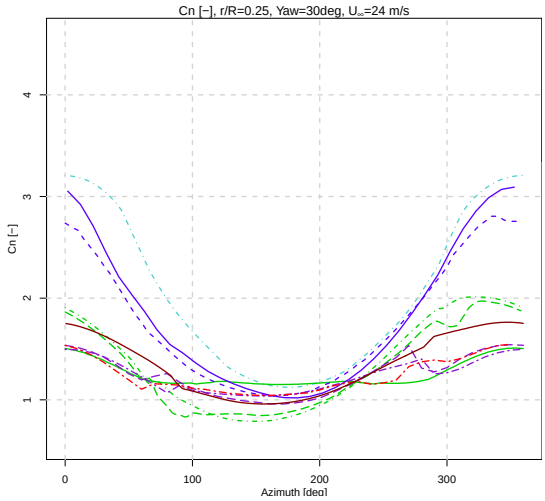

(a) Cn, 25%R

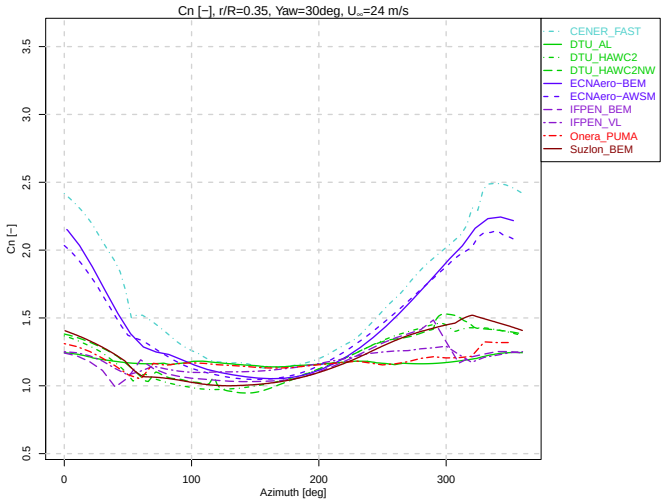

(b) Cn, 35%R

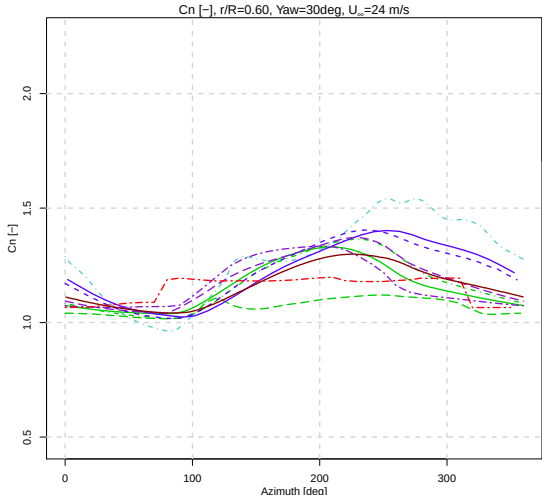

(c) Cn, 60%R

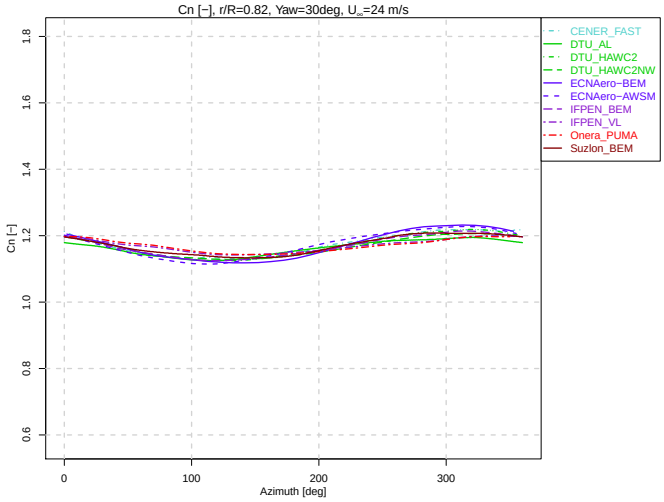

(d) Cn, 82%R

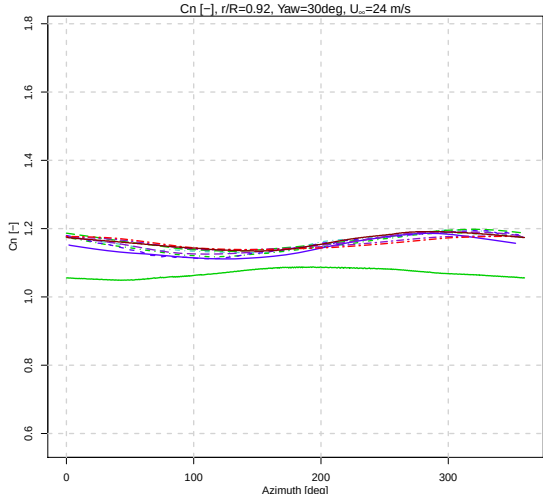

(e) Cn, 92%R

Figure B.15: Cn, Case 2.3

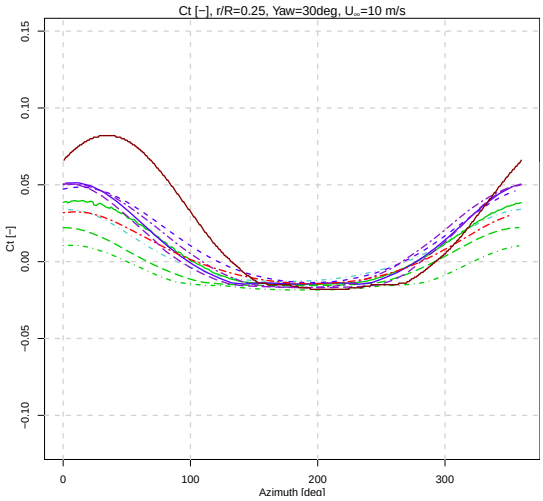

(a) Ct, 25%R

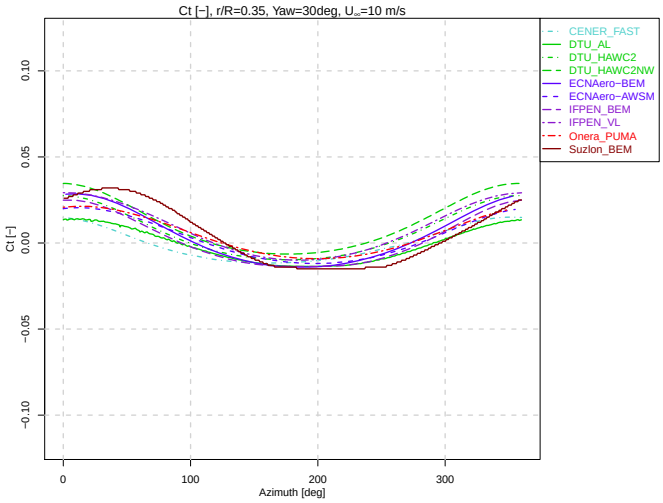

(b) Ct, 35%R

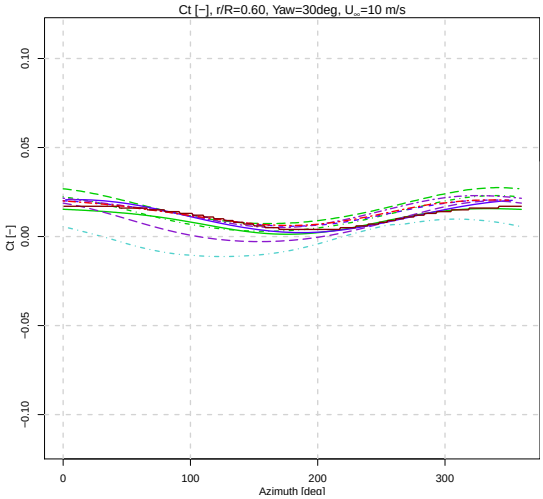

(c) Ct, 60%R

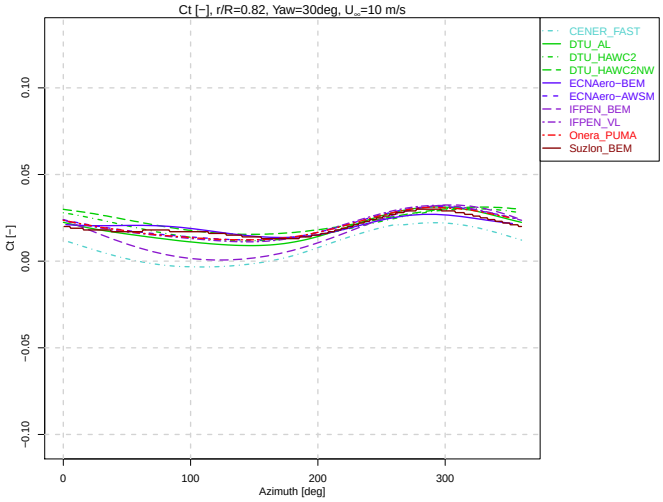

(d) Ct, 82%R

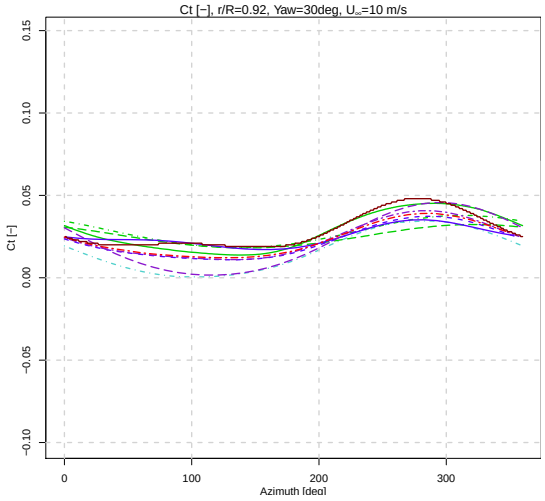

(e) Ct, 92%R

Figure B.16: Ct, Case 2.1

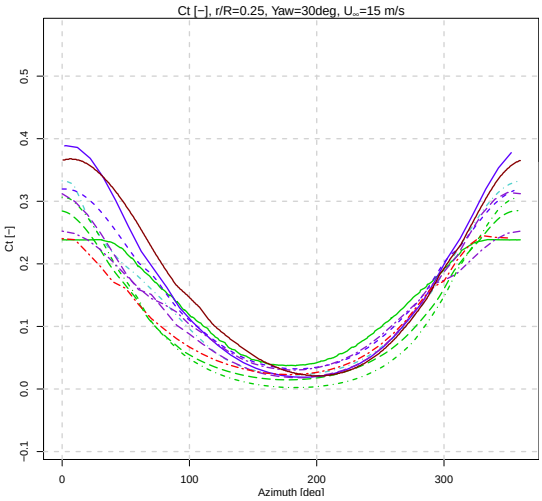

(a) Ct, 25%R

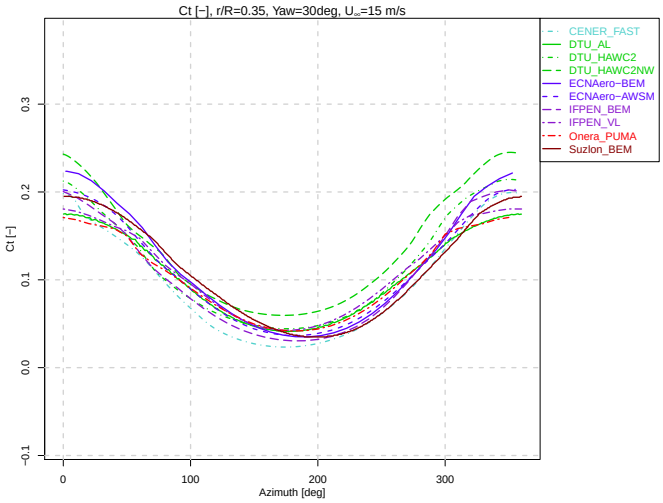

(b) Ct, 35%R

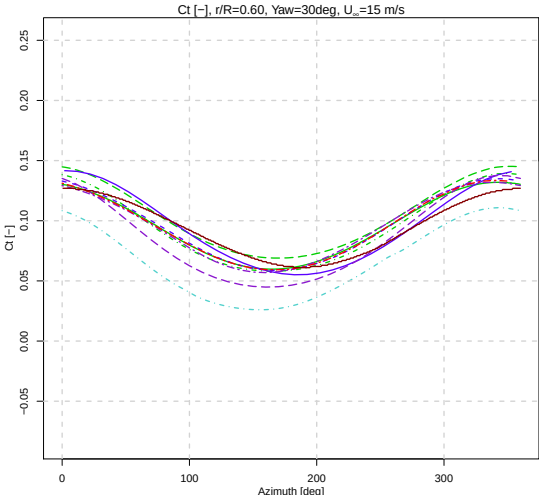

(c) Ct, 60%R

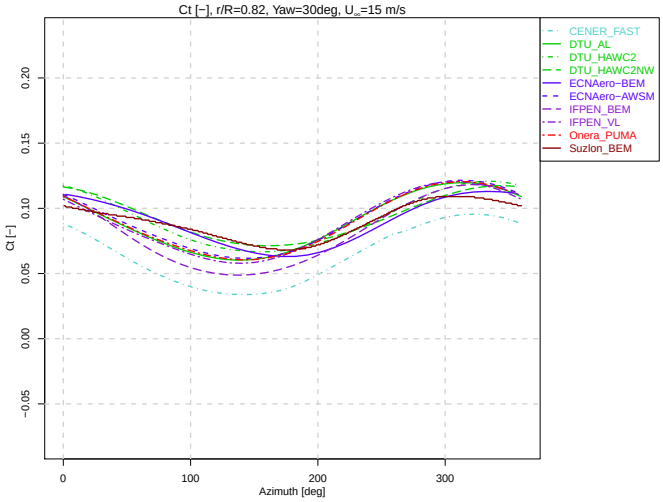

(d) Ct, 82%R

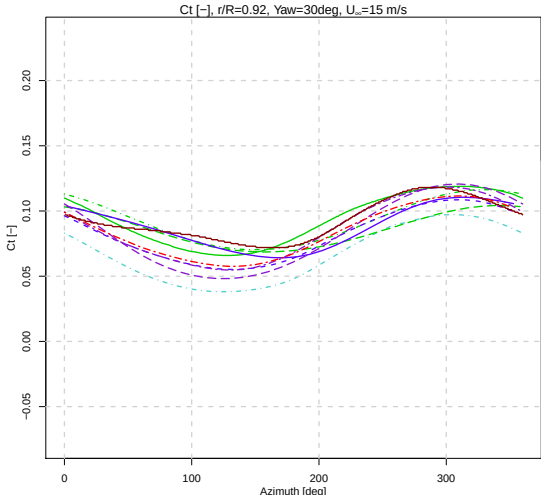

(e) Ct, 92%R

Figure B.17: Ct, Case 2.2

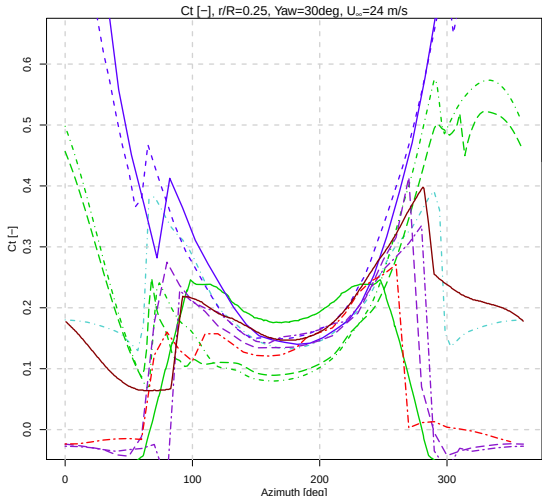

(a) Ct, 25%R

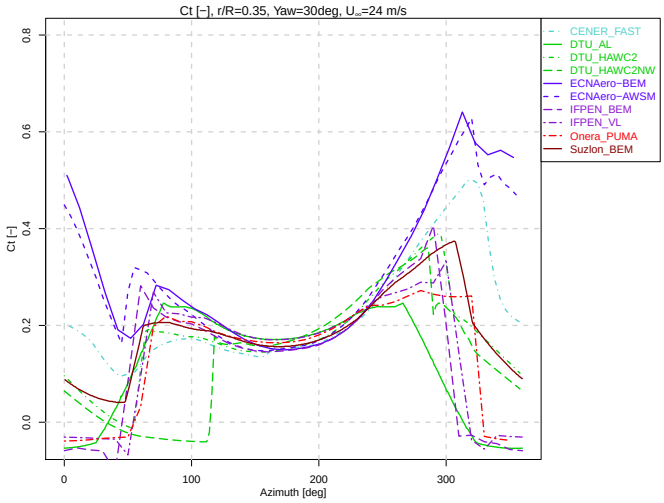

(b) Ct, 35%R

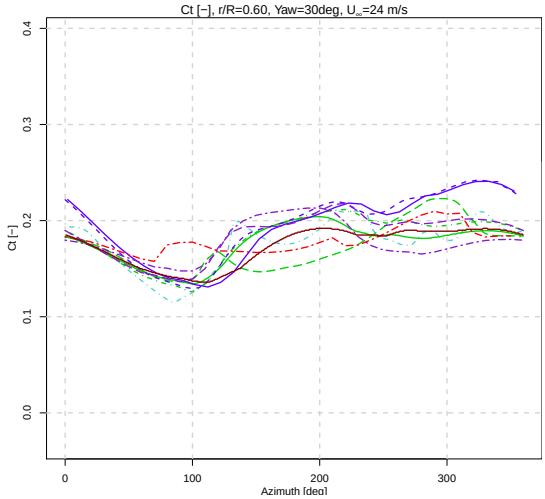

(c) Ct, 60%R

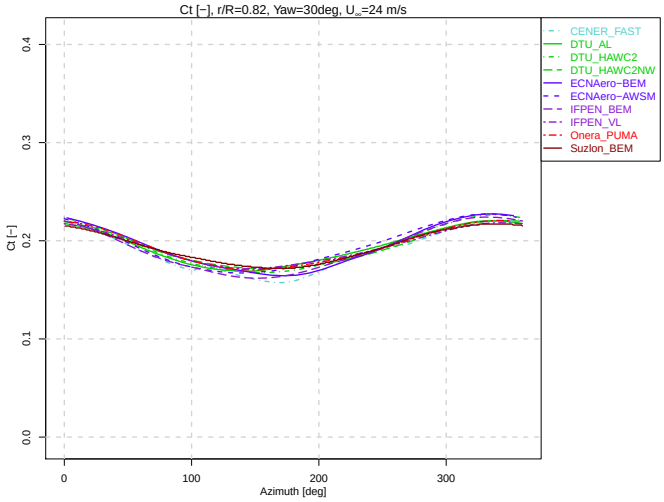

(d) Ct, 82%R

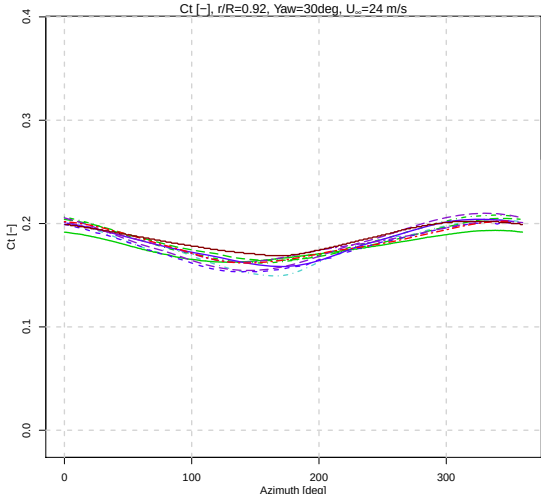

(e) Ct, 92%R

Figure B.18: Ct, Case 2.3

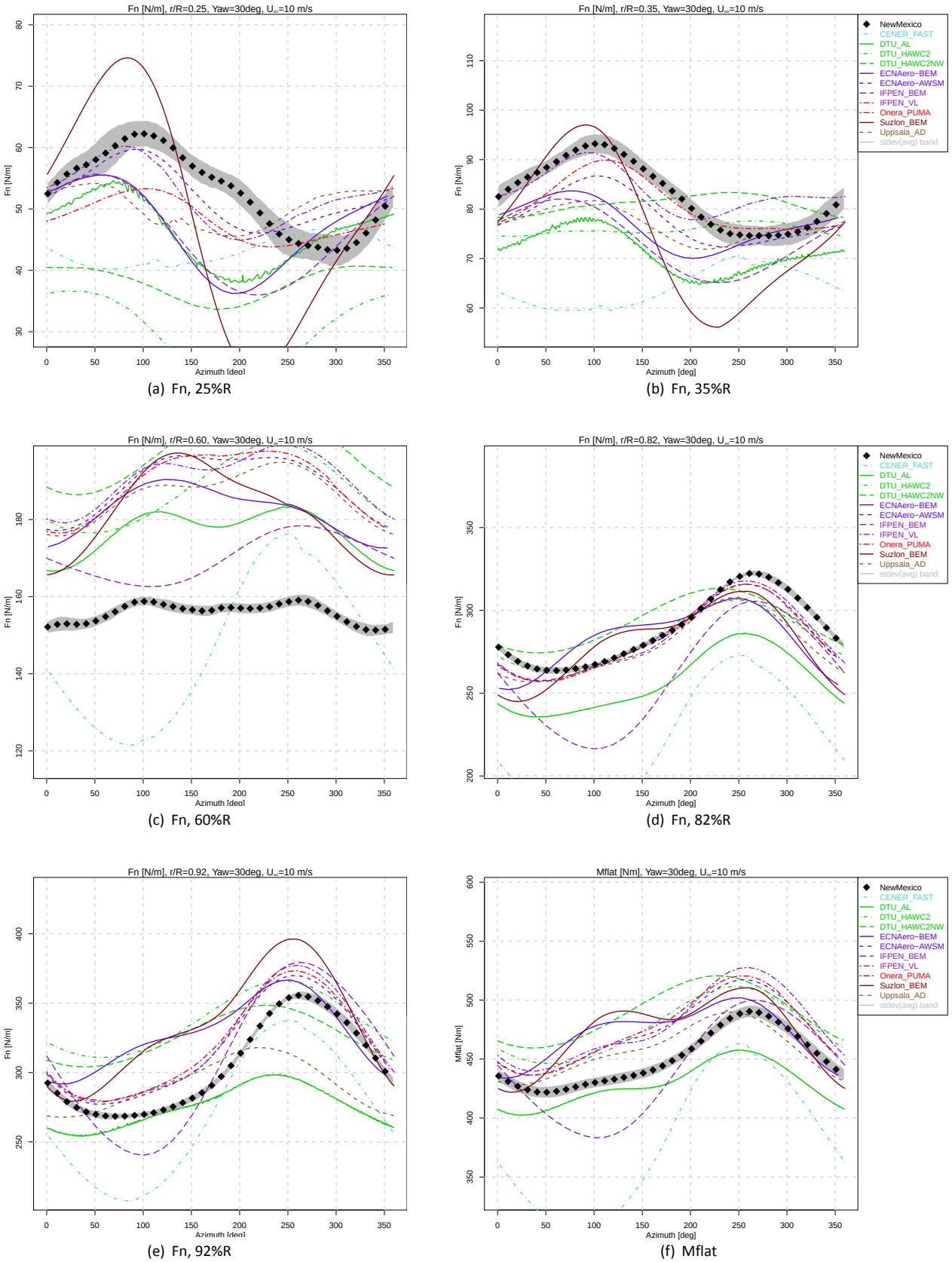

Figure B.19: Chord normal force and flatwise blade root moment, Case 2.1

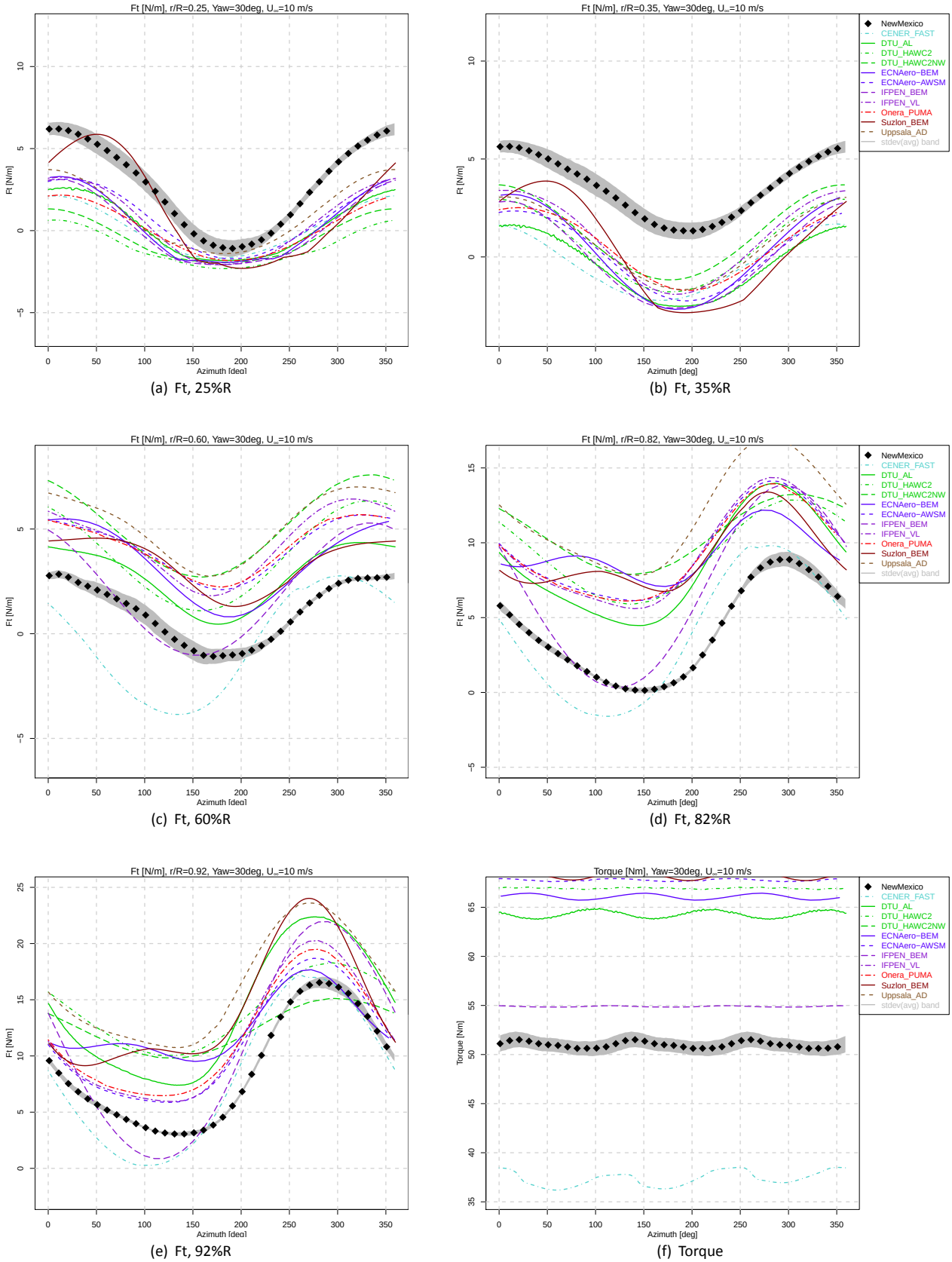

Figure B.20: Chord tangential force and torque, Case 2.1

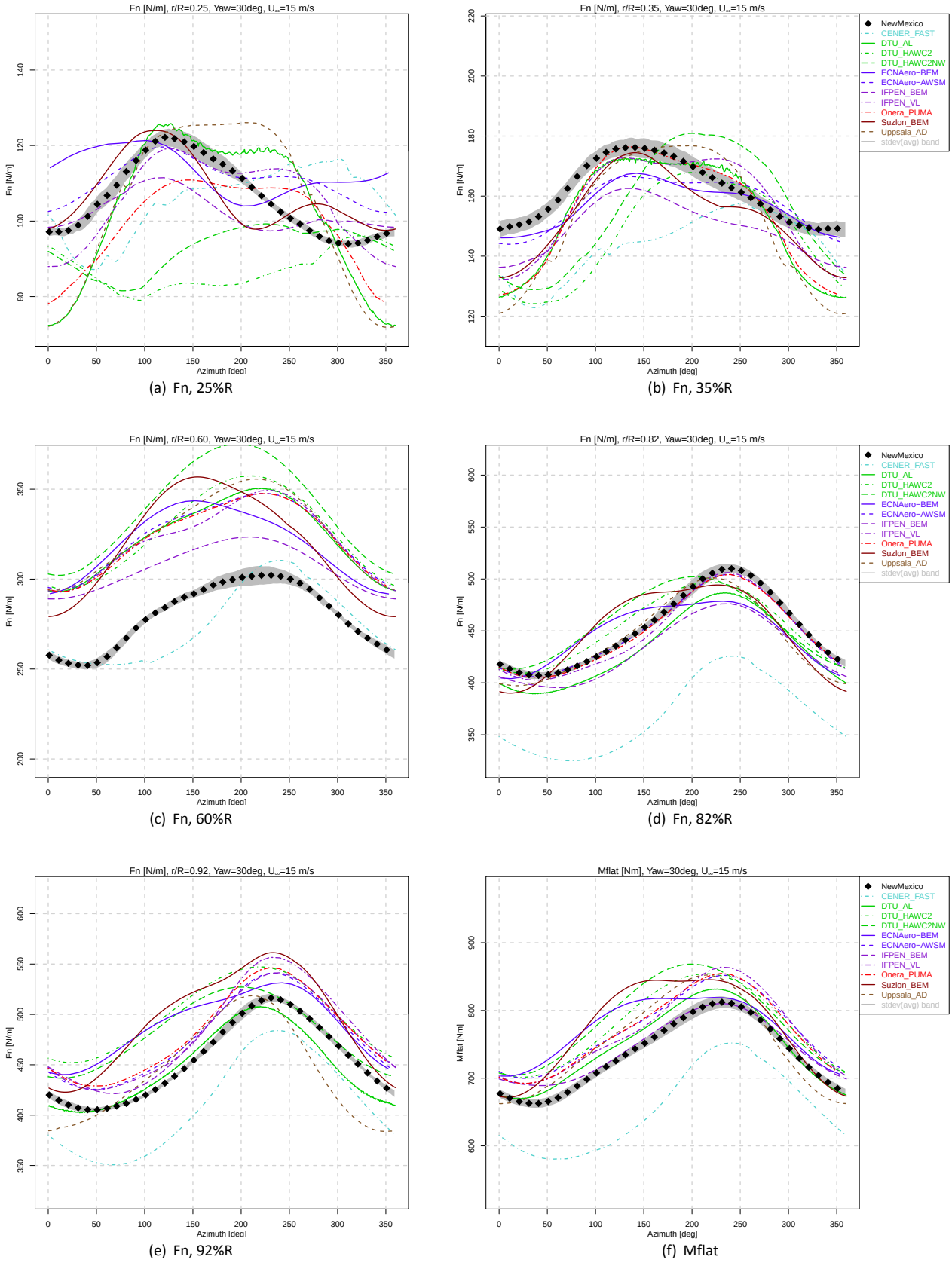

Figure B.21: Chord normal force and flatwise blade root moment, Case 2.2

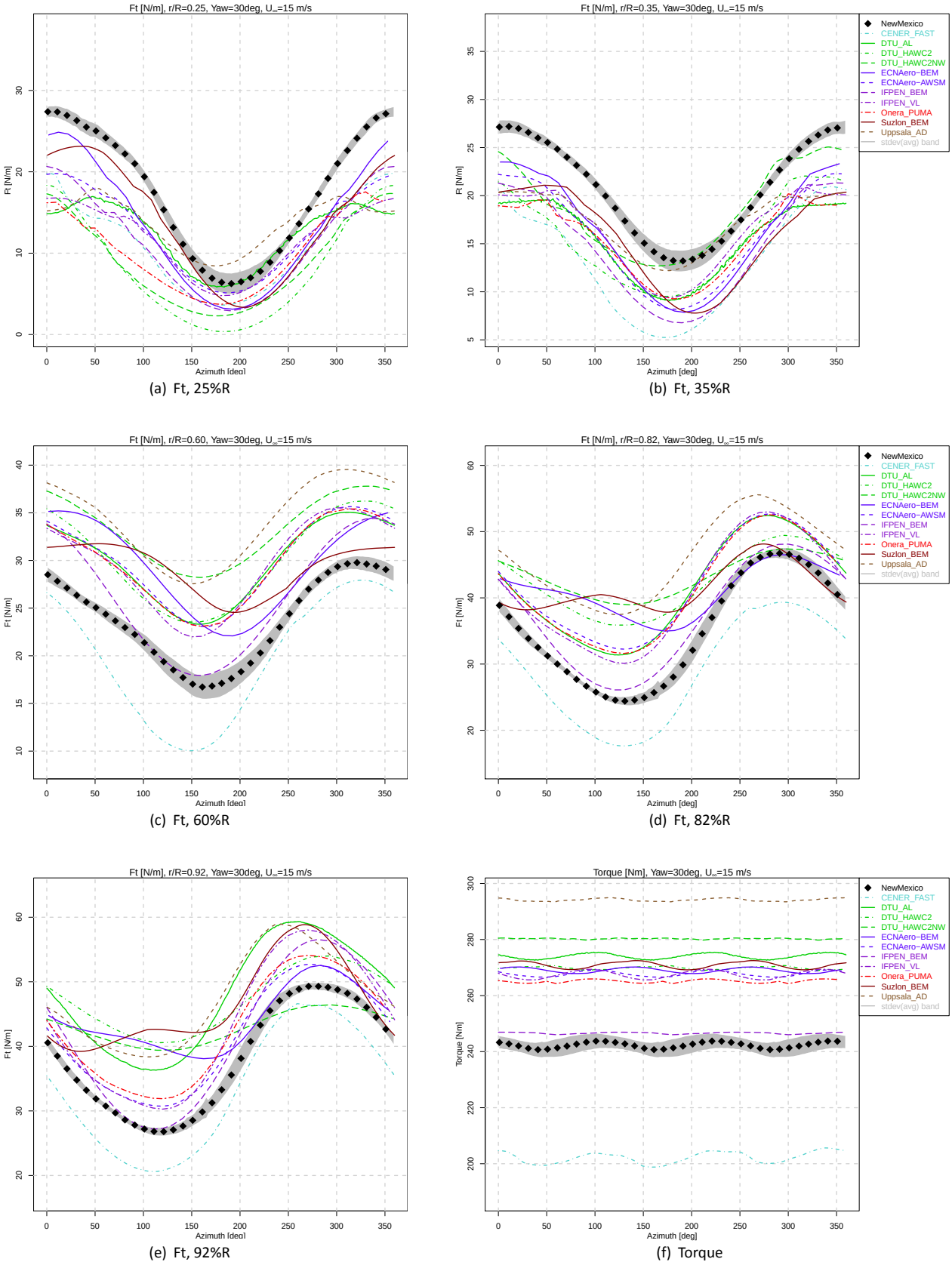

Figure B.22: Chord tangential force and torque, Case 2.2

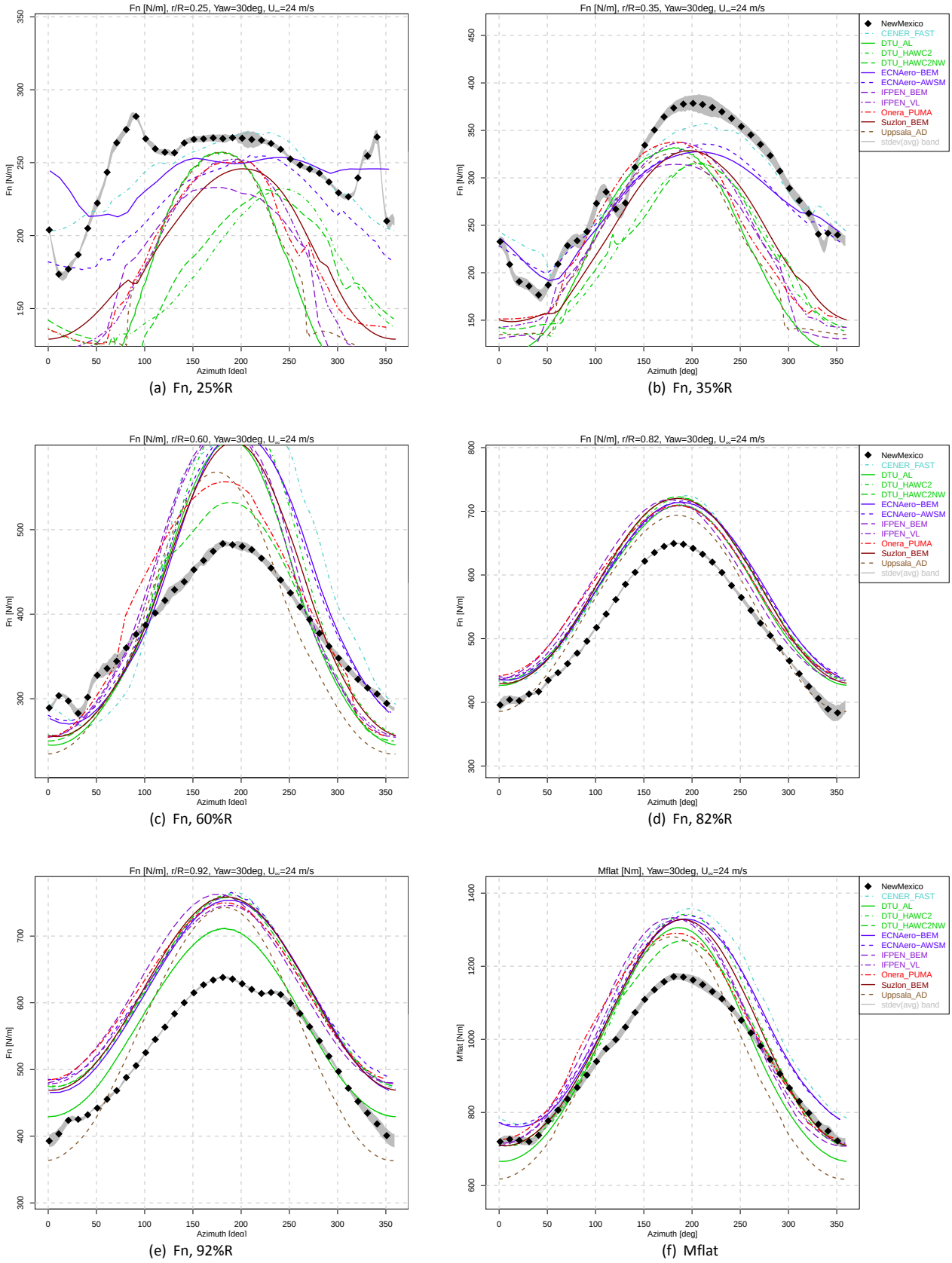

Figure B.23: Chord normal force and flatwise blade root moment, Case 2.3

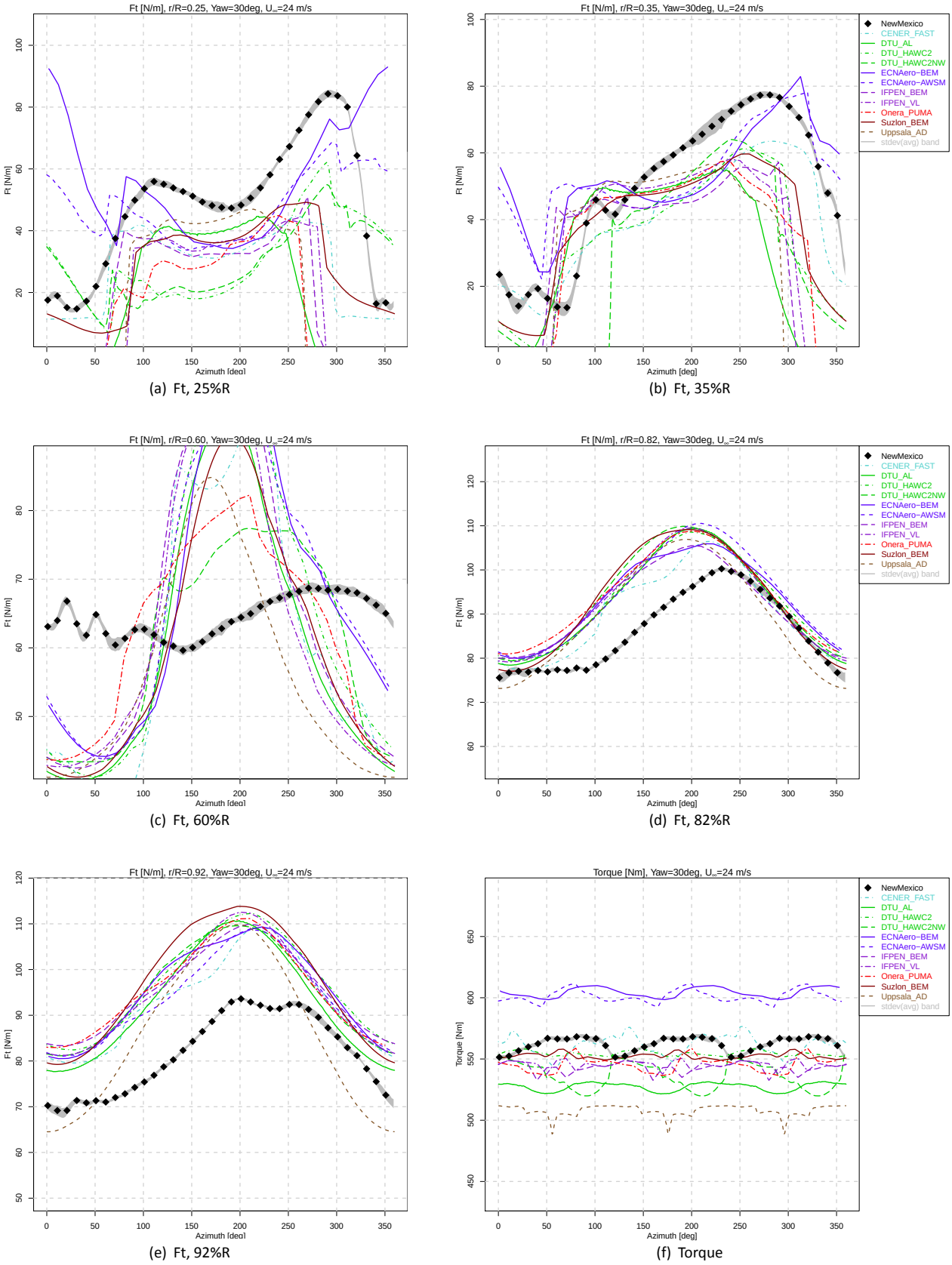

Figure B.24: Chord tangential force and torque, Case 2.3

B.2 CFD codes

Pressure distributions

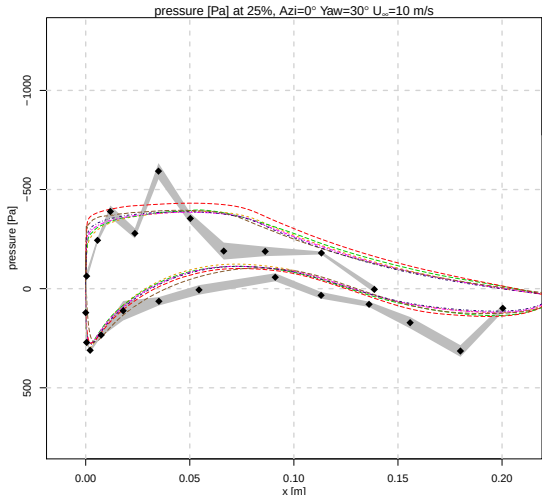

(a) Azimuth=0°

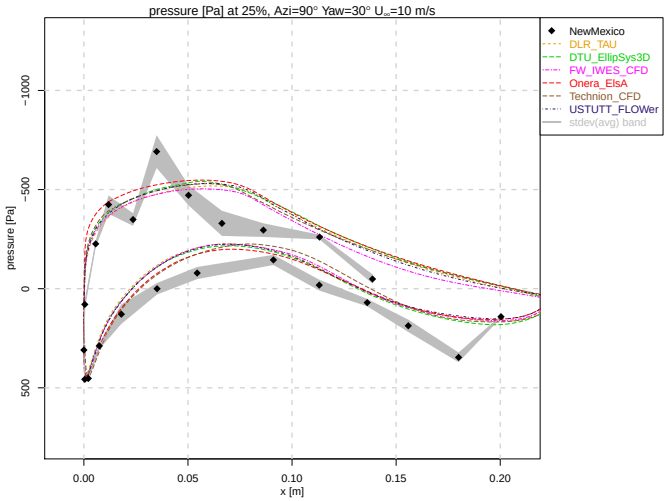

(b) Azimuth=90°

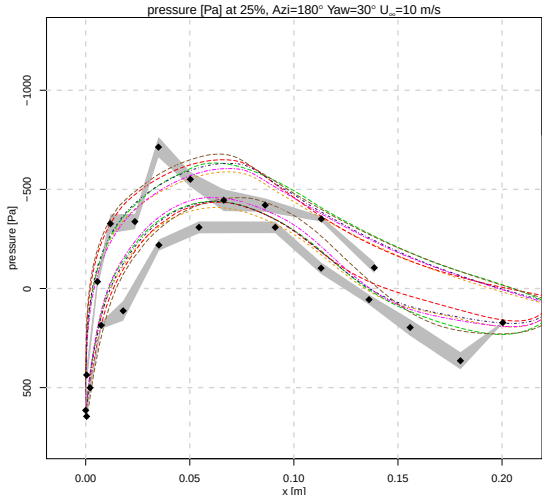

(c) Azimuth=180°

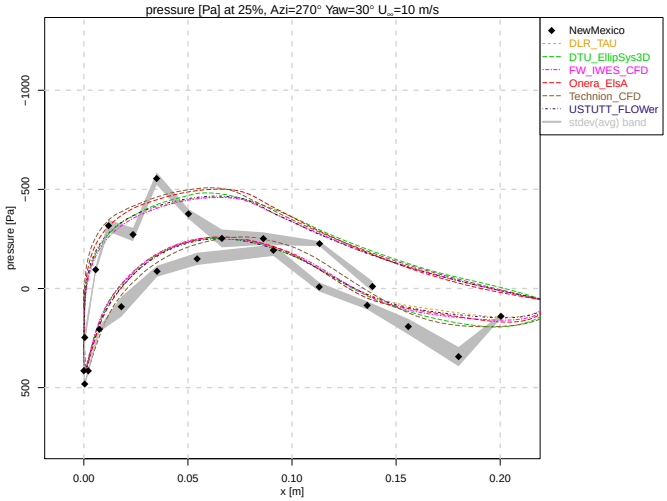

(d) Azimuth=270°

Figure B.25: 25%R, Case 2.1

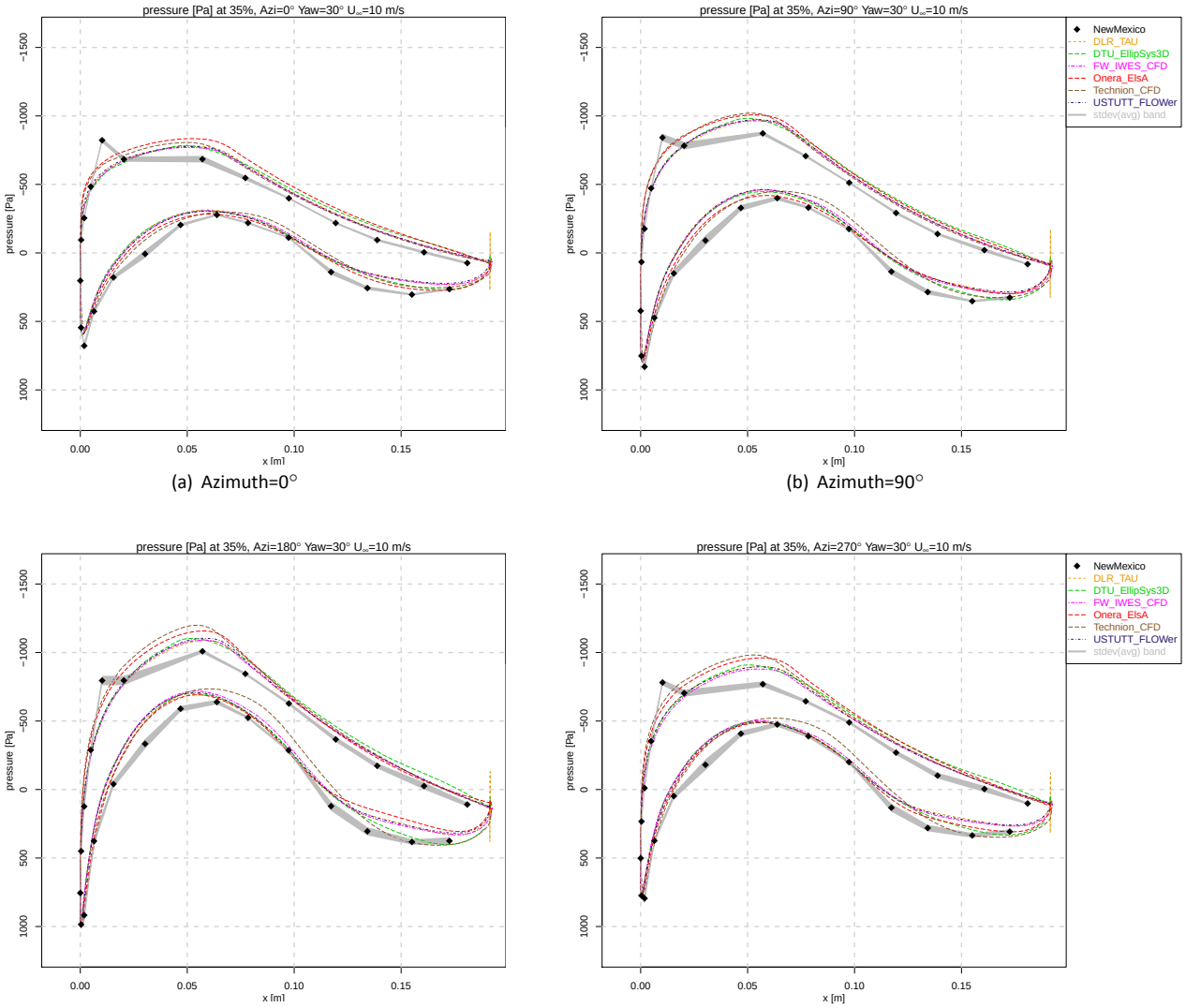

(a) Azimuth=0°

(b) Azimuth=90°

(c) Azimuth=180°

(d) Azimuth=270°

Figure B.26: 35%R, Case 2.1

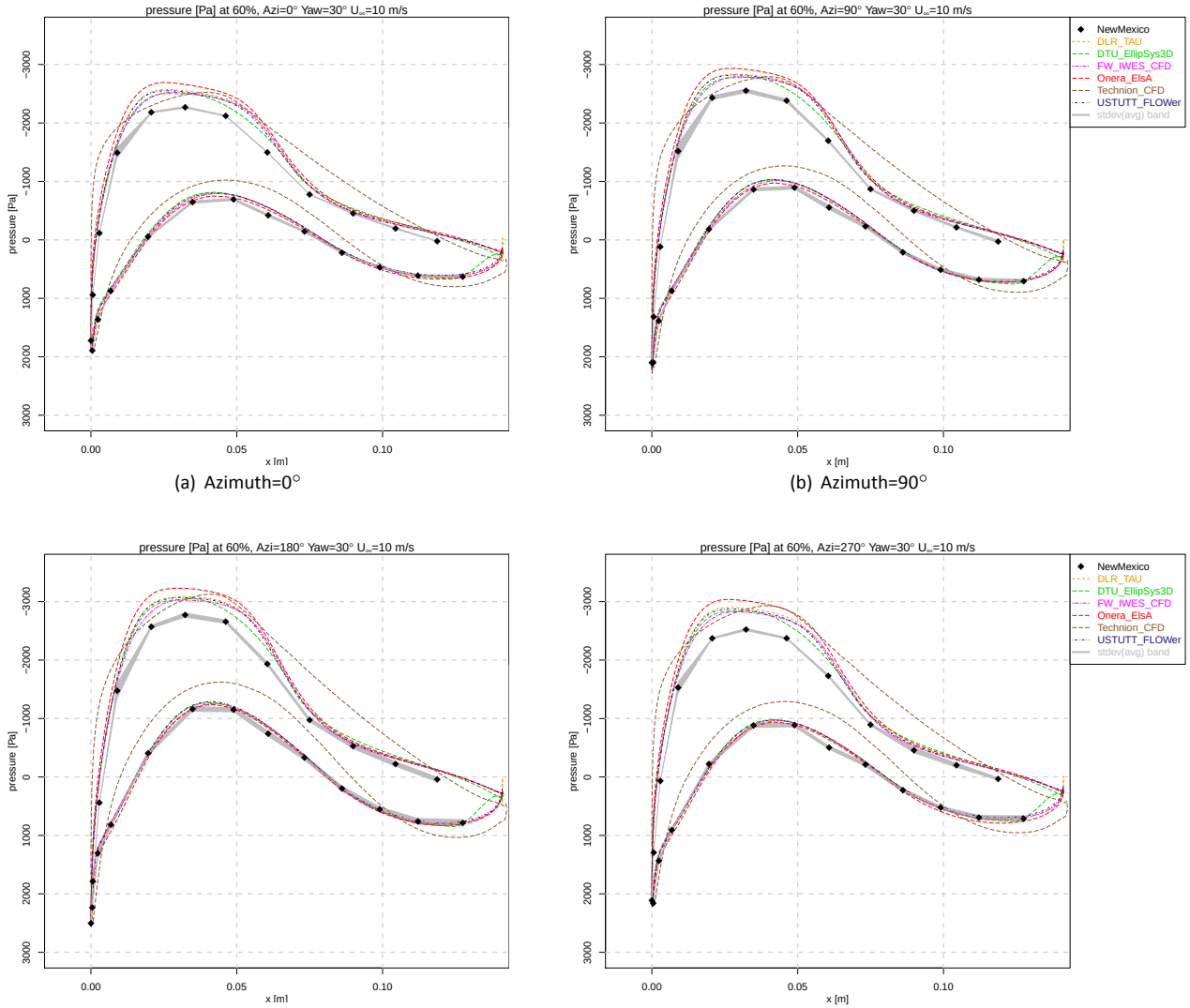

(a) Azimuth=0°

(b) Azimuth=90°

(c) Azimuth=180°

(d) Azimuth=270°

Figure B.27: 60%R, Case 2.1

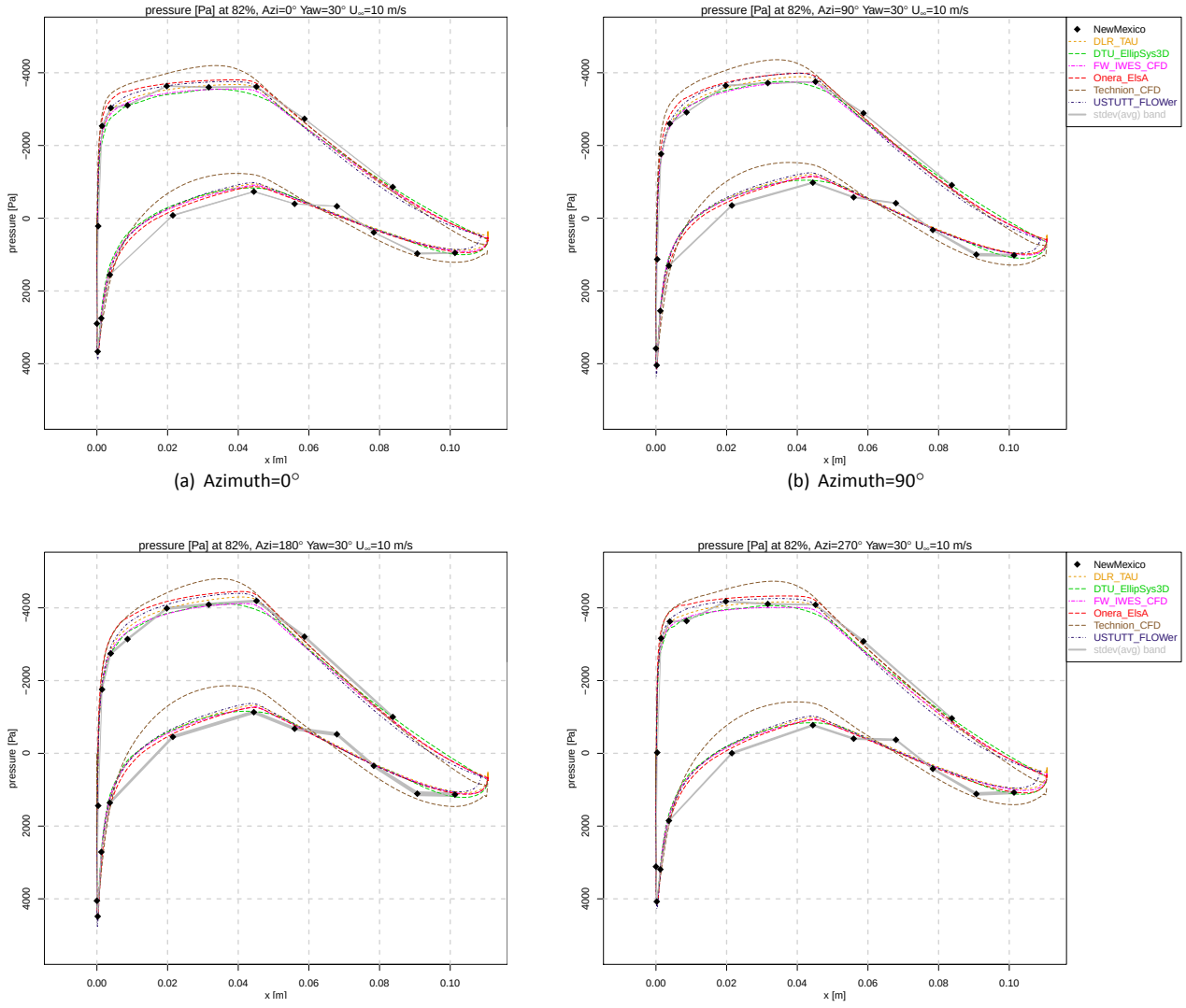

(a) Azimuth=0°

(b) Azimuth=90°

(c) Azimuth=180°

(d) Azimuth=270°

Figure B.28: 82%R, Case 2.1

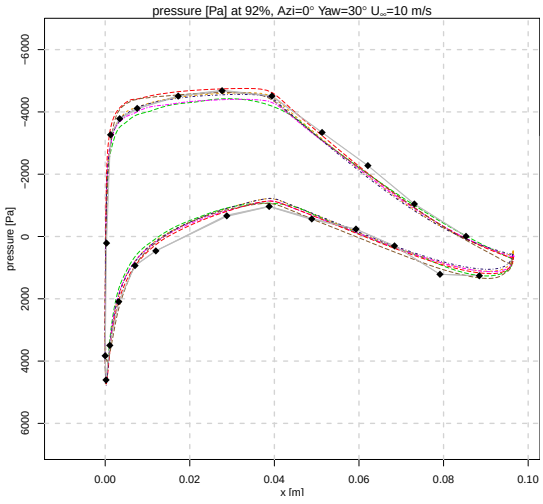

(a) Azimuth=0°

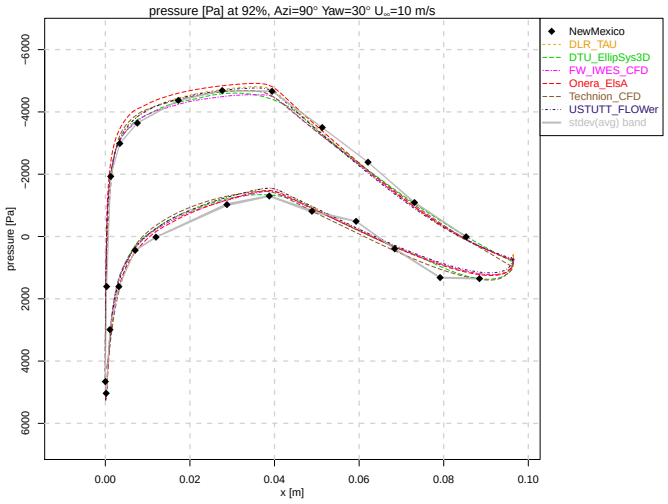

(b) Azimuth=90°

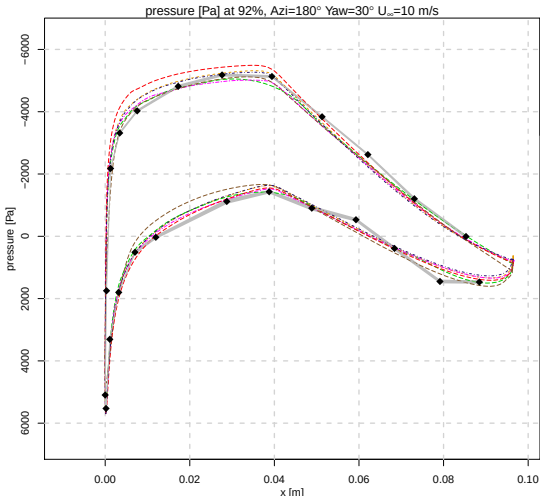

(c) Azimuth=180°

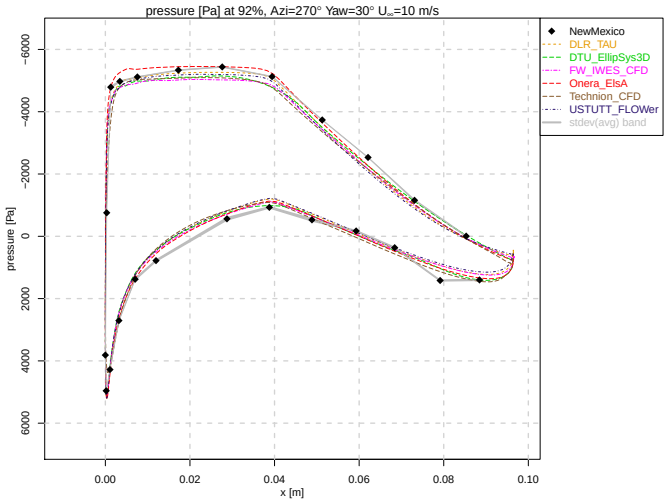

(d) Azimuth=270°

Figure B.29: 92%R, Case 2.1

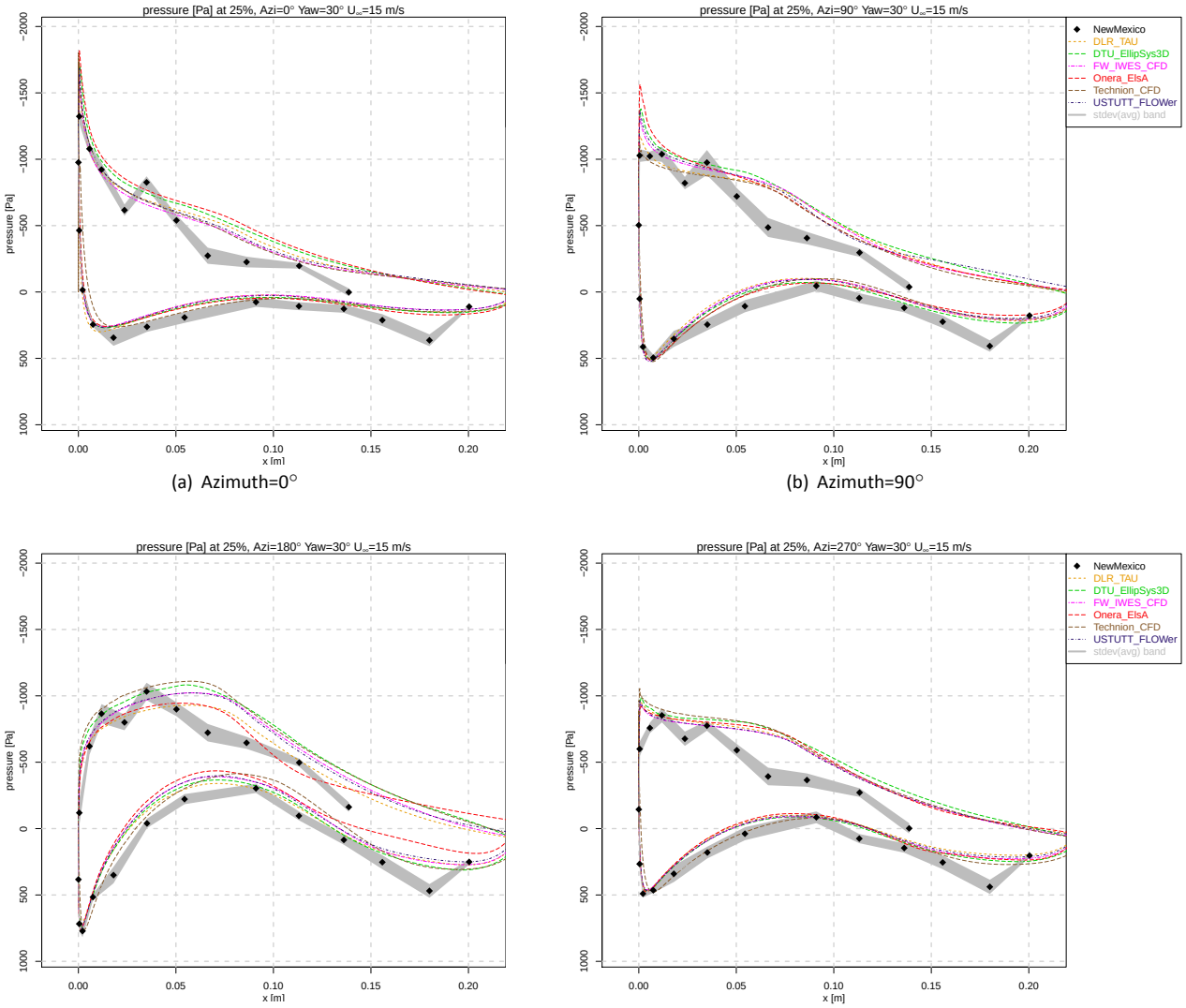

(a) Azimuth=0°

(b) Azimuth=90°

(c) Azimuth=180°

(d) Azimuth=270°

Figure B.30: 25%R, Case 2.2

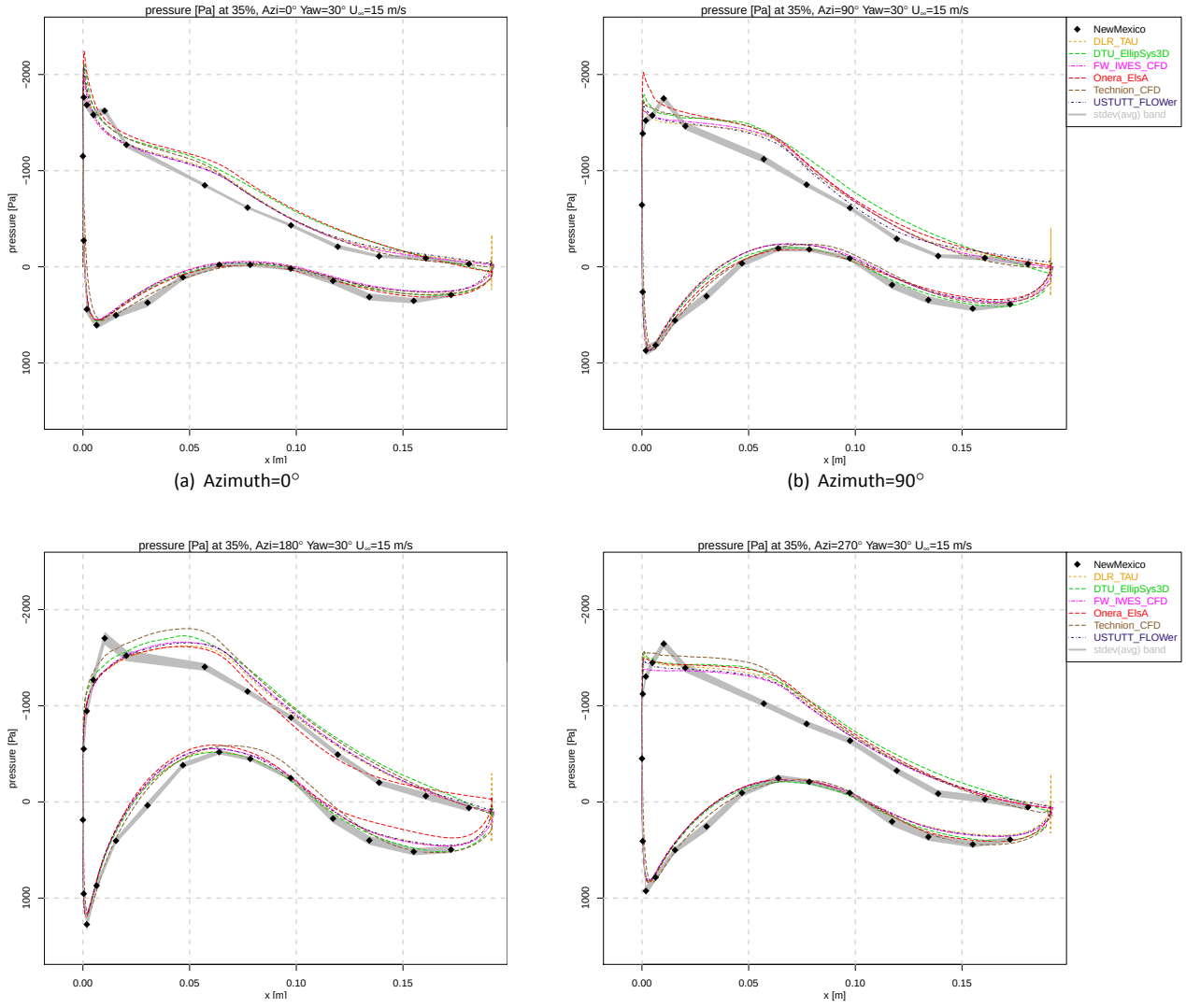

(a) Azimuth=0°

(b) Azimuth=90°

(c) Azimuth=180°

(d) Azimuth=270°

Figure B.31: 35%R, Case 2.2

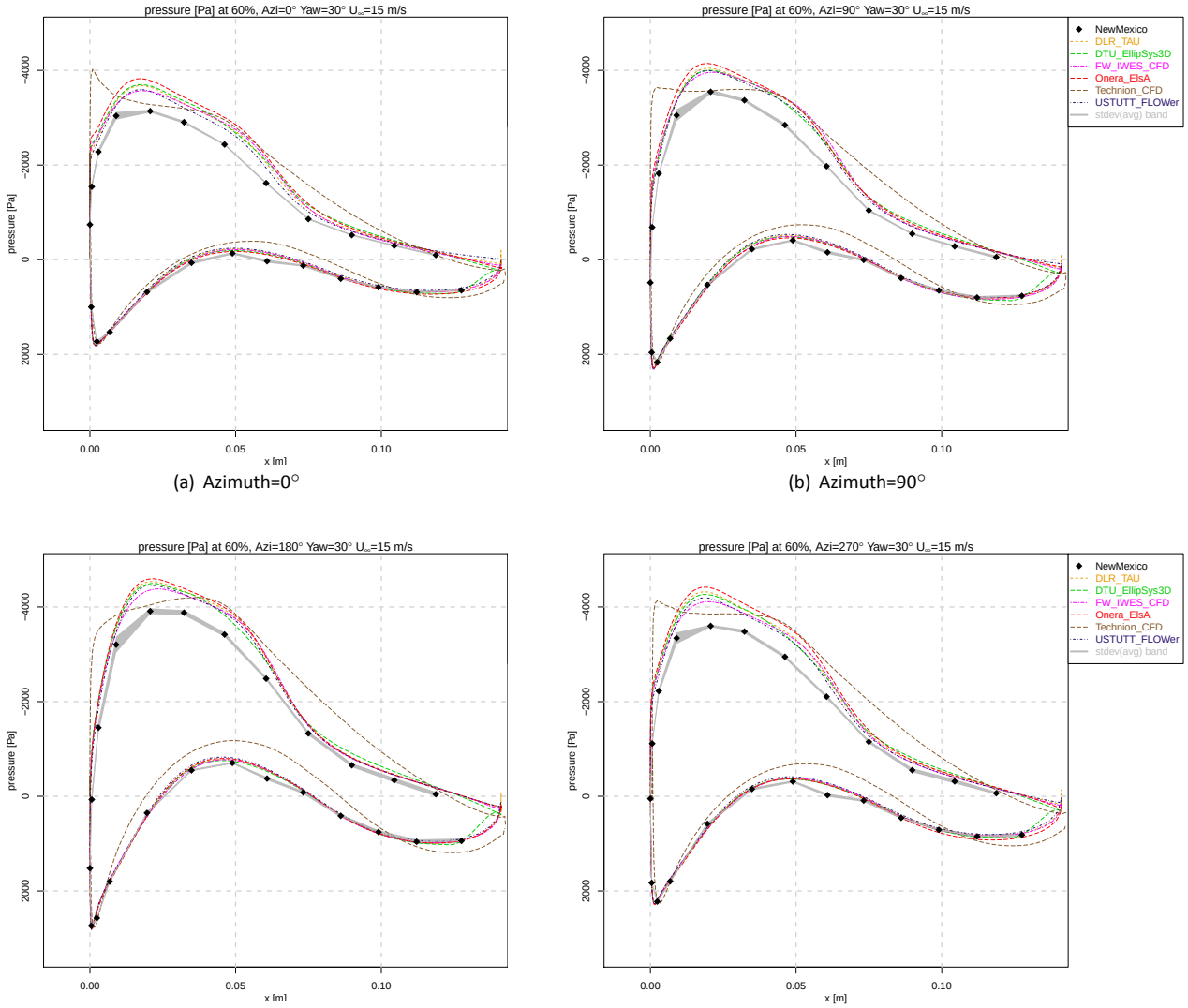

(a) Azimuth=0°

(b) Azimuth=90°

(c) Azimuth=180°

(d) Azimuth=270°

Figure B.32: 60%R, Case 2.2

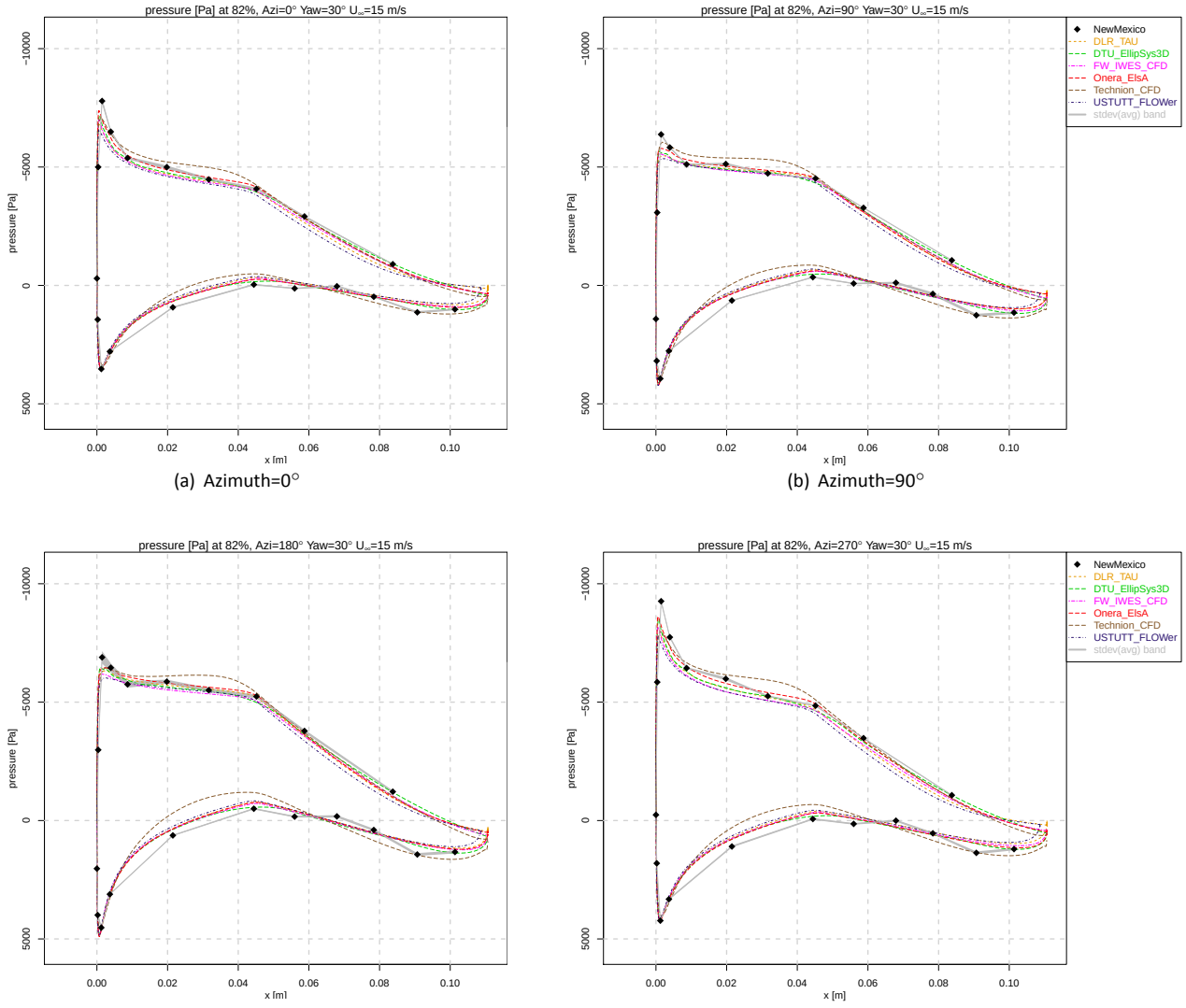

(a) Azimuth=0°

(b) Azimuth=90°

(c) Azimuth=180°

(d) Azimuth=270°

Figure B.33: 82%R, Case 2.2

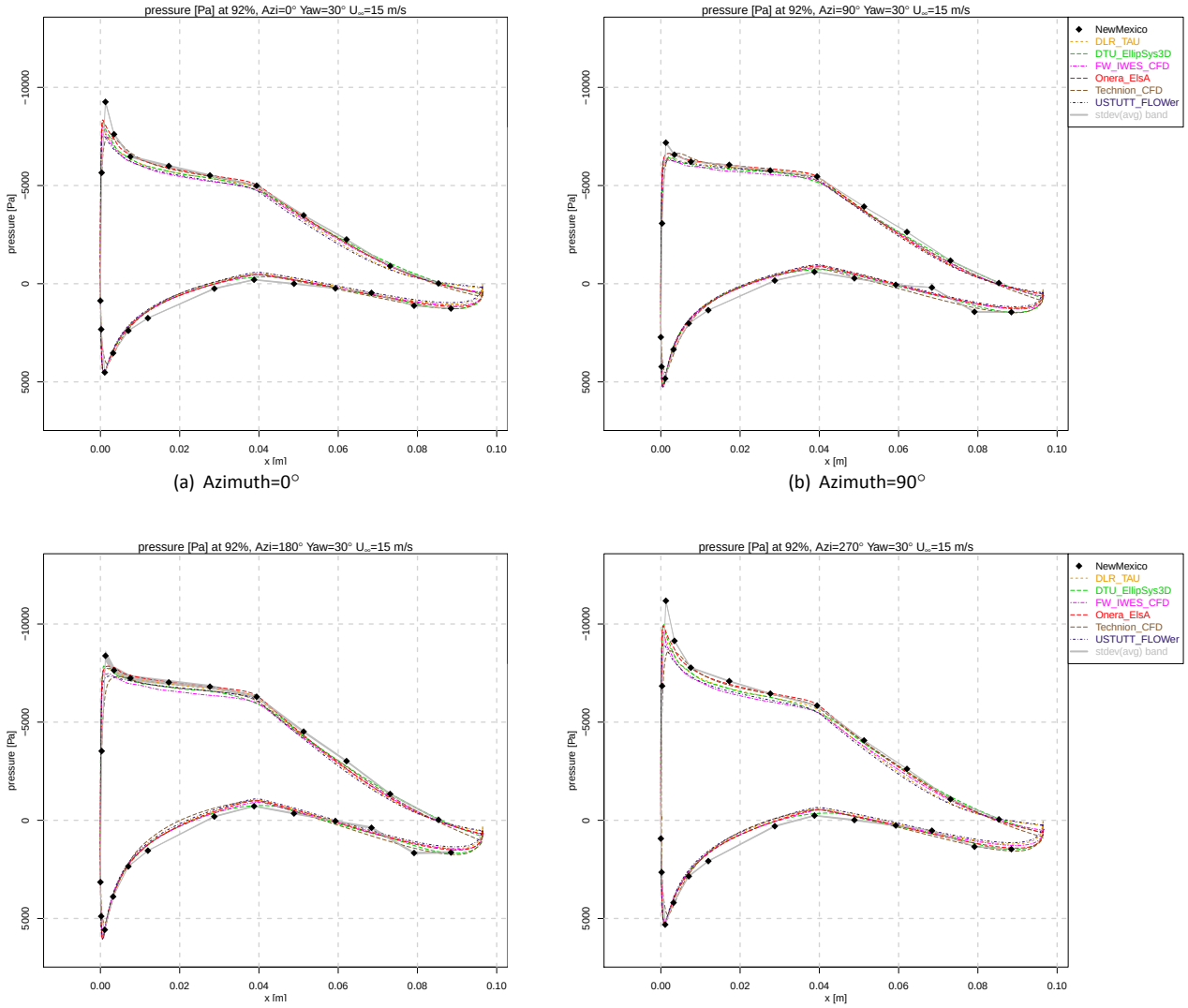

(a) Azimuth=0°

(b) Azimuth=90°

(c) Azimuth=180°

(d) Azimuth=270°

Figure B.34: 92%R, Case 2.2

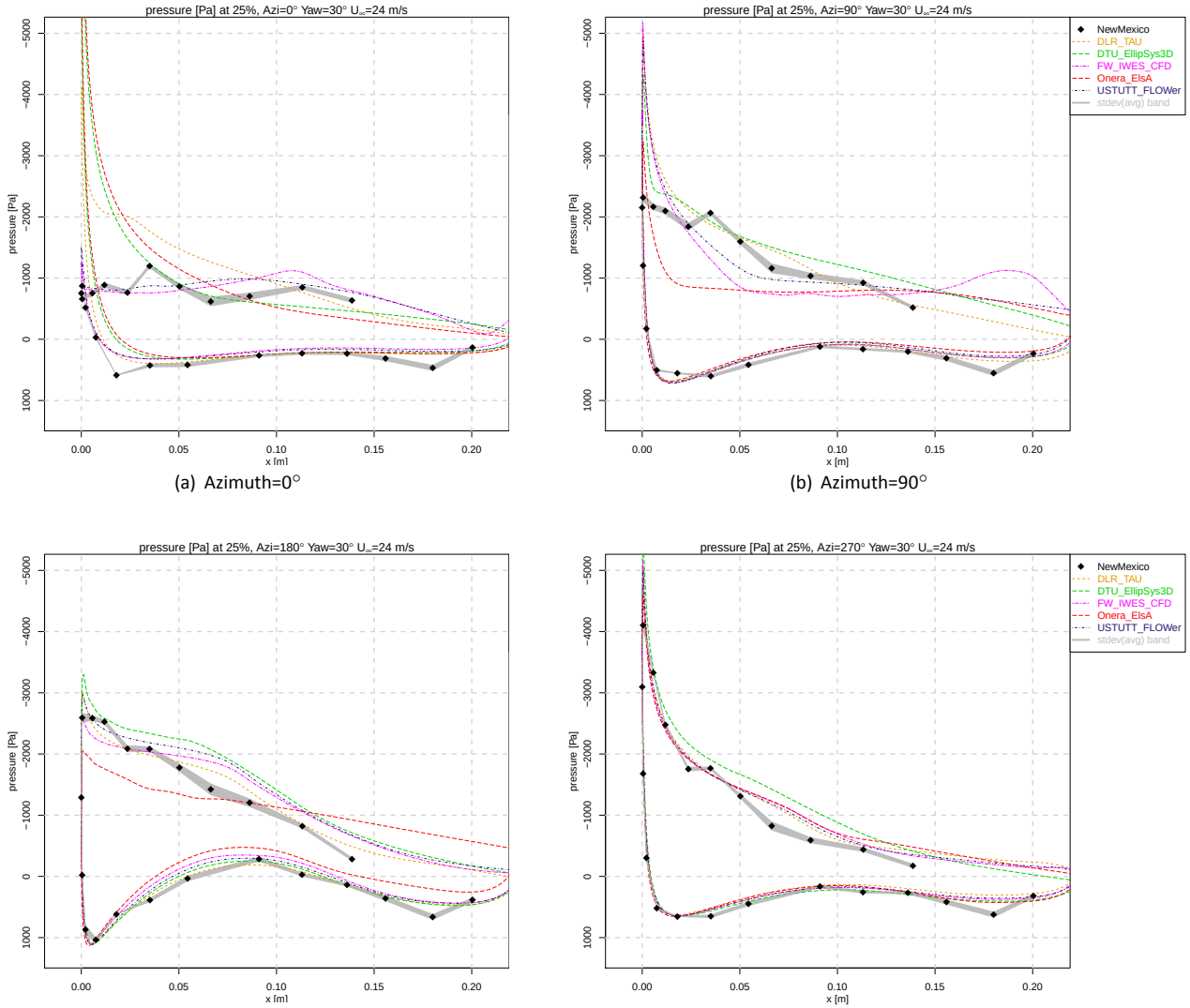

(a) Azimuth=0°

(b) Azimuth=90°

(c) Azimuth=180°

(d) Azimuth=270°

Figure B.35: 25%R, Case 2.3

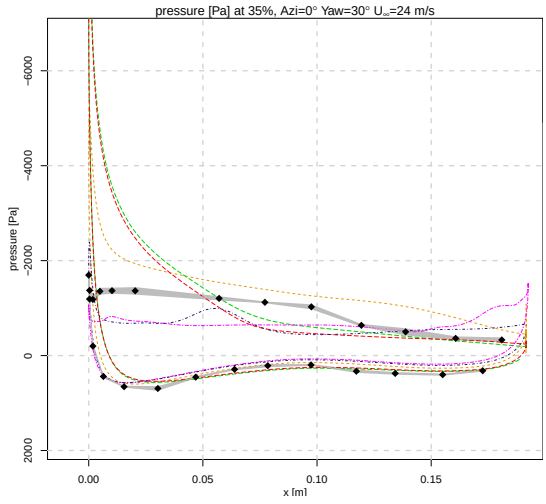

(a) Azimuth=0°

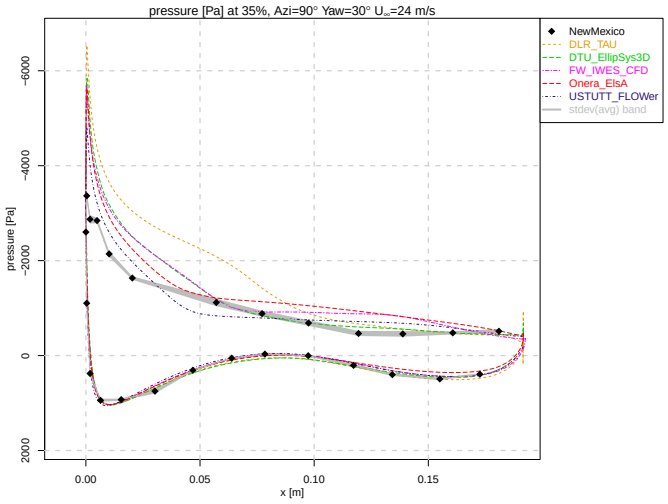

(b) Azimuth=90°

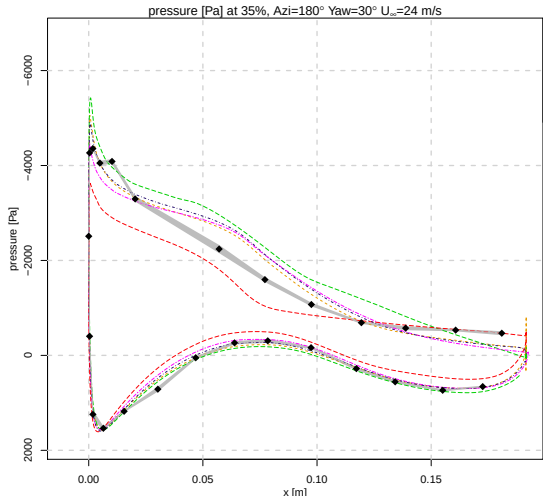

(c) Azimuth=180°

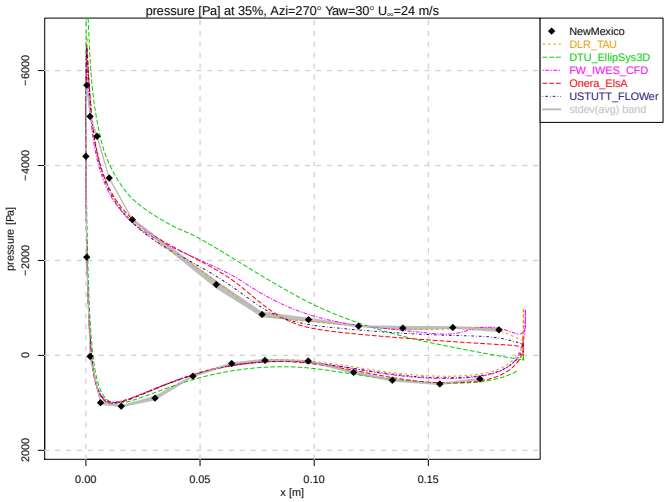

(d) Azimuth=270°

Figure B.36: 35%R, Case 2.3

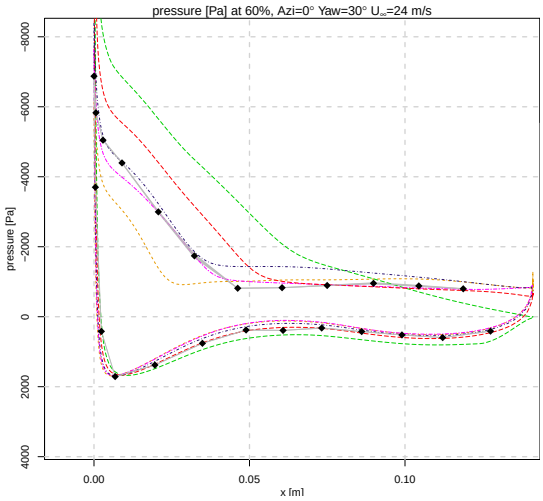

(a) Azimuth=0°

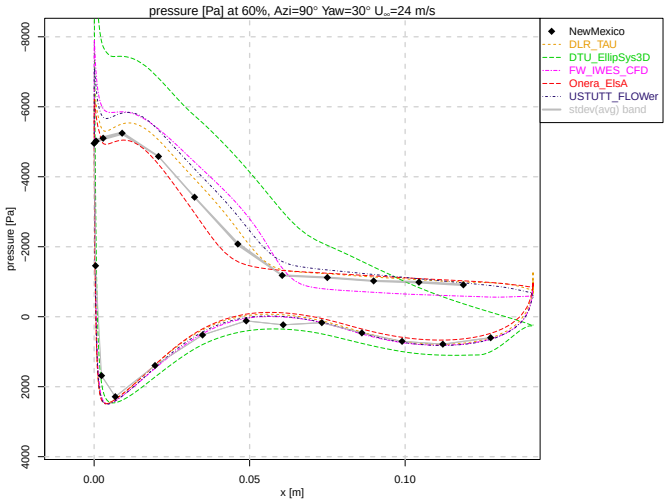

(b) Azimuth=90°

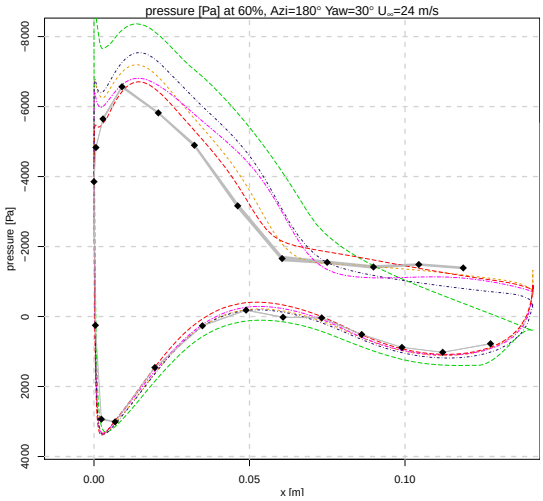

(c) Azimuth=180°

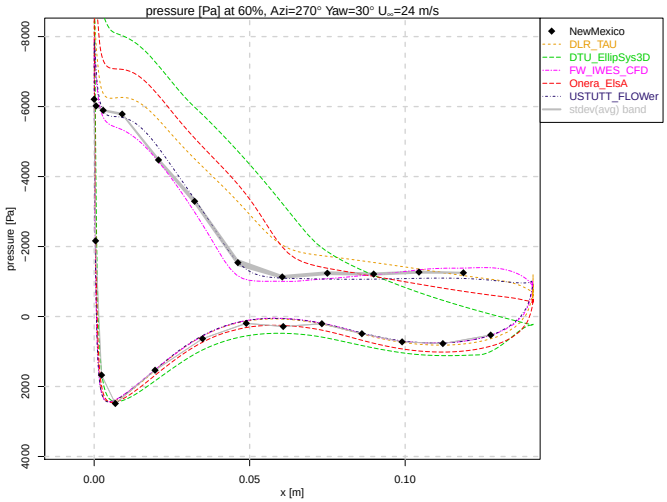

(d) Azimuth=270°

Figure B.37: 60%R, Case 2.3

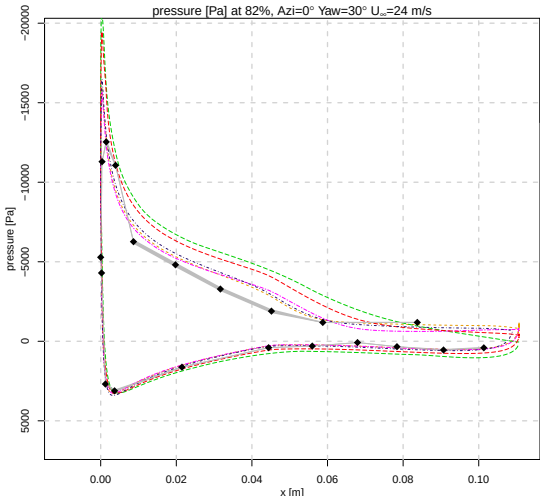

(a) Azimuth=0°

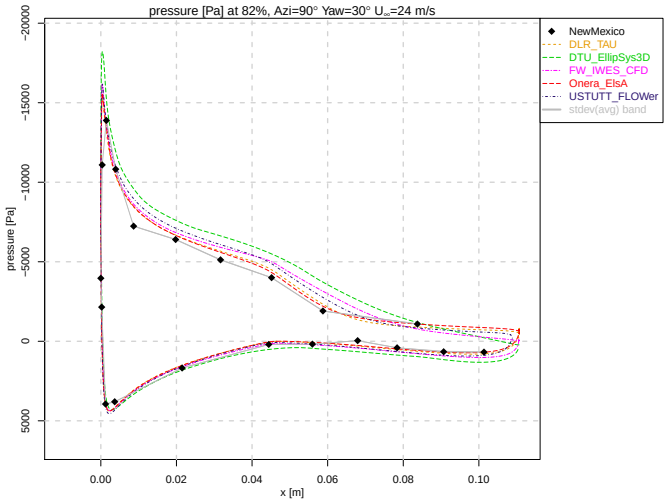

(b) Azimuth=90°

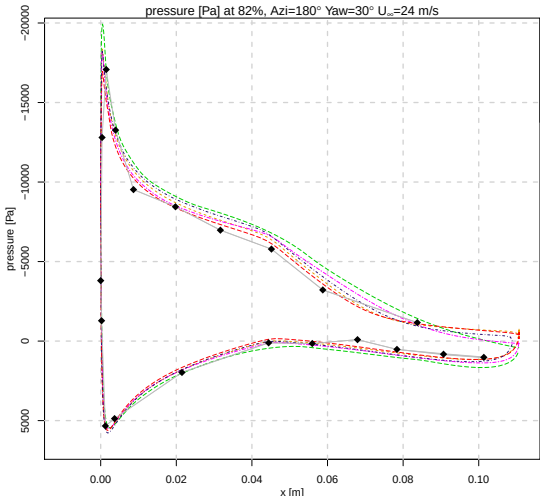

(c) Azimuth=180°

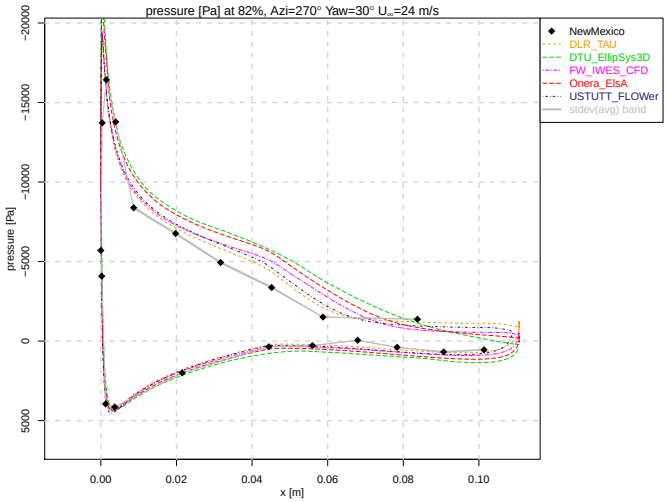

(d) Azimuth=270°

Figure B.38: 82%R, Case 2.3

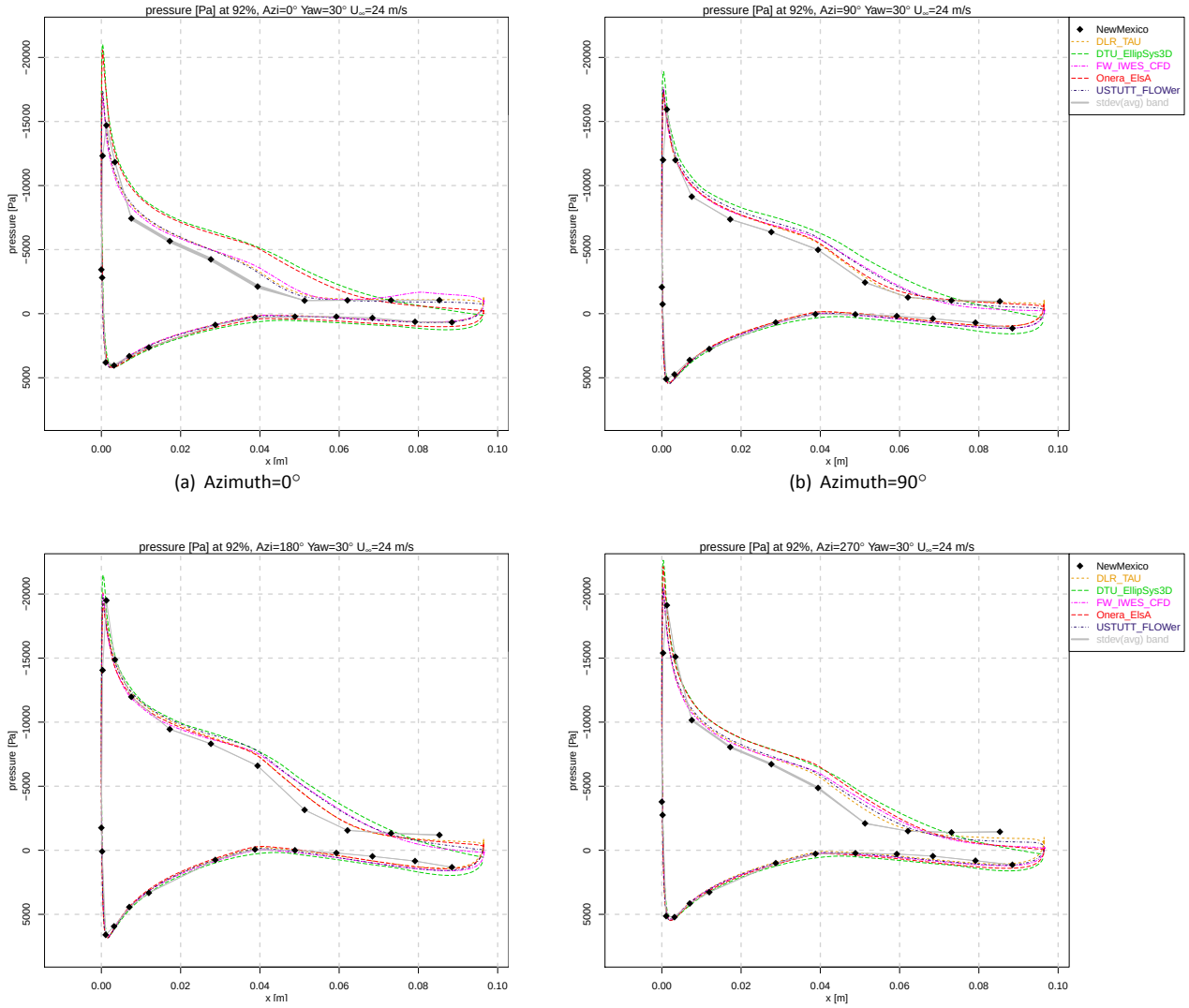

(a) Azimuth=0°

(b) Azimuth=90°

(c) Azimuth=180°

(d) Azimuth=270°

Figure B.39: 92%R, Case 2.3

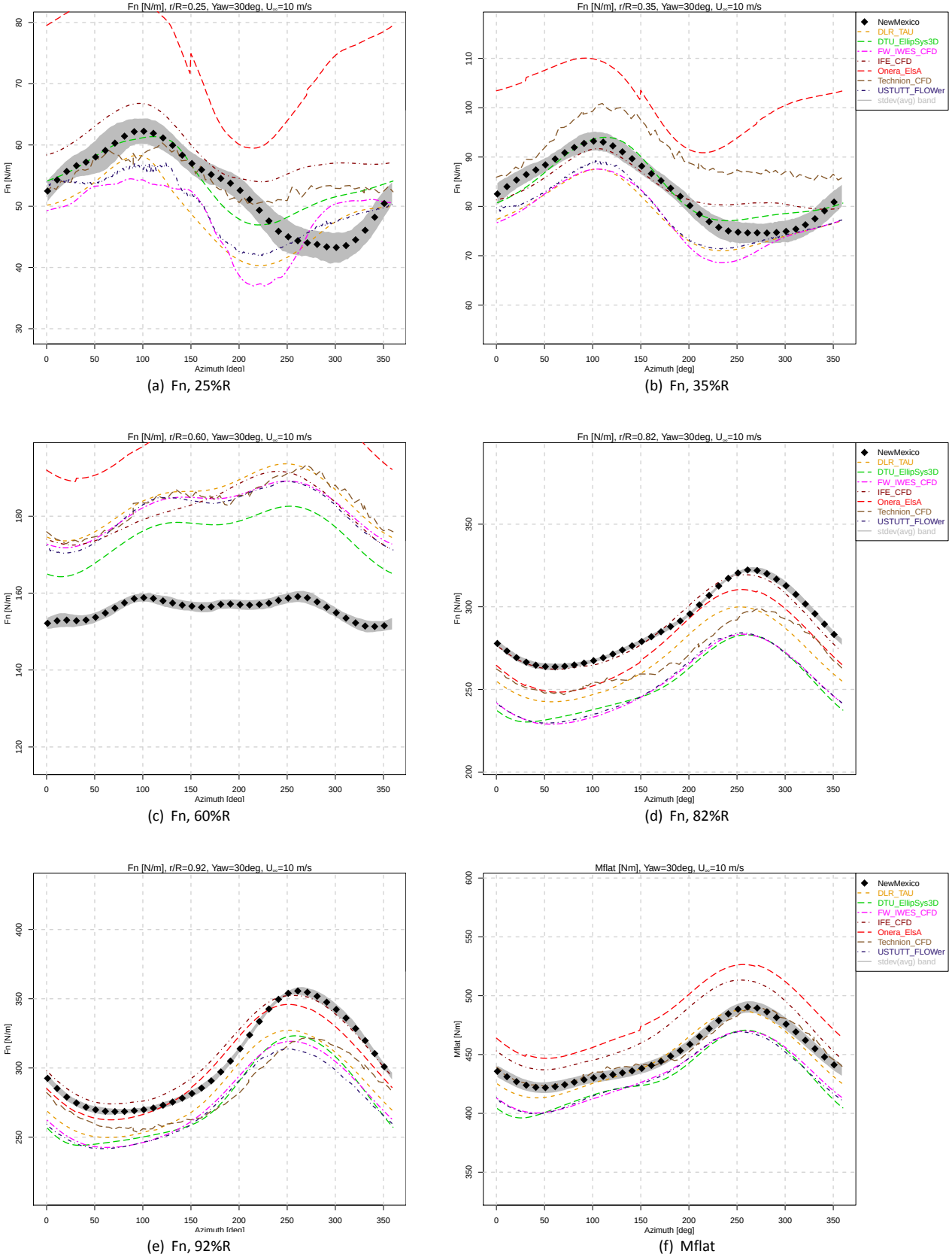

Figure B.40: Chord normal force and flatwise blade root moment, Case 2.1

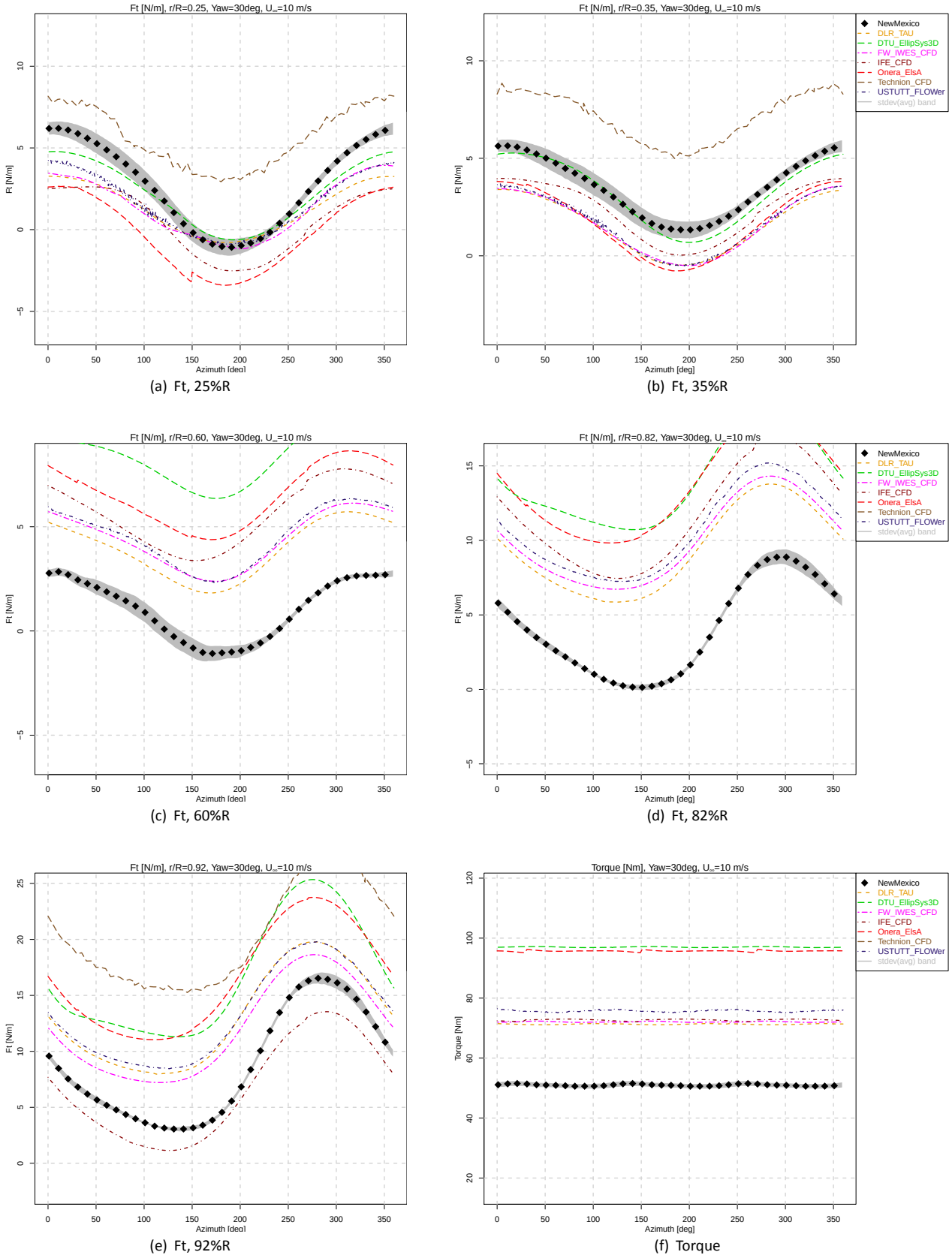

Figure B.41: Chord tangential force and torque, Case 2.1

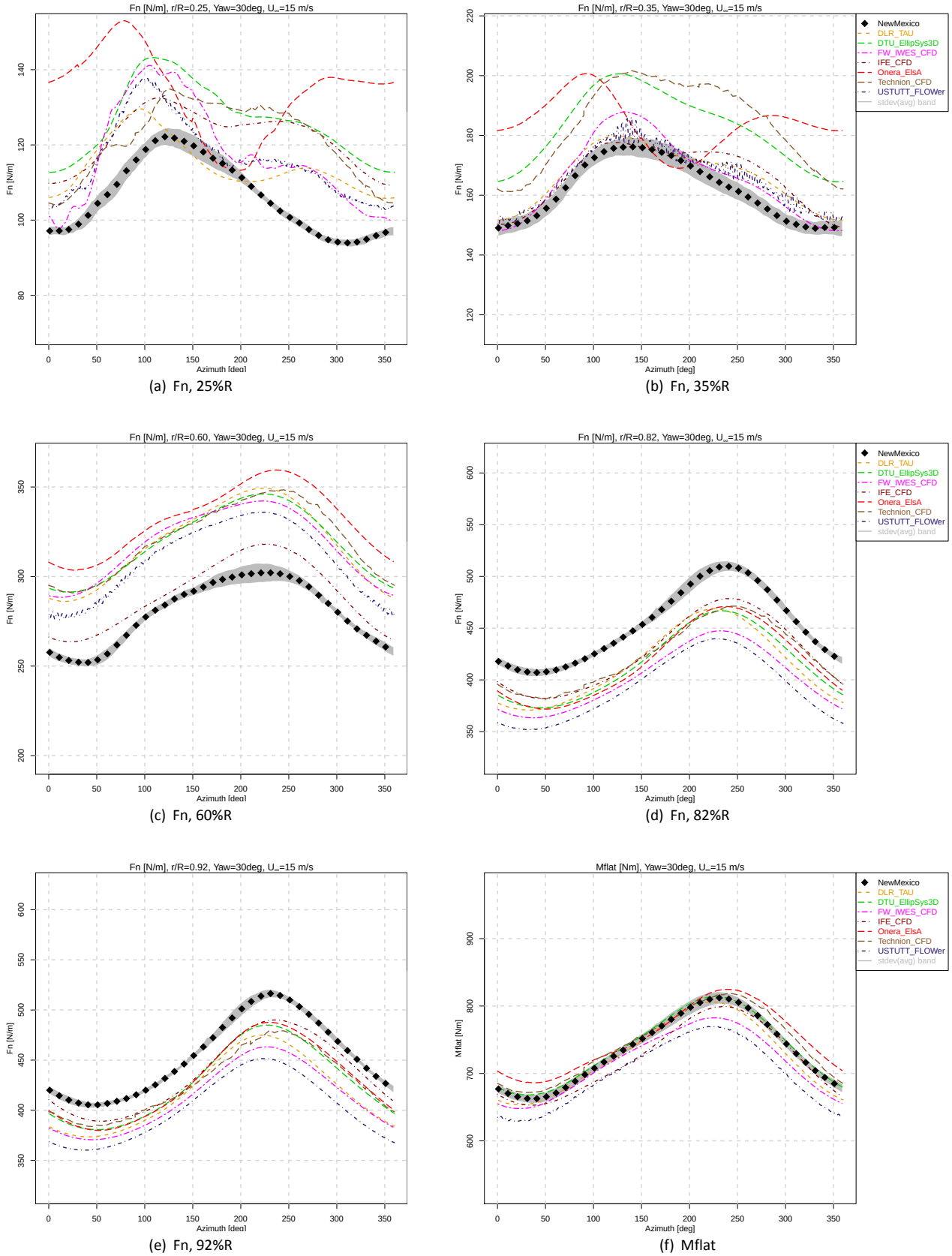

Figure B.42: Chord normal force and flatwise blade root moment, Case 2.2

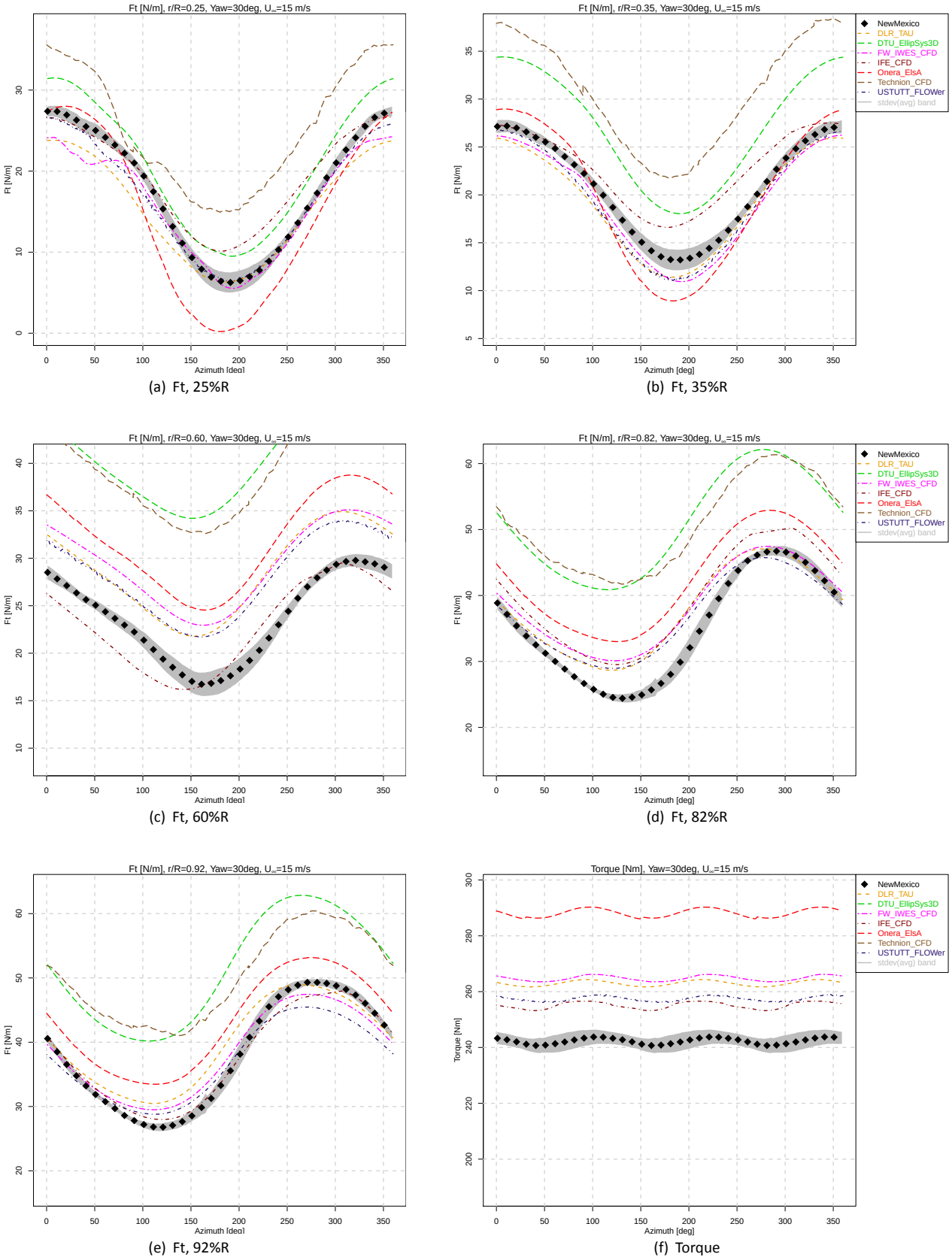

Figure B.43: Chord tangential force and torque, Case 2.2

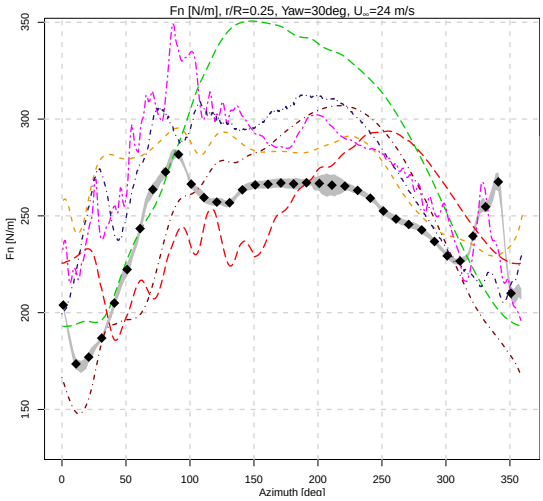

(a) Fn, 25%R

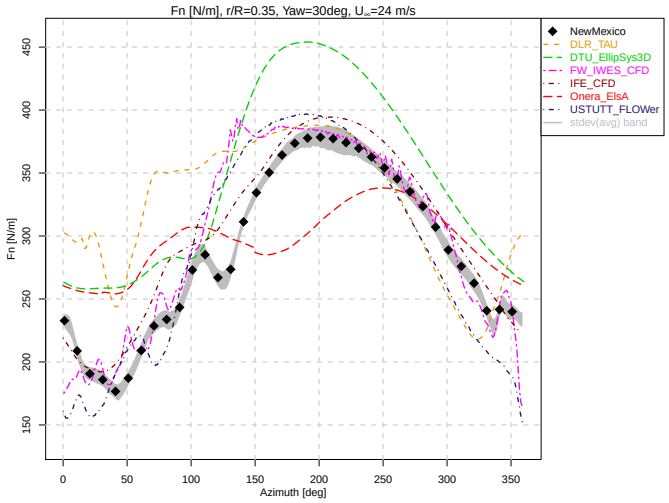

(b) Fn, 35%R

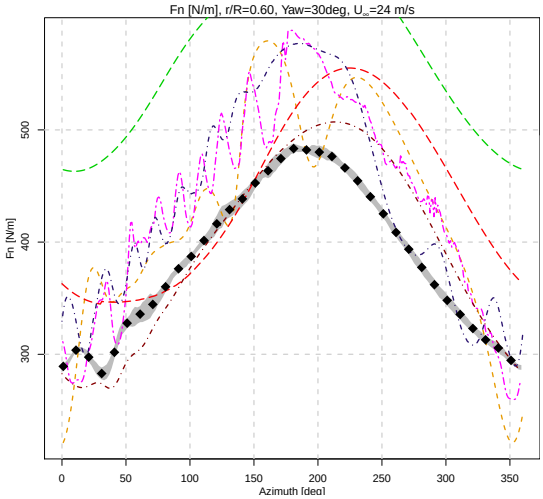

(c) Fn, 60%R

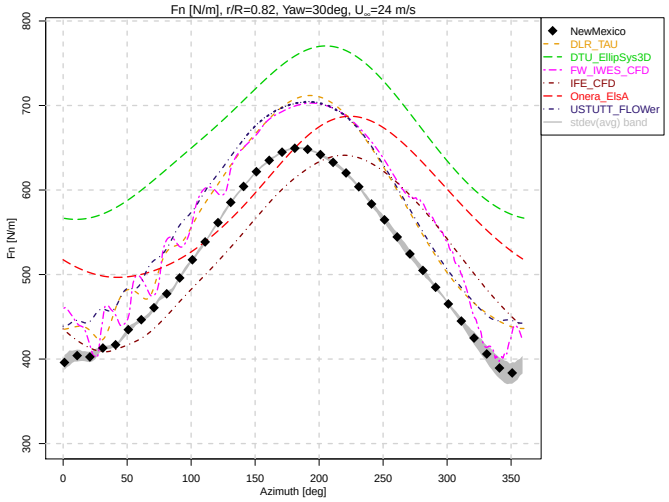

(d) Fn, 82%R

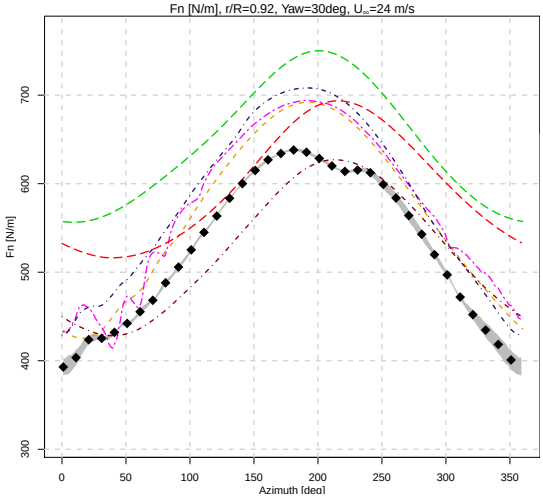

(e) Fn, 92%R

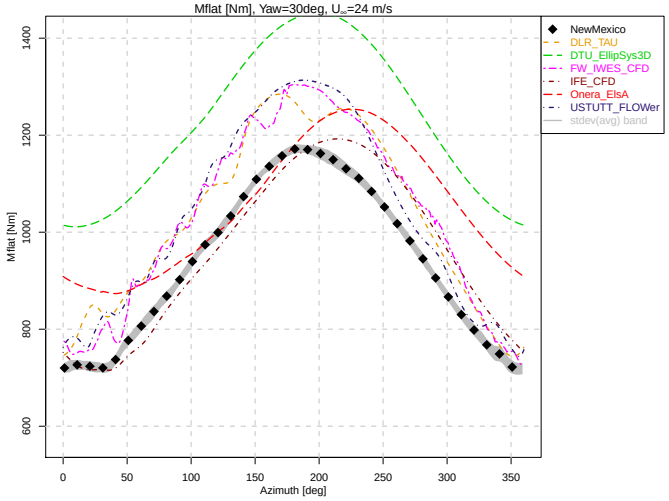

(f) Mflat

Figure B.44: Chord normal force and flatwise blade root moment, Case 2.3

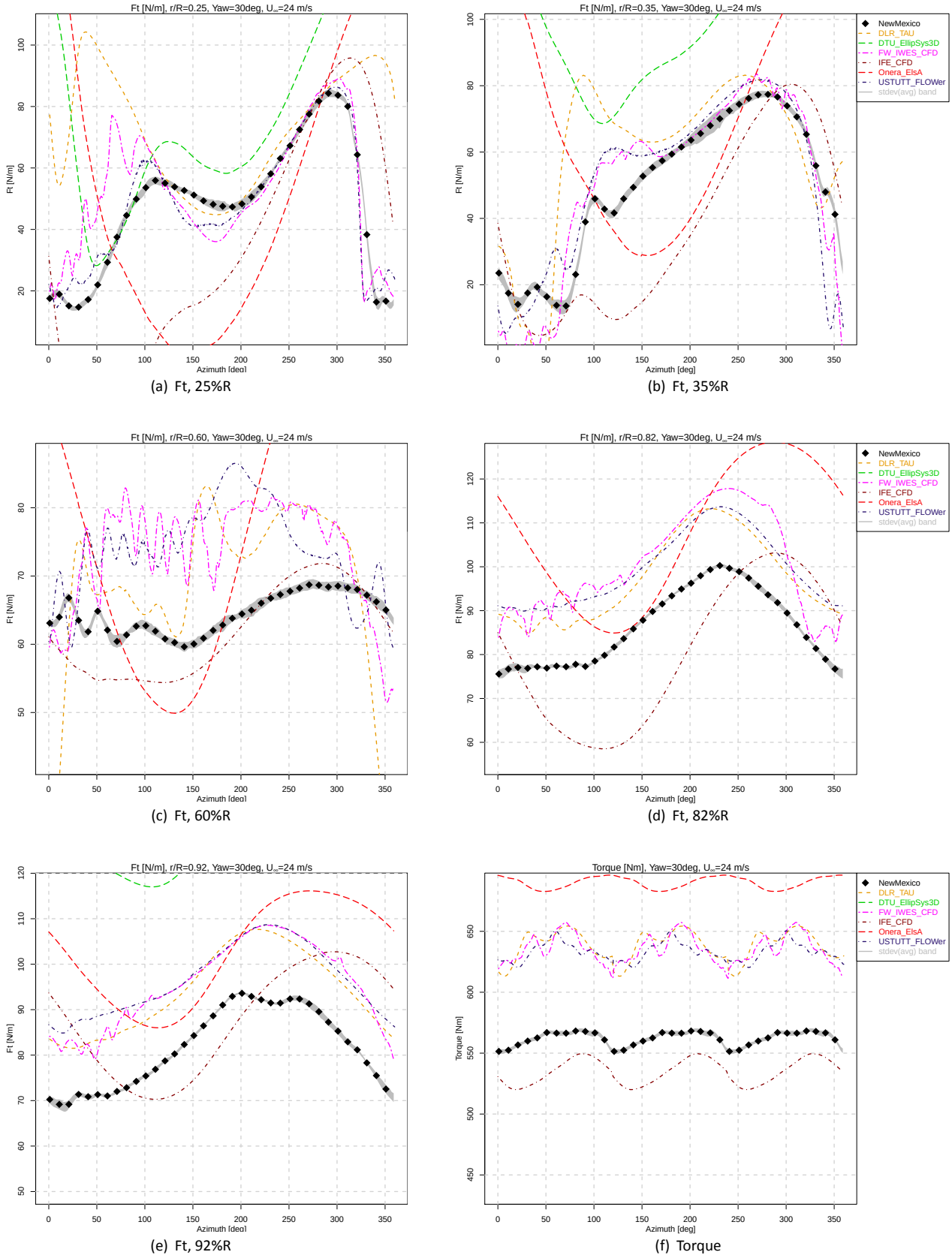

Figure B.45: Chord tangential force and torque, Case 2.3

B.3 Velocity traverses

Axial traverse

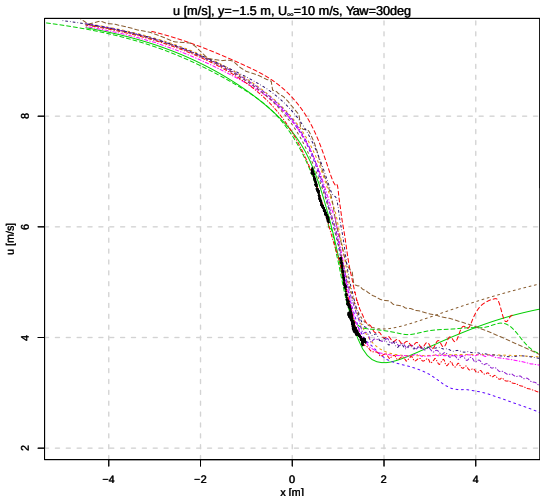

(a) u, y=-1.5 m

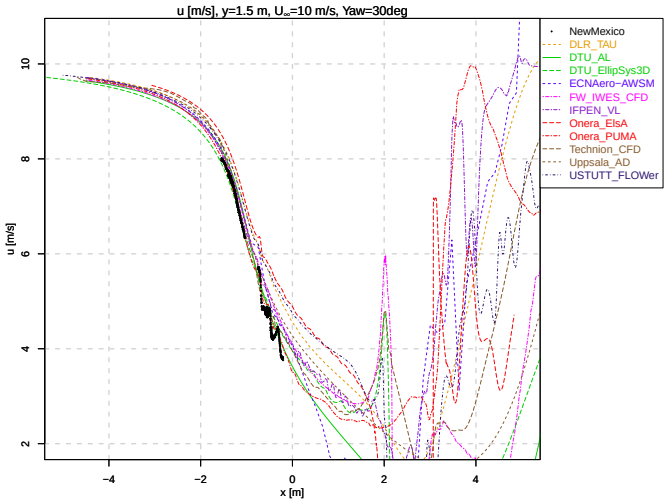

(b) u, y=+1.5 m

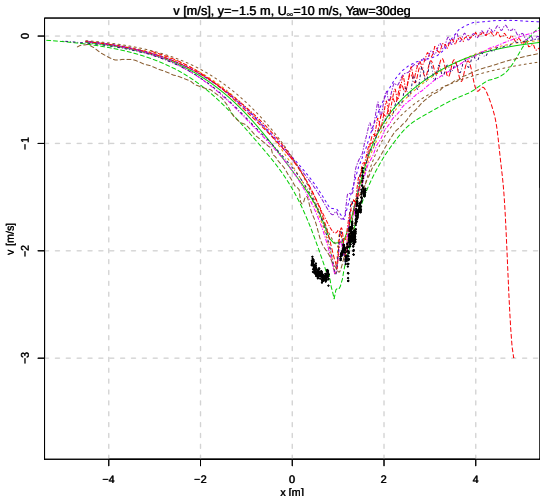

(c) v, y=-1.5 m

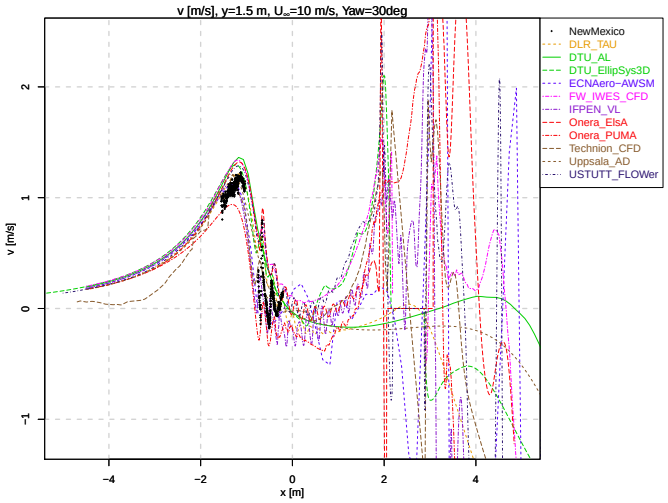

(d) v, y=+1.5 m

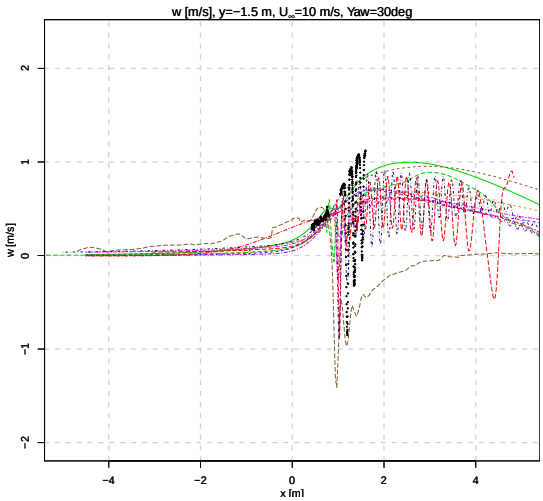

(e) w, y=-1.5 m

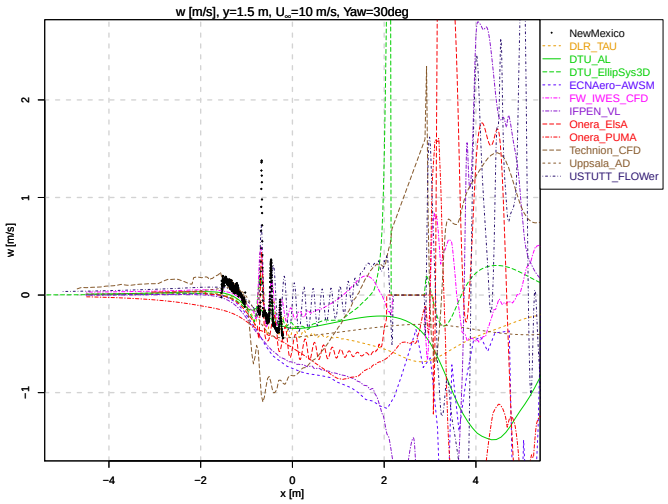

(f) w, y=+1.5 m

Figure B.46: Axial traverse of velocity , Case 2.1

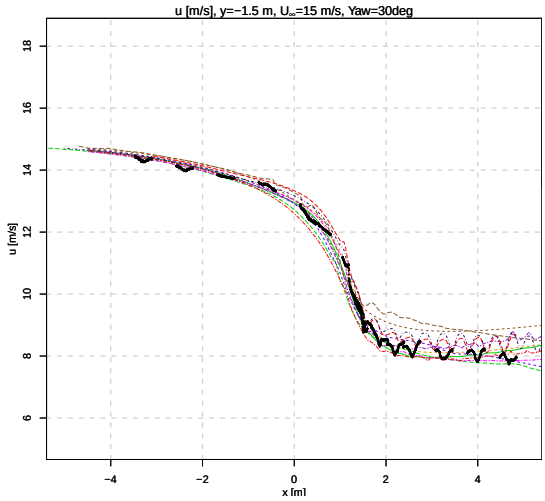

(a) u, y=-1.5 m

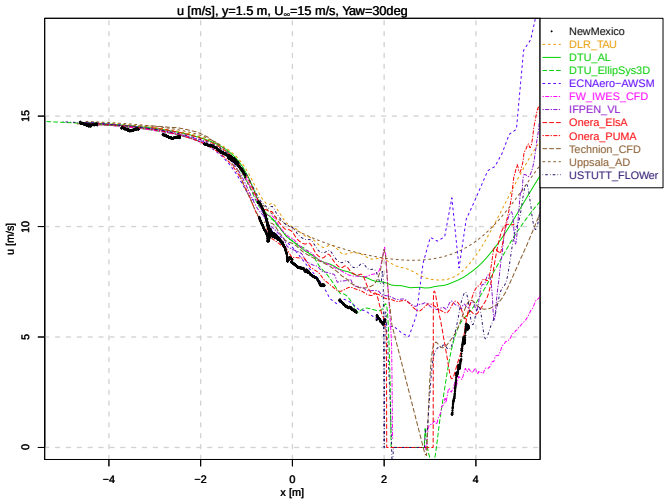

(b) u, y=+1.5 m

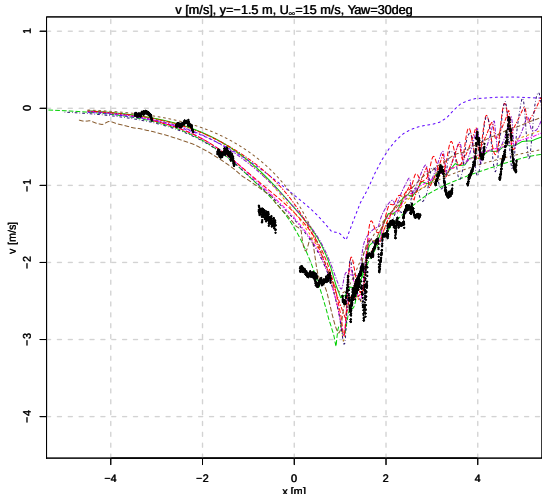

(c) v, y=-1.5 m

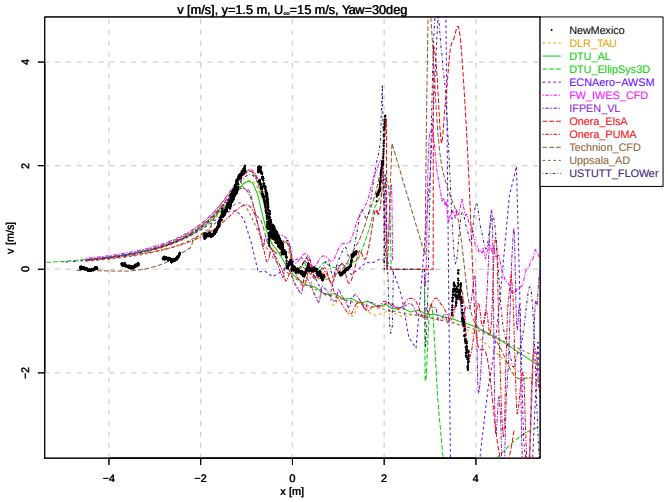

(d) v, y=+1.5 m

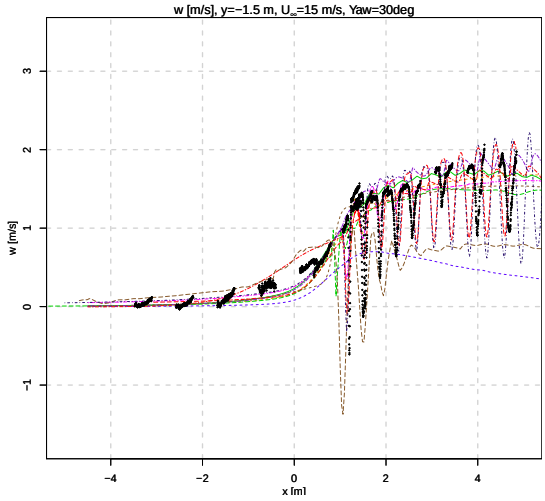

(e) w, y=-1.5 m

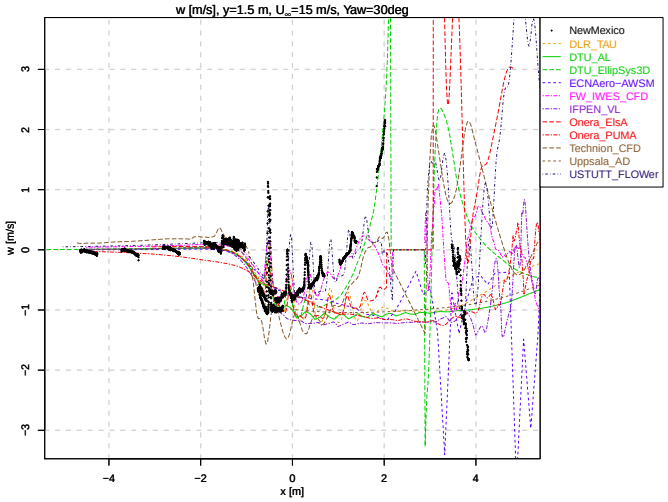

(f) w, y=+1.5 m

Figure B.47: Axial traverse of velocity , Case 2.2

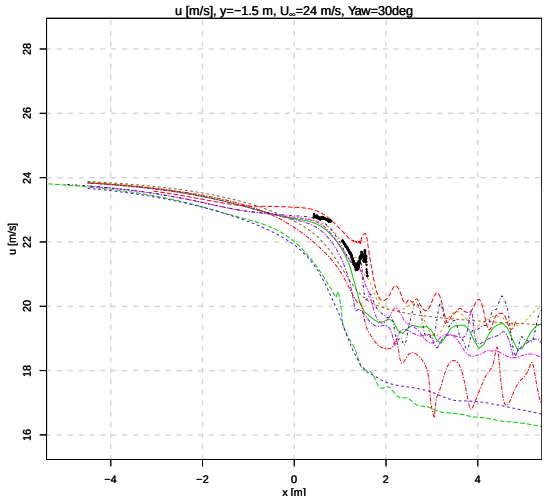

(a) u, y=-1.5 m

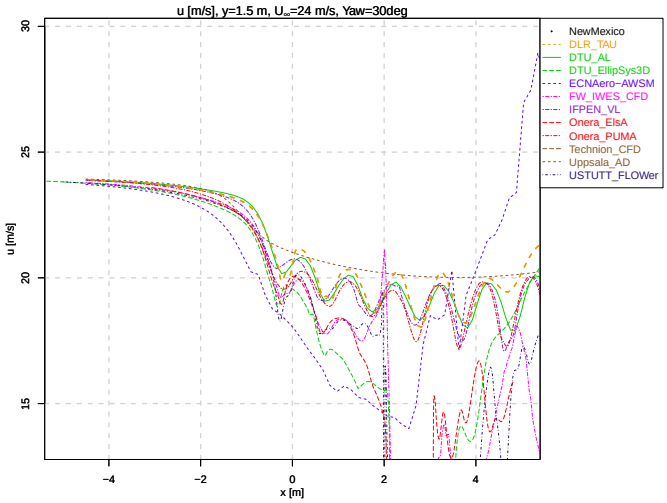

(b) u, y=+1.5 m

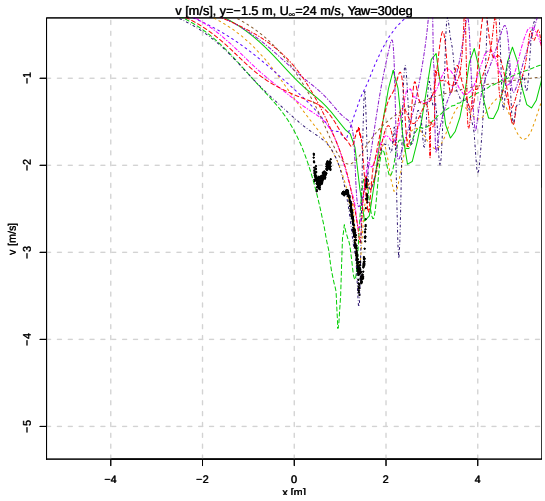

(c) v, y=-1.5 m

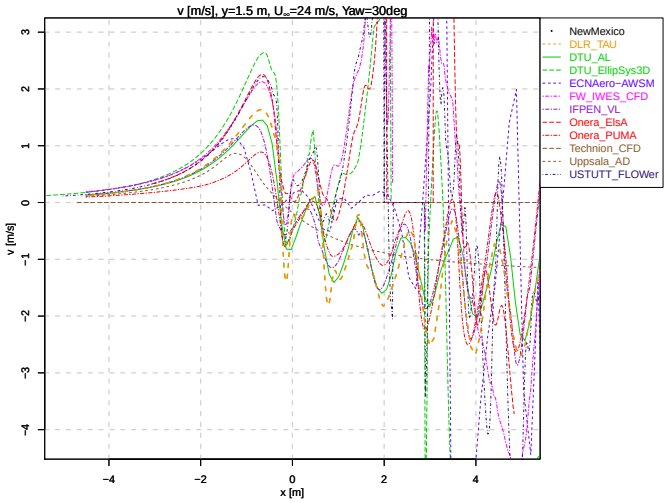

(d) v, y=+1.5 m

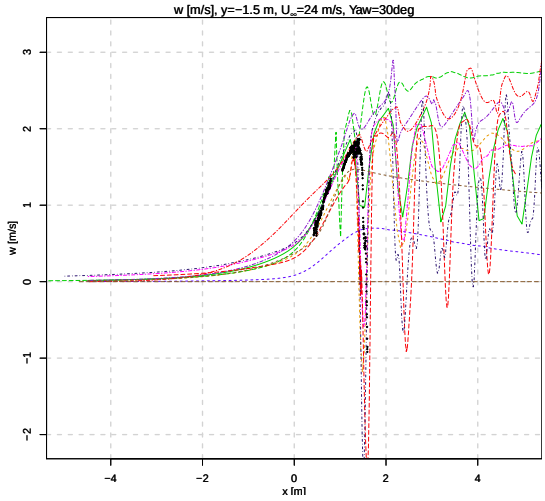

(e) w, y=-1.5 m

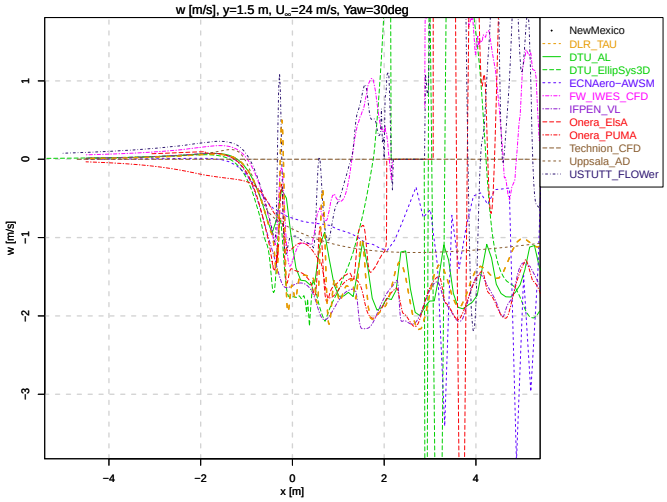

(f) w, y=+1.5 m

Figure B.48: Axial traverse of velocity , Case 2.3

Radial traverse

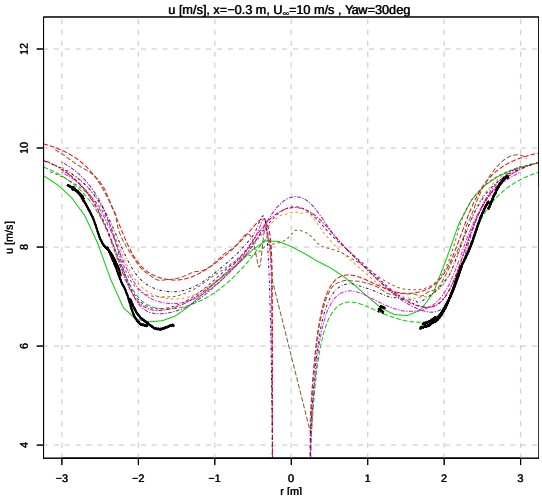

(a) u, x_m=-0.3 m

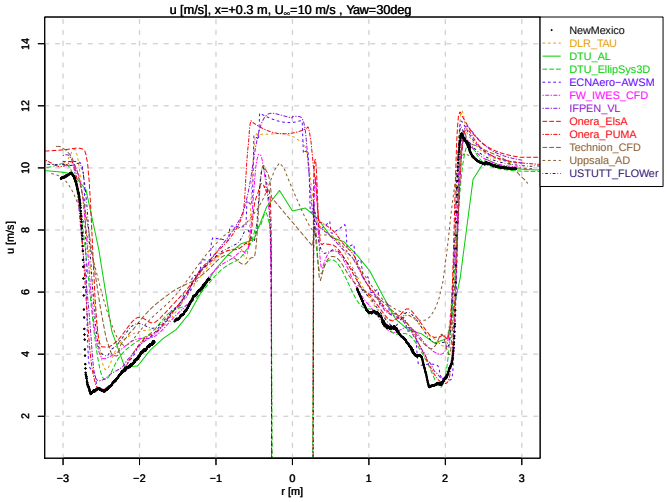

(b) u, x_m=+0.3 m

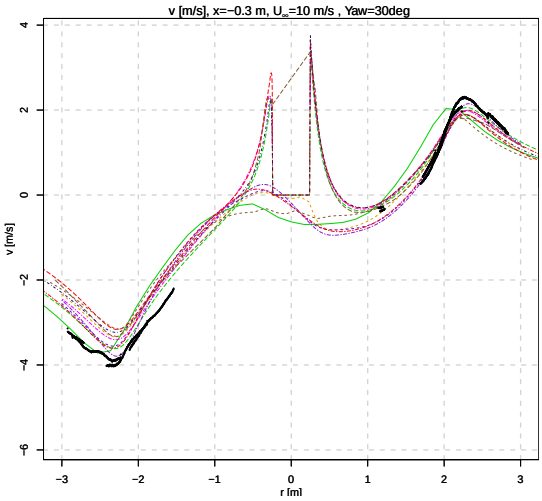

(c) v, x_m=-0.3 m

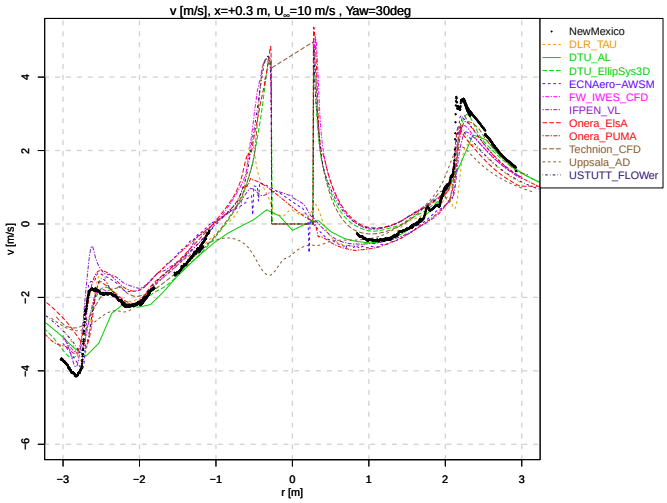

(d) v, x_m=+0.3 m

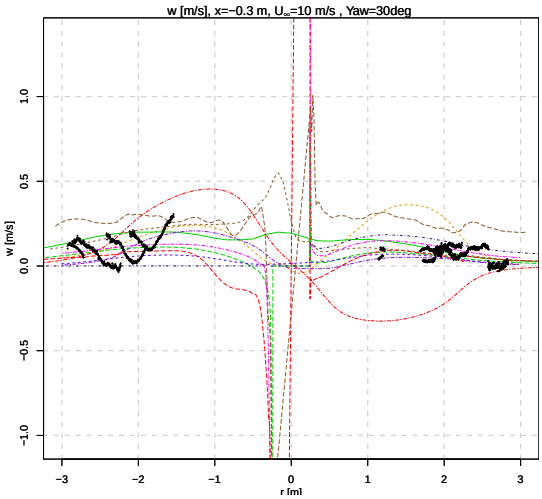

(e) w, x_m=-0.3 m

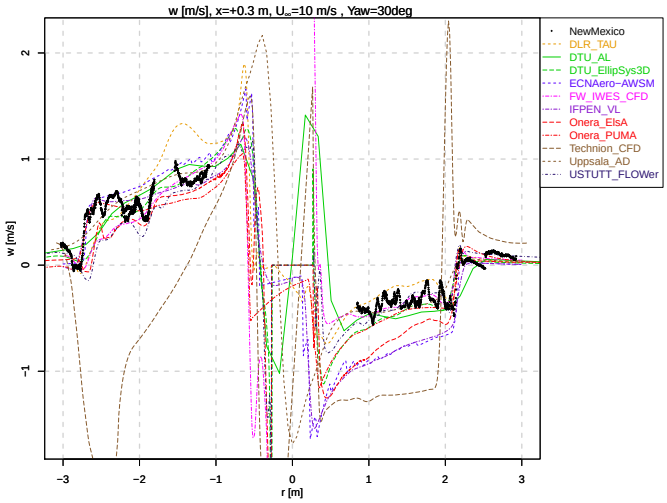

(f) w, x_m=+0.3 m

Figure B.49: Radial traverse of velocity , Case 2.1

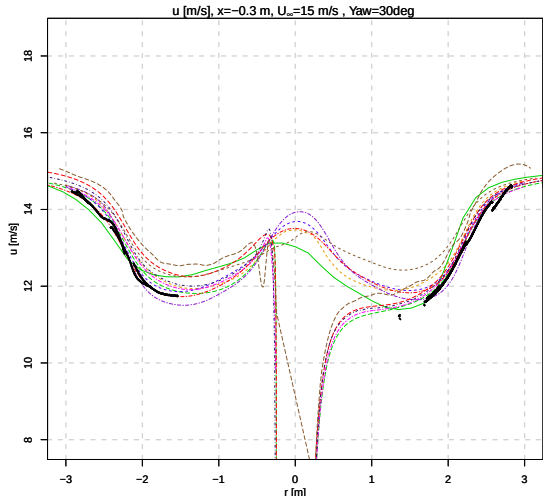

(a) u, x_m=-0.3 m

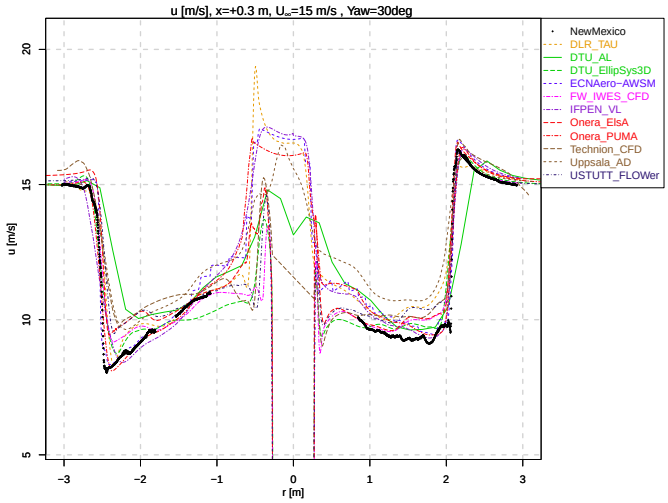

(b) u, x_m=+0.3 m

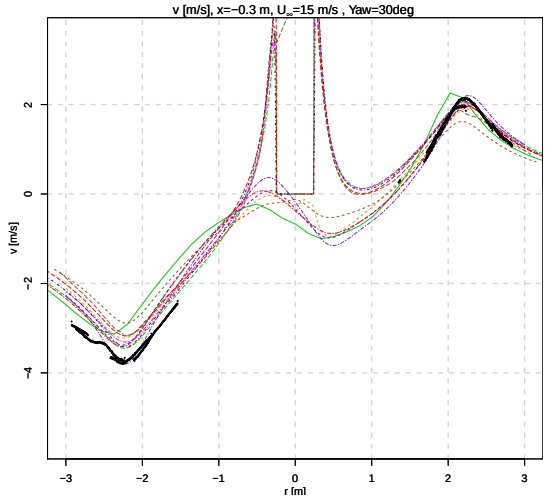

(c) v, x_m=-0.3 m

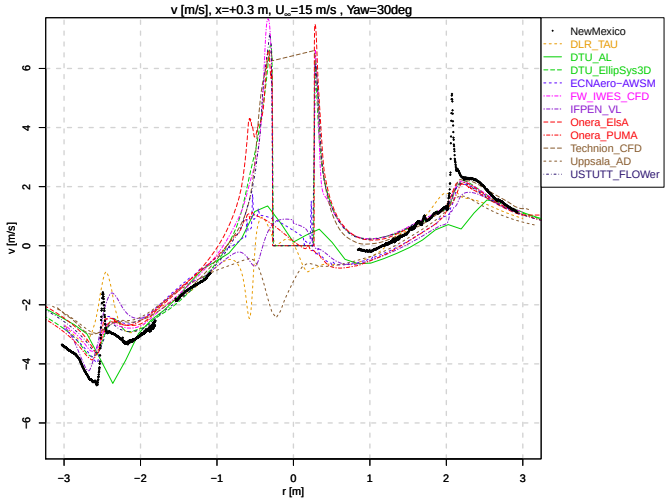

(d) v, x_m=+0.3 m

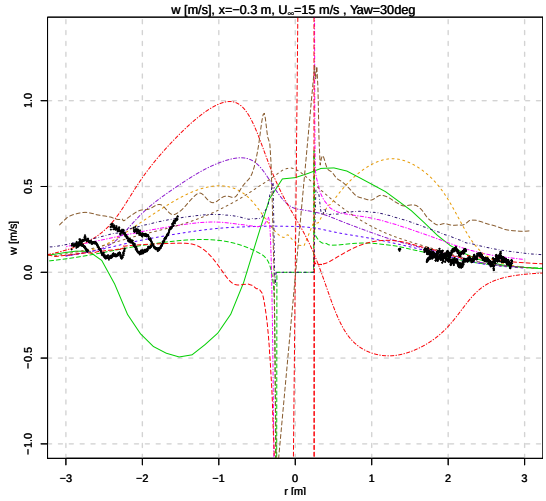

(e) w, x_m=-0.3 m

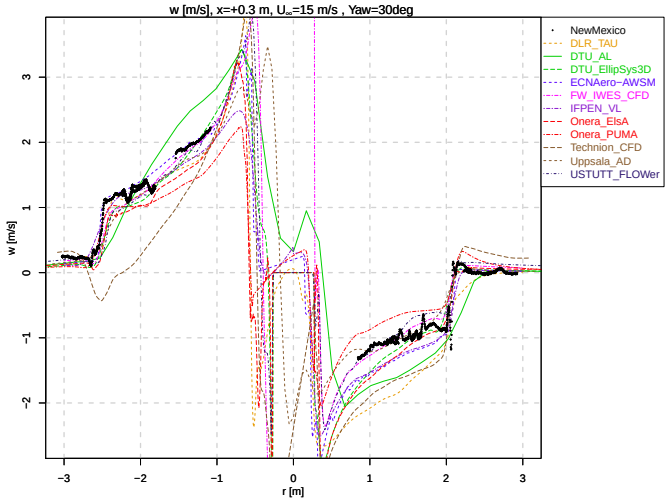

(f) w, x_m=+0.3 m

Figure B.50: Radial traverse of velocity , Case 2.2

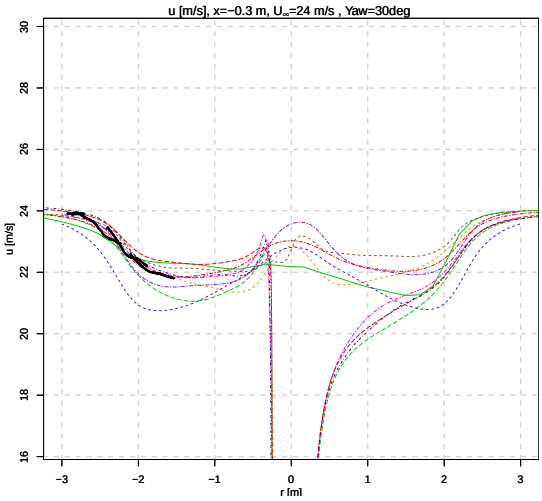

(a) u, x_m=-0.3 m

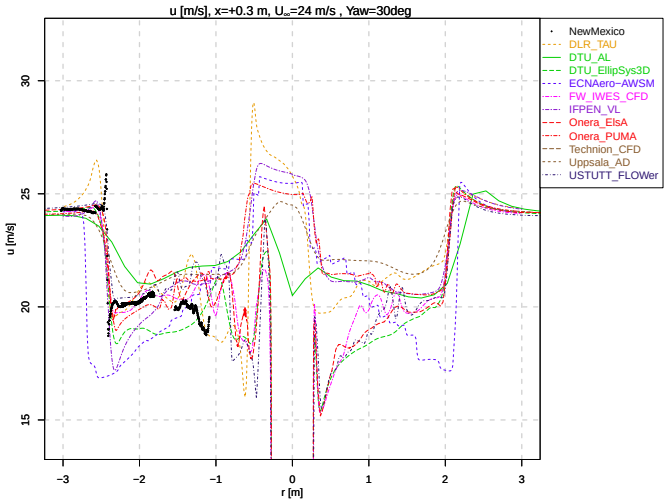

(b) u, x_m=+0.3 m

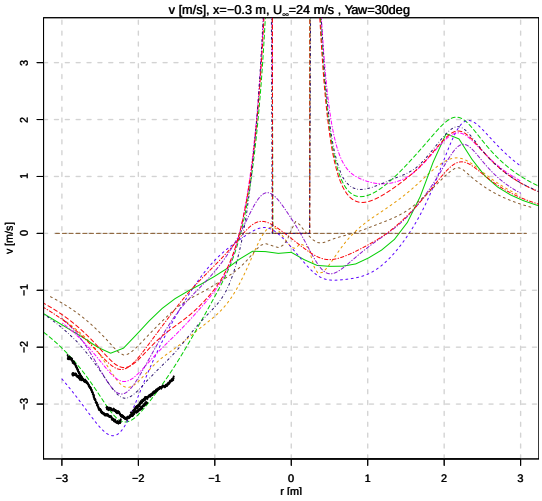

(c) v, x_m=-0.3 m

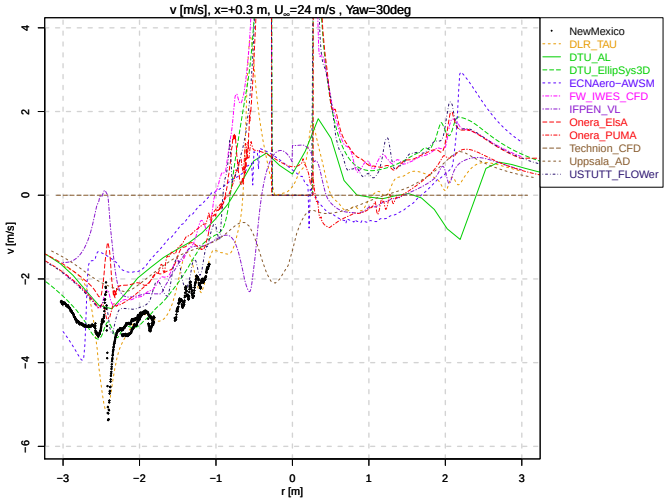

(d) v, x_m=+0.3 m

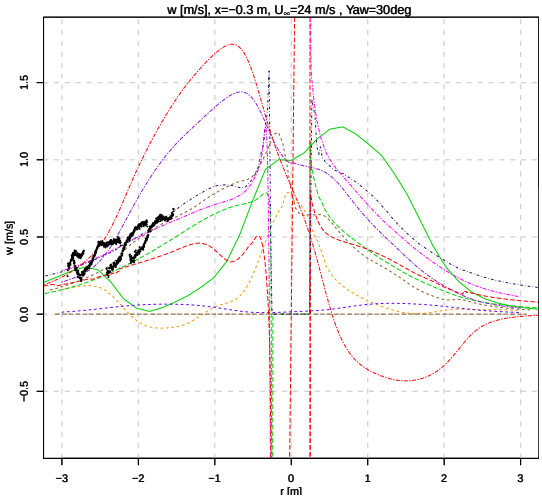

(e) w, x_m=-0.3 m

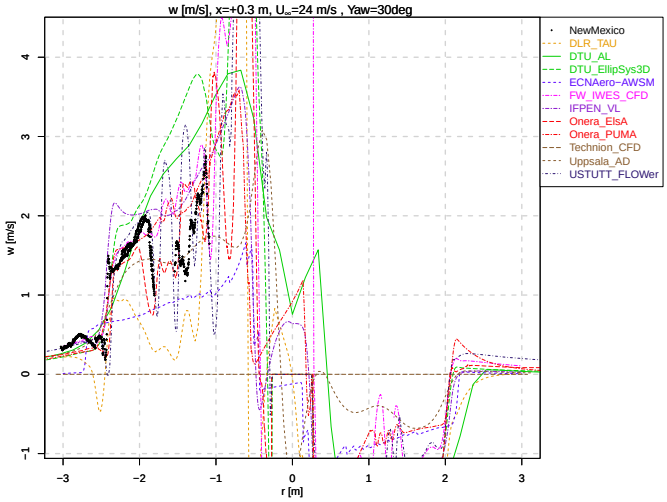

(f) w, x_m=+0.3 m

Figure B.51: Radial traverse of velocity , Case 2.3

C. WP3 Data Format and Test Cases

This section describes the data format and test cases for the purpose of the comparison between calculations and measurements (chapter 4).

C.1 First round: Axial flow

Mexnext III: Definition of first round of calculations

K. Boorsma and J.G. Schepers
February 13th, 2017

1. Description of the tunnel and the wind turbine model:

See the tunnel definition document ECN-x--15-093 and related data files on the EPOS site, https://mexnext.ecn.nl/do/document/?id=14921-766f66646f63 (Please note that depending on your browser settings this link and the ones below may not work. In that case please copy and paste the address to your browser address bar). To make sure that everybody uses the same input, the following airfoil coefficient data sets are prescribed from "ExperimentDescriptionNewMexico.xlsx" (https://mexnext.ecn.nl/do/document/?id=14920-766f66646f63, marked yellow) or the tunnel definition document:

- DU91-W2-250 : $Re_c = 0.5 \times 10^6$ dataset (rough)
- RISØ A1-21 : $Re_c = 1.6 \times 10^6$ dataset (rough)
- NACA64-418 : $Re_c = 0.7 \times 10^6$ dataset (**clean**)

For the CFD modellers please use the supplied CAD files from the EPOS site.

- Design geometry of the blades as supplied by Technion, https://mexnext.ecn.nl/do/folder/?id=4000-766f66666f6c
  Please note that the blade geometry does not yet include the pitch angle.
- If tower and nacelle geometry are desired, the simplified geometry as supplied by IAG University of Stuttgart, https://mexnext.ecn.nl/do/folder/?id=14460-766f66666f6c

The information on size and location of roughness strips can be found in ECN-x--15-093, Table 4 and 6 (Blade config 3, r/R>0.7 transition free).

2. Description of cases.

- Pitch angle: -2.3 degrees (see also Figure 1 for definition)
- Rotor speed: 425.1 rpm
- Tunnel speeds, air density, static ambient pressure and temperature (note that these numbers are supplied by DNW but apparently they donot precisely fulfill the ideal gas law):
  - Case 1.1: $V_{tunnel} = 10.05$ m/s, $\rho = 1.197$ kg/m^3 ($T_{inf} = 293.63$ ^{o}K, $p_{inf} = 101398$ N/m^2)
  - Case 1.2: $V_{tunnel} = 15.06$ m/s, $\rho = 1.191$ kg/m^3 ($T_{inf} = 294.91$ ^{o}K, $p_{inf} = 101345$ N/m^2)
  - Case 1.3: $V_{tunnel} = 24.05$ m/s, $\rho = 1.195$ kg/m^3 ($T_{inf} = 294.25$ ^{o}K, $p_{inf} = 101407$ N/m^2)
- Yaw angle: 0 degrees

3. Results to be supplied:

3.1 Lifting line codes:

The comparison of results from lifting line codes (e.g. BEM codes) mainly focusses on the local aerodynamic forces and the angle of attack at several radial stations. In addition the axial force on the rotor is calculated. The axial force on the rotor and the local aerodynamic forces can be compared with the measured values.

3.1.1 Loads

- Requested data and units:
  - F_{ax} : Axial force on the rotor [N]. For the spanwise integration, please use the experimental resolution, i.e. only five points at 25%, 35%, 60%, 82% and 92%R. Please see Table 1 for the relevant weighting factors. The factors assume a linear integration with zero loading at blade root and tip. Application of the factors results in the full rotor axial force and hence already take into account the number of blades.
  - Torque: Aerodynamic torque of the rotor [Nm]. For the spanwise integration, please use the experimental resolution, i.e. only five points at 25%, 35%, 60%, 82% and 92%R (CFD contributions please exclude skin friction). Please see Table 2 for the relevant weighting factors. The factors assume a linear integration with zero loading at blade root and tip. Application of the factors results in the full rotor torque and hence already take into account the number of blades.
  - For a minimum of 10 (preferably more) radial locations:
    - F_{normal} (i.e. the force normal to the local chord, positive pointing in downwind direction) [N/m]
    - $F_{tangential}$ (i.e. the force parallel to the local chord, positive pointing from trailing to leading edge) [N/m]. To compare with the measurements this should be the 'pressure' tangential force without skin friction (CFD only).
- Files to be supplied:
  - Please supply the data in one ASCII file which should contain the data for all three wind speeds.
  - Format: Each row contains 7 columns with data. Separate the columns by tabs or blanks. The first row gives the identification of data. The second row gives the axial force for the three wind speeds (10, 15 and 24 m/s). Please duplicate the values for F_{ax} since 2 columns are available for each wind speed. The next rows give the data at the three wind speeds for the chosen radial locations (a total of n), increasing from root to tip. The variable r is defined to start at the rotor center (r=0m) increasing towards the blade tip (r=2.25m). Hence, the format is as follows

r	F_{n10}	F_{t10}	F_{n15}	F_{t15}	F_{n24}	F_{t24}
F_{ax}	--	--	--	--	--	--
Torque	--	--	--	--	--	--
r_1	--	--	--	--	--	--
|	|	|	|	|	|	|
|	|	|	|	|	|	|

r_n -- -- -- -- -- --

Note that this makes the total number of rows to be n + 3
(1 (header) + 1 (axial force) + 1 (torque) + n radial locations)

3.1.2 Lifting line variables

- Requested data and units
  - For a minimum of 10 (preferably more) radial locations:
    - V_{eff} (i.e. the resultant incoming velocity at the blade section) [m/s]
    - α Angle of attack [deg]
    - u_i, the local axial induced velocity [m/s]
      The sign is positive pointing in upwind direction.
    - u_{tan}, the local velocity induced in tangential (rotational) direction [m/s]
      The sign is positive pointing opposite to the direction of rotation.
    - c_n normal force coefficient = $F_{normal}/(0.5\ \rho\ V_{eff}^2\ c)$ [-]
      Orientation in agreement with F_{normal} from loads (section 3.1.1)
    - c_t tangential force coefficient = $F_{tangential}/(0.5\ \rho\ V_{eff}^2\ c)$ [-]
      Orientation in agreement with $F_{tangential}$ from loads (section 3.1.1)

- Files to be supplied:
  - Please supply the data in one plain ASCII file which should contain the data for all three wind speeds.
  - Format: Each row contains 19 columns, separated by tabs or blanks. The first row gives the identification of data. The next rows give the data at the three wind speeds for the chosen radial locations (a total of n), increasing from root to tip. Hence, the format is as follows:

r	V_{eff10}	α_{10}	u_{i10}	u_{tan10}	c_{n10}	c_{t10}	V_{eff15}	α_{15}	u_{i15}	u_{tan15}	c_{n15}	c_{t15}	V_{eff24}	α_{24}	u_{i24}	u_{tan24}	c_{n24}	c_{t24}
r_1	--	--	--	--	--	--	--	--	--	--	--	--	--	--	--	--	--	--
|	|	|	|	|	|	|	|	|	|	|	|	|	|	|	|	|	|	|
|	|	|	|	|	|	|	|	|	|	|	|	|	|	|	|	|	|
r_n	--	--	--	--	--	--	--	--	--	--	--	--	--	--	--	--	--	--

Note that this makes the total number of rows to be n + 1
(1 (header) + n radial locations)

3.2 CFD codes

It is anticipated that many CFD (and free vortex wake) codes calculate the flow field around the rotor and in the wake. Hence results from these codes can be compared with PIV flow field measurements. Some of these codes will also model the pressures (and resulting loads) around the blades which can be compared with the measured data as well.

It is proposed to calculate 3D velocities in the form of

- Radial traverses, just upstream of the rotor and just downstream of the rotor (azimuthally averaged).
- Axial traverses at fixed radial positions and azimuth angle of 0 deg.
- Azimuth traverse, just upstream and downstream of the rotor, at 5 radial positions.

Note that the blade position refers to the position of blade 1 where blade position = 0 degrees indicates blade 1 pointing vertically upward. The velocities need to be calculated in the horizontal plane at the 9 o clock position.
For actuator disc codes the velocities the dependency on blade position is lost and a (more or less averaged) velocity can be supplied only. This obviously makes a comparison with measured values useless near the rotor plane but we still propose to supply the calculated values for a mutual comparison with other simulation results.

3.2.1 Loads

See the format specification of the file in section 3.1.1.

3.2.2 Pressure data

- Requested data and units.
  - For all instrumented sections: Azimuthally averaged pressure data in dimensional form [Pa] relative to the ambient pressure as function of x (along the chord) and y (perpendicular to the chord). Note that (x=0,y=0) is at the nose of the airfoil. Positive y at the suction side. Units of x and y are [m]. Note that x and y donot necessarily need to coincide with the position of the sensors.
- Files to be supplied
  - For every instrumented section and every wind speed a separate (ASCII) file needs to be supplied. Hence a total of 5 (radial positions) * 3 (wind speeds) = 15 files need to be supplied.
  - Format: Three columns with pressures as function of x (along the chord) and y (perpendicular to the chord) starting at the trailing edge, then going along the suction side to the leading edge and then back to the trailing edge along the pressure side. Separate the columns by tabs or blanks. The format is as follows:

x[m]	y[m]	Pressure [Pa]
chord (t.e.)	0	--
--	positive	usually negative
0(l.e.)	0	--
--	negative	usually positive
Chord(t.e.)	0	--

3.2.3. Radial traverses

Radial traverses need to be calculated in the horizontal plane at the 9 o' clock position at:

- x = -0.30m (upstream of the rotor) and x=+0.30m (downstream of the rotor). Note that x=0m is in the rotor plane with positive x directed towards the collector), see also Figure 1.
- **Average the velocities with repect to blade azimuth angle** (or time). Here it is noted that the large velocity variations around the blade passage require sufficient azimuthal resolution to determine a proper weighted average. The measurement resolution was not constant and consisted of the following azimuth angles (focusing on blade 2 passage): 10/17/22/26/29/31/34/38/43/50/70/90/110deg. If possible please use this experimental resolution in azimuth direction to determine the average. Please see Table 3 for the relevant weighting factors.
- The radial coordinate should anyhow cover the measurement range from r =y= 0.30 m to r =y= 2.68m (i.e. part of the wake expansion is included), see also Figure 1.

- Requested data and units
  - All three wind components (u, v and w) as function of r. Note that r=0 m is in the rotor centre. The r-positions donot necessarily need to coincide with the measurement locations. However the measurements are done with a spatial resolution of 2 mm and we recommend a resolution which is more or less comparable to that.
  - Unit of r = [m].
  - u is the axial component (positive from nozzle to collector), v is the radial component (positive from root to tip) and w is the vertical component (tangential, positive upward).
  - Unit of u, v and w = [m/s].

- Files to be supplied:
  - Please supply the data in ASCII files. Separate files should be supplied for the upstream position and the downstream position. Each file contains the data for all three wind speeds (10, 15 and 24 m/s). Hence the total number of files should be 2 (2 x-positions).
  - Format: Each row contains 10 columns. Please separate the columns with blanks or tabs. The first row is for identification of the signals. Then the 3D (u, v and w) velocity components are given as function of the radial position for all three wind speeds

r	u_{10}	v_{10}	w_{10}	u_{15}	v_{15}	w_{15}	u_{24}	v_{24}	w_{24}
r_1	--	--	--	--	--	--	--	--	--
|	|	|	|	|	|	|	|	|	|
|	|	|	|	|	|	|	|	|	|
r_n	--	--	--	--	--	--	--	--	--

3.2.4 Axial traverses

Axial traverses need to be calculated in the horizontal plane at the 9 o clock position at:

- r =y= 1.5 m and r=y=0.5 m. Note that r = 0 m is in the rotor centre.
- Blade (1) position: 0 degrees (i.e. blade 1 pointing vertically upward).
- The axial coordinate should anyhow cover the measurement range from x = -4.5 m (upstream) to x = 5.9 m (downstream)

- Requested data and units
  - All three wind components (u, v and w) as function of x. Note that x=0 m is in the rotor plane with positive x directed towards the collector), see also Figure 1. The x-positions donot necessarily need to coincide with the measurement locations but measurements are done with a spatial resolution of 4 mm and we recommend a resolution which is more or less comparable to that.
  - Unit of x = [m].
  - u is the axial component (positive from nozzle to collector), v is the radial component (positive from root to tip) and w is the vertical component (tangential, positive upward).
  - Unit of u, v and w = [m/s].

- Files to be supplied:
  - Please supply the data in 2 ASCII files. One file for the r=1.5m position and one file for the r=0.5m position, where each file contains the data for all three wind speeds (10, 15 and 24 m/s).
  - Format: Each row contains 10 columns. Please separate the columns with blanks or tabs. The first row is for identification of the signals. Then the 3D (u, v and w) velocity components are given for all three wind speeds as function of x.

x	u_{10}	v_{10}	w_{10}	u_{15}	v_{15}	w_{15}	u_{24}	v_{24}	w_{24}
x_1	--	--	--	--	--	--	--	--	--
|	|	|	|	|	|	|	|	|	|
|	|	|	|	|	|	|	|	|	|
x_n	--	--	--	--	--	--	--	--	--

3.2.5 Azimuth traverses

Azimuth traverses need to be calculated in the horizontal plane at the 9 o' clock position at:

- x = -0.30m (upstream of the rotor) and x=+0.30m (downstream of the rotor). Note that x=0 m is in the rotor plane with positive x directed towards the collector.
- The data is requested at 5 radial locations in agreement with the instrumented sections on the blades. This means r=0.56, 0.79, 1.35. 1.85 and 2.07m.
- The rotor azimuth range should anyhow cover the measurement range between 0 and 120 degree with sufficient resolution to capture the blade passage, see also Figure 1. The measurement resolution was not constant and consisted of the following azimuth angles (focusing on blade 2 passage): 10/17/22/26/29/31/34/38/43/50/70/90/110deg

- Requested data and units
  - All three wind components (u, v and w) as function of rotor azimuth angle (see also Figure 1). See the comments above for the required range and resolution
  - Unit of rotor azimuth angle = [deg].
  - u is the axial component (positive from nozzle to collector), v is the radial component (positive from root to tip) and w is the vertical component (tangential, positive upward).
  - Unit of u, v and w = [m/s].

- Files to be supplied:
  - Please supply the data in ASCII files. Separate files should be supplied for the upstream position and the downstream position and for every radial location. Each file contains the data for all three wind speeds (10, 15 and 24 m/s). Hence the total number of files should be 5 (radial positions) * 2 (x-positions) =10.
  - Format: Each row contains 10 columns. Please separate the columns with blanks or tabs. The first row is for identification of the signals. Then the 3D (u, v and w) velocity components are given as function of the radial position for all three wind speeds

Azimuth	u_{10}	v_{10}	w_{10}	u_{15}	v_{15}	w_{15}	u_{24}	v_{24}	w_{24}
0°	--	--	--	--	--	--	--	--	--
|	|	|	|	|	|	|	|	|	|
|	|	|	|	|	|	|	|	|	|
120°	--	--	--	--	--	--	--	--	--

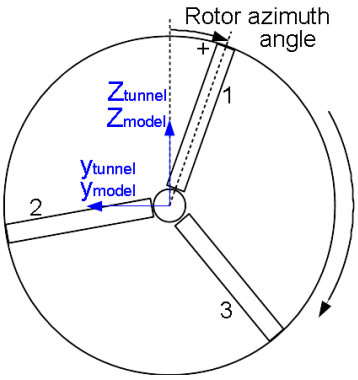

(a) Front view

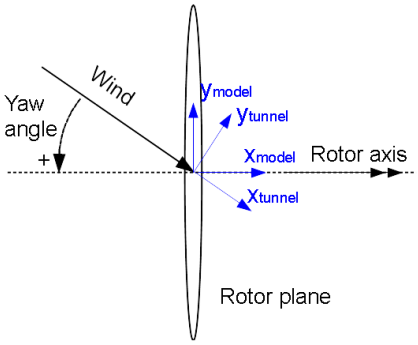

(b) Top view

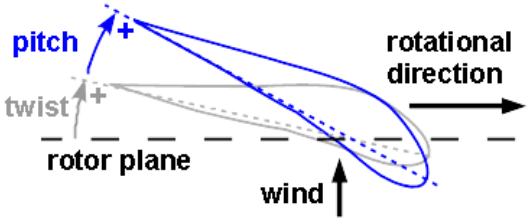

(c) Sectional view: Pitch angle

Figure 1: Definitions and conventions of the (New) Mexico experiment

Table 1: Weighting factors to convert Mexico normal and tangential force [N/m] from the 5 specified radial sections to full **rotor** axial force in [N] for pitch=-2.3deg
(Hence Fax = 0.847477*Fn25 - 0.179634*Ft25 + ……. + 0.607397*Fn92 + 0.011208*Ft92)

Fn25 [N/m]	**0.847477**	Ft25 [N/m]	**-0.179364**
Fn35 [N/m]	**1.170039**	Ft35 [N/m]	**-0.162356**
Fn60 [N/m]	**1.584740**	Ft60 [N/m]	**-0.069191**
Fn82 [N/m]	**1.079999**	Ft82 [N/m]	**-0.001508**
Fn92 [N/m]	**0.607397**	Ft92 [N/m]	**0.011208**

Table 2: Weighting factors to convert Mexico normal and tangential force [N/m] from the 5 specified radial sections to full **rotor** torque in [Nm] for pitch=-2.3deg
(Hence Torque = 0.089458*Fn25 + 0.422679*Ft25 + …….. - 0.022949*Fn92 + 1.243645*Ft92)

Fn25 [N/m]	**0.089458**	Ft25 [N/m]	**0.422679**
Fn35 [N/m]	**0.155253**	Ft35 [N/m]	**1.118850**
Fn60 [N/m]	**0.091073**	Ft60 [N/m]	**2.085914**
Fn82 [N/m]	**0.002579**	Ft82 [N/m]	**1.846798**
Fn92 [N/m]	**-0.022949**	Ft92 [N/m]	**1.243645**

Table 3: Weighting factors to convert New Mexico velocities [m/s] from the 13 specified azimuth angles to azimuth averaged velocity [m/s] for the radial traverse
(Hence u_avg = 0.1125*u_10deg + 0.0500*u_17deg +.....+ 0.166667*u_90deg + 0.166667*u_110deg)

10deg	**0.112500**	38deg	**0.037500**
17deg	**0.050000**	43deg	**0.050000**
22deg	**0.037500**	50deg	**0.112500**
26deg	**0.029167**	70deg	**0.166667**
29deg	**0.020833**	90deg	**0.166667**
31deg	**0.020833**	110deg	**0.166667**
34deg	**0.029167**		

C.2 Second round: Yawed flow

Mexnext III: Definition of second round of calculations

K. Boorsma and J.G. Schepers
February 13th, 2017

1. Description of the tunnel and the wind turbine model:

See the tunnel definition document ECN-x--15-093 and related data files on the EPOS site, https://mexnext.ecn.nl/do/document/?id=14921-766f66646f63 (Please note that depending on your browser settings this link and the ones below may not work. In that case please copy and paste the address to your browser address bar). To make sure that everybody uses the same input, the following airfoil coefficient data sets are prescribed from "ExperimentDescriptionNewMexico.xlsx" (https://mexnext.ecn.nl/do/document/?id=14920-766f66646f63, marked yellow) or the tunnel definition document:

- DU91-W2-250 : Re_c = 0.5 x 10^6 dataset (rough)
- RISØ A1-21 : Re_c = 1.6 x 10^6 dataset (rough)
- NACA64-418 : Re_c = 0.7 x 10^6 dataset (**clean**)

For the CFD modellers please use the supplied CAD files from the EPOS site.

- Design geometry of the blades as supplied by Technion, https://mexnext.ecn.nl/do/folder/?id=4000-766f66666f6c
  Please note that the blade geometry does not yet include the pitch angle.
- If tower and nacelle geometry are desired, the simplified geometry as supplied by IAG University of Stuttgart, https://mexnext.ecn.nl/do/folder/?id=14460-766f66666f6c

The information on size and location of roughness strips can be found in ECN-x--15-093, Table 4 and 6 (Blade config 3, r/R>0.7 transition free).

2. Description of cases.

- Pitch angle: -2.3 degrees (see also Figure 1 for definition)
- Rotor speed: 425.1 rpm
- Tunnel speeds, air density, static ambient pressure and temperature (note that these numbers are supplied by DNW but apparently they don't precisely fulfill the ideal gas law):
  - Case 2.1: Yaw angle=30 deg, V_{tunnel} = 10.03 m/s, ρ = 1.198 kg/m^3 (T_{inf} = 293.93 ^oK, p_{inf} = 101612 N/m^2)
  - Case 2.2: Yaw angle=30 deg, V_{tunnel} = 15.01 m/s, ρ = 1.198 kg/m^3 (T_{inf} = 294.16 ^oK, p_{inf} = 101625 N/m^2)
  - Case 2.3: Yaw angle=30 deg, V_{tunnel} = 24.08 m/s, ρ = 1.198 kg/m^3 (T_{inf} = 293.92 ^oK, p_{inf} = 101595 N/m^2)

3. Results to be supplied:

3.1 Lifting line codes:

The comparison of results from lifting line codes (e.g. BEM codes) mainly focuses on the local aerodynamic forces and the angle of attack at the 5 instrumented sections. In addition the axial force on the rotor is calculated. The axial force on the rotor and the local aerodynamic forces can be compared with the measured values.

3.1.1 Loads

- Requested data and units as a function of bin averaged rotor azimuth angle [deg] between 0 and 360 deg. Preferably in steps smaller than 5 deg azimuth.
  - F_{ax} : Axial force on the rotor [N]. For the spanwise integration, please use the experimental resolution, i.e. only five points at 25%, 35%, 60%, 82% and 92%R. Please see Table 1 for the relevant weighting factors. The factors assume linear integration with zero loading at blade root and tip and result in the **blade** axial force. After the separate contribution for each blade is determined these still need to be summed for each azimuth to obtain rotor axial force.

    Torque: Aerodynamic torque of the rotor [Nm]. For the spanwise integration, please use the experimental resolution, i.e. only five points at 25%, 35%, 60%, 82% and 92%R (CFD contributions please exclude skin friction). Please see Table 2 for the relevant weighting factors. The factors assume linear integration with zero loading at blade root and tip and result in the **blade** torque. After the separate contribution for each blade is determined these still need to be summed for each azimuth to obtain rotor torque.
  - For the 5 instrumented radial locations:
    - F_{normal} (i.e. the force normal to the local chord, positive pointing in downwind direction) [N/m]
    - $F_{tangential}$ (i.e. the force parallel to the local chord, positive pointing from trailing to leading edge) [N/m]. To compare with the measurements this should be the 'pressure' tangential force without skin friction (CFD only).
- Files to be supplied:
  - Please supply the data in three ASCII files which should contain the data for the three cases (case 2.1, 2.2 and 2.3).
  - Format: Each row contains 13 columns with data containing axial force, torque and normal and tangential forces at 5 sections. Separate the columns by tabs or blanks. The first row gives the identification of data. The next rows give the data at the specified azimuth positions (a total of n) between 0 and 360 deg. Hence, the format is as follows

Azi	F_{ax}	Torq	F_{n25}	F_{t25}	F_{n35}	F_{t35}	F_{n60}	F_{t60}	F_{n82}	F_{t82}	F_{n92}	F_{t92}
Azi_1	-	-	-	-	-	-	-	-	-	-	-	-
|	|	|	|	|	|	|	|	|	|	|	|	|
|	|	|	|	|	|	|	|	|	|	|	|	|
Azi_n	-	-	-	-	-	-	-	-	-	-	-	-

Note that this makes the total number of rows to be n + 1
(1 (header) + n azimuth positions)

3.1.2 Lifting line variables

- Requested data and units as a function of bin averaged rotor azimuth angle [deg] between 0 and 360 deg. Preferably in steps smaller than 5 deg azimuth.
    - For the 5 instrumented radial locations:
        - V_{eff} (i.e. the resultant incoming velocity at the blade section) [m/s]
        - α Angle of attack [deg]
        - u_i, the local axial induced velocity [m/s]
          The sign is positive pointing in upwind direction.
        - u_{tan}, the local velocity induced in tangential (rotational) direction [m/s]
          The sign is positive pointing opposite to the direction of rotation.
        - c_n normal force coefficient = $F_{normal}/(0.5\ \rho\ V_{eff}^2\ c)$ [-]
          Orientation in agreement with F_{normal} from loads (section 3.1.1)
        - c_t tangential force coefficient = $F_{tangential}/(0.5\ \rho\ V_{eff}^2\ c)$ [-]
          Orientation in agreement with $F_{tangential}$ from loads (section 3.1.1)

- Files to be supplied:
    - Please supply the data in three plain ASCII files which should contain the data for the three cases (case 2.1, 2.2 and 2.3)
    - Format: Each row contains 31 columns, containing the 6 variables at 5 radial stations. Separate the columns by tabs or blanks. The first row gives the identification of data. The next rows give the data at the specified azimuth positions (a total of n) between 0 and 360 deg. Hence, the format is as follows:

Azi	V_{eff25}	α_{eff25}	u_{i25}	u_{tan25}	c_{n25}	c_{t25}	V_{eff35}	α_{eff35}	----	u_{tan92}	c_{n92}	c_{t92}
Azi_1	-	-	-	-	-	-	-	-	----	-	-	-
|	|	|	|	|	|	|	|	|	---	|	|	|
|	|	|	|	|	|	|	|	---	|	|	|
Azi_n	-	-	-	-	-	-	-	-	---	-	-	-

Note that this makes the total number of rows to be n + 1
(1 (header) + n azimuth positions)

3.2 CFD codes

It is anticipated that many CFD (and free vortex wake) codes calculate the flow field around the rotor and in the wake. Hence results from these codes can be compared with PIV flow field measurements. Some of these codes will also model the pressures (and resulting loads) around the blades which can be compared with the measured data as well.

It is proposed to calculate 3D velocities in the form of

- Radial traverses, just upstream of the rotor and just downstream of the rotor (azimuthally averaged).
- Axial traverses at fixed radial positions and azimuth angle of 0 deg.

Note that the blade position refers to the position of blade 1 where blade position = 0 degrees indicates blade 1 pointing vertically upward. The velocities need to be calculated in the horizontal plane intersecting the rotor center. Please note that experimental data is not available for all traverses and conditions but a comparison between codes can also be very useful.

3.2.1 Loads

See the format specification of the file in section 3.1.1.

3.2.2 Pressure data

- Requested data and units.
    - For all instrumented sections: Pressure data in dimensional form [Pa] relative to the ambient pressure as function of x (along the chord) and y (perpendicular to the chord) for 4 different azimuth angles (0 degrees (12 o' clock), 90 degrees (3 o' clock), 180 degrees (6 o'clock) and 270 degrees (9 o'clock). Note that (x=0,y=0) is at the nose of the airfoil. Positive y at the suction side. Units of x and y are [m]. Note that x and y donot necessarily need to coincide with the position of the sensors.
- Files to be supplied
    - For every instrumented section and every wind speed a separate (ASCII) file needs to be supplied. Hence a total of 5 (radial positions) * 3 (wind speeds) = 15 files need to be supplied.
    - Format: Ten columns with pressures as function of x (along the chord) and y (perpendicular to the chord) starting at the trailing edge, then going along the suction side to the leading edge and then back to the trailing edge along the pressure side. Separate the columns by tabs or blanks. The format is given below: It starts with 2 columns with x and y of the pressure points, then the first azimuth angle (0 degrees) followed by the pressures, then the azimuth angles and the pressures at the remaining azimuth angles. We explicitly ask you to specify the azimuth angle to assure that the pressures are supplied for the correct azimuthal position. We recall that pressures should be supplied in Pascal relative to ambient pressure.

x[m]	y[m]	Azi_0	P_{azi0} [Pa]	Azi_1	P_{azi1}	Azi_2	P_{azi2}	Azi_3	P_{azi3}
chord (t.e.)	0	0	--	90	--	180	--	270	--
--	positive	0	negative *)	90	--	180	--	270	--
0(l.e.)	0	0	--	90	--	180	--	270	--
--	negative	0	positive **)	90	--	180	--	270	--
Chord(t.e.)	0	0	--	90	--	180	--	270	--

*) Usually suction (negative) pressures **) Usually positive pressures

3.2.3. Radial traverses

Radial traverses need to be calculated in the horizontal plane (rotor center height) at:

- x = -0.3 m (upstream of the rotor) and x=+0.3 (downstream of the rotor). Note that **x** is expressed in the **model coordinate system** as defined in Figure 1 included below.
- The radial coordinate should anyhow cover the measurement range from y = -3.0 m to y = 3.0 m (roughly going from one tip to the other). Note that **y** is expressed in the **model coordinate system** as defined in Figure 1.
- Average the velocities with respect to blade azimuth angle (or time). Here it is noted that the large velocity variations around the blade passage require sufficient azimuthal resolution to determine a proper weighted average. The measurement resolution was not constant and consisted of the following azimuth angles to capture the blade passage:
  -For **positive** y values: **10/17/22/26/29/31/34/38/43/50/70/90/110**deg
  -For **negative** y values: **10/30/50/70/77/82/86/89/91/94/98/103/110**deg
- If possible please use this experimental resolution in azimuth direction to determine the average. Please see Table 3 and 4 for the relevant weighting factors.

- Requested data and units
  - All three wind components (u, v and w) as function of y. Note that y=0 m is the projection of the rotor center on the off-setted (x=0.3 or x=-0.3m) radial traverse line. The measurements are done with a spatial resolution smaller than 4 mm and we recommend a resolution which is more or less comparable to that.
  - Unit of y = [m].
  - Please note that u, v and w are defined respectively in the x, y and z directions of the **tunnel coordinate system** (see Figure 1).
  - Unit of u, v and w = [m/s].

- Files to be supplied:
  - Please supply the data in ASCII files. Separate files should be supplied for the upstream position and the downstream position. Each file contains the data for case 2.1, 2.2 and 2.3. Hence the total number of files should be 2.
  - Format: Each row contains 10 columns. Please separate the columns with blanks or tabs. The first row is for identification of the signals. Then the 3D (u, v and w) velocity components are given as function of the y-position for both cases:

y	$u_{2.1}$	$v_{2.1}$	$w_{2.1}$	$u_{2.2}$	$v_{2.2}$	$w_{2.2}$	$u_{2.3}$	$v_{2.3}$	$w_{2.3}$
y_1	--	--	--	--	--	--	--	--	--
|	|	|	|	|	|	|	|	|	|
|	|	|	|	|	|	|	|	|	|
y_n	--	--	--	--	--	--	--	--	--

3.2.4 Axial traverses

Axial traverses need to be calculated in the horizontal plane (rotor center height) at:

- y = -1.5 m and y = 1.5 m. Please note that **y** is expressed in the **tunnel coordinate system** (see Figure 1).
- Blade (1) position for y = 1.5 m: **0** degrees
  Blade (1) position for y = -1.5 m: **60** degrees
- The axial coordinate should anyhow cover the measurement range from x = -4.5 m (upstream) to x = 5.9 m (downstream). Note that **x** is expressed in the **tunnel coordinate system** (see Figure 1).

- Requested data and units
  - All three wind components (u, v and w) as function of x.
  - The x-positions don't necessarily need to coincide with the measurement locations but measurements are done with a spatial resolution of 4 mm and we recommend a resolution which is more or less comparable to that.
  - Unit of x = [m].
  - Please note that u, v and w are defined respectively in the x, y and z directions of the **tunnel coordinate system** (see Figure 1).
  - Unit of u, v and w = [m/s].

- Files to be supplied:
  - Please supply the data in 2 ASCII files, one file for every radial position where every file contains the data for case 2.1, 2.2 and 2.3.
  - Format: Each row contains 10 columns. Please separate the columns with blanks or tabs. The first row is for identification of the signals. Then the 3D (u, v and w) velocity components are given as function of x for both cases:

x	$u_{2.1}$	$v_{2.1}$	$w_{2.1}$	$u_{2.2}$	$v_{2.2}$	$w_{2.2}$	$u_{2.3}$	$v_{2.3}$	$w_{2.3}$
x_1	--	--	--	--	--	--	--	--	--
|	|	|	|	|	|	|	|	|	|
|	|	|	|	|	|	|	|	|	|
x_n	--	--	--	--	--	--	--	--	--

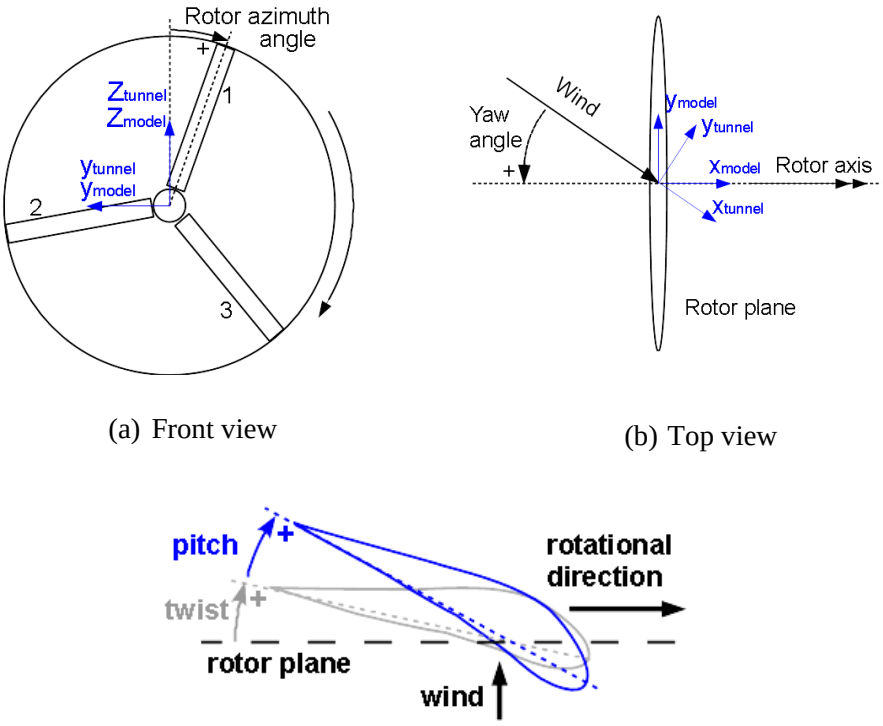

(a) Front view

(b) Top view

(c) Sectional view: Pitch angle

Figure 1: Definitions and conventions of the (New) Mexico experiment

Table 1: Weighting factors to convert Mexico normal and tangential force [N/m] from the 5 specified radial sections to **blade** axial force in [N] for pitch=-2.3deg
(Hence Fax = 0.282492*Fn25 - 0.059788*Ft25 + ……. + 0.202466*Fn92 + 0.003736*Ft92)

Fn25 [N/m]	**0.282492**	Ft25 [N/m]	**-0.059788**
Fn35 [N/m]	**0.390013**	Ft35 [N/m]	**-0.054119**
Fn60 [N/m]	**0.528247**	Ft60 [N/m]	**-0.023064**
Fn82 [N/m]	**0.360000**	Ft82 [N/m]	**-0.000503**
Fn92 [N/m]	**0.202466**	Ft92 [N/m]	**0.003736**

Table 2: Weighting factors to convert Mexico normal and tangential force [N/m] from the 5 specified radial sections to **blade** torque in [Nm] for pitch=-2.3deg
(Hence Torque = 0.029819*Fn25 + 0.140893*Ft25 + …….. - 0.007650*Fn92 + 0.414548*Ft92)

Fn25 [N/m]	**0.029819**	Ft25 [N/m]	**0.140893**
Fn35 [N/m]	**0.051751**	Ft35 [N/m]	**0.372950**
Fn60 [N/m]	**0.030358**	Ft60 [N/m]	**0.695305**
Fn82 [N/m]	**0.000860**	Ft82 [N/m]	**0.615599**
Fn92 [N/m]	**-0.007650**	Ft92 [N/m]	**0.414548**

Table 3: Weighting factors to convert New Mexico velocities [m/s] from the 13 specified azimuth angles to azimuth averaged velocity [m/s] for the radial traverse (**positive** radial coordinate)
(Hence u_avg = 0.1125*u_10deg + 0.0500*u_17deg +.....+ 0.166667*u_90deg + 0.166667*u_110deg)

10deg	**0.112500**	38deg	**0.037500**
17deg	**0.050000**	43deg	**0.050000**
22deg	**0.037500**	50deg	**0.112500**
26deg	**0.029167**	70deg	**0.166667**
29deg	**0.020833**	90deg	**0.166667**
31deg	**0.020833**	110deg	**0.166667**
34deg	**0.029167**		

Table 4: Weighting factors to convert New Mexico velocities [m/s] from the 13 specified azimuth angles to azimuth averaged velocity [m/s] for the radial traverse (**negative** radial coordinate)
(Hence u_avg = 0.166667*u_10deg + 0.166667*u_30deg +.....+ 0.05*u_103deg + 0.1125*u_110deg)

10deg	**0.166667**	89deg	**0.020833**
30deg	**0.166667**	91deg	**0.020833**
50deg	**0.166667**	94deg	**0.029167**
70deg	**0.112500**	98deg	**0.037500**
77deg	**0.050000**	103deg	**0.050000**
82deg	**0.037500**	110deg	**0.112500**
86deg	**0.029167**		

D. WP3 Description of experimental data reduction

This chapter describes the data reduction of the measurements for the purpose of the comparison between calculations and measurements (chapter 4). Here we can distinguish three axial flow and yawed flow cases as defined in Tables 4.1 and 4.3 and appendix C.

D.1 Datapoints

The New MEXICO datapoints used for data reduction have been summarized in Table D.1. The corresponding tunnel velocity, air density and atmospheric conditions for each case have been obtained by averaging over the relevant pressure datapoints. The datapoints for the pressure runs have been selected minimizing differences in tunnel speed. For the traverses the datapoint selection is based on PIV sheet location and discrepancies of ± 0.1 m/s between tunnel speeds can be present.

Table D.1: Overview of New MEXICO datapoints used for data reduction

Case	U_∞[m/s]	Yaw angle[$^\circ$]	Datapoints		
			Pressure	Axial traverse	Radial/Azi traverse
1.1	10.05	0	452,595-602,636-647	595-602	636-647
1.2	15.06	0	547,553,556,558,561 571,572,576,579,580 582,584,585,587,589 590,603-610,624-627	547-554,569-573,575-582 585,586,589,590	603-610
1.3	24.05	0	447,611-618,648-659	648-659	611-618
2.1	10.03	$\pm 30^\dagger$	674,676-684,699 716-727	674,676-684,716-727	674,676-684,716-727
2.2	15.01	$\pm 30^\dagger$	663-673,742-753 703-715,728-738	664-673,742-753 703-715,728-738	664-773,703-715
2.3	24.08	$\pm 30^\dagger$	688-698,942	688-698	688-698

† Datapoints of positive and negative yaw angle have been combined using rotor and blade symmetry

D.2 Pressure distributions

An overview of the pressure sensors used for data reduction is given in Table D.2. Malfunctioning pressure sensors that were certain to give erroneous values have been removed fro the list. The pre-calibrated pressure data are used that assume a linear variation of atmospheric reference pressure between the zero measurements taken before and after each polar. This calibration is described in [110] and [27].

Table D.2: Overview of pressure sensors used for data reduction

Signal nr‡	Spanwise location∓ [%]	Blade nr	x/c† [%]	y/c† [%]	Signal nr‡	Spanwise location∓ [%]	Blade nr	x/c† [%]	y/c† [%]	Signal nr‡	Spanwise location∓ [%]	Blade nr	x/c† [%]	y/c† [%]
58	25	1	62.04	9.49	43	35	1	8.05	-7.91	100	82	3	3.47	3.80
63	25	1	50.66	11.53	41	35	1	15.73	-10.58	98	82	3	1.29	2.28
61	25	1	38.58	12.79	40	35	1	24.35	-12.01	105	82	3	0.32	1.16
59	25	1	29.67	12.68	38	35	1	33.18	-12.18	104	82	3	0.00	0.00
57	25	1	22.49	11.73	36	35	1	40.74	-11.42	103	82	3	0.20	-0.89
56	25	1	15.64	10.10	34	35	1	50.59	-9.31	102	82	3	1.10	-1.98
54	25	1	10.57	8.36	39	35	1	60.90	-6.05	101	82	3	3.24	-3.13
52	25	1	5.30	5.80	37	35	1	69.73	-2.96	151	82	3	18.99	-6.35
50	25	1	2.54	3.90	35	35	1	80.54	0.02	147	82	3	39.24	-7.08
32	25	1	0.20	1.16	27	35	1	89.65	0.88	145	82	3	49.44	-6.17
30	25	1	0.00	0.00	93	60	2	83.61	3.24	144	82	3	60.01	-4.65
28	25	1	0.19	-1.22	91	60	2	73.55	5.09	142	82	3	69.23	-3.12
26	25	1	0.95	-2.71	89	60	2	63.29	7.10	140	82	3	80.11	-1.34
31	25	1	3.33	-5.13	88	60	2	52.80	9.45	138	82	3	89.53	-0.14
53	25	1	8.05	-7.91	86	60	2	42.59	11.64	128	92	3	86.34	2.95
51	25	1	15.73	-10.58	84	60	2	32.54	12.50	126	92	3	73.98	5.83
49	25	1	24.35	-12.01	69	60	2	22.74	11.90	124	92	3	62.86	8.13
46	25	1	40.74	-11.42	82	60	2	14.57	10.21	122	92	3	51.90	9.89
44	25	1	50.59	-9.31	87	60	2	6.34	6.63	127	92	3	39.90	10.85
42	25	1	60.90	-6.05	85	60	2	2.04	3.29	125	92	3	27.97	10.28
47	25	1	69.73	-2.96	83	60	2	0.44	1.31	123	92	3	17.47	8.61
45	25	1	80.54	0.02	81	60	2	0.00	0.00	121	92	3	7.66	5.76
29	25	1	89.65	0.88	80	60	2	0.32	-0.85	120	92	3	3.47	3.80
19	35	1	93.99	1.94	78	60	2	1.67	-1.76	119	92	3	1.29	2.28
17	35	1	83.49	4.57	76	60	2	4.79	-3.04	118	92	3	0.32	1.16
16	35	1	72.11	7.29	79	60	2	13.79	-6.18	116	92	3	0.00	0.00
14	35	1	62.04	9.49	77	60	2	24.55	-8.23	117	92	3	0.20	-0.89
12	35	1	50.66	11.53	75	60	2	34.44	-8.41	114	92	3	1.10	-1.98
10	35	1	40.09	12.70	73	60	2	42.81	-7.55	115	92	3	3.24	-3.13
15	35	1	29.67	12.68	72	60	2	51.56	-5.93	160	92	3	7.13	-4.36
13	35	1	19.69	11.15	68	60	2	60.62	-3.72	158	92	3	12.12	-5.40
11	35	1	10.57	8.35	70	60	2	69.73	-1.54	154	92	3	29.10	-7.07
9	35	1	5.30	5.80	66	60	2	78.96	0.01	159	92	3	39.24	-7.08
25	35	1	2.54	3.90	71	60	2	89.79	0.60	157	92	3	49.44	-6.17
24	35	1	0.94	2.32	112	82	3	73.98	5.83	155	92	3	60.01	-4.65
22	35	1	0.20	1.16	108	82	3	51.90	9.89	153	92	3	69.23	-3.12
20	35	1	0.00	0.00	106	82	3	39.90	10.85	152	92	3	80.11	-1.34
18	35	1	0.19	-1.22	111	82	3	27.97	10.28	150	92	3	89.53	-0.14
23	35	1	0.95	-2.71	109	82	3	17.47	8.61					
21	35	1	3.33	-5.13	107	82	3	7.66	5.76					

‡ The signal number is correlated to the column number in the resulting measurement file.
∓ Spanwise location is measured from the rotor center and normalized with the rotor radius.
† Coordinates are normalized using the airfoil chord c. x/c is in chordwise direction, positive from leading edge to trailing edge. y/c is perpendicular to the chord, positive pointing towards the suction side of the airfoil.

If multiple datapoints are available within one case, the standard deviation between the average values gives an indication of the repeatability. The standard deviation is indicated in the graphs by a grey band around the mean value.

D.3 Loads

All loads are derived from the pressure distributions. The underlying procedures are highlighted below.

Sectional forces

Sectional forces (normal and tangential force) are obtained by integrating the pressure distributions assuming a linear line between the sensor values for each sample (around 27000) in a datapoint. The trailing edge pressure at x/c=1 is assumed to be the average of the pressures measured by the sensor closest by, located on the pressure and suction side.

Contrary to the normal force, the contribution of friction to the tangential force is significant in addition to the pressures. This contribution is however not taken into account in the experimental value, which consist solely of the pressure forces. In addition to that, the resulting tangential pressure force is highly dependent on location and number of pressure sensors. These two effects are more dominant for high angles of attack.

For the first round, the average over all these samples is calculated for each datapoint. For the second round, the sectional forces are presented as a function of the rotor azimuth angle. The azimuth angle is determined by means of the 1P trigger.A spline is drawn through the discrete pulses of the sensor, which allows determination of azimuth angle at a given time instance.

A bin analysis with a width of 2° azimuth is performed to average the sectional forces between 0° and 360° for each datapoint. These bin averaged sectional forces are then averaged over the datapoints to obtain the experimental data plotted in the graphs. Like the pressure distributions for axial flow, a grey standard deviation band in the plots gives an indication of the repeatability between the datapoints.

Axial force and torque

Axial force and torque are calculated by integrating the distributed forces linearly between instrumented sections assuming zero loads at the blade root and tip. This procedure is equivalent to using the weighting factors as reported in appendix C. For axial flow the average loading is assumed to be equal for all three blades. For the yawed flow case, these variables are a function of rotor azimuth angle and the contribution of each blade varies with the blade azimuth angle. The variation of blade loading with **blade** azimuth angle is assumed equal between the blades to determine the rotor azimuth dependent axial force and torque.

D.4 Velocity traverses

For each PIV datapoint the average over 31 samples is taken. The velocities of the sheets are concatenated to obtain a radial or axial traverse. The exact location taken for the traverses is described in section C.1 and C.2. The overlap between the sheets gives a satisfactory image on the accuracy of the PIV data. The data close to the rotor plane for the axial traverse is complimented with the radial traverse sheets.

It must be noted that the PIV measurements were performed phase locked and hence the data is for a fixed azimuth angle. Hence close to the rotor plane the phase locked measurements can differ significantly from the azimuth averaged velocities. For the axial traverses the data at a rotor azimuth angle of 0° is taken. For the radial traverses it was decided to compare azimuthally averaged velocities which are determined from a weighted average over a rotor revolution, using the weighting factors given in appendix C.2 applied to the phase locked angles that were obtained during the PIV campaign. For the yawed flow

E. WP3 Codes Descriptions: Lifting line codes

This chapter describes computational models that are used in the comparison between calculations and measurements (chapter 4).

The codes described in this chapter can be characterized as lifting line codes, which indicates that they need input of the aerodynamic coefficients of the airfoils used in the blade. Many of these lifting line codes use Blade Element Momentum (BEM) or vortex line theory. The descriptions as provided by the participants are included below.

E.1 CENER BEM and FAST BEM

FASTv8 CODE DESCRIPTION:

1. Model description

1. *We assume that your model basically combines the axial and tangential momentum equation with the axial and tangential force from the blade element theory.*

For both rounds of comparisons CENER has used FAST v8.12, but with different versions of AeroDyn v15 (see [1] and [2]):

- 1st Round with AeroDyn v15.01.00a-gjh
- 2nd Round with AeroDyn v15.01.02a-gjh

"For operating wind turbine rotors, AeroDyn calculates the influence of the wake via induction factors based on the quasi-steady Blade-Element/Momentum (BEM) theory, which requires an iterative nonlinear solver (implemented via Brent's method)."

2. *In how many elements have you divided the blade*

The blade has been divided in 30 sections as it could be seen in Table 1.

Section	Blade span, l [m]	Section	Blade span, l [m]
1	0	16	1.224
2	0.02	17	1.265
3	0.09	18	1.365
4	0.165	19	1.465
5	0.24	20	1.53
6	0.3525	21	1.59
7	0.42	22	1.635
8	0.465	23	1.73
9	0.51	24	1.815
10	0.5775	25	1.86
11	0.69	26	1.9
12	0.815	27	1.955
13	0.915	28	1.983
14	1.015	29	2.012
15	1.14	30	2.04

Table 1: Blade sections that have been considered in FAST's simulations

3. Describe which airfoil data along the blade have been applied. Also describe the origin of these data and possible manipulations (e.g. 3D corrections)

CENER has used two different set of airfoil polars for the simulations:

- Without corrections:
  - DU91-W2-250 (Re=0.5*10^6), RISO A1-21 (Re=1.6*10^6) and NACA64-418 (Re=0.7*10^6, clean) data was used as provided in ECN report, [3].
  - CYLINDER: used a cylinder with a drag coefficient of 1. For a clean cylinder, CD at 24m/s is around 0.7, and at 10m/s is around 1.3. An average value has been taken.

- Transitions: information calculated using AirfoilPrep_v2.02.01. The influence of each of the profiles used for calculating each transition has been weighted equally (50% each one).

- With 3D corrections:
  - DU91-W2-250 (Re=0.5*10^6): for each span section with this airfoil, a 3D correction has been calculated using AirfoilPrep_v2.02.01 (see [4]), resulting in 8 different airfoil data (corresponding to sections 5 to 12 from Table 1). The maximum angle of attack that has been considered in AirfoilPrep for this correction is 30º. RISO A1-21 (Re=1.6*10^6) and NACA64-418 (Re=0.7*10^6, clean) data was used as provided in ECN report, [3].
  - CYLINDER: used a cylinder with a drag coefficient of 1. For a clean cylinder, CD at 24m/s is around 0.7, and at 10m/s is around 1.3. An average value has been taken.
  - Transitions: information calculated using AirfoilPrep_v2.02.01. The influence of each of the profiles used for calculating each transition has been weighted equally (50% each one).

For the 1st Round CENER has used both set of polars with and without corrections, and for the 2nd Round CENER has used only the set with corrections.

4. Describe unsteady airfoil aerodynamics modeling (e.g. dynamic stall)

CENER has used the in-house model for unsteady aerodynamics called DYSTOOL based on the work of Beddoes and Leishman that has been coupled with AeroDyn v15, see [5].

5. Describe tip and root correction

AeroDyn uses a theory originally developed by Prandtl to account for the tip effect. To account for the hub effects, a hub loss model is used, that has an identical implementation as the Prandtl tip loss model, see [6].

6. Describe correction for turbulent wake

The effect of the wake is only included in the computations via induction factors see [6].

7. Describe tower shadow modelling

The cases of the 1st Round have been calculated without Tower shadow, while the cases of the 2nd Round have been calculated using a tower influence on wind based on potential flow around the tower with Bak correction, see [6]: “This model uses a potential flow solution around a cylinder as the base flow field along with a downwind wake model dependent on tower drag coefficient (based on diameter), Cd, and a tower dam model for upwind influence”.

The drag coefficient of the tower for each case of the 2nd Round has been calculated for each Reynolds number, see Figure 1 and Table 2.

WindSpeed (m/s)	Towr_Diam (m)	KinVisc (m^2/s)	Re (-)	**Twr_Cd (-)**
10.03	0.508	1.53E-05	3.34E+05	**0.778**
15.01	0.508	1.53E-05	5.00E+05	**0.310**
24.08	0.508	1.53E-05	8.02E+05	**0.352**

Table 2: Drag coefficient of the tower for each wind speed

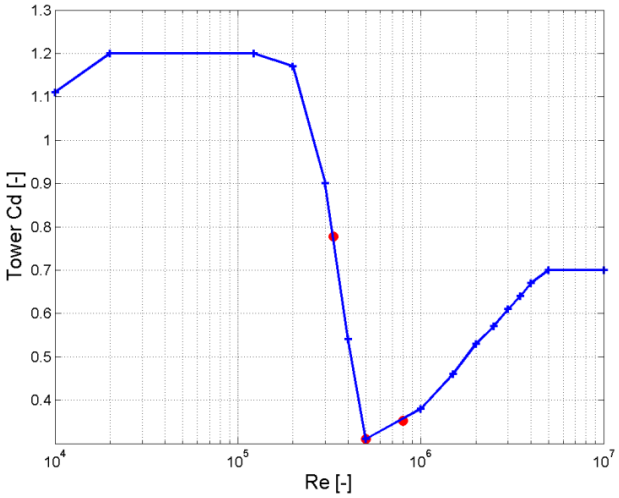

Figure 1: Drag coefficient of a cylinder against the Reynolds Number

8. Describe yaw model

In AeroDyn (see [7]), the effect of yaw is considered in the calculation of the in-plane velocities and also in the calculation of the induction factor. The effect of the yaw over the in-plane velocities is included as a geometric relation between the yaw, tilt and azimuth angles. The effect on the induction factor is computed based on Glauert's model for the skewed-wake effect, Pitt and Peters model but with a different coefficient suggested by Snel and Schepers. Resulting in the following expression:

$$a = a_0 * \left[1 + \frac{15\pi}{64} \tan\left(\frac{\chi}{2}\right) * \frac{r}{R} * \sin(\psi)\right]$$

9. Describe dynamic inflow model

The inflow has been considered as uniform wind for all cases.

10. Is drag included in the calculation of induction

The drag is included in the calculation of both axial and tangential induction factors.

11. Miscellaneous remarks

All the cases have been simulated considering both, blades and tower, as rigid structures with a fixed rotational speed of 425.1rpm and a pitch = -2.3deg

2. Other information

1. Describe the wind excitation used (e.g. no turbulence, uniform flow, shear)

Uniform flow, no turbulence, no shear.

2. What time step (and corresponding azimuth angle step) has been used in the case of unsteady calculations?

The time step for the 1st Round has been 0.005s. As the rotational speed is 425.1rpm, the corresponding azimuth angle step is 12.75deg.

The time step for the 2nd Round has been 0.0017s. As the rotational speed is 425.1rpm, the corresponding azimuth angle step is 4.34deg.

3. How many seconds have been simulated? Which result (what time instance or averaging procedure) was taken in the case of unsteady simulations?

All cases endure 80s and the first 70s have been eliminated from the output.
As the output requested for the 2nd Round cases was a single revolution data, the mean values of the last 70 revolutions (10s) of each variable, at each azimuthal position, have been considered. Then a lineal interpolation has been made to obtain the data with an azimuth step of 3.02deg.

4. What was the CPU time of the computations?

Round	1st Round	2nd Round
Time Step [seconds]	0.005	0.0017
Simulated Time [seconds]	80	80
Simulation CPU Time [seconds]	368	1211

5. Do the given normal and tangential force results contain the contribution of friction (CFD only)?

(-)

6. How have axial force and torque results been obtained (interpolation procedure, resolution)?

Axial force and torque results have been obtained considering the integrating factors given for the five experimental sections (25%, 35%, 60%, 82%, 92%) at [3] and [8]. For the 2nd Round the separate contribution of each blade at each azimuthal position have been considered to obtained the global forces of the rotor.

7. How have azimuth averaged velocities been obtained (interpolation procedure, resolution)?

(-)

CENER_BEM CODE DESCRIPTION:

1. Model description

1. *We assume that your model basically combines the axial and tangential momentum equation with the axial and tangential force from the blade element theory.*

CENER BEM is a pure code with a pure implementation of the Blade Element/Momentum theory that calculates the axial and tangential force iteratively.

2. *In how many elements have you divided the blade*

The blade has been divided in 28 sections as it could be seen in Table 1.

Section	Blade span, l [m]	Section	Blade span, l [m]
1	0.02	15	1.224
2	0.09	16	1.265
3	0.165	17	1.365
4	0.24	18	1.465
5	0.3525	19	1.53
6	0.42	20	1.59
7	0.465	21	1.635
8	0.51	22	1.73
9	0.5775	23	1.815
10	0.69	24	1.86
11	0.815	25	1.9
12	0.915	26	1.955
13	1.015	27	1.983
14	1.14	28	2.012

Table 3: Blade sections that have been considered in CENER BEM's simulations

3. Describe which airfoil data along the blade have been applied. Also describe the origin of these data and possible manipulations (e.g. 3D corrections)

The BEM CENER code has calculated the 1st Round cases, and it has used the polars without corrections:

- DU91-W2-250 ($Re=0.5\cdot10^6$), RISO A1-21 ($Re=1.6\cdot10^6$) and NACA64-418 ($Re=0.7\cdot10^6$, clean) data was used as provided in ECN report, [3].
- CYLINDER: used a cylinder with a drag coefficient of 1. For a clean cylinder, CD at 24m/s is around 0.7, and at 10m/s is around 1.3. An average value has been taken.
- Transitions: information calculated using AirfoilPrep_v2.02.01 [4]. The influence of each of the profiles used for calculating each transition has been weighted equally (50% each one).

4. Describe unsteady airfoil aerodynamics modeling (e.g. dynamic stall)

The BEM CENER code is a steady model, and it does not include unsteady aerodynamic model. The calculations with this code have been the steady calculations of the 1st round.

5. Describe tip and root correction

It uses a theory originally developed by Prandtl to account for the tip effect. To account for the hub effects, a hub loss model is used, that has an identical implementation as the Prandtl tip loss model, see [6].

6. Describe correction for turbulent wake

The effect of the wake is only included in the computations via induction factors see [6].

7. Describe tower shadow modelling

The cases of the 1st Round have been calculated without Tower shadow. However, the BEM CENER code includes different tower shadow models: potential, Bak and downwind, but these models have not been used in the calculations for MexNext3.

8. Describe yaw model

The BEM CENER code is a steady model, and it does not include unsteady aerodynamic model. The calculations with this code have been the steady calculations of the 1st round.

9. Describe dynamic inflow model

The inflow has been considered as uniform wind for all cases.

10. Is drag included in the calculation of induction

The drag is included in the calculation of both axial and tangential induction factors.

11. Miscellaneous remarks

All the cases have been simulated considering both blades and tower as rigid structures with a fixed rotational speed of 425.1rpm and a pitch = -2.3deg.

2. Other information

1. Describe the wind excitation used (e.g. no turbulence, uniform flow, shear)

Uniform flow, no turbulence, no shear.

2. What time step (and corresponding azimuth angle step) has been used in the case of unsteady calculations?

The azimuth angle step of the 1st round cases was 10 deg (dt= $3.92 \cdot 10^{-3}$).

3. How many seconds have been simulated? Which result (what time instance or averaging procedure) was taken in the case of unsteady simulations?

This code calculates a single revolution.

4. What was the CPU time of the computations?

Round	1st Round
Time Step [seconds]	$3.92 \cdot 10^{-3}$
Simulation Time [seconds]	2

5. Do the given normal and tangential force results contain the contribution of friction (CFD only)?

(-)

6. How have axial force and torque results been obtained (interpolation procedure, resolution)?

Axial force and torque results have been calculated integrating the results of the five experimental sections (25%, 35%, 60%, 82%, 92%) considering zero loading at the blade root and tip

7. How have azimuth averaged velocities been obtained (interpolation procedure, resolution)?

(-)

References

[1] B.Jonkman and J.Jonkman, «FAST v8.12.00a-bjj,» National Renewable Energy Laboratory, 2015.

[2] J.M.Jonkman; G.J.Hayman; B.J.Jonkman and R.R.Damiani, "AeroDyn v15 User´s Guide and Theory Manual," National Renewable Energy Laboratory, 2016.

[3] K. B. a. J. Schepers, «Mexnext III: Definition of first round of calculations,» February 13th, 2017.

[4] "NWTC Information Portal (AirfoilPrep)," 19 December 2014. [Online]. Available: https://nwtc.nrel.gov/AirFoilPrep.

[5] A. González, S. Gomez-Iradi and X.Munduate, «Validation of DYSTOOL for unsteady aerodynamic modeling of 2D airfoils,» *Proceedings of the Science of Making Torque from Wind,* 2014.

[6] P. J. Moriarty, «AeroDyn Theory Manual,» NREL/EL-500-36881, National Renewable Energy Laboratory, December 2004.

[7] S.A.Ning; G.Hayman; R.Damiani and J.Jonkman, "Development and Validation of a New Blade Element Momentum Skewe-Wake Model within AeroDyn," NREL/Cp-50000-63217, National Renewable Energy Laboratory, 2014.

[8] K. Boorsma and J.G. Schepers, «Mexnext III: Definition of second round of calculations,» February 13th, 2017.

Model description of the CFD/LES/AL model at DTU

Wen Zhong Shen

Department of Wind Energy, Technical University of Denmark

1. General Description of the model

In the IEA-Mexnext III project, DTU's Actuator Line (AL) technique [1] is used. The AL technique is implemented in the in-house EllipSys3D code [2-3] which is based on a multi block/cell-centered finite volume discretization of the steady/unsteady incompressible Navier-Stokes equations in primitive variables (pressure-velocity). The predictor-corrector method is used. In the predictor step, the momentum equations are discretized using a second-order backward differentiation scheme in time and second-order central differences in space, except for the convective terms that are discretized by the QUICK upwind scheme. In the corrector step, the improved Rhie-Chow interpolation [4] is used in order to avoid numerical oscillations from pressure decoupling. The obtained Poisson pressure equation is solved by a five-level multi-grid technique. Since the EllipSys3D code is programmed using a multi-block topology, it can be parallelized relatively easily using Message Passing Interface (MPI).

The SGS turbulence model used for Large Eddy Simulation is the mixed scale turbulence model developed at LIMSI [5]

$$\nu_t = C\left|\bar{\bar{\omega}}\right|^{\alpha} k^{(1-\alpha)/2}\Delta^{(1+\alpha)}$$

where $\Delta = \left(\Delta_x\Delta_y\Delta_z\right)^{1/3}$ is an average grid size, and $\alpha = 0.5$. Assuming similarity between two grid levels, the turbulent kinetic energy can be estimated by using the following filter

$$k = \frac{1}{2}\sum_{j=1}^{3}\left(U_j - \bar{U}_j\right)^2 \approx \frac{1}{2}\sum_{j=1}^{3}\left(\bar{U}_j - \tilde{\bar{U}}_j\right)^2$$

where $\tilde{\bar{U}}_j$ is the filtered velocity of the resolved velocity, $\bar{U}_j$, by the second filter, i.e. the double filtered velocity.

In the Actuator Line model, the Beddoes--Leishman type dynamic stall model is implemented.

2. Modeled components

The blades are included as a line-distributed body force in the Navier-Stokes equations, obtained from the Actuator Line technique. The tower is not included in the computations. Concerning the nacelle of the MEXICO rotor, computations with and without the nacelle are performed, which are used to study the nacelle effects. However, in the late computations for the MEXICO rotor in yaw, the nacelle is not included. In Mexnext-I, the open DNW wind tunnel was considered in order to study the tunnel effects. But in Mexnext-III, the open tunnel is not included.

3. Origin of geometrical description

The origin of geometrical description (blade and nacelle) is obtained from the report by Boorsma and Schepers [6].

4. Mesh and blade resolution

The computations are performed using two computational grid configurations which consider the presence and absence of the hub and nacelle geometry. The first setup, where the geometry of hub and nacelle is not considered, is a structured Cartesian grid with 45 blocks and approximately 11.8 million grid points in a domain of size [-16R, 16R] x [-16R, 16R] x [-16R, 16R] with the finest cell size equal to R=40. R is the rotor radius.

The second setup is a structured grid containing five blocks in both radial and axial directions and three blocks in the azimuthal direction. The mesh extends to 26R in all three directions. This results in a total number of 75 blocks and 19.66 million grid points. The geometry of the hub and nacelle are reproduced based on the experimental model and it can be described as a cylinder with a cone shaped front and spherical end, see Figure 1. The resolution in the blade area is almost uniform with $\Delta r=0.015R$, except in the boundary layer of the nacelle. The cell height away near the nacelle is approximately $2 \times 10^{-4}R$ which results in y+ of 4 ~ 5.

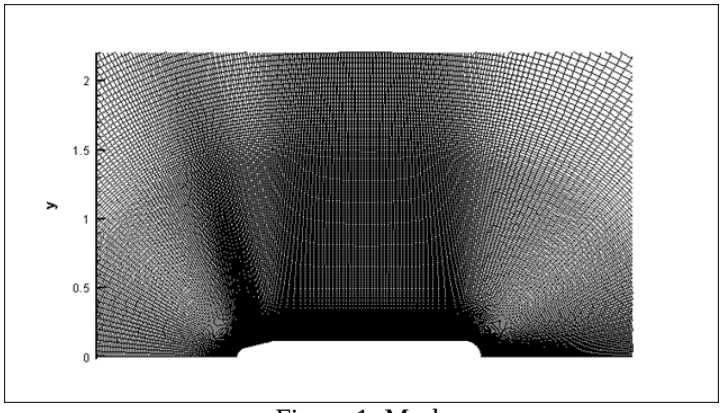

Figure 1: Mesh

5. Boundary conditions

At the inflow and lateral boundaries, the velocity is imposed to be uniform in the axial direction. No inflow turbulence is considered as the measured turbulence intensity in the wind tunnel is very small. At the outlet boundary, the convective outflow boundary condition is used. At the nacelle way, no-slip condition is used.

6. Numerical algorithm

See the model description in Section 2.

7. Convergence

Unsteady time-true computations are performed for the MEXICO rotor with and without nacelle. In the nacelle case, a dimensionless time-step of 5×10^{-4} R/V (~0.285 deg) based on the length scale of rotor radius R and the velocity scale of wind speed V is used while

in the absence of nacelle, a time-step of 10^{-3} R/V (~0.57 deg) is used. Computations are performed until a time of T=30 R/V (=6.75 s) for the wind speed of 10 m/s and 20 R/V (=4.5 s) for the 15 m/s and 24 m/s cases. The presented results are extracted at the final time instant.

For the cases without hub, each computation was carried out with 45 CPUs and the computations lasted 28 hours. For the cases with hub, each computation was carried out with 75 CPUs and the computations lasted 53 hours

8. Airfoil data

In the Mexnext project, 2D airfoil data (OAD: original airfoil data) is used in both axial flow and yaw flow conditions, which is obtained from [6]. Airfoil data with 3D corrections on rotational effects (MAD: modified airfoil data) wre used in the paper [7] and are also in the axial flow condition.

9. Other information

The normal and tangential force results are calculated with airfoil data and thus friction is contained.

The original results were calculated without the “Weighting Factor” procedure. However, it is applied in the new results.

In the test cases, the pitch angle of the MEXICO rotor is -2.3 deg.

References

[1] Sørensen JN, Shen WZ (2002), Numerical computations of wind turbine wakes. Journal of Fluids Engineering 124: 393-399.
[2] Michelsen JA (1992), Basis3D - a Platform for Development of Multiblock PDE Solvers. Technical Report, AFM 92-05, Technical University of Denmark, Denmark.
[3] Sørensen NN (1995), General Purpose Flow Solver Applied to Flow over Hills. Risø-R-827-(EN), Risø National Laboratory, Roskilde, Denmark.
[4] Shen WZ, Michelsen JA and Sørensen JN (2001), An improved Rhie-Chow interpolation for unsteady flow computations. AIAA Journal, 39: 2406-2409.
[5] Ta Phuoc L (1994), Modèles de sous maille appliqués aux écoulements instationnaires décollés. Proceedings of the DRET Conference: Aérodynamique Instationnaire Turbulente-Aspects Numériques et Expérimentaux, Paris, France: DGA/DRET editors.
[6] Boorsma K and Schepers G (2014), New MEXICO experiment: Preliminary overview with initial validation. Tech. Rep. ECN-E-14-048, ECN.
[7] Shen WZ, Zhu WJ and Sørensen JN (2012), Actuator line / Navier-Stokes computations of flows past the MEXICO rotor: Comparisons with Detailed Measurement. Wind Energy Vol. 15(5), pp. 811-825.

E.3 DTU HAWC2

E.3.1 Introduction

The HAWC2 code has been developed at Risoe National Laboratory of Denmark (now DTU Wind Energy) over the last more than 10 years. The structural part of the code is a multibody formulation based on the roating frame of reference method as described in [78]. In the particular formulation of the code, the turbine structure is subdivided into a number of bodies where each body has its own coordinate system. Within each body, the structure consists of an assembly of linear Timoshenko beam elements. The nonlinear effects of the body motion (rotations and deformations) are accounted for in the coupling constraints in between the individual bodies, ensuring small deflections within the linear beam elements. This means that effects of large rotations and deflections are included using a proper subdivision of a blade to a number of bodies. The suggested method has been validated with another existing nonlinear multibody formulation with the classical spin-up maneuver example [78].
The aerodynamic part of the code is based on the blade element momentum (BEM) theory [46], however implemented in a way that is comparable with an actuator disc approach [39], [82], which means that the induction at each time step is computed in a number of points distributed over the swept area in order to respond to instantaneous changes in loading from shear and turbulence in the inflow. The present BEM implementation has the advantage that rotor designs where the swept surface deviates from a plane circular disc like coned rotors or rotors with wing lets can be analyzed if induction characteristics can be imported from a CFD based actuator disc simulation [39]. Below the present BEM implementation will be described in more details.

E.3.2 The BEM model

The fundamental part of the blade element momentum model is the relation between thrust on the rotor and the induced velocities in the rotor plane. A 1D momentum balance between axial forces on the turbine and the flow within a stream tube is $T = \dot{m}\Delta U$. Following the classical theory by Glauert [46] this leads to a relationship between a thrust coefficient C_T and the induction factor a

$$C_T = 4a(1-a) \tag{E.1}$$

where

$$C_T = \frac{T}{\frac{1}{2}\rho A \mathbf{V}_\infty^2} \tag{E.2}$$

and a is the induction factor defined $a = \frac{V_\infty - u_r}{V_\infty}$ and
For thrust values causing higher induced velocities than $a = 0.5$, (E.1) breaks down since the flow velocity in the wake far downstrean according to the momentum theory is $(1-2a)$ which in this cases is equal to zero. This results in an infinite expansion of the flow behind the rotor and the flow can no longer be approximated by simple momentum theory. More complex flow models are needed such as CFD or an empirically based relation can be used.
In HAWC2 we use a C_T vs. a curve at high loading that is based on a combination of the Glauert empirical relation and results from actuator disc simulations at high loading [92] shown in Figure E.1. The actuator disc simulations were run with a uniform disc loading and with a turbulence model. Up to a $C_T = 1.2$ there is a good correlation between the Glauert curve and the AD results but for higher loadings the AD simulations give higher induction. It should be noted that AD results are shown for two different radial positions and although the loading is uniform they differ. Typically an increase in induction is seen towards the edge of the disc.
For different reasons explained below we use a BEM implementation in HAWC2 where the induction in the whole operational range from negative C_T to a high positive C_T is expressed through the following third order polinomial shown in Figure E.1 :

$$a = k_3 C_t^3 + k_2 C_t^2 + k_1 C_t + k_0 \tag{E.3}$$

where the coefficient $k_0 \ldots k_3$ are defined. $k_0 = -0.0017077$, $k_1 = 0.251163$, $k_2 = 0.0544955$ and $k_3 = 0.0892074$
As seen in Figure E.1 the C_T vs. a follows the momentum relation up to about a $C_T = 0.9$ after which it continues into the empirical relation described above. One important reason for using this approach is that we find that it is a more robust and fast method to compute the induction instead of solving eq. 1 using a nonlinear Newton-Raphson iteration solver combined with an empirical relation at high loading. Another reason

is that it makes it possible in an easy way to modify this C_T vs. a relation for e.g. a coned rotor as illustrated in [39], using actuator disc simulations for the coned rotor.

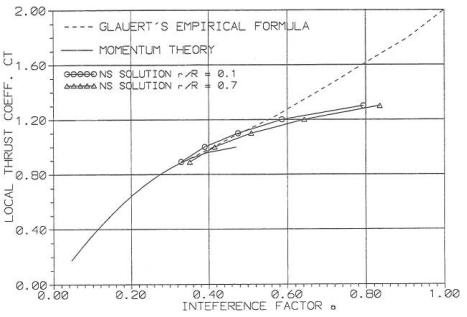

Computed axial induction at high loading at two different radial positions. Turbulent mixing included.

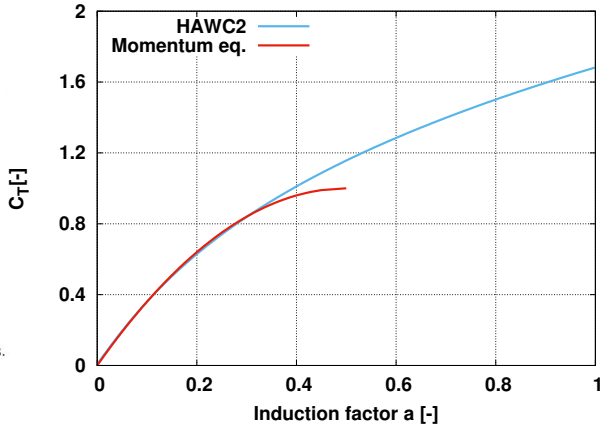

Figure E.1: To the left is shown the C_T vs. a relation from actuator disc simulations in comparison with momentum theory results and the Glauert empirical relation, Madsen 1996 [92]. To the right the C_T vs. a relation used in HAWC2 in comparison with the momentum theory based curve.

Now, a next step in implemeting the momentum theory by Gauert is to apply equation (E.2) on a ring element of the rotor with the radial extension dr as illustarted in Figure 2 E.2

$$C_T = \frac{dT}{\frac{1}{2}\rho A \mathbf{V}_\infty^2 2\pi r dr} = \frac{V_r^2 C_y c N_B}{\mathbf{V}_\infty^2 2\pi r} \tag{E.4}$$

where V_r is the relative velocity to the blade section, c is the blade chord, N_B is the number of blades and C_y is the projection of the lift coefficient C_l and the drag coefficient C_d on a line perpendicular to the rotor plane. Besides the elemtal thrust dt on the ring element there is also a torque dQ and we can defive a torque coefficient dQ by:

$$C_Q = \frac{dQ}{\frac{1}{2}\rho A \mathbf{V}_\infty^2 r 2\pi r dr} = \frac{V_r^2 C_x c N_B}{\mathbf{V}_\infty^2 2\pi r} \tag{E.5}$$

where C_x is the projection of the lift coefficient C_l and the drag coefficient C_d on a line tangential to the rotor plane.
Applying the angular momentum equation across the disc we get:

$$D_Q = \rho(2\pi r dr) r V_\infty (1-a)(2ra'\omega) \tag{E.6}$$

Combining equation(E.5) and (E.6) we find:

$$a' = \frac{V_r^2\, C_x(\alpha)\, c\, N_B}{8\pi r^2 (1-a) V_\infty \Omega} \tag{E.7}$$

where a' is the tangential induction coefficient.

Tip correction The relation between thrust and induced velocities is changed due to the presence of tip effects, caused by a finite number of blades. These effects consist of mainly two contributions. The first effect is the direct effect of a tip vortex caused by the pressure difference between the pressure and suction side of the blade tip, where the second is from the uneven axial flow velocity through the rotor. The wind speed is higher in between the blade than close to the blade. In HAWC2 we use the Prandtl tip correction factor F as presented by Glauert [46]:

$$F = \frac{2}{\pi} \cos^{-1}\left(\exp\left(-\frac{N_B}{2}\frac{R-r}{r\sin\varphi}\right)\right) \tag{E.8}$$

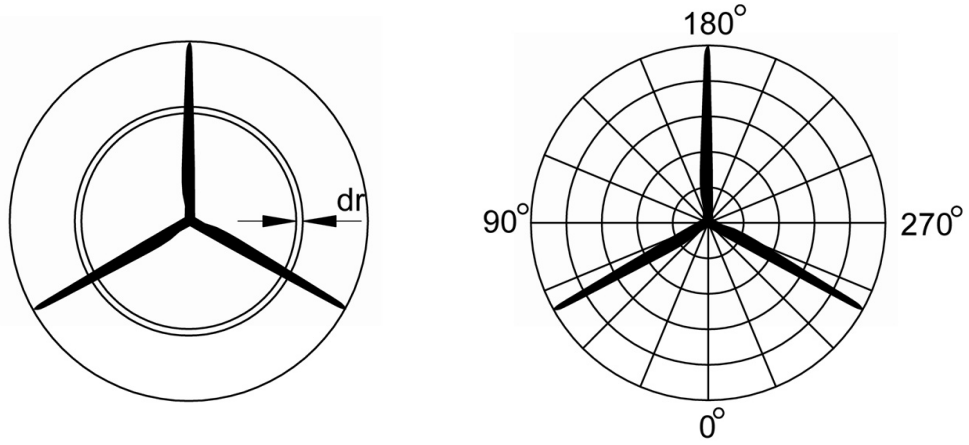

Figure E.2: Illisutration of the BEM approach. Left: Classic approach using an annular element to which the load is assumed contant over or the element (mean value of blade forces). Right: New induction grid with annular elements and further subdivided azimuthally

We insert it into the the momentum equation(E.1) as:

$$\frac{C_T}{F} = 4a(1-a) \tag{E.9}$$

where $\frac{C_T}{F}$ has to be inserted instead of C_T in (E.3).

Specific BEM implementation in HAWC2 Even though the BEM relationship is originally derived for a full rotor, it is generally implemented on an annular element form as proposed by Glauert [46] where it is assumed that the loading and induction within this annular element is constant and that the annular elements are independent of each other. The C_T coefficient now represents the average axial loading of the blades on an annular ring element.
In order to model azimuthal variations of induction due to azimuthal variations of blade loading caused by shear in inflow or turbulence we propose to expand this relationship from an annular element to an annular element subdivided into azimuthal sub parts, see right part of Figure E.2. The induced velocity is found in each grid point using the relationship in (E.3). For a situation, where the free wind speed is constant over the rotor, this leads to exactly same induction as the classic annular element approach, whereas differences are seen for non-uniform wind loading over the rotor. An important part of this azimuthal annular element approach is the definition of the local induction factor where the local instantaneous wind speed at a point in the grid is normalized with the local wind speed at exactly same point assuming no influence from rotor induction (the free wind speed).

$$a \equiv -\frac{\mathbf{u}_{induc,y}}{|\mathbf{V}_{\infty,local}|} \tag{E.10}$$

As seen in Figure E.2, a question arises how to find the local load in grid points not being exactly at the location of the blades. This is for the classic annular element approach done by assuming equal loading over the element, hence the average blade load is assumed to be constant over the annular element. The solution for the azimuthal divided annular element is in each grid point to find the load if the blade had been there. This can be justified by the assumption of an infinite number of blades, which is already the basic assumption for blade element momentum analysis. This means that the local angle of attack as well as relative velocity is calculated in the grid point based on the blades own velocity, at the location of the blade, and the local wind speeds at the location of the grid point:

$$\mathbf{V}^S_{grid} = \mathbf{T}_{gs}(\mathbf{V}^G_{grid} + \mathbf{V}^G_{induc,grid} - \mathbf{x}^G_{blade}) \tag{E.11}$$

The angle of attack α is computed by:

$$\alpha = \arctan \frac{\mathbf{V}^S_{grid,y}}{-\mathbf{V}^S_{grid,x}} \tag{E.12}$$

and the relative velocity V_r by:

$$V_r = \sqrt{{\mathbf{V}^S_{grid,x}}^2 + {\mathbf{V}^S_{grid,y}}^2} \tag{E.13}$$

and the local thrust in the grid points are calculated

$$d1T = \frac{1}{2}\,\rho\,V_r^2\,C_y(\alpha)\,c\,N_B \tag{E.14}$$

where $C_y(\alpha)$ is the lift and drag coefficient projected into the axial direction.

Yaw modeling When the rotor operates in yaw there are two main effects on the induced velocities as described by Glauert [46]. One effect is the change in mean level of the induced velocities and the other effect is an azimuthal variation of the induced velocities as the wake vortex system is relatively closer to the rotor on the one side compared to the other side.

Mean induction in yawed inflow

The general equation relating the thrust and induction at a rotor operating in yaw, see Figure E.3, as proposed by Glauert is:

$$T = \rho A|\mathbf{V}_\infty + \mathbf{u}_{induc}|(-2\,u_{induc}) \tag{E.15}$$

The equation has not been proved but generally accepted as a good assumption. Now the following equation relating the thrust coefficient to the induction can be derived:

$$C_T = 4a(1 + a^2 - 2a\cos\Phi)^{\frac{1}{2}} \tag{E.16}$$

where Φ is the yaw angle.
The modified relation of C_T vs. a for different yaw angles is shown in Figure E.4 (left). Based on these results a reduction factor for the induction a as function of C_T for different yaw angles can be derived as shown in Figure E.5. The induction computed by (E.3) is now reduced by this factor.

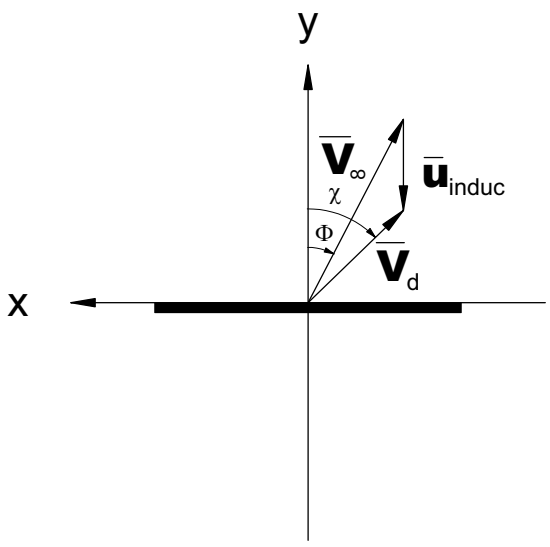

Figure E.3: Angles used for skew wake expressions, observing the rotor from above. The y-direction is the default wind direction without any skew inflow.

The wake skew angle χ is as default found based on the average wake angle using vectors $\bar{\mathbf{V}}_\infty$ and $\bar{\mathbf{u}}_{induc}$ representing the average local wind speed and induction over the whole rotor, see also Figure E.3.

$$\tan(\chi) = \frac{|\bar{\mathbf{V}}_\infty|\sin(\Phi)}{|\bar{\mathbf{V}}_\infty|\cos(\Phi) - |\bar{\mathbf{u}}_y|} \tag{E.17}$$

The wake skew angle χ depends on the thrust coefficient, which is illustrated in Figure E.3. At low loading χ is close to the yaw angle but for high loading it is seen that the wake can be deflected more $10deg.$ from the mean wind direction.

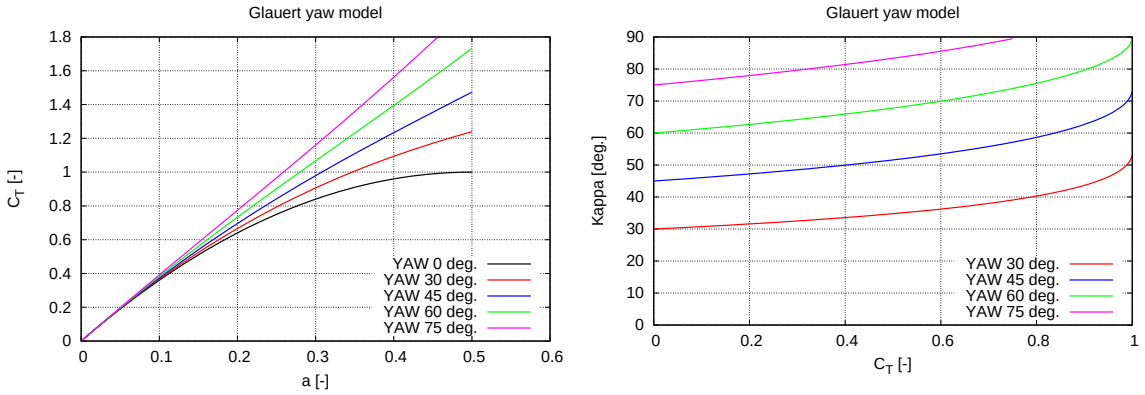

Figure E.4: Left: Relation between the thrust coefficient C_T and the induced wind speed factor a in yawed inflow. Right: The wake skew deflection angle χ. For zero loading the angle is similar to the yaw angle, whereas the deflection angle increases in combination with an increased thrust level on the turbine.

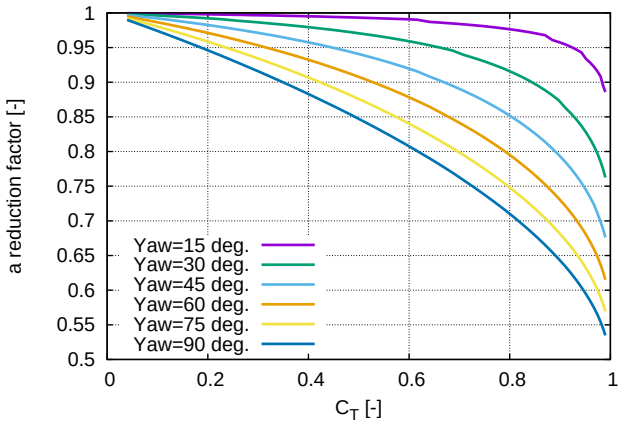

Figure E.5: Figure showing the reduction factor of the induction$a$ as function of C_T for different yaw angles.

Azimuthal variations of induction in yawed inflow

As the wake in the yawed conditions is skewed behind the rotor disc expressed by the skew angle κ, see Figure E.3 the induction will be higher on the side of the rotor where the wake bends towards. This is because the wake votices are closer to the rotor on that side.

The following variation has been proposed by Leishman [84] :

$$u_{induc,y,new} = u_{induc,y}(1 + +k_x r \sin(\Psi) + k_y r \cos(\Psi)) \tag{E.18}$$

where Ψ is the rotor azimuth, r is non-dimensional radius and k_x and k_y are constants.

In the book of Leishman [84] several proposals from different authors for the values of k_x and k_y are presented. It should be noted that these proposals are mainly thought for applicatiuon on helicopter rotors. As we will se below we found by comparison with results from an Actuator Disc in yaw that the best correlation was found for $k_y = \tan(0.4\chi)$ and k_x equal to 0. This is close to the model of Coleman, table in Figure E.6.

Table 3.1. *Various Estimated Values of First Harmonic Inflow*

Author(s)	k_x	k_y
Coleman et al. (1945)	$\tan(\chi/2)$	0
Drees (1949)	$(4/3)(1-\cos\chi-1.8\mu^2)/\sin\chi$	-2μ
Payne (1959)	$(4/3)(\mu/\lambda/(1.2+\mu/\lambda))$	0
White & Blake (1979)	$\sqrt{2}\sin\chi$	0
Pitt & Peters (1981)	$(15\pi/23)\tan(\chi/2)$	0
Howlett (1981)	$\sin^2\chi$	0

Figure E.6: Figure showing the reduction factor of the induction$a$ as function of C_T for different yaw angles.

Comparison of the yaw model with Actuator Disc results

In the fiures E.7 and E.8 the above described yaw model is compared with actutor disc results for a uniform, presribed loading with a thrust coefficient of 0.8. In the BEM simulations the constant C_T was like-wise prescribed.

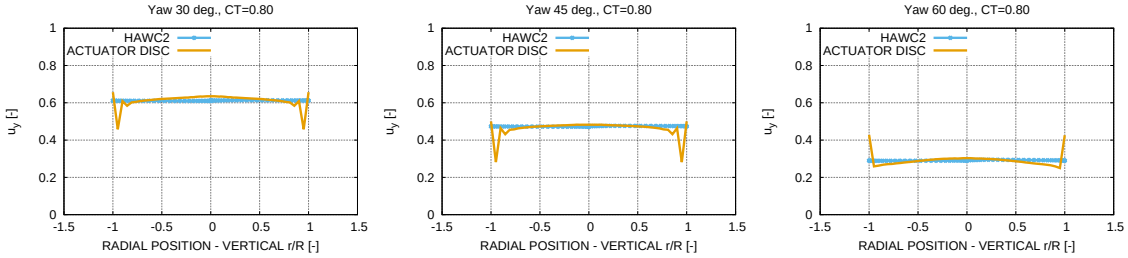

Figure E.7: Comparison of axial velocity through a vertical line (z axis in Figure E.3) through the rotor disc. The rotor loading is prescribed to a constant loading of $C_T = 0.8$.

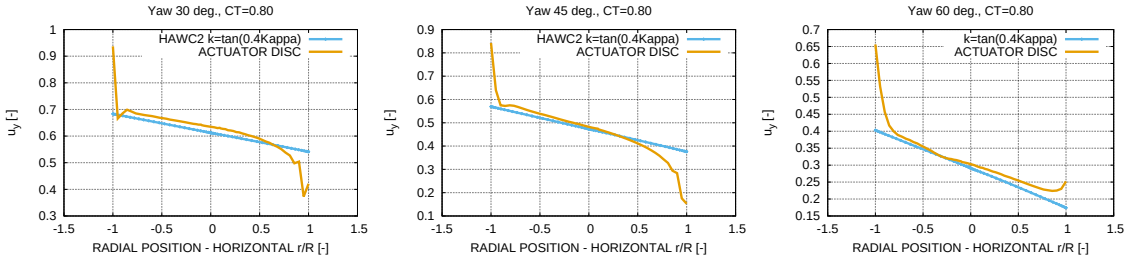

Figure E.8: Comparison of axial velocity through a horizontal line through the rotor disc. The rotor loading is prescribed to a constant loading of CT=0.8.

As seen in Figure E.7 the axial wind speed distribution at the rotor disc is seen to match very well in the vertical plane (z-y plane), which clearly illustrates the good performance of Glauert's yaw expression for the mean induction at different yaw angles. Results for the horizontal plane are depicted in E.8 and the slope of the velocity variation across the disc is seen to correlate well between the AD and the BEM yaw model. However, towards the rotor edge the AD induction is higher on the side where the wake is deflected to.

Dynamic inflow modeling A first order filter with the time constant τ is formulated in the LaPlace domain. The raw signal is here denoted q, where the filtered signal is noted y :

$$y = \frac{1}{1+s\tau}q \tag{E.19}$$

which can be formulated in discrete time domain using eg. an indicial function formulation. The index $(_1)$ refers to one time step earlier, assuming a constant discrete time step ΔT

$$y = y_1 \exp\left(-\frac{\Delta T}{\tau}\right) + q\left(1 - \exp\left(-\frac{\Delta T}{\tau}\right)\right) \tag{E.20}$$

We used AD simulations with a uniform loading and step changes in C_T to provide dynamic inflow data to calibrate our empirical model. An example of such simulation is shown in Figure E.9 where the flow velocity at different radial positions are shown for a step change in C_T from 0.0 to 0.9. It can be noticed that the velocity decreases a little bit faster towards the edge of the actuator disc. Each of the curves were now approximated with a first order filter with two time constants. An example of the approximation is shown to the right in Figure E.9. It is seen that a quite good correlation is obtained using two time constants. The same was done for AD simulations where the loading was changed from 0.9 to 0.0.
These two sets of derived time constants are now shown in Figure E.10 as function of radial position and it is seen that the smallest time constant decreases more towards the tip than the other time constant. We approximated the variation of the two time constants along the radius with a 2^{nd} order polynomium in non-dimensional radius. These two time constants with their radial variation are now used in the dynamic inflow filter where the induced velocities at each grid point are filtered according to this.
As a validation case we have run the HAWC2 dynamic inflow model with the same prescribed variation of C_T as used above to derive the time constants. The comparison of the AD and HAWC2 model results in Figure E.11 shows a very good correlation as should be expected.

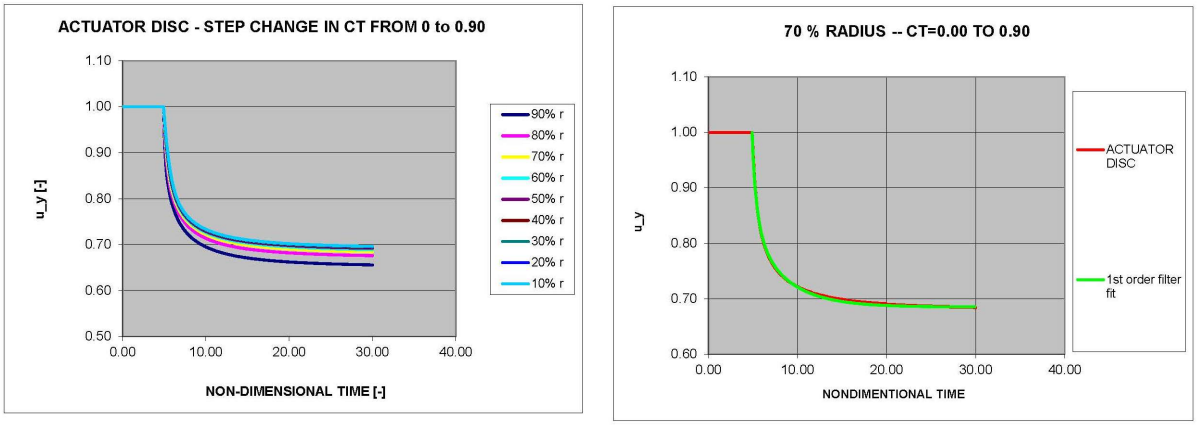

Figure E.9: In the left figure is shown the axial velocity at the actuator disc for different radial positions as function of non-dimensional time at different radial positions. To the right is shown a first order filter approximation using two time constants for one radial postion.

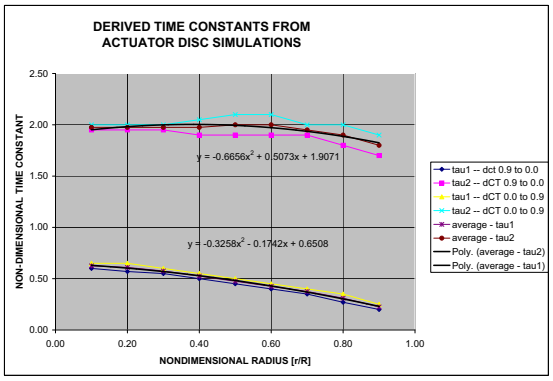

Figure E.10: The two time constants derived from actuator disc simulations of a step change in C_T.

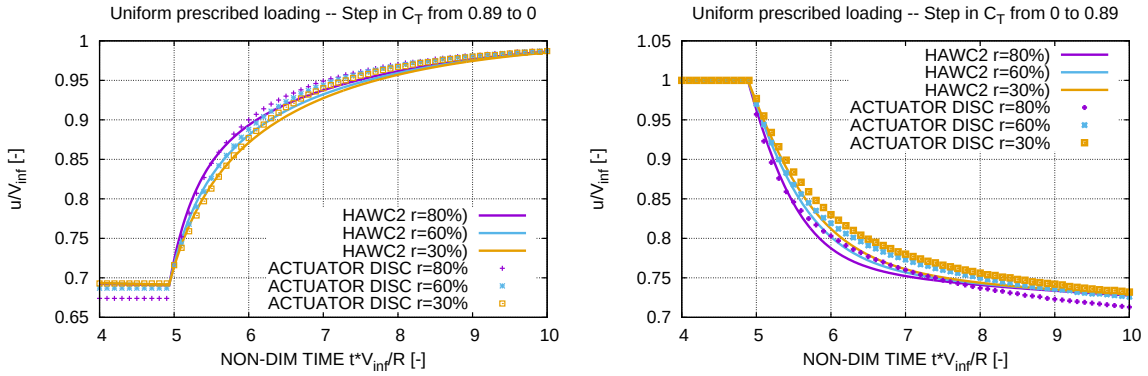

Figure E.11: Comparison of simulated response to change in C_T by an actuator disc and the above dynamic inflow simulation model.In the left figure the uniform loading step change in C_T is from 0.89 to 0 and in the right from 0 to 0.89

Near wake trailed vorticity modeling A fast near wake trailed vorticity model has recently been included in the HAWC2 code, [115, 116, 118, 117]. The near wake model only accounts for the trailed vorticity near the individual blades and has to be coupled to a BEM model without tip loss correction and with a reduced thrust coefficient C_T in the thrust-induction Equation E.3.

The addition of the near wake model to the BEM based aerodynamics code in HAWC2 has been shown to:

- Improve the radial load distribution for the NREL 5 MW reference turbine at high wind to more closely match CFD predictions [116]
- Increase the predicted flutter speed for the NREL 5MW reference turbine (flapwise and torsional stiffnesses varied between 70 and 130 % of the original value) by 4-10% [115]
- Predict the aerodynamic work response to prescribed edgewise and flapwise vibrations of the NREL 5 MW blades more closely to a free wake vortex code [118]
- Improve the prediction of dynamic stall loops of the Phase VI rotor in standstill [117]

The coupled near and far wake model has several limitations to ensure fast computation: Every blade can only see the near wake trailed from itself, so there is no interaction with the wake trailed from the other blades. Also, the wake is not a free wake, where the vortices in the wake influence each other. Instead the vorticity trailed from each vortex trailing point follows a helical path that is entirely determined by the in-plane and out-of-plane velocities at the blade section at a given time step. Also, a reference BEM model is run in parallel to the coupled wake model to determine how much the thrust of the far wake model has to be reduced. This means that the addition of the near wake model will not lead to significantly different integrated thrust of the whole rotor. The effect on the steady state results is therefore limited to the radial induction distribution, rather than the mean induction of the whole rotor.

E.4 ECNAero-BEM and AWSM

E.4.1 Model

The ECN Aero-Module [21, 22] includes both BEM as well as a lifting line free vortex wake formulation, allowing the same external input (e.g. wind, tower, airfoil data) to be used for both models. The BEM formulation is based on PHATAS [89], including state of the art engineering extensions which have matured over decades of research in wind turbine rotor aerodynamics. The free vortex wake method is based on the AWSM code [165]. The 3D correction is based on the model of Snel [150] as modified in PHATAS, dependent on chord over radius and tip speed ratio. As such it is embedded in the overall code, applied during the calculation and restricted to the inboard region below 50° angle of attack. The dynamic stall model of Snel [147] has been used as well.

BEM specific submodels

A skewed wake model is used in yawed inflow, based on wind tunnel measurements and described in [129]. To correct for the Prandtl effect in the BEM simulations, a Prandtl factor has been calculated and applied to root and tip regions. For axial induction factors exceeding 0.38 the momentum line (or Ct-a curve) has been replaced by a straight line tangent to a=0.38. Drag has been excluded from contributing to the induction calculation. The ECN dynamic inflow model [151] has been implemented to add another term to the axial momentum equation to account for the aerodynamic rotor 'inertia' in the case of pitch action, rotational speed variation or wind speed variation. The term is proportional to the time derivative of the annulus averaged axial rotor induction and has a dependency on the radial position.

E.4.2 Settings

The number of elements per blade used for both simulation types is around 20. Time step is set to a 10° azimuth step. About 20 rotor revolutions are calculated which for AWSM takes around 10 minutes on a 40 node cluster. The results are averaged or bin-averaged with azimuth angle over the last revolution for the axial and yawed inflow case respectively. The supplied weighting factors have been used to calculate the rotor integral forces from interpolated loads at the five sections that were instrumented in the experiment.

E.5 IFPEN solvers

BEM solver "AeroDeep"

AeroDeep is based on the widely used Blade Element Momentum method. Induction factors are computed in both axial and tangential directions along the blade span. Both lift and drag coefficients are used and taken into account in the calculation of the induction factors. In the present calculations, blades have been divided in 30 elements, using a cosine distribution, so that the blade tip and root are well refined. Airfoil data have been used according to each comparison round definition. If required, Snel's correction for three-dimensional effects Snel [150] has been used. This correction acts on the lift only, and has not been used in the yawed inflow cases. Rotor thrust and torque have been computed using the experimental resolution and assuming zero forces at the root and tip. The weighting factors given in the comparison round descriptions have been used.

In order to overcome the major limitations of the classical BEM theory, corrections have been implemented to account for hub and tip losses, turbulent wake state, tower shadowing, dynamic inflow (i.e. unsteady BEM), dynamic stall, as well as skewed rotor configurations. The tip and root corrections have been applied in both axial and yawed inflow cases, and are based on the classical formulation of Prandtl. The turbulent wake state correction is based on Buhl's work [28] in the axial flow cases, and the extension of Buhl's work by Ning [103] has been used in the yawed inflow cases. AeroDeep is able to take the tower into account, but the tower shadow effect have not been activated in the presented calculations, as the tower presence has almost no impact on the results. A stall model is also implemented in AeroDeep. This model is based on the work by Øye, as presented in [53]. For the yawed inflow cases, both dynamic stall and yaw models have been activated. The Øye dynamic stall model has been used [108]. Small modifications have been made to the original model, regarding the calculation of the fully separated lift coefficient. A yaw model has been specially developed for the comparison rounds. This model can be seen as a compromise between the standard Glauert model [46], which is not able to represent the root vortex effect, and the more recent yaw model by Schepers [131], which depends on many empirical constants. In the model, only two phase angle are defined: the first one for the root vortex effect and the second for the tip vortex effects. Based on the analysis of vortex solver results, it has been noticed that the phase of the normal force due to the tip and phase shift due to the root vortex were constant along the span: only the intensity of the normal force fluctuations is changing. Thus, we simply combined two identical models, the first being related to the tip vortex influence and the second to the root vortex influence. Then, a linearly increasing function is used to increase the influence of the tip vortex with blade span, and a linearly decreasing function is used to decrease the influence of the root vortex with blade span. One can notice that the correction is directly applied to the local values of the induction factor. Tests have been made using an average induction factor, leading to less good results. No corrections are applied to the tangential induction factor.

Finaly, our model simply reads:

$$a_{yaw} = a\left[1 + k_1(r/R)\frac{r}{R}tan(\chi/2)sin(\psi+\phi_1) + k_2(r/R)\left(1-\frac{r}{R}\right)tan(\chi/2)sin(\psi+\phi_2)\right] \quad \text{(E.21)}$$

In the expression above, ψ is the blade azimuth angle and χ the wake skew angle. We defined the wake skew angle as follows:

$$\chi = \gamma(0.6a_{rotor}+1), \quad \text{(E.22)}$$

with γ the yaw angle and a_{rotor} the rotor averaged induction factor. After some calibration, phases offset and linear functions have been defined as:

$$\phi_1 = -\pi/9 \qquad \phi_2 = \pi \quad \text{(E.23)}$$

$$k_1(r/R) = 0.65 + 0.35\frac{r-r_{hub}}{R-r_{hub}} \qquad k_2(r/R) = 1 - 0.35\frac{r-r_{hub}}{R-r_{hub}} \quad \text{(E.24)}$$

Free-wake lifting-line solver "CASTOR"

CASTOR is a free-wake vortex filament lifting-line solver based on the generalized Prandtl lifting-line theory. In the present calculations, the blade have been divided in 30 elements, using a cosine distribution, so that the blade tip and root are well refined. Airfoil data have been used according to each comparison round definition.

If required, Snel's correction for three-dimensional effects has been used. In order to reduce the computational cost, CASTOR is based on an hybrid $OpenMP$ / GPU implementation, thereby reducing the computational times up to two orders of magnitude when compared to sequential CPU implementations. The presence of the ground can be taken into account through the mirror technique, also it has not been used in the presented calculations. The dynamic stall model by Øye, together with the modifications described above, has been used in the calculations. In all cases, the wake was able to freely deform. For the axial flow cases, 16 rotor rotations have been kept in the wake, together with an azimuth step of 10 degres per time step. For the yawed inflow cases, 20 rotor rotations have been kept in the wake, together with an azimuth step of 10 degres per time step. Computational time for both axial and yawed inflow cases is below 30 minutes per case. As for the BEM solver, tower shadow models are available in CASTOR, but have not been used in the presented calculations. Rotor thrust and torque have been computed using the experimental resolution and assuming zero forces at the root and tip. The weighting factors given in the comparison round descriptions have been used for rotor thrust, torque, and radial traverse velocities averaging.

Mexnext: Check list for code descriptions from participants of the comparison rounds

1. Suzlon model description

BEM

1. We assume that your model basically combines the axial and tangential momentum equation with the axial and tangential force from the blade element theory. *That is what Suzlon's Flex5 is doing.*

2. In how many elements have you divided the blade? *29 cross sections. Cross sections evaluated are r = 0.30, 0.40, …, 2.00, 2.05, 2.10, 2.15, 2.20, 2.25 m. Extra cross sections are added at 25%, 35%, 60%, 82% and 92% to get "exact" output. See file.*

3. Describe which airfoil data along the blade have been applied. Also describe the origin of these data and possible manipulations (e.g. 3D corrections). *Airfoil data that were prescribed were used, i.e.*

Cylinder
DU91-W2-250 t/c=25% Re=5e5
Risoe A1-21 t/c=21% Re=1.6e6
NACA 64-418 t/c=18% Re=7e5

Where necessary, interpolation is done based on thickness. The 3D correction applied is a version of the Snel correction:

$$C_{L,3D} = C_{L,2D} + f(\alpha)3.1\left(\frac{c}{r}\right)^2\left(C_{L,pot} - C_{L,2D}\right) \qquad C_{L,3D} \le C_{L,pot}$$

$$C_{D,3D} = C_{D,2D} + f(\alpha)\ 2.2\left(\frac{c}{r}\right)^2 \cos^4(\theta)\left(C_D - C_{D,0}\right)$$

Where f(α) is a fading factor:

$$f(\alpha) = 1 \quad \text{for} \quad |\alpha - \alpha_0| \le 25$$
$$f(\alpha) = \frac{|\alpha - \alpha_0 - 45|}{20} \quad \text{for} \quad 25 < |\alpha - \alpha_0| \le 45$$
$$f(\alpha) = 0 \quad \text{for} \quad |\alpha - \alpha_0| > 45$$

See attached file for detailed data for each cross section.

Suzlon Energy Ltd 10 March 2017 - p1

4. Describe unsteady airfoil aerodynamics modeling (e.g. dynamic stall). *Øye dynamic stall model.*

5. Describe tip and root correction. *Tip correction is standard Prandtl-Glauert (based on lift only). There is no root correction.*

6. Describe correction for turbulent wake. *A version of the Glauert correction is used according to Wilson & Walker (see M.O.L. Hansen "Aerodynamics of Wind Turbines, eqn 6.37):*

$$C_T = 4a(1-a) \quad \text{for} \quad a \le 1/3$$
$$C_T = 4a(1-(1.25-0.75a)\,a) \quad \text{for} \quad a > 1/3$$

7. Describe tower shadow modelling. *Standard potential flow model.*

8. Describe yaw model. *Schepers skew wake model.*

9. Describe dynamic inflow model. *Model as derived in the European dynamic inflow project, with one global time constant for the wake and another dependent on radius.*

10. Is drag included in the calculation of induction. *No.*

11. Miscellaneous remarks
Added files: blade input file mexico2.bda, profile file mexico2.aer, 3D correction file 3d.cor.

2. Other information

1. Describe the wind excitation used (e.g. no turbulence, uniform flow, shear) *Uniform flow as prescribed.*

2. What time step (and corresponding azimuth angle step) has been used in the case of unsteady calculations? Δt *= 0.001 s. At 325 rpm this is 2.0 deg/s, at 425 rpm this is 2.5 deg/s. Note that the Runge_Kutta algorithm used also calculates values at half steps (0.0005 s).*

3. How many seconds have been simulated? Which result (what time instance or averaging procedure) was taken in the case of unsteady simulations? *Steady simulation: 20 s run in + 2 s (= 14 revolutions). Unsteady simulations: 20 s run in + 15 s as prescribed.*

4. What was the CPU time of the computations? *Ca. 0.7 s/s.*

5. Do the given normal and tangential force results contain the contribution of friction (CFD only)?

6. How have axial force and torque results been obtained (interpolation procedure, resolution)? *Procedure with weighing factors as prescribed.*

7. How have azimuth averaged velocities been obtained (interpolation procedure, resolution)? *Averaging over time for each blade (run in is discarded).*

Suzlon Energy Ltd 10 March 2017 - p3

Description of simulations performed with EllipSys3D at Uppsala University Campus Gotland

1. Model description

CFD

1. General description of model (RANS (turbulence model)/LES/panel code, incompressible/compressible, steady/unsteady, transition/fully turbulent etc.)

This is an LES code, the flow is considered incompressible.

2. Which components have been modeled (e.g. blades, tower, nacelle, tunnel etc.)

The rotor has been modelled, using a rotating actuator disc.

3. Origin of geometrical description

N/A (unless I do not understand the question)

4. Describe meshing (chordwise and spanwise resolution, structured/unstructured, number of cells, grid convergence study? etc.)

A structured Cartesian grid is used, inside which a local polar mesh is used to model the actuator disc.
Finest cell resolution of the grid: 1/40R
Number of cells: about 11.8 million

A grid convergence study has not been made in this case per se, but this resolution is based on previous works using this method.

5. Describe boundary conditions and domain size

Domain size:
X: 32R
Y: 32R
Z: 40R

The tunnel walls are not modelled.
Boundary conditions:
Inlet: constant value
Outlet: Convective outflow
Sides: symmetry plane

6. Describe numerical solution algorithm (scheme, order etc.)

Uses a blend of a third-order quadratic upwind interpolation for convective kinematics (QUICK) scheme (10%) and a fourth-order central differences scheme (CDS) (90%) for the convective terms. Uses a second-order CDS for the remaining

terms. Pressure correction equation based on the semi-implicit method for pressure-linked equations (SIMPLE) algorithm.

7. How was convergence of the solution assessed (simulation length, number of revolutions)?

Simulation length

8. Miscellaneous remarks
   Airfoil data values as included from "ExperimentDescriptionNewMexico.xlsx" have been used. No 3D corrections have been performed, but a tip loss model has been applied directly in the model.

2. Other information

1. Describe the wind excitation used (e.g. no turbulence, uniform flow, shear)
   No turbulence
2. What time step (and corresponding azimuth angle step) has been used in the case of unsteady calculations?

   The rotor turns at 425.1rpm*2pi/rotation*1min/60s=44.5rad/s

   V0=10m/s: time step= 4.5000e-04s corresponds to 1.15deg
   V0=15m/s: time step= 3.0000e-04s corresponds to 0.76 deg
   V0=24m/s: time step= 1.8750e-04s corresponds to 0.48 deg

3. How many seconds have been simulated? Which result (what time instance or averaging procedure) was taken in the case of unsteady simulations?
   40000 timesteps were simulated in each case
   V0=10m/s: 18s
   V0=15m/s: 12s
   V0=24m/s: 7.5s

The last fourth of the simulation was used for averaging.
   V0=10m/s: last 4.5s
   V0=15m/s: last 3s
   V0=24m/s: last 1.9s

4. What was the CPU time of the computations?
   About 20000 CPU hours for each wind speed

5. Do the given normal and tangential force results contain the contribution of friction (CFD only)?
   The rotor is modelled as an actuator disc using airfoil data.

6. How have axial force and torque results been obtained (interpolation procedure, resolution)?
   They have been determined using weighting factors (provided by Koen Boorsma) and forces normal and tangential to the local chord of the blade at 5 positions.
7. How have azimuth averaged velocities been obtained (interpolation procedure, resolution)?
   We are using the actuator disc method in the axial case, from which averaged values are readily obtained.

E.8 USTUTT Actuator Line

E.8.1 Model description

At the Institute of Aerodynamics and Gas Dynamics of the University of Stuttgart the block-structured finite volume solver FLOWer by DLR [81] has been extended by the actuator line approach (AL) as tool for wake studies, wake interaction and wind farm effects. The basic implementation of the actuator line method is aligned with literature [98, 163, 162], where the source term distribution representing the two dimensional lift and drag forces of each blade element are distributed over the surrounding grid cells using a three dimensional Gaussian smearing with a radially constant factor ϵ. The velocities are interpolated on the rotating actuator line points using an octree search algorithm and trilinear interpolation. Tait-Bryan angles are used to transform these sampled velocities into the airfoil coordinate system by taking into account the turbine kinematics of yaw, tilt, cone and the current azimuthal position of the blade. It is to be noted, that for the approximation of the angle of attack (AoA), the sampling points of the velocities do not coincide with the locations of the actuator points. Theoretically, the up- and down-wash in the center of a potential vortex is discontinuous. In reality, at least high gradients can be expected. In order to circumvent the problem that the sampled velocity might be deteriorated by the induced velocity of the bound vortex, the sampling is applied at some distance upstream of the airfoil and is then corrected iteratively by the induced velocity of the bound vortex applying Biot-Savart's law. Comparisons of AL and fully resolved turbines have been shown for different inflow conditions in [173, 174].

Regarding the present simulations in MexNext, the AL was applied to the axial flow cases. In order to save grip points, the implementation of the AL has been extended to be able to handle a rotating one-third model with periodic boundary conditions. The measured airfoil data have been used with clean conditions for $r/R \geq 0.7$. Between these polars, the lift and drag coefficients have been interpolated. At the root a cylinder is assumed. It is to be noted, that no further modifications have been applied to the airfoil data, i.e. no tip correction and no corrections for three dimensional stall effects. The computational setup includes the geometrically resolved nacelle and spans 25 meters upstream and 30 meters downstream. In radial direction it extends 25 meters. The simulations have been performed with a time step equivalent to one degree of azimuthal movement. The initial transient phase was 20 revolutions before flow data and loads were extracted for one more revolution.

E.8.2 Other information

Regarding the post processing, the calculated BEM loads are used. For the axial, radial and azimuthal traverses those are extracted from the one-third volume segment and taking into account the relative azimuthal position to the blade. To determine the azimuthally averaged velocities in the radial traverses, the provided weighting factors have been used.

F. WP3 Codes Descriptions: CFD codes

This chapter describes computational models that are used in the comparison between calculations and measurements (chapter 4).

The models described in this chapter can be categorized as Computational Fluid Dynamics (CFD) codes, for which the actual geometry of the blade surface is taken into account instead of using aerodynamic lift and drag coefficients of the airfoil sections. The descriptions as provided by the participants are included below.

F.1 CENER CFD

F.1.1 Model

WMB (Wind Multi-Block) is the CFD method developed together between CENER and the University of Liverpool and validated for HAWT [47, 49]. Two of the key aspects of this method that make it appropriate for relatively high wind speeds and complex geometries is that it is capable of solving the compressible Unsteady Reynolds Averaged Navier-Stokes (URANS) flow equations on multi-block structured grids using a cell-centered finite-volume method for spacial discretization. A second-order implicit method [157] was employed, and the resulting linear system of equations was solved using a pre-conditioned Generalised Conjugate Gradient (GCG) method.

F.1.2 Computations

The computations shown in this report were done simulating just one third of the domain (that includes the hub, nacelle and a single blade) and assuming periodicity in time and space. Menter's k-w SST turbulence model was used.

F.1.3 Mesh

The structured mesh was generated with ANSYS ICEMCFD v17 and its main characteristics are given below. Domain size is 20R towards inlet and another 20R towards outlet, having in radial direction 5R distance. This domain has a total number of cells of 83 million, having 417 cells chord-wise (plus another 37 at the trailing edge), 412 cells along the span of the blade and the first cell height of 1×10^{-5}c. Figure F.1 shows the domain and topology simulation meshes.

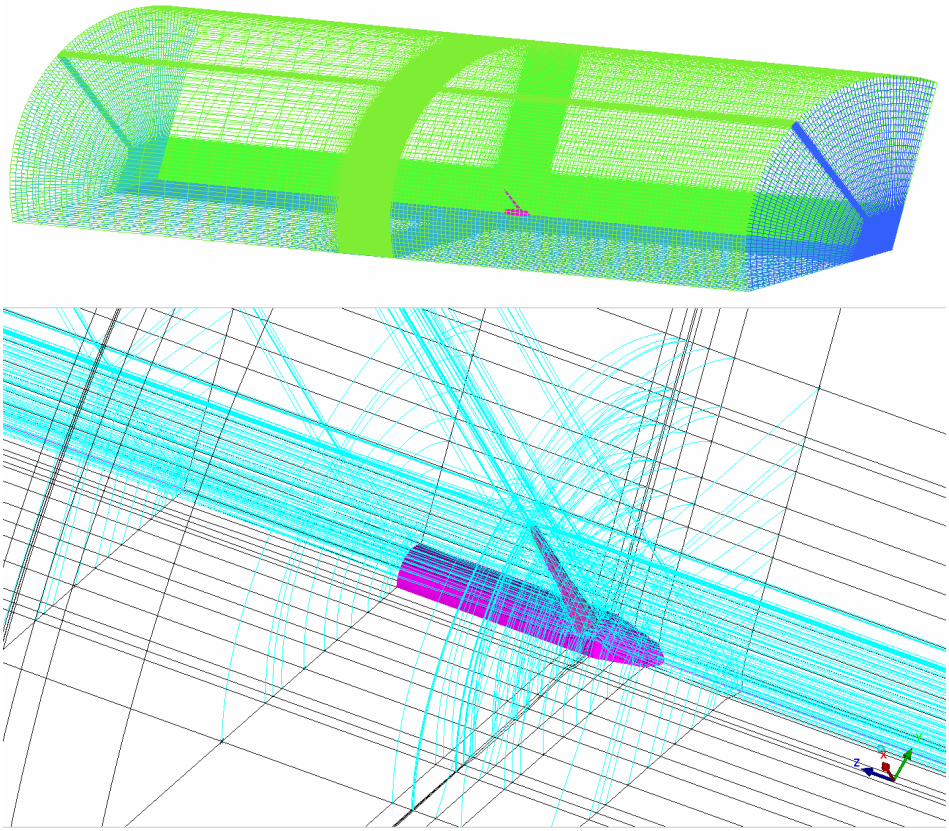

Figure F.1: Illustration of grid and domain details

F.2 DLR Tau

F.2.1 Axial flow

For the presented RANS simulations of the MEXICO rotor an isolated and rigid rotor geometry was assumed as shown in Figure F.2(a). The rotor spinner and nacelle were omitted as well. Simplified geometries of the MEXICO rotor have also been studied in the investigations by e.g. Bechmann et al. [11] or Sørensen et al. [155]. Lutz et al. [159] performed full turbine simulations with and without the tower geometry. For the present simulations the geometry of the open wind tunnel test section was neglected since its influence on the rotor was found to be small (Réthoré et al. [122]). Due to the axial symmetry of the present flow problem an overset grid consisting of a cylindrical background grid and three blade grids was used. The outer dimensions of the complete grid are shown in Figure F.2(b) in relation to the rotor diameter D. Farfield boundary conditions were set at the inflow, outflow and outer plane of the cylindrical background grid. A total of 29 million points was used to discretize the complete flow domain. To improve the flow field resolution in the region of the PIV measurements a structured grid domain was used upstream and downstream of the rotor, see Figure F.3. This structured domain had a diameter of 1.3D and a total length of 3D. Outside of the structured domain, unstructured elements were used up to the farfield. The three blade grid domains were discretized using an O-O topology with mainly hexaeder elements. The blade surface was resolved with 140 points in radial and 256 points in chordwise direction. The blunt blade trailing edge was resolved with 17 points. In wall normal direction 35 points were distributed along a distance corresponding to approximately 10% of local chord length. The grid point distance near the wall was chosen to assure a non-dimensional wall distance of $y^+<1$.

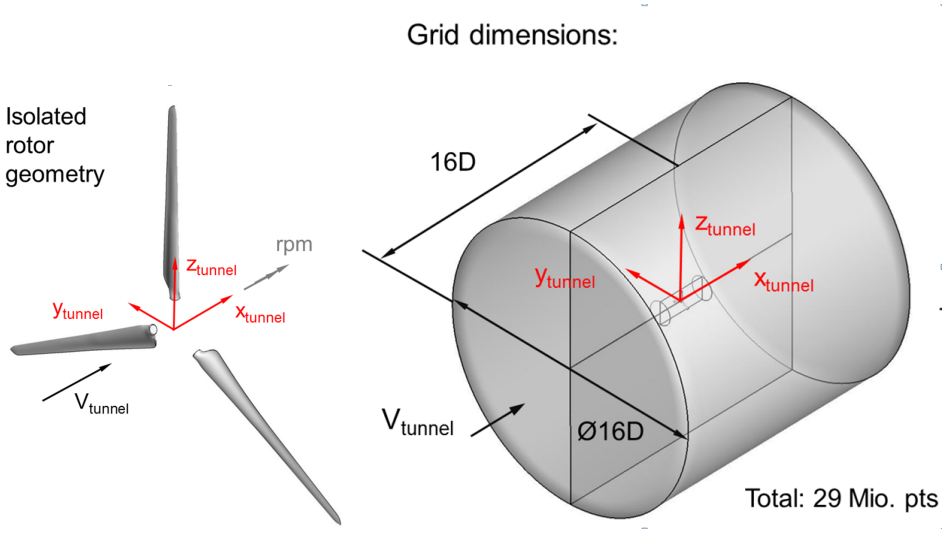

(a) Geometry of the isolated rotor

(b) Overall dimensions of the overset grid scaled relative to the rotor diameter length D=4.5m as used for the TAU-RANS simulation

Figure F.2: New MEXICO rotor simulation. The rotor axis is oriented along the x-axis of the fixed wind tunnel coordinate system (red).

For the present RANS simulation of the New MEXICO experiment the TAU-Code [140] of the German Aerospace Center (DLR) has been used. The rotor flow field was assumed to be steady for the considered test cases. A central scheme with scalar dissipation was used for spatial discretization. The implicit Backward Euler scheme was applied for relaxation. To accelerate the solution procedure a 3v multigrid algorithm was applied. The TAU rotor simulations for the three different windtunnel test cases (see Table F.1) were run as fully turbulent as well as laminar-turbulent calculations [57]. For turbulent closure the two-equation turbulence model Wilcox-kω was employed. The Menter-SST model was used in addition to the Wilcox-kω model for test case 1.3. For the laminar-turbulent calculations, an approximate method for rotor blade transition prediction [56] was used, which has been implemented in the TAU Transition module developed by Krimmelbein and Radespiel [80]. To account for the effect of experimental roughness strips the TAU Transition module allows the prediction of transition onset upstream of predefined tripping lines. This mode is used at the inner 70% of the blade radius during the present rotor simulations. At the remaining tip region, transition is predicted freely. The

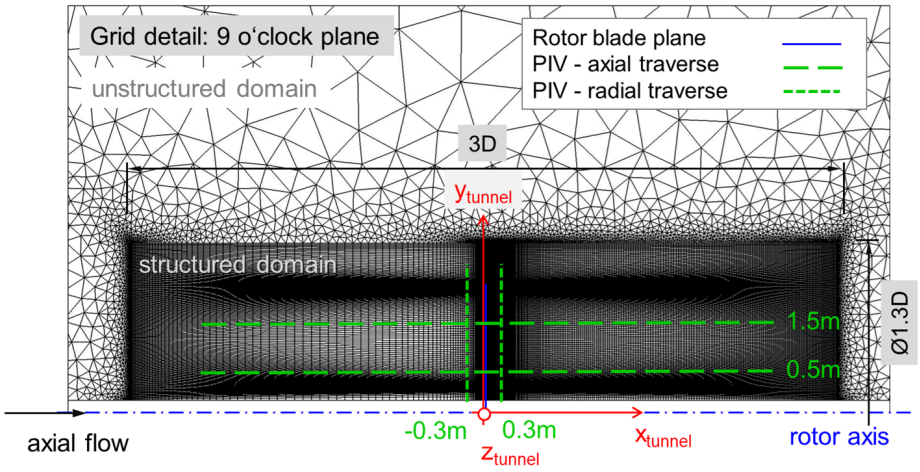

Figure F.3: New MEXICO rotor simulation. Detail of the TAU grid near the rotor plane (blue) of the isolated rotor. Note the structured domain enclosing four PIV measurement planes indicated in green for axial and radial traverses.

laminar boundary layer quantities were computed by an integral method correlated with a Pohlhausen method. Transition onset due to Tollmien-Schlichting and crossflow instabilities was accounted for using the empirical criteria AHD and C1 of Arnal et al. [7]. The prediction of laminar separation was based on the integral solution of the laminar boundary layer quantities. The turbulence level for transition prediction was set to Tu=0.4% based on the reported measurements in the DNW-LLF facility [25, 27].

Table F.1: New MEXICO rotor experiment – Wind tunnel speed and atmospheric reference conditions measured in the DNW-LLF for three axial flow cases [25, 27]

Test case	V_{tunnel} [m/s]	ρ_{ref} [kg/m3]	T_{ref} [°K]	p_{ref} [N/m2]	Rotor blade flow
1.1	10.05	1.197	293.63	101398	attached
1.2	15.06	1.191	294.91	101345	attached
1.3	24.05	1.196	294.25	101407	stalled

F.2.2 Yawed flow

The aerodynamics are computed using the DLR TAU code developed at the Institute of Aerodynamics and Flow Technology as described by Schwamborn et al [140]. The code solves the compressible, three-dimensional Reynolds-Averaged Navier-Stokes (RANS) equations using a finite volume formulation. An implicit backward Euler LUSGS algorithm is used to advance the solution in time. In order to meet the requirements of the experimental setup (of the yawed flow case), time-accurate simulations are performed using a dual time-stepping approach. While an azimuthal resolution of 1°/time-step was sufficient for the first two test cases (low and medium inflow velocity), the time-step had to be reduced to 0.05°/time-step for the last test case (high inflow velocity) in order to achieve a converged solution. For modelling the turbulence Menter's two equation k-ω SST model has been chosen as it can cope with partially detached flow. The convergence was assessed by examining the weighted density residual and by visual inspection of the gradient of the lift and drag coefficient for various arbitrarily chosen time-steps. For the spatial discretization a cell-vertex formulation with a dual-grid approach is used. For high quality results and for a better comparison between simulation and experiment hexahedral elements have been used in the blade grid and the nearfield of the background grid as can be seen in Figure F.4(a). Tetrahedral elements are used from the boundary of the nearfield to the farfield boundary in

order to keep the size of the complete grid within acceptable limits, i.e. 30 million grid points. Viscous and inviscid fluxes are computed with a central scheme. The scheme is stabilized by applying matrix dissipation which usually improves the solution over the standard scalar dissipation. The simulations are carried out fully turbulent. For simplicity only the blades of the rotor are modeled as shown in Figure F.4(b); hub, nacelle, tower and wind tunnel are omitted. The rotation of the blade grids in the stationary background grid is realized by using the chimera technique. In order to keep interference effects and mesh complexity as low as possible, the background mesh was chosen to be cylindrical. The origin is situated at the rotor center which coincides with the center of the background mesh. The diameter of the cylinder measures 16 rotor diameters and extends 8 rotor diameters from the rotor center to the upstream inflow and to the downstream outflow. The set-up is sketched in Figure F.5(a). The boundary conditions on the outer domain are set to farfield meaning a Riemann problem is solved with the prescribed inflow velocity. The geometry is based on the CAD data from the EPOS site (BladeCore-B_Airfoil_11.igs). The volume mesh around the blade is also of cylindrical shape having a diameter of approximately four chord lengths. The three blade meshes are identical hybrid meshes formed primarily of hexahedral elements but also containing a small percentage of tetrahedras, prisms and pyramids (see Figure F.5(b)). On the blade surface a no-slip condition is imposed. The boundary layer is modeled with approximately 35 layers in normal direction. In the chordwise direction the blade is made-up of 257 points on the upper and lower surface and an additional 15 points on the trailing edge. 145 points are used in spanwise direction giving a total of 2.5 million grid points for each blade mesh. The length of the simulation differs between the different cases. The relevant numbers are shown in Table F.2. The longest simulation has to be carried out for case1. The rotor force and torque need a long time to reach steady state due to the small inflow velocity. As can be seen in Table F.2 the total wall-clock time is 30 days on 240 cores resulting in 18 revolutions or 2.54s simulation time. Case2 with the medium inflow velocity still needs approximately 23 days for 1.98s simulation time while case3 needs 41 days for 0.42s of simulation time. The normal and tangential force for each radial cut has been obtained by transforming the force contribution of all chordwise surface elements from the wind tunnel to the airfoil coordinate system. The transformed loads contain only the pressure part of the force. In a second step the force contribution from all chordwise elements is integrated and smeared over the element length. In order to obtain the axial force and torque of the rotor for each azimuth the force contribution of each radial cut has been weighed with its appropriate weighing coefficient as described in the description document (Chapter C). Subsequently the axial force and torque has been integrated over one revolution to obtain the force and torque per blade. The rotor force and torque is calculated by summing up the contribution of each blade. In order to obtain the radial velocities a similar procedure has been adopted. In contrary to the azimuthal positions that have been used in the experiment, all azimuthal positions available of the CFD calculation, i.e. 360 solutions for the last revolution, have been used for interpolation.

Table F.2: Simulation and wall-clock time of the three cases

Test case	revolutions	Time [s]	cores	Wall-clock/rev [h]	Total wall-clock [h]
1	18	2.54	240	41	740
2	14	1.98	240	40	566
3	3	0.42	240	330	990

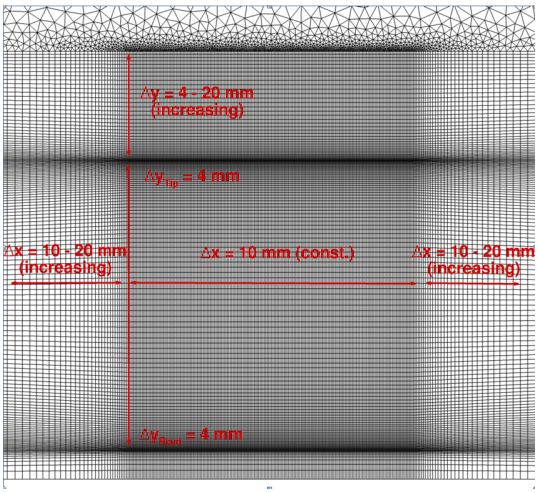

(a) Resolution of the background grid in the vicinity of the rotor

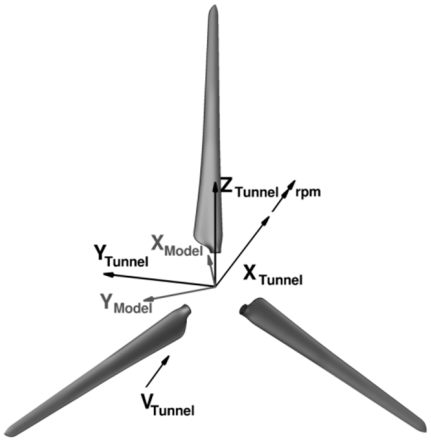

(b) Simulated components and coordinate systems

Figure F.4: Background grid resolution and coordinate system

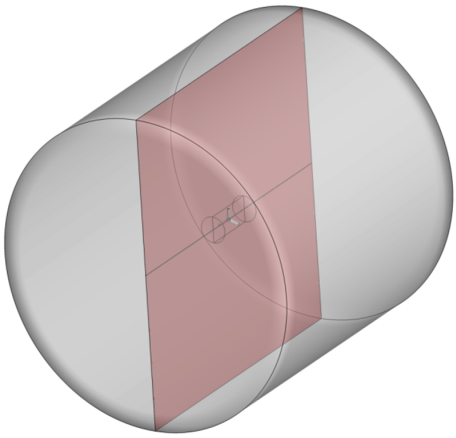

(a) Chimera set-up of background mesh and blade meshes

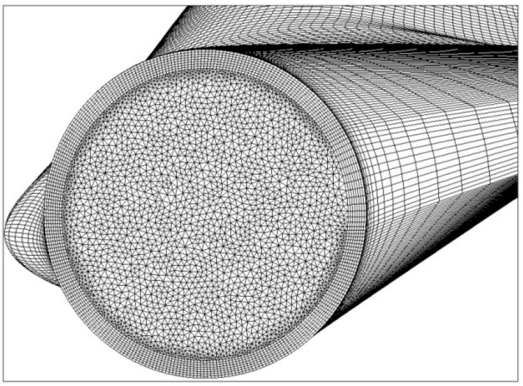

(b) Discretization of blade surface

Figure F.5: Chimera set-up and blade surface discretization

'

Risø-DTU EllipSys3D code description

Niels N. Sørensen

March 1, 2017

1 Code description

The in-house flow solver EllipSys3D is used for the present series of MexNext computations. The code is developed in co-operation between the former Department of Mechanical Engineering at the Technical University of Denmark and The Department of Wind Energy at Risø National Laboratory, see [1, 2] and [3], now both institutions are merged into DTU Wind Energy. The EllipSys3D code is a multi-block finite volume discretization of the incompressible Reynolds Averaged Navier-Stokes (RANS) equations in general curvilinear coordinates.

The code uses a collocated variable arrangement, and Rhie/Chow interpolation [4] is used to avoid odd/even pressure decoupling. As the code solves the incompressible flow equations, no equation of state exists for the pressure, the pressure correction approach is used. In the present work the pressure/velocity coupling is enforced through the Semi-Implicit Method for Pressure-Linked Equations (SIMPLE) algorithm of Patankar and Spalding [5, 6], alternativeley the Pressure Implicit with Splitting of Operators (PISO) algorithm of Issa [7, 8] is also available in the code.

For unsteady computations the solution is advanced in time using a 2nd order iterative time-stepping (or dual time-stepping) method. In each global time-step the equations are solved in an iterative manner, using under relaxation. First, the momentum equations are used as a predictor to advance the solution in time. At this point in the computation the flowfield will not fulfill the continuity equation. The rewritten continuity equation (the so-called pressure correction equation) is used as a corrector making the predicted flowfield satisfy the continuity constraint. Finally, any additional transport equations $k-$equation and $\omega-$equation in case of the $k-\omega$ model are solved. This two step procedure corresponds to a single sub-iteration, and the process is repeated until a convergent solution is obtained for the time step. When a convergent solution is obtained, the variables are updated, and we continue with the next time step. Thus, when the sub-iteration process is finished all terms are evaluated at the new time level.

For steady state computations, as used in the present work, the global time-step is set to infinity and dual time stepping is not used, this corresponds to the use of local time stepping.

The convective terms are discretized using a third order Quadratic Upstream Interpolation for Convective Kinematics (QUICK) upwind scheme, implemented using the deferred correction approach first suggested by Khosla and Rubin [9]. Central differences are used for the viscous terms, in each sub-iteration only the normal terms are

treated fully implicit, while the terms from non-orthogonality and the variable viscosity terms are treated explicitly.

In the present work the turbulence in the boundary layer is modeled by the k-ω Shear Stress Transport (SST) eddy viscosity model [10], considering both fully turbulent and transitional scenarios.Two options are available for modeling transitional flows, one is based on the $\gamma - \widetilde{Re}_\theta$ correlation based transition model of Menter [11], see Sørensen [12], while the other is based on the semi-empirical e^n model by Drela and Giles [13], see Michelsen [14]. In this first set of computiations, the flow is computed as fully turbulent, which is not equavivalent with the tripped flow in the experiment.

The code can solve both moving frame and moving mesh, in the present simulations the moving mesh option is used even for the steady state case were the special 'Steady state moving mesh algorithm' is used, see Sørensen [15].

The three momentum equations, are solved decoupled using a red/black Gauss-Seidel point solver, similar to any additional scalar transport equation. The solution of the Poisson system arising from the pressure correction equation is accelerated using a multi-grid method. In order to accelerate the overall algorithm, a multi-level grid sequence is used in the steady state computations.The EllipSys3D code is parallelized with the Message-Passing Interface (MPI) for executions on distributed memory machines, using a non-overlapping domain decomposition technique.

- Solver type: Incompressible, Reynolds Averaged Navier Stokes (RANS) solver, steady/unsteady, with full turbulent and transitional options.
- Turbulence model: k-omega SST model, combined with e^N model.
- Modeled Components: Rotor only featuring the full three bladed rotor, and a combined rotor nacelle geometry have been used.
- Geometry Origin: The grid is based on the CAD description from Technion, BladeCore-B_Airfoil_11.igs.
- Mesh setup: Several meshes has been used over time, the present version is a standard EllipSys3D setup with an O-O grid, with 256 cells in chordwise direction, 128 cells in span-wise direction, and 256 cells in normal direction, with a wall cell height of 1e-5 meter. Total number of cells 33 millions.
- Numerical Algorithm: Second order accurate QUICK scheme, second order in time.
- Convergence Steady State: For steady state simulations the criteria is that the normalized residual is reduced by five orders of magnitude from the initital value. For high wind speeds it is not always possible to reduce to reduce five order of magnitude, and in this case the results are averaged over a sustained period of iterations, typically 20000 iterations .
- Convergence of Unsteady Simulations: The unsteady simulations used 1440 time-steps per revolution and run for 50 revolutions.

- Miscellaeous: The integrated loads are based on only the five spanwise sections measured in the campaign, but not using the weight factors. For the axial cases the forces are only based on pressure while for the yaw cases the viscous contribution is included.

References

[1] J. A. Michelsen. Basis3D - a Platform for Development of Multiblock PDE Solvers. Technical Report AFM 92-05, Technical University of Denmark, Department of Fluid Mechanics, Technical University of Denmark, December 1992.

[2] J. A. Michelsen. Block structured Multigrid solution of 2D and 3D elliptic PDE's. Technical Report AFM 94-06, Technical University of Denmark, Department of Fluid Mechanics, Technical University of Denmark, May 1994.

[3] N. N. Sørensen. General Purpose Flow Solver Applied to Flow over Hills. Risø-R-827-(EN), Risø National Laboratory, Roskilde, Denmark, June 1995.

[4] C. M. Rhie. *A numerical study of the flow past an isolated airfoil with separation*. PhD thesis, Univ. of Illinois, Urbana-Champaign, 1981.

[5] S. V. Patankar and D. B. Spalding. A Calculation Prodedure for Heat, Mass and Momentum Transfer in Three-Dimensional Parabolic Flows. *Int. J. Heat Mass Transfer*, 15:1787, 1972.

[6] S. V. Patankar. *Numerical Heat Transfer and Fluid Flow*. Hemisphere Publishing Corporation, 1980. ISBN: 0891165223.

[7] R. I. Issa. Solution of the Implicitly Discretised Fluid Flow Equations by Operator-Splitting. *J. Computational Phys.*, 62:40–65, 1985.

[8] R. I. Issa, A. D. Gosman, and A. P. Watkins. The Computation of Compressible and Incompressible Recirculating Flows by a Non-iterative Implicit Scheme. *J. Computational Phys.*, 62:66–82, 1986.

[9] P. K. Khosla and S. G. Rubin. A diagonally dominant second-order accurate implicit scheme. *Computers Fluids*, 2:207–209, 1974.

[10] F. R. Menter. Zonal Two Equation k-ω Turbulence Models for Aerodynamic Flows. *AIAA paper 1993-2906*, 1993.

[11] F. R. Menter, R. B. Langtry, S. R. Likki, Y. B. Suzen, P. G. Huang, and S. Völker. A Correlation-Based Transition Model Using Local Variables, Part I - Model Formulation. In *Proceedings of ASME Turbo Expo 2004, Power for Land, Sea, and Air*, Vienna, Austria, June 14-17 2004. ASME. GT2004-53452.

[12] N. N. Sørensen. CFD modeling of laminar-turbulent transition for airfoils and rotors using the gamma - Retheta model. In *2008 European Wind Energy Conference and Exhibition*, , pages 106–112, Brussels (BE), 31 Mar - 3 Apr 2008 2008. EWEC.

[13] M. Drela and M. B. Giles . Viscous-Inviscid Analysis of Transonic and Low Reynolds Number Airfoils. *AIAA Journal*, 25(10):1347–1355, October 1987.

[14] J. A. Michelsen. *Forskning i aeroelasticitet EFP-2001*, chapter Beregning af laminar-turbulent omslag i 2D og 3D, page 73. Risø-R1349(DA). 2002. In Danish.

[15] N. N. Sørensen. Rotor computations using a 'Steady State' moving mesh. IEA Joint Action Committee on aerodynamics, Annex XI and 20, Annex XI and 20. Aero experts meeting, Pamplona, Spaine, May 2005.

F.4 EDF Saturne

F.4.1 General description of the CFD solver

The CFD solver used is Code_Saturne [6]. It is a general CFD solver developed by EDF since 1997. It is mainly dedicated to incompressible or weakly dilatable flows, based on a PISO algorithm. It enables the resolution of 2D or 3D flows, steady or unsteady, laminar or turbulent, isothermal or not. A wide variety of turbulence models are available, including $k-\varepsilon$ or $k-\omega$ SST eddy-viscosity modelling, second moment SSG modelling, Large Eddy Simulation (Smagorinsky, dynamic Smagorinsky, WALE)...

A range of specific physics can be modelled: turbomachinery flows, atmospheric flows, Lagrangian particle tracking, fire modelling, homogeneous mixture or VOF modelling, ...

The spatial resolution is finite volume with collocated arrangement on unstructured mesh. Several mesh format are supported (MED, CGNS, Ensight, ...). The solver is reliable for massively parallel applications (HPC).

The data setting is done through a *G*raphical User Interface and Code_Saturne can also be used as part of the *S*alome platform.

Code_Saturne and *S*alome are open-source and freely downloadable (`www.code-saturne.org`, `www.salome-platform.org`).

F.4.2 MEXICO CFD modelling

Geometry The geometry used comes from the CAD files delivered by Technion and IAG University of Stuttgart, available on the Mexnext website of ECN (`https://mexnext.ecn.nl`). We have considered the blade and the nacelle but not the tower. Only one blade passage is modelled. Periodicity of rotation $2\pi/3$ is assumed. The flow is modelled in a rotating frame of reference such that the rotor is *frozen* on the CFD model. The domain is cylindrical. It extends 10 m upstream the blade and 40 m downstream. The radial extension is about 3 blade radii.

Mesh The mesh has been mainly generated with the NUMECA/Autogrid software, dedicated to turbomachinery mesh. Then it has been finalized, downstream the nacelle, with the IGG software which is the general bock-structured mesh processor of NUMECA. The mesh topology is visible on Figure F.6–F.7. It is composed of 4.55 million hexaedral cells. The resolution around the blade is 161 x 85 in the chordwise and spanwise direction respectively. The cells thickness at walls is about 10^{-5} m on the blade and 10^{-4} m on the nacelle. Mesh views are given on Figure F.8–F.11.

A mesh sensitivity was performed using a second mesh of about 10 million cells with a thickness at wall of 10^{-5} m everywhere and a finer resolution in the spanwise direction (125 cells). The results were almost identical to those obtained with the first mesh of 4.55 million cells. As a result, the first mesh was kept for the study.

Boundary conditions The boundary conditions are summarized on Figure F.12. The flow is axial uniform at inlet:

$$\mathbf{u} = U_0 \mathbf{e}_z$$

where $\mathbf{e}_z$ is the rotation axis unit vector. Note that the walls are divided into two parts: the rotor part, $z < 0.20$ m, with zero *relative* velocity and the stator part, $z \geq 0.20$ m, with zero *absolute* velocity ($z = 0$ is the blade position on the rotation axis). The relative velocity **w** and the absolute velocity **u** are related by:

$$\mathbf{u} = \mathbf{w} + \boldsymbol{\Omega} \times \mathbf{x}$$

where $\boldsymbol{\Omega}$ is the rotation vector and **x** the position. Finally, it is recalled that periodicity planes are not treated as boundary faces but as internal faces thanks to halo cells [6, 2].

Turbulence modelling The turbulence model used is the RANS $k-\omega$ SST eddy-viscosity model, associated with a two-scale wall function (see [6, 2]).

Numerical method An unsteady time-stepping method is used with a first order backward Euler scheme. The convective and diffusive fluxes are centered, second order. The flow is incompressible and the velocity/pressure coupling is provided by a PISO algorithm.

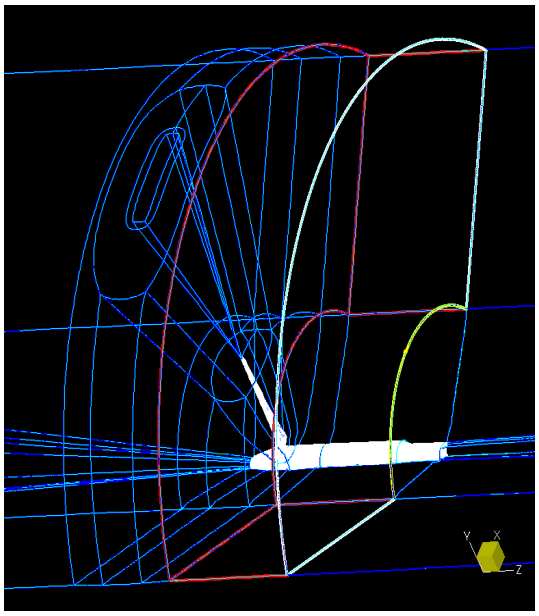

Figure F.6: Mesh topology around the rotor

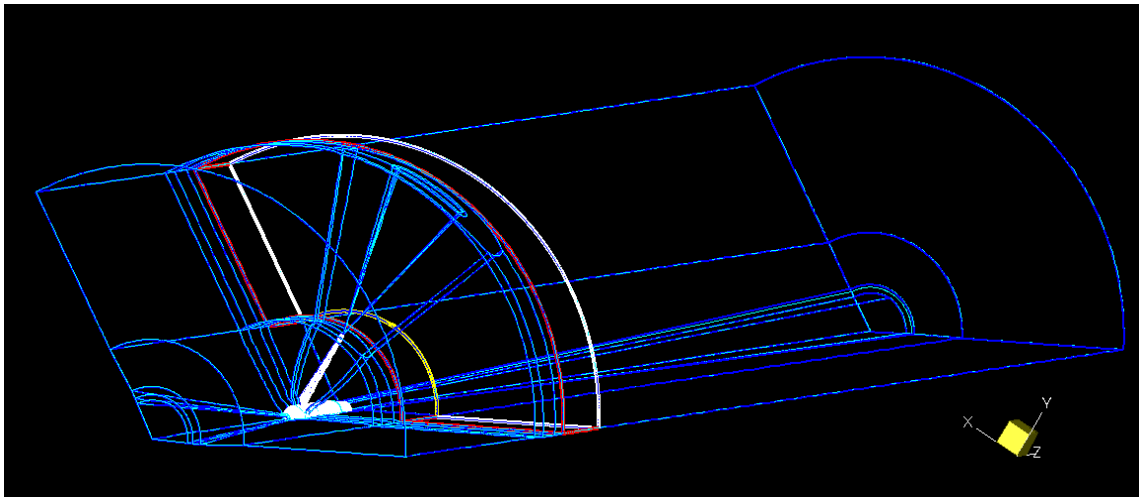

Figure F.7: Global mesh topology

Convergence/performance The calculations were started with a time step $\Delta t = 10^{-5}$ during 100,000 time steps. Then the solution was refined with a time step $\Delta t = 2 \cdot 10^{-6}$ for another 100,000 time steps. The flow evolution was monitored at several probes showing an almost steady behaviour in the regions of interest for the post-processing (see Figure F.13–F.14).

The calculations were distributed on 224 CPUs of the EDF's *Porthos* supercomputer. The total simulation time for one case (200,000 time steps) was between 80 and 90 hours.

F.4.3 Results supplied

The post-processing has followed the indications given by ECN, applied to our periodic computational domain containing one frozen blade in the 0 o'clock position. In particular, since the rotor is frozen in our CFD model, the u, v and w components of velocity in the model coordinate system correspond to the axial, radial and azimuthal components of velocity in our frozen rotor model.

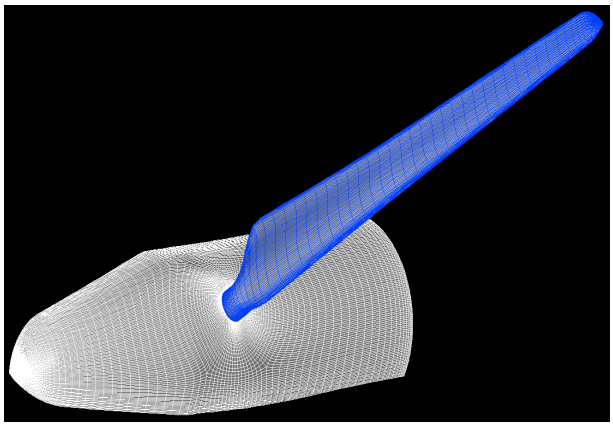

Figure F.8: Mesh: rotor view

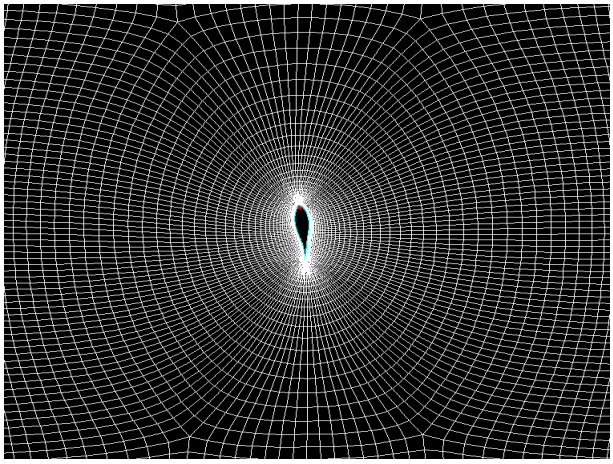

Figure F.9: Mesh: spanwise view

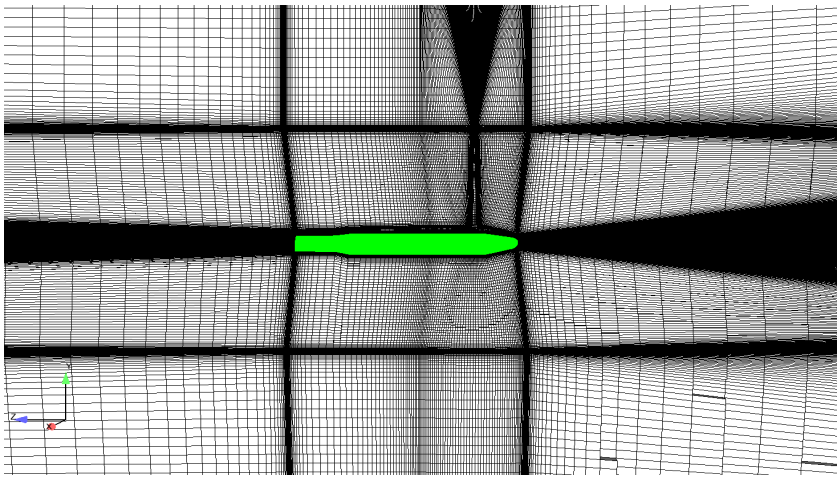

Figure F.10: Mesh: side view

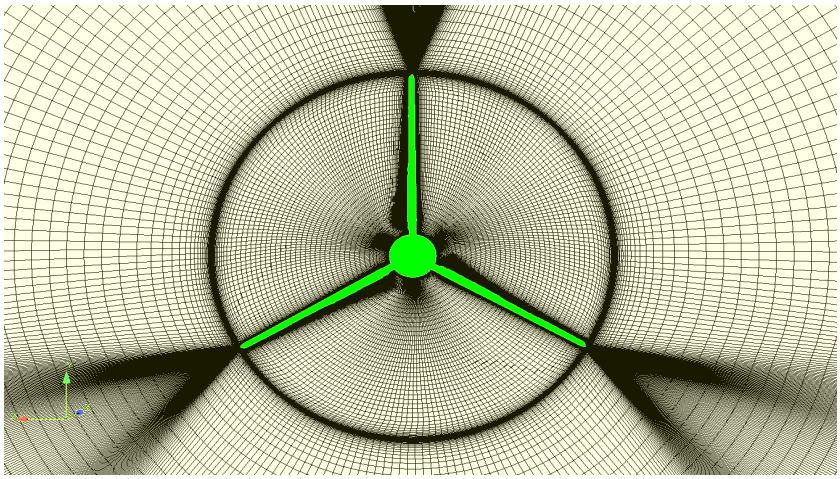

Figure F.11: Mesh: front view

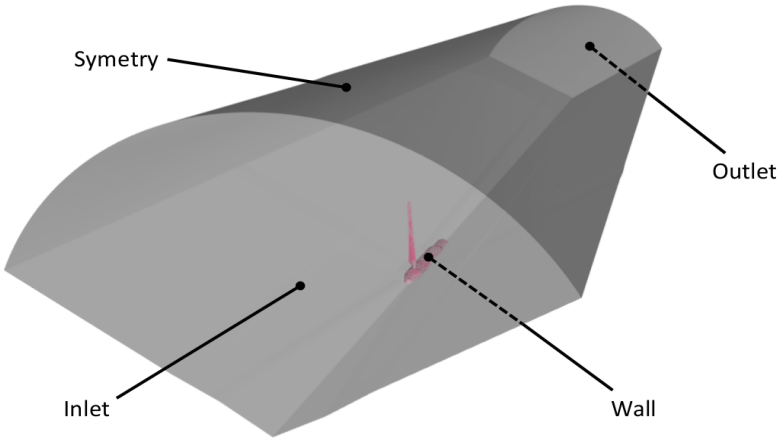

Figure F.12: Boundary conditions

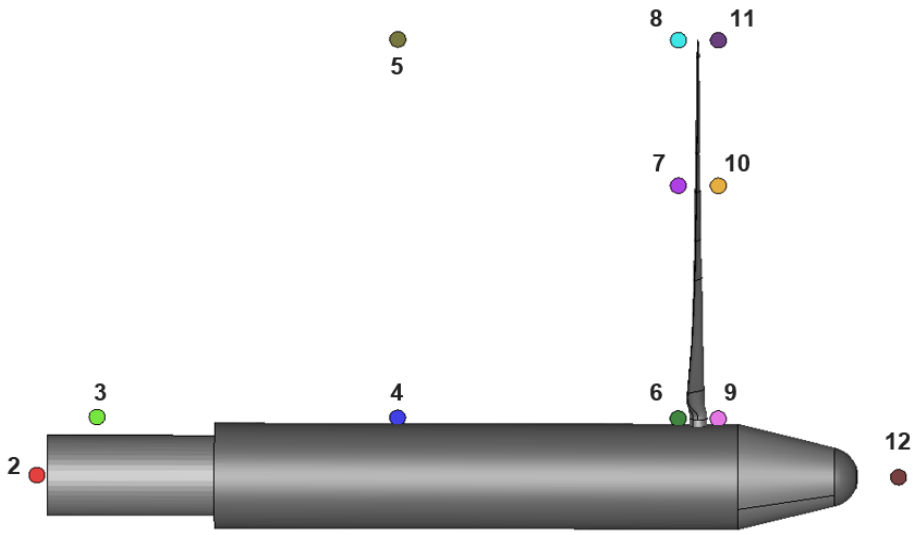

Figure F.13: Monitoring probes location

Loads The normal and tangential force are computed by integrating the *pressure stress only* on the chordwise set of blade faces having the same span. In order to define the chord of the blade at a specific span, the coordinates of the leading edge (resp. trailing edge) are defined as the coordinates of the boundary face center of maximum (resp. minimum) azimuth angle in the corresponding chordwise set (the positive azimuth direction comes from the trailing to the leading edge). Then the resulting pressure stress on a chordwise set is projected onto the chord (resp. perpendicular to the span-chord plane) to obtain the tangential (resp. normal) force. Finally, these forces [N] are divided by the radial expansion of the corresponding chordwise set in order to obtain the requested 2D forces [N/m]. 72 span locations between $r = 0.45$ and $r = 2.25$ are considered for the load profiles.

Axial force and torque are calculated by integration of the tangential and normal forces [N/m] at experimental spanwise locations (25%, 35%, 60%, 82% and 92%) with the provided weighting factors.

Pressure data The pressure profiles are built on 50 chordwise locations for each experimental spanwise location (25%, 35%, 60%, 82% and 92%).

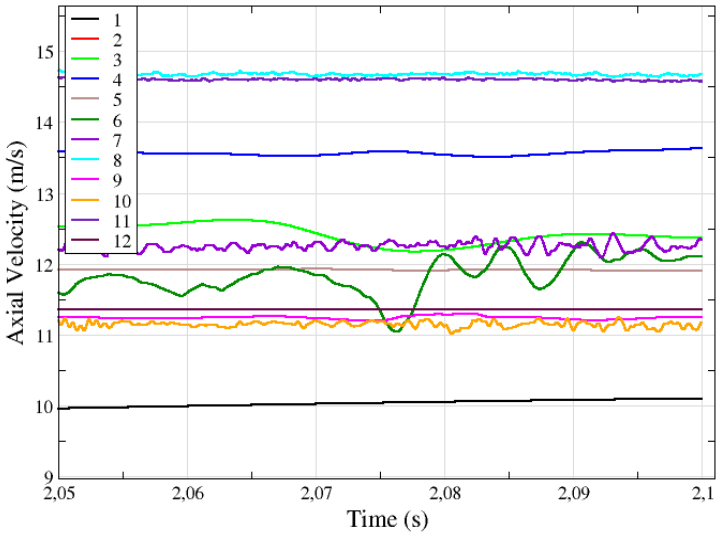

Figure F.14: Time evolution of axial velocity at monitoring probes ($U_0 = 15$ m/s)

Radial traverse For the radial traverse profiles, the upstream and downstream planes are divided into 54 radial intervals. The size of these intervals is given on table F.3.

$$\begin{aligned} 0.3 < r \leq 0.5 : &\quad \Delta r = 0.02 \\ 0.5 < r \leq 2.0 : &\quad \Delta r = 0.1 \\ 2.0 < r \leq 2.1 : &\quad \Delta r = 0.05 \\ 2.1 < r \leq 2.4 : &\quad \Delta r = 0.02 \\ 2.4 < r \leq 3.0 : &\quad \Delta r = 0.05 \end{aligned}$$

Table F.3: Radial resolution for the radial traverse curves

In one radial interval, the azimuthal averaging is performed using the experimental azimuth angles: 10/17/22/26/29/31/34/38/43/5 and the corresponding weighting factors. Note that the corresponding angles around the blade 1 in 0 o'clock position are: 10/17/22/26/29/31/34/38/43/50/-50/-30/-10.

Axial traverse For the axial traverse profiles, 200 points equally spaced between $x = -4.5$ and $x = 5.9$ are examined for each radial location, $r = 0.5$ and $r = 1.5$. Once doubloons are removed, 117 (resp. 108) points remain for the inner (resp. outer) profiles. Note that, since the experimental 9 o'clock position is out of our computational domain, the 1 o'clock position is used in place (periodicity is assumed).

Azimuth traverse In the azimuth traverse profiles, the experimental radial and azimuthal resolutions are respected. Note that, assuming periodicity, the azimuthal resolution considered was 10/17/22/26/29/31/34/38/43/50/-50/-30/-10 around the blade 1 in 0 o'clock position.

F.5 Forwind Fraunhofer IWES

F.5.1 Model description

1. General description of model (RANS (turbulence model)/LES/panel code, incompressible/compressible, steady/unsteady, transition/fully turbulent etc.)

   All provided CFD results were obtained with the open-source CFD software OpenFOAM. The simulations were performed using a Delayed Detached Eddy Simulation (DDES) model, which uses the Spalart-Allmaras turbulence model in the vicinity of the walls. Furthermore, an incompressible and fully turbulent flow was assumed. For this benchmark, only unsteady simulations were performed.

2. Which components have been modeled (e.g. blades, tower, nacelle, tunnel etc.)

   The complete wind turbine geometry including blades, tower, nacelle and hub was modeled.

3. Origin of geometrical description

   The simplified geometry as supplied by IAG University of Stuttgart.

4. Describe meshing (chordwise and spanwise resolution, structured/unstructured, number of cells, grid convergence study? etc.)

   In total 32 million cells were used to discretize the domain in space. In regions close to the blade, the mesh is fully structured (hex). The chordwise resolution was set to 273 cells, the spanwise resolution to 356 cells. The rest of domain is meshed using an unstructured grid, mainly consisting of quads and hexahedrons. Behind the rotor, several refinement regions were arranged to better resolve the tip and root vortex. To check the dependence of the solution from the grid, several meshes with different meshes were tested.

5. Describe boundary conditions and domain size

   We used a half spherical shaped domain with a radius of 100m. For the outer boundary we used an standard InletOutlet boundary condition. The boundary layer at the blade surface is resolved, therefore no wall functions were used.

6. Describe numerical solution algorithm (scheme, order etc.)

   The equations were solved using the PIMPLE algorithm which is a combination of the loop structures of SIMPLE and PISO. A second-order linearUpwind scheme was used for the discretization of the convective terms. Integration in time was performed using an implicit second order backward scheme.

7. How was convergence of the solution assessed (simulation length, number of revolutions)?

   Due to issues with our cluster only 22-revolutions could be simulated. To assess the convergence of the solution, all used local and global quantities were processed and averaged over complete revolutions. The global quantities were converged for all simulated cases with a difference below 0.25% comparing the last and the forelast revolution. The local quantities were mostly converged. For some conditions, the local quantities at the inner blade sections suffered from flow separation and didn't converge down to 0.25%. The traverses were not perfectly converged after 22 revolutions, as the wake still developed.

8. Miscellaneous remarks

F.5.2 Other information

1. Describe the wind excitation used (e.g. no turbulence, uniform flow, shear)

   Uniform flow, no turbulence, no shear.

2. What time step (and corresponding azimuth angle step) has been used in the case of unsteady calculations?

   For the first 15 rotations 0.5 degree/per iteration and the last 7 rotations with 0.25 degree/per iteration.

3. How many seconds have been simulated? Which result (what time instance or averaging procedure) was taken in the case of unsteady simulations?

   3 Seconds of physical time were simulated, and the results were averaged using a binning of 4 time steps (1 degree). The provided cp-distributions for yawed flow at different azimuthal positions, were not processed or averaged.

4. What was the CPU time of the computations?

   For all cases, 600 cores were used for 5 days of calculation on the cluster. The time needed for one rotation accounts was 5.4 hours.

5. Do the given normal and tangential force results contain the contribution of friction (CFD only)?

   The provided forces do not contain the contribution of friction.

6. How have axial force and torque results been obtained (interpolation procedure, resolution)?

   Based on the table with weighting factors which was provided in the Definition of cases.

7. How have azimuth averaged velocities been obtained (interpolation procedure, resolution)?

   Based on the table with weighting factors which was provided in the Definition of cases.

Description of CFD simulations of IFE

1. Model description

CFD

1. General description of model (RANS (turbulence model)/LES/panel code, incompressible/compressible, steady/unsteady, transition/fully turbulent etc.)
   Code : The multipurpose StarCCM+ code from CD-Adapco was used for the simulations. In the present work, an unsteady RANS (Reynolds Average Navier Stokes) approach was used for the simulations

   a. **Round1 -** RANS, incompressible, Steady, fully turbulent.
   b. **Round 2** - URANS, incompressible, unsteady, fully turbulent

   Turbulence Model: The k-ω-SST Menter SST with second order convection and Low Re damping Modification was used in the simulations. The Durbin scale limiter used as realizability option and second order convection. The realizability coefficient was 0.6.

2. Which components have been modeled (e.g. blades, tower, nacelle, tunnel etc.)
   3 blades and nacelle were simulated both in round 1 and round 2. The tower was neglected.

3. Origin of geometrical description
   0,0,0

4. Describe meshing (chordwise and spanwise resolution, structured/unstructured, number of cells, grid convergence study? etc.)
   a. **Round1**- Trimmed mesh (unstructured) with at least 180 cells chordwise, 21million cells in total, 25 cells in the boundary layer growing with a growing factor of 1.25 were used. In order to reach a y+ of ca. 1 all over the surface, the first cell in the boundary layer was placed at ca. 7×10^{-6} m. A preliminary grid dependency test was carried out on a simpler configuration (one blade, 1/3 of the domain and Steady State configuration) in order to ensure a grid independent solution in steady state conditions. Three different grids consisting respectively of ca. 2million, ca. 3millions and ca. 6 millions cells were used in the grid dependency study and torque and thrust generated by the blades in the three load cases were monitored. A difference of ca. 1% in torque and ca 2% in thrust was found between the 3millions cells mesh an the 6 millions cells.
   b. **Round 2-** A blended approach with two different meshing techniques was used for the simulations. A polyhedral mesh was used on the blade surface

and in the rotor plane region while a trimmed mesh was used in the domain. The volume region was divided in two sub-regions: a rotating region (extending from -0.3 to 0.3 m from the rotor plane in rotor coordinates where the polyhedral mesh was used) and a fixed region. A sliding mesh technique where cells at the interface are updated at each time step was used. 180 cells chordwise, 21million cells in total, 25 cells in the boundary layer growing with a growing factor of 1.25 were used. In order to reach a y+ of ca. 1 all over the surface, the first cell in the boundary layer was placed at ca. $7\times10-6$ m.

WAKE refinement (both rounds) The volume grid consisted of cubical cells with three cylindrical levels of grid refinement, progressive coarsening upstream and downstream was obtained by doubling the cell's characteristic length. The first refinement region, closer to the rotor plane, extends from -0.3m upstream to 0.3m downstream and it has a radius of 2.5m and a characteristic length of 0.02m in the rotor reference system, the second refinement region extends from -5m upstream to 7m downstream, it has a radius of 3m and it has a characteristic length of 0.4m. A progressive coarsening was used in the rest of the domain (**Error! Reference source not found.**). The numerical wind tunnel has a circular section with a radius of 10D and a length of 20D. The rotor was placed at a distance of 10D from the inlet. The final mesh consisted of ca. 20.000.000 cells where 13.000.000cells were in the rotating rotor area and the rest in the domain area.

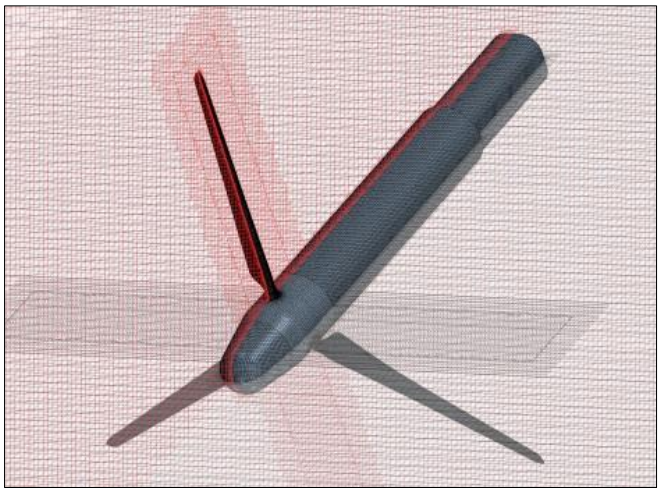

Figure 1 – Grid on the blade surface and in the wake area

5. Describe boundary conditions and domain size

A cylidrical Domain, 10D upstream, 10D downstream, 5Diameter Radius. Velocity inlet at the inlet, pressure outlet at the outlet and symmetry at the sides

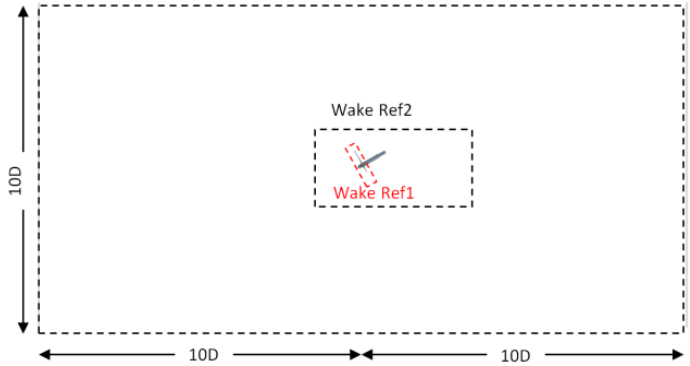

Figure 2 – Domain and wake refinement for the yawed case. The axial flow case was treated similarly

6. Describe numerical solution algorithm (scheme, order etc.)
    a. **Round1**- A coupled flow method was used in the simulations. In general, a normal initialization followed by the computation of an approximate inviscid solution to the flow problem was done by grid sequencing. The AMG Linear Solver node (The algebraic multigrid methods) was used to solve the discrete linear system of equations. An implicit second order central difference scheme with constant density was used in the simulations and the Roe FDS flux with flow boundary diffusion was activated. A Gauss Seidel relaxation scheme was used to improve robustness. A wall y+ treatment was used. A variable CFL routine was used where the CFL was checked every 5 iterations and corrections were automatically made to improve convergence.
    b. **Round2 –** Like for Round 1, an implicit second order central difference scheme with constant density was used. The Roe FDS flux with flow boundary diffusion was. A wall y+ treatment was used.

7. How was convergence of the solution assessed (simulation length, number of revolutions)?
    a. **Round 1**- Convergence was obtained by monitoring the residuals and the total torque and thrust generated by the rotor. The simulations were considered converged when the residuals dropped of three orders of magnitude and the toque and thrust had negligible fluctuations.
    b. **Round 2**- The flow was initialized with a steady state solution. One degree per time step and 10 iterations per time step resulted to be sufficient in order to ensure convergence in residuals and torque and thrust. A total number of 2 complete rotor revolutions were recorded and torque, thrust and pressure fields were averaged in time after the monitored values converged

2. Other information

1. Describe the wind excitation used (e.g. no turbulence, uniform flow, shear)
   No turbulence, uniform flow and no shear was used in the simulations.

2. What time step (and corresponding azimuth angle step) has been used in the case of unsteady calculations?
   a. 1 degree per time step

3. How many seconds have been simulated? Which result (what time instance or averaging procedure) was taken in the case of unsteady simulations?
   a. Two full rotations were recorded and averaged

4. What was the CPU time of the computations?
   a. ND

5. Do the given normal and tangential force results contain the contribution of friction (CFD only)?
   a. YES

6. How have axial force and torque results been obtained (interpolation procedure, resolution)?
   a. Axial force and torque results were obtained interpolating the 5 normal and tangential forces at the 5 stations where the pressure taps are placed.

7. How have azimuth averaged velocities been obtained (interpolation procedure, resolution)?

F.7 Onera ElSa (CFD) and PUMA (lifting line)

Mexnext: ONERA codes descriptions

1. Lifting line (Axial and tangential flow)

Numerical parameters used are based on Onera background and parametric study on case 1.1, which is the "worst" one:

- Free wake model
- Computation time step: 10 degrees
- Number of radial stations for blade definition : 45
- Number of wake revolutions kept for induced velocity computations: 25
- Number of revolution computed: 35
- Radial position of first blade section: 0.21m for axial flow and 0.45m for yaw flow
- Used provided airfoil datas without any corrections
- No dynamic stall models
- Not accounting for nacelle and tower
- Postprocessing is performed according to the instructions given in "*MexNext III: Definition of first round of calculations*", February 13th 2017 version. Except for azimuthal averages that are performed from the computed data each 10 degrees and not from the provided azimuthal positions.

2. Fully turbulent CFD computation, Axial Flow

2.1. Mesh

- Only one blade passage meshed, using periodic assumption
- Spanwise number of points: 265
- Chordwise number of points (per side): 167
- Azimuth number of points (per degree): 2.9
- Trailing edge number of points: 33
- Number of cells in the boundary layer: approximately 60
- First cell high [m]: 1E-6
- Mesh extend 5 radius in all directions
- Nacelle is taken into account
- Mast is not taken into account
- Total number of mesh points: 67 millions

2.2. Numerical method

- Steady RANS computation in relative reference frame
- Backward Euler with LU-relax decomposition
- K-ω Menter turbulent model with Zheng limiter and SST correction
- AUSMP second order spatial scheme
- Adiabatic walls using low Reynolds approach for blade and nacelle
- Non reflecting far field boundary condition on external mesh faces

- Fully turbulent computation

2.3. Computations

- Convergence criteria: periodicity of the loads (reached after 90000 iterations)
- 219 Nehalem processor
- Approximately 72 hours wall clock for the computation

2.4. PostProcessing

- Postprocessing is performed according to the instructions given in "*MexNext III: Definition of first round of calculations*", February 13th 2017 version.

3. Free transition CFD computation, Axial Flow

3.1. Mesh

- Same mesh as for the fully turbulent computation

3.2. Numerical method

- Same numerical parameters as for the fully turbulent computation
- Laminar / Turbulent boundary layer transition computation is added using criteria approach: combined AHD and Gleyzes criteria, additional criterion for cross-flow instability mode[1]
- Turbulence level prescribed to 0.5%;

3.3. Computations

- Convergence criteria: periodicity of the loads (reached after 90000 iterations)
- 219 Nehalem processor
- Approximately 75 hours wall clock for the computation

3.4. PostProcessing

- Postprocessing is performed according to the instructions given in "*MexNext III: Definition of first round of calculations*", February 13th 2017 version.

4. Fully turbulent CFD computation, Yaw flow

4.1. Mesh

- One blade passage is meshed and duplicated to have the full turbine mesh
- Spanwise number of points: 139
- Chordwise number of points (per side): 113
- Azimuth number of points (per degree): 1.6
- Trailing edge number of points: 25
- Number of cells in the boundary layer: approximately 30
- First cell high [m]: 1e-6
- Nacelle is taken into account
- Mast is not taken into account

---

[1] CLIQUET, Julien, HOUDEVILLE, Robert, et ARNAL, Daniel. Application of laminar-turbulent transition criteria in Navier-Stokes computations. AIAA journal, 2008, vol. 46, no 5, p. 1182-1190.

- Turbine mesh extends roughly 0.4m downstream, 1.0m upstream and 2.4m in radial direction. It is immersed in a background Cartesian grid of cell size 0.0165m
- Background mesh extends 6 radius in all direction, except under the wind turbine where the ground is modeled at its actual position.
- Total number of mesh points: 155 millions

4.2. Numerical method

- Unsteady RANS computation
- Time step: 0.5 degrees
- Backward Euler with LU-relax decomposition
- K-ω Menter turbulent model with Zheng limiter and SST correction
- AUSMP second order spatial scheme
- Adiabatic walls using low Reynolds approach for blade and nacelle
- Non reflecting far field boundary condition on background external faces
- Wall slip boundary condition on the lower face of the background mesh to model the ground
- Fully turbulent computation

4.3. Computations

- Convergence criteria: no evolution of axial force fluctuations between two consecutive revolutions.
- 6 revolutions computed (case 2.1 and 2.2 not yet fully converged)
- 480 Ivy Bridge processor
- Approximately 44 hours wall clock per revolution

4.4. PostProcessing

- Postprocessing is performed according to the instructions given in "*MexNext III: Definition of second round of calculations*", February 13th 2017 version.

F.8 TECHNION CFD

The results were obtained with the STARCCM+ code. The mesh is composed of two meshes: A cylindrical inner mesh built around the turbine nose and blades that rotates with the turbine blades and nose, and an outer cylindrical mesh fixed in space in time that encompasses the inner mesh. Both the inner and outer meshes are built of several structured / unstructured blocks. The mesh is built of about 14,500,000 cells: around 10,000,000 cells in the inner mesh and 4,500,000 in the outer mesh. The results for case 1.1 (U=10.05 m/s) were obtained for incompressible flow with the k-ϵ model. Results were also obtained with the k-ω/SST model. However, the calculated results with the k-ω/SST model showed somewhat less agreement with the experimental data, and are not included here. The results for case 1.2 (U=15.06 m/s) were obtained for incompressible flow with the k-ϵ model. The calculated results for this case with the k-ω/SST model were very similar to those with the k-ϵ model , but are not included here. The results for case 1.3 (U=24.05 m/s) were obtained for compressible flow with the k-ω/SST model. The calculated results for this case with the k-ϵ model were in less agreement with the experimental data and are not included here. The results for the pressure distribution on the 3 blades are somewhat different. Hence the results on each of the 3 blades are included.

F.9 USTUTT FLOWer

F.9.1 Model description

At the Institute of Aerodynamics and Gas Dynamics of the University of Stuttgart the block-structured finite volume solver of the compressible Navier-Stokes equations FLOWer by DLR [81] has been used. This code is well suited for simulation of rotary wings, since the fluxes caused by relative grid movements are taken into account. Thereby, the movements of the different components are realized with the overset grid technique [12]. Convergence is accelerated by a three-level multigrid method. For unsteady simulations, time discretization is conducted using the dual-time stepping algorithm by Jameson [64], whereas the convective fluxes are discretized by default with the central Jameson-Schmidt-Turkel (JST) scheme [66]. In order to improve conservation of vortical structures, the latter has been extended at IAG [79] by implementing the fifth-order WENO scheme in conjunction with a HLLC Riemann solver. The high order scheme was employed for the yawed cases and the 24m/s case of the axial inflow.

Turbulence is modeled using in the unsteady RANS approach using the one equation Spalart-Allmaras model (for the yawed cases and the 24m/s axial case) as well as the two equation model *k-ω-SST* (for the other axial cases). All runs were performed fully turbulent.

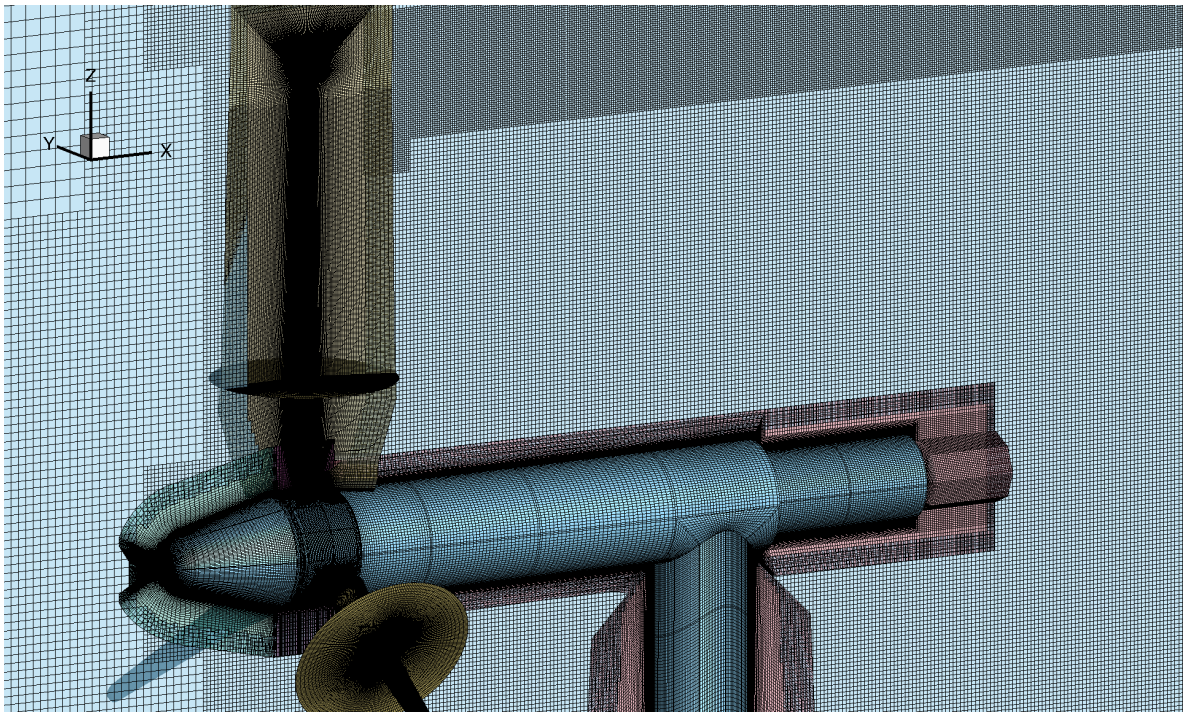

Figure F.15: Overset grid topology of the MEXICO rotor

Regarding the simulated turbine components, the blades the tower and nacelle, as well as the rotating and non-rotating part of the spinner have been taken into account (see Fig. F.15). The blades used the provided CAD geometry.

The meshing of the blades generally uses a C-O topology for the axial cases and a C-H topology for the yawed inflow. The meshes were created parametrically using the IAG tool *Automesh*, that generates meshes with boundary layer resolutions adapted to the local Reynolds number dependent, guaranteeing $y^+ = 1$. The dimension and distribution of the cells especially in span-wise direction has been adapted to the requirements of the specific case. For the 24m/s case for example the span-wise resolution has been increased in order to better resolve three dimensional vortex structures. More details on this as well as grid study are shown in [172]. In cases where the flow is attached a coarser distribution is employed in span-wise direction, particularly in the mid span region. The number of cells vary between 10 and 20 Mio. depending on the case.

The background mesh into which all components are embedded with the overset grid technique is Cartesian and locally refined to accurately capture the expected wake. Therefore, it is adapted according to the wake expansion, direction and wake length. For example the refinement is wider and longer for the turbulent wake state case compared to the low tip speed ration cases.

All other component meshes were created manually in a body conforming way with resolved boundary layers and $y^+ = 1$.

As for the grids, also the time step has been adjusted for the specific problem. For axial and attached flow the time step was set equivalent to an azimuth increment of 1°. For the yawed cases, as well as for the separated case in axial flow, the time step was reduced to 0.25° azimuth. Each time step was iterated towards a pseudo-steady state using 40 sub-iterations. Investigations on the time step can be found in [172].

The domain size spans 30 meters upstream and 30m downstream of the rotor. In lateral direction 15 meters are used in each side, whereas in vertical direction the ground is set 9 meters below the hub and the vertical top of the domain 20 meters above the hub. Except for the ground, where a slip wall was specified, the domain boundaries use far field conditions. The surfaces of the turbine components imply no-split walls.

Before data extraction, the simulations were run until a fully developed periodic wake state has been achieved and the thrust between each revolution did not vary by more than 1%.

F.9.2 Other information

Regarding the post processing surface data as well as slices in the wake were extracted every time step. The blade forces were calculated solely by pressure integration, hence without friction. To derive thrust and torque the integration is conducted in axial and circumferential direction. The line load of the blade forces is then obtained by transforming the individual thrust and torque forces into the airfoil coordinate system. In addition, for the axial inflow the forces and pressures have been time averaged over at least two revolutions.

To determine the azimuthally averaged velocities each solution that corresponds to the azimuth position of the measurements was multiplied with the corresponding weighting factor representing each azimuthal increment and then summed over the measurement period of 120°. To obtain better converged statistics the whole simulation time signal (only the when data was extracted) was subdivided in 120° packages and then phase averaged, before doing the azimuthal averaging described above.

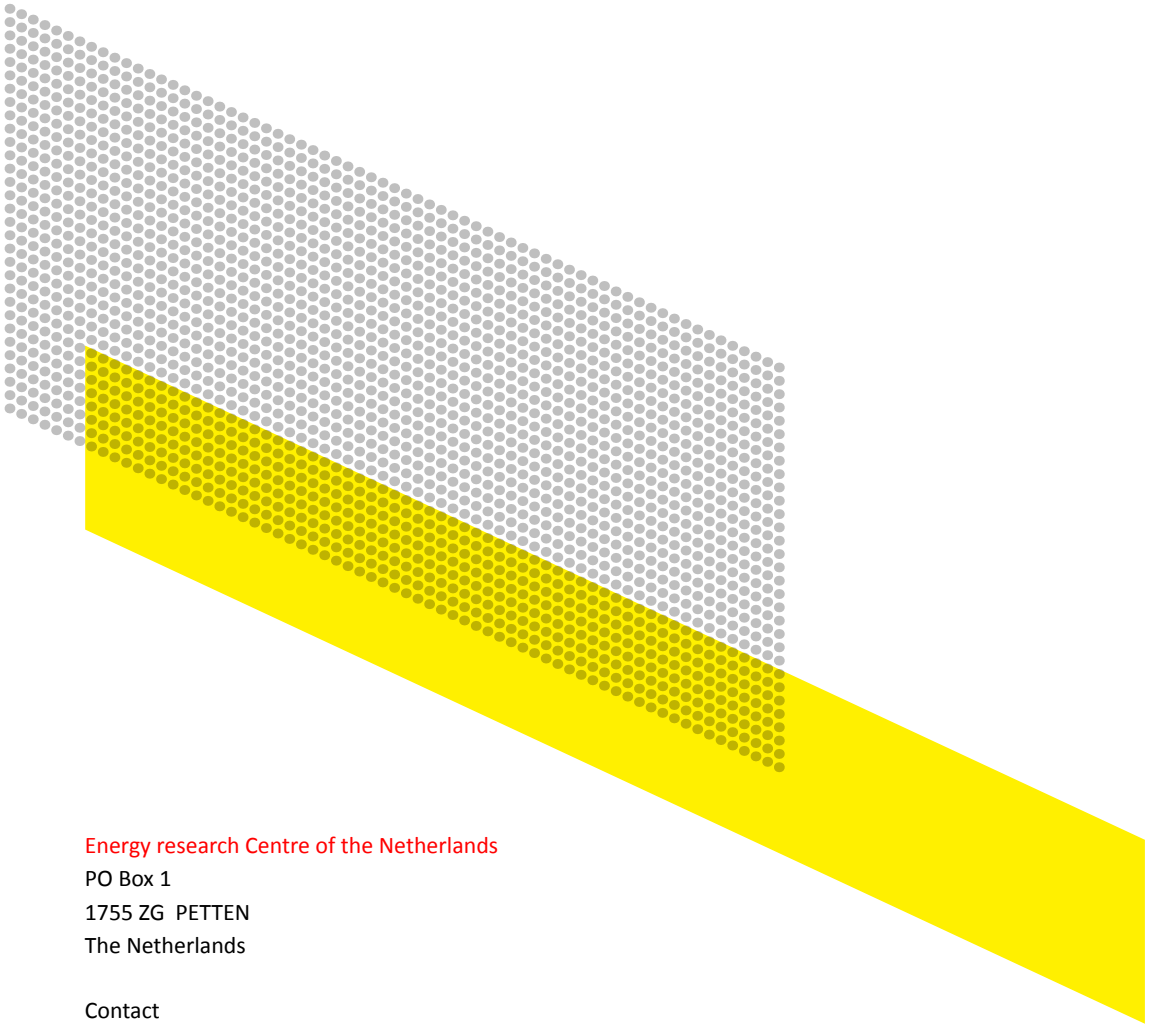

Energy research Centre of the Netherlands
PO Box 1
1755 ZG PETTEN
The Netherlands

Contact
088 515 4949
info@ecn.nl

www.ecn.nl